European Commission

JRC CONFERENCE AND WORKSHOP REPORTS

Proceedings of the 11th International Conference on NDE in Relation to Structural Integrity for Nuclear and Pressurized Components

19-21 May 2015

Jeju, KOREA

Kaisa Simola (Ed.)

2016

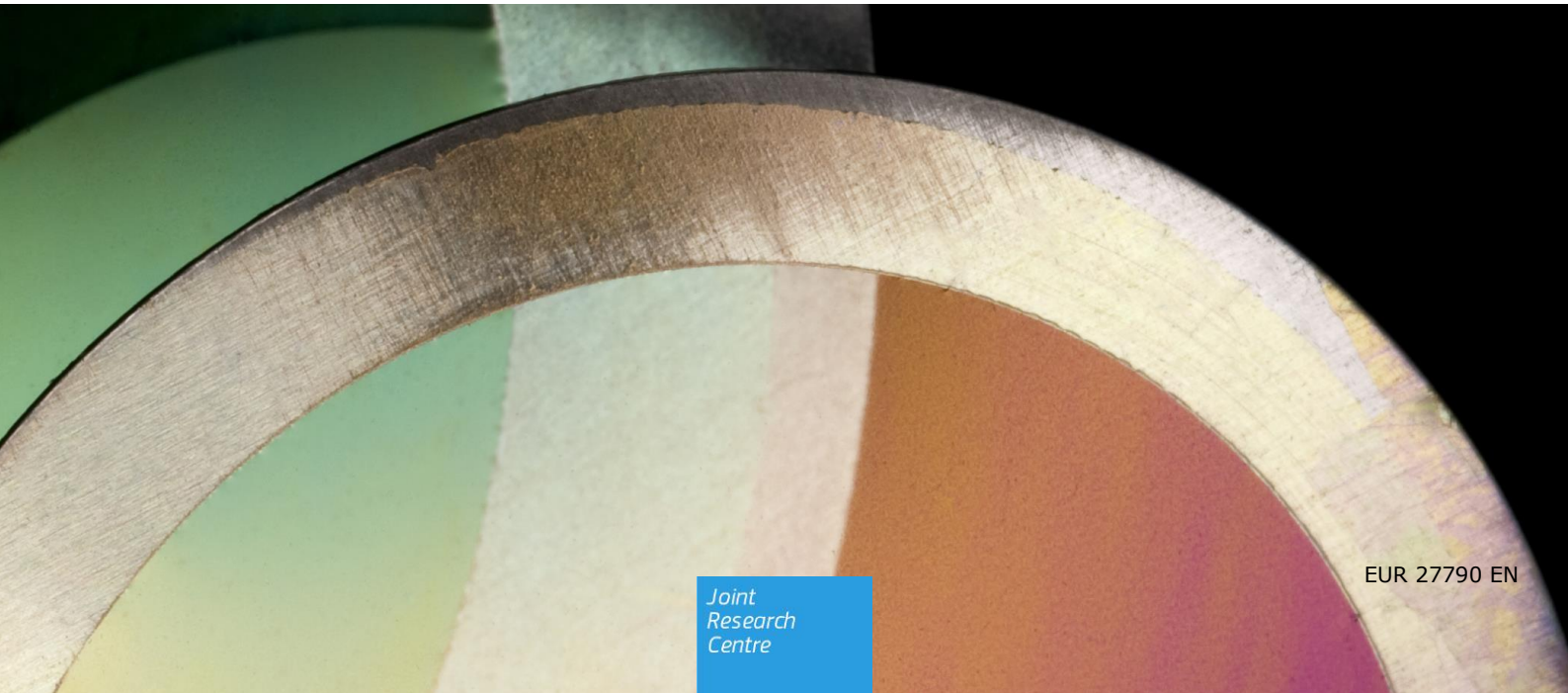

Joint Research Centre

EUR 27790 EN

Proceedings of the 11th International Conference on NDE in Relation to Structural Integrity for Nuclear and Pressurized Components

This publication is a Conference and Workshop report by the Joint Research Centre, the European Commission's in-house science service. It aims to provide evidence-based scientific support to the European policy-making process. The scientific output expressed does not imply a policy position of the European Commission. Neither the European Commission nor any person acting on behalf of the Commission is responsible for the use which might be made of this publication.

Contact information
Name: Kaisa Simola
Address: Institute for Energy and Transport, P.O. Box 2, 1755 ZG Petten, The Netherlands
E-mail: kaisa.simola@ec.europa.eu
Tel.: +31-224-565180

JRC Science Hub
https://ec.europa.eu/jrc

JRC100801

EUR 27790 EN

ISBN 978-92-79-57266-1 (PDF)

ISSN 1831-9424 (online)

doi: 10.2790/13215 (online)

Table of contents

Abstract

This Conference, the eleventh in a series on NDE in relation to structural integrity for nuclear and pressurized components, was held in Jeju Island, Korea, from 19th to 21st of May 2015. The scientific programme was co-produced by the European Commission's Joint Research Centre, Institute for Energy and Transport (EC-JRC/IET). Previous conferences were held in Amsterdam in October 1998, New Orleans in May 2000, Seville in November 2001, London in December 2004, San Diego in May 2006, Budapest in October 2007, Yokohama in May 2009, Berlin in September 2010, Seattle in May 2012, and Cannes in October 2013. All were highly successful in the quality and scope of the technical programs and the number of attendees from all countries with an interest in the structural integrity of nuclear and pressurized components.

The overall objectives of the Conference were to provide an up-to-date assessment of the development and application of NDE and to allow technical interchange between experts on an international basis. The Conference covered all aspects of this extremely important subject, with special regard to the links between structural integrity requirements and NDE performance. The development of improved NDE systems and methods was highlighted. Determination of NDE performance by development of qualification systems or performance demonstration, and experience of their use in practice was prominently featured.

1. Introduction

We are very pleased to introduce the proceedings of the Eleventh International Conference on NDE in Relation to Structural Integrity for Nuclear and Pressurized Components.

This Conference, held in Jeju Island, Korea, from 19th to 21st of May 2015, was the 11th in a series devoted to the use of NDE to demonstrate the structural integrity of nuclear and pressurized components. Previous conferences were held in Amsterdam in October 1998, New Orleans in May 2000, Seville in November 2001, London in December 2004, San Diego in May 2006, Budapest in October 2007, Yokohama in May 2009, Berlin in September 2010, Seattle in May 2012, and Cannes in October 2013. All were highly successful in the quality and scope of the technical programs and the number of attendees from all countries with an interest in the structural integrity of nuclear and pressurized components.

The overall objectives of the Conference were to provide an up-to-date assessment of the development and application of NDE and to allow technical interchange between experts on an international basis. The Conference covered all aspects of this extremely important subject, with special regard to the links between structural integrity requirements and NDE performance. The development of improved NDE systems and methods was highlighted. Determination of NDE performance by development of qualification systems or performance demonstration, and experience of their use in practice was prominently featured.

Country	Participants
Austria	1
Canada	5
China	7
Croatia	2
Czech	1
Denmark	1
Finland	5
France	22
Germany	3
Hungary	1
Japan	20
Korea	76
Singapore	1
Spain	1
Sweden	8
Switzerland	3
UK	6
USA	11
Vietnam	1
Total	**175**

In the event, the Conference was highly successful. The 111 presentations maintained the high promise suggested by the written abstracts and the programme was chaired in a professional and efficient way by the session chairmen who were selected for their international standing in the subject. The number of delegates, 175 representing 19 countries showed the high level of international interest in the subject. We want to express our thanks to all chairmen – without their support, the conference could not have been the success that it was. We also acknowledge the authors themselves, without whose expert input there would have been no conference.

Finally, our thanks are due to Prof. Sung-Jin Song, Prof. Hak-Joon Kim, and our fellow members of the Local Organising Committee for excellent arrangements for the conference, making a great contribution to its success. The conference was co-ordinated jointly by Safety and Structural Integrity Research Center at Sungkyunkwan University (SAFE/SKKU), Korea Institute of Nuclear Safety (KINS), Korea Atomic Energy Research Institute (KAERI) and Korea Research Institute of Standards and Science (KRISS).

These Proceedings provide the permanent record of what was presented. They indicate the state of development at the time of writing of all aspects of this important topic and will be invaluable to all workers in the field for that reason. The proceedings were prepared by the European Commission Joint Research Centre, whose support to the conference is acknowledged.

We are looking forward to a continuous success of this conference series, and meeting all NDE experts at the 12th ICNDE to be held in Dubrovnik, Croatia, 4-6 October 2016.

G. Selby, T. Takagi and K. Simola

2. Organising Committees

International Organising Committee

Prof. Takagi Toshiyuki
Tohoku University
Institute of Fluid Science, Katahira 2-1-1, Aoba-ku, Sendai 980-8577
JAPAN
takagi@ifs.tohoku.ac.jp

Mr. Greg Selby
Electric Power Research Institute
1300 West W. T. Harris Boulevard
Charlotte, NC 28262
USA
gselby@epri.com

Dr. Kaisa Simola
European Commission
DG JRC, Institute for Energy and Transport (IET)
P.O. Box 2, 1755 ZG Petten
THE NETHERLANDS
kaisa.simola@ec.europa.eu

Local Programme Committee

Prof. Sung-Jin Song
Safety and Structural Integrity Research Center (SAFE) /
Sungkyunkwan University (SKKU)
School of Mechanical Eng. 23340, 2066, Seobu-ro, Jangan-gu, Suwon
KOREA
sjsong@skku.edu

Dr. Sung-Sik Kang
Korea Institute of Nuclear Safety (KINS)
62 Gwahak-ro, Yuseong-gu, Daejeon 305-338
KOREA
sskang@kins.re.kr

Dr. Yong-Moo Cheong
Korea Atomic Energy Research Institute (KAERI)
111, Daedeok-Daero 989Beon-Gil, Yuseong-gu, Daejeon
KOREA
ymcheong@kaeri.re.kr

Dr. Dong-Jin Yoon
Korea Research Institute of Standards and Science (KRISS)
267 Gajeong-ro, Yuseong-gu, Daejeon 305-340
KOREA
djyoon@kriss.re.kr

Secretary

Prof. Hak-Joon Kim
Sungkyunkwan University (SKKU)
1st Research Complex Building. 81507, 2066, Seobu-ro, Jangan-gu, Suwon
KOREA
hjkim21c@skku.edu

3. Technical Programme

Day1 (Tuesday, 19 May)

Time	Plenary Session
09:15	Opening
09:30	NDE Research Issues Focus for Integrity of NPPs in Korea *Sung-Jin Song, Sungkyunkwan University, Korea*
10:00	Deep Learning in the Future of NDE *G.Selby, EPRI Charlotte Office, USA*
10:30	Break
10:50	Activities and Future Trends of the ENIQ Network *Etienne Martin, EDF Generation Nuclear Engineering Division, France* *Oliver Martin, European Commission, Joint Research Centre, Institute for Energy and Transport, Netherlands* *Tommy Zetterwall, Swedish Qualification Centre (SQC), Sweden* *Anders Lejon, Vattenfall, Ringhals NPP, Sweden* *Samuel Perez, Iberdrola, Madrid, Spain*
11:20	Fukushima Daiichi Muon Imaging *Haruo Miyadera, Toshiba Corporation Power Systems Company, Japan*
11:50	Lunch

Time	Session A InspectionQualification Ⅰ	Session B Pipe inspection Ⅰ	Session C Reactor Pressurized Vessel
	Co-chairpersons: Tommy Zettervall Keiji Watanabe	Co-chairperson: Kyung-Cho Kim Ari Koskinen	Co-chairperson: Yong-Sang Cho Jason Van Velsor
	TUE.1.A	TUE.1.B	TUE.1.C
01:20	*TUE.1.A.1* Development of a Comprehensive Risk-informed Categorization Process for CANDU Conventional Systems and Components Mehdi Rezaie-Manesh, Ontario Power Generation, Canada; Paul Lafreniere, CANDU Owners Group, Canada; Patrick O'Regan, Electric Power Research Institute, USA; Scott Chesworth, Structural Integrity Associates, Inc., USA	*TUE.1.B.1* Development of Ultrasonic Techniques for the Examination of ITER VV T-joint Welds P.I. Resa, F. Fernández, C.M. Pérez, R. Martínez-Oña, Tecnatom Group, Spain; P. Vessio, Ansaldo, Italy; A. Dans, A. Bayón, Fusion for Energy, Spain	*TUE.1.C.1* Human Errors of Reactor Pressure Vessel Examinations in Korean Nuclear Plants Euisoon Doh, Chang-Hun Lee, Jae-Yoon Kim, Wi-Hyun Kim, Plant Service & Engineering, Korea Electric Power Corporation, Korea
01:40	*TUE.1.A.2* Inspection Qualification of a FMC/TFM Based UT System R.L. ten Grotenhuis, Y.Verma, A.Hong, Ontario Power Generation, Canada; N.Saeed, Toronto University, Canada; E.Schumacher, EXTENDE Inc, USA; S.Bannouf, EXTENDE S.A., France; M.Hetmanczuk, McMaster University, Canada	*TUE.1.B.2* The Study on Defect Quantified Program of the Inside Wall Thinning Pipe Using Infrared Thermography KooAhn Kwon, Man-Yong Choi, Jung-Hak Park, Won-Jae Choi, Korea Research Institute of Standards and Science; Hee-Sang Park, Korea Research Institute of Smart Material and Structures System Association; Won-Tae Kim, Kongju National University, Korea	*TUE.1.C.2* Understanding of Sub-cooled Nucleate Boiling on the Nuclear Fuel Cladding Surface Using Acoustic Emission Energy Parameter Kaige Wu, Seung-Heon Baek, Hee-Sang Shim, Do Haeng Hur, Deok Hyun Lee, Korea Atomic Energy Research Institute, Korea

02:00	*TUE.1.A.3* The EPR's NDE program: a technical and industrial challenge Pascal Blin, EDF Nuclear Engineering Division, France	*TUE.1.B.3* Conceptual Optimization of Sample Size for POD Determination for Cast Austenitic Stainless Steel Components Owen Malinowski, Jason Van Velsor, Timothy Griesbach, David Harris, Nat Cofie, Structural Integrity Associates, Inc., USA	*TUE.1.C.3* Implementation of Special PA UT Techniques for Manufacturing Inspection of Welds in Thick Wall Components Dirk Verspeelt, Dominic Marois, Guy Maes, Zetec, Canada; Jean Marc Crauland, Michel Jambon, Frédéric Lasserre, AREVA Nuclear Power, France
02:20	*TUE.1.A.4* Consideration of Operators in the Qualifications of Non Destructive Testing Systems P. Jardet, V. Didier, P. Huet, EDF Qualification Body, France	*TUE.1.B.4* Influence of the dimensions of an elbow on defect sensitivity of guided wave testing at elbow part ToshihiroYamamoto, Takashi Furukawa, Japan Power Engineering and Inspection Corporation, Japan; Hideo Nishino, Tokushima University, Japan	*TUE.1.C.4* Energy Contour Map Based Acoustic Emission Source Location for Pressurized Vessel Byeong-Hee Han, Chungnam National University; Il-Sik Kim, Korea University of Science and Technology; Choon-Su Park, Dong-Jin Yoon, Korea Research Institute of Standards and Science, Korea
02:40	*TUE.1.A.5* Modeling-Assisted Justification of the Ultrasonic Inspection of a Clad Repair in NI-Based Alloy Lhuillier Pierre-Emile, Chassignole Bertrand, EDF R&D, MMC Department, France; Gelebart Yann, Deydier Sébastien, EDF CEIDRE, France	*TUE.1.B.5* Guided Wave Signals for a Monitoring of Buried Pipe Mockup by a Magnetostrictive Sensor Method Yong-Moo Cheong, Duck-Hyun Lee, Korea Atomic Energy Research Institute, Korea	*TUE.1.C.5* Defect Sizing using Ultrasonic Phased Array Techniques and SAFT A. Erhard, Th. Heckel, R. Boehm, J. Kitze, Bundesanstalt für Materialforschung und –prüfung, Germany
3:00	Break		

Time	Session A Inspection Qualification Ⅱ/ Steam Generator Primary Ⅰ	Session B Pipe Inspection Ⅱ	Session C Modeling Ⅰ
	Co-chairperson: Patrice Jardet Ki-bok Kim	Co-Chairpersons: Satoshi Okada Sung-sik Kang	Co-Chairpersons: Seung-Hyun Cho Erhard Anton
	TUE.2.A	TUE.2.B	TUE.2.C
03:20	TUE.2.A.1 Qualification pursuant to EPRI PDI methodology of Phased Array UT techniques for the inspection of PWR reactor vessels using advanced robot equipment José R. Gadea, Francisco Fernández, Pablo González, Pedro Gómez, Tecnatom, Spain	TUE.2.B.1 Evaluation of Thinning Pipe Wall Having Complicated Surface by EMAR Tetsuya Uchimoto, Toshiyuki Takagi, Ryoichi Urayama, Shoichiroh Hara, Tohoku University, Japan; Kazuhiro Tanji, Tohoku Electric Power Co., Inc., Japan	TUE.2.C.1 Model Based Simulation of Liquid Level Measurement using Ultrasonic Lamb Wave Ziqiao Tang, Maodan Yuan, Hak-Joon Kim, Sung-Jin Song, Sungkyunkwan University, Korea
03:40	TUE.2.A.2 Assessment of Reliability of NDE for CSS and DMW Components Lili Ducousso-Ganjehi, Damien Gasteau, Fréderic Jenson, CEA, LIST, France; Gérard Cattiaux, Thierry Sollier, Institut de Radioprotection et de Sûreté Nucléaire, France	TUE.2.B.2 Detection of Incipient SCC Damage in Primary Loop Piping Using Acoustic Emission & Fiber Optic Strain Gages Benjamin K. Jackson, Jonnathan L. W. Warwick, Intertek AIM, USA; James J.Wall, Electric Power Research Institute, USA	TUE.2.C.2 Evaluations of Various Scan-Images with Ultrasonic NDE Simulator Yasushi Ikegami, Yukihiro Sakai, ITOCHU Techno-Solutions Corporation, Japan

04:00	*TUE.2.A.3* Safety Improvements and Burden Reductions Using a Streamlined, Risk-informed, Approach to Inspection Program Development James Agold, Southern Nuclear Company, USA; Kimberly Herman, Dominoin Generation, USA; Patrick O'Regan, Electric Power Research Institute, USA	TUE.2.B.3 An Innovative Steam Generator Dissimilar Metal Weld Inspection System Using Phased Array Ultrasonic and Eddy Current Techniques Steven J. Todd, Ramon Villagomez, and Carlos M. Barrera, IHI Southwest Technologies, Inc., USA	TUE.2.C.3 Validation of an EMAT Code based on a Two-Dimensional FEM Coupled Electromechanical Formulation D. Garcia-Rodriguez, O. Mihalache, T. Japan Atomic Energy Agency, Japan; T. Yamamoto, W. Cheng, Japan Power Engineering and Inspection Corporation, Japan
04:20	*TUE.2.A.4* Assessing Reliability of Remote Visual Testing – Status of Round Robin Exercise John Lindberg, Jeff Landrum, Chris Joffe, Electric Power Research Institute, USA; Pradeep Ramuhalli, Michael Anderson, Aaron Diaz, Pacific Northwest National Laboratory, USA	TUE.2.B.4 Comparison of Conventional and Phased Array TRL Ultrasonic Testing for Case Austenite Stainless Steel in Nuclear Power Plant Byungsik Yoon, Yongsik Kim, Chanhee Cho, KHNP Central Research Institute, Korea	TUE.2.C.4 Conventional X-Ray Radiography versus Image Plates : A Simulation and Experimental Performance Comparison David Tisseur, B. Rattoni, CEA, LIST, France; G. Cattiaux, T. Sollier, Institut de Radioprotection et de Sûreté Nucléaire, France
04:40	TUE.2.A.5 Separator Reheater Tubes: 38 Years of Experience In Non Destructive Examination Mathieu Lheureux, Vallourec Heat Exchanger Tubes, France	TUE.2.B.5 On-line Monitoring of Pipe Wall Thinning for Flow Accelerated Corrosion in a Piping at High Temperature Yong-Moo Cheong, Dong-Jin Kim, Duck-Hyun Lee, Korea Atomic Energy Research Institute, Korea	TUE.2.C.5 Simulation Based Design of Eddy Current Sensor for Thickness Change Measurement of Multi-Layer Seul-Gi Lee, Hak-Joon Kim, Sung-Jin Song, Chang-Sung Seok, Sungkyunkwan University, Korea

05:00		TUE.2.B.6 Sizing of Pipe Wall Thinning using Pulsed Eddy Current Signals Shejuan Xie, Zhenmao Chen, Xi'an Jiaotong University, China; Toshiyuki Takagi, Tetsuya Uchimoto, Tohoku University, Japan	

Day2 (Wednesday, 20 May)

Time	**Session A** **Inspection Qualification Ⅲ** **- Performance Demonstration**	**Session B** **Pipe Inspection Ⅲ** **- Nozzle / Complex**	**Session C** **Advanced Technologies Ⅰ**
	Co-Chairperson: Greg Selby Jin-yi Lee	Co-Chairperson: Hitoshi Ishida Yong-Moo Cheong	Co-Chairperson: Frédéric Lasserre Martin Bolander
	WED.1.A	WED.1.B	WED.1.C
09:00	*WED.1.A.1* Technical Support Developing Performance Demonstration Programs in Japan P. Ashwin, C. Latiolais, L. Esp, R.Grizzi, J. Langevin, Electric Power Research Institute, USA	*WED.1.B.1* Austenitic Weld Inspection for Long-Term Fuel Storage Canisters A. Brockett, J. M. Dagen, R. Hague, Doosan Babcock Ltd, Scotland	*WED.1.C.1* Development of the improved PECT system to evaluate thermal degradation of thermal barrier coatings Zhang Jianhai, Hak-Joon Kim, Sung-Jin Song, Chang-Sung Seok, Sungkyunkwan University, Korea; Koo-Kab Chung, Korea Institute of Nuclear Safety, Korea

09:20	*WED.1.A.2* The Progressive Statistical Analysis Results of Performance Demonstration for Piping Welds Hung-Fa Shyu, Institute of Nuclear Energy Research, Taiwan ROC	*WED.1.B.2* Ultrasonic Phased Array Technique for Check Valve Evaluation in Comparison with Magnetic Flux and Acoustic Method H. Calás, B. de la Fuente, V. Barcenilla, R. Martínez-Oña, F. Fernández, Tecnatom Group, Spain	*WED.1.C.2* Effects of Metallic Diaphragm on Sensitivity Characteristics of Optical Ultrasonic Sensor for Under-Sodium Inspection Koichi Saruta, Toshihiko Yamaguchi, Masashi Ueda, Japan Atomic Energy Agency, Japan
09:40	*WED.1.A.3* Current Status of Japanese Performance Demonstration in FY 2014 Keiji Watanabe, Hajime Shohji, Koichiro Hide, Joji Ohta, PD center, Central Research Institute of Electric Power Industry, Japan	*WED.1.B.3* Detection of Artificial Defects at Storage Vessels for Liquefied Hydrogen by Ultrasonic Guided Wave Mu-Kyung Seo, Hak-Joon Kim, Sung-Jin Song, Sungkyunkwan University; Ki-Bok Kim, Korea Research Institute of Science and Standards; Geonwoo Kim, University of Science& Technology; Chi-Hwan Oh, Daum Energy Co,,Ltd; Minsu Park, KEPCO plant service & Engineering Co.,Ltd; YongSang Cho, Korea Electric Power Corporation Research Institute, Korea	*WED.1.C.3* Liquid Sodium Test Results of an 8 Element Phased Array EMAT Probe for Nuclear Applications Florian Le Bourdais, Thierry Le Pollès, CEA, LIST, France

10:00	*WED.1.A.4* Development of Virtual Ultrasonic Testing System Hajime Shohji, Koichiro Hide, Central Research Institute of Electric Power Industry, Japan.	*WED.1.B.4* Development of Sizing Techniques of SCC Height in Dissimilar Metal Welds of Vessel Nozzle Safe-End by means of Phased Array TOFD Technique with Asymmetrical Ultrasonic Beams and Multi-Angle Synthesis Technique K. Endoh, J. Kitasaka, Non-Destructive Inspection Co., Ltd., Japan; H. Ishida, Institute of Nuclear Safety System, Inc., Japan	*WED.1.C.4* Open Phased Array Ultrasonic Instrument for Advanced Applications and Full-Matrix Capture Gavin Dao, Advanced OEM Solutions, USA; Dominique Braconnier, The Phased Array Company, USA
10:20	**Break**		

Time	**Session A** **Steam Generator Primary Ⅱ**	**Session B** **Emerging Techniques Ⅰ**	**Session C** **Modeling Ⅱ**
	Co-Chairperson: Kwang-Hee Im Sung-Sik Kang	Co-Chairperson: Dong-Jin Yoon Koichi Saruta	Co-Chairperson: Ovidu Mihalache Yong-Sang Cho
	WED.2.A	WED.2.B	WED.2.C
10:40	*WED.2.A.1* High Performance Equipment for the Steam Generator Tubes Inspections Hervé Gac, Rock Samson, SG NDT Sarl, France	*WED.2.B.1* Effect of Vibration Reflection on Vibrothermography Wonjae Choi, Manyong Choi, Jeounghak Park, Korea Research Institute of Standards and Science, Korea	*WED.2.C.1* Computation of Inspection Parameters on Complex Component using CIVA Simulation Tools Arnaud Vanhoye, Séverine Paillard, Stephane Leberre, Commissariat à l'Energie Atomique, France

11:00	*WED.2.A.2* Effect of NDE Signal Variation by Chemical Cleaning on the Steam Generator Tube Integrity for Axial Cracks Yong-Seok Kang, KHNP Central Research Institute, Korea; In Chul Kim, Jai-Hak Park, Chungbuk National University, Korea	*WED.2.B.2* Comparison of PZT and PMN-PT Based Sensors for Detection of Partial Discharge at Electric Transformer Geonwoo Kim, Namkyoung Choi, University of Science & Technology; Mu-Kyung Seo, Sungkyunkwan University; Ki-Bok Kim, Korea Research Institute of Science and Standards; Jae-Ki Jeong, Hong-Sung Kim, Hanbit EDS. Co., Ltd.,; Minsu Park, KEPCO Plant Service & Engineering Co. Ltd., Korea	*WED.2.C.2* Numerical Study of Ultrasonic Nonlinearity Parameter in Solids with Rough Surfaces Maodan Yuan, Jianhai Zhang, Hak-Joon Kim, Sung-Jin Song, Sungkyunkwan University, Korea
11:20	*WED.2.A.3* Advanced Inspection Technique for Tube Seal Welds of Steam Generators H. Yonemura, N. Kawai, M. Morikawa, H. Murakami, T. Hanaoka, T. Tsuruta, K. Kawata, M. Kurokawa, Mitsubishi Heavy Industries, Japan	*WED.2.B.3* New Improved Piezoelectric Detection Method to Measure Ultrasonic Nonlinearity Parameters for Incipient Damages in Nuclear Engineering Materials To Kang, Jin-Ho Park, Korea Atomic Energy Research Institute, Korea; JeongK.Na, Wyle Lab, USA; Sung-Jin Song, Sungkyunkwan University, Korea	*WED.2.C.3* Eddy-Current Non Destructive Testing with the Finite Element Tool Code_Carmel3D Thomas P., Goursaud B., EDF R&D, France; Maurice L., Cordeiro S., EDF CEIDRE, France

11:40	*WED.2.A.4* Automated Correlation of Historical with Present Eddy Current Inspection Data Using HDC® for Understanding Change in Steam Generator Tubing Conditions and Visual Flaw Morphology Tom O'Dell, Tom Bipes, Kevin Newell, Zetec, USA	*WED.2.B.4* Application of Fiber-optic Sensors to CFRP Pressure Tanks for Internal Strain Monitoring Donghoon Kang, Korea Railroad Research Institute, Korea	*WED.2.C.4* Modelling Ultrasonic Image Degradation due to Beam-Steering Effects in Austenitic Steel Welds O. Nowers, D.J. Duxbury, Rolls-Royce plc, UK; B.W. Drinkwater, Bristol University, UK
12:00	**Lunch**		

Time	**Session A** **PARENT**	**Session B** **Pipe Inspection Ⅳ** **- Weld**	**Session C** **Reactor Pressurized Vessel / BOP**
	Co-Chairpersons: Ryan M. Meyer Kyung-cho Kim	Co-Chairpersons: Younho Cho Joe Agnew	Co-Chairpersons: Phil Ashwin Euisoon Doh
	WED.3.A	**WED.3.B**	**WED.3.C**
01:20	*WED.3.A.1* Overview and Status of the International Program to Assess the Reliability of Emerging Nondestructive Techniques Ryan M. Meyer, Pacific Northwest National Laboratory, USA; Ichiro Komura, Japan Power Engineering and Inspection Corporation, Japan; Kyung-cho Kim, Korea Institute of Nuclear Safety, Korea; Tommy Zetterwall, Swedish Qualification Center, Sweden; Stephen E. Cumblidge, Iouri Prokofiev, Nuclear Regulatory Commission,	*WED.3.B.1* Experimental Visualization of Ultrasonic Wave Propagation in Dissimilar Metal Welds Masaki Nagai, Shan Lin, Central Research Institute of Electric Power, Japan; Audrey Gardahaut, Hugues Lourme, Frédéric Jenson, CEA, LIST, France	*WED.3.C.1* New Magnetic Crawler Inspection Manipulators Mats Wendel, Torbjörn Sjö, David Eriksson, DEKRA Industrial AB, Sweden

	USA		
01:40	*WED.3.A.2* Challenge for the Detection of Crack in the Dissimilar Weld Region using PECT(Pulsed Eddy Current Technology) Duck-Gun Park, M.B Kishore, Korea Atomic Energy Research Institute, Korea	*WED.3.B.2* Application of a 3D Ray Tracing Model to the Study of Ultrasonic Wave Propagation in Dissimilar Metal Welds Audrey Gardahaut, Hugues Lourme, Frédéric Jenson, CEA, LIST, France; Shan Lin, Masaki Nagai, Central Research Institute of Electric Power Industry, Japan	*WED.3.C.2* CRONOS, an Advanced System for RCCA Inspection A Sola, F.Fernández, Tecnatom, Spain
02:00	*WED.3.A.3* TOFD Technique and Field Applications in Korean Nuclear Plants Euisoon Doh, Jae-yoon Kim, Chang-ho Song, Tack-su Lee, KEPCO Plant Service & Engineering Co., Ltd, Korea	*WED.3.B.3* Comparison of Artificial Flaws in Austenitic Steel Welds with NDE Methods Ari Koskinen, Esa Leskelä, VTT Technical Research Centre of Finland, Finland	*WED.3.C.3* Nondestructive Testing of Ferromagnetic Heat Exchanger Tube using Bobbin-Type Solid-State Hall Sensor Array with Low Exciting Frequency Jung-Min Kim, Jong-Hyung Seo, Sol-A Kang, Jinyi Lee, Chosun University, Korea

02:20	*WED.3.A.4* Nonlinear Ultrasonic Technique for Assessment of Thermal Aging Jongbeom Kim, Kyung Young Jhang, Hanyang University, Korea	*WED.3.B.4* Manufacturing of a New Type of NDE Test Samples with Laboratory-grown Intergranular SCC Cracks in a Nickel Base Weld-Comparison of Various NDE Techniques Applied to a Challenging Crack Morphology Klaus Germerdonk, Swiss Federal Nuclear Safety Inspectorate; Hans-Peter Seifert, Paul Scherrer Institute; Hardy Ernst, Swiss Association for Technical Inspections –Nuclear Inspectorate; Alex Flisch, Swiss Federal Laboratories for Materials Science and Technology; Dominik Nussbaum, ALSTOM Power Products, Switzerland	*WED.3.C.4* Development of ROV systems for Narrow Environment Inspection Satoshi Okada, Ryosuke Kobayashi, Hitachi, Ltd, Japan
02:40	*WED.3.A.5* A Feasibility Study on Detection and Sizing of Defects in the Reference Block Specimen by Using Ultrasonic Infrared Thermography Hee-Sang Park, Korea Res. Institute of Smart Material and Structures System Association; Jeong-Hak Park, Dong-Jin Yoon, Man-Yong Choi, Korea Res. Institute of Standards and Science; Kyoung-cho Kim, Korea Institute of Nuclear Safety, Won-Tae Kim, Kongju National University, Korea	*WED.3.B.5* Advanced Ultrasonic Technologies Applied to the Inspection of HDPE Piping Fusion Welds Andre Lamarre, Olympus NDT Canada, Canada	*WED.3.C.5* Helium Leak Test In-Line: Enhanced Reliability for Heat Exchanger Tubes Mathieu Lheureux, Pascal Gerard, Vallourec Heat Exchanger Tubes, France
03:00	**Break**		

Time	Session A PARENT	Session B Pipe Inspection Ⅴ	Session C Advanced Technologies Ⅱ
	Co-Chairperson: Yongsik Kim Toshiyuki Takagi	Co-Chairperson: Philippe Benoist Ki-bok Kim	Co-Chairperson: Masaki Nagai Donghoon Kang
	WED.4.A	WED.4.B	WED.4.C
03:20	*WED.4.A.1* Effectiveness Evolution of DMW Inspection Techniques Assessed Through Three International RRT's Tommy Zettervall, SQC Swedish Qualification Centre, Sweden; Steven R Doctor, Pacific Northwest National Laboratory, USA	*WED.4.B.1* Higher Harmonic Imaging of SCC in Dissimilar Metal Weld with Ni-Based Alloy and Fatigue Crack in Cast Stainless Steel Hitoshi Ishida, Institute of Nuclear Safety System, Japan, Koichiro Kawashima, Ultrasonic Material Diagnosis Lab. Ltd, Japan	*WED.4.C.1* Improvements to Surface Detection Algorithms for the TFM Beam Former R.L. ten Grotenhuis, N. Saeed, A. Hong, Y. Verma, Ontario Power Generation, Inspection & Maintenance Division; R. Fernandez-Gonzalez, M. Wang, T. Zulueta, Toronto University, Canada;
03:40	*WED.4.A.2* Integrity Evaluation Case Subject to Replacement & Preventive Maintenance for NPP Ni-alloy Components Changkuen Kim, Jooyoul Hong, Dongjin Lee, Doosan Heavy Industries & Construction, Korea	*WED.4.B.2* Automated Ultrasonic Nondestructive Evaluation of High Density Polyethylene Mitered Joints and Butt Fusion Welds Jeff Milligan, Cliff Searfass, Joseph Agnew, Structural Integrity Associates, Inc., USA	*WED.4.C.2* Evaluation of Interface Property for Thin Film by Laser Interferometer Hae-Sung Park, Ik-Keun Park, Seoultech, Korea, Sanichiro Yoshida, David Didie, Southeastern Louisiana University, USA
04:00	*WED.4.A.3* Long Range Guided Wave technique for Nuclear Power Facility Jaesun Lee, Younho Cho, Pusan National University, Korea	*WED.4.B.3* Developments of Portable Pulsed Eddy Current Equipment for the Detection of Wall Thinning in the Insulated Carbon Steel Pipe Duck-Gun Park, M.B. Kishore, D.H. Lee, Korea Atomic Energy Research Institute, Korea	*WED.4.C.3* Development of Ultrasonic Inspection Techniques using a Matrix Array Transducer for Acoustical Anisotropic Media Naoyuki Kono, So Kitazawa, Hitachi, Ltd, Japan

04:20	*WED.4.A.4* Simulation of Inspection for Dissimilar Metal Welds by Phased Array UT with Focusing Techniques Young-In Hwang, Jae-Hyun Bae, Hak-Joon Kim, Sung-Jin Song, Sungkyunkwan university, Korea; Kyung-Cho Kim, Yong-Buem Kim, Korea Institute of Nuclear Safety, Korea; Hun-Hee Kim, Doosan Heavy Industries & Construction, Korea	*WED.4.B.4* New Developments in the use of Flexible PCB-Based Eddy Current Array Probes for the Surface Inspection of Welds and Pipes Andre Lamarre, Tommy Bourgelas, Benoit Lepage, Olympus NDT Canada, Canada	*WED.4.C.4* A Study of Laser Generated Guided Ultrasonic Waves for Measuring Elastic Modulus of Metal Thin Film Layers on Silicon Substrate Taehoon Heo, Bonggyu Ji, Bongyoung Ahn, Seung Hyun Cho, Korea Research Institute of Standards and Science, Korea; Gang-Won Jang, Sejong University, Korea
04:40	*WED.4.A.5*	*WED.4.B.5* A Study on Development of RFECT System for Inspection of Ferromagnetic Pipelines Jae-Ha Park, Hak-Joon Kim, Sung-Jin Song, Sungkyunkwan University, Korea; Dae-Kwang Kim, Hui-Ryong Yoo, Sung-Ho Cho, Korea Gas Corporation, Korea	*WED.4.C.5* Real-time Adaptive Imaging for Ultrasonic Nondestructive Testing of Structures with Irregular Shapes Sébastien Robert, Léonard Le Jeune, Vincent Saint-Martin, CEA, LIST, France; Olivier Roy, M2M, France
05:00	*WED.4.A.6*	*WED.4.B.6* Evaluation of Effect of the Magnetic Field on the Exciter Tilting of RFECT System Module in Pipeline Jeong-Won Park, Jae-ha Park, Sung-Jin Song, Hak-Joon Kim, Sungkyunkwan University, Korea	*WED.4.C.6* Improved Inspection Technique for Large Rotor Shafts, Using a Semi-Flexible Phased Array UT Probe Guy Maes, Dany Devos, Patrick Tremblay, Zetec, Canada; Nobuyuki Hoshi, Hiroki Nimura, Hideaki Narigasawa, The Japan Steel Works, Ltd., Japan

Day3 (Thursday, 21 May)

Time	Session A Surface Examination	Session B Emerging Techniques Ⅱ	Session C Material Properties / Concrete
	Co-Chairperson: Shan Lin Yong-Moo Cheong	Co-Chairperson: Dong-Jin Yoon Hajime Shohji	Co-Chairperson: Tetsuya Uchimoto Jin-yi Lee
	THU.1.A	THU.1.B	THU.1.C
09:00	*THU.1.A.1* Evaluation of dispersion characteristics for leaky surface acoustic wave on aluminum thin film with scanning acoustic microscopy Byung-seok Jo, Tae-sung Park, Seung-bum Cho, Ik-keun Park, Seoul National University of Science and Technology, Korea	*THU.1.B.1* Acceleration of Total Focusing Method for Ultrasonic Imaging Ewen Carcreff, Dominique Braconnier, The Phased Array Company, USA	*THU.1.C.1* Residual Stress Evaluation of an IN 600 Shot Peening Specimen by using the Minimum Reflection Taek-Gyu Lee, Hak-Joon Kim, Sung-Jin Song, Sungkyunkwan University, Korea, Sung-Sik Kang, Korea Institute of Nuclear Safety, Korea; Sung-Duk Kwon, Andong National University, Korea
09:20	*THU.1.A.2* Study for Microcrack of steel wire rods using EMAR Method Seung-Wan Cho, Sungkyunkwan University; Taehoon Heo, University of Science and Technology; Seung-Hyun Cho, Korea Research Institute of Standards and Science; Zhong-Soo Lim, Research Institute of Industrial Science & Technology, Korea	*THU.1.B.2* Experimental Visualization of Ultrasonic Pulse Waves Using Piezoelectric Films Yoshinori Kamiyama, Takashi Furukawa, Japan Power Engineering and Inspection Corporation, Japan	*THU.1.C.2* Monitoring Microstructural Evolution in Steel Components with Nonlinear Ultrasound James J. Wall, Electric Power Research Institute, USA; Kathryn Matlack, Eidgenösische Technische Hochschule, Switzerland; Jin-Yeon Kim, Laurence J. Jacobs, Georgia Institute of Technology, USA; Jianmin Qu, Northwestern University, USA

09:40	*THU.1.A.3* Surface Property Measurement of the Cylinder Liner Using the Honing Polishing Ho-Girl Lee, Taek-Gyu Lee, Hak-Joon Kim, Sung-Jin Song, Seung-Mok Kim, Yeong-Jae Lee, Sungkyunkwan University, Korea	*THU.1.B.3* Monitoring of Pipe Wall Thinning Using High Temperature Thin-Film UT Sensor T.Kodaira, I. Seki, N.Kawase, T. Matsuura, Y.Yamamoto, S. Kawanami, Mitsubishi Heavy Industries, Ltd,Japan	*THU.1.C.3* Corrosion Behavior of 304L Stainless Steel using Confocal Laser Scanning Microscopy (CLSM) and Atomic Force Microscopy (AFM) Joe-Ming Chang, Tai-Cheng Chen, Hsiao-Ming Tung, Institute of Nuclear Energy Research Atomic Energy Council, Taiwan ROC
10:00	*THU.1.A.4* Study on Ultrasonic Method for Detection of Micro-Defects in Pipeline Using the Rayleigh Wave Yun-Taek Yeom, Hak-Joon Kim, Sung-Jin Song, Sungkyunkwan University; Sung-Duk Kwon, Andong National University; Ki-Bok Kim, Korea Research Institute of Standards and Science, Korea	*THU.1.B.4*	*THU.1.C.4* Water Content Distribution in Concrete using the FDR Method Denis Vautrin, F. Taillade, EDF R&D STEP, France; T. Clauzon, A. Courtois, EDF DPIH DTG, France
10:20	**Break**		

Time	Session A Modeling III / Others	Session B Pipe Inspection VI - Embedded	Session C Advanced Technologies III / Alternative to RT
	Co-Chairpersons: Wonjae Choi Yasushi Ikegami	Co-Chairpersons: Jaesun Lee Myles Duncan	Co-Chairpersons: Seung-Hyun Cho Toshihiro Yamamoto
	THU.2.A	THU.2.B	THU.2.C
10:40	*THU.2.A.1* Two Dimensional FEM Simulation of Ultrasonic Guided Wave Propagation in Multilayered Pipe with Delamination Vu Anh Hoang, Sung-Jin Song, Hak-Joon Kim, Sungkyunkwan University, Korea	*THU.2.B.1* Inspection of Inaccessible Areas: The Heysham Case Martin Bolander, WesDyne International, Germany	*THU.2.C.1* A New State of the Art Portable Phased Array Equipment Dedicated to Defect Characterization Philippe Benoist, Olivier Roy, M2M, France; François Cartier, CEA, France
11:00	*THU.2.A.2* Advanced Tools Based on Simulation for Analysis of Ultrasonic Data Souad Bannouf, Sébastien Lonné, EXTENDE, France; Stéphane LeBerre, David Roué, Florence Grassin, CEA, LIST, France	*THU.2.B.2* Short-Range Guided Wave Testing of Dry Cask Storage Systems Using EMATs Matthew S. Lindsey, Jason K.Van Velsor, Owen M.Malinowski, Structural Integrity Associates, Inc., USA; Jeremy Renshaw, Nathan Muthu, Electric Power Research Institute, USA	*THU.2.C.2* Detection and Sizing of Cracks in Bolts Based on Ultrasonic Phased Array Technology Shan Lin, Central Research Institute of Electric Power Industry, Japan

11:20	*THU.2.A.3* Model-Aided Design of Purpose Built Ultrasonic Probes Lars Skoglund, WesDyne Sweden AB, Sweden	*THU.2.B.3* Detection of Corrosion on Non-Accessible Areas using Rayleigh-like Waves Laura Taupin, Frederic Jenson, CEA, LIST, France; Sylvain Murgier, EDF CEIDRE, France; Pierre-Emile Lhuillier, EDF Lab Les Renardières, France	*THU.2.C.3* Ultrasonic Phased Array Inspection of Small Bore Tubing - A Replacement for Radiography Toufik Cherraben, Francis Hancock, Doosan Babcock, UK; Jérôme Delemontez, EDF, Division Technique Générale, France; Thierry Le Guevel, Philippe Cornaton, EDF, Centre d'Ingénierie Thermique, France
11:40	*THU.2.A.4*	*THU.2.B.4* Use of Creeping Wave/Head Wave Ultrasonic Method for Inspection of a Carbon Steel Pipe Hidden Areas Under Bedplate S. Murgier, C. Herault, EDF CEIDRE, France; P. Bergalonne, COMEX Nucléaire, France	*THU.2.C.4* Development of Alternatives to Radiographic Testing at AREVA. Comparison and Challenges Frédéric Lasserre, Sophie Hem, Bruno Bader, Jean-Marc Crauland, AREVA Nuclear Power, France

4. List of Authors

Author name		Full paper	Abstract only
Agnew	J.		WE_4_B_2
Agold	J.		TU_2_A_3
Ahn	B.		WE_4_C_4
Anderson	M.		TU_2_A_4
Ashwin	P.		WE_1_A_1
Bader	B.		TH_2_C_4
Bae	J.-H.	WE_4_A_4	
Baek	S.-H.	TU_1_C_2	
Bannouf	S.	TU_1_A-2 TH_2_A_2	
Barcenilla	V.	WE_1_B_2	
Barrera	C.M.		TU_2_B_3
Bayón	A.	TU_1_B_1	
Benoist	P.		TH_2_C_1
Bergalonne	P.		TH_2_B_4
Bey	S.	WE_2_C_1	
Bipes	T.		WE_2_A_4
Blin	P.		TU_1_A_3
Boehm	R.		TU_1_C_5
Bolander	M.	TH_2_B_1	
Bourgelas	T.		WE_4_B_4
Braconnier	D.		WE_1_C_4 TH_1_B_1
Brockett	A.		WE_1_B_1
Calás	H.	WE_1_B_2	
Carcreff	E.		TH_1_B_1
Cartier	F.		TH_2_C_1
Cattiaux	G.	TU_2_A_2 TU_2_C_4	
Chang	J.-M.		TH_1_C_3
Chassignole	B.	TU_1_A_5	
Chen	T.-C.		TH_1_C_3
Chen	Z.		TU_2_B_6
Cheng	W.	TU_2_C_3	
Cheong	Y.-M.		TU_1_B_5 TU_2_B_5
Cherraben	T.		TH_2_C_3
Chesworth	S.		TU_1_A_1
Cho	C.		TU_2_B_4
Cho	S.-B.		TH_1_A_1
Cho	S.H.		WE_4_C_4 TH_1_A_2
Cho	S.-H.	WE_4_B_5	
Cho	S.W.		TH_1_A_2
Cho	Y.S.		WE_1_B_3
Choi	M.-Y.	TU_1_B_2	WE_2_B_1 WE_3_A_5

Author name		Full paper	Abstract only
Choi	N.		WE_2_B_2
Choi	W.-J.	TU_1_B_2	WE_2_B_1
Clauzon	T.	TH_1_C_4	
Cofie	N.		TU_1_B_3
Cordeiro	S.	WE_2_C_3	
Cornaton	P.		TH_2_C_3
Courtois	A.	TH_1_C_4	
Crauland	J.-M.	TU_1_C_3	TH_2_C_4
Cumblidge	S.E.	WE_3_A_1	
Dagen	J.M.		WE_1_B_1
Dans	A.	TU_1_B_1	
Dao	G.		WE_1_C_4
De la Fuente	B.	WE_1_B_2	
Delemontez	J.		TH_2_C_3
Devos	D.	WE_4_C_6	
Deydier	S.	TU_1_A_5	
Diaz	A.		TU_2_A_4
Didie	D.		WE_4_C_2
Didier	V.	TU_1_A_4	
Doctor	S.R.		WE_4_A_1
Doh	E.		TU_1_C_1 WE_3_A_3
Drinkwater	B.W.	WE_2_C_4	
Ducousso-Ganjehi	L.	TU_2_A_2	
Duxbury	D.J.	WE_2_C_4	
Endoh	K.	WE_1_B_4	
Erhard	A.		TU_1_C_5
Eriksson	D.	WE_3_C_1	
Ernst	H.		WE_3_B_4
Esp	L.		WE_1_A_1
Fernández	F.	TU_1_B_1 TU_2_A_1 WE_1_B_2 WE_3_C_2	
Fernandez-Gonzalez	R.	WE_4_C_1	
Flisch	A.		WE_3_B_4
Furukawa	T.	TU_1_B_4 TH_1_B_2	
Gac	H.		WE_2_A_1
Gadea	J.R.	TU_2_A_1	
Garcia Rodriguez	D.	TU_2_C_3	
Gardahaut	A.	WE_3_B_1 WE_3_B_2	
Gasteau	D.	TU_2_A_2	
Gelebart	Y.	TU_1_A_5	
Gerard	P.		WE_3_C_5
Germerdonk	K.		WE_3_A_5
Gómez	P.	TU_2_A_1	
González	P.	TU_2_A_1	

Author name		Full paper	Abstract only
Goursaud	B.	WE_2_C_3	
Grassin	F.	TH_2_A_2	
Griesbach	T.		TU_1_B_3
Grizzi	G.		WE_1_A_1
Hague	R.		WE_1_B_1
Han	B.-H.		TU_1_C_4
Hanaoka	T.		WE_2_A_3
Hancock	F.		TH_2_C_3
Hara	S.		TU_2_B_1
Harris	D.		TU_1_B_3
Heckel	Th.		TU_1_C_5
Hem	S.		TH_2_C_4
Heo	T.		WE_4_C_4 TH_1_A_2
Herault	C.		TH_2_B_4
Herman	K.		TU_2_A_3
Hetmanczuk	M.	TU_1_A-2	
Hide	K.	WE_1_A-3 WE_1_A-4	
Hoang	V.A.	TH_2_A_1	
Hong	A.	TU_1_A-2 WE_4_C_1	
Hong	J.		WE_4_A_2
Hoshi	N.	WE_4_C_6	
Huet	P.	TU_1_A_4	
Hur	D.H.	TU_1_C_2	
Hwang	Y.-I.	WE_4_A_4	
Ikegami	Y.	TU_2_C_2	
Ishida	H.	WE_1_B_4 WE_4_B_1	
Jackson	B.K.		TU_2_B_2
Jacobs	L.J.		TH_1_C_2
Jambon	M.	TU_1_C_3	
Jang	G.-W.		WE_4_C_4
Jardet	P.	TU_1_A_4	
Jenson	F.	TU_2_A_2 WE_3_B_1 WE_3_B_2	TH_2_B_3
Jeong	J.-K.		WE_2_B_2
Jhang	K.-Y.		WE_3_A_4
Ji	B.		WE_4_C_4
Jianhai	Z.		WE_1_C_1
Jo	B.-S.		TH_1_A_1
Joffe	C.		TU_2_A_4
Kamiyama	Y.	TH_1_B_2	
Kang	D.	WE_2_B_4	
Kang	S.-A.		WE_3_C_3
Kang	S.-S.		TH_1_C_1
Kang	T.		WE_2_B_3

Author name		Full paper	Abstract only
Kang	Y.S.	WE_2_A_2	
Kawai	N.		WE_2_A_3
Kawanami	S.	TH_1_B_3	
Kawase	N.	TH_1_B_3	
Kawashima	K.	WE_4_B_1	
Kawata	K.		WE_2_A_3
Kim	C.		WE_4_A_2
Kim	D.-J.		TU_2_B_5
Kim	D.-K.	WE_4_B_5	
Kim	G.		WE_1_B_3 WE_2_B_2
Kim	H.-H.	WE_4_A_4	
Kim	H.-J.	TU_2_C_5 WE_2_C_2 WE_4_A_4 WE_4_B_5 TH_2_A_1	TU_2_C_1 WE_1_B_3 WE_1_C_1 WE_4_B_6 TH_1_A_3 TH_1_A_4 TH_1_C_1
Kim	H.-S.		WE_2_B_2
Kim	I.C.	WE_2_A_2	
Kim	I.-S.		TU_1_C_4
Kim	J.		WE_3_A_4
Kim	J.-M.		WE_3_C_3
Kim	J.-Y.		TU_1_C_1 WE_3_A_3
Kim	J.-Y.		TH_1_C_2
Kim	K.-B.		WE_1_B_3 WE_2_B_2 TH_1_A_4
Kim	K.-C.	WE_3_A_1 WE_4_A_4	WE_3_A_5
Kim	S.-M.		TH_1_A_3
Kim	W.-H.		TU_1_C_1
Kim	W.-T.	TU_1_B_2	WE_3_A_5
Kim	Y.		TU_2_B_4
Kim	Y.-B.	WE_4_A_4	
Kishore	M.B.	WE_3_A_2 WE_4_B_3	
Kitasaka	J.	WE_1_B_4	
Kitazawa	S.		WE_4_C_3
Kitze	J.		TU_1_C_5
Kobayashi	R.		WE_3_C_4
Kodaira	T.	TH_1_B_3	
Komura	I.	WE_3_A_1	
Kono	N.		WE_4_C_3
Koskinen	A.	WE_3_B_3	
Kurokawa	M.		WE_2_A_3
Kwon	K.-A.	TU_1_B_2	
Kwon	S.-D.		TH_1_A_4 TH_1_C_1
Lafreniere	P.		TU_1_A_1
Lamarre	A.		WE_3_B_5 WE_4_B_4
Landrum	J.		TU_2_A_4
Langevin	J.		WE_1_A_1
Lasserre	F.	TU_1_C_3	TH_2_C_4

Author name		Full paper	Abstract only
Latiolais	C.		WE_1_A_1
Le Berre	S.	WE_2_C_1 TH_2_A_2	
Le Bourdais	F.		WE_1_C_3
Le Guevel	T.		TH_2_C_3
Le Jeune	L.		WE_4_C_5
Le Pollès	T.		WE_1_C_3
Lee	C.-H.		TU_1_C_1
Lee	D.		WE_4_A_2
Lee	D.H.	WE_4_B_3	
Lee	D.-H.	TU_1_C_2	TU_1_B_5 TU_2_B_5
Lee	H.-G.		TH_1_A_3
Lee	J.		WE_3_C_3
Lee	S.-G.	TU_2_C_5	
Lee	T.-G.		TH_1_A_3 TH_1_C_1
Lee	T.-S.		WE_3_A_3
Lee	Y.-J.		TH_1_A_3
Lejon	A.	TU_O_P_3	
Lepage	B.		WE_4_B_4
Leskelä	E.	WE_3_B_3	
Lheureux	M.		TU_2_A_5 WE_3_C_5
Lhuillier	P.-E.	TU_1_A_5	TH_2_B_3
Lim	Z.S.		TH_1_A_2
Lin	S.	WE_3_B_1 WE_3_B_2 TH_2_C_2	
Lindberg	J.		TU_2_A_4
Lindsey	M.S.		TH_2_B_2
Lonne	S.	TH_2_A_2	
Lourme	H.	WE_3_B_1 WE_3_B_2	
Maes	G.	TU_1_C_3 WE_4_C_6	
Malinowski	O.M.		TU_1_B_3 TH_2_B_2
Marois	D.	TU_1_C_3	
Martin	E.	TU_O_P_3	
Martin	O.	TU_O_P_3	
Martínez-Oña	R.	TU_1_B_1 WE_1_B_2	
Matlack	K.		TH_1_C_2
Matsuura	T.	TH_1_B_3	
Maurice	L.	WE_2_C_3	
Meyer	R.M.	WE_3_A_1	
Mihalache	O.	TU_2_C_3	
Milligan	J.		WE_4_B_2
Miyadera	H.		TU_O_P_4
Morikawa	M.		WE_2_A_3
Murakami	H.		WE_2_A_3
Murgier	S.		TH_2_B_3 TH_2_B_4

Author name		Full paper	Abstract only
Muthu	N.		TH_2_B_2
Na	J.K.		WE_2_B_3
Nagai	M.	WE_3_B_1 WE_3_B_2	
Narigasawa	H.	WE_4_C_6	
Newell	K.		WE_2_A_4
Nimura	H.	WE_4_C_6	
Nishino	H.	TU_1_B_4	
Nowers	O.	WE_2_C_4	
Nussbaum	D.		WE_3_B_4
O'Dell	T.		WE_2_A_4
Oh	C.-H.		WE_1_B_3
Ohta	J.	WE_1_A-3	
Okada	S.		WE_3_C_4
O'Regan	P.		TU_1_A_1 TU_2_A_3
Paillard	S.	WE_2_C_1	
Park	C.-S.		TU_1_C_4
Park	D.-G.	WE_3_A_2 WE_4_B_3	
Park	H.-S.	TU_1_B_2	WE_3_A_5
Park	H.-S.		WE_4_C_2
Park	I.-K.		WE_4_C_2 TH_1_A_1
Park	J.H.	WE_2_A_2	
Park	J.-H.	TU_1_B_2	WE_2_B_1 WE_3_A_5
Park	J.-H.		WE_2_B_3
Park	J.-H.	WE_4_B_5	WE_4_B_6
Park	J.-W.		WE_4_B_6
Park	M.		WE_1_B_3 WE_2_B_2
Park	T.-S.		TH_1_A_1
Perez	S.	TU_O_P_3	
Pérez	C.M.	TU_1_B_1	
Prokofiev	I.	WE_3_A_1	
Qu	J.		TH_1_C_2
Ramuhalli	P.		TU_2_A_4
Rattoni	B.	TU_2_C_4	
Renshaw	J.		TH_2_B_2
Resa	P.I.	TU_1_B_1	
Rezaie-Manesh	M.		TU_1_A_1
Robert	S.		WE_4_C_5
Roue	D.	TH_2_A_2	
Roy	O.		WE_4_C_5 TH_2_C_1
Saeed	N.	TU_1_A-2 WE_4_C_1	
Saint-Martin	V.		WE_4_C_5
Sakai	Y.	TU_2_C_2	
Samson	R.		WE_2_A_1
Saruta	K.	WE_1_C_2	

Author name		Full paper	Abstract only
Schumacher	E.	TU_1_A-2	
Searfass	C.		WE_4_B_2
Seifert	H.-P.		WE_3_B_4
Seki	I.	TH_1_B_3	
Selby	G.		TU_O_P_2
Seo	J.-H.		WE_3_C_3
Seo	M.-K.		WE_1_B_3 WE_2_B_2
Seok	C.-S.	TU_2_C_5	WE_1_C_1
Shim	H.-S.	TU_1_C_2	
Shohji	H.	WE_1_A-3 WE_1_A-4	
Shyu	H.-F.		WE_1_A_2
Sjö	T.	WE_3_C_1	
Skoglund	L.		TH_2_A_3
Sola	A.	WE_3_C_2	
Sollier	T.	TU_2_A_2 TU_2_C_4	
Song	C.-H.		WE_3_A_3
Song	S.		TU_2_C_1
Song	S.-J.	TU_2_C_5 WE_2_C_2 WE_4_A_4 WE_4_B_5 TH_2_A_1	TU_O_P_1 WE_1_B_3 WE_1_C_1 WE_2_B_3 WE_4_B_6 TH_1_A_3 TH_1_A_4 TH_1_C_1
Taillade	F.	TH_1_C_4	
Takagi	T.		TU_2_B_1 TU_2_B_6
Tang	Z.		TU_2_C_1
Tanji	K.		TU_2_B_1
Taupin	L.		TH_2_B_3
ten Grotenhuis	R.L.	TU_1_A-2 WE_4_C_1	
Thomas	P.	WE_2_C_3	
Tisseur	D.	TU_2_C_4	
Todd	S.J.		TU_2_B_3
Tremblay	P.	WE_4_C_6	
Tsuruta	T.		WE_2_A_3
Tung	H.-M.		TH_1_C_3
Uchimoto	T.		TU_2_B_1 TU_2_B_6
Ueda	M.	WE_1_C_2	
Urayama	R.		TU_2_B_1
Van Velsor	J.K.		TU_1_B_3 TH_2_B_2
Vanhoye	A.	WE_2_C_1	
Vautrin	D.	TH_1_C_4	
Verma	Y.	TU_1_A-2 WE_4_C_1	
Verspeelt	D.	TU_1_C_3	
Vessio	P.	TU_1_B_1	
Villagomez	R.		TU_2_B_3
Wall	J.J.		TU_2_B_2 TH_1_C_2
Wang	M.	WE_4_C_1	
Warwick	J.L.W.		TU_2_B_2

Author name		Full paper	Abstract only
Watanabe	K.	WE_1_A-3	
Wendel	M.	WE_3_C_1	
Wu	K.	TU_1_C_2	
Xie	S.		TU_2_B_6
Yamaguchi	T.	WE_1_C_2	
Yamamoto	Y.	TH_1_B_3	
Yamamoto	T.	TU_1_B_4 TU_2_C_3	
Yeom	Y.-T.		TH_1_A_4
Yonemura	H.		WE_2_A_3
Yoo	H.-R.	WE_4_B_5	
Yoon	B.		TU_2_B_4
Yoon	D.-J.		TU_1_C_4 WE_3_A_5
Yoshida	S.		WE_4_C_2
Yuan	M.	WE_2_C_2	TU_2_C_1
Zetterwall	T.	TU_O_P_3 WE_3_A_1	WE_4_A_1
Zhang	J.	WE_2_C_2	
Zulueta	T.	WE_4_C_1	

5. Conference Papers

This section contains the full papers of the conference. When a full paper was not submitted, the abstract is provided.

NDE Researches for Structural Integrity of Nuclear Power Plant Components in Korea

Sung-Jin Song

Sungkyunkwan University, School of Mechanical Engineering, 300 Chunchun-dong, Jangan-gu, Suwon 440-746, South Korea

E-mail address : sjsong@skku.edu

Since Kori Nuclear power Plant (NPP) operated from 1978, 23 NPPs are currently operating for generation of electric power and 5 more plants are under construction in Korea. More than 30 year nuclear power plant operation history, various accident including S/G tube rupture at 2002 have experience. Especially, after Fukushima accidents, safety of nuclear power plants is one of major concern. Nondestructive evaluation (NDE) techniques play key role for insurance of structural integrity of NPPs.

In this presentation, review of NDE issues related on technical and/or social needs to NPPs in Korea during last 30 years. Also, technical progress or movement of NDE in order to meet those needs for NPP's safety will be discussed. Especially, research activity by SAFE (Safety and structural Integrity Research Center), established at 1997 in Sungkyunkwan University and carried out many researches including NDE fields for insuring safety of NPPs, related to NDE issues focused on structural integrity of NPPs. Also, major stream of NDE research topics in KOREA during last three decade will be touched in this presentation.

Deep Learning in the Future of NDE

Greg Selby
Electric Power Research Institute, USA

gselby@epri.com

Three factors are coming together to bring a revolution in the way people interact with the electronic environment and with data. They are: first, the development of deep neural networks (also called deep convolutional networks, or deep learning); second, the rapid development of massively parallel, low-cost supercomputing systems using general-purpose graphics processor units; and third, the availability of huge amounts of data to train the systems.

The NDE community will access the first item through the efforts of large commercial enterprises such as Google, Microsoft, Baidu, Facebook, NVIDIA, Tesla, and Apple, all of whom are investing heavily in deep learning research. Our small industry of nuclear NDE cannot contribute meaningfully to these seminal developments, but as the research progresses and the field matures, powerful general-purpose deep learning engines will become available to us, perhaps even before the next conference in this series.

The second item, the computing platform, is not an issue; today a researcher can purchase for USD15k a desktop workstation that five years ago would have been one of the world's top 500 supercomputers. Also, engines will become available as netware.

The biggest question for us is the third item, the data. To work robustly, deep learning engines require huge amounts of training data. It's possible that no single NDE institution will be able to gather enough information to train the systems; will we be able to work together to accomplish it, when the prize at the end of the work could be uniform NDE reliability and repeatability for the world fleet of nuclear power plants?

Keywords:

Deep learning
GPU computing
Artificial intelligence
Deep neural networks

Activities and future Trends of the ENIQ Network

Oliver Martin[1], Tommy Zetterwall[2], Etienne Martin[3], Anders Lejon[4], Samuel Perez[5]

[1]European Commission, Joint Research Centre, Institute for Energy and Transport, Petten, Netherlands
[2]Swedish Qualification Centre (SQC), Täby, Sweden
[3]EDF Generation Nuclear Engineering Division, Ceidre, France
[4]Vattenfall, Ringhals NPP, Sweden
[5]Iberdrola, Madrid, Spain

Abstract

The European Network for Inspection and Qualification (ENIQ) is a utility driven network that works towards a harmonized European approach on reliable and effective in-service inspection (ISI). It is Technical Area 8 (TA8) of the international association NUGENIA on R&D on Gen II / III reactors. ENIQ has a steering committee and two sub-areas: the sub-area on Qualification (SAQ), which works on issues related to the qualification of in-service inspection (ISI) systems and the Sub-area on Risk (SAR), which is focused on risk-informed ISI (RI-ISI).

Recently SAQ launched a comprehensive study on the performance of computed and digital radiography (CR / DR) with the name COMRAD. The aim of the study is to identify the essential parameters that affect the performance of CR and DR and thereby providing a consistent approach to inspection design and the production of technical justifications. Also SAQ is currently performing a study to identify the main barriers for transport of qualifications between countries and how to overcome these and recently drafted a position paper on the re-qualification and maintaining proficiency of ISI personnel. The reason for this paper is the significantly different practices of countries with operating NPPs on re-qualification of ISI personnel. Some countries require re-qualification of ISI personnel every five years, where as others do not demand such (re-)qualifications at all. The on-going discussion inside SAQ on re-qualification and maintaining proficiency of ISI personnel will most probably result in a study on the issue.

SAR is currently launching a study to quantify the benefit from ISI and to indicate the level of risk reduction that can be expected from ISI and is currently updating the ENIQ Framework Document on RI-ISI. The aim of this paper is to describe these activities in more detail plus the challenges for ENIQ in the next couple of years.

Keywords: ENIQ, in-service inspection, inspection qualification, inspection qualification body, risk-informed in-service inspection, NUGENIA

1. ENIQ: Objectives and Organisation

The European Network for Inspection and Qualification (ENIQ) is a network dealing with the reliability and effectiveness of non-destructive testing (NDT) for nuclear power plants (NPP). ENIQ is driven by European nuclear utilities and is working mainly in the areas of qualification of NDT systems and risk-informed in-service inspection (RI-ISI). Since its establishment in 1992 ENIQ has performed two pilot studies on in-service inspection (ISI) qualification [1] [2] and has issued 50 documents. Among them are the two ENIQ framework documents, the "European Methodology for Qualification of Non-Destructive Testing" [3] and the "European Framework Document for Risk-Informed In-Service-Inspection"[1] [4], 11 recommended practices [5] [6] [7] [8] [9] [10] [11] [12] [13] [14] and a significant number of technical reports and discussion documents[2]. ENIQ is recognized as one of the main contributors to today's global qualification guidelines for in-service inspection (ISI).

ENIQ is part of the European based R&D association on Gen II & III reactors NUGENIA established in November 2011. NUGENIA has more than 100 member organisations with all major nuclear organisations (i.e. utilities, reactor vendors, nuclear research organisations, technical service organisations, universities with nuclear faculties) among them. NUGENIA has 8 technical areas (TA), in which then scientific / technical work of the association is carried out,

[1] The European Framework Document for RI-ISI is currently revised and the revised version will be published later this year.
[2] All valid ENIQ documents can be found on the website of NUGENIA (www.nugenia.org).

with ENIQ being the 8th TA. ENIQ has two sub-areas (SA), the Sub-area for Qualification (SAQ), which is dealing with ISI qualification, and the Sub-area for Risk (SAR), which is dealing with RI-ISI. Beside these two ENIQ used to have a separate Sub-area for Inspection Qualification Bodies (SAIQB) for two years, which served as an exchange forum for IQBs. Because there was quite some overlap in topics and members SAIQB and SAQ were merged to one sub-area called SAQ. ENIQ has a steering committee (SC), which is the decision making body of ENIQ. It approves all the documents drafted inside the SAs, but also serves as an exchange forum for ISI related issues in NPPs of ENIQ members. ENIQ SC members have contributed to the recently published NUGENIA Global Vision Document, which summarizes all the scientific / technical challenges (short-, mid- and long-term) of the individual TAs, including the ones of ENIQ (TA8) [15].

2. Current Activities of ENIQ

2.1 Sub-area for Qualification

COMRAD

Since May 2014 SAQ members are performing a comprehensive study on the performance of computed and digital radiography called COMRAD. The aim of this study it to identify the essential parameters that affect the performance of both methods and thus provide a consistent approach to inspection design and production of technical justifications. Computed radiography (CR) and digital radiography (DR) are two contenders as replacement technologies for traditional film based industrial radiography. In CR the film is replaced by an imaging plate containing photostimuable storage phosphors, which store the radiation level received at each point in local electron energies. A scanner employs a laser beam to read out the imaging plate via photostimulated luminescence, where the emitted light in the visible spectrum is detected by a photomultiplier and converted to an electronic digitised signal. In DR a digital detector array (DDA), also known as flat panel detector, the image is directly captured in the detector.

Both techniques share a number of potential advantages over film, such as their linear detection characteristics over a wide dose range, allowing the examination of a wider range of thicknesses in one exposure and making CR and to a lesser extent DR less vulnerable to under- or overexposure, unlike conventional film. Another potential advantage concerns the increased sensitivity at lower energies and the consequential ability to reduce the radiation exposure (which in turn reduces inspection times and the potential radiological hazard). However, the transition from traditional silver film to digital radiography requires an in-depth understanding of the relative performances of CR/DR and film based radiography. As detection, processing and interpretation of the two methods are significantly different there are many technical aspects that need to be explored.

COMRAD was launched in May 2014 has a duration of two years. The first stage of the project is a review of the state-of-the-art of CR / DR and identification of key aspects that determine their performance. The second stage of the project is the writing of a recommended practice on qualification of CR and DR, which is the final output of the project.

MUREC

In 2011 SAQ carried out a survey to identify the barriers that preclude transfer of inspection qualifications from one country to another. The survey involved a questionnaire on different aspects of inspection qualification. Beside a section with general questions (e.g. if ENIQ Methodology is followed, which codes & standards are followed, etc.) the questionnaire contained sections with questions on regulatory requirements, IQB requirements, test pieces and practical trials, use of modelling, utilisation of foreign validations and personnel qualification. The questionnaire was sent to one organisation per country with ENIQ members, either IQB or utility, and with one exception all countries submitted answers.

Based on the outcomes of the above survey the idea was to launch a project on the transfer of inspection qualifications between countries called MUREC[3]. In the first stage of the project a comparison of the inspection requirements and inspection specifications of different countries was planned. In a second step a pilot study was planned, in which each participant is requested to perform a qualification on a simple case (real or fictitious) according to his national rules, guidelines and methodologies. In the third and last stage of the project the results of these qualifications are compared with each other and recommendations are formulated. In particular the second step would require significant efforts (personnel & time) from the participants and for this reason SAQ members decided to take a different approach.

[3] MUREC = Pilot study on mutual recognition of inspection qualifications between countries.

SAQ will perform an in-depth review of the questions of the questionnaire and decide for each question whether it is relevant or non-relevant for the transfer of inspection qualifications between countries and thus re-write the questionnaire. The resulting re-written questionnaire will be distributed to one organization per country with ENIQ members again and the answers will be reviewed. By taking this approach SAQ members are confident to infer the possibility to facilitate transfer of inspection qualifications between countries and at least achieve transfers of parts of technical justifications, since there are practically only two scenarios for the exchange of parts of a technical justification, either that providers want to use the same NDT system in different countries or that utilities operate the same type of plant in different countries and use the same provider with the same specifications. The survey based on the re-written questionnaire might evolve into an ENIQ position paper.

Maintaining proficiency of ISI personnel

In the last 1 ½ years there was quite some discussion within SAQ on (re-)qualification of ISI personnel. The discussions revealed that there are different approaches with regards to (re-)qualification of ISI personnel in different countries. Where as some countries require re-qualification of ISI personnel after a couple of years, normally 5 years, as it is the case for e.g. Finland, others have no legal requirements concerning re-qualification of ISI personnel (e.g. France). The discussions also revealed that two items need to be distinguished:

- Re-qualification in general (which rather concerns systems than ISI personnel alone) and
- Maintaining proficiency of ISI personnel.

The latter is a matter of demonstrating of maintaining the proficiency of ISI personnel and some ENIQ members perform it already via technical justifications. Discussions focused on the issue of maintaining proficiency of ISI personnel and a position paper was produced [16]. In the position paper it was concluded that a study on the needs, experience, benefits and recommended approaches for maintaining the proficiency of ISI should be carried out. The study should answer the following questions:

- What similar schemes exist in the nuclear industry or other relevant industrial areas, where an individual is expected to maintain his proficiency, e.g. qualification of welders?
- What is the experience and lessons learned with existing schemes?
- What are the arguments in favor and against re-qualification of ISI personnel?
- What is the recommended common approach for future qualification of ISI personnel?

ENIQ will discuss the issue of maintaining proficiency of ISI personnel further and will launch a study with the aim of answering the above questions later this year.

2.2 Sub-area for Risk

Lessons learned from the application of RI-ISI to European NPP

SAR is currently in the process of finalizing a report on the lessons learned from the application of RI-ISI to European NPPs. It summarises the experience from RI-ISI programs of Finland, Spain and Sweden, where RI-ISI is commonly used (i.e. where RI-ISI is approved by the regulator), and the experience of pilot studies performed in Bulgaria, Lithuania and Romania. The report covers the experience from different types and designs, such as BWR (Asea-Atom, GE), PWR (Westinghouse), VVER, Candu and RBMK. The report is in the final editorial stage and will be published within the next months. The main conclusion from the RI-ISI programs is that they help to focus on most risk significant locations of the plants and thus lead to a reduction in ISI efforts. Also RI-ISI led to a reduction in doses of ISI personnel.

Update of the ENIQ Framework Document on RI-ISI

The ENIQ Framework Document on RI-ISI was firstly published in 2005 and the experience gained from RI-ISI programs since then prompted SAR members to update the document. The updated document also contains considerations on external events, which was one of the main drivers for updating the document. The new version of the ENIQ Framework Document on RI-ISI will be published later this year.

REDUCE

A month ago a number of SAR members launched a project on risk reduction through ISI called REDUCE. The main objective of the project is to evaluate the parameters that influence the risk reduction that can be achieved via ISI.

In the project the effect of alternative ISI strategies on the level of risk reduction will be investigated for different situations that are typical for European NPPs. The influence of key parameters will be systematically analysed by using structural reliability models, considering a range of components, materials, degradation mechanisms, loading conditions, NDT reliability (POD[4] curves) and inspection intervals. The final output of the project will be a document that supports utilities in assessing risk reduction when applying RI-ISI approaches. When entering long-term operation (LTO) the number of positions susceptible to fatigue is expected to increase when considering environmental effects and the document will cover issues of an ISI strategy for control of this specific degradation mechanism.

3. Summary

The main activities of ENIQ SAQ at the moment are the comprehensive study on the performance of computed and digital radiography (COMRAD), the transfer of inspection qualifications between countries (MUREC) and maintaining the proficiency of ISI personnel and linked to the latter the re-qualification of ISI personnel. Main activities of ENIQ SAR are the recently launched project on risk reduction through ISI and the update of the ENIQ Framework Document on RI-ISI. With its on-going and new activities ENIQ will maintain its role as one of the main contributors to today's global ISI qualification codes and guidelines.

References

[1] ENIQ technical report, "Final Report of the 1st ENIQ Pilot Study", ENIQ Report no. 20, EUR 19026 EN, 1999.

[2] ENIQ technical report, "Final Report of the 2nd ENIQ Pilot Study", ENIQ Report no. 27, EUR 22539 EN, 2006.

[3] ENIQ, "European Methodology for Qualification of Non-Destructive Testing – Issue 3", ENIQ Report no. 31, EUR 22906 EN, 2007.

[4] ENIQ, "European Framework document for Risk-Informed In-Service Inspection", ENIQ Report no. 23, EUR 21581 EN, 2005.

[5] "ENIQ RP1: Influential / Essential Parameters – Issue 2", ENIQ Report no. 24, EUR 21751 EN, 2005.

[6] "ENIQ RP2: Strategy and Recommended Contents for Technical Justifications – Issue 2", ENIQ Report no. 39, EUR 24111 EN, 2010.

[7] "ENIQ RP4: Recommended Contents for the Qualification Dossier", ENIQ Report no. 13, EUR 18685 EN, 1999.

[8] "ENIQ RP5: Guidelines for the Design of Test Pieces and Conduct of Test Piece Trials", ENIQ Report no. 42, EUR 24866 EN, 2011.

[9] "ENIQ RP6: The Use of Modelling in Inspection Qualification – Issue 2", ENIQ Report no. 45, EUR 24914 EN, 2011.

[10] "ENIQ RP7: Recommended General Requirements for a Body operating Qualification of Non-Destructive Tests", ENIQ Report no. 22, EUR 20395 EN, 2002.

[11] "ENIQ RP8: Qualification Levels and Approaches", ENIQ Report no. 25, EUR 21761 EN, 2005.

[12] "ENIQ RP9: Verification and Validation of Structural Reliability Models and associated Software to be used in Risk-Informed In-Service Inspection Programmes", ENIQ Report no. 30, EUR 22228 EN, 2007.

[13] "ENIQ RP10: Personnel Qualification", ENIQ Report no. 38, EUR 24112 EN, 2010.

[14] "ENIQ RP11: Guidance on Expert Panels in RI-ISI", ENIQ Report no. 34, EUR 22234 EN, 2008.

[4] POD = Probability of detection

[15] NUGENIA Association, “NUGENIA Global Vision Report”, 2015.

[16] ENIQ position paper “NDE Personnel Re-Qualification or a Need to Maintain Proficiency”, ENIQ report no. 49, 2015, *in press*.

Fukushima Daiichi muon imaging

Haruo Miyadera
Power and Industrial System R&D Center, Toshiba Corporation,
8 Shinsugita-cho, Isogo-ku, Yokohama 235-8523, Japan

E-mail address : haruo.miyadera@toshiba.co.jp

Japanese government announced cold-shutdown condition of the reactors at Fukushima Daiichi by the end of 2011, and mid- and long-term roadmap towards decommissioning has been drawn. However, little is known for the conditions of the cores because access to the reactors has been limited by the high radiation environment. The debris removal from the Unit 1 – 3 is planned to start as early as 2020, but the dismantlement is not easy without any realistic information of the damage to the cores, and the locations and amounts of the fuel debris.

Soon after the disaster of Fukushima Daiichi, several teams in the US and Japan proposed to apply muon transmission or scattering imagings to provide information of the Fukushima Daiichi reactors without accessing inside the reactor building. GEANT4 modeling studies of Fukushima Daiichi Unit 1 and 2 showed clear superiority of the muon scattering method over conventional transmission method. The scattering method was demonstrated with a research reactor, Toshiba Nuclear Critical Assembly (NCA), where a fuel assembly was imaged with 3-cm resolution.

The muon scattering imaging of Fukushima Daiichi was approved as a national project and is aiming at installing muon trackers to Unit 2 in FY15. A proposed plan includes installation of muon trackers on the 2nd floor (operation floor) of turbine building, and in front of the reactor building. Two 7m x 7m detectors are assembled at Toshiba and tested.

Keywords: Fukushima Daiichi, muon scattering, imaging, core damage, fuel debris

Inspection Qualification of a FMC/TFM Based UT System

R.L. ten Grotenhuis[1], Y. Verma[1], A. Hong[1], N. Saeed[1,2], E. Schumacher[4] , S. Bannouf[5] and M. Hetmanczuk[1,3]
[1]Ontario Power Generation, Inspection & Maintenance Division, Toronto, Canada
[2]University of Toronto, Division of Engineering Science, Toronto, Canada
[3]McMaster University, Mechanical Engineering Department, Hamilton, Canada
[4]EXTENDE Inc., Ballston Spa, USA
[5]EXTENDE S.A., Massy, France

E-mail address (corresponding author): ray.tengrotenhuis@opg.com

Abstract

The Matrix Inspection Technique (MIT) consists of the Full Matrix Capture (FMC) UT acquisition technique in combination with an automated analysis beamformer applying the Total Focusing Method (TFM) algorithm. The MIT system was developed by Ontario Power Generation (OPG) and deployed in several field inspection campaigns beginning in 2010 to the most recent work in spring 2015. During this time a series of enhancements have been implemented to improve overall system performance. Thus while the system has evolved, a sufficient body of operational experience (OPEX) has been obtained to enable inspection qualification efforts to proceed.

The Canadian Nuclear Safety Commission (CNSC) is the regulatory authority for all nuclear facilities operating in Canada. The CNSC has mandated all nuclear utilities to qualify their inspection systems as a condition of their operating license. The European Network for Inspection Qualification (ENIQ) methodology has been adopted as the basis for inspection qualification programmes. An organization known as the CANDU Inspection Qualification Bureau (CIQB) has been tasked by the CNSC with programme oversight as well as evaluation of the licensee's submissions. The ENIQ methodology tailors the scope of the Technical Justification (TJ) effort based upon the degree of novelty of the inspection system and the severity of the consequence of failure of the component inspected. MIT's use of automated FMC and automated TFM for inspection is unprecedented in any industry. Furthermore the components inspected are part of the nuclear pressure boundary, failure of which could result in a single channel Loss of Coolant Accident (LOCA) and a potential release of activated products. Thus in both respects the MIT system is obligated to undergo the complete process defined by ENIQ. Major sections of the TJ will address simulation/modelling, parametric studies, experimental studies and examination of ex-service samples.

This paper summarizes the application of the ENIQ process to the MIT system as well as the progress to date in preparation of the Technical Justification.

Keywords: Inspection Qualification, FMC, TFM

1. Introduction

Over several decades of commercial operation most CANDU nuclear units have experienced varying degrees of Flow Accelerated Corrosion (FAC) in the carbon steel piping components of the Primary Heat Transport system, see Figure 1. Thinning rates were found to vary in a range of 0.01mm/EFPY to 0.14 mm/EFPY where EFPY stands for Effective Full Power Years. In extreme cases the FAC progressed to the stage where replacement of the components was necessary in order to maintain pressure boundary thickness margins. Regions prone to acute attack are the surfaces under and immediately downstream from the weld as shown in Figure **2**. Fitting geometry, access, as fabricated weld caps combined with the Inspection Specification requirements make this inspection particularly challenging. At Ontario Power Generation an inspection system was developed that applied the FMC data acquisition technique with a proprietary version of the TFM beam former, [1] and [2]. The system, called the Matrix Inspection Technique or MIT, has been deployed since mid-2010 and in four separate inspection campaigns has inspected 83 locations comprising not fewer than 115 welds.

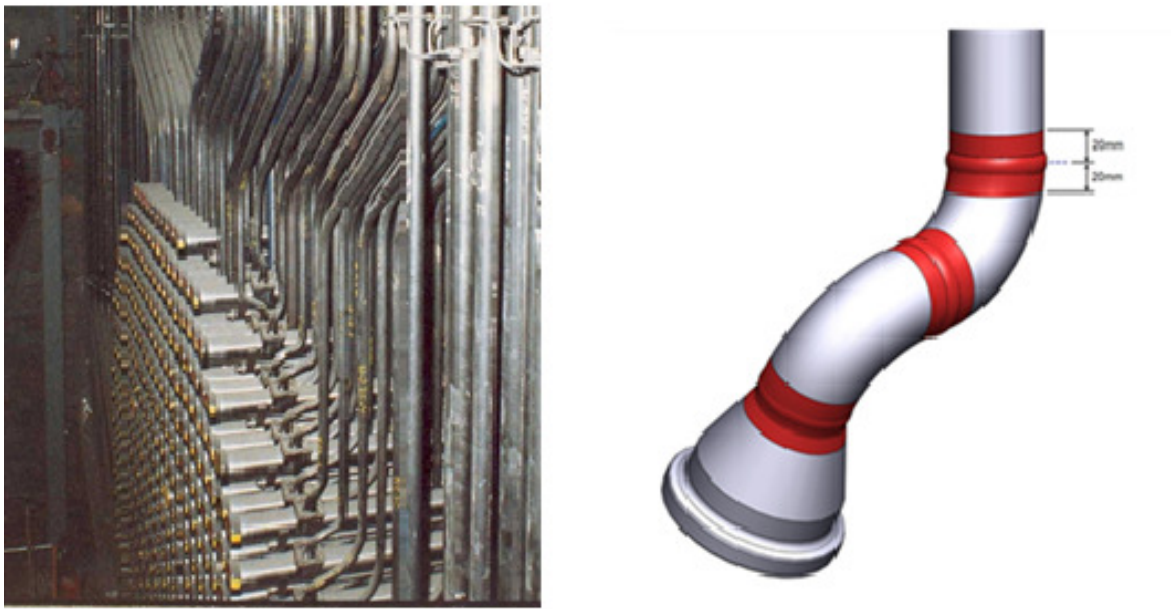

Figure 1 Portion of the reactor face with associated carbon steel piping - left, isometric of piping spool piece with inspection zones - right.

Figure 2 Examples of localized FAC located at weld root.

Typical profiles for fitting to fitting welds and the 3D evolution are presented in Figure 3. The results have generally exceeded expectations with respect to coverage and accuracy particularly in the volume of the weld material under the weld cap. The MIT system represents the first large scale application of this method in the power generation industry. Understandably there have been changes to the system reflecting the OPEX obtained in the field. The changes are directed toward three general objectives:

- enhancement of system capabilities,
- remediation of system deficiencies,
- efficiency/productivity improvements

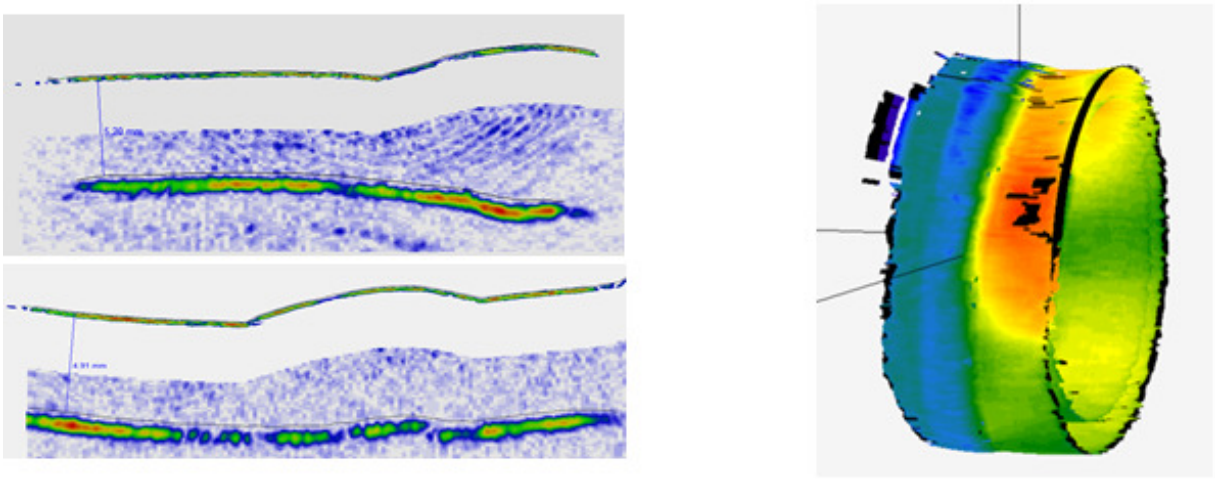

Figure 3 Typical axial cross sections through the weld - left, 3D colour coded thickness map - right.

Facets of the MIT system that were identified for modification were: manipulators, analysis software, acquisition software and instrumentation. Many of the desired changes have been implemented to date. Some enhancements to the manipulators and analysis code remain outstanding and are to be addressed within the next year. The ultrasonic parameters and underlying methodology on the other hand were deemed to be apposite in their initial form adopted.

2. Inspection Qualification

In Canada, the CNSC has mandated licensees to implement a qualification programme for inspections performed. The licensees in concert with the CNSC have adopted the ENIQ qualification regime under the administration of the CIQB. At this juncture in the MIT system development it is appropriate to begin the preparation of the TJ document based on the body of inspection OPEX established. High level objectives for the TJ of the MIT system may be identified as:

- Demonstration of performance meeting the Inspection Specification (IS) [4] over the target volume for the range of inspection geometries encountered
- Identification of influential and essential variables as well and factors that ultimately manifest in unit time or distance error
- Provide evidence that the acquisition system and analysis software are capable of yielding consistent results when applied with the established procedures.

Now many readers will be familiar with the ENIQ recommended structure of the TJ in general as found in **Error! Reference source not found.**. The ENIQ TJ guidelines allow for a simplified approach if the conditions of a reasonably well established inspection technique are coupled with a relatively low consequence as a result of component failure. In the case of the MIT system the technology is both novel and relatively complex. Furthermore, the consequence of a failure of the subject component is potentially a single channel LOCA. Clearly then, in light both of these factors, the MIT TJ requires the full rigour as defined by ENIQ.

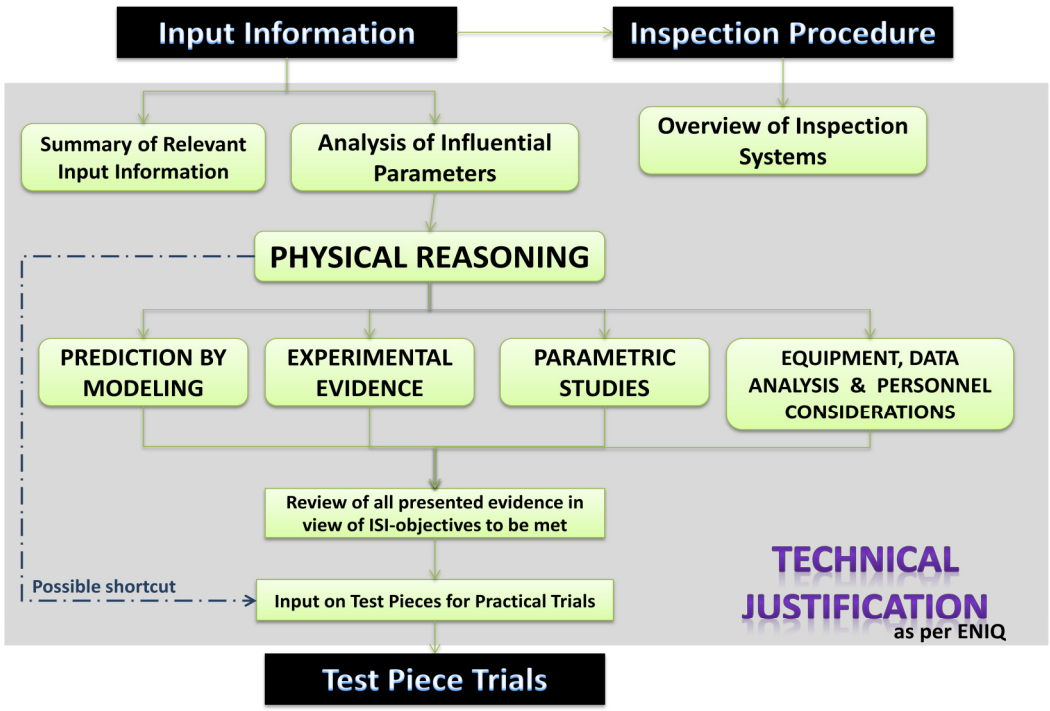

Figure 4 ENIQ recommended structure of the Technical Justification as adopted by CIQB.

With reference to **Error! Reference source not found.**, the full format TJ introduces additional avenues for investigation beyond that of the basic structure. This includes: Prediction by Modelling, Experimental Evidence, Parametric Studies and Equipment, Data Analysis & Personnel Considerations. The section, Analysis of Influential Parameters, remains at the core of the MIT TJ. The MIT system has few analogues to conventional UT approaches that would be applicable as a reference. Hence the Physical Reasoning portion of the MIT TJ has a somewhat reduced significance relative to the corresponding element in TJs for standard techniques. The principal focus of the MIT TJ then is to direct efforts to the four additional areas introduced in the extended TJ structure as to support the Influential Parameters section.

Prediction by Modelling and Experimental Evidence sections are treated as complementary avenues of investigation within the MIT TJ. The transducer beam characteristics are modelled using EXTENDE's CIVA application and then confirmed via an immersion test rig, see Figure 5. The purpose is to verify the beam characteristics and then establish the statistical variation for the series of essential variables that define the transducer performance. Simulations of the UT responses for the range of Test Geometries are created with CIVA and then will be verified in the immersion scanning apparatus. The simulations generate FMC data sets containing idealized UT responses. These data sets once converted into the appropriate format, are processed by the MIT automated analysis software. The goal of the exercise is to demonstrate accurate reconstruction of the test geometry. Idealized data sets are used in the Parametric Study to isolate the effects of parameter variation from those introduced by experimental error.

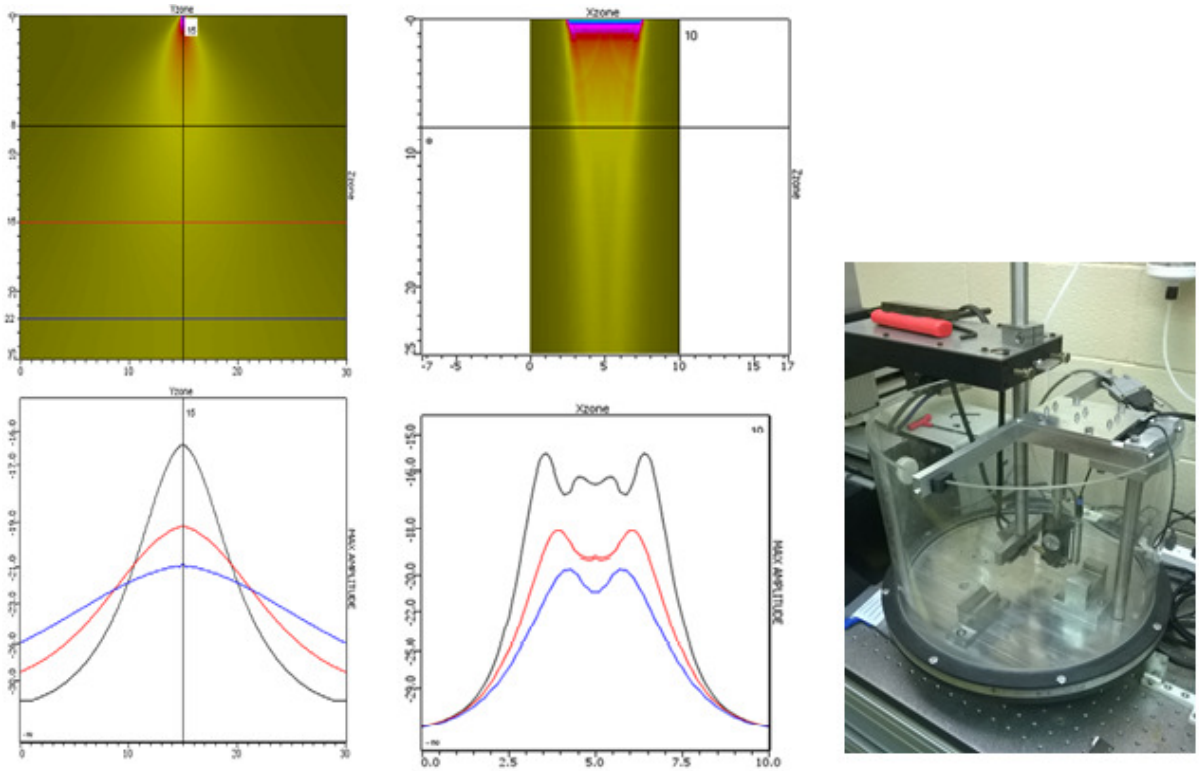

Figure 5 Beam modelling with CIVA, active plane - left, passive plane – centre. Relative amplitudes at 8, 15 and 22 mm water column denoted as black, red and blue profiles respectively. Five axis immersion tank - right.

2.1 Test Geometry Design

The function of the test geometry series is to facilitate demonstration of adequate inspection coverage, accuracy and repeatability of the inspection. These samples are a series of controlled surfaces that bound the range of inspection geometries encountered. Five basic samples are simulated: planar, plano-convex, plano-concave, double convex or dome, convex-concave or saddle. A concave-concave sample would be required if inspection from the interior of the specimen were contemplated. Since the application is thickness monitoring of fitting to fitting welds, a series of contours for the interior surface would seem to be an obvious choice. However this choice would have required an inordinate number of samples to address the possible configuration permutations. Conventional reflectors, specifically side drilled holes and EDM notches were used instead. These reflectors are widely accepted, easier to control to the desired accuracy, and less expensive to produce. Use of samples with conventional reflectors provides an opportunity to evaluate volumetric inspection performance should this type of inspection become necessary. The permutations of geometry, water path distance to sample with the number of target reflectors resulted in 192 individual simulations to be performed. Examples of the Test Geometries are given in Figure 6.

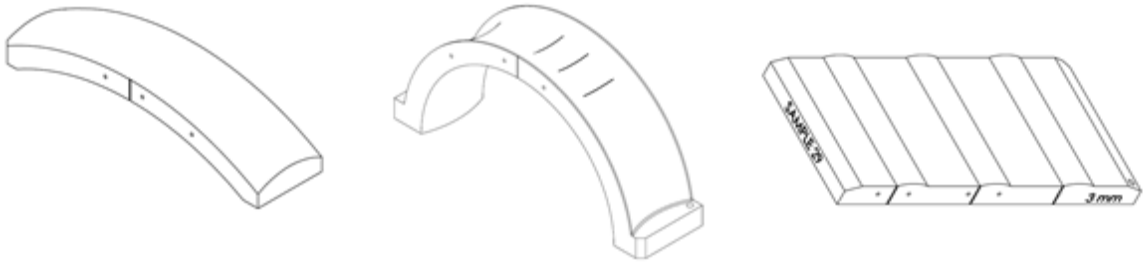

Figure 6 Test Geometry Samples: left - dome, centre - saddle, right - weld cap

Initial attempts at machining controlled surfaces with characteristics representative of weld pool ripple did not meet with success. The characteristic response from the machined ripples did not match that of ex-service samples. Furthermore the cost to manufacture these samples was substantial relative to the benefits obtained. Rather than pursue manufacture of idealized welds it was decided to fabricate welds according to the original weld procedure, acquire and process the FMC data sets and then destructively analyse the welds.

2.2 FMC Simulations

The Inspection Specification requires a precision of measurement of 0.03 mm with an accuracy of +/- 0.06 mm. As a consequence a higher degree of resolution is required for both simulations and experimentation in order to observe and assess the contribution of individual 3rd order effects. Recall application of the FMC acquisition method results in dramatically larger data sets compared with other UT methods. With respect to the MIT application, the data sets are roughly 2 orders of magnitude larger than the corresponding linear electronic B scan sets. Commensurate simulation of FMC data sets consumes markedly greater computation resource. Careful consideration must then be given to the design of the simulation and the input parameters. The simulation parameters were optimized following several test runs and with consultation of the CIVA specialists at EXTENDE. Factors considered were: Level of Accuracy, Computation mode, Number of modes and reflections calculated, and Sampling frequency, see reference [6]. Though CIVA can simulate basic weld configurations in plate or pipe welds, complex geometries such as dome, saddle and weld cap do not pre-exist in CIVA and must be imported as 3D CAD models. Discrepancies between surface of the specimen defined by the original 3D CAD model and the surface automatically meshed by CIVA do influence simulation accuracy. In CIVA, the mesh accuracy corresponds to the maximum discrepancy between the surface of the specimen defined by the CAD file and the surface meshed into triangles. Decreasing the size of the mesh accuracy reduces the discrepancy but requires more computation time. Typical responses to reflectors in; weld, dome and saddle geometries are found in Figures 7, 8 and 9 respectively.

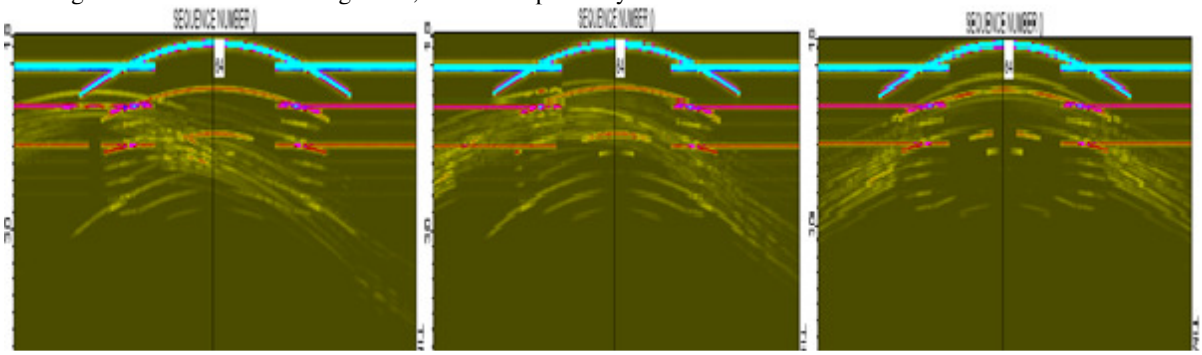

Figure 7 Simulated response to 1 mm diameter SDH under weld cap, main diagonal of the FMC data array. Adjacent cap- left, under weld toe – centre, mid weld – right.

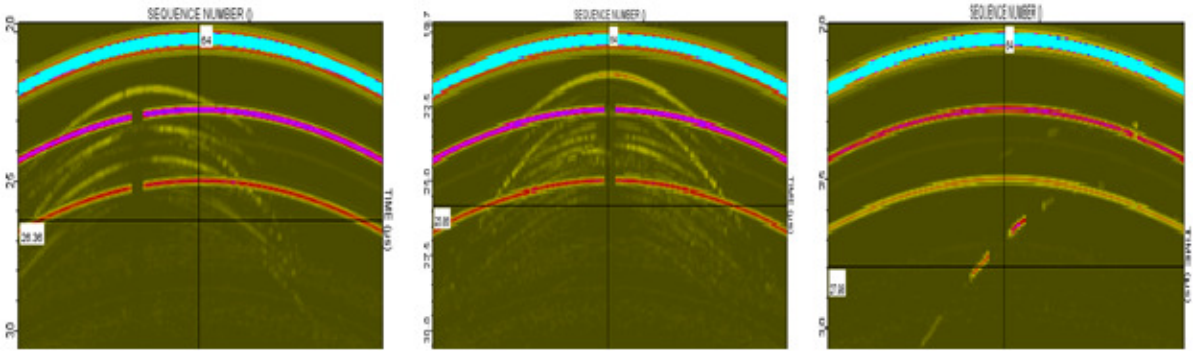

Figure 8 Simulated response to 1 mm diameter SDH in the dome geometry, main diagonal of the FMC data array. 10 mm from centreline - left, mid dome – centre, 1 mm EDM notch – right.

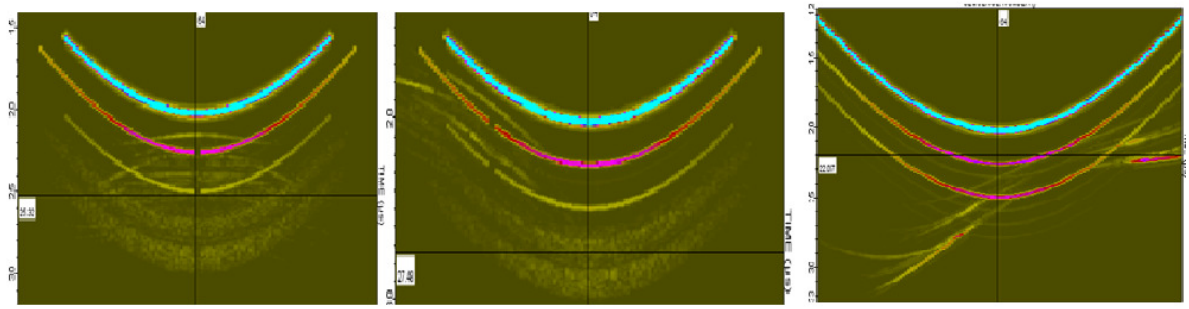

Figure 9 Simulated response to 1 mm SDH in saddle geometry, main diagonal of FMC data array. Centre saddle – left, 15 mm offset from centre line – centre, and 1 mm EDM notch 5 mm offset – right.

There are slight differences between the CIVA treatment of waveforms and the conventions adopted for inspection with MIT. The most realistic signal type for the transducer excitation waveform built-in CIVA is a Gaussian envelope, which departs from that of the actual UT signals. As a consequence there are slight variations between simulated and experimental results. The convention used within CIVA to define the distance to the target is the peak of the simulated waveform envelope, whereas MIT defines the onset of the waveform envelope as the distance to the target. These differences, while subtle, must be accommodated when comparing simulation results with experimental results.

The simulations were run on a dual processor, 6 core PC workstation operating in batch file mode. Computation times ranged from a low of 4 hours to a maximum of 133 hours. The median computation time was 48.1 hours with over 9000 hours required to complete all simulations. The entire effort was performed over a period of 15 months. Figure 10 illustrates the computation times for a range of simulations performed.

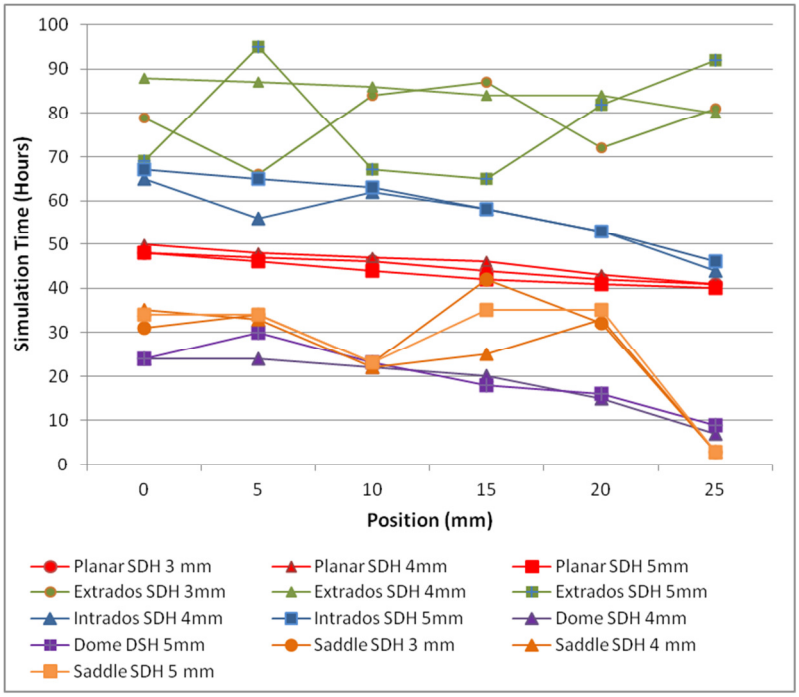

Figure 10 Simulation times versus geometry and reflector location.

2.3 Experimental Evidence

Verification of the UT beam characteristics, see Figure **11**, and test geometry responses are two fundamental components of the Experimental Evidence. But in addition to these, the experimental evidence also includes results from controlled samples such as reference blocks, fabricated spool pieces and ex-service components. When MIT was first commissioned, the validity of the results was established via a performance demonstration exercise on reference blocks and ex-service samples. The results obtained on the blocks were accurate to within 0.01 mm and on ex-service samples to within +/- 0.02 mm. Going forward, once all the desired changes are implemented, the Experimental Evidence will expand upon this base to improve the statistical significance of the results.

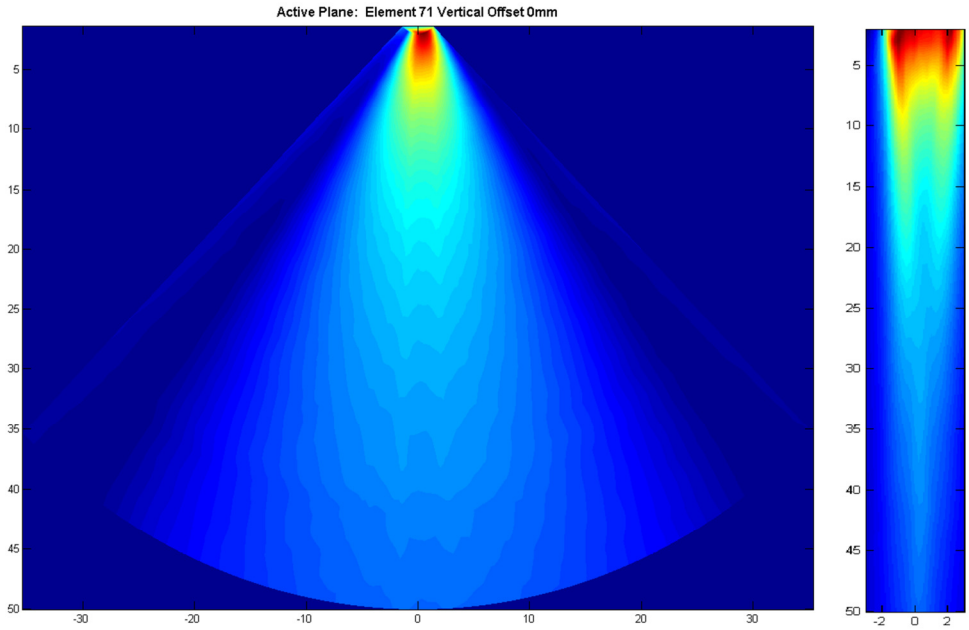

Figure 11 Element sound field plot in water, right - active plane, left - passive plane.

2.4 Parametric Study

The Parametric Study portion of the TJ is divided into three main sections. One section addresses the essential parameters underpinning the TFM analysis code; the second examines the essential parameters of the UT data acquisition system, while the third examines the essential parameters introduced by factors related to materials, geometry, inspection conditions, and manipulator performance. At the current stage a cursory effort has been directed to the Parametric Study, however even this limited effort has already identified desirable changes to the MIT system. Some examples are:

1. Increasing the reconstructed sampling rate from 100 MHz to 200 MHZ enhanced with linear interpolation.
2. Compensation for temperature based velocity variation in the carbon steel media.
3. Correction for transducer element to element delay variation.

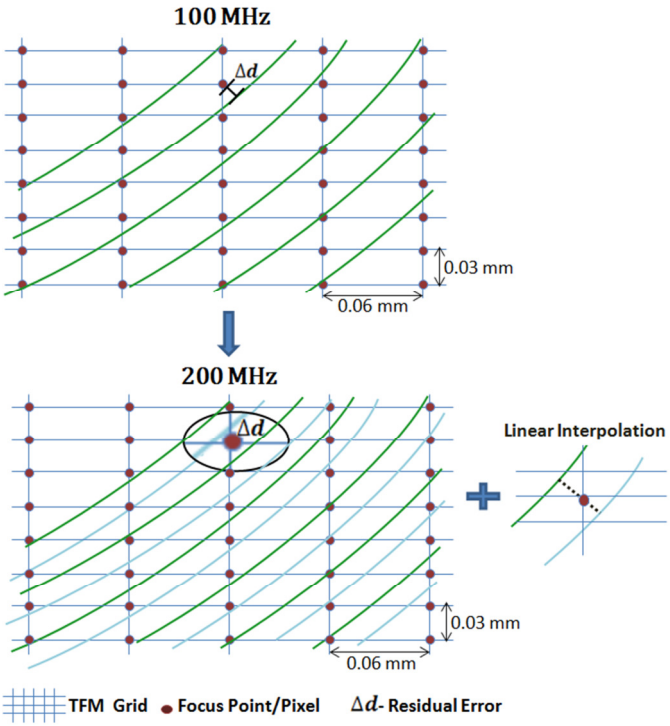

Figure 12 Enhanced analytic signal resolution - up sampling to 200 MHz combined with linear interpolation.

When reconstructing the interior volume TFM image, for any given focal point P, the time index of the analytic signal will most often not correspond precisely to the point imaged. The magnitude of the error is a function of the TFM grid spacing and the sampling frequency. This intrinsic error can be reduced by up-sampling to 200 MHz, see Figure **12**. Further improvement to the estimate of the analytic signal is obtained via linear interpolation. For a focal point P the worst case timing error using this strategy is typically on the order of 1 ns.

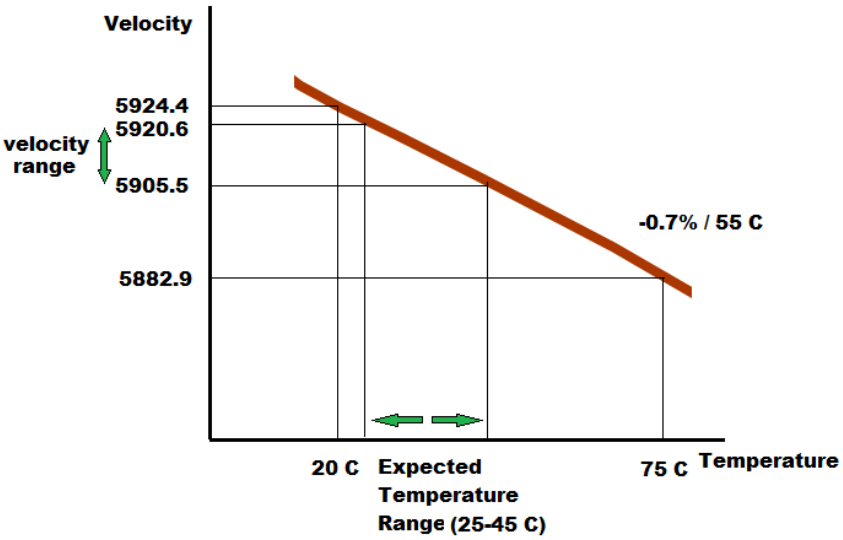

Figure 13 Velocity of ASME SA106 Gr. B as a function of temperature.

Error can be introduced under the assumption that velocity remains fixed. Rather, velocity of ASME SA106 Gr B is a function of temperature as shown in Figure 13. For a mean path to the interior surface of 15 mm given a nominal aperture, the resultant timing error can be as large as 6.47 ns or equivalently 19.1 µm. A linear velocity correction with a coefficient of -0.7% per 55 C is applied to reduce the error, see reference [5].

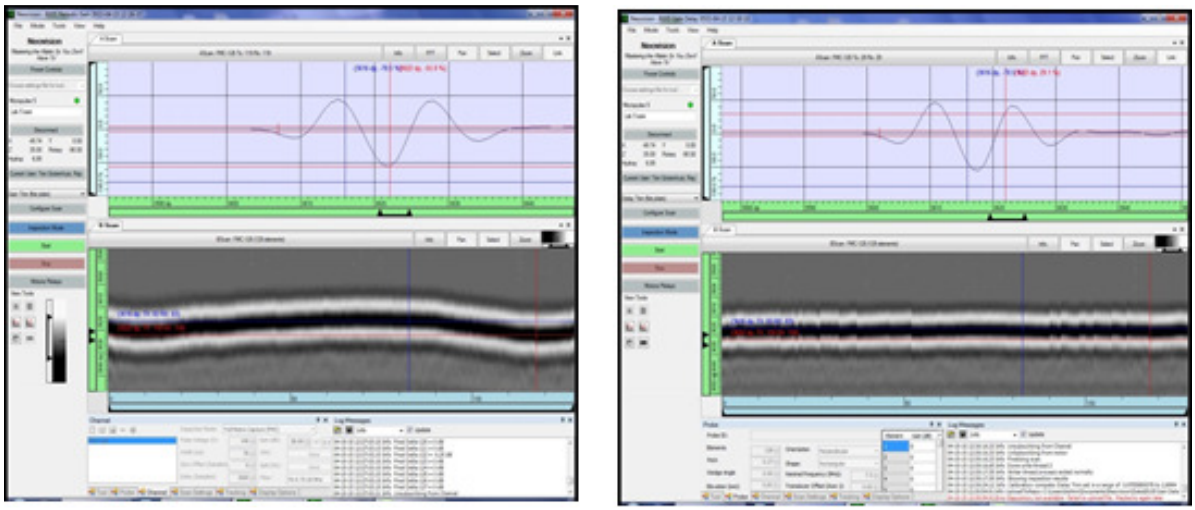

Figure 14 Transducer element delay variation, left - as found, right - corrected.

The distribution of timing errors associated with variation in transducer element delay is unique to each transducer. A statistical approach is necessary to quantify this effect. An example is shown in Figure **14**. Observations to date report a nominal range of +/- 35 ns with a standard deviation of 14 ns. Compensation of this variation is performed by measuring arrival of the peak of the signal envelope. Individual element delay compensations are calculated and applied as needed during the TFM imaging operations. Applying compensation reduces the timing error to +/- 5 ns with a standard deviation of 2 ns.

Further changes arising from Parametric Study work are anticipated. As the changes are identified they will be incorporated into the MIT system. Near term activities will include: procurement of Test Geometry samples, completion of the experimentation on the Test Geometry samples and initiation of work on the Equipment, Data Analysis & Personnel Considerations document.

3. Conclusions and Summary

The Canadian nuclear power industry has adopted the ENIQ strategy for inspection qualification. Since its introduction in 2010, the MIT system has developed a body of inspection OPEX over the course of four inspection campaigns. The nature of the inspection coupled with the characteristics of the MIT system mandates the use of the enhanced format ENIQ TJ. Several changes have been made to the system, however many the fundamental aspects of the original approach remain intact.

The TJ for the MIT system is in progress. A series of bounding geometry samples incorporating standard reflectors have been developed. UT beam characteristics have been evaluated via modelling with CIVA, confirmation of which is provided by direct measurement. Inspection coverage has been demonstrated via simulation. Judicious selection of parameters (such as sampling frequency, computation mode, etc.) is required for balancing both simulation accuracy and efficiency. FMC data sets generated using CIVA are exported to the MIT analysis software to support parametric study of the analysis code. Initial efforts in the Parametric study have identified desirable improvements. Going forward further improvements to the MIT analysis code are anticipated. The current schedule projects the completion date of the TJ in mid-2016.

References

[1] ten Grotenhuis R, Hong A and Sakuta A, "Inspection of complex geometries using the full matrix capture (FMC) method", 9th Int Conf on NDE in Relation to Structural Integrity for Nuclear and Pressurized Components, Seattle WA, USA, 2012.

[2] ten Grotenhuis R and Hong A, "Imaging the weld volume via the total focus method", 9th Int Conf on NDE in Relation to Structural Integrity for Nuclear and Pressurized Components, Seattle WA, USA, 2012.

[3] CANDU Inspection Qualification Bureau, "Instructions for the Contents of a Technical Justification" , Toronto, Ontario Canada August 28, 2008

[4] CANDU OWNER'S GROUP, "Feeder Pipes Inspection Specification", COG-JP-4059-V03 Rev3, Toronto, Ontario, Canada March 2011

[5] Biagiotti S, "Effect of Temperature on Ultrasonic Velocity in Steel", NACE Corrosion '97, New Orleans LA, USA 1997

[6] "CIVA 2015 (V11.1) User Manual" by CEA List

The EPR's NDE program: a technical and industrial challenge.

Pascal BLIN
EDF Nuclear Engineering Division, Ceidre, 2 rue Ampère, 93206 ST DENIS, FRANCE

pascal.blin@edf.fr

The "Flamanville 3" EPR™ unit is the first one to be subjected to the French Ministerial Orders of the 10th November 1999 and of the 13th December 2005 from the design phase. According to these orders, the non destructive examination (NDE) planned for the in service inspection (ISI) and for the pre service inspection (PSI) must be operational with a compulsory formal qualification. The PSI is a complete inspection of the main primary and secondary systems. The PSI's objective is to perform before the first core loading all the NDE planned for the future ISI in the same conditions, in order to have a reliable reference for the detection or for the evaluation of the possible damages during the ISI. The program consists of the development and the qualification of the NDE compatible with this new generation reactor's challenges. This program, composed of 40 NDE applications is today achieved. At present, EDF is preparing the PSI implementation planned from 2015 until 2016.
The paper is about:
- the main EPR's objectives and the approach to set up the ISI program,
- the mainlines of the ISI program,
- a reminder of the NDE qualification process,
- the exchanges with the design, the manufacturing and the regulatories,
- a presentation of the main NDE: MCL welds (UT), CRDM housing welds (UT & ET), RPV (UT)..
- the first feed-back (difficulties, good practises),
- the organization for the PSI,
- the future prospects.

CONSIDERATION OF OPERATORS IN THE QUALIFICATIONS OF NON DESTRUCTIVE TESTING SYSTEMS

P. Jardet[1], V. Didier[1] and P. Huet[1]

[1]EDF Qualification Body, France

Abstract

Nowadays NDE qualification is required for in service inspections of nuclear pressurized components in most countries where nuclear power plants are being exploited. The practices notably differ as regards the taking into account of the operators.

The aim of this communication is to:

- Present the different approaches to take into account the operators in the qualifications.

- Briefly describe the context and qualification process established by the Qualification Commission of EDF.

- Develop the approach taken by the Qualification Commission of EDF to take into account the competence of operators during the review of the dossiers.

Keywords: Qualification, Operator, Competence, In-Service Inspection.

1. Different Qualification Approaches – Taking operators into account

Providing a performance guarantee for the tests carried out on in-service surveillance of components important for security or safety (see example in Figure 1) is an expectation common to various industries in many countries. As far as the nuclear industry is concerned, the question on NDE reliability was asked in the mid-sixties, in the framework of an American committee involved in the behaviour of reactor pressure vessels (specifically for ultrasonic testing): the Pressure Vessel Research Committee (PVRC). International programs based on blind trials aimed at comparing the results of the various procedures and teams operating worldwide were therefore launched.

The variability of the results obtained led to the establishment of performance demonstration methodologies and to gradually taking into account the obligation to qualify in-service inspections in the regulations of the various countries.

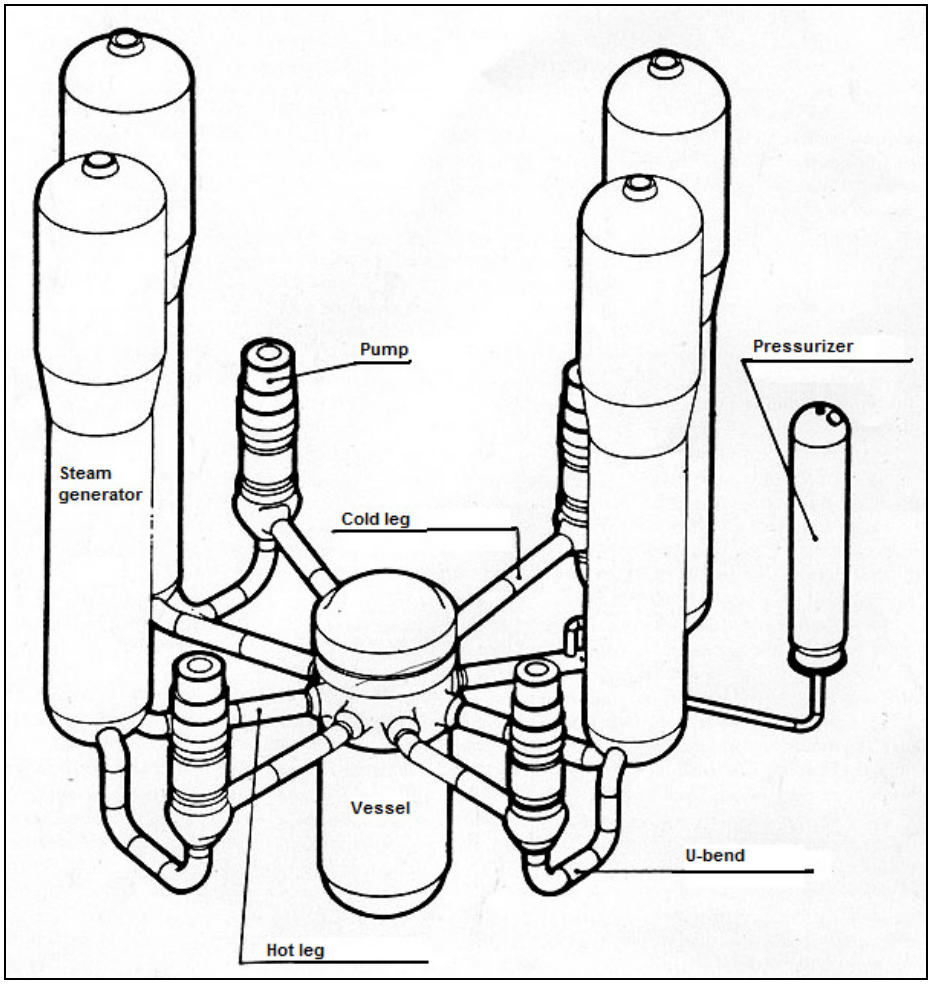

Figure 1. Examples of primary circuit components in the EDF fleet, inspected with NDE systems submitted to qualification

The references dedicated to qualification or performance demonstration of NDE systems which are applied in Europe and in the United States for the in-service inspection of nuclear components are the following (see their distribution in figure 2):

- the ASME Code, section XI appendix VIII [1],
- the European methodology by ENIQ (European Network for Inspection Qualification) [2],
- the RSE-M code, appendix 4.3 [3],
- the IAEA methodology for VVER type reactors [4].

In some countries, article 14 in the ASME code section V [5] is used complementarily to the references listed above.

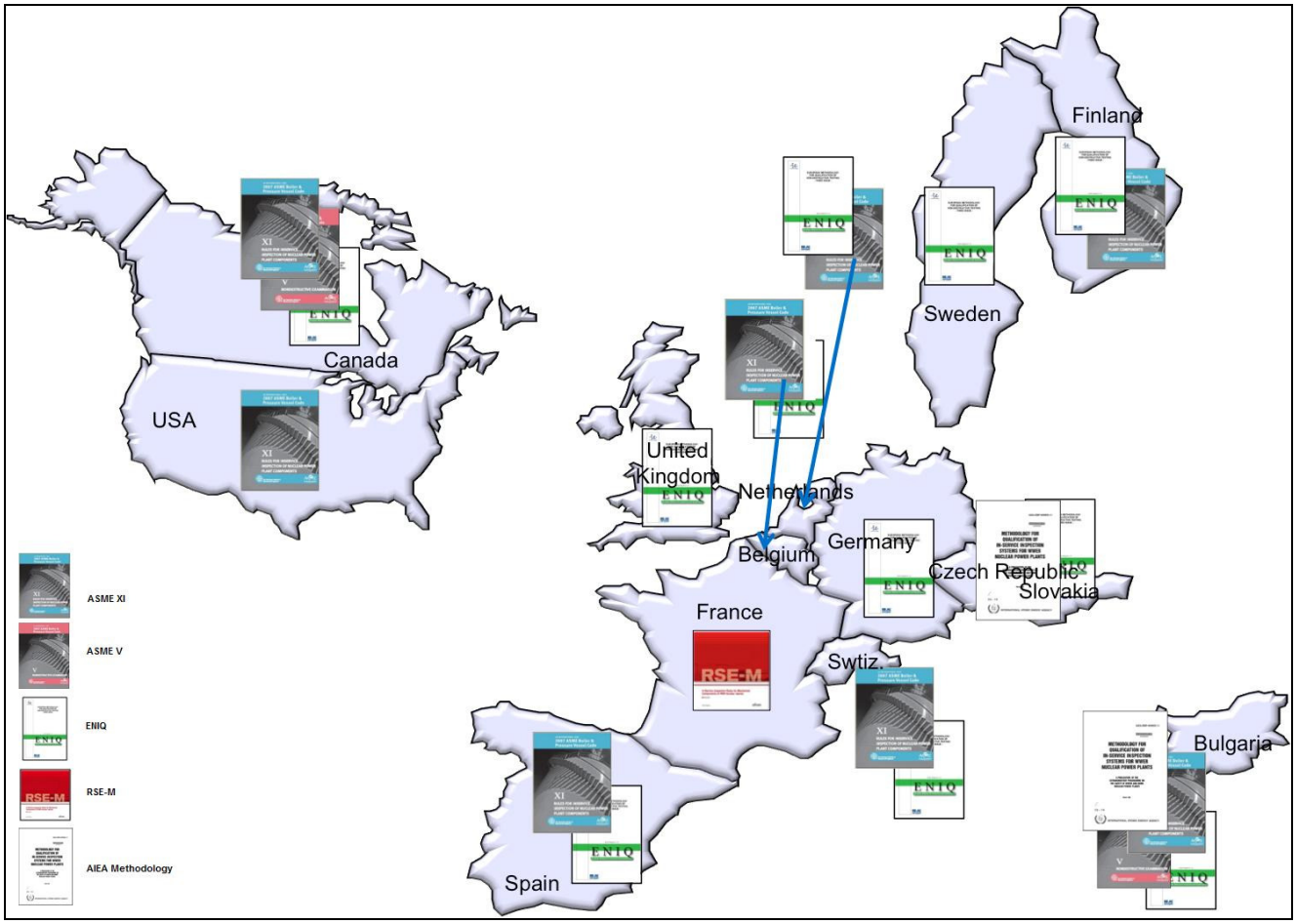

Figure 2. Qualification references used in Europe and North America

In the following sections, we shall limit our analysis to the Appendix VIII of section XI in the ASME code, the ENIQ methodology, and the appendix 4.3 in the R-SEM code. Indeed the IAEA methodology established in the 90s to consolidate the safety of VVER plants built in Eastern Europe is directly derived from the ENIQ methodology. As for article 14 in the ASME V, not specifically dedicated to nuclear components, it is used in some countries complementarily to section XI in the ASME XI.

A comparison between the main elements in the three references is given in Table 1.

When specifically comparing the dispositions for taking into account operators, then significant differences exist between the three qualification references.

Appendix VIII of ASME XI is essentially based on blind trials on blocks featuring artificial defects. Operators' qualification is almost not separated from the NDE system qualification.

The ENIQ methodology clearly separates the system qualification (NDE equipment and procedure), based on technical justifications complemented or not by open trials (defects with characteristics known by the operators), from personnel qualification, which, if requested or required, is performed through blind trials (defects in mock-ups are not known by the operators, the comparison between test results and defects characteristics is carried out by a specific organisation).

Finally, the RSE-M, rather similar to the ENIQ methodology as far as system qualification is concerned (technical justifications, open trials on realistic mock-ups…), does not request blind trials to qualify the personnel but prescribes that the operators expected competencies be formalised and justified as well as the dispositions taken to reach them and verify them. The complete file is submitted to a qualification body.

Items	ASME XI, Appendix VIII	ENIQ Methodology	RSE-M Appendix 4.3
Scope	Ultrasonic examination for crack detection and sizing (mainly fatigue cracks)	Any inspection (any method) enabling detection, sizing and location of a specified defect.	Any inspection (any method) enabling detection, sizing and location of a specified defect, or the surveillance for in-depth defence when no defect is postulated
Input data	- Component type - Examination procedure -Description of UT equipment.	- qualification objectives (what shall be demonstrated) - precise description of the components to be inspected. - size, orientation, location and morphology of the defects to be detected/sized	- inspection objectives - precise description of the components to be inspected. - size, orientation, location and morphology of the defects to be detected/sized - or conventional threshold to be applied (defence in depth)
Technical Justifications (TJ)	Not required	Recommended, TJs are based on: - results of tests on blocks or mock-ups - engineering reasoning - elements of feedback from experience - elements from previous qualifications - modelling results - laboratory studies -…	Required, separating the NDE technique, and the in-situ implementation. TJs are based on: - results of tests on blocks or mock-ups - engineering reasoning - elements of feedback from experience - elements from previous qualifications - modelling results - laboratory studies -…
Mock-ups, test blocks; **Associated trials**	Blind trials are required. The test blocks must fulfil precise specifications. (dimensions, defect type: crack, semi-elliptic notch …), and number of defects per size category. Acceptance criteria are defined in terms of minimum number of defects to be detected, maximum number of false calls and RMS error on height measurement.	It is found preferable to perform open trials for the qualification of the procedure and the equipment and blind trials for personnel qualification. Mock-ups are intended to be representative of the components but the use of simpler mock-ups is also accepted (extrapolation shall then be justified).	Open trials are required for NDE systems where searched defects are specified. The number and type of defects in the test mock-ups is justified in a case-by-case mode, coherent with the TJs. Trial acceptance criteria are also defined in a case-by-case mode coherent with TJs.
NDE Equipment, procedure qualification	NDE equipment, procedure and personnel are qualified	Procedure and NDE equipment may be qualified by TJ, open and/or blind trials.	Required
Personnel Qualification	See above.	If required, then a combination of the following : - certification according to a national NDE certification system - theoretical exam and/or open trial - blind trial	Not required. The procedure shall specify whether a specific training or qualification is expected. In the latter case, the qualification content is documented (training, test…).
Qualification Body	Not specified	Required : independent, third party, internal or ad-hoc	Required, organisation in conformity with ISO 17020

Table 2. Comparison between ASME XI Appendix VIII, ENIQ Methodology and RSE-M appendix 4.3 references

2. Qualification Process in place at EDF- Role of the Qualification Commission Section

EDF, a pressurised water reactor Utility, is bound as such to obey the 10 November 1999 order [6], which defines the expectations as far as NDE system qualification is concerned. As a reminder:

- obligation to qualify NDE systems prior to their implementation,
- qualification consists in the demonstration that inspection performance is sufficient to reach the expected objectives when the degradation mode is presumed or established, or to specify the performance in all other cases.
- qualifications shall be awarded by a competent independent authority, accredited by COFRAC or equivalent, chosen by the Utility,
- NDE operators implementing those systems shall be certified by an independent organisation.

Note: the application letter of the order stipulates that qualification shall « specify how the specific competency of operators is verified for the operation submitted to qualification».

The Commission, internal organization accredited by COFRAC, consisting of a college of experts, is the body chosen by EDF to award qualification of NDE systems in the framework of the compliance with the 10 November 1999 order.

Several actors are involved in the qualification process (see Figure 3):

- the Utility, defines the objectives in terms of performance requirements,
- the Instruction organisation to which the utility has delegated the project management for the design and constitution of the qualification file, establishes a checking form specifying the performance and presents elements of its demonstration (gathered in a qualification synthesis) to the Commission,
- the Contractor, who designs and develops the NDE system and establishes the elements of the qualification file, assists the Instruction organisation during the presentations to the Commission.

The Commission testifies the qualification of the NDE systems by examining the files submitted to it. The files brought before the Commission are in conformity with qualifications according to appendix 4.3 of the RSE-M code.

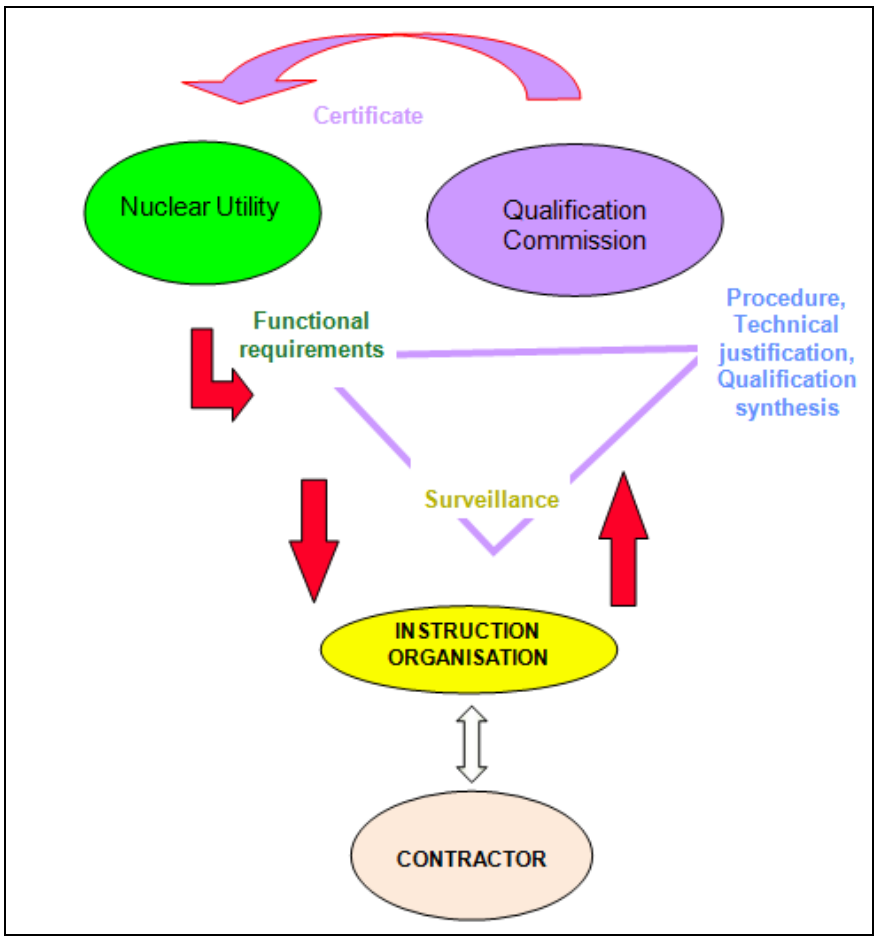

Figure 3: EDF qualification process, links between parties

3. Approach chosen by EDF's qualification Commission for taking operators into account.

The Commission examines the conformity of a file in three steps in connection with the qualification process:

- the first step occurs at the stage of the qualification approach and of the design of test blocks and mock-ups,
- the second one, prior to the performance of qualification trials,
- the third and last one, once the trials have been carried out and the elements of the file are gathered.

At each of these steps, the Commission gives an approval or formulates reservations or a refusal. The third step ratifies the award of the qualification.

Elements concerning the operators are examined at each step.

3.1 Examination of the qualification approach and of the design of test blocks and mock-ups Subsection

At this stage, the Commission assesses that the defects which will be in a block are appropriate for the performance to be demonstrated. Defects shall be representative of the investigated degradation modes and the physical phenomenon being exploited. Concerning more specifically operators, the Commission verifies that the difficulties in accessing the area to be examined (see the example in Figure 4) have actually been taken into account in the actions planned (qualification approach) and in the test blocks. It must be stressed that this notion of accessibility and neighbourhood constraints has a most significant impact when the inspection is carried out manually (probe scanning movement, source and film positioning more or less difficult ….). For automated inspections, these considerations essentially influence the design of robotic tools. However the set-up and steering of a manipulator generally requires adequate competencies from the operators.

Figure 4. Example of manual UT test performed in a rather awkward position

Figure 5. Example of robot installation for automated UT on the pressurizer surge line

3.2 Examination prior to the performance of the tests

When presenting qualification trials, all the equipment (instrument, probe, manipulator…), the software and the inspection procedure are defined and settled (the inspection procedure shall specify the operators' qualifications required for its implementation). The constitution of the inspection team is also defined. The qualification trials are aimed at carrying out all the phases of the inspection procedure on blocks with realistic defects and to verify the achievement of the assumed performance.

The Commission makes sure that inspection conditions are actually representative of the environmental constraints in the real situation as far as obstacles, nearby walls and inspection zone location are concerned. In the case of manual NDE, the Commission sees that inspection in the most unfavourable positions (for example in UT, testing in lower position, close to the ground….) be performed. The Commission is led to ask the trial supervisors to specifically report that the inspection is operable and to point out any specific skill needed for a correct inspection.

3.3 Examination at final stage

At final stage and complementarily to the examination before tests, the Commission makes sure that the prescriptions in the inspection procedure concerning the qualification of operators are sufficient. In the case of manual NDE, a certification in accordance with ISO 9712 may be enough. However, complements are sometimes indispensable due to the specificity of the inspection. It is frequently the case for automated inspections which require on the one hand a specific know-how for the installation of the manipulator on the component (see illustration in figure 5) and on the other hand, the control of signal analysis software and the associated analysis rules, (examples of automated UT and ET inspection signals are shown in figure 6 and 7). The Commission then examines the pedagogic files including the specific training syllabi and the conditions for the delivery of a qualification for such or such position in the inspection team.

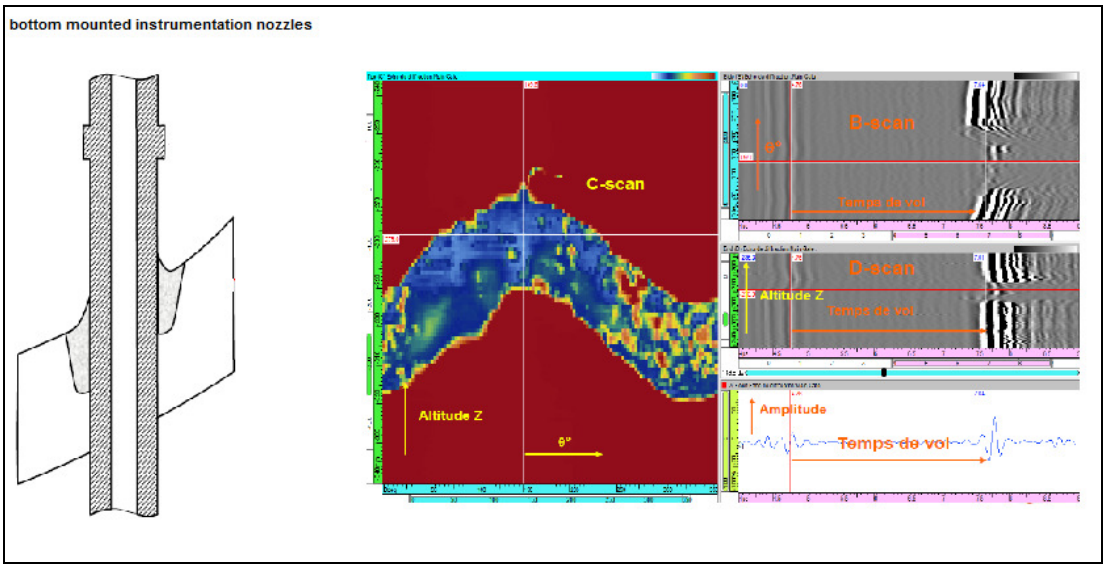

Figure 6. L0° UT and TOFD inspection of bottom mounted instrumentation nozzles: Example of signals

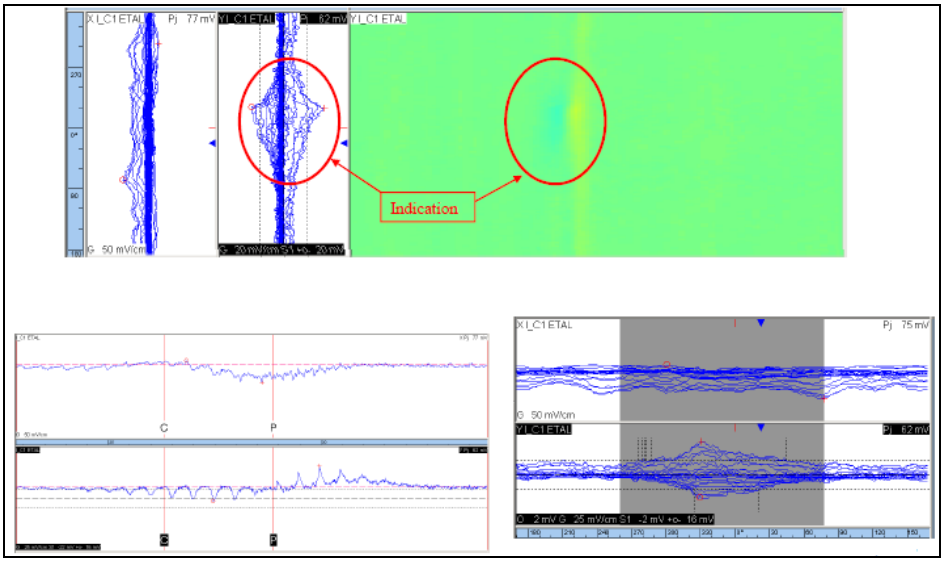

Figure 7: SG tube inspection using a rotating probe: examples of ET signals

4. Conclusion

NDE performance partly depends on the competencies of the personnel carrying out the inspections. The main NDE system qualification references implemented for the in-service inspection of nuclear plant components i.e. Appendix 8 of ASME XI, the ENIQ qualification methodology and appendix 4.3 of the RSEM, deal with this point but in different ways.

Indeed, performance demonstration in conformity with the ASME code covers altogether the procedure, the equipment and the personnel and is pronounced for each operator implementing the inspection, while qualification in accordance with the R-SEM code is established for one system, taking into account the expected necessary competencies; the ENIQ methodology includes individual qualification prescriptions for operators without explicitly requiring them.

EDF's qualification commission, in conformity with the regulatory national reference, examines the files and awards qualification of NDE systems excluding the personnel.

While not formally considering the qualification of each operator in charge of implementing an NDE system submitted to qualification, the Commission is extremely careful regarding the adequacy of the operator's competencies required to achieve the expected performance. The three steps of the conformity examination by the Commission are turned into account to assess the dispositions taken to ensure the competency of operators.

References

[1] ASME Section XI - Rules for Construction of Nuclear Facility Components, 2011.

[2] ENIQ- European Methodology for Qualification of Non-Destructive Testing- 3rd Issue, 2007.

[3] RSE-M - Règles de surveillance en exploitation des matériels mécaniques des îlots nucléaires REP – AFCEN, 2010.

[4] IAEA-EBP-WWER-11 - Methodology for Qualification of In-Service Inspection Systems for WWER Nuclear Power Plants, 1998.

[5] ASME Section V - Non-destructive Examination, 2011.

[6] 10 November 1999 order, concerning operating surveillance of the main primary and secondary circuits in pressurised water reactors.

Modeling-assisted justification of the ultrasonic inspection of a clad REPAIr in Ni-BASED ALLOY

LHUILLIER Pierre-Emile[1], GELEBART Yann[2], CHASSIGNOLE Bertrand[1], DEYDIER Sébatien[2]

[1] EDF R&D, MMC Department, EDF Lab Les Renardières, France
[2] EDF CEIDRE, Saint Denis, France

Abstract

The Ni-based alloy clad repairs encountered on the primary circuit of nuclear power plant exhibit complex anisotropic and heterogeneous structures which lead to important disturbances of the ultrasonic waves. During ultrasonic inspections, the structure is thus responsible for beam skewing or splitting, attenuation, and the appearance of spurious echoes. The objective of this study is to show the benefits of the numerical simulation by finite elements in the frame of the performance evaluation of a Non Destructive Examination (NDE) system.

The inspection of a clad repair has been investigated for two particular welding positions with the use of the finite element code ATHENA 2D. The description of the weld repair was obtained from metallurgical observations. The simulation of the amplitudes of the tip diffraction echo of notches and side drilled hole echoes located in the weld were compared with experimental acquisitions. A good agreement between simulation and experiment was found. In particular, the simulation tool has enabled to predict the influence of the welding position on the inspection performances.

In addition the implementation of the complex and anisotropic structure of the weld has enabled to highlight particular configurations which lead to the appearance of spurious echoes. The origin of these echoes was identified thanks to advanced simulation tools such as the visualization of the ultrasonic beam and wavefront propagation. Finally, this study demonstrates that the finite elements simulation code which takes into account the complexity of the clad is an efficient tool both to demonstrate the performance of the NDE system and also to identify the configurations which will require a particular analysis.

1. Introduction

For several years, EDF R&D has launched a consistent research program on ultrasonic inspection of austenitic stainless steel welds. In particular, a methodology was developed to improve the understanding of the disturbances of the ultrasonic waves (beam deviation, distortion and attenuation) in components welded with a SMAW process (Shielded Metal Arc Welding) [1]. This methodology, based on UT modelling, was applied to various components such as: a butt weld of the surge line [2], the branch pipe weld connecting the Chemical and Volume Control System (CVCS) and the primary coolant piping of PWR circuits [3], or even nickel-based alloy welds [4]. This study deals with the application of the methodology to a Ni based alloy clad weld repair of the primary circuit of Nuclear Power Plant. This work is based on both experimental analyses on representative welded mock-ups and the use of a finite element modeling tool (ATHENA 2D code) which allows realistic simulation of the propagation phenomena in complex mediums. The aim of this study was to provide quantitative and qualitative estimations of the performances of the ultrasonic NDE system.

2. Inspection configuration

2.1. Inspected component

The inspected component is a special area of the inner surface of cladded primary circuit pipes. During manufacturing, defects were revealed by Non Destructive Examinations, the affected zone was removed by machining and repaired by manual Shielded Metal Arc Welding (SMAW). The welding material is a Ni based alloy (alloy 182). The generic geometry of the welded zone is given in Figure 1. The inspection zone is thus composed of a trapezoidal welded zone filled by manual multi pass welding.

Owing that the components have been repaired in place and that the repaired defects might have been observed all around the circumference of the pipe, the welding position might differ from one weld to another. In addition, the results of former studies [5] suggest that the welding position is most likely to show a major influence on the performances of the ultrasonic NDE system. Two particular welding positions have been analyzed: the Horizontal / vertical and Flat welding position (see Figure 1).

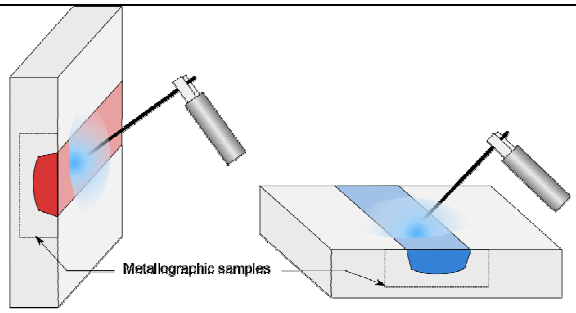

Figure 1 : Schematic view of (left) horizontal / vertical and (right) Flat welding position.

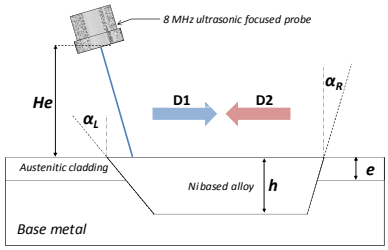

Figure 2 : Generic geometry of the weld repair inspected area.

Table 1 : Geometric parameters of the configuration.

Left and right weld chamfer angle	α_L & α_R	°	10 to 40 *depending on the welding position*
Weld depth	h	mm	20
Cladding thickness	e	mm	9

2.2. NDE System

The weld repair is inspected by a focused single element ultrasonic probe at the frequency of 8 MHz with longitudinal waves. The probe is designed in order to get a good sensitivity of the ultrasonic beam in the range of 3 to 10 mm depths in steel. The main characteristics of the inspection probe are given in Table 2.

Table 2 : Characteristics of the ultrasonic inspection probe.

Mode	Immersed / focused P-Wave
Frequency	8 MHz
Water height	60 mm
Refraction angle	50°

3. Material and method

3.1. Mock-ups

A preliminary study has thus been performed in order to evaluate the impact of the welding position on the inspection performances. The weld microstructures have been modeled with the MINA [6, 7] code for both flat and horizontal / vertical welding positions and used as input of the finite elements code ATHENA 2D for the weld description. The results of this study have shown that the horizontal / vertical welding position might affect the inspection performances. The horizontal / vertical welding position exhibits a main columnar grain orientation at about 45° from the piece surface normal. Thus in the particular inspection configuration displayed in Figure 3 (left), the angle between the ultrasonic beam and the main axis of the columnar grain is close to 90°. In this configuration the ultrasonic attenuation reaches its higher value as it is shown on the Figure 3 (right). It induces a drastic decrease of the echo amplitude of calibrated defects located in the weld. In particular, the echo amplitude of a 2 mm side drilled hole (SDH) at the depth of 12 mm is 17 dB lower than the same SDH located in the base metal. As a comparison, the modeling predicts that the same SDH located in a flat weld exhibits an echo which amplitude is only 2.5 dB lower than the reference configuration. The conclusion of this preliminary study has led to the manufacturing of 2 different representative mock-ups respectively executed in horizontal / vertical and flat welding position (see Figure 1).

Different calibrated flaws have been machined in the mock-ups:

- 4 SDH, at the depth of 9, 15, 15 and 9 mm (of length 80 mm)
- 3 vertical notches in the weld with a tip located at the depth of 5 and 10 (of length 15 mm).

The Figure 4 and Table 3 show the location of the calibrated defects in the flat and horizontal / vertical mock-ups.

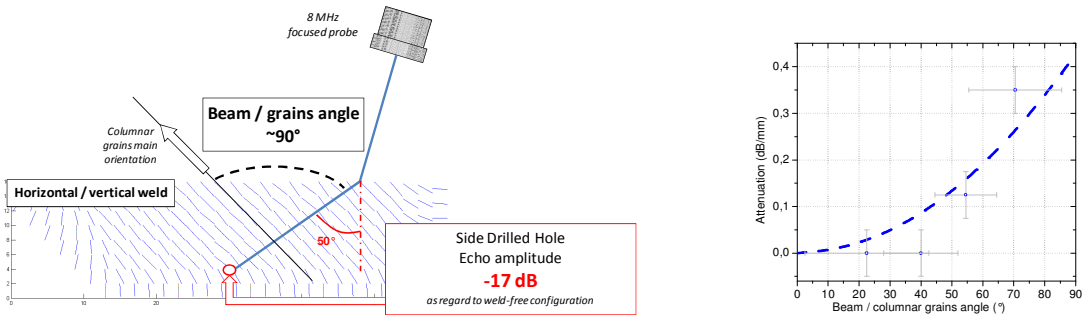

Figure 3 : (Left) Special inspection configuration of the horizontal / vertical welding position causing a highly degraded inspection performances. (Right) Variations of the anisotropic ultrasonic attenuation as a function of the angle between the ultrasonic beam and the columnar grain axis.

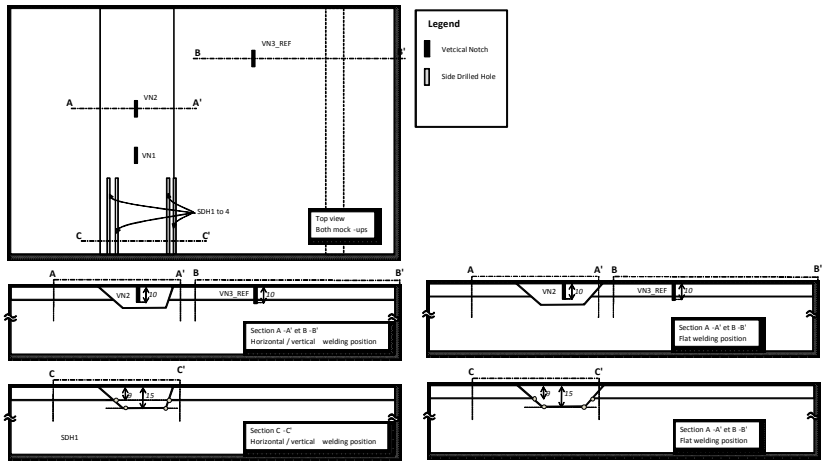

Figure 4: General Implantation scheme of the calibrated defects in the (Left) horizontal / vertical (Right) and Flat welding position.

Table 3: Dimensions of the calibrated defects.

Horizontal / vertical and Flat welding position mock-up					
Vertical Notch (VN)			Side Drilled Holes (Φ 2mm)		
Defect	Height (mm)	Length (mm)	Defect	Depth (mm)	Length (mm)
VN1	5	15	SDH1	9	80
VN2	10	15	SDH2	15	80
VN3_REF	10	15	SDH3	15	80
			SDH4	9	80

3.2. Modeling approach – The ATHENA Code

The main features of the 2D version of the ATHENA code are presented here, more details can be found in [8]. ATHENA 2D is a finite element code for elastodynamic developed by EDF R&D. The code solves the equation of elastodynamic expressed in a mixed formulation combining stress and velocity terms. The code is dedicated to the simulation of wave propagation in all kinds of elastic media and in particular, heterogeneous and anisotropic materials. One important feature of the code is the use of the fictitious domain method [9]. It relies on the combined use of a regular discretization of the calculation zone with a non-regular meshing of the defects. It takes advantage of the rapidity of regular mesh calculation with the possibility to model arbitrary shaped defects. Furthermore, ATHENA 2D gives the possibility to use Perfectly Matched Layers (PML) to define the boundaries of the calculation domain [10]. The use of PML removes spurious reflections on artificial edges of the calculation zone and thus enables to model virtually infinite components. Finally, ATHENA 2D integrates the possibility to simulate various inspection configurations (pulse-echo, tandem, TOFD) with a wide range of transducers (single element and phased array), inspection mode (contact or immersion), materials and defects. The code has been widely used by EDF to simulate the inspection of complex structures such as austenitic welds [4, 11, 12].

3.3. Weld characterizations and simulation inputs

On each mock-up, a sample has been removed for metallographic characterization (see Figure 3 for position). Figure 5 shows the metallographic pictures and the resulting grain orientation maps. The regular discretized orientation maps have been obtained with an image processing tool based on Hough transform. Those maps have been integrated as input in the ATHENA 2D code to describe the welds. Each square of the maps represents an homogeneous area of the weld with anisotropic and constant elastic properties. The contrast of acoustic impedance from one area to another – which lies at the origin of the beam disturbances in the weld – comes from the difference of grain orientation from the different zones. The elastic properties assigned to each area are the same and are given in Table 4.

3.4. Data analysis

In order to ensure the comparison between the experimental and simulated data, each echo amplitude, respectively in experiment and simulation, have been compared to the echo amplitude of a SDH located at the depth of 10 mm in an isotropic and homogeneous ferritic steel plate.
For the notches, only the tip diffraction echoes have been analyzed.

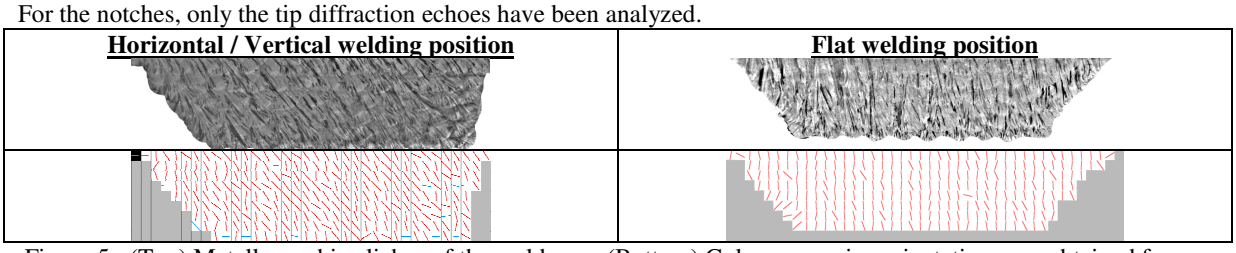

Figure 5 : (Top) Metallographic cliches of the weld area. (Bottom) Columnar grains orientation map obtained from an image processing tool based on Hough transform (regular grid of 2*2mm²).

Table 4 : Elastic coefficients (in GPa) of Ni-based alloy (alloy 182) deposited by Shielded Metal Arc Welding (SMAW). The 3rd axis corresponds to the fiber axis.

C_{11}	C_{22}	C_{33}	C_{44}	C_{55}	C_{66}	C_{12}	C_{13}	C_{23}
265	264	247	111	111	84	121	139	140

4. Results

4.1. Comparison between experimental and modeling data

Firstly the experimental and simulated data have been compared in order to validate the simulation conditions. The Table 5 compares the simulated and experimental amplitudes of the notch tip diffraction echoes and of the SDH echoes. The data are given for both Horizontal / Vertical and Flat welding position mock-ups.

Last column of Table 5 also displays the differences between simulation and experiment for a given defect. A positive value corresponds to an overestimation of the echo amplitude by the simulation.
For the SDH, the simulation results are very close to the experimental data since the larger difference between experiment and simulation is -3.2 dB. In addition, the average of the difference between simulation and experiment for SDH echoes is 1.7 dB. Concerning the notch echoes, only 2 experimental data are available for the horizontal / vertical mock-up. Nevertheless for those 2 data, the maximum difference between simulation and experience is -3.9 dB.
On the Flat mock-up the tip diffraction echoes are always slightly overestimated by the simulation and the higher discrepancy is 5.5 dB.
Nevertheless the average of the simulation to experiment difference on the notch echoes is only 2.3 dB.
Finally, it can thus be considered that the simulation configuration based on a fine characterization of the weld structure and the implementation of a model for the scattering attenuation shows rather good performances to predict the amplitude of SDH echoes and vertical notch tip diffraction echoes.

Table 5 : Comparison of the experimental and simulated amplitudes of defect echoes. Diff = Expe / Simulation difference

				Horizontal vertical mock-up			Flat mock-up		
Mock-up	Dir	Ref	Depth	Expe	Simulation	Diff	Expe	Simulation	Diff
Notch Data	D1	VN1	5	not detected	-18	_	-21,4	-20,4	1
		VN1	10	-26,7	-26,6	0,1	-26,7	-23,4	3,3
	D2	VN2	5	-20,5	-24,4	-3,9	-18,7	-18,5	0,2
		VN2	10	not detected	-34,6	_	-28,6	-23,1	5,5
SDH Data	D2	SDH1	9	-14,9	-11,8	3,1	-11,5	-10	1,5
		SDH2	15	-27,2	-30,4	-3,2	-18,7	-18,9	-0,2
	D1	SDH3	9	-15,9	-16,3	-0,4	-10,2	-9,1	1,1
		SDH4	15	-19,4	-21,8	-2,4	-16,7	-18,7	-2

4.2. Artifact identification

In addition to the good prediction of the echo amplitudes, the simulation tool also enables to reproduce the beam disturbances. In particular, the heterogeneous orientation map of the weld causes beam splitting and deviation which might be at the origin of the appearance of artifacts. To highlight this phenomenon, a particular case of inspection is exposed in this section.
The configuration corresponds to the inspection of a 10 mm notch located on the bottom side of horizontal / vertical welding process. Figure 6 shows the inspection configuration and the resulting BScan is displayed on Figure 7.b. In this particular configuration the BScan shows two particular echoes, denoted Echo A and Echo B on Figure 7.b. For comparison, Figure 7.a. displays the BScan of a similar notch located in an isotropic and homogeneous base metal. One can note the tip diffraction echo is clearly seen and that Echo A is not present. The Echo A could be interpreted as the tip diffraction echo of the notch. Nevertheless, complementary simulations – not displayed here – suggest that the origin of this echo is not due to the notch tip diffraction. Indeed, the amplitude and position of Echo A does not change if the height of the notch is increased up to 20 mm.
The visualization of the ultrasonic beam at the position of Echo A and Echo B, displayed on Figure 8 helps to understand the origin of both echoes.
On Figure 8.a, the ultrasonic beam exhibits a division and deviation on the upper part (marked with the white arrow). The deviated beam propagates quasi perpendicularly to the notch and thus interacts specularly with it. The reflected beam is thus also quasi perpendicular to the notch. Moreover, the analysis of the local anisotropy of the weld in this region has shown that the local orientations are favorable to the skewing of the beam in the direction of the probe. The appearance of this echo is thus not related to the notch height. In particular conditions, the echo can be misinterpreted as a notch tip diffraction echo and thus cause a severe overestimation of the defect height.
The origin of Echo B is more difficult to identify. Nevertheless a fine analysis of the wavefront propagation suggest that this echo can be attributed to a mode conversion after reflection at the notch (LT) followed by a wave deviation due to the anisotropic local structure.
In this frame, the use of the simulation code with a fine description of the microstructure enables to highlight special configurations which might show complex ultrasonic signature or artifact. The numerical simulation can thus become a useful tool to drive the focus of the expert in charge of the interpretation of a particular complex result.

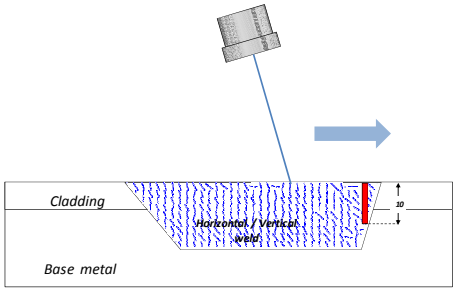

Figure 6 : Simulation configuration of the inspection of a 10 mm notch located on one side of the horizontal / vertical weld.

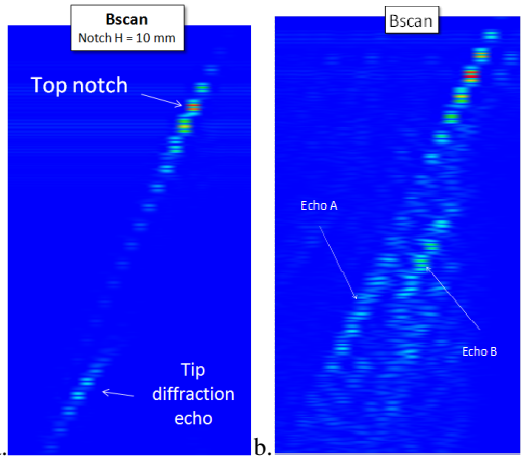

a. b.

Figure 7: Simulated BScan of the inspection of a 10 mm notch located (a) in a homogeneous and isotropic metal (b) on one side of the horizontal / vertical weld.

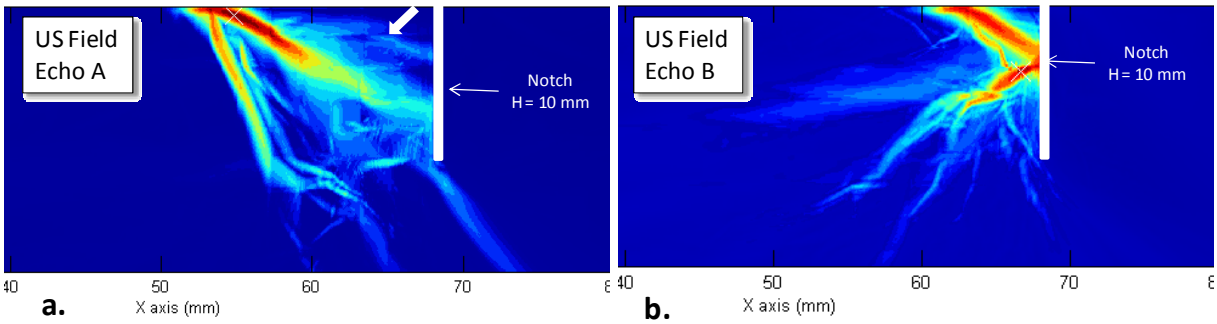

Figure 8 : Simulated ultrasonic field of the inspection of a 10 mm notch located on one side of the horizontal / vertical weld.

5. Conclusion

The objective of this study was to evaluate the performance of an NDE system for the inspection of austenitic weld repairs. In particular, the aim was to investigate the influence of the welding position on the ultrasonic beam disturbances.

Firstly the microstructures resulting from different welding positions (from flat to horizontal / vertical) have been obtained via metallographic observations. The metallurgical analysis enables to get the grain orientation map which is used as input of the Finite Elements code ATHENA 2D for the fine description of the anisotropic and heterogeneous weld structure. The modelling configuration enables to evaluate the performance of the NDE system. Two particular welding positions have been investigated with the use of the finite element code ATHENA 2D. The results were compared with experimental acquisitions and a good agreement was found between simulation and experiment.

Taking into account the complex and anisotropic structure of the weld in ATHENA simulations has enabled to highlight particular configurations which lead to the appearance of spurious echoes. Indeed, the anisotropy of the weld may induce an additional echo which if misinterpreted may lead to a drastic overestimation of the height.

Finally, the simulation code which accounts for the complexity of the weld appears to be an efficient tool both to demonstrate the performance of the inspection process and also to identify the configurations which will require a particular analysis.

References

1. Dupond, O., et al., *Methodology for modelling ultrasonic inspection of an austenitic stainless steel weld.* 6th ICNDE, 2007.
2. Chassignole, B., et al., *Ultrasonic modelling of austenitic stainless steel welds: improvement in the comprehension of anisotropic and heterogeneous structure effects.* 4th ICNDE, 2004.
3. Chassignole, B., O. Paris, and E. Abittan. *Ultrasonic examination of a CVCS weld.* in *6th International Conference on NDE in Relation to Structural Integrity for Nuclear and Pressurized Components, Budapest, Hungary*. 2007.

4. Chassignole, B., et al. *Ultrasonic examination of a weld repair in Ni-based alloy*. in *9th International Conference on NDE Relation to Structural Intergity for Nuclear and Pressirized Components*. 2012. Seattle, Washington, USA: European Commission.
5. Chassignole, B., *Influence de la Structure Métallurgique Des Soudures En Acier Inoxydables Austénitique sur Le Contrôle Non Destructif*. 2000, INSAL: Lyon. p. 217.
6. Apfel, A., *Modélisation de l'orientation cristalline des soudures multi-passes en acier inoxydable austénitique : application au contrôle non destructif ultrasonore - Bilan du* in *ECOLE DOCTORALE DE PHYSIQUE, MODELISATION, ET SCIENCES POUR L'INGENIEUR*. 2005, Université de la Méditerranée.
7. Moysan, J., et al., *Modelling the grain orientation of austenitic stainless steel multipass welds to improve ultrasonic assessment of structural integrity.* International Journal of Pressure Vessels and Piping, 2003. **80**(2): p. 77-85.
8. Becache, E., P. Joly, and C. Tsogka, *Fictitious domains, mixed finite elements and perfectly matched layers for 2D elastic wave propagation.* 2000.
9. Bécache, E., P. Joly, and C. Tsogka, *An analysis of new mixed finite elements for the approximation of wave propagation problems.* SIAM Journal on Numerical Analysis, 2000. **37**(4): p. 1053-1084.
10. Berenger, J.-P., *A perfectly matched layer for the absorption of electromagnetic waves.* Journal of Computational Physics, 1994. **114**(2): p. 185-200.
11. Chassignole, B., et al., *Modelling the attenuation in the ATHENA finite elements code for the ultrasonic testing of austenitic stainless steel welds.* Ultrasonics, 2009. **49**(8): p. 653-658.
12. Chassignole, B., et al., *Ultrasonic and structural characterization of anisotropic austenitic stainless steel welds: Towards a higher reliability in ultrasonic non-destructive testing.* NDT & E International, 2010. **43**(4): p. 273-282.

Development of a Comprehensive Risk-informed Categorization Process for CANDU Conventional Systems and Components

Mehdi Rezaie-Manesh[1], Paul Lafreniere[2], and Patrick O'Regan[3]
Scott Chesworth[4]
[1]Ontario Power Generation, Toronto, Ontario, Canada
[2]CANDU Owners Group, Toronto, Ontario, Canada
[3]Electric Power Research Institute, Charlotte, North Carolina, USA
[4]Structural Integrity Associates, San Jose, California, USA

poregan@epri.com :

The Canadian Nuclear Safety Commission (CNSC) raised a concern in 2009 regarding adequacy of secondary side inspections, particularly the impact of the failure of balance of plant systems on nuclear safety and the lack of consistency in the inspection of these systems among utilities. In response to this concern, the Canadian Nuclear Executives (CNE) decided to develop a new CSA Standard N285.7, "Periodic inspection of CANDU nuclear power plant balance of plant systems and components".

In support of this, the CANDU Owner's Group (COG) has embarked on a project (JP-4425) to conduct a pilot study in order to develop, test and assess a risk-informed inservice inspection (RI-ISI) methodology for CANDU conventional systems and components. In particular, the objectives of the pilot study were to:

- Develop a methodology for the periodic inspection of NPP conventional systems and components that is practical, repeatable, broadly-applicable, and has a firm technical basis.
- Implement the methodology on ten (10) selected conventional systems and identify the scope of inspection for those systems and components.
- Compare the results with current augmented inspection programs.

Additionally, given the nature of a CANDU nuclear power plant, there are a large number of possible conventional systems that could be subject to evaluation (e.g., 168 systems/subsystems at the pilot plant), and as such a system-by-system evaluation has the possibility to become quite resource intensive. Therefore, a pre-screening process needed to be developed that efficiently identifies those systems, or portions of systems that need to be subject to the full methodology while providing a technical justification for excluding other, less important, systems.

This presentation will present the alternatives considered, the methodology that was developed and application of that methodology to the pilot study systems and components.

Keywords: risk-informed inservice inspection (RI-ISI)

Development of ultrasonic techniques for the examination of ITER VV T-joint welds

P.I. Resa[1], F. Fernández[1], C.M. Pérez[1], R. Martínez-Oña[1], P. Vessio[2], A. Dans[3], A. Bayón[3]

[1] Tecnatom Group, Avda. de Montes de Oca 1, 28703 San Sebastián de los Reyes, Spain

[2]Ansaldo Nucleare, C.so F.M. Perrone 25,16152 Genova, Italy

[3]Fusion for Energy, c/ Josep Pla 2, 08019 Barcelona, Spain

Abstract

The vacuum vessel of International Thermonuclear Experimental Reactor (ITER) is a double wall torus made of austenitic stainless steel that houses the fusion reaction and acts as a first safety containment barrier. A consortium led by Ansaldo Nucleare (including Mangiarotti and Walter Tosto) is in charge of manufacturing seven out of its nine sectors. Tecnatom is responsible for developing the ultrasonic inspection techniques (UT) for the examination of one and two-side access welds.

Two-side access welds –to be examined by UT– consist of full penetration welded T-joints with two different chamfer geometries: (i) Form B, with rib thicknesses between 20 and 80 mm and plate thicknesses between 40 and 60 mm; and (ii) Form C, with rib thickness of 40 mm and plate thickness of 60 mm.

Demonstration of the non-destructive inspection procedures for thick austenitic welds is required by RCC-MR Code. Detection and characterization capabilities have to be shown in representative test pieces with a wide range of postulated defects, simulated by side drilled holes and notches (parallel and transverse to the weld).

Tecnatom has developed a fully comprehensive set of ultrasonic techniques, based on phased-array (PA) technology, including multiple beam angles and different wave modes. Normal incidence, sectorial longitudinal and sectorial shear wave techniques are simultaneously applied using one single linear PA probe. Space limitations and accessibility interferences have been overcome by the generation of delay laws without the use of refraction wedges, shear mode included.

Tecnatom's approach significantly increases the capabilities of the ultrasonic method in terms of detection and characterization, at the same time as inspection, calibration and verification activities are notably simplified.

Keywords: ITER, ultrasonic, phased-array, austenitic steel, T-joint.

1. Introduction

The Vacuum Vessel (VV) is the largest component of the International Thermonuclear Experimental Reactor (ITER) machine. It is composed of nine sectors made of thick austenitic stainless steel 316L (N) – IG ITER Grade. All of the sectors are similar in shape and are built with double-walls containing shielded plates. Forty four additional ports allow access and instrumentation during fabrication and further vacuum vessel maintenance (Figure 1).

Both the design and manufacturing of ITER VV and the corresponding non-destructive examinations must be compliant with the requirements of the 2007 edition of RCC-MR Code [1]. This Code requires radiographic testing (RT) of all category 1 and 2 welds of the component. Most welded joints have conventional configurations and can be inspected by RT to ensure their integrity. However, given the geometric characteristics and the construction sequence, a significant number of welds are not accessible from both sides. The alternative consists of using ultrasonic techniques (UT), being their qualification required according to CEN/TR 14748:2004 code [2]. Main types of welds to be examined by ultrasonic testing are: (1) longitudinal and circular (Flexible Housing) welds with access only from one-side, and (2) T-joint and cruciform welds with access from at least two surfaces.

Seven out of the nine sectors of the ITER VV are being manufactured by the European consortium of AMW (Ansaldo Nucleare S.p.A, Mangiarotti S.p.A and Walter Tosto S.p.A) and Tecnatom is responsible for developing and qualifying the inspection system and non-destructive techniques **[3,4]**.

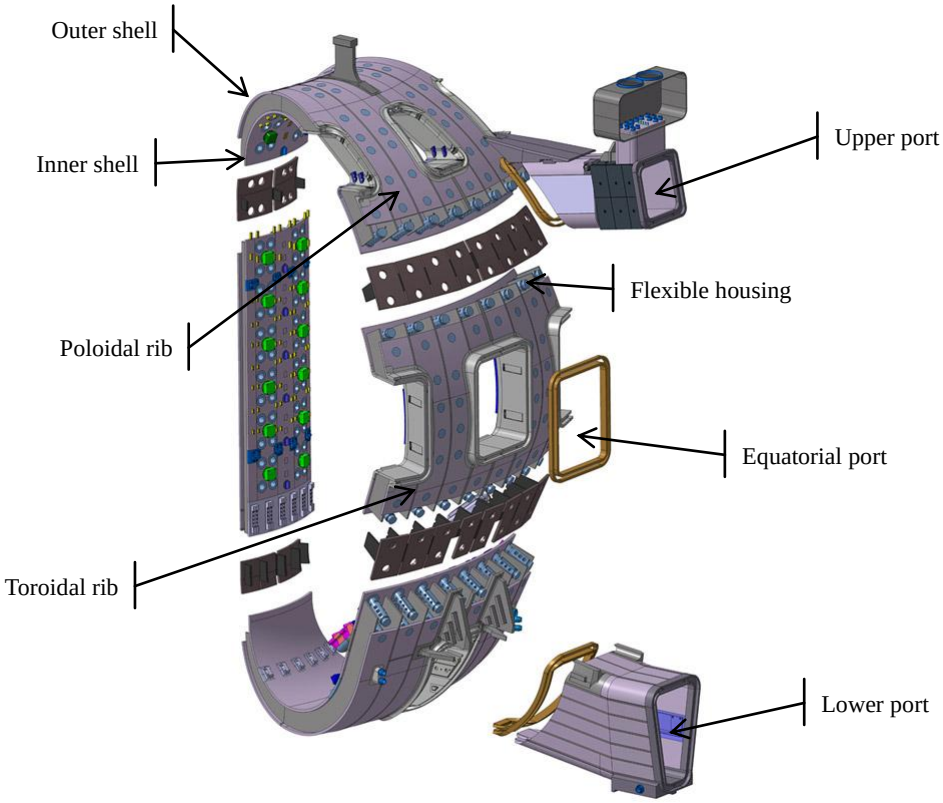

Figure 1. ITER VV sector (courtesy of Fusion for Energy)

Due to the access limitations, the geometrical constraints, the diversity of configurations, the challenging postulated defects in terms of sizes and orientations and the difficulties on UT of austenitic material, the need for advanced UT techniques is evident.

The present paper focuses on the advances in the development of ultrasonic techniques for the non-destructive inspection of ITER VV T-joint welds.

2. Material and methods

2.1 Test pieces

Test pieces, reproducing the geometry and characteristics of two-side access joints of ITER VV and containing representative artificial defects, are required by RCC-MR Code [1] to demonstrate that the ultrasonic inspection procedures are able to identify and characterize the postulated defects. These welds have different bevel forms (B, C, CA) and are filled by different welding processes (GTAW and SMAW). The required examination volume includes 100% of the fused material plus 10 mm of base metal corresponding to the heat affected zone adjacent to the weld (Figure 2).

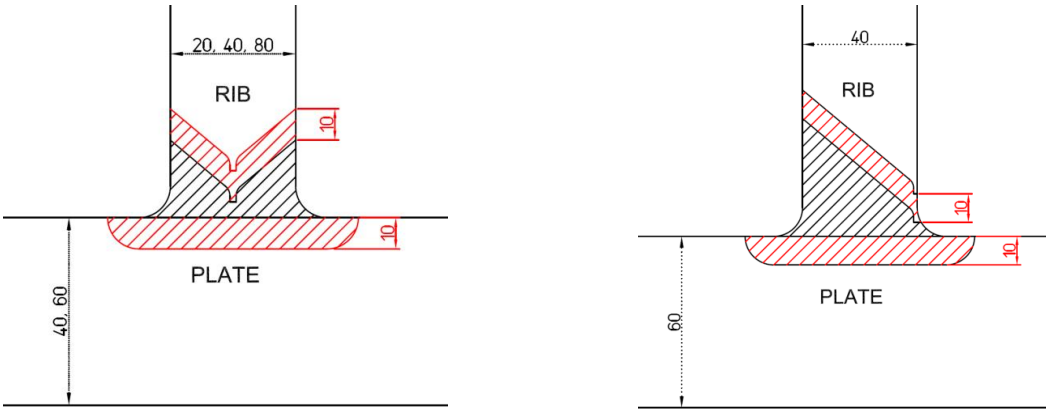

Form B *Form C*

Figure 2. Weld forms, thicknesses and examination volumes of ITER VV T-joint welds (UT).

2.2 Postulated defects

Postulated defects are volumetric and planar (open and embedded), and with orientations longitudinal and transversal to the weld. These reflectors have been reproduced in the test pieces by:

- Side-drilled holes (SDH), 2 mm in diameter

- Open and embedded notches of different heights (open notches: 1.0, 1.3, 2.0 and 2.7 mm; and embedded notches: 1.3, 2.7 and 5.3 mm), depending on the thickness of the rib.

According to RCC-MR code [1]:

- Any planar defect is unacceptable.

- For volumetric defects, criteria based on amplitude and length must be applied.

2.3 Ultrasonic techniques

RCC-MR code [1] recommends the use of two refraction angles, between 35º and 70º, using shear waves, with a difference of 15º at least, that are selected based on the weld geometry and perpendicular to the bevel. Besides, weld volume must be examined at least in two directions.

For the ITER VV T-joint welds, in addition to code recommendations, a more comprehensive set of ultrasonic techniques has been developed including multiple beam angles and different wave modes. Normal incidence, sectorial longitudinal, sectorial shear and Creep wave techniques have been proposed, which can be simultaneously applied using one single linear PA probe. Space limitations and accessibility interferences have been overcome by the generation of delay laws without the use of refraction wedges, shear mode included (Table 1). This approach significantly increases the capabilities of the ultrasonic method in terms of detection and characterization, at the same time as inspection, calibration and verification activities are notably simplified.

In order to adequately detect, characterize and size flaws, examinations from three different surfaces and with different probe skews have been devised (Figure 3).

Table 1. UT techniques defined for T-joint welds.

Postulated defect	Position	Main UT technique
Defects open to surface	HAZ or interface, inspection surface	Creeping waves or sectorial scan using shear waves
	HAZ or interface, opposite surface	Sectorial scan using shear waves
	Fused area, in opposite surface	Sectorial scan using shear or longitudinal waves
Volumetric embedded defects	Base material or fused material	Sectorial scan using longitudinal waves
Planar embedded defects	HAZ or interface	Sectorial scan using shear or longitudinal waves
	Fused material	Sectorial scan using longitudinal waves

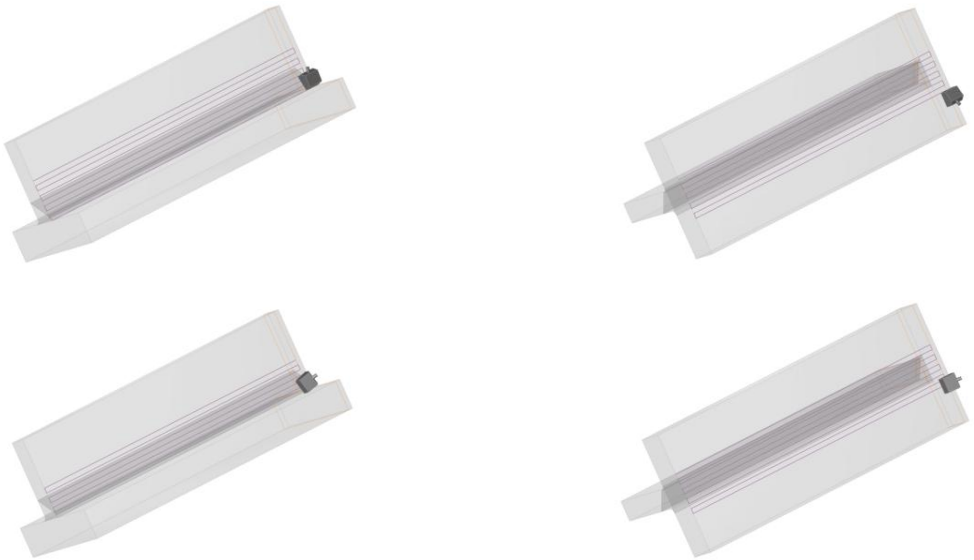

Figure 3. Inspection of T-joint welds.

2.4 Mechanical scanner

A semi-automatic mechanical scanner has been designed for the ultrasonic inspection of ITER VV T-weld joints (Figure 3). The device is divided into two main assemblies, the encoded guide system and the guiding probe assembly. All the parts are manufactured in light resistant materials, with the appropriate surface finishing being corrosion protected, and complying with the given material restrictions of ITER VV.

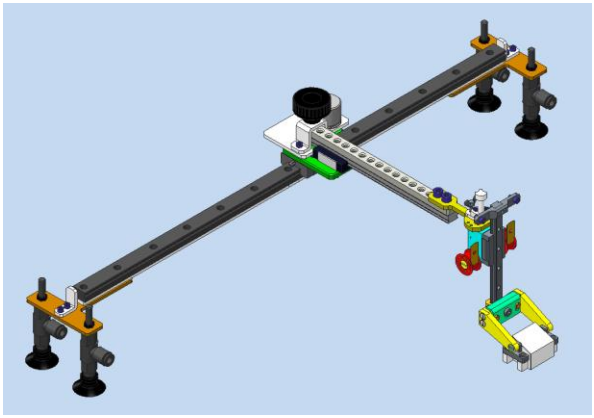

Figure 4. General overview of the semi-automatic scanning system.

3. Results and discussion

3.1 Ultrasonic radiated beam

Ultrasonic probes have been selected taking into account geometrical considerations and the performance in thick austenitic specimens. Probe characteristics (aperture, frequency, pitch, etc.) have been evaluated by simulating the ultrasonic beams in complex structural specimens, so as to assess steering capabilities, focal range, resolutions, grating and side lobes. In a first approach, austenitic steel has been simulated as an oriented polycrystalline aggregate of cubic crystals. Ultrasonic beam simulations are illustrated in Figure 5 for two delay laws proposed for the inspection of ITER VV T-welds.

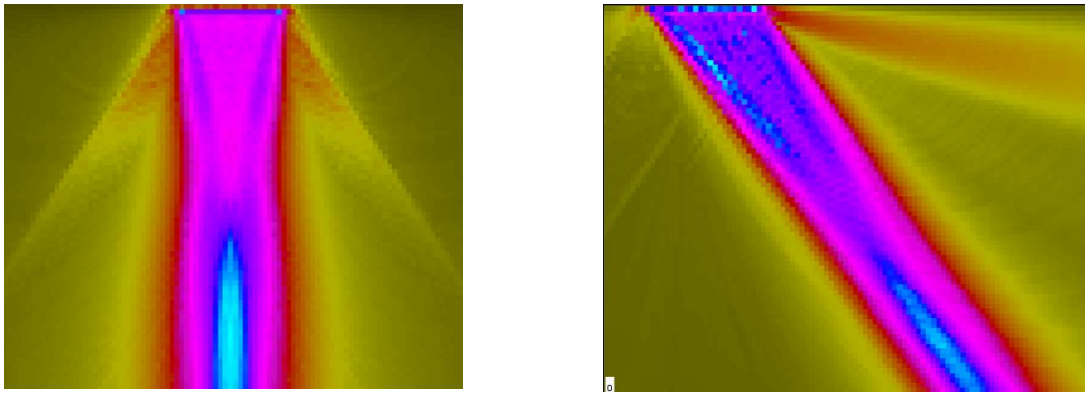

0ºL *35ºT*

Figure 5. Simulation of ultrasonic beam in an 80 mm plate using PA in direct contact (not normalized).

3.2 Results on test pieces

Besides the difficulties on account of the intrinsic properties of the material (granular noise and anisotropy), ITER VV T-joints present very diverse configurations: weld forms, plate and rib thicknesses, etc. In order to cover all the possibilities, a comprehensive number of test pieces are being inspected and completed with inspection simulations.

Figure 6 shows the inspection simulation parallel to the weld with a PA probe skewed 90º for the detection of a side-drilled hole, 2 mm in diameter, located in fused material, using a sectorial longitudinal wave technique focused at 40 mm.

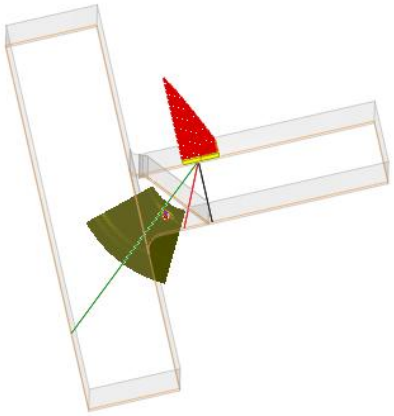

Figure 6. Illustration of inspection simulation: weld form C, 2 mm diameter SDH.

Figure 7 presents the experimental results obtained in a validation block with planar (open to inspection surfaces) and volumetric defects (embedded).

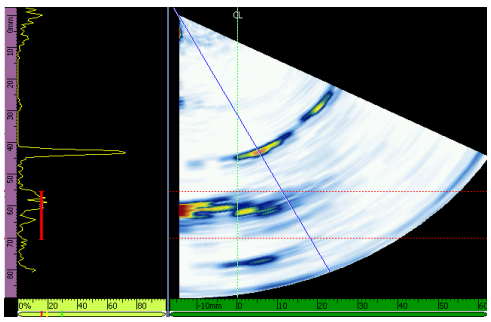

Embedded SDHs, 2 mm in diameter, in fused metal (longitudinal wave)

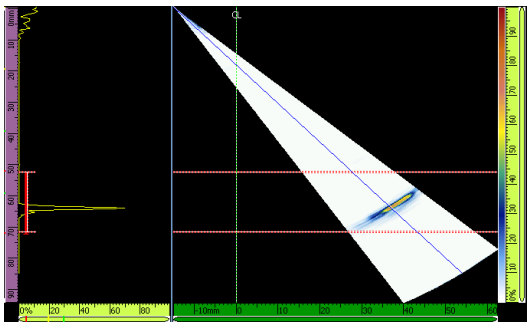

EDM notch, 2 mm in height, open to opposite surface in HAZ (shear wave)

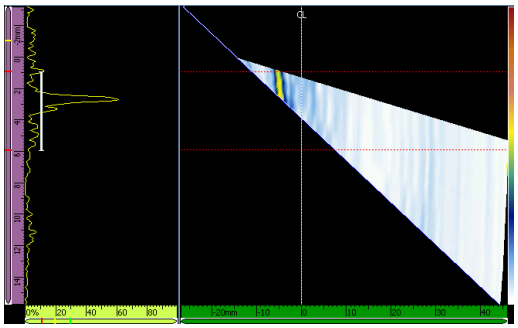

EDM notch, 2 mm in height, open to the inspection surface in HAZ (Creeping wave).

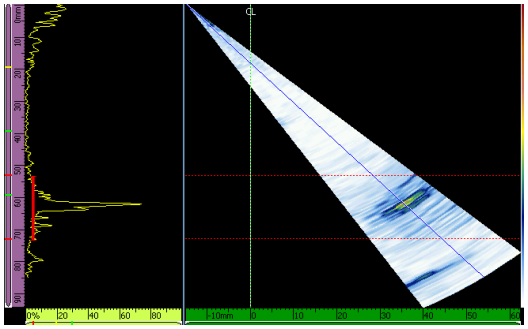

EDM notch, 2 mm in height, open to the opposite surface in fused metal (shear wave).

Figure 7. Ultrasonic acquisition results on test piece.

Hitherto, all the postulated defects have been clearly detected using the ultrasonic techniques developed. In next steps, the effect of access limitations in cruciform geometries, the interference by weld fillets and potential obstacles at the inspection stage has to be assessed.

Acknowledgements

This paper has been written in the frame of the contract between the consortium composed by Ansaldo Nucleare-Walter Tosto-Mangiarotti (AMW) and Fusion For Energy (F4E), for the manufacture of 7 out of 9 sectors of ITER Vacuum Vessel, and thanks to an efficient collaboration among Tecnatom, AMW, F4E, ITER Organization and ANB (Authorized Notified Body).

References

[1] "Design and Construction Rules for Mechanical Components of Nuclear Installations, Section 3: Examination Methods and Section 4: Welding", RCC-MR Code (2007).

[2] "Non-destructive testing – Methodology for qualification of non-destructive tests", CEN/TR 14748 (2004).

[3] R. Martínez-Oña, A. García, C. Pérez, G. Pirola, "Qualification of ultrasonic inspections in the ITER vacuum vessel manufacturing project", Proceedings of the 9th International Conference on NDE in Relation to Structural Integrity for Nuclear and Pressurised Components (22 – 24 May, Seattle, 2012).

[4] A. García, F.J. Fernández, M.C. Pérez, R. Martínez-Oña, G. Pirola, "Inspection of austenitic welds in ITER vacuum vessel welds with ultrasonic phased-array technology", Proceedings of the 9th International Conference on NDE in Relation to Structural Integrity for Nuclear and Pressurised Components (22 – 24 May, Seattle, 2012).

Quantitative Evaluation Program of the Wall Thinning Pipe Using Infrared Thermography

Koo-Ahn Kwon[1], Man-Yong Choi[1], Jung-Hak Park[1], Won-Jae Choi[1],Hee-Sang Park[2], Won-Tae Kim[3]

[1]Korea Research Institute of Standards and science, Daejeon, Korea

[2]Korea Research Institute of Smart Material and Structures System Association, Korea

[3]Kongju National University, Chungnam, Korea

Abstract

For the diagnosis of defects in pipes used in nuclear power plants that currently produce the majority of domestic electricity, a variety of non-destructive test methods such as ultrasonic testing (UT) and radiographic testing (RT) have been conducted. However, there is still a lack of studies on the quantification of defects and inspection standards for pipes with a thickness of less than 4 inches. In this regard, this study sought to quantify wall thinning defects that occur in pipes of less than 4 inches using infrared thermography. After fabricating an artificial defect specimen for development of programs to quantify defects and performance evaluation, defect quantification was performed using a calibration reflective tape. Experimental results confirmed that the measurement accuracy of the defect quantification program ranged from about 80% up to 90%, and the error of quantification was greater in smaller defects.

Keywords : Quantitative Evaluation Program, Wall Thinning Pipe, Infrared Thermography, Lock-in Method, Calibration Reflection Tape.

1. Introduction

Among problems that occur in nuclear power plant, the problem related to piping accounts for a large portion, with exception of the problem arising from electric power systems. At present, pipes of various materials and shapes are used, and various methods are applied to diagnose the defects of the pipes. In the case of pipes used in nuclear power plants, the type of defects is divided into wall thinning defect and micro-crack defect. As methods to detect these defects, ultrasonic testing (UT), radiographic testing (RT) and eddy current testing (ECT) have been used. However, test standards for the pipes of less than 4 inches in diameter have not yet been established.[1,2] In this regard, this study was conducted to quantify defects using infrared thermography with respect to wall thinning defects that occur in pipes of less than 4 inches in diameter.[3,4]

2. Specimen and experiment configuration

2.1 Specimen

A pipe specimen with a diameter of 89.3mm was produced to quantify defects. A black matt radiation tape was applied to maintain a constant emissivity of more than 0.95. In addition, a calcification reflective tape (40.0 mm X 30.0 mm, 10.0 mm X 10.0 mm) was produced and attached to the outside of the pipe for quantification of defects in the pipe. This is what uses the principle that the defective image is formed on the pipe surface because thermal behavior generated in the inside is delivered to the outside of the pipe, resulting in the radiation of thermal energy. The large reflective tape is 40±0.5 mm wide and 30±0.5 mm long, and the small reflective tape is 10±0.5 mm in length and width. The experiment was performed to detect defects in the angle of the front direction and eccentric direction..

Figure 1. Specimen

2.2 Experiment configuration

A experimental configuration are shown in Figure 2. Digital lock-in method was used to improve the detection sensitivity and minimize the defect detection error. Excitation is Halogen lamp(1kW X 2).[5,6]

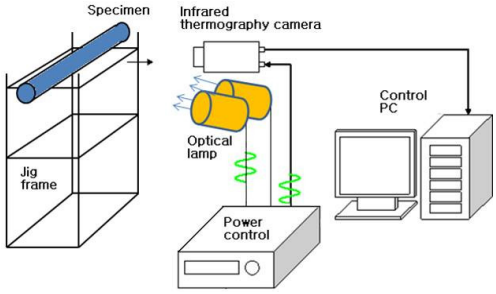

Figure 2. Active IR Thermography

3. Quantitative evaluation program

3.1 Quantifying defects

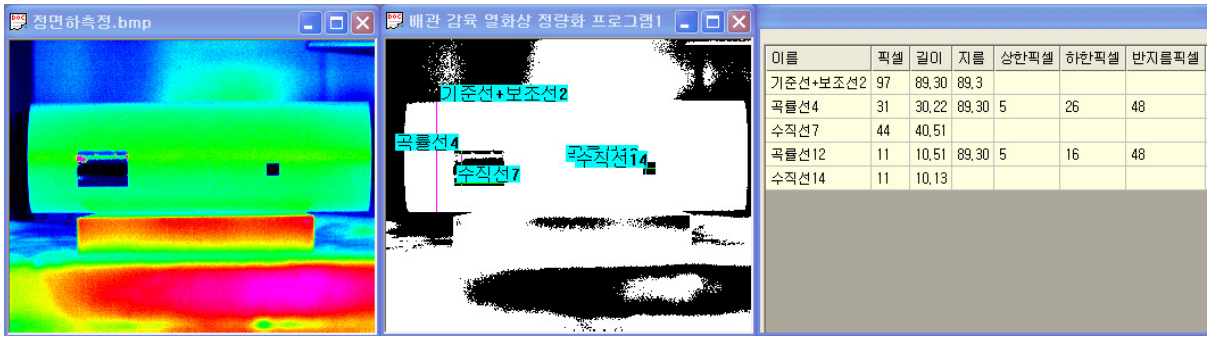

Figure 3 Quantifying wall thinning defects(centric direction)

In this study, a program for quantifying defects in pipes was developed. The diameter of the pipe is 89.30 mm. The number of measured pixels is 97, and the length of a pixel is 0.92 mm. This means that an error of 0.92 mm occurs each time a measurement error of one pixel occurs. The results of being measured by using a defect quantification program are shown in Figure 3. The measurements of the large defect tape were 40.51 mm in width and 30.22 mm in length, which shows that the measurement results are close to the error margin (±0.5 mm) of the defect tape. The small defect tape was measured at 10.13 mm in an axial direction and 10.51 mm in a curvature direction, which can be also said to be an excellent measurement result as it is close to the error margin of the tape.

Fig. 4 shows the measurement results of defects obtained by adjusting the angle of the same specimen in the eccentric direction. As in the results of the front direction, the large defect tape was measured at 40.09 mm in length of axial direction and 30.37 mm in length of circumferential direction, which shows an exact measurement result within a dimensional error of the tape.

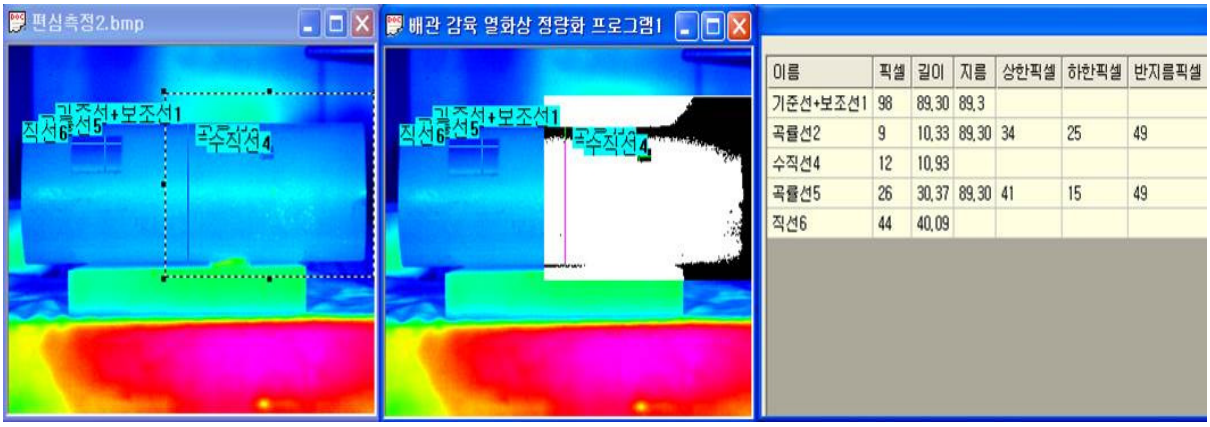

Figure 4. Quantifying wall thinning defects(eccentric direction)

3.2 Infrared Thermography

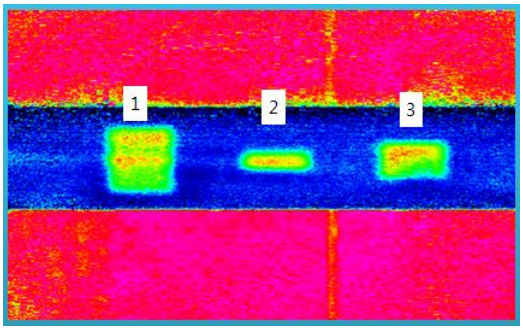

Figure 5. Infrared thermography of 4 inch pipe

Fig. 5 shows the actual pipe with a full length of 500.00 mm, into which a wall thinning defect is inserted. It was produced through welding after inserting the defect that has a rectangular shape without a slope into the inside of the pipe. It was measured at 4.00 inches in diameter and 7.50 mm in thickness, and the depth of the defect was located at 50% of the pipe thickness.

Table 2. Measurement comparison of defect length

Measurements Location	**Length (mm)**		
	defect 1	**defect 2**	**defect 3**
Vertical real value	85.8	21.4	42.9
Vertical measurements	77.3	24.4	41.7
Horizontal real value	56.5	56.5	56.5
Horizontal measurements	57.3	58.6	58.6

A comparison between the actual defect and defect in the infrared thermal image revealed that the error of the vertical measurement value of defect 2, which is smallest in size, was most significant with 2.98mm (13.90 %) as shown in Table 1. This means that there was a difficulty in selection of thermal boundary since less thermal variation occurs as the size of the defect is smaller. In addition, it seems that it is most important to detect defect images at the optimum time in the process of heat diffusion in the quantification of defects.

4. Conclusion

In this study, an experiment was conducted to quantify wall thinning defects of nuclear power plant pipes using infrared thermography. To this end, a program for defect quantitative evaluation through a spatial resolution was applied to measurement. According to the results of the measurement, the defect 2 of the smallest size showed an accuracy of at least 86%, and the largest defect 1 an accuracy of up to 98.6%, indicating a high accuracy of more than 94% on average. This suggests that due to the limit of the spatial resolution, the error of defect quantification is greater as the size of the defect is smaller.

Acknowledgements

This work was supported by Radiation Technology R&D program through the National Research Foundation of Korea funded by the Ministry of Science, ICT & Future Planning(2013M2A2A9043706) This work was supported by the Nuclear Power Core Technology Development Program of the Korea Institute of Energy Technology Evaluation and Planning(KETEP) granted financial resource from the Ministry of Trade, Industry & Energy, Republic of Korea (No. 20121620100020)

References

[1] M. Y. Choi, K. A. Kwon, H. S. Park, J. H. Park, Y. H. Huh, W. J. Choi, “Quantitative Defects Detection in Wind Turbine Blade Using Optical Infrared Thermography”, Journal of the Korean Society for Nondestructive Testing, Vol. 35, No. 1: 25-30, 2015

[2] K.W. Yun, G. U. Go, J. W. Kim, H. C. Jung, K. S. Kim, “Application Angle of Defects Detection in the Pipe Using Lock-in Infrared Thermography.”, Journal of the Korean Society for Nondestructive Testing, Vol. 33, No.4: 323-329, 2013.

[3] K. J. Lee, H. S. Jang, H. C. Jung and K. S.Kim, "Quantitative out-of-plane deformation measurement of pressure vessel with the defect using shearography," Journal of the Korean Society for Precision Engineering, Vol. 23, No. 10, pp. 36-42, 2006

[4] X. P. V. Maldague, "Trends in Optical Nondestructive Testing and Inspection," P. K.Rastogi, D. Ibaudi, Editors Elsevier Science,Switzerland , 2000

[5] K. S. Kim, H. C. Chang, D. P. Hong, C. J. Park, S. W. Na, K. S. Kim, H. C. Jung, “Defect Detection of the Wall Thinning Pipe of the Nuclear Power Plant Using Infrared Thermography”, Journal of the Korean Society for Nondestructive Testing, Vol. 30, No. 2, 2010

[6] K. W. Yun, D. L. Kim, H. C. Jung, D. P. Hong, K. S. Kim, “Application Defects Detection in the Small-Bore Pipe Using Infrared Thermography Technique”, Journal of the Korean Society for Nondestructive Testing, Vol. 33, No. 1: 34-39, 2013

Conceptual Optimization of Sample Size for POD Determination for Cast Austenitic Stainless Steel Components

Owen Malinowski (omalinowski@structint.com)[1], Jason Van Velsor[1], Timothy Griesbach[1], David Harris[1], and Nat Cofie[1]
[1]Structural Integrity Associates, Inc., 1951 Pine Hall Road, Suite 100, State College, Pennsylvania, 16801, USA

Inspection of cast austenitic stainless steel (CASS) components is very challenging due the coarse grain structure present in the microstructure. Inspections, together with flaw tolerance evaluations, are needed to demonstrate piping reliability. In order to meet piping reliability targets, a certain level of probability of detection (POD) is required that can be demonstrated by a qualification process. Traditionally, NDE qualification to determine the POD curve requires a relatively large number of samples and trials. This could be very challenging for CASS piping components where the sample sizes and number of flawed components is limited by the availability of flawed specimens. As such, methods have to be sought to reduce the sample size in determining the POD curve without loss of accuracy while retaining high confidence. This paper presents a summary of statistical POD modeling methods and discusses the potential of these techniques to minimize the required number of test samples needed to produce adequate POD curves for future inspections of CASS piping in nuclear plant applications.

Keywords: Nondestructive Evaluation, NDE, Cast Austenitic Stainless Steel, CASS, Probability of Detection, POD, Statistical POD

Influence of the dimensions of an elbow on defect sensitivity of guided wave testing at elbow part

Toshihiro Yamamoto[1], Takashi Furukawa[1] and Hideo Nishino[2]

[1]Japan Power Engineering and Inspection Corporation, Japan

[2]The University of Tokushima, Japan

Abstract

This paper investigates characteristics of defect sensitivity of guided wave testing at an elbow of piping for efficient defect detection at an elbow of piping. Along with experimental results, the results of finite element method (FEM) simulations imply that constructive and destructive interference of guided waves causes unevenness of defect sensitivity at an elbow. From the simulation results, it is assumed that the ratio of the wavelength of guided waves to the pipe size determines the interference behavior and thus the location of a defect-sensitive region at an elbow.

Keywords: guided wave testing, piping, elbow, defect detection, simulation

1. Introduction

Guided wave testing offers an efficient screening method to detect wall thinning of piping owing to its long inspection range and ability to inspect pipes with limited access (covered with insulation, buried, etc.) However, there is a problem in signal interpretation of guided wave testing. While interpretation of echo signals is relatively simple for straight pipes, it becomes much more difficult when the wave propagation path includes an elbow. This problem needs to be solved for applying guided wave testing to evaluation of local wall thinning of piping because local wall thinning frequently occurs around an elbow such as liquid droplet impingement (LDI) erosion or flow-accelerated corrosion (FAC).

In the previous study [1], we conducted experiments of guided wave testing using aluminum alloy 50A Schedule 40 (60.5 mm in outer diameter and 3.9 mm in wall thickness) piping that includes an elbow to investigate defect sensitivity at an elbow with different frequencies of guided waves. The results of the experiments showed that the defect sensitivity tends to be higher at the concave side of the elbow for 30 kHz and in contrast it tends to be higher at the convex side of the elbow for 40 and 50 kHz. We also performed computer simulations corresponding to these experiments and observed the transient changes in the amplitude distribution of the particle displacement caused by guided waves. To indicate the places where the amplitude becomes high with a single image, distributions of the maximum amplitude over time at each position were depicted. Then, the maximum amplitude shows a similar frequency-dependent distribution trend as the defect sensitivity obtained in the experiments. Namely, the concave side of the elbow gets higher amplitudes for 30 kHz, whereas the convex side of the elbow gets higher amplitudes for 40 and 50 kHz. This similarity is understandable because a high-amplitude region is expected to be a defect sensitive region. Since it requires a much smaller computational cost to obtain a distribution of the maximum amplitude of the particle displacement compared with the defect sensitivity, this maximum amplitude is a convenient parameter to estimate the defect sensitivity at an elbow under certain conditions.

The uneven distributions of the maximum amplitude are thought to be attributed to interference of guided waves at an elbow. Even if guided waves entering an elbow are coherent, the shape of the elbow gives rise to constructive and destructive interference of the guided waves. In the present study, we performed computer simulations using several different-sized simulation models of piping that includes an elbow to investigate influence of the dimensions of an elbow on defect sensitivity of guided wave testing at elbow part.

2. Experiments to investigate characteristics of defect sensitivity

This section provides a summary of the results of the laboratory experiments conducted in our past study.

2.1 Experimental setup

Figure 1 shows a schematic illustration of the piping specimen used in our experiments. This piping specimen is made of aluminum alloy, and it consists of two straight pipes and an elbow connecting these two pipes. The pipes are 50A Schedule 40 (60.5 mm in outer diameter and 3.9 mm in wall thickness). The elbow is a long radius elbow complying with JIS B2313 (comparable to ASME B16.9). Either end of the elbow was welded to one of the straight pipes. The dry-coupled piezoelectric ring-shaped sensor system already presented in the past studies [2, 3] was used to transmit and receive guided waves in the experiments. The sensor system consists of two sets of eight transducer elements aligned to be placed at equal intervals in the circumferential direction of the outer surface of the pipe. These transducer elements are oriented to vibrate in the circumferential direction of the pipe to transmit and receive the fundamental torsional guided wave mode T(0,1) preferentially. One set of eight transducer elements is used as a transmitter, and the other is used as a receiver. The transmitter was placed 485 mm before the inlet of the elbow, and the receiver was placed 30 mm before the transmitter.

To find out how the observed signals vary according to the position of a defect at the elbow, 12 piping specimens of the same configuration as shown in Fig. 1 were prepared. On the outer surface of each specimen, a single defect was made by a carbide cutting bit at one of the 12 positions indicated in Fig. 2. The diameter of the carbide cutting bit is 9.5 mm. The depth of each defect was gradually increased up to 2.0 mm with 0.25 mm increments. The observed signals were stored for each step of the defect depth on the 12 piping specimens.

In the measurements on each specimen, the three frequencies 30, 40 and 50 kHz were used as the center frequency of the excitation signal for the transmitter to find out how the characteristics of the observed signals are changed according to the frequency of guided waves.

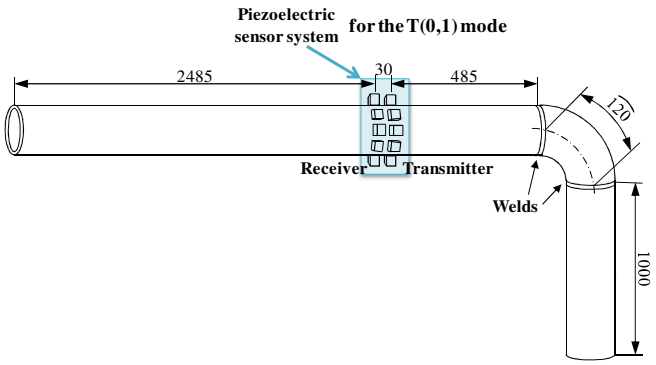

Figure 1. Piping specimen with piezoelectric sensor system

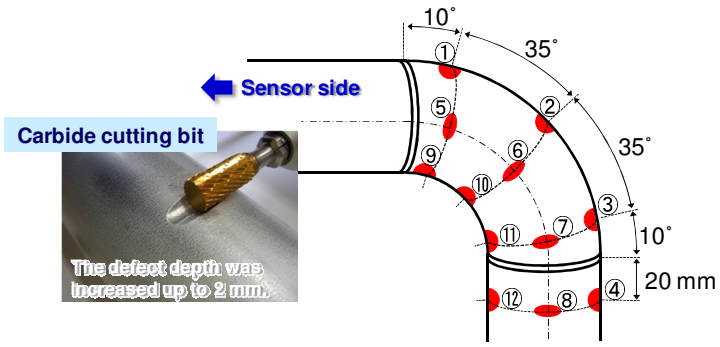

Figure 2. 12 positions of artificial defects

2.2 Observation of defect signals

Figure 3 shows a typical waveform obtained from the measurements on the piping specimens before the defect was made at the elbow. The signal labeled ① represents the guided waves that propagate directly from the transmitter to the receiver. The signal labeled ② is formed by several wave packets reflected around the elbow. This group of wave packets mainly consists of the two wave packets reflected from the two butt welds at both ends of the elbow, respectively. The signal labeled ③ arises from the waves reflected by the lower right end of the piping specimen shown in Fig. 1.

Figure 4 shows the waveforms of the observed signals with the increasing depth of the defect when the frequency of the excitation signal is 50 kHz and the defect position is ①. To focus on the signal variations according to the defect depth, only the range from 350 μs to 600 μs is displayed. The signal amplitudes are normalized such that the maximum amplitude of the signal that corresponds to the signal labeled ① in Fig. 3 is unity. The normalized amplitudes are expressed in permil (‰). Because the signal variations due to the defect depth are relatively small compared with the original signal, the baseline subtraction was adopted to clarify the signal variations. The lower graph in Fig. 4 shows the resulting signals that were obtained by subtracting the baseline signal (the signal when the defect depth is 0 mm) from all the signals in the upper graph in Fig. 4. Then, only the defect signals were extracted by this subtraction.

2.3 Defect sensitivity

To quantify the increasing rate of the amplitude of the defect signal with respect to the defect depth, Fig. 5 shows the correlation between the cross-sectional loss caused by the defect and the maximum amplitude of the defect signal for 50 kHz of the guided wave frequency and the defect position ①. In this graph, the cross-sectional loss is represented as the proportion (%) of the maximum cross-sectional area of the defect to the cross-sectional area of the intact pipe wall. The filled circles indicate the data obtained from the experiments. The solid line is the least squares regression line derived from the data. In this study, the defect sensitivity is defined as the slope of this least squares regression line at each defect position for each guided wave frequency.

The measurements on the 12 piping specimens provide the defect sensitivity values at the 12 positions presented in Fig. 2. Figure 6 shows the defect sensitivity values at these 12 positions for the three frequencies 30, 40 and 50 kHz. From the figure, it is observed that the defect sensitivity depends on both the position and the frequency. For 30 kHz higher sensitivity values are presented at the concave side of the elbow, whereas for 40 and 50 kHz higher sensitivity values are presented at the convex side of the elbow.

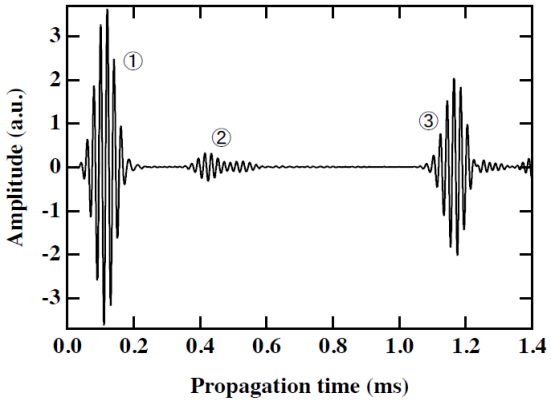

Figure 3. Typical waveform obtained from measurement on piping specimen

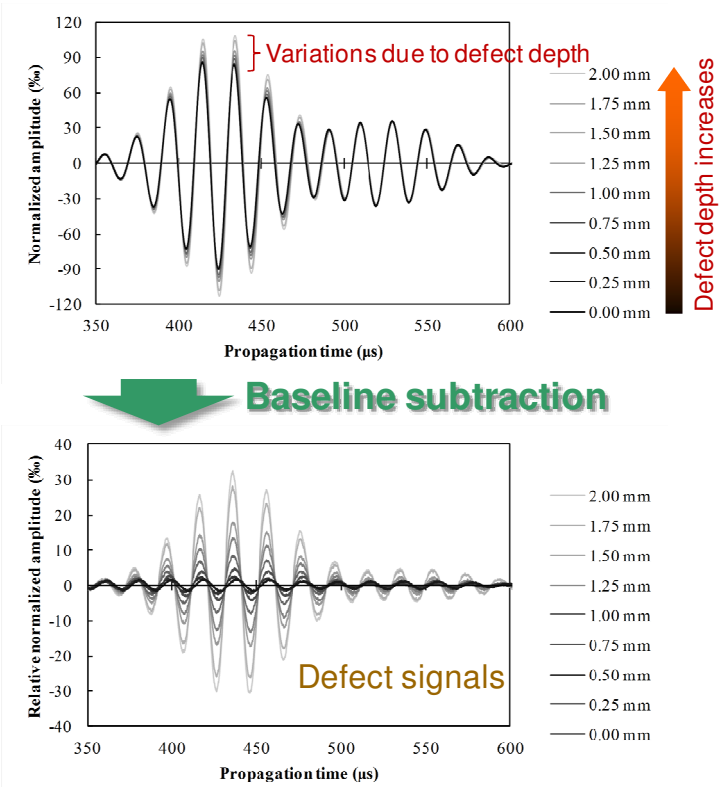

Figure 4. Signal variations due to defect depth (frequency 50 kHz, defect position ①)

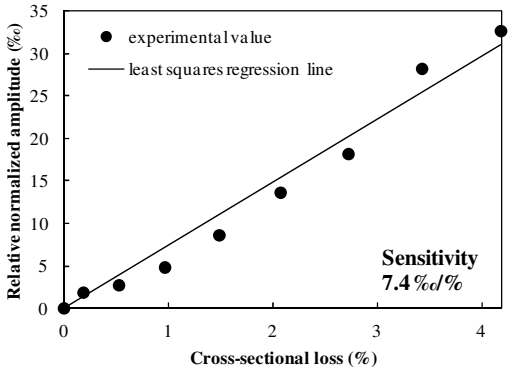

Figure 5. Increasing rate of signal variation (frequency 50 kHz, defect position ①)

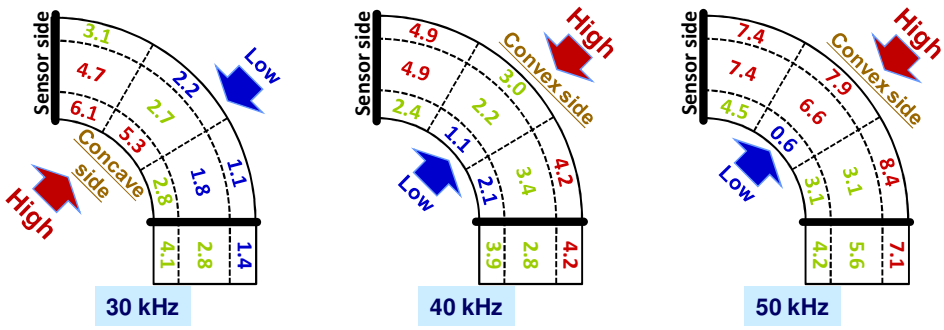

Figure 6. Distributions of defect sensitivity

3. FEM simulations to investigate characteristics of guided wave propagation

To figure out how the frequency of guided waves causes the differences of the sensitivity distribution shown in Fig. 6, finite element method (FEM) simulations were conducted.

3.1 Configuration of FEM simulations

The commercial software ComWAVE, developed by ITOCHU Techno-Solutions Corporation, was used to conduct FEM simulations [4]. The shape of the specimens used in the experiments was reconstructed by the combination of basic geometric shapes in the simulations. The two straight pipes were modeled as hollow cylinders, and the elbow was modeled as a quarter of a hollow torus. The weld beads at both ends of the elbow cause the reflection of guided waves but they were omitted in the simulation model because they did not make a significant difference in our analysis.

The specimens are made of aluminum alloy. The velocities of longitudinal and shear waves in the pipe wall were set to 6,400 m/s and 3,120 m/s, respectively. The density of aluminum alloy was set to 2,700 kg/m^3. Materials properties were not defined in the other regions besides the pipe walls. In ComWAVE, these non-defined regions are treated as a perfect reflector, and computations are not performed inside these regions. This saves much computation time.

To reduce the size of the simulation model, a transmitter was placed 200 mm before the inlet of the elbow. Because ultrasonic attenuation was not considered in these simulations, the amplitude of guided waves propagating along a straight pipe did not diminish with distance. Therefore, the distance between the transmitter and the inlet of the elbow did not affect the propagation behavior at the elbow. The transmitter consists of eight blocks aligned at equal intervals in the circumferential direction of the outer surface of the pipe. All the blocks were synchronously vibrated in the same circumferential direction to generate the fundamental torsional guided wave mode T(0,1). Because the aim of the simulations was to observe how guided waves propagate through an elbow, the receiver was omitted in the simulation model.

The whole simulation model was built up with 0.5 mm voxels. It takes approximately two hours to obtain the simulation results for each condition in parallel on four cores of a processor of the computer with two Intel Xeon X5660 processors (2.8 GHz, six cores for each) and 32 GB of the main memory.

3.2 Simulation results

Because ComWAVE calculates the output parameters at each time step, ComWAVE can display propagation of ultrasonic waves as transient changes in the amplitude distribution of the particle displacement caused by ultrasonic waves.

The three images on the left-hand side in Fig. 7 show the amplitude distributions of the displacement on the outer surface of the piping at three moments when a wave packet is passing through the elbow. The color changes from blue to red as the amplitude increases. To indicate where the amplitude becomes high with a single image, the distribution of the maximum amplitude at each element is presented as shown in the image on the right-hand side in Fig. 7.

Figure 8 shows the distributions of the maximum amplitude around the elbow when the center frequency of the excitation signal is 20, 30, 40, 50 and 60 kHz, respectively. The pipe size is 50A Schedule 40, which is the same as that used in the experiments. As compared with Fig. 6, these distributions show that the maximum amplitude of the displacement has a similar frequency-dependent distribution trend as the defect sensitivity obtained in the experiments. Namely, the maximum amplitude tends to be higher at the concave side of the elbow for lower frequencies, whereas it tends to be higher at the convex side of the elbow for higher frequencies. It is understandable that the defect sensitivity and

the maximum amplitude of the displacement have similar distribution trends because a high-amplitude region is expected to be a defect-sensitive region for guided wave testing.

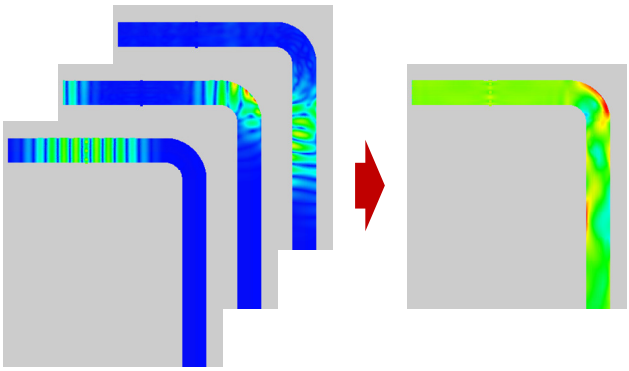

Figure 7. Amplitude distribution of displacement on outer surface of piping

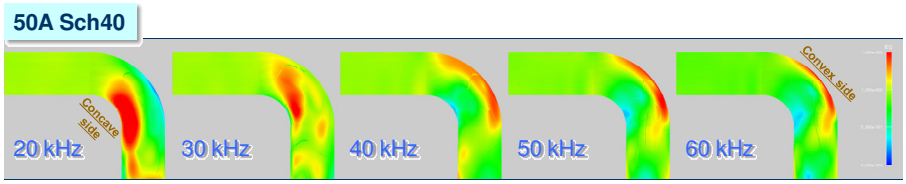

Figure 8. Distributions of maximum amplitude (50A Sch. 40)

The uneven distributions of the maximum amplitude shown in Fig. 8 are thought to be attributed to interference of guided waves at an elbow. Even if guided waves entering an elbow are coherent, the shape of the elbow gives rise to constructive and destructive interference of the guided waves as shown in Fig. 7. In this process, the relation between the pipe size and the wavelength of the guided waves should determine the interference behavior.

To investigate the effect of the pipe size on the distribution of the maximum amplitude, the simulation results obtained with different pipe sizes were compared. Table 1 shows the pipe sizes used for the simulations. Because the finite element used in the simulations is a 0.5 mm voxel, these values are rounded. Figure 9 shows the distributions of the maximum amplitude around the elbow when the pipe size is 100A Schedule 10S, which has twice the outer diameter and the same wall thickness compared with 50A Schedule 40. To keep the same ratio between the wavelength of the guided waves and the pipe size, the frequencies of the guided waves were reduced to half of those used for 50A Schedule 40. Then, a variation trend observed in these distributions is similar to that found in Fig. 8. This supports that the uneven distributions of the maximum amplitude are caused by constructive and destructive interference of guided waves.

Table 1. Pipe sizes used in FEM simulations

Nominal Size	Outer Diameter	Wall Thickness		
		10S	20S	40
15A	22.0	2.0	2.5	3.0
20A	27.0	2.0	2.5	3.0
50A	61.0	3.0	3.5	4.0
100A	114.0	3.0	4.0	6.0

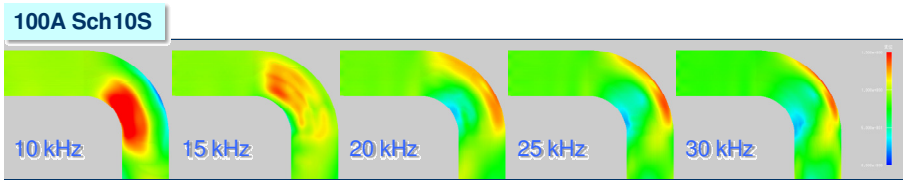

Figure 9. Distributions of maximum amplitude (100A Sch. 10S)

Figure 10 compares the distributions of the maximum amplitude around the elbow when the pipe size is 50A Schedule 10S, 50A Schedule 20S and 50A Schedule 40. The outer diameter is 61.0 mm for all the cases but the wall thickness is 3.0, 3.5 and 4.0 mm, respectively. The comparison shows that the wall thickness has little influence on whether constructive interference occurs at the concave or convex side of the elbow.

To confirm that the same ratio between the wavelength of guided waves and the pipe size provide a similar distribution of the maximum amplitude, the highest frequency with high amplitudes at the concave side of the elbow is marked for each pipe size in Fig. 11 (The wall thickness is 10S for all the pipe sizes). For example, both the third and forth images from the left in the row of 15A in Fig. 11 show high amplitudes at the concave side of the elbow but the view given on the top left corner of each image exhibits that the high-amplitude region is split in the middle of the concave side of the elbow for 60 kHz. Therefore, 50 kHz was determined to be the highest frequency with high amplitudes at the concave side of the elbow for the pipe size 15A. In a similar manner, such frequencies were determined to be 40, 20 and 10 kHz for the pipe sizes 20A, 50A and 100A, respectively. Figure 12 shows that there is an almost linear correlation between the outer diameter of the pipe and the highest frequency with high amplitudes at the concave side of the elbow. It is plausible that the ratio of the wavelength of guided waves to the pipe size determines the interference behavior of the guided waves and thus the locations of high-amplitude regions at the elbow.

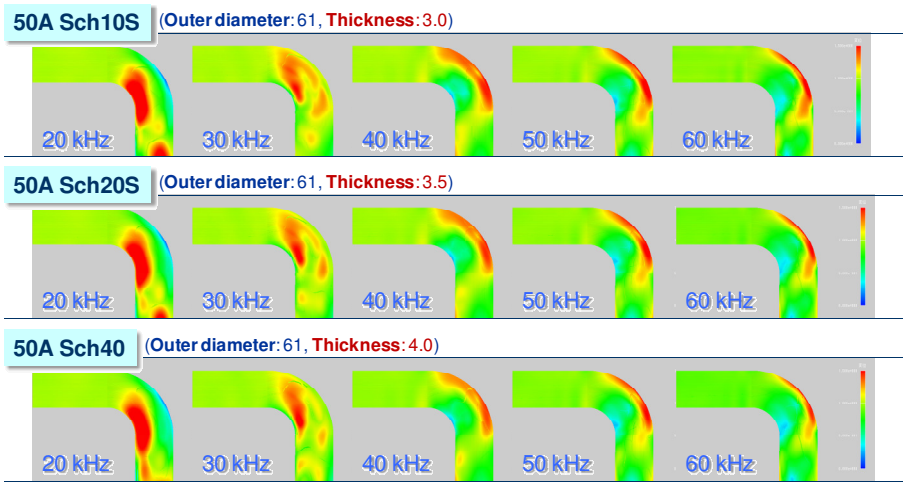

Figure 10. Distributions of maximum amplitude (50A with different wall thicknesses)

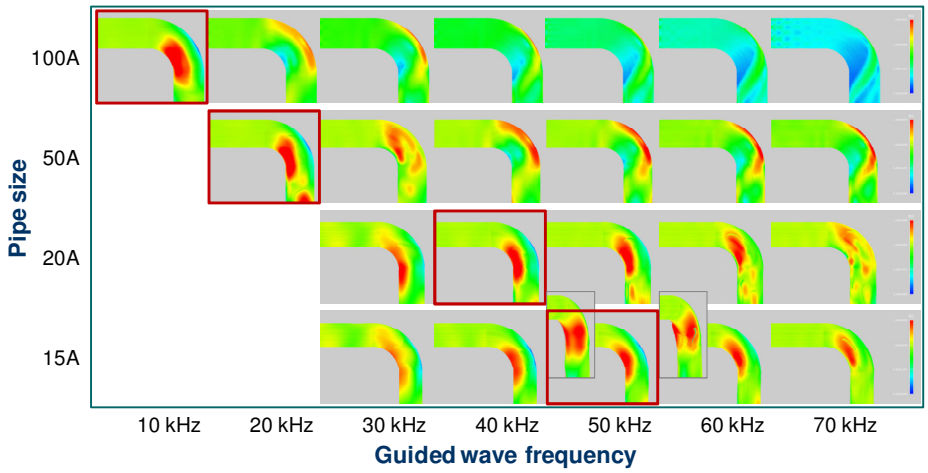

Figure 11. Highest frequencies with high amplitudes at concave side for different pipe sizes (The wall thickness is 10S)

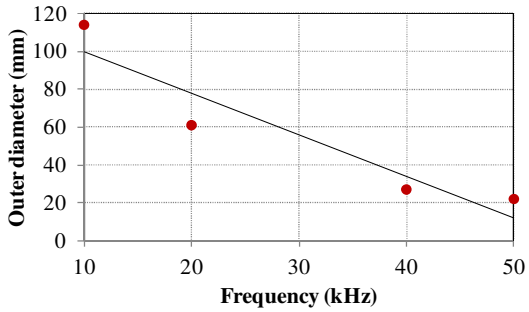

Figure 12. Correlation between highest frequency with high amplitudes at concave side and pipe size

4. Summary

FEM simulations were conducted to investigate the mechanism of the sensitivity characteristics at an elbow of piping. Constructive and destructive interference was observed in the simulation results using simulation models with different combinations of the pipe size and the frequency of guided waves. These simulation results support that the ratio of the wavelength of guided waves to the pipe size determines the places where the amplitude of guided waves tends to be high (especially, the concave or convex side of an elbow). From the comparison between experimental results and simulation results, a high-amplitude region is expected to be a defect-sensitive region. Then, it is assumed that the location of a defect-sensitive region is controlled by the ratio between the pipe size and the wavelength of guided waves. Efficient defect detection at an elbow of piping is accomplished by making the target area of the elbow (e.g., the concave or convex side) a defect-sensitive region with an appropriate frequency for each pipe size.

References

[1] T. Yamamoto, T. Furukawa and H. Nishino, “Efficient defect detections of elbow pipes using propagation characteristics of guided waves,” 40th Annual Review of Progress in Quantitative Nondestructive Evaluation, Vol. 33A, D. E. Chimenti, L. J. Bond and D. O. Thompson (Eds.), AIP Conference Proceedings, Vol. 1581, pp. 373–379, AIP Publishing LLC (2014)

[2] H. Nishino, S. Masuda, Y. Mizobuchi, T. Asano and K. Yoshida, “Long-range testing of welded elbow pipe using the T(0, 1) mode ultrasonic guided wave,” Jpn. J. Appl. Phys. 49 (2010), pp. 116602-1–6

[3] H. Nishino, T. Tanaka, S. Katashima and K. Yoshida, “Experimental investigation of mode conversions of the T(0, 1) mode guided wave propagating in an elbow pipe,” Jpn. J. Appl. Phys. 50 (2011), pp. 046601-1–7

[4] Y. Ikegam, Y. Sakai and H. Nakamura, “A highly accurate ultrasonic simulator capable of over one billion elements for non-destructive evaluations,” Proceedings of the 7th International Conference on NDE in Relation to Structural Integrity for Nuclear and Pressurised Components, M. Bieth (Eds.), pp. 177–190, European Communities (2009)

Guided Wave Signals for Monitoring of Buried Pipe Mockup using a Magnetostrictive Sensor Method

Yong-Moo Cheong [1], and Duck-Hyun Lee[1]
[1]Korea Atomic Energy Research Institute, 111, Daedeok-daero, 989-beon-gil, Yuseong-gu, Daejeon, 305-353, Korea

E-mail address(corresponding author) : ymcheong@kaeri.re.kr

When a pipe is buried in the ground, it is difficult to detect a defect until the defect grows even to the point of leakage. To prevent the leakage of a buried pipe, a guided wave method can be a promising technique. Among the various vibration modes, the torsional guided wave T(0,1) mode has many advantages, such as no dispersion, no radial displacement, and a low attenuation.
Because the torsional guided wave T(0,1) mode has many advantages for long-range guided wave examination, such as no dispersion, no radial displacement, and a low attenuation, it can be a promising tool for an evaluation of flaws from a buried pipe as well as the structural health monitoring of pipes for a long period. A guided wave method with a magnetosrictive sensor was studied for practical application to an examination of a buried pipe. The signal amplitude from various reflectors is compared with two different sensor techniques, one by a variation of DC bias and the other by a remnant magnetic bias technique. Based on the signal amplitude, attenuation owing to the surrounding sand and soil on the buried pipe mockup was estimated. The guided wave signals from various reflectors were also compared with two different sensor techniques, one through a variation of DC bias and the other using a remnant magnetic bias technique.

Keywords: Torsional guided wave, magnetostrictive sensor, buried pipe monitoring.

Human errors of reactor pressure vessel Examinations in Korean nuclear plants

Euisoon DOH, Chang-hun LEE, Jae-yoon KIM, Wi-hyun KIM
KEPCO KPS, Busan, Korea

E-mail : dohes@kps.co.kr

More than 20 PWR units are under commercial operations in Korea. Every nuclear plant shall be examined periodically in accordance with regulatory guides and codes in Korea and in the world. 40 Month examination of reactor pressure vessel is performed in the second outage, and 10 Year RPV ISI is performed in the sixth outage of the interval in Korea.
Welds, components and structures in the nuclear plants shall be examined very accurately per regulatory guides, code and fabrication drawings. Reactor pressure vessel is the most important component among the examination parts.
However, some critical mistakes of reactor pressure vessel examination have been reported in Korean nuclear plants.
The first error in the examination of reactor pressure vessel was occurred at Yonggwang (Hanbit) unit 5 in 2001. A weld location of Yonggwang unit 5 and 6 was changed from that of the previous units of KSNP(Korean Standard Nuclear Plant) to get more examination coverage. However, an American inspection company which is no more existence now did not use the right drawings of Yonggwang unit 5. They used another drawing from the previous plant. Fortunately, they got to know their mistake before getting a fuel load approval from authority while they were preparing PSI of unit 6.
The next error was revealed at Kori unit 4 in 2014. The same American company with Yonggwang unit 5 has performed the PSI of Kori unit 4 about 30 years ago, they has used wrong drawings, and examined 2 wrong welds for Kori unit 4. They have used drawings for Kori unit 3 to establish the Examination Scan Plan for Kori unit 4. They might have thought that Kori unit 3 and 4 should have been same fabrications, but they have been wrong. These drawings and fabrication of Kori unit 4 have been different from Kori unit 3. No body after the PSI has found the error for 30 years. Wrong welds have been examined after the PSI before verification of the error by KPS in 2014 during the preparation of the examination for the 3rd interval. Korean the only nuclear utility, KHNP investigated all nuclear plants after revelation of error at Kori unit 4 to check their integrity of examinations for major components. Unfortunately, KHNP found another fatal error of RPV examination at Hanbit unit 2. The cause of the error was same as Kori unit 4.
KPS carried out inspections for both units of errors in 2014, and reported their keeping integrity of their original welds which must have been examined.

The learned lesson from these errors in the examination is the importance of using right and accurate drawings and the mental concentration of examiners not to make mistake in the PSI. Otherwise, it would be very difficult to find the any error in the successive examination after PSI.

Keywords: Reactor vessel, Reactor vessel Examination, RPV Examination, RPV Inspection, RPV, PSI

Understanding of Sub-cooled Nucleate Boiling on the Nuclear Fuel Cladding Surface Using Acoustic Emission Energy Parameter

Kaige Wu, Seung-HeonBaek, Hee-Sang Shim, DoHaengHur, Deok Hyun Lee*

Korea Atomic Energy Research Institute, 989-111 Daedeok-daero,Yuseong-gu, Daejeon, Republic of Korea

Abstract

In the primary coolant system of a pressurized water reactor, it has been known that CRUD deposition on the fuel cladding surfaces is accelerated under sub-cooled nucleate boiling (SNB) conditions. Anomalous neutron absorption from accumulated boron in the CRUD can lead to an axial offset anomaly (AOA). Thus, the detection and monitoring of SNB in terms of a non-destructive evaluation is of great importance for analyzing the behavior of CRUD deposition and AOA. In this work, an acoustic emission (AE) method is proposed to investigate and understand the SNB phenomenon.

An internal electric heater was inserted within a Zirlo cladding tube to control the boiling process. A high sensitivityAE sensor was connected to the upper end of thecladding tube, which acted as a waveguide. The internal heater temperature was controlled from 120 to 260 °C in the simulated primary watercontaining 3.5 ppm Li and 1500 ppm B under atmospheric pressure. The tests were conducted in a cylindrical glass cell whereby the boiling occurrence could be visibly checked. The AE data were collected and photographic observations were also made during the boiling process.

When the heater temperature was low, no bubbles were generated and the AE signals obtained should be background owing to heating and other electrical noises. As the water was heated to the temperature under saturation, bubbles began to form on the cladding surface but immediately collapsed nearby. The detected AE signals might be associated with the bubble growth and collapse. After the water temperature reached the saturation temperature, the bubbles grew, departed from the cladding surface,then rose up and burst at the water/air interface.The AE signals were distinguished as four groups in the AE energy criterion, which might be associated with the bubble growth, bubbles departure, bubbles collapse, and bubbles burst, respectively. The results indicate that the SNB phenomenon can be understood through the characteristics of the AE signals, and AE NDT can be proposed as an effective tool for monitoring the evolution of nucleate boiling on the fuel cladding surface.

Keywords: Fuel cladding, CRUD, Sub-cooled nucleate boiling, Boling process, Acoustic emission.

1.Introduction

The axial offset anomaly (AOA), which is also known as crud-induced power shift (CIPS), refers to a neutron flux depression in upper region of a pressurized water reactor core, which can lead to operational issue of the plants with long-period cycle operation [1-3].It is well known that AOA is caused by anomalous neutron absorption due to accumulated boron hide out in porous crud deposited on the cladding. Furthermore, large scale laboratory experiments elaborated and confirmed the mechanism of boiling assisted deposition that porous crud layer on the cladding was accelerated under sub-cooled nucleate boiling (SNB) condition [4-10].Obviously, the degree of SNB is interrelated to the crud deposition on the cladding surface. Accordingly, evaluation of the SNB and crud deposition is an important approach to understand the occurrence of AOA. Indeed, a great many attempts have been made with such consideration by various methods, such as thermal-hydraulic analysis [4], model analysis of particle transportation [5-6], micro-layer evaporation and dry-out (MED) model calculation [7], post-morphological analysis [8-9], and high fidelity digital imaging apparatus [10].Unfortunately, despite much effort focusing on this topic, much still remains to be investigated for the realization of a comprehensive understanding. Moreover, these methods have their own disadvantages like that most of these methods are usually off-line and must be performed during plant outage. Therefore, we are encouraged to get a better understanding of SNB on the cladding surface and the behavior of the bubbles formed in SNB from the dynamic point of view, using an in-situ nondestructive evaluation (NDE)technique.

Acoustic emission method (AE) is an in situNDE method that senses transient elastic waves resulting from a rapid release of energy within a dynamic process [11], such as corrosion process [12-14], cracks evolution [15-16] andvarious chemical engineering processes concluding bubbles dynamic [17]. Of many methods proposed for evaluation of the crud deposition and AOA phenomenon, monitoring and detection of AE signals generated along with boiling process is considered to be one of the most promising techniques because of its high sensitivity of detection, real time monitoring and in-situ full body scanning of research target.Up to now, many attentions has been paid to AE investigation on the boiling process, such as SNB, nucleate boiling (NB) and transition boiling [18-27]. It has been well acceptedthatthe bubble dynamic is critical for the generation of acoustic emission along with the boiling process. Nishihara et al. [18] and Zhang et al. [19] investigated the boiling behavior on the surface of a horizontal metal wire under atmospheric pressure. The AE in boiling was reported to have frequency components up to 50 kHz.

At the beginning of the bubble growth, a significant pressure pulse was found by Robinson and Schmidt [20]. Moreover, the mechanism of the pressure wave generation in bubble growth is shown to follow the Young-Laplace equation [21-23]. The amplitude increase of AE was thought to be directly proportional to the overheating of the liquid and indirectly proportional to the critical radius of the bubble.

In the departure or detachment of bubbles from the surface, AE was reported to be generated dependent on the distribution of surface temperature in the vicinity of the boiling nucleus [22-25]. The detailed source in bubble departure was believed to be the swirl and turbulence induced by the pulsing vapor nucleus.

Bubble collapsein SNB, or called as bubble implosion, were frequently reported to generate AE signals with larger amplitude, higher energy comparing with the bubble growth and bubble departure [20, 24]. Bubble collapse due to heat transfer from the subcooled liquid was assumed to be very fast and the generated acoustic pulses were directly proportional to sub-cooling and practically independent on the diameter of the collapsing bubbles [24].

In NB, the bubbles rise and burst at the free surface of liquid. Husin and Mba [26], and Divoux et al. [27] found that bubble rising does not produce AE, while the bubble burst caused AE with large amplitude and high energy which have a correlation with bubble length. They also observed that the duration of AE increases with the bubble length [27].

Motivated both by the will to understand the dynamic of SNB on the nuclear fuel cladding surface, and the hope to use AE NDT as a tool to predict the crud deposition and AOA phenomenon, we carried out an experimental work with AE sensor directly coupled to the surface of a simulated cladding tube, to investigatethe dynamic of bubbles formed inSNB under atmospheric pressure by AE method.

2. Experimental procedure

Figure 1 shows a series of schematic drawings of the test section in the present work. A Zirlo cladding tube with an internal electric heater inserted was placed vertically to provide the surface for boiling process. The internal heater temperature was controlled from 120 to 260 °C in the simulated primary water containing 3.5 ppm Li and 1500 ppm B under atmospheric pressure. 500 seconds was held on at each temperature for observation of the boiling behavior and collection of the AE signals.The test was conducted in a cylindrical glass cell whereby the boiling occurrence could be visibly checked. The photographic and video observations were made during the boiling process.The video was taken with a common camera by 30 frames / s. After the test, all the videos taken in each temperature were analyzed by frames comparison.

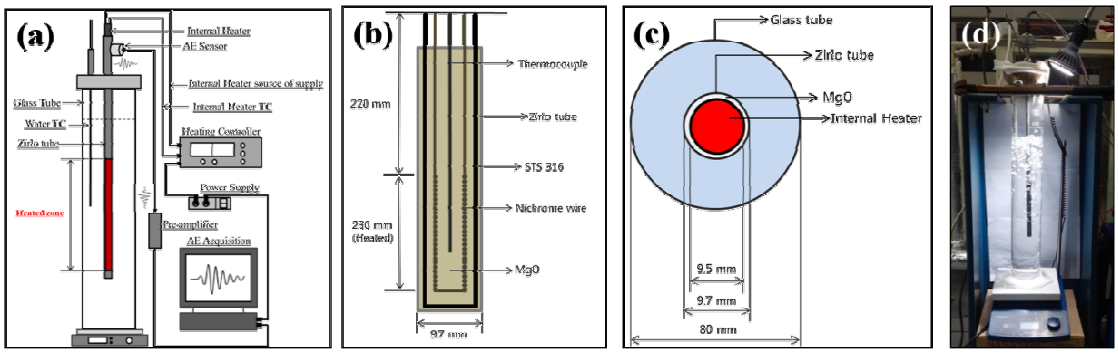

Figure 1. (a) A schematic illustration of experimental apparatus used in the present research; (b) and (c) Theschematics of the detailed structure of internal heater. (d) A real photo showing the experimental setup.

As shown in Fig. 1, a high sensitivity AE sensor (Type R15, MISTRAS from Physical Acoustic Corporation, USA) was directly coupled with an ultrasonic couplantto the upper end of the cladding tube which also acted as a waveguide.

The other end of AE sensor was connected to a pre-amplifier (2/4/6 Preamplifier, Physical Acoustic Corporation, USA), the other end of which was connected to the AE system. The AE signals and various parameters were collected by an acquisition device (Model: PCI-2, Physical Acoustic Corporation, USA). The background noises from the surrounding were tried to be minimized and the threshold value was carefully to determine as 40 dB and the preamplifier was set to 40 dB, respectively. For detected AE signals, following AE parameters are studied:

(i) Counts: The number of times the AE signal excursions over the AE threshold;
(ii) Amplitude: the maximum AE signal excursion during an AE hit;
(iii) Energy: the parameter derived from the integral of the rectified voltage signal over the duration of the AE hit;
(iv) Rise Time: the time between the AE Hit start and the peak amplitude of the AE Hit;
(v) Duration: the time from the first threshold crossing to the end of the last threshold crossing of the AE signal from the AE Threshold.
(vi) Average Frequency: the parameter derived from AE Counts and Duration determines an average frequency over the entire AE hit.

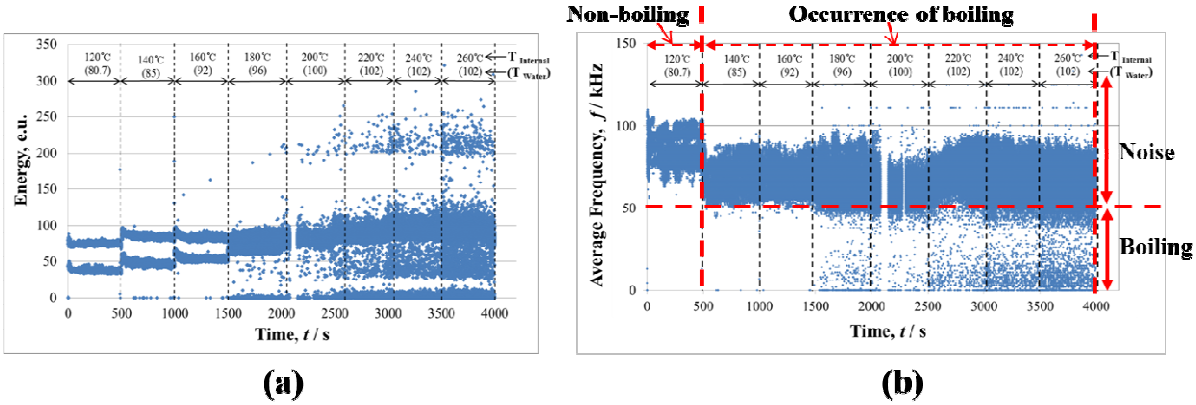

3. Results and discussion

Figure 2. Evolution of raw AE data obtained during process of boiling test with controlling the temperature of internal heater from 120 to 260℃: (a) AE signals in energy parameter; (b) AE signals in average frequenc

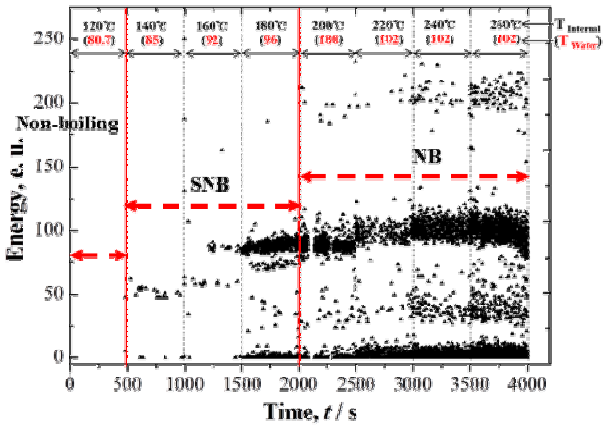

y parameter.

Figure3. Evolution of AE signalsfrom boiling process with frequency range of between 0 and 50 kHzextractedfrom the raw data.

Figure 2 shows the evolution of raw AE data obtained during the test process in energy and average frequency parameters, respectively. AE signals presented to be in dependence on the temperatures of internal heater and water. Considering the direct coupling of sensor to tube surface, it is believed that the raw data were mixed with boiling signals and noises signals that derived from such as electricity noises, heating shut-off, and the contraction or friction of the heating elements. Based on the photographical monitoring, it was non-boiling period when the temperatures of heater and water were 120 and 80.7 °C, respectively. In this period the AE frequency was in a band over 50 kHz.It was from the 500 s,at which the heater temperature was increased to 140 °C,when boiling began to be observed. Along with the occurrence of boiling, the component offrequency below 50 kHz was collected. It was thought, therefore, that the AE signals from the boiling process cluster below 50 kHz. Similar frequency of boiling process up to 50 kHz under atmospheric pressure was also reported by Nishihara and Bessho [18] and Zhang et al. [19].

Based this conclusions of AE frequency of boiling, the raw AE data was filtered by a frequency range between 0 and 50 kHz. Then the signals extracted were believed to be from the boiling process, as shown in Figure 3. It clearly showed that the boiling AE signals in energy appeared to be dependent on water temperature. Based on the water temperature and the photographical observations, the boiling process could be divided into two periods: SNB before saturationtemperature was surpassed and the NB after saturation was reached, which were indicated in Fig. 3. Moreover, it was noticed that the saturation increased to be 102 °C since 2500 s, despite the test was finished under atmospheric pressure. It might be due to the pressure changes nearby the thermal couple, which was again due to the volume changes because of bubbles evolution [20].

Figure 4 shows the cross-plot analysis of the parameters of boiling AE concluding amplitude, energy, rise time, d uration, and counts number. This analysis suggested that the AE signals clustered clearly into four distinct groups, i.e., group 1, 2, 3, and 4, respectively.

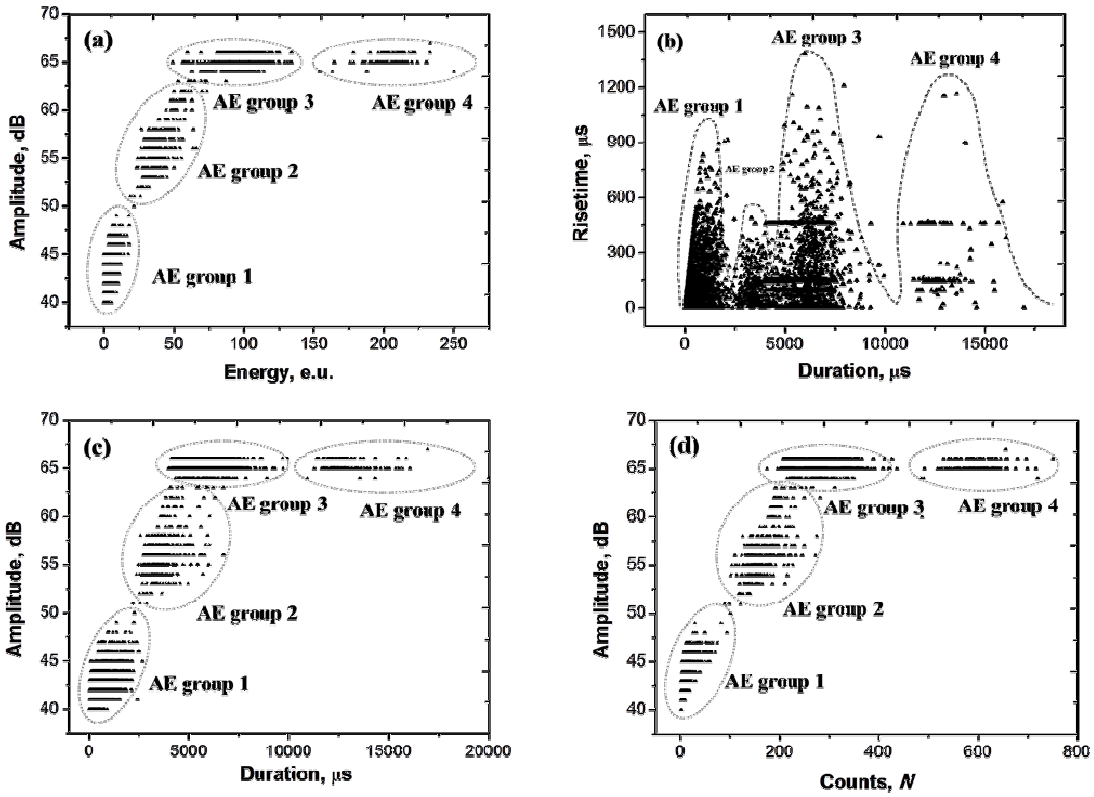

Figure4.Cross-plot analysis of the parameters of boiling AE: (a) amplitude versus energy; (b) rise time vers

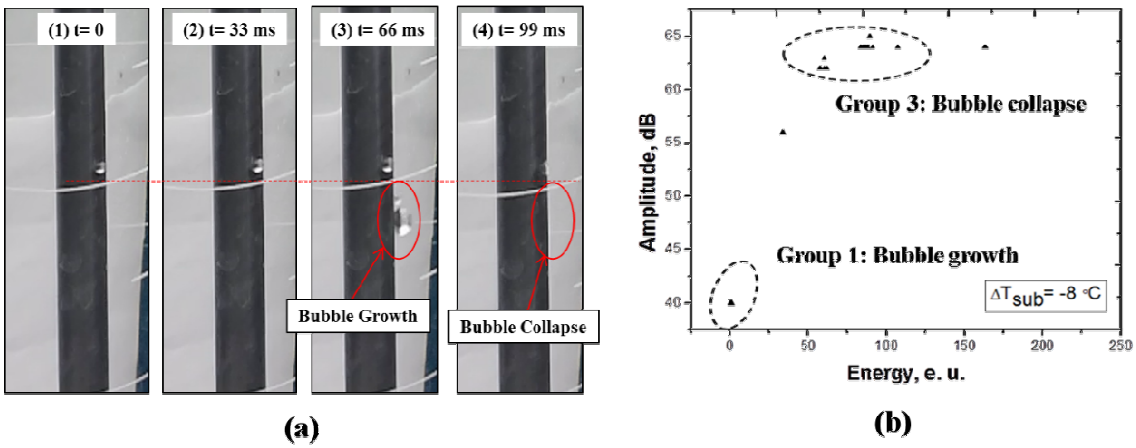

us duration; (c) amplitude versus duration; (d) amplitude versus counts.

Figure 5. (a) Photographical analysis and (b) the corresponding AE data in the condition of $T_{Internal\ heater}$ = 160°C, T_{water} = 92°C.

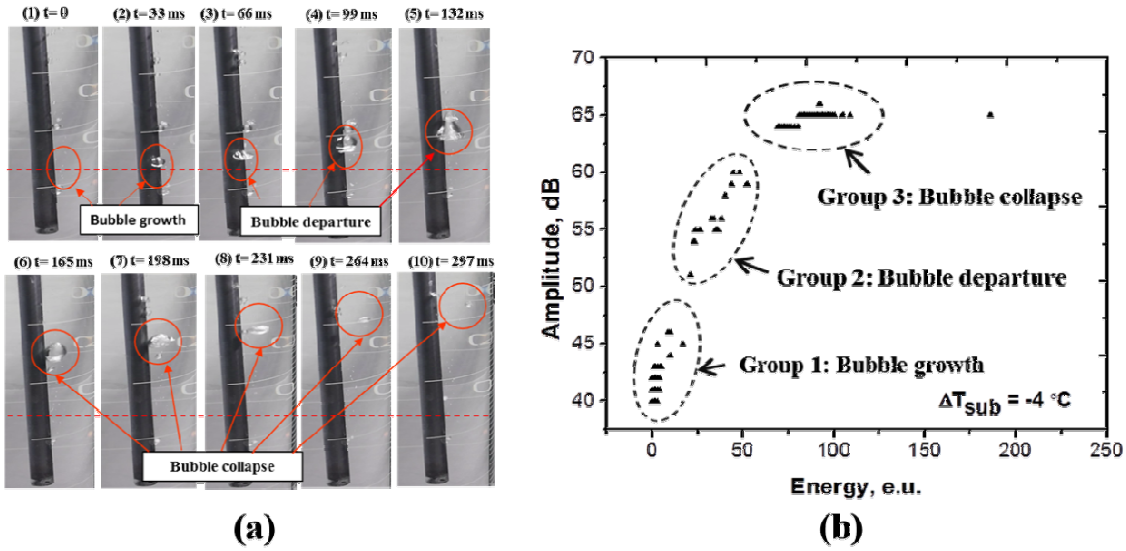

Figure 6. (a) Photographical analysis and (b) the corresponding AE data in the condition of $T_{Internal\ heater}$ = 180°C, T_{water} = 96°C.

In attempting to uncover the physical mechanism between the AE groups and the dynamic of bubbles formed during boiling, photographical analysis was carried out based on frame comparison of the video taken during boiling process.

Figure 5(a) shows a series of frames extracted from the video taken in the condition of $T_{Internal\ heater}$ was 160°C, T_{water} was 92°C. When t = 66ms, a bubble was captured to grow on the cladding surface, and collapsed immediately at the surface after 33ms. The main physical changes during this process were bubble growth and bubble collapseon thecladding surface, which clearly suggested the occurrence of SNB. Figure 5(b) shows the AE signal in cross-plot analysis of amplitude and energy, which indicated the appearance of AE signals located in group 1 and 3 in comparison with the all-process signals in Fig. 4. It has been well known that the bubble collapse produced AE signals with higher energy and larger amplitude than bubble growth [20-24]. Consequently, it was concluded that AE group 1 and 2 were contributed to the bubble growth and bubble collapse, respectively, as marked in Fig. 5(b).

Figure 6(a) shows a series of frames extracted from the video taken in the condition of $T_{Internal\ heater}$ was 180°C, T_{water} was 96°C. When t = 33ms, a bubble was observed to grow on the claddingtube surface, subsequently the bubble departed from the surface. Then it rose upwardly and collapsed nearby the tube surface after 264ms. In this SNB process, the physical evolutions were bubble growth, bubble departure, bubble rising and bubble collapse. Figure 6(b) shows the AE signal in this period. It clearly indicated that AE signals appeared to be with three groups, which were corresponding to the AE groups 1, 2, 3, respectivelycomparing with the total signals in Fig. 4. According to the report by Husin and Mba [26], bubble rising does not produce AE. Considering that AE groups 1 and 3 were associated with bubble growth and bubble collapse, the AE group 2 was therefore believed to be the results of bubble departure. This conclusion shows that the AE signals from bubble collapse are with larger amplitude and higher energy than bubble

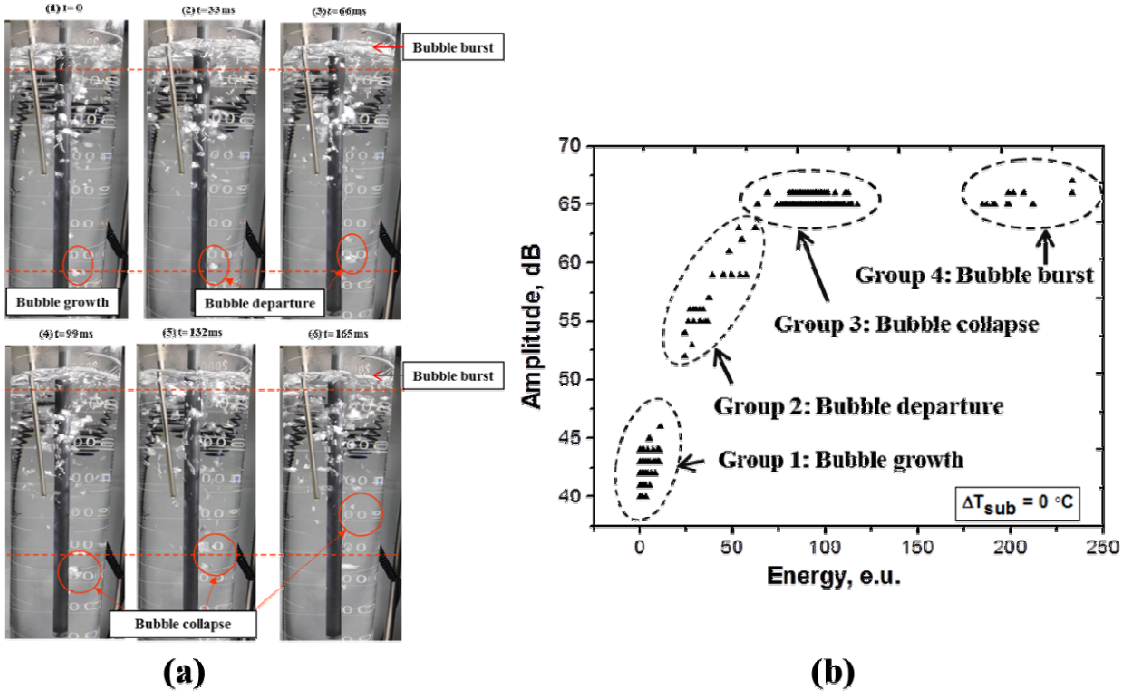

growth and bubble departure, which is in good consistent with previous reports [22-24].

Figure 7. (a) Photographical analysis and (b) the corresponding AE data in the condition of $T_{Internal\ heater}$ = 200°C, T_{water} = 100°C.

Figure 7(a) shows another series of frames extracted from the video taken in the condition of $T_{Internal\ heater}$ was 200°C, T_{water} was 100 °C. First, this period was featured by the bubbles burst at the free surface of water after rising to the free surface, which suggested the beginning of NB. In the bottom of cladding tube, it was observed that the bubble grew, subsequently departed from the cladding surface, and finally collapsed nearby the cladding surface. While in the upper of tube, the bubbles rose to the water surface and burst.This phenomenon could be explained that the temperature of water near the bottom of tube was below saturation, and the surface temperature was very high. However, the saturation of water near the upper of tube was reached and NB started to be generated. Figure 7(b) shows the AE signals in this period. AE signals clearly clustered into four groups which were corresponding to the AE groups 1-4 in comparison with the total signals in Fig. 4. According to the photographic analysis, bubble burst was first found in this period in comparison with the bubbling in SNB. As a result, bubble burst were proposed to be responsible for the AE group 4.

Based on analysis above, two proposed schematic diagrams for SNB and the transition from SNB to NB were shown in Figure 8. Moreover, AE characteristics and detectabilityof the dynamic of bubbles formed during the boiling were given in Table 1. The AE groups 1-4 were associated with the bubble growth, bubble departure, bubble collapse in sub-cooled water, and bubble burst in NB process, respectively. This conclusions show the most powerful source for AE signals during NB are bubble burst at the free surface, while the AE with largest amplitude and highest energy are contributed to the bubble collapse in sub-cooled liquid. It could be concluded that the AE group 3 from bubble

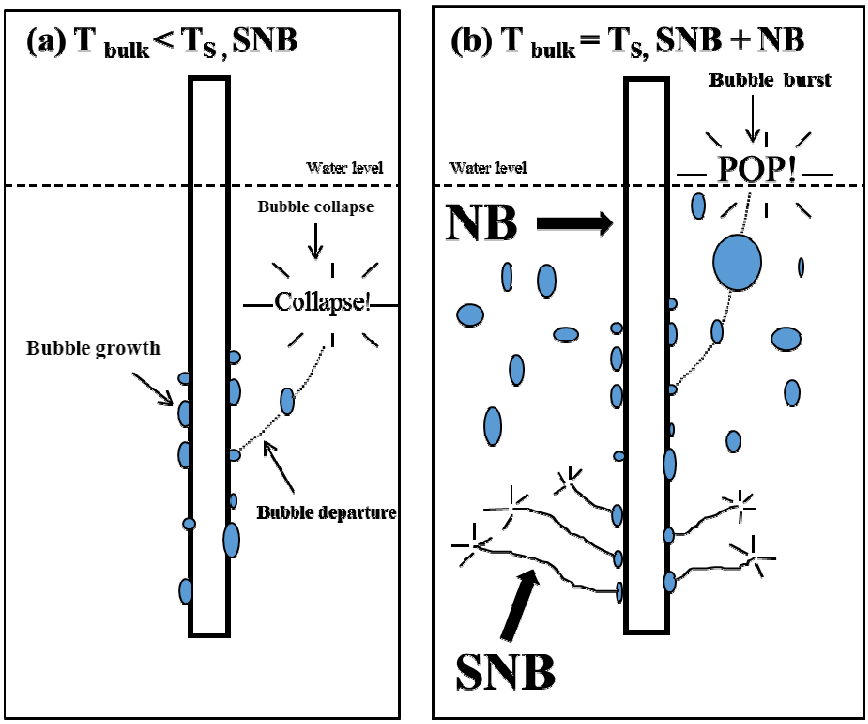

collapse and AE group 4 from bubble burst could be used as the featured indicator for the occurrence of SNB and NB, respectively. Moreover, the transition from SNB to NB could be distinguished by AE signal monitoring.

Figure 8.The proposed schematic diagrams for SNB (a) and the transition from SNB to NB (b).

Table1. Summary of AE characteristics and detectabilityof the dynamic of bubbles formed during the boiling.

AE groups	Characteristics of the corresponding AE groups					Physical mechanism
	Energy (e.u.)	Amplitude (dB)	Duration (μs)	Rise time (μs)	Counts (N)	
Group 1	0-9	40-49	0-2178	0-903	0-65	Bubble growth
Group 2	19-73	51-65	2173-6313	0-487	90-282	Bubble departure
Group 3	57-134	64-66	4004-9706	0-1210	201-437	Bubble collapse
Group 4	163-233	64-67	11283-16942	0-460	520-655	Bubble burst

4. Conclusions

In this work, AE method was employed to investigate the dynamic of bubbles formed in SNB at atmospheric pressure in the perspective of in-situ NDE monitoring. Some conclusions can be drawn based on the present work as follows:

1). AE in-situ monitoring was confirmed to with good feasibility in investigating the dynamic of bubbles formed in SNB and NB;

2). The frequency of boiling AE was confirmed to be lower than 50 kHz, and the boiling AE could be divided into four distinct groups based on cross-plot analysis of AE parameters;

3). Based on analysis of boiling AE and the corresponding photographic observations, AE groups 1-4 could be contributed to the dynamic of bubble growth, bubble departure, bubble collapse in subcooled water, and bubble burst at water surface, respectively.

4). The AE group 3 from bubble collapse and AE group 4 from bubble burst could be used as the featured indicator for the occurrence of SNB and NB, respectively.

5). AE energy and amplitude could contribute to monitor the dynamic process of SNB well.The transition from SNB to NB could be clearly distinguished by AE signals.

6). The obtained AE characteristics of boiling dynamic could provide a good basis for the following experiments in high temperature and high pressure.

Acknowledgements

This work was supported by the National Research Foundation of Korea (NRF) grant funded by the Korea government (MSIP).

References

[1] J. Deshon, D. Hussey, B. Kendrick, J. McGurk, J. Secker and M. Short, “Pressurized water reactor fuel crud and corrosion modeling”, JOM J. Miner. Met.Mater. Soc., Vol.63, No. 8, pp. 64-72 (2011)

[2] E. Decossion and O. Bremnes, “Axial offset anomaly modeling studies on EDF cores” In: Proc. Int. Conf. on Nuclear Engineering, Orlando, Florida, USA., May 11-25, p.271, 2008

[3] W. Byers and J. Deshon, “Structure and chemistry of PWR crud” In: Proc. Int. Conf. on Water Chemistry of Nuclear Reactor Systems, San Francisco, USA, p.1722, 2004

[4] M.H. Kim, U.C. Kim, C.W. Won and W.Y. Maeng, “Experimental evaluation of primary water chemistry for prevention of axial offset anomaly”, Thermochim. Acta, Vol. 542, No. 20, pp. 80-88 (2012)

[5] H. Bindra and B.G. Jones, “Deposition of metallic colloids under sub-cooled nucleate boiling”, Colloids and Surfaces A: Physicochemical and Engineering Aspects, Vol. 397, No. 5, pp. 85-91 (2012)

[6] H. Bindra, “Effect of boiling in deposition of metallic colloids”, PhD Thesis, University of Illinois, 2010

[7] S. Uchida, Y. Asakura and H. Suzuki, “Deposition of boron on fuel rod surface under sub-cooled boiling conditions-An approach toward understanding AOA occurrence”,Nucl. Eng. Des., Vol. 241, No. 7, pp. 2398-2410 (2011)

[8] S.H. Baek, H.S. Shim, C.H. Won, D.H. Hur and U.C. Kim, “Effects of Ni, Fe chemicals and hydrogen on deposits formed on Zirlo fuel cladding material in nuclear primary water chemistry conditions at 325 °C”, Ann. Nucl. Energy, Vol. 70, pp. 233-239 (2014)

[9] T. Iwahori, T. Mizuno, and H. Koyama, “Role of surface chemistry in crud deposition on heat transfer surface”, Corros., Vol. 35, No. 8, pp. 345-350, (1979)

[10] W. Wu, P. Chen, B. Jones, and T. Newell, “Measurement and analysis of bubble behavior in sub-cooled boiling

flows", In: Proc. 13th Int. Conf. on Nuclear Engineering, Beijing, China, May 16-20, p.545, (2005)

[11] ASTM E1316, "Standard Terminology for Nondestructive Examinations", American Society for Testing and Materials, (2011)

[12] J.W. Byeon, K. Wu and H. Y. Kim, Korean Patent No. 10-1477962, (2014)

[13] K. Wu, W.S. Jung and J.W. Byeon, "Evaluation of corrosion critical variables of 304 stainless steel by delay time of acoustic emission", Mater. Trans., Vol. 56, No. 3, pp. 398-403, (2015)

[14] K. Wu, W.S. Jung and J.W. Byeon, "Acoustic emission of hydrogen bubbles on the counter electrode during pitting corrosion of 304 stainless steel", Mater. Trans., Vol. 56, No. 4, pp. 587-592, (2015)

[15] M. Huang, L. Jiang, P.K. Liaw, C.R. Brooks, R. Seeley, and D.L. Klarstrom, "Using acoustic emission in fatigue and fracture materials research", JOM Nondestructive Evaluation, Vol. 50, No. 11, Presented as JOM-e, (1998)

[16] J.H. Han, D.H.Hur, K.M. Kim, M.S. Choi, D.H. Lee, "Analysis on the Acoustic Emission Signals in the Crack Evolution of Steam Generator Tube", Transactions of the Korean Nuclear Society Autumn Meeting, PyeongChang, Korea, October 25-26, pp. 321-322, (2007)

[17] J.W.R. Boyd, and J. Varley,"The use of passive measurement of acoustic emissions from chemical engineering processes", Chem. Eng. Sci., Vol. 56, No. 5, pp. 1749-1767, (2001)

[18] H. Nishihara and Y. Bessho, "Acoustic emission in subcooled nucleate pool boiling", J.Nucl. Sci.Technol., Vol. 14, No. 6, pp. 407-415, (1977)

[19] Q. Zhang,K. Dong, Z. Huang, J. Wang and Y. Yang, "Mode identification of pool boiling of water by acoustic emission", CIESC Journal, Vol. 64, No. 10, pp. 3527-3533, (2013)

[20] G.E. Robinson, F.W. Schmidt, H.R. Block, and G. Green, "An experimental determination of isolated bubble acoustics in nucleate boiling system", in: Proc. 5th Int. Heat Transfer Conf., Tokyo, September 3-7, Vol. 4, pp. 75-79, (1974)

[21] P. Benes and M. Uher, "Identification of liquid boiling by acoustic emission", In: Proceedings of XIX IMEKO World Congress Fundamental and Applied Metrology, September 6-11, Lisbon, Portugal, pp. 1396-1401, (2009)

[22] V. P. Carey, Liquid Vapor Phase Change Phenomena: An Introduction to the Thermophysics of Vaporization and Condensation Processes in Heat Transfer Equipment. New York: Hemisphere Publishing Corporation, ISBN: 0-89116-836-2, (1992)

[23] G.F. Hewitt, "Boiling", In: W.M. Rohsenow, J.P. Hartnett, Y.I. Cho, ed., Handbook of Heat Transfer. 3rded. New York: McGraw-Hill, Chapter 15, pp. 15.1-15.167, ISBN: 978-0-07-053555-8, (1998)

[24] A.F. Mills, Basic Heat and Mass Transfer, 2nd Ed., New Jersey: Prentice-Hall, ISBN: 978-0-13-096247-3, (1999)

[25] T.G. Leighton, The Acoustic Bubble, Academic Press, London, 1997.

[26] S. Husin and D. Mba, "Acoustic emission of a single bubble activities", in: Proceedings of the World Congress on Engineering 2010 Vol II, WCE 2010, June 30-July 2, London, U.K.

[27] T. Divoux, V. Vidal, F. Melo, and J.C. Geminard, "Acoustic emission associated with the bursting of a gas bubble at the free surface of a non-Newtonian fluid", Phys. Rev. E, Vol. 77, 056310, pp. 1-7, (2008)

Implementation of Special PA UT Techniques for Manufacturing Inspection of Welds in Thick Wall Components

Dirk Verspeelt [1], Dominic Marois [1], Guy Maes [1],
Jean Marc Crauland [2], Michel Jambon [2], Frédéric Lasserre [3]

[1] Zetec, zNDT Solutions, Québec, Canada
[2] AREVA Nuclear Power, Chalon / St Marcel, France,
[3] AREVA Nuclear Power; Paris, France

Abstract

The AREVA-NP/EFF/SAINT-MARCEL factory have selected advanced automated UT based on phased array and TOFD techniques, in view of replacing manual UT and radiographic testing, for circular welds in thick-wall components. The principles of the applied phased array and TOFD examination techniques, and the on-site implementation will be briefly reviewed.

This paper will then address how special UT examination techniques are implemented using phased array technology, to complement the generic techniques.

Tandem configurations, using the LLT technique, are used to obtain enhanced detection capability on planar flaws perpendicular to the inspection surface. Both single probe and two-probe configurations are used to cover the complete wall thickness.

Asymmetric TOFD configurations (Delta technique), generated with phased array probes, are used to maximize TOFD coverage in areas where access is limited to one side of the weld.

For both techniques, theoretical considerations on probe design will be presented, as well as the practical implementation of the focal laws using the UltraVision® phased array calculator.

The performance of the special techniques will be illustrated with ultrasonic data from practical trials on representative specimens with artificial and realistic flaws. It will be shown how the UltraVision software supports comprehensive visualization of the data generated by the special techniques, and how the advanced tools allow for efficient data analysis.

Keywords: phased array, TOFD, weld inspection, reactor vessel

1. Introduction

Manufacturing of Steam Generators (SG) and Pressurizers (PZR) involves non-destructive testing of the circumferential welds according to the French Design and Construction Rules for Mechanical Components of PWR Nuclear Islands (RCC-M) code. This includes surface and volumetric NDT methods.

The low alloy steel pieces of PZR and SG (

Figure **1**: Pressurizer (PZR) and Steam Generator (SG) weld outline

) are assembled by means of narrow gap submerged arc welds. The weld thickness range varies between 100 mm and 180 mm. Shell diameters varying between 3.077 m and 5.165 m yield weld lengths up to more than 16 m.

Historically, Radiographic Testing (RT) was applied before heat treatment while manual UT was used in complement for examination of the welds before and after heat treatment.

For productivity and environment reasons, the AREVA-NP/EFF/SAINT-MARCEL have decided to replace manual UT and RT by advanced automated phased array pulse-echo (PE) and TOFD techniques.

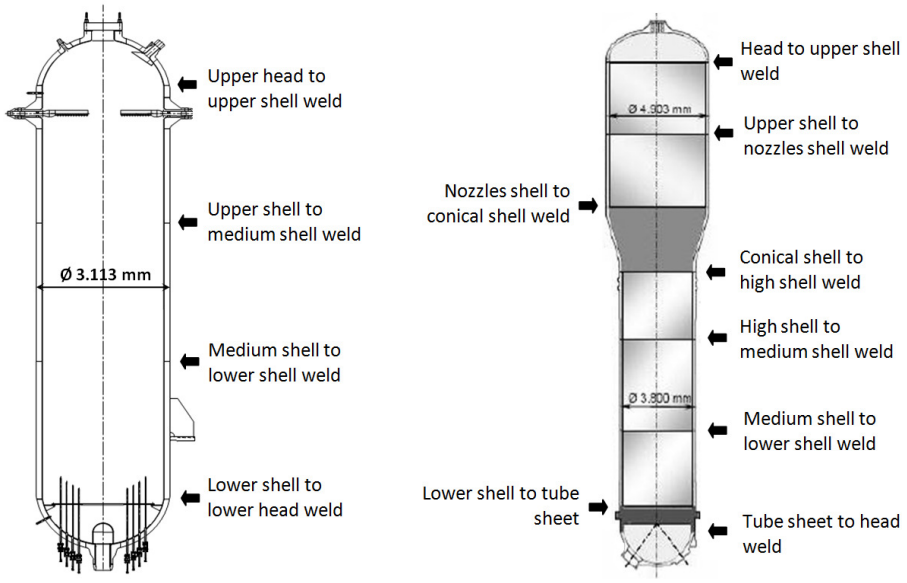

Figure 1: Pressurizer (PZR) and Steam Generator (SG) weld outline

2. Dedicated Advanced Automated UT System

2.1. Generic Inspection Techniques

In order to demonstrate the best possible equivalence between the current methods (RT and manual UT) and the proposed alternative UT techniques (PE and TOFD), and instead of a qualification (very time consuming), the development of the new UT phased array PE technique was at the start based as much as possible on the existing manual UT characteristics [1],[2]. Figure **2** shows a schematic representation of the pulse-echo examination techniques that were selected. The phased array beam steering capability is used for reproducing the refracted angles required by the code (0ºLW, 45ºSW, 60ºSW and 70ºSW) while reducing the number of probes. In order to optimize the response for various defects orientations, the beam skewing capability is used to replace manual optimization (turning the probe) in conventional UT.

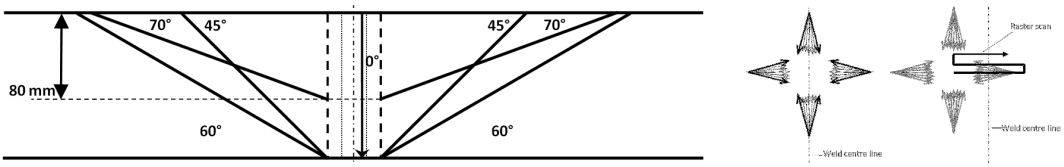

Figure 2: Weld coverage using beam steering and skewing with phased array pulse-echo techniques

A typical inspection result from the pulse-echo techniques is shown on Figure 3. Since more than 90 pulse-echo beams are used (different beam orientations, refracted angles and skew angles), analysing the weld data beam by beam would require too much time. Therefore, the merge tool in the UltraVision software is used to calculate and visualize, considering all beams, the maximum amplitude found for each unitary volume of the inspected weld zone. The left view (VC-Side) shows a cross section of the weld with all indications found along the weld seam. The top right view (VC-End) shows a “front” view of the weld, whereas the lower right view (VC-Top) shows the top view of the weld.

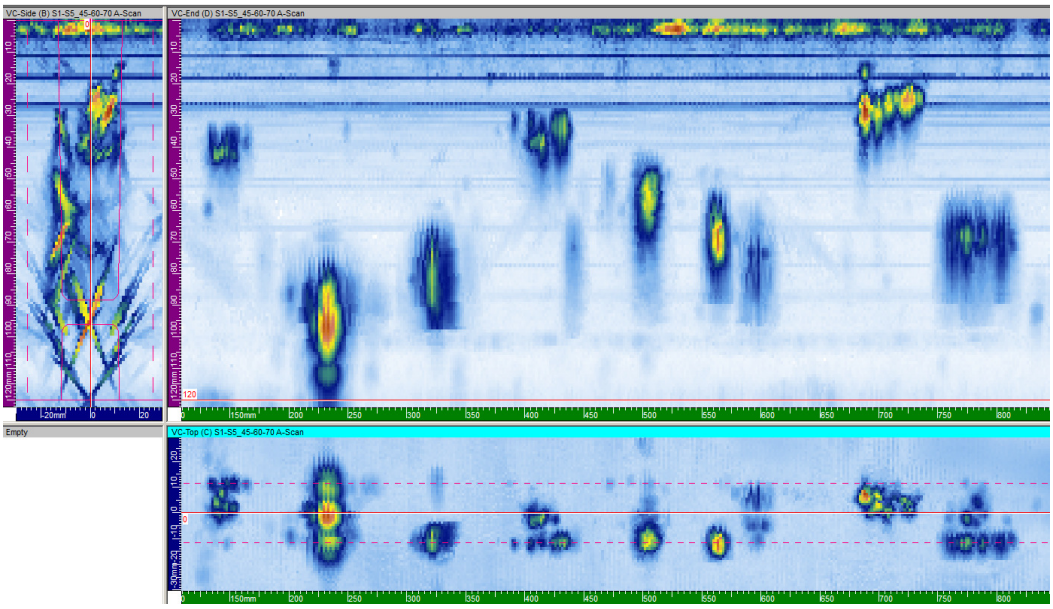

Figure 3: Typical inspection result from pulse-echo techniques, using Merged Data from all beams

The TOFD technique is implemented using a combination of conventional and phased array probes (see Figure 4. The near-surface depth range is covered by two conventional configurations. The phased array probe set covers the deeper range. Besides a reduction of the number of probes, this allows for flexible adaptation of zone division to fit various weld thicknesses, and a good control of the beam spread for a given depth range resulting in a high signal-to-noise ratio (SNR) and reduced back-wall dead zone.

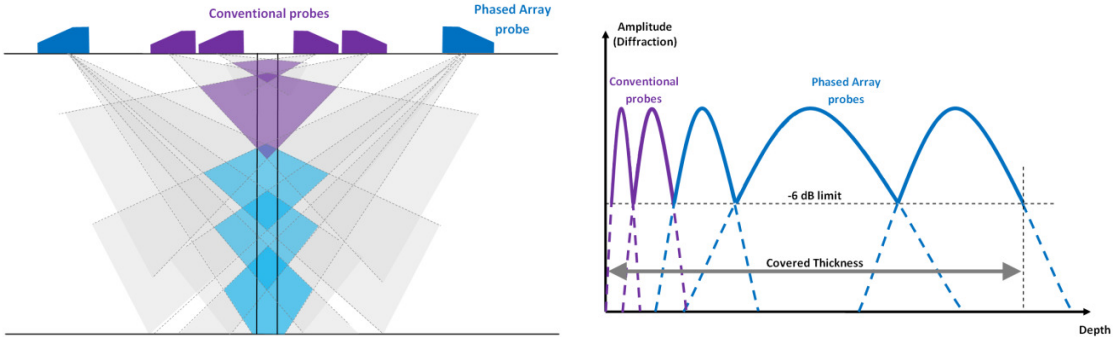

Figure 4: Depth zone coverage for TOFD inspection techniques

The excellent SNR obtained with the phased array TOFD configuration is shown in Figure 5. The left image shows the signals from an alumina insert, known to yield low diffraction amplitudes: the quality of the signal is very good and the obtained SNR is about 16 dB. The right image shows a 2 mm deep far-surface breaking notch in a 165mm test block. The back-wall dead zone is reduced to a minimum.

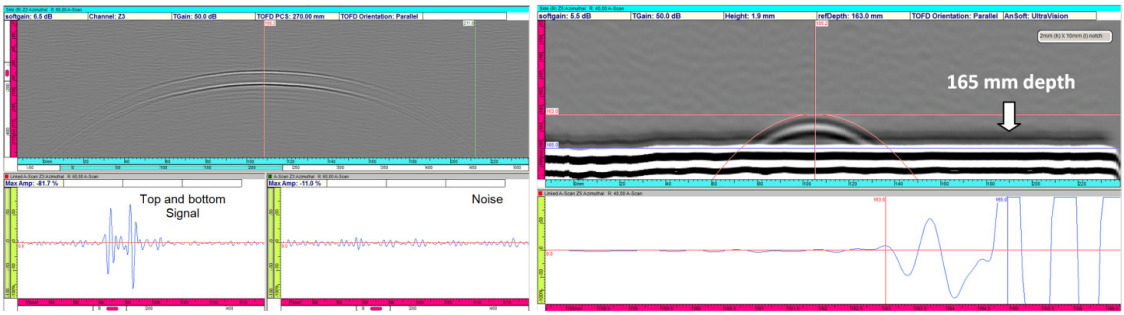

Figure 5: PA-TOFD images from an embedded 4 mm height Alumina insert (left), and a 2 mm height far-surface EDM notch (right)

2.2. On-Site Implementation

A dedicated industrial system for the UT inspection during manufacturing of large narrow gap submerged welds has been developed, and the manufacturing was finalized end 2013. It was commissioned in the factory in France in the spring of 2014 (see **Error! Reference source not found.**). This system is used to deploy all inspection techniques discussed in the previous paragraph.

Figure 6: Dedicated automated UT system during commissioning in factory

The system includes a dedicated 2 axis-scanner system with magnetic wheels, shown on the left image of Figure 7. A detector on the scanner allows for the steering of 2 circumferential motors, to follow the trajectory projected by a laser tracking device onto the component. The axial movement is performed by a linear arm that carries the probe holder. The height of the linear movement allows travel over obstacles (nozzles), and the position of the legs can be adapted to move between obstacles.

The phased array UT & TOFD probe sets are mounted in several probe holders, as shown on the right image of Figure 7.

The system is controlled by the Zetec DYNARAY® 256/256PR phased array UT system and the UltraVision 3 software. A dedicated calibration table, with calibration blocks and an encoded manually driven 2-axis mechanism has been developed to allow for an efficient and reliable calibration process, without removing the individual probes from their respective probe holders.

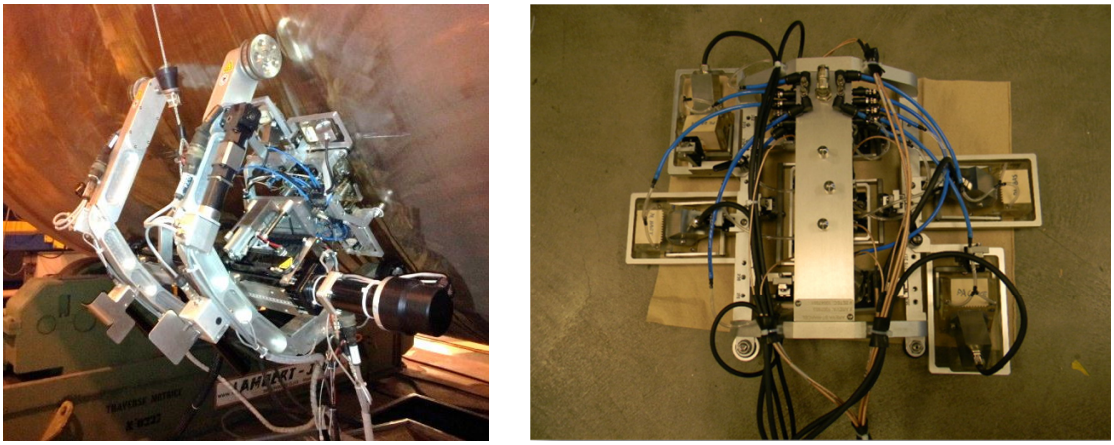

Figure 7: Dedicated scanning mechanism (left) and example of probe holder (right)

3. LLT Technique

In order to obtain enhanced detection capability on planar flaws perpendicular to the inspection surface, the LLT technique has been selected to complement the pulse-echo techniques discussed in § 2. The principle of this technique, and the reason for its high sensitivity is shown in Figure **8** : the transmitter generates a longitudinal wave (shown in blue) with a refracted angle between 5º and 45º. This longitudinal wave is reflected at the back wall and impinges on the planar reflector with an angle between 45º and 85º. Here, most of the energy is converted to a shear wave (shown in orange), which travels to the receiver with a beam angle around 60º **Error! Reference source not found.**.

Implementing the LLT technique with phased array technology offers a drastic improvement in flexibility for the selection of the beam angles. To cover the complete wall thickness of the component, one single phased array probe (self-tandem) and one two-probe (tandem) phased array configuration have been implemented. The single probe configuration covers the upper depth range, down to 2/3 of the wall-thickness, whereas the last 1/3 near the far-surface is covered by the two-probe configuration (see Figure 8). The probe frequency was set at 2 MHz, similar to the shear wave probes used for the pulse-echo inspection techniques.

The UltraVision software includes a dedicated tool to generate the focal law groups for tandem configurations with phased array probes. It allows selecting the size of transmitting and receiving apertures, and the probe separation in case of a two-probe configuration. After computation, the beam forming of each focal law can be visualized (blue for LW beams, orange for SW beams). Each focal law covers a depth range of approximately 5 mm. The black “trace” in the focal law calculator, the “L-T conversion point locus”, shows the total depth range covered by a group of focal laws, and the scanning extent required to cover the complete weld and heat-affected zone volume in the given depth range (see Figure 8 and Figure 9). A single scanning sequence, using the two configurations provides complete coverage of the volume to be examined. Since the back-wall reflection is used in the beam path, the focal law groups are specific for a given wall-thickness.

The mechanical setup of the two-probe configuration for the LLT technique is shown on **Error! Reference source not found.**. The probe holder allows to adapt the probe separation for various weld thicknesses.

Sensitivity calibration of the individual focal laws is performed using a calibration block with the same wall-thickness as the weld to inspect, and containing a set of flat bottom holes (FBH). Around 30 focal laws are

required to cover a wall-thickness of 150 mm, therefore, the automated calibration tool in UltraVision 3 is used to perform this operation efficiently.

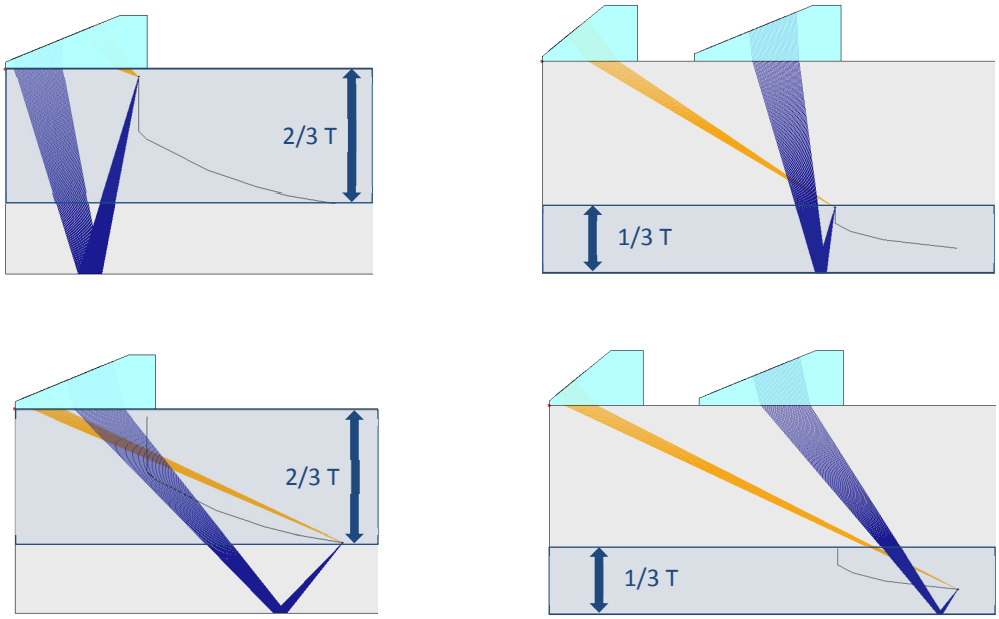

Figure 8 : Depth coverage for LLT techniques, with single probe configuration (left) and two-probe configuration (right)

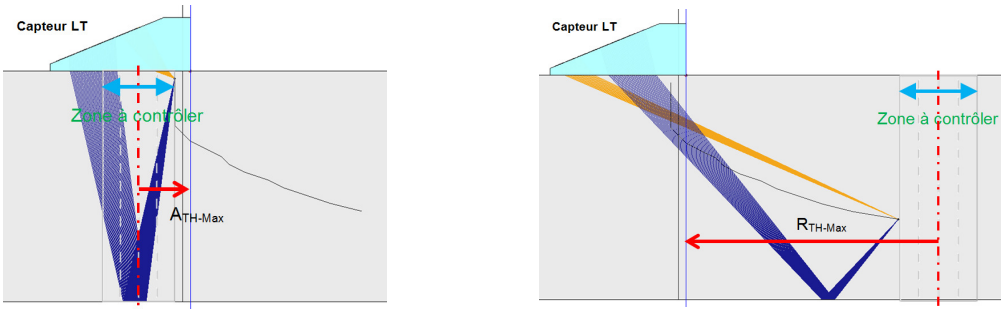

Figure 9 : Scanning extent for single probe LLT technique

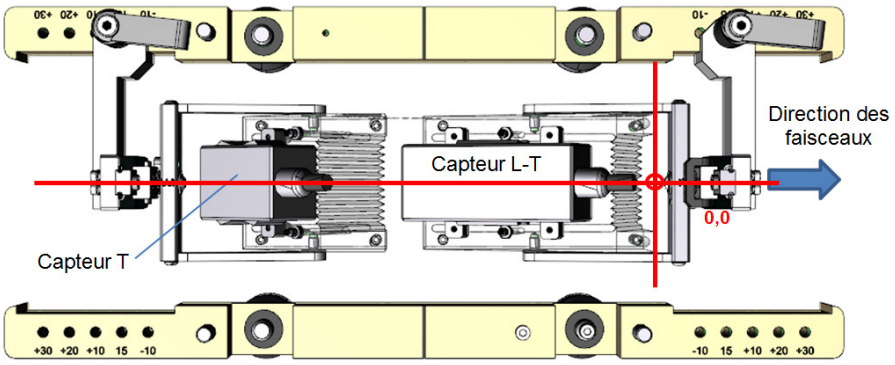

Figure 10 : Mechanical setup of two-probe configuration for LLT technique

Specific consideration was given to the analysis of LLT technique data. A large number of focal laws are used, but for each law only a ± 5 mm depth range around the "L-T conversion point" is considered, to avoid "double" indications from other mode conversions. The volumetric merge feature in UltraVision is an essential tool for this analysis: a merge is generated for each focal law in the appropriate depth range, and afterwards the resulting data are merged together to generate a single data group for each LLT configuration (see Figure 11).

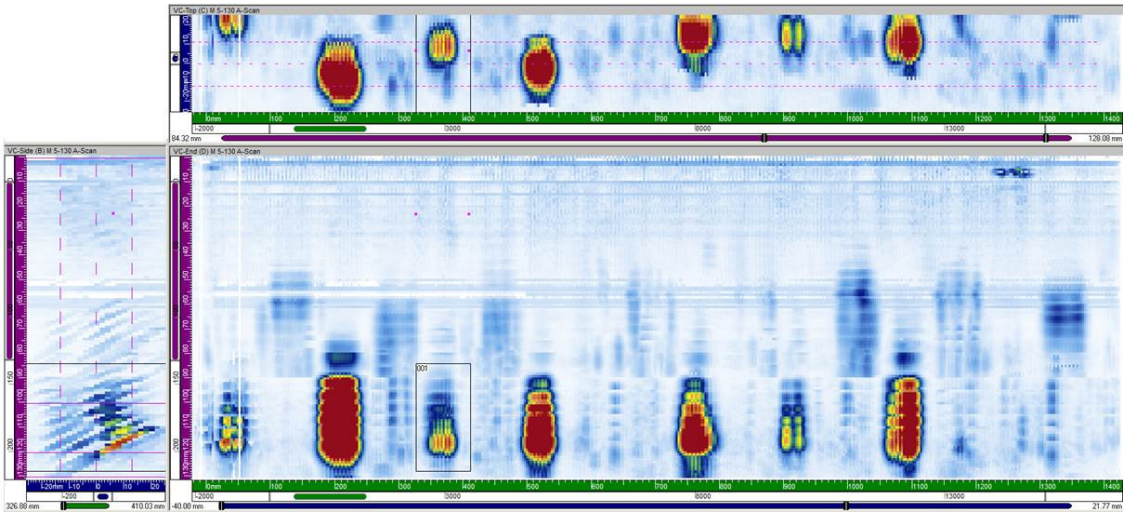

Figure 11 : Final merged data group from LLT technique, showing indications from realistic flaws

4. Asymmetric TOFD Technique

In some zones of the circumferential welds to be inspected, access is restricted to one side of the weld. One example is the region of the weld close to a nozzle, as shown in Figure 12. Except for the near-surface zone, the standard TOFD technique cannot be applied for detection, sizing and characterization of embedded flaws.

To ensure adequate TOFD coverage, an asymmetric TOFD technique was developed, using a longitudinal wave angle beam from the transmitter probe to insonify the flaw, and a straight beam from the receiver probe to detect the signals diffracted from the flaw edges (see Figure 13). This type of configuration is also known as the "delta technique".

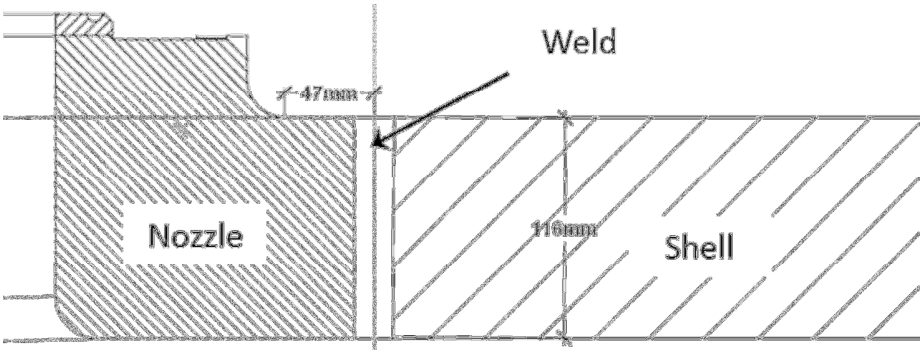

Figure 12 : Nozzle in the region of the conical shell to high shell weld of a steam generator

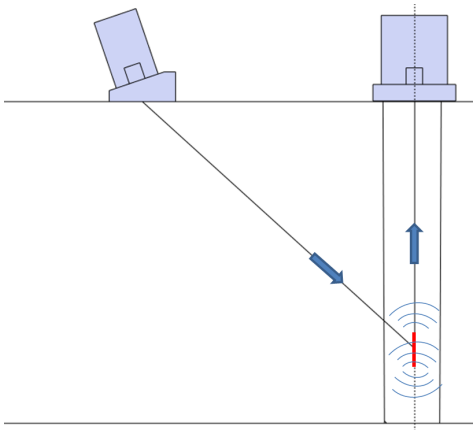

Figure 13 : Principle of asymmetric TOFD: angle beam transmitter, straight beam receiver

A large depth range (from 8 to 160 mm) needs to be covered with the asymmetric TOFD technique, therefore it was appropriate to divide the range in several depth zones and set up appropriate transmit-receive configurations for each zone. It was decided to use phased array probes for more flexibility, and to allow for focusing of the receiving beam in order to optimize the detection capability at various depths. Based on previous experiments, a probe frequency of 5 MHz was selected, and acoustic beam simulations in UltraVision were used to optimize the active aperture of the probes, the refracted angle of the transmitter beam (between 45ºLW and 60ºLW) and the probe center separation (PCS) of the configurations. Examples for 2 depth zones are shown in Figure 14.

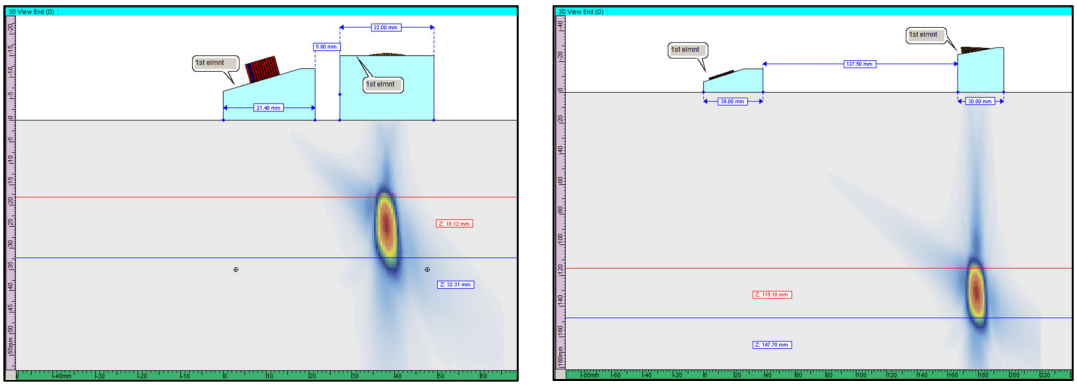

Figure 14 : Sensitivity of asymmetric TOFD configurations for depth zone 18 mm to 32 mm (left) and depth zone 115 mm to 147 mm (right)

Initial validation work has shown very promising results. A test specimen with various types of realistic flaws was scanned with both standard PA TOFD and asymmetric PA TOFD configurations, parallel to the weld. Figure 15, shows that the flaws are detected with good signal-to-noise ratio (SNR) by both techniques, although the flaw signature is slightly different. It can also be seen that the data analysis for the asymmetric TOFD data is relatively simple and very similar to the standard TOFD technique. The final validation of the asymmetric TOFD technique is on-going.

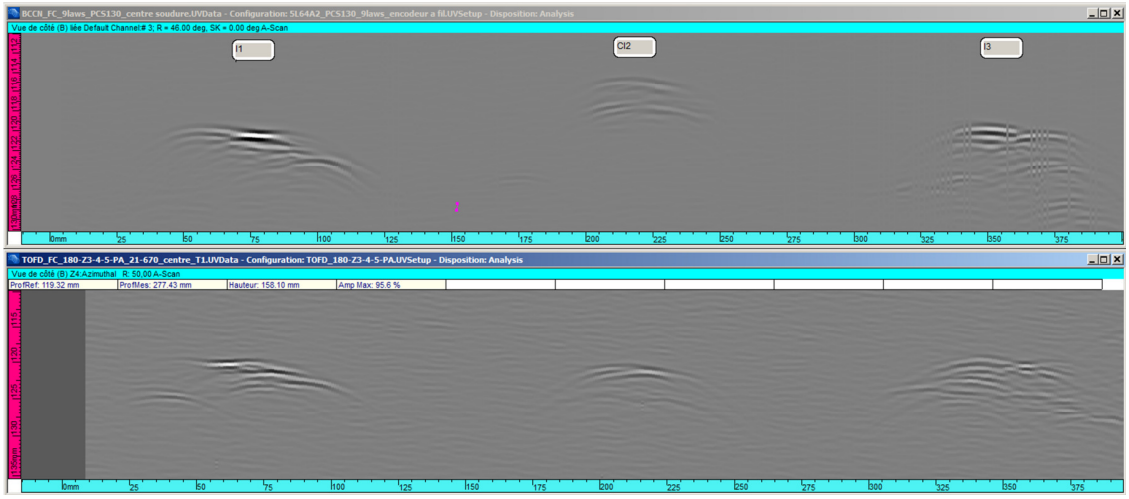

Figure 15 : Data from asymmetric PA TOFD technique (above) and standard PA TOFD technique (below) on realistic flaws in depth range 110 mm to 130 mm

5. Conclusions

A dedicated system for the UT inspection during manufacturing of large narrow gap submerged welds has been developed and commissioned on site. The system allows to efficiently deploy phased array pulse-echo and TOFD techniques, with an inspection speed of 2 m per hour.

The standard phased array pulse-echo and TOFD techniques have been complemented with additional phased array techniques to improve specific aspects of the inspection capability. The LLT technique is used as a complementary inspection technique to obtain enhanced detection capability on planar flaws perpendicular to the inspection surface, and asymmetric TOFD configurations are used to maximize TOFD coverage in areas where access is limited to one side of the weld.

All the characteristics and capabilities of the final system have been implemented and studied in the equivalency file. This study will allow for using the system as an alternative to conventional UT and RT.

References

[1] F. Lasserre, J.Y. Gourdin, J.M. Crauland, M. Jambon, D. Verspeelt, D. Marois, "Use of Combined UT Advanced Techniques in Lieu of Conventional UT Associated to Radiography for End of Manufacturing of Primary Component Circumferential Welds", 10th Int. Conf. on NDE in Relation to Structural Integrity for Nuclear and Pressurized Components, Cannes, September 2013

[2] D. Verspeelt, D. Marois, B. Cliché, J.M. Crauland, M. Jambon, F. Lasserre, "Development and Implementation of Advanced UT Techniques in Lieu of Manual UT and RT for the Inspection of Narrow Gap Welds during Manufacturing of Primary Component Circumferential Welds", 10th Int. Conf. on NDE in Relation to Structural Integrity for Nuclear and Pressurized Components, Cannes, September 2013

[3] W. Gebhardt, F. Walte, "Crack Detection and Defect Classification using the LLT-Technique", Annual Review of Progress in Quantitative Nondestructive Evaluation, La Jolla (CA) USA, 1989 .

Energy Contour Map Based Acoustic Emission Source Location for Pressurized Vessel

Byeong-Hee Han[1,2], Il-Sik Kim[1,3], Choon-Su Park[1] and Dong-Jin Yoon[*1]
[1]Center for Safety Measurement, Korea Research Institute of Standards and Science
267 Gajeong-ro, Yuseong-gu, Daejeon, 305-340, Republic of Korea
[2]Department of Mechanical Engineering, Chungnam National University
99 Daehak-ro, Yusung-gu Daejeon 305-764, Republic of Korea
[3]KRISS Campus, Korea University of Science and Technology
217 Gajeong-ro, Yuseong-gu, Daejeon, 305-350, Republic of Korea

E-mail address (corresponding author) : djyoon@kriss.re.kr

Nuclear power plant consists of many kinds of pressurized component such as pressurized vessel and pipeline system. Recently, in-situ monitoring and maintenance for these kinds of high pressurized system is one of the issues for prevention of catastrophic failure. So, the structural health monitoring technique is necessary for real time monitoring of these components. Acoustic emission (AE) technology is one of the powerful techniques for real time monitoring in the large and complex structures. However conventional acoustic emission technique is not suitable sometimes for damage location that is applied to complicated structures. So, we developed a new source location method, which uses the propagation energy of elastic wave instead of time arrival difference in the tested structures. This new source location algorithm is very useful for the structures which consist of inhomogeneous material or complex geometry, and also good for materials affected by the speed of wave propagation.
In this study, we have prepared commercial pressurized storage vessel. The new source location algorithm which is self-developed technique based on AE energy contour map was applied to these vessels. And also the activities of AE signals obtained from artificial impact damage sources were used for assessing the degree of damages as well as for locating the damage source in the tested vessel. From this experimental study, the new source location method shows much better performance compared to conventional AE source location which is based on arrival time difference. And we also suggested the methodology for assessing impact damages based on damage indexing algorithm.

Keywords: acoustic emission, source location, pressurized vessel, energy contour map

Defect Sizing using Ultrasonic Phased Array Techniques and SAFT

A. Erhard, Th. Heckel, R. Boehm, J. Kitze

Bundesanstalt für Materialforschung und –prüfung (BAM)

Unter den Eichen 87, 12205 Berlin, Germany

anton.erhard@bam.de

Abstract

In-service inspection at the safety components of the primary circuit of pressurized water reactors are an essential for the evaluation of the component integrity. One of the assumptions for integrity assessment is the properties of the material, the stresses and the defect size. The information about the defect size is provided through nondestructive testing methods. In the present contribution nondestructive testing methods based on ultrasonic phased array technique are employed to find material imperfections, i.e. in the particular case cracks in the surfaces areas. Such cracks are generated due to material fatigue during operation. The measured data processing using Synthetic Aperture Focusing Technique (SAFT) is carried out for crack depth estimation. Examples measured at a mock-up pressure vessel with a base metal wall thickness of 180 mm and 6 mm austenitic cladding are presented. For this example the phased array probe was coupled at the outer surface. Inspection from the outside is normally carried out for the BWR pressure vessel examination. A further example is demonstrates the examination of a nozzle in the thermos-sleeve area is. The aims of these investigations were, to find out the potential of the SAFT method for the depth evaluation of surface breaking cracks realized due to notches.
Another degradation mechanism for crack generation is stress corrosion cracking which requires tensile stress and a corrosive environment based on chlorides or sulfides containing substances. The shape of such cracks came often along with branching's, which means the surface of stress corrosion cracks are irregular shaped. Only a multitude of different beam angles, like the application of the phased array technique, produces enough reflections at the different crack surfaces to reconstruct the complete defect shape from measured ultrasonic data. In the presentation examples are described.

Keywords: In-service inspection, pressure vessel, surface breaking cracks, phased array technique, synthetic aperture focusing technique (SAFT)

"Qualification pursuant to EPRI PDI methodology of Phased Array UT techniques for the inspection of PWR reactor vessels using advanced robot equipment"

José R. Gadea, Francisco Fernández, Pablo González, Pedro Gómez

Tecnatom, S.A., Avda. Montes de Oca, 1, 28703 San Sebastián de los Reyes (Madrid), Spain

Abstract

Within the framework of the overall qualification project forming part of the PDI Programme for ultrasonic techniques for the inspection of PWR type vessel welds, Tecnatom decided to address Supplements 4, 6 and 7 of ASME XI Appendix VIII, which corresponds to the reactor vessel wall welds (4 and 6) and the welds between the nozzles and the vessel (7). This constitutes the stage following the qualification of Supplement 14 –PWR piping bimetal welds, culminated in early 2013, and carried out at the EPRI facilities in Charlotte (USA).

For this case phased array technology has been used, implemented in the SONIA-F1 Compact PA ultrasonic system and managed in both data acquisition and analysis by means of the InspectView, software, both developed by Tecnatom and reflecting the state-of-the-art in this type of systems. A novelty aspect in this project is the use of an industrial robot for qualification, integrated into the data acquisition system. The programming of the inspection trajectories executed by the robot is accomplished by means of the Gentray software, also developed by Tecnatom, on the basis of 3D models of the mock-ups to be examined.

The techniques and procedures qualified in the EPRI PDI programme are directly applicable at plants having ASME XI – specifically Appendix VIII – as their reference code, mainly plants in the USA and in countries in which the American PWR technology is implemented. Although in countries having ABB technology reactors (Sweden) or VVER type reactors (Finland and Eastern countries) in operation a specific ENIQ technique qualification is required, the PDI qualification is a valuable reference since it allows this specific qualification to be addressed with guarantees.

Keywords: Qualification, ultrasonic techniques, robot equipment

1. Introduction

The use of phased array (from here on PA) techniques for the inspection of vessel wall welds and nozzle to shell welds constitutes an update of the inspection process performed using conventional UT techniques, with advantage taken of the progress made in the field of PA and data acquisition systems, the electronic management capacity of which is increasingly high, in parallel with the increasing capacity of the software equipment associated with the aforementioned acquisition systems.

Tecnatom habitually uses a conventional ultrasonic technique for the inspection of vessel wall and nozzle welds, this having been qualified within the framework of the 1998 EPRI PDI programme for wall welds. Furthermore, the need to revise the technique with a view to achieving a PDI qualification that will remain unchanged for several years makes it advisable to apply the most modern or updated technique available, within the framework of effectiveness and reliability required by the in-service inspections to which these qualified techniques will be applied.

The ultimate objective of the PA, beyond maintaining the quality of the data acquired using conventional probes, is to attempt to reduce PWR vessel inspection times by optimising scan plans. In this case, reducing the radiological component is not such a determining factor as with BWR vessels, but does reduce the number of interventions on the mechanical equipment since it is not necessary to replace one detection module with another to dimension flaws, for example.

The choice of an industrial robot as the ultrasonic technique manipulating system was the result of Tecnatom's wide experience of working on this type of systems in the aeronautical inspection sector, and implied the pioneering application of these robots to inspection in a nuclear environment, with its different technical demands, with a view to application in the pre-service inspection of nuclear components in the factory.

2. Main stages of the process

The process of preparing the qualification of Supplements 4 and 6 begins with the specification of a mechanical system suitable for the application of ultrasonic techniques. With a view to addressing the qualification of these Supplements, and subsequently Supplement 7 (nozzle-vessel weld), the decision was taken to use a system capable of providing the simple trajectories involved in scanning of the wall and also the complex trajectories necessary for scanning of the nozzle-vessel weld, as a result of which the project team opted for an industrial robot. Given Tecnatom's experience in the application of these systems in the aeronautical sector, and the possibilities they offer, industrial robots are a useful mechanical tool not only for qualification activities, but also for pre-service inspections in the factory. In this case the industrial robot is simply a tool for qualification, as the techniques are to be implemented on the actual inspection machine (currently the TIME equipment).

As regards the ultrasonic technique proposed, prior to the decision to use PA as the UT technique for qualification, a study was performed on improvement of the conventional ultrasonic techniques used up until that time, supported both by simulations using CIVA (ultrasonic simulation software) and data acquisitions on wall mock-ups. The objective of the study focused on reducing the number of probes and angles used up to that time, fundamentally the large focused probes used for the dimensioning of defects or flaws located further along the sound path in the material. From the tests performed it was concluded that it could be done without these sizing probes, and furthermore the number of detection techniques was simplified, as a result of which the suite of probes to be used was reduced.

One consequence of the switch to the PA technique was the need to update an inspection activity that Tecnatom had been using for years with conventional probes, and the qualification was a perfect opportunity to do this. Furthermore, there was the demand from the overseas market that in a sense boosted the use of this technology by including it as a requirement in calls for bids for inspection services.

The next stage was the integration of the mechanical system – KUKA industrial robot – with Tecnatom's InspectView data acquisition software, initially designed for operation with ordinary coordinates from machines, normally using two encoders (X-Y), which in the case of the KUKA robot now includes six axes operating with a reference system different from that habitually used. This integration has been particularly laborious since it has been linked to development of the PA application itself in the InspectView data acquisition system.

The UT technique preparation stage has been carried out using a wall mock-up belonging to Tecnatom and another provided by EPRI for practical exercises, both with induced flaws having the characteristics indicated in Supplements 4 and 6 of ASME XI. For Supplement 7 – nozzle to vessel welds – a full-scale PWR nozzle mock-up belonging to Tecnatom, also with induced flaws, was used.

The main project team is made up of a Level III UT Project Manager, four Data Analysts, 1 UT Data Acquisition Operator and 1 Robot Operator, in addition to the necessary mechanical and electrical maintenance and software support. Also involved in the project are Mechanical Design/Development and Manufacturing personnel.

3. Ultrasonic equipment and data acquisition system

The two most important elements for data acquisition are the ultrasonic equipment and the software for the management of the electronics of this equipment and for data acquisition.

The ultrasonic system that generates the electrical pulses required by the probe consists of the SONIA-F1 Compact PA equipment and the FPA128M PA connection module, both developed by Tecnatom. The overall assembly has a multi-channel electronic management capacity, such that up to four 32-crystal array probes or other configurations may be connected to each FPA128M module (figure 1), until the 128 channels of this module are occupied. In turn, each SONIA-F1 Compact PA rack may have two (2) FPA128M modules connected. The FPA128M modules are connected to the main rack by an optical fibre, which opens up enormous possibilities as regards the distance at which the modules may be placed from the feed source, since optical fibre does not suffer any appreciable losses and in this way the ultrasonic cable connecting the PA probe to the module may be very short, this benefitting signal amplitude.

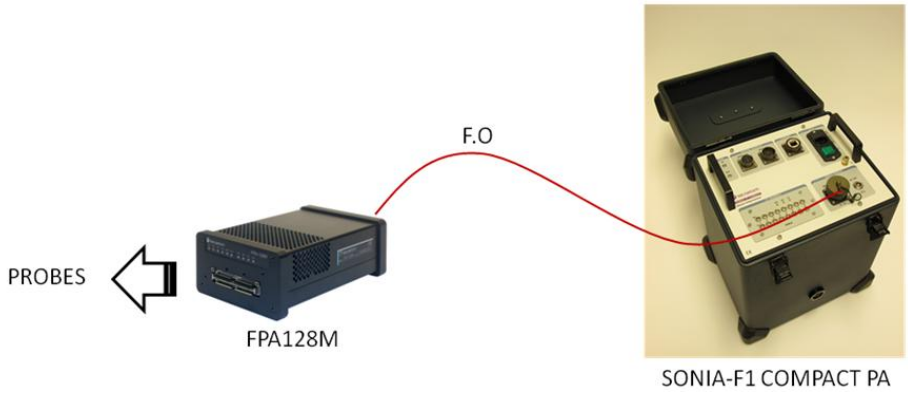

Figure 1. FPA128M array probe management module and connection to SONIA-F1 rack

InspecView-ACQ is the software that manages the aforementioned electronics and ultrasonic data acquisition, maintaining the required conditions (resolution, sample frequency, channel triggering order, etc.). This programme module is part of the general InspectView inspections suite, which is made up of InspectView-ACQ (data acquisition) and InspectView-EVA (data analysis).

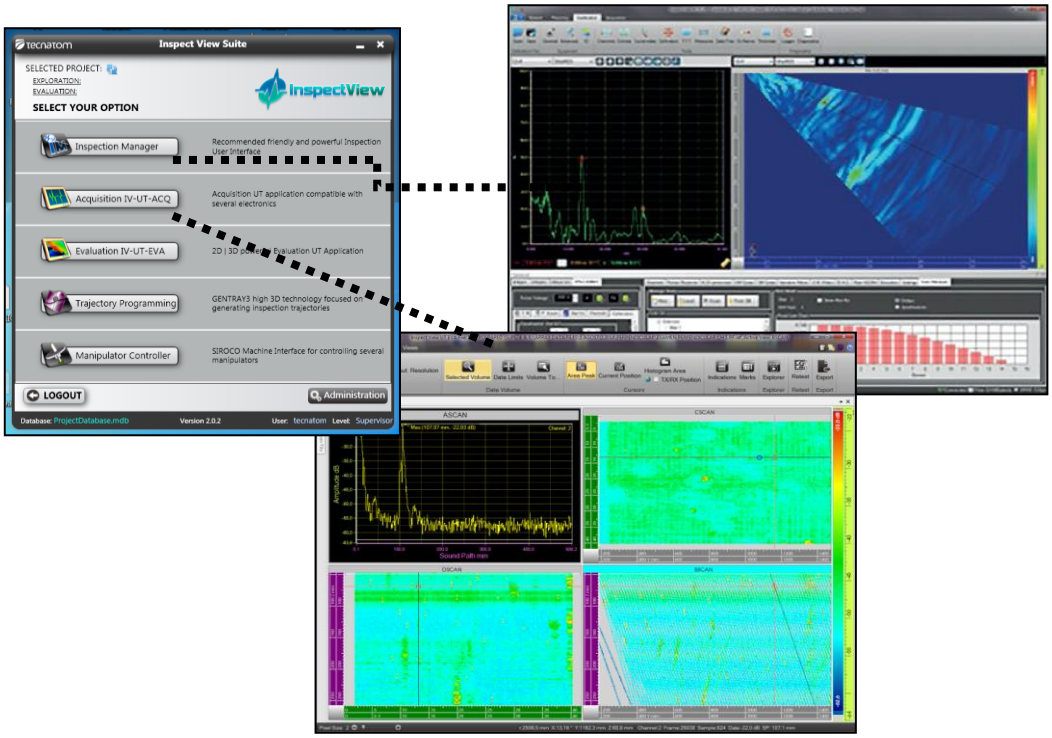

Figure 2. InspectView-ACQ data acquisition programme screens

4. Mechanical equipment

The mechanical equipment used for the validation of PWR wall weld and nozzle-vessel weld areas consists of a KUKA industrial robot that, in addition to its own robot control software (Robomove), includes a trajectory generation software (Gentray 3), originally developed by Tecnatom for the aeronautical sector and applied for the first time on this occasion in the industrial nuclear environment.

The choice of an industrial robot for this application springs on the one hand from Tecnatom's experience in the

aeronautical field, applying these robots integrated in inspection systems, and on the other from the possibilities offered as regards versatility of use, the tracking of complex trajectories, precision of movements, etc. Finally, also positive is the motivation of applying robotics in the field of nuclear inspection, both for the validation of processes and for the pre-service inspection of components in the factory.

The mechanical equipment is in charge of executing the necessary trajectories with the speed and accuracy required and of transmitting the position coordinates to the InspectView data acquisition system at each moment in time, in addition to generating the ultrasonic equipment triggering order, with the separation between triggers indicated by the procedure.

The part to be inspected is first modelled in 3D in the Gentray 3 programme, which also designs the trajectories with the separation between runs required by procedure. Subsequently, the 3D model is passed to the robot control system (Robomove), where the scan is simulated with all its parameters and possible problems or interferences are detected before the trajectory is physically executed with the robot. Finally, the scan is launched via the InspectView screens, from where all the ultrasonic parameters are prepared. Figure 3 shows a general Gentray 3 screen.

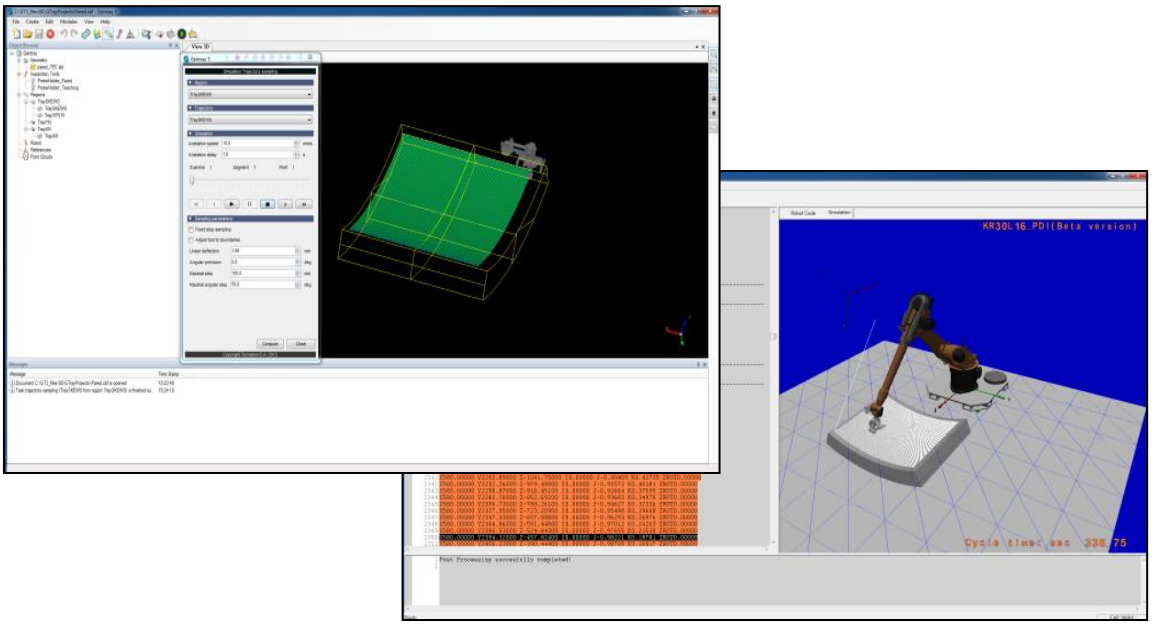

Figure 3. Gentray 3 trajectory modelling screen and Robomove robot simulation screen

5. Inspection techniques

5.1 Supplements 4 and 6 (Vessel wall welds)

The design of the inspection techniques aims to achieve a compromise between the capacity to detect flaws with the required characteristics and inspection time, an important parameter since inspection of the vessel is performed on the critical path of refuelling outages. In this respect, optimisation of the scan plans is very important to reduce inspection time in each of the areas. It should be remembered that examination of the reactor vessel wall welds constitutes approximately 60%-70% of the scanning activity of the mechanical equipment, and improving the times required without reducing the effectiveness of the inspection is a key objective in the application of UT techniques.

With this objective in mind, two types of probes were finally defined for the qualification of the wall (Supplements 4 and 6): one dual 2 x 16-element PA probe for scanning to an approximate depth of 25% of material thickness (Supplement 4), and a linear 32-element PA probe for scanning of the rest of the material thickness (Supplement 6).

The probe-holder module carries three (3) PA units: 2 dual linear PA's with shoe, one oriented in the positive direction and the other in the negative direction, and a linear PA without shoe, which performs sequential scans in the positive and negative directions by programming adequate focal laws. Figure 4 shows the module with PA probes.

The ASME XI code establishes the need to perform weld scans in four perpendicular directions, Y+, Y-, X+ and X-, to an extent covering the width of the weld extended on either side to a distance equivalent to half the thickness of the wall. Consequently, scanning is required from both sides of the weld if access is available in both cases. The

positioning and orientation of the PA probes in the module have been accomplished such that the required scans are covered with two sweeps of the mechanical equipment, one perpendicular to the other, by rotating the module 90°. In the case of vessel welds that cannot be examined in four opposing directions due to the inevitable physical interferences to access on either of the two sides of the weld – for example in the case of the weld between the vessel flange and the first shell course – qualification pursuant to Appendix VIII of ASME XI includes a method known as "single side", in accordance with which the procedure to be validated must demonstrate the capacity to detect unfavourably oriented flaws by scanning from only one of the two sides of the weld. This demonstration is performed on a special open block containing flaws with a tilt of up to 45°, which must be detected from the side implying less reflectivity to ultrasounds. In this case, the PA probe is seen to be more advantageous than a conventional one, due to its capacity to perform the scan with various focal laws covering a range of angles offering a higher possibility of impinging on the faces of the flaw in an unfavourable orientation.

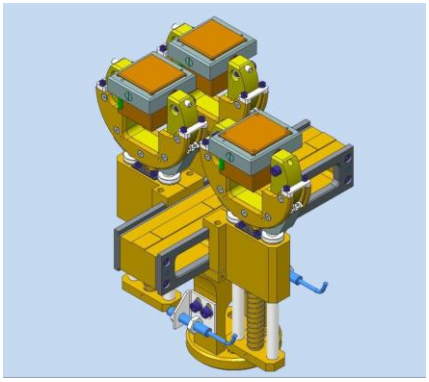

Figure 4. PA probe holder module for RPV wall scanning (Supplements 4 and 6)

Going into greater detail as regards the PA elements that make up the module, the dual PA probes with shoes for the scanning of Supplement 4 have been programmed with scanning focal laws at angles of 60°, 65° and 70°, although their total design range covers from 0° to 70°, with longitudinal waves. This type of PA probes is made up of two parallel lines of 16 crystals with an angle of tilt towards the interior (known as the "roof angle" in probe parameter terminology), which allows for focusing of the ultrasonic beam at short distances, such that the maximum energy of this beam is concentrated in an area close to the examination surface (figure 5).

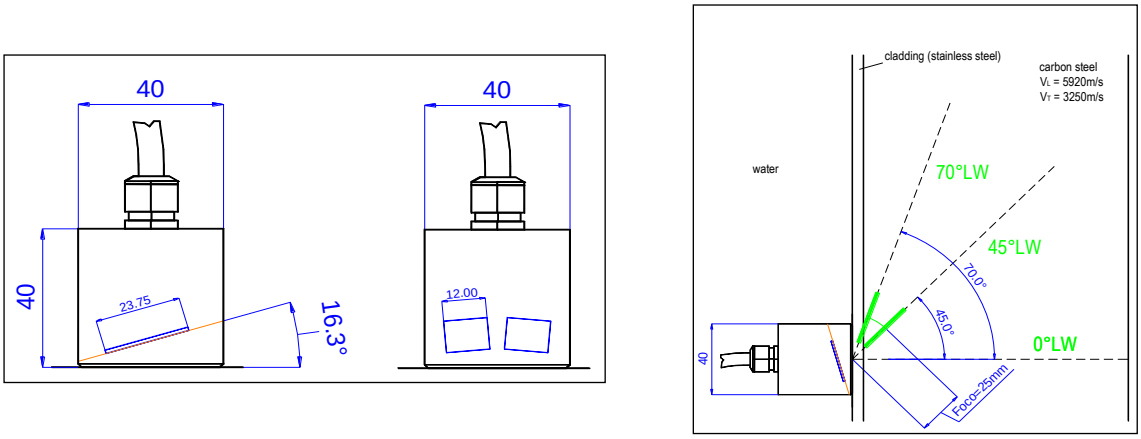

Figure 5. Main dual PA probe parameters and scanning capacity

Figure 6. KUKA robot performing a scan on a wall mock-up

The linear probe without shoe for the scanning of Supplement 6 (intermediate zones and depth of material) has been programmed with focal laws of 45° to 55°, with increases of 5°, with sequential emission of the UT beams in the positive and negative scan directions, as a result of which examination is performed in two opposing directions simultaneously with a single forward or reverse movement (figure 6).

The overlapping between scan lines in flaw detection has been established in such a way as to achieve a compromise between detection capacity and a rational inspection time, which as has been pointed out above is a key objective. The inspection time depends on the number of runs to be performed to cover the entire area of interest and on the scan speed of the mechanical equipment. However, it should be remembered in this respect that the speed should be suitable for the data acquisition system to acquire the data (perform triggering) at the rhythm or frequency established, as a result of which the scan speed and triggering frequency parameters of the ultrasonic system are closely linked.

Management of the focal laws is accomplished by the FocalSIM programme, which is integrated in the InspectView data acquisition and evaluation system. This is the programme module that plans and simulates previously the focal laws to be applied with the corresponding scans, verifying their feasibility and detecting planning errors where appropriate. Once the focal laws are correct and in keeping with the probe required and specific part and material conditions, they are incorporated in the InspectView data acquisition programme. Figure 7 presents a general view of the FocalSIM screen.

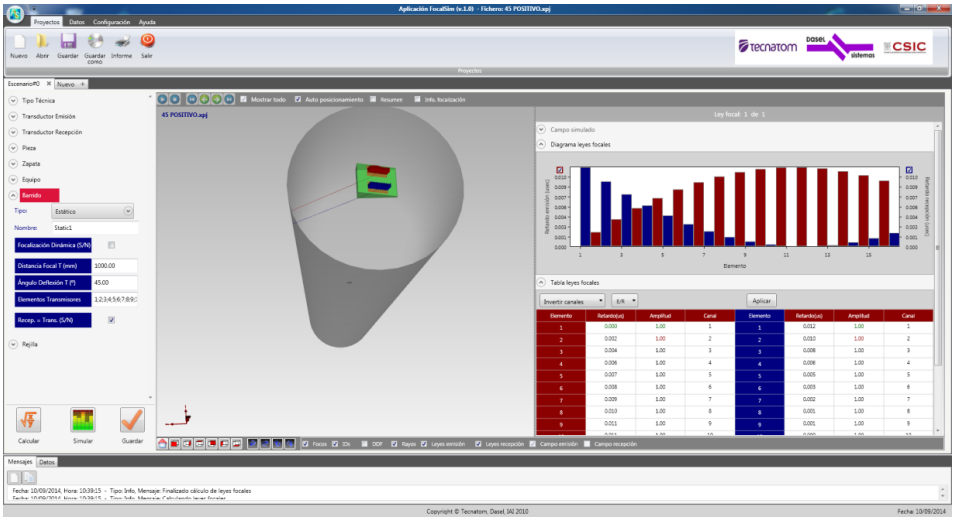

Figure 7. General view of the FocalSIM programme screen for the verification of phased array focal laws

The dimensioning of flaws is performed using the same PA probes, optimising focusing to the suitable distance to the flaw to be measured by displacing the probe perpendicular to the flaw.

5.2 Supplement 7 (Nozzle-vessel welds)

The validation of Supplement 7 – weld between nozzle and vessel – is planned to be performed using a single PA probe emitting ultrasounds with focal laws of 0°, 35° and 45° forwards and in reverse. This probe also has 32 crystals and replaces the conventional technique used to date with the same sound angles but issued by independent probes. Dimensioning of flaws is performed using the PA probe, focussing at the depth required to optimise the impingement of the energy on the area containing the flaw detected. During the inspection for detection, the nozzle is examined from the bore by rotating the module circumferentially, while the ultrasonic beam is kept oriented axially. For the dimensioning of each flaw, however, the movement is performed perpendicular to the flaw.

The tests have been performed on a full-scale mock-up of the inlet nozzle of a PWR vessel, containing induced flaws located in the areas of interest of Supplement 7.

The validation of Supplement 7 is linked to Supplements 4 and 6 in the sense that successful completion of the latter is a pre-requisite for the former to be addressed.

Figure 8 shows the configuration of the probe in preparation for a nozzle inspection, using a type scan plan.

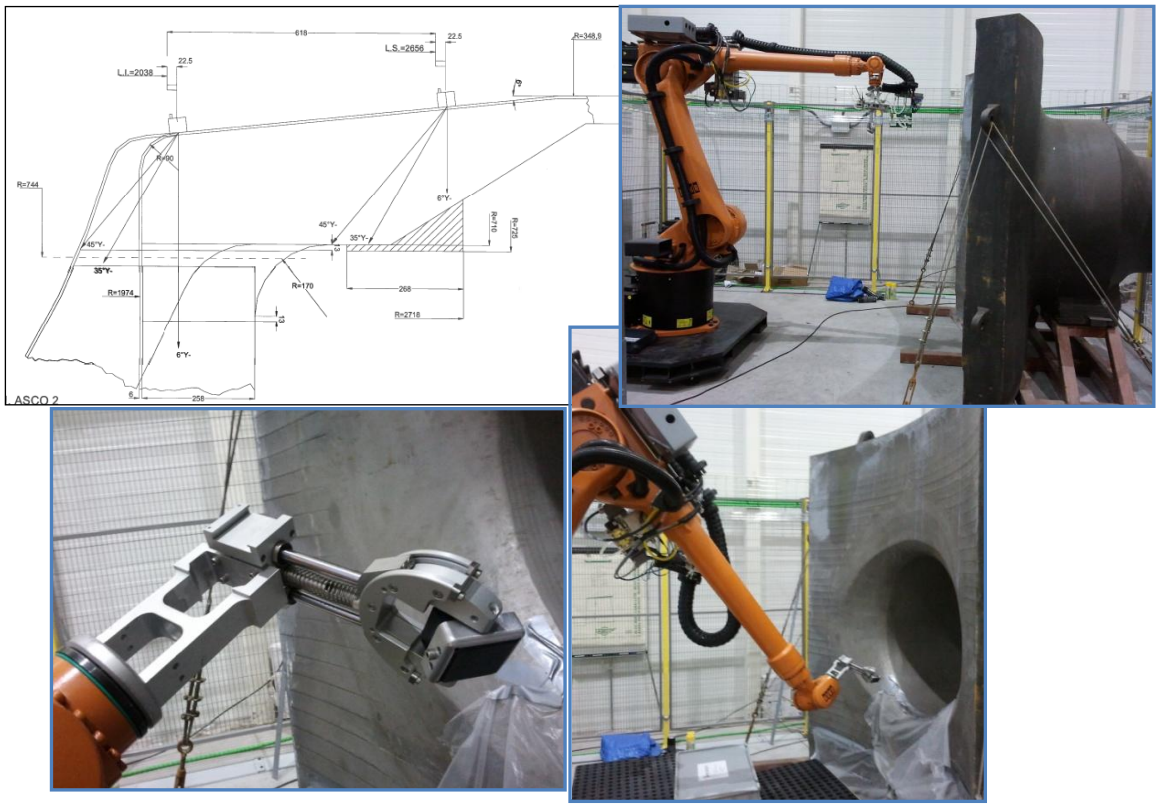

Figure 8. Configuration of the robot for nozzle inspection (Supplement 7)

6. Conclusions and results of the tests performed

The tests performed using the PA probes on open mock-ups show similar results to conventional techniques as regards detection capacity, although the PA is more versatile due to its capacity for various focusing arrangements from one same probe and to optimisation of the trajectory of the probes in the scan plans. The population of flaws provided is sufficient to appreciate the sensitivity of the system to different working depths in the material. The evaluation of the results of the acquisitions has been blind, with two chief analysts analysing the data separately, such that conclusions might be drawn regarding the effectiveness of the procedure.

Validation of the techniques proposed, which are set out in two procedures, were carried out at EPRI (facilities in Charlotte, USA) during the last quarter of 2014, using blind mock-ups. As a result of this demonstration, the inspection procedures and analyst were qualified.

Assessment of reliability of NDE for CSS and DMW components

Lili DUCOUSSO-GANJEHI[1], Damien GASTEAU[1,3], Fréderic JENSON[1], Gérard CATTIAUX[2], Thierry SOLLIER[2]

[1]CEA, LIST, DigitéoLabs, Bât. 565, PC 120, F-91191 Gif-sur-Yvette, France

[2]Institut de Radioprotection et de Sûreté Nucléaire, B.P. 17 92262 Fontenay-Aux-Roses, France

[3]LAUM, UMR-CNRS 6613, Université du Maine, Av. Olivier Messiaen, 72085 Le Mans, France

Abstract

Cast stainless steel material (CSS) are used in the primary pressure boundary of U.S. and French pressurized water reactors due to its relatively low cost and resistance to corrosion. However, potential damage is difficult to detect with in-service ultrasound inspection systems because of the complex metallurgical structure of these components. The coarse-grained and anisotropic microstructure of CSS materials makes them difficult to inspect. Similar inspection problems may occur for dissimilar metal welds for U.S. and French nuclear power plants. In 2012 during the in-service ultrasonic inspection of DMW in an inlet steam generator nozzle at North Anna Power Station Unit 1, several axially oriented flaws in varied locations around the weld circumference went undetected. These flaws were then classified as primary water stress corrosion cracking (PWSCC). In France, almost all of the dissimilar metal welds are made of austenitic stainless steel, only a few of them are made of nickel based alloys, therefore the solving of the issue is an important challenge in all cases.
The U.S. Nuclear Regulatory Commission (NRC) and the Institute for Radiological Protection and Nuclear Safety (IRSN) have each initiated research programs with the objective of assessing the ability of advanced ultrasonic methods to detect and size defects in CSS and DMW specimens. The overall objectives of the program are to enhance NDE simulation and modeling to better understand the effects of the parameters such as the microstructure on ultrasonic inspection performances, to enhance transducers and signal processing for the inspection of components with complex geometries and material properties, and to improve the reliability of the inspections.
At CEA, the challenge is to identify the most effective ultrasound technologies by using simulation to assess the microstructure impact on the inspection performances. The simulation depends strongly on the material input data. Here, the first results on the investigation of an opto-acoustic method to characterize the elastic properties of CSS and DMW specimens are presented.

Keywords : Ultrasonic Testing, CASS, DMW, Opto-acoustic

1. Introduction

Cast austenitic stainless steel (CASS) material is known to be very ductile, flaw tolerant, and resistant to stress corrosion cracking. That's why CASS materials are present in many safety-related nuclear power plant (NPP) components in France and in the U.S.. Unfortunately, CASS materials are also difficult to inspect with conventional UT. UT inspections do not provide useful information and, currently, cannot be qualified. The challenge of CASS materials UT inspection is to develop new UT inspection methods to limit the influence of the metallurgical structure on the reliability of the inspection methods. Similar inspection problems may occur for dissimilar metal welds (DMW) for U.S. and French NPP. In 2012 during the in-service ultrasonic inspection of DMW in an inlet steam generator nozzle at North Anna Power Station Unit 1, several axially oriented flaws in varied locations around the weld circumference went undetected. These flaws were classified as primary water stress corrosion cracking (PWSCC) [1]. NRC continues to assess the event and its causes. It must however be emphasized that the problem of stress corrosion cracking of bimetallic welds is more important to the United States because many dissimilar metal welds are made of an alloy sensitive to stress corrosion cracking (alloy 82/182). The solving of the issue is therefore an important challenge.

NRC and IRSN signed an agreement in 2008 to conduct cooperative research to assess the reliability and effectiveness of NDE for CASS components. The results and findings from the cooperative research have proved very useful to both organizations. Additional research is required to improve the reliability and effectiveness of the inspection methods. One of the identified remaining challenges is the assessment of UT inspection reliability of CSS and DMW specimens by using simulation studies. The CIVA software [2] allows to simulate the impact of the metallurgical structure on UT inspection performances. To do that, user has to enter the input material data in CIVA summarized in Table 1.
The material characterization essentially includes the evaluation of material microstructure, elastic and morphologic properties.

Table 1. Input data materials in CIVA software for CSS and DMW specimen

	Size of macrograins D	Size of colony d	Percentage of colony	Morphological texture	Crystallographic orientation	Type of symetry	Elastic Constants
CSS	Required	Required	Required	Required	Not required (statically isotropic)	Required	Required Per grain Per colony
DMW	Not required	Not required	Not required	Not required	Required - Per domain > wavelength	Not required	Required In the entire weld

Part of the required input data is given by metallographic analysis or EBSD, which give access to information such as the macrograin sizes and shapes and the texture. The determination of the elastic properties at the grain scale remains very difficult to date. In this context, the investigation of reliable and easy-to-use techniques to characterize the elastic properties of complex materials is very important. In our project, the task dedicated to the evaluation of the opto-acoustic method for material characterization has started in July 2013 with the academic laboratory LAUM (Laboratoire d'Acoustique de l'Université du Maine) located at Le Mans in France. It deals with the evaluation of an opto-acoustic method to determine elastic properties without prior knowledge of crystallographic orientation.

2. Opto-acoustic method

The objective is to determine the elastic properties of a polycrystalline material by means of a noncontact experimental device that includes laser generation and detection of acoustic waves. One of the difficulties is to determine the elastic properties without prior knowledge on the metallurgical structure.

The so-called laser ultrasonic techniques or opto-acoustic techniques have several advantages for material characterization which are: contactless ultrasonic measurements on the sample, broadband system providing information from the kHz to the GHz range, operating on curved and rough surfaces and at hard-to-access locations and providing a high spatial resolution because of the possibility to focus the beam down to tens of micrometers. These advantages show that opto-acoustic methods are very attractive for material characterization studies.

2.1. Principles of laser-based generation and detection of ultrasound

The generation of an acoustic wave in a solid can be achieved with a laser excitation. The material itself acts as an elastic wave source: the thermal induced dilatation acts as a source of compression, shear and Rayleigh surface waves in the sample. At high energy density, a thin layer located on the component surface melts. This leads to an ablation process where particles are emitted from the surface, thus giving rise to forces which generate the ultrasonic waves. As opposed to generation in the ablation range, laser generation of ultrasound in the thermoelastic range does not damage the surface of the material.

The main parameters of the laser are the wavelength, pulse duration, energy, and repetition rate. The repetition rate is a limiting factor for the overall speed of inspection.The pulse duration impacts on the frequency content of the ultrasound generated. Laser pulses of 10 ns are used to generate ultrasounds in the order of 10-MHz frequency range. For higher frequencies, pulse widths of 100ps (ultrasounds in the order of 100-MHz frequency range) or femtoseconde (for GHz range) laser systems may be used. The optical power depends on the material to be tested and whether laser damage is acceptable or not. Power ranging from nanojoules to microjoules to several hundred millijoules have been used. Finally, the choice of laser wavelength depends on the material absorption. Wavelength ranging from the ultraviolet to the infrared have been used for laser generation of ultrasound.

Ultrasound waves can be detected using piezoelectric, EMAT or a laser interferometer. Laser detection of ultrasound is attractive because it is non-contact, with high detection bandwidth and it can provide absolute measurement of the material displacement or velocity fields. To measure ultrasound using an optical interferometer, a laser beam is directed on the object surface. The intensity of the light beam reflected by the surface can change due to ultrasound induced modifications. For instance, modifications can occur in the refractive index of the medium due to the ultrasound. These changes are typically very small for most materials. Another technique utilizes the surface tilt associated with ultrasonic motion. The probe light beam is focused onto the specimen surface. The reflected light beam

will undergo a slight tilt because of the ultrasonic displacement. This action will cause an intensity change at the photodetector.

2.2. Experimental setup

The pump-probe experimental setup developed by LAUM [3] has been used by CEA to determine the elastic properties of different polycrystalline samples such as austenitic, CASS and DMW specimens.

The pump beam is created by laser at 1064 nm at a pulse rate of 1kHz with a pulse duration of around half a nanosecond. The pump beam excites local deformation on the surface of the sample. Afterwards an optically delayed probe pulse reflects from the area of the deformation to provide the information about displacement or strain. The method is based on the measurement of an intensity change at the photodetector. Figure 1 (left part) shows the simplified version of the experimental setup without the set of mirrors and lenses to understand the principle of the experimental method. The detailed version is represented in Figure 1(right part).

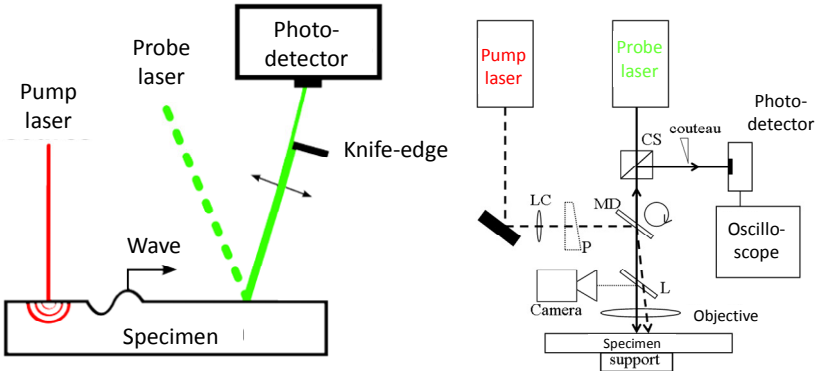

Figure 1. The pump-probe experimental setup – Simplified version (left part) and detailed version (right part)

Figure 2 presents a typical time signal recorded by the pump-probe setup. One can see the clear contribution of the surface wave and in a lower order the contribution of the longitudinal wave. Figure 2 shows that the setup is mainly sensitive to the deformations normal to the surface, in this way, the Surface Acoustic Wave (SAW). The determination of elastic properties is based on the analysis of the velocities measured through the material and their probability of apparition which is detailed just below.

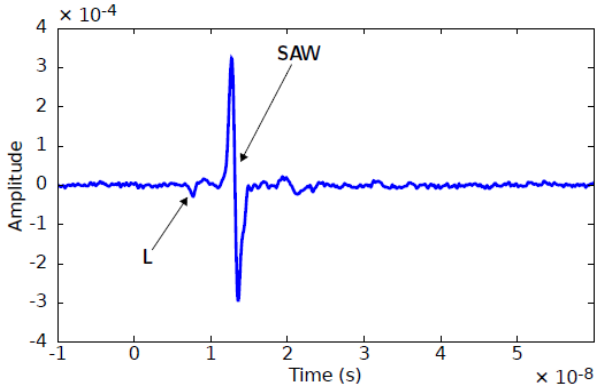

Figure 2. Typical time signal measured by a pump-probe setup.

3. Determination of elastic parameters

3.1 Test samples

The first samples studied are austenitic steels. The crystal grain or grain size is heterogeneous, but following the NF A 04-102 norm, the mean size of the crystals of three samples has been analyzed on different cut plans and the results are presented in Table **Error! Reference source not found.** and Figure 3 .

Table 2. Crystal samples sizes

Name	Norm size (G)	Norm size (μm)
P1	$3-4$	$88-125$
N1	$1-4$	$88-250$
S1	$-6-0$	$434-2800$

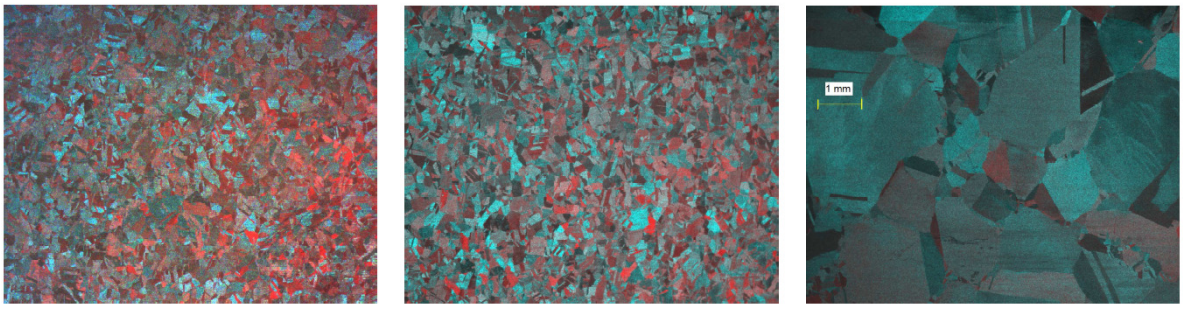

Figure 3. Grain structure observed using light microscope technique: P1 (left part), N1 (middle part), S1 (right part).

3.2 Statistical method

The anisotropic behavior of the medium modifies the existence and the properties of the waves that propagate at the surface of the medium. A surface wave theory was developed to link the measurement of SAW velocities to the elastic properties of materials. For instance, the speeds of the SAW are related to the crystal lattice orientation in the vicinity of the surface and by the direction of propagation. First, a numerical estimation of the SAW velocities and their frequency of apparition are obtained through N grains of P1 sample. This step allows to obtain a theoretical histogram. In parallel, the pump-probe experimental setup is used to determine the time of flight of SAW wave through N grains of austenitic sample. The measurement of time of flight is related to the measurement of SAW speed of sound. A thousand of measurements have been done by scanning the surface along 20 different lines of 50 different positions. The representation is an histogram in which the velocity space [1500:4500] is divided in bins of 50m/s width. Finally, an inversion procedure optimizes the elastic parameters to minimize the difference between the experimental histogram and the numerical one (Fig. 4). Thanks to this statistical method, Table 1 gives the values of elastic constants of the P1 sample. SEED values correspond to the initial parameters of the inversion procedure. As written previously, the determination of elastic constants should be calculated without prior knowledge on the crystallographic orientation. Because of these constraints, the calculation time of the inversion procedure could be long. Therefore, the procedure must be optimized to minimize the computation time. To do that, several optimization tests (OPTIM1, OPTIM2, OPTIM3, OPTIM4 and OPTIM5) were performed with different number of propagation direction (200, 400 and 800). Then, the average values are calculated. These values are closed to the literature values (c_{11} = 200.4 GPa, c_{12} = 129.3 GPa, c_{44} = 125.8 GPa) [4].

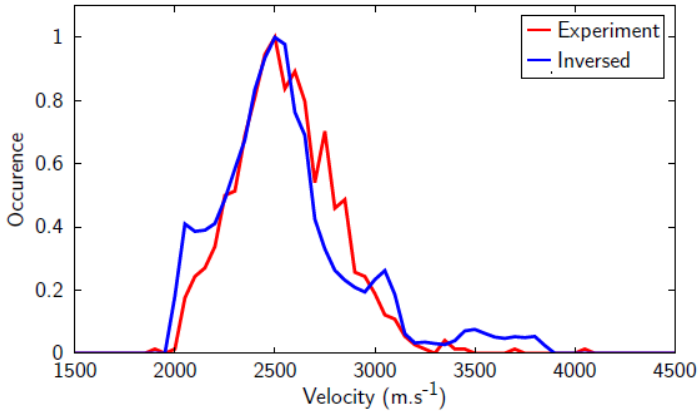

Figure 4. Histogram measured with pump-probe setup (red) and obtained by numerical inversion (blue)

Table 1. Optimized elastic parameters of P1 sample

	$c_{11}(GPa)$	$c_{12}(GPa)$	$c_{44}(GPa)$
SEED	200	120	100
OPTIM1	196.90	136.05	134.46
OPTIM2	198.31	137.24	140.60
OPTIM3	190.64	128.99	116.93
OPTIM4	189.51	126.30	121.77
OPTIM5	188.03	127.95	117.91
Average	192.678	131.3060	126.3340

3.3 Estimation of errors

The first source of error on the evaluation of the SAW velocities comes from the metallurgical structure of the material. As shown on Figure 5 the probability that the surface wave crosses a grain boundary can be very high and depends on the ratio between the size of the crystal and the propagation distance. One can easily predict that the smaller the propagation distance is, the smaller the probability of crossing boundary is.

Figure 5. Surface sample representation. Pump focusing is represented in red and probe focusing is represented in green.

Moreover, as the velocity is inversely proportional to the time of flight, the impact of an error on the time detection of the wave can be also important. This induces to be careful about the data processing of the time signal acquired experimentally. In this way, the surface wave time of flight is measured by the zero amplitude crossing of its dipolar profile. Because of the sampling of the time axis, the error is estimated around 1%.

4. First applications on CSS and DMW specimens

Experimental results were obtained on CSS specimens manufactured by MANOIR and DMW specimens (Fig. 6).

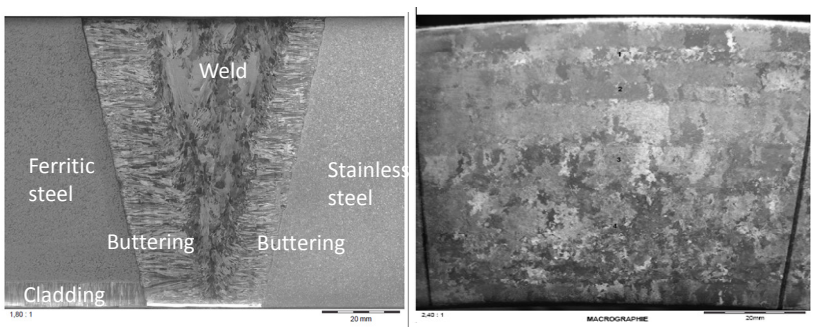

Figure 6. Macrographic representations of DMW (left part) and CASS components (right part)

On CSS specimens, the photoacoustic signals are represented in Figure 7. The measurements were performed for two

distances between probe-pump: d= 65 µm and d = 156 µm. For both distances, the SAW is well characterized by a bipolar signal and the L-wave by a monopolar signal. The measurements were performed at different positions on the specimen surface and show important signal variations. These variations reflect the complexity and the heterogeneity of the medium. For several scanning positions, the main difficulty is to extract the SAW signals with a level of signal to noise ratio sufficient to determine the time of flight. .work is performed on the improvement of the experimental setup to improve the signal to noise ratio.

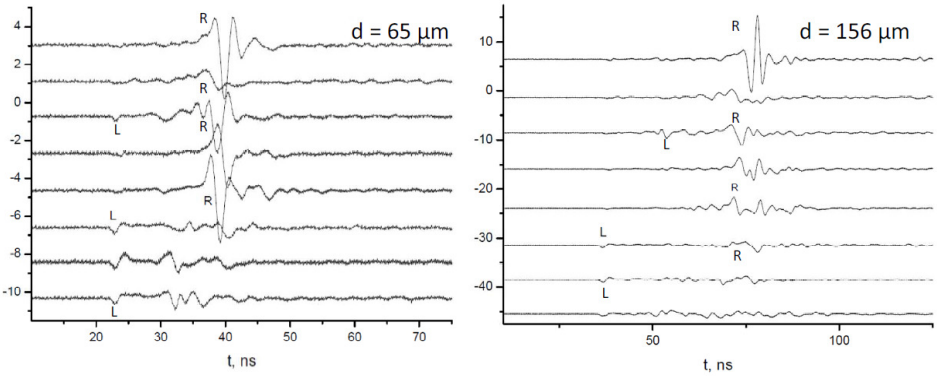

Figure 7. Photoacoustic signals measured on MANOIR specimen for d = 156 µm (right part) and d = 65 µm (left part) at different positions of the specimen surface.

Another result obtained on CSS specimens shows that the opto-acoustic method may be very useful to characterize the metallurgical structure. Figure 8 shows the measurements of SAW time of flight for different positions of the CSS specimen. The length of scanning is 5 mm. We observe clearly the variation of time of flight located at the boundary between two different macrograins (designated by a yellow line on Figure 8). Figure 9 gives the values of SAW speed measured along the 5mm scanning. This result shows clearly two different values of SAW speed of sound corresponding to the presence of two different macrograins and the fluctuation of speed around the mean values due to the biphasic structure of CSS specimens (the measurements through test samples in austenitic material don't show these fluctuations). Figure 10 shows the measurements of SAW time of flight on another area of CSS specimen. This result shows the variations of SAW time of flight through different macrograins and confirm that the setup is sensitive to the modification of elastic properties from a macrograin to the other.

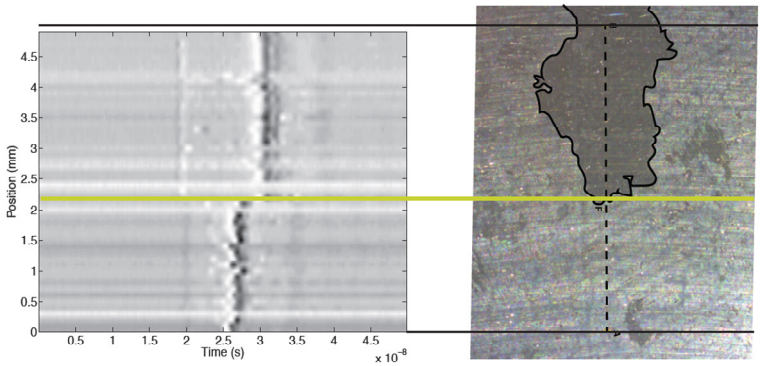

Figure 8. Measurement of SAW time of flight along the 5mm scanning. Macrography of CSS specimen.

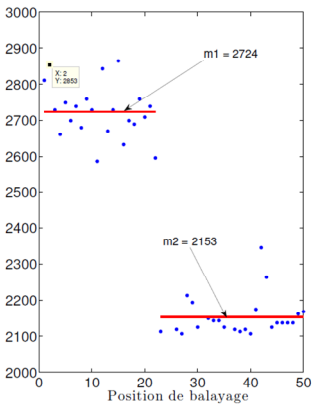

Figure 9. Measurement of SAW speed of sound along the 5 mm scanning on CSS specimen

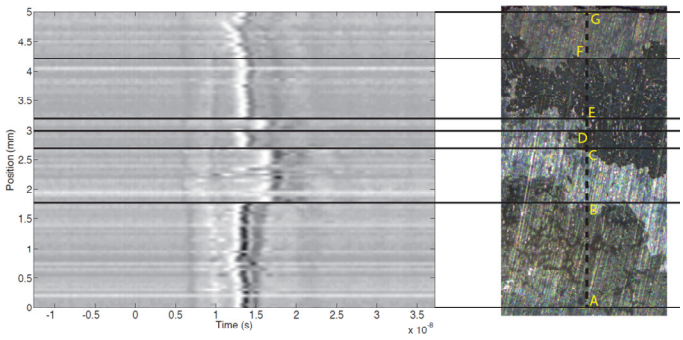

Figure 10. Measurement of SAW time of flight along the 5mm scanning (left part). Macrography of CSS specimen (right part).

This experimental method was performed on DMW specimens. This specimen is much more complex because of the crystallographic texture of DMW specimens. For instance, Figure 11 shows the structure of an austenitic sample and a DMW sample. The first one is characterized by an equiaxed and single grain structure and the second one is characterized by an elongated and complex structure. The rectangular box shows the surface of DMW sample after a polishing processing.

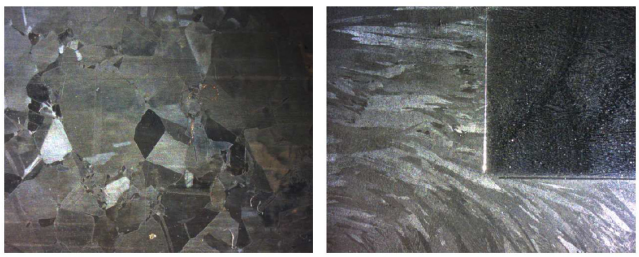

Figure 11. Macrographic representations of austenitic sample (left part) and DMW components (right part)

Figure 12 shows the photoacoustic signals measured on DMW specimen for a propagation distance equal to 5 mm at different positions separated by 200 µm. The shapes of signals are much more complex than the ones measured in austenitic samples and the signal to noise ratio is too low to detect the SAW time of flight.

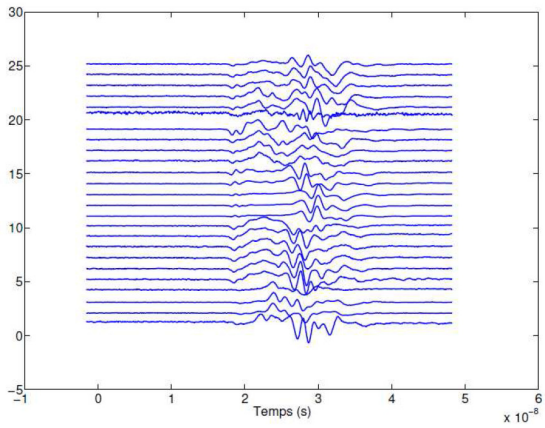

Figure 12. Photoacoustic signals measured on DMW specimen for d = 5 mm at different positions of the specimen surface (step = 200 µm between each measurement).

5. Conclusion

This paper presents the experimental setup selected by CEA to evaluate a nondestructive method to characterize the elastic properties of CSS and DMW specimens. The experimental setup has been performed on three different types of specimens: austenitic, CSS and DMW specimens. The measurements were performed on polycrystalline, monophasic and equiaxed samples such as austenitic samples. The determination of elastic parameters is in good comparison with the literature. The measurements on CSS specimens give quantitative informations on the positions of macrograins and anisotropic characteristics. Work is currently performed to extract the elastic constants of CSS specimens from these measurements and to estimate the size of colony (which is a very challenging objective). Unfortunately, measurements on DMW specimens don't give quantitative informations on materials. However, the samples were not enough polished to obtain a mirror surface which will be the next step.

References

[1] M.T. Anderson *et al*., "Evaluation of manual ultrasonic examinations applied to detect flaws in primary system dissimilar metal welds at North Anna Power Station", Technical report, PNNL-21546,(2012)

[2] CIVA website http://www-civa.cea.fr

[3] N. Chigarev *et al.,* "All-optical monitoring of acoustic waves guided by confined micro-fluidic layers", Applied physics letters, Vol. 100, 144102, doi 10.1063/1.3701576 (2012).

[4] K. Benyelloul *et al.,* "Elastic constants of austenitic stainless steel: Investigation by the first-principles calculations and the artificial neural network approach", Computational Materials Science, Vol. 67, 353-358 (2013)

Safety Improvements and Burden Reductions Using a Streamlined, Risk-informed, Approach to Inspection Program Development

James Agold[1], Kimberly Herman[2], and Patrick O'Regan[3]
[1]Southern Nuclear Company, Birmingham, Alabama, USA
[2]Dominoin Generation, Richmond, Virginia, USA
[3]Electric Power Research Institute, Charlotte, North Carolina, USA

poregan@epri.com

The US Nuclear Regulatory Commission (USNRC) recently issued revision 17 to Regulatory Guide 1.147 "Inservice Inspection Code Case Acceptability, ASME Section XI, Division 1." In this document, the USNRC identifies those ASME Code Cases that can be used by licensees (plant operators) without requiring USNRC review and approval. One of the code cases endorsed in RG1.147 is code case N716-1 which contains what is known as the EPRI streamlined risk-informed inservice inspection (RI-ISI) methodology.

This streamlined RI-ISI methodology provides an alternative to existing deterministic and traditional risk-informed inservice inspection (RI-ISI) methodologies. A main advantage of this new approach is that it is more cost-effective to implement and maintain as compared to traditional RI-ISI approaches. Benefits to this new approach consist of not only reductions in reactor coolant pressure boundary piping inspections but cost-effectively extending the scope of application to other systems such as those that perform a mitigative function. As importantly, this streamlined approach has been demonstrated to efficiently identify safety significant piping that may lie outside the traditional deterministic inspection scope thereby providing safety benefits beyond that typically identified by other risk-informed methods. These safety benefits consist of a better understanding of risk (e.g. more realistic analyses) as well as concrete actions (e.g. new or revised operating procedures, plant hardware modifications) to eliminate risk significant scenarios.

While previous RI-ISI methodologies have been limited to examination of piping welds, the updated streamlined RI-ISI methodology (N716-1) has been expended to address additional pressure boundary components (e.g. a number of tanks, vessels, heat exchangers, pump/valve bodies).

The presentation will provide a description of the RI-ISI process and results of its application to two pilot plants (a BWR and PWR plant) to demonstrate the application of the revised streamlined RI-ISI methodology on real plant ISI programs and systems as well as identify lessons learned that could be used by future applicants.

Keywords: risk-informed inservice inspection (RI-ISI)

Assessing Reliability of Remote Visual Testing – Status of Round Robin Exercise

Authors

John Lindberg, Jeff Landrum, Chris Joffe; Electric Power Research Institute

Pradeep Ramuhalli, Michael Anderson, Aaron Diaz; Pacific Northwest National Laboratory

Abstract

The nuclear industry relies heavily on the use of remote visual examination (VT) for assessing reactor pressure vessel internals and related components. Because of variability in the implementation of remote VT, global regulators have challenged the reliability and capabilities of remote visual examinations for reactor internals inspections. In the United States, the Electric Power Research Institute (EPRI) has been collaborating with the U.S. Nuclear Regulatory Commission (NRC) - Research Branch, and their contractor, Pacific Northwest National Laboratories (PNNL)[1] to determine the capabilities and reliability of remote visual examination. This project is currently in progress, and consists of a complex multi-year, three phase industry round robin program that began in 2010.

The focus of this round robin program is to quantify the current capabilities of remote visual examination technology, including equipment, procedures, and personnel; to determine the reliability of remote visual examination for detection of stress corrosion cracking type flaws in austenitic stainless steel reactor internals components; and to identify potential improvements in remote visual examination technology, if necessary. The first two phases of the round robin testing and data analysis have been completed, and the final testing phase began in 2015. This paper will discuss the phased testing approach, the key attributes being tested, the testing methodology, and provide a current status of the industry round robin.

Keywords: Remote visual examination, round robin test, NDE reliability, visual examination, reactor internals, vessel internal examinations

[1] The work was sponsored by the U.S. Nuclear Regulatory Commission under U.S. Department of Energy Contract DE-AC05-76RL01830; NRC JCN N6398 and V6323; Mr. Wallace Norris, Program Monitor

SEPARATOR REHEATER TUBES:

38 YEARS OF EXPERIENCE IN NON DESTRUCTIVE EXAMINATION

Mathieu Lheureux[1]
[1]Vallourec Heat Exchanger Tubes, ZI Rue Marthe Paris, 21150 Venarey-Les-Laumes, France

E-mail address:
mathieu.lheureux@vallourec.com

A Moisture Separator Reheater (MSR) is a key component in the steam cycle of nuclear power plants. By drying the exhaust steam leaving the high pressure turbine and reheating the dry steam before entering the low pressure turbine, it increases the overall efficiency of the nuclear steam supply system and protects the low pressure turbine from damage.

Subject to stringent operating conditions, any potential residual defect on a tube can possibly lead to failure. For this reason, it is particularly critical to select high quality tubes when building or revamping MSR equipment. Although ferritic stainless steels have been around for a long time, their use for MSR tubes was thwarted by toughness and weldability limitations. Today, finned welded tubes in material TP439 have been chosen as the industry-wide new standard material and design.

Along with optimization of the 439 chemical composition, good control of the welding process and strong non-destructive tests (NDT) are necessary to produce high quality tube for critical MSR applications. Vallourec Heat Exchanger Tubes has acquired expert know-how in this matter with its over 38 years of experience and is fully aware of TP439 potential welding risks and how to avoid them. This paper will review potential defects that can be generated during the manufacturing process of MSR tubes and the non-destructive examinations needed to detect them.

The objective of this paper is to share Vallourec Heat Exchanger Tube's 38 years of experience in the detection, analysis and prevention of tubes defects and to contribute to nuclear reliability.

Keywords: Moisture Separator Reheater Tubes, Return of Experience, Welding

Evaluation of Thinning Pipe Wall Having Complicated Surface by EMAR

Tetsuya Uchimoto[1], Toshiyuki Takagi[1], Ryoichi Urayama[1],
Shoichiroh Hara[1], and Kazuhiro Tanji[2]
[1] Institute of Fluid Science, Tohoku University, 2-1-1Katahira, Aoba, Sendai 980-8577, Japan
[2]Thermal & Nuclear Power Division, Tohoku Electric Power Co., Inc. Japan
E-mail address (corresponding author): uchimoto@ifs.tohoku.ac.jp

Keywords: Pipe wall thinning, EMAT, Resonance Method.

Electromagnetic acoustic resonance method (EMAR) has a high capability of evaluating thickness or ultrasonic velocity, and it is applied to measurement of thickness, elastic constants, damping properties and so on [1]. Since the principle of the method is based on the through-thickness resonances of bulk waves, that is, thickness oscillations, targets are usually limited to ones with simple geometry such as plates. Authors have proposed the signal processing method, Superposition of nth compression method (SNC) to extract thickness information of piping from EMR spectral response, and thickness of a pipe cut from a mock-up corrosion test loop was accurately evaluated by the signal processing [2].

In this study, EMAR with the signal processing method of SNC is investigated aiming at application of monitoring pipe wall thickness in a nuclear power plants. For the pipes having long-term services, the thinning may have scale-like surfaces, and complicated geometry. To evaluate the wall thickness of complicated surface, the structure of EMAT probes and test conditions such as excitation and signal processing are discussed and optimized.

Figure 1 (left) shows an example of SNC spectrum of EMAR together with three parameters discussed in this study: the peak value, full width half maximum (FWHM) and fundamental frequency. The right side of Fig. 1 shows the evaluated thickness of a 10 mm-thick carbon steel plate with a dent having the length of 70 mm and the curvature radius of 300 mm. Thickness of plate with curved surface is evaluated by EMAR with high accuracy. In addition, the peak value and FWHM may work as the parameters showing the reliability of evaluation.

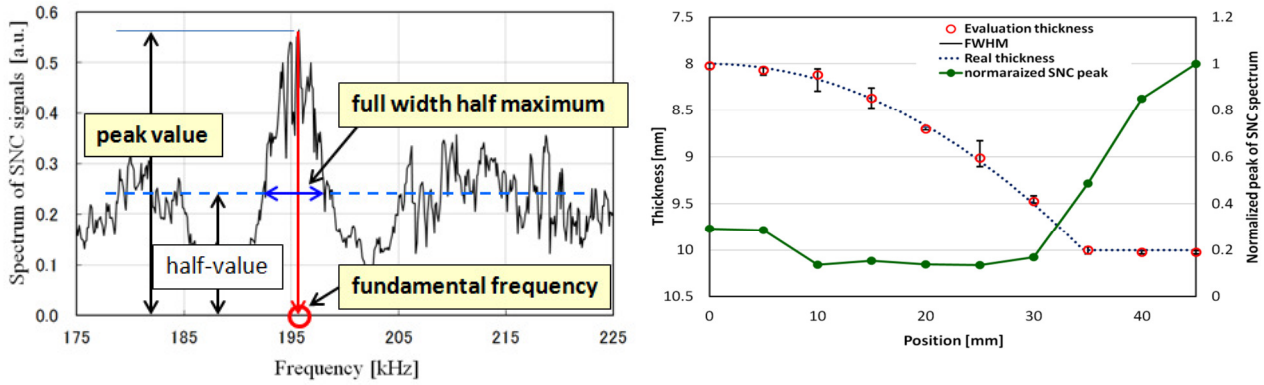

Figure 1: An example of SNC spectrum of EMAR (left) and evaluated thickness of a carbon steel plate having curved dent (right).

References
1. M. Hirao and H. Ogi, EMAT for Science and Industry, Kluwer Academic Publishers, (2003), pp.83-102.
2. R. Urayama, T. Uchimoto, T. Takagi, S. Kanemoto, Quantitative Evaluation of Pipe Wall Thinning by Electromagnetic Acoustic Resonance, E-Journal of Advanced Maintenance, 2, (2010), pp.25-33.

DETECTION OF INCIPICIENT SCC DAMAGE IN PRIMARY LOOP PIPING USING ACOUSTIC EMISSION & FIBER OPTIC STRAIN GAGES

Dr. Benjamin K. Jackson[1], Dr. Jonnathan L. W. Warwick[1] and Dr. James J. Wall[3]
[1]Intertek AIM, 601 W. California Ave., Sunnyvale, CA 94086, USA
[2]Electric Power Research Institute, 1300 W.T. Harris Blvd., Charlotte, NC 28221, USA

E-mail address: ben.jackson@intertek.com

Stress corrosion cracking (SCC) of austenitic stainless steel components is a materials degradation issue that the nuclear industry has been addressing to ensure safe, long term operation of operating plants. Utilities are required to devote a significant quantity of resources and time to the characterization and mitigation of SCC in primary loop piping. Current nondestructive examination (NDE) technology detection capabilities limit our ability to detect SCC damage until it has progressed significantly. This work describes the continued development of an *in-situ* monitoring technique to detect and characterize mechanical damage caused by SCC, allowing the detection of the incipient stages of damage to components/piping. The application of this study is to prevent failures in the primary cooling loop piping in nuclear plants. The main benefit to the industry will be improved safety and component lifetime assessment with fewer and more efficient inspections.

This research focuses on the use of acoustic emission (AE) to detect the initiation and subsequent growth of SCC cracks using AE sensors mounted to the outer diameter (OD) of a pipe mock up. Previous work related to this study has resulted in a methodology to create accelerated realistic SCC in laboratory scale pipe mock-ups using boiling magnesium chloride ($MgCl_2$). Acoustic events were monitored and recorded over a 2-month period during the course of an accelerated SCC experiment. The results of this study are presented here, and the effectiveness of AE as a detection method for this type of damage is discussed.

The paper also describes a summary of the initial work performed in the study that utilized high-resolution fiber optic strain gages mounted on the pipe OD. The strain gage technique has successfully detected changes in the residual stress profile caused by cracks propagating from the pipe inside diameter (ID). The results of two accelerated tests, one run for 12 days, and the other for 2 months are discussed, and the suitability for strain gage monitoring compared to AE is also presented.

Keywords: Stress corrosion cracking (SCC), acoustic emission (AE), fiber optic strain gages, primary loop piping, 304L stainless steel, in-situ monitoring, accelerated SCC simulation.

An Innovative Steam Generator Dissimilar Metal Weld Inspection System Using Phased Array Ultrasonic and Eddy Current Techniques

Steven J. Todd, Ramon Villagomez, and Carlos M. Barrera
IHI Southwest Technologies, Inc. 6766 Culebra Rd. San Antonio, TX 78238, USA

mvillagomez@ihiswt.com

Abstract

Due to recent issues concerning primary water stress corrosion cracking (PWSCC) in dissimilar metal welds (DMW) in pressurized water reactors, the American Society of Mechanical Engineers issued Code Case N-770-1, "Alternative Requirements and Acceptance Standards for Class 1 PWR Piping and Vessel Nozzle Butt Welds Fabricated with UNS N06082 or UNS W86182 Weld Filler Material With or Without Application of Listed Mitigation Activities". At the time of the issuance, the only approved method for performing Steam Generator (SG) Nozzle DMW was ultrasonic examinations (UT) from the outside surface (OD). Additionally examinations had not been established for the corresponding (S/G) inlet/outlet nozzle-to-reactor coolant piping welds.

As a result, IHI developed the SG Nozzle Examination Tool (SG-NExT), the first of a kind SG Examination Delivery System that allows the application of a phased array ultrasonic (PAUT) and Eddy Current (ECT) examination that was previously qualified for examination of RPV nozzle DMWs to meet the requirements of examination of DMWs at the SG nozzle from the nozzle interior (ID). The SG-NExT is a remotely operated automated delivery system capable of performing automated PAUT and ECT ID examinations on Alloy 82/182 SG DMWs.

The performance of conventional OD UT examinations of these welds encounters many challenges, such as high radiation exposure, significant grinding of tapered areas, less effective coverage, and in most cases, inability to obtain encoded data. The SG-NExT not only overcomes these problems, but also provides many additional benefits. The compact SG-NExT is remotely deployed from the outside of the SG manway to minimize human exposure to high radiation doses. Applying this technology also allows utilities to drastically reduce the inspection frequency of Hot and Cold leg DMWs. The reduction in ISI scope will result in significant dose and dollar savings.

Comparison of Conventional and Phased Array TRL Ultrasonic Testing for Case Austenite Stainless Steel in Nuclear Power Plant

Byungsik Yoon[1], Yongsik Kim[1] and Chanhee Cho[1]
[1]KHNP Central Research Institute, 70, 1312-Gil, Yuseung-Daero Yuseung-Gu Daejeon 305-343, Korea

E-mail address(Byungsik Yoon) : bsyoon@khnp.co.kr

Cast austenitic stainless steel(CASS) is used in the primary cooling piping system of Westinghouse designed nuclear power plant for its relative low cost, corrosion resistance and easy of welding. However, the coarse-grain structure of cast austenitic stainless steel can strongly affect the inspectability of ultrasonic testing. The major problems encountered during inspection are beam skewing, high attenuation and high background noise of CASS component. So far, the best inspection performance involving CASS components have been known using low frequency TRL(Transmitter/Receiver side-by-side L wave) angle beam probe. But TRL technique could not detect shallow defect and it contains an uncertainty for sizing capability. Currently, most researchers are studying to overcome these challenging issues.

In this study, we compared conventional TRL ultrasonic testing with phased array TRL ultrasonic testing technique using plant ultrasonic testing reference block that was manufactured when the nuclear power plant built. The reference block represents same metallographic characteristics of RCS piping because the block was made by same heat number and same heat treatment. The reference blocks contain side drilled holes and mechanical grooves. We acquired four reference blocks from Korean nuclear power plants. We assessed the detectability and sizing accuracy by changing ultrasonic probe frequency from 0.5 MHz to 1.25 MHz. The inspection angle in conventional TRL method is 35˚, 45˚ and 60˚ and the phased array TRL focal law is generated from 20˚ to 60˚ by 1.5 ˚step. Each reference block is compared by macro metallographic scale with chemical etching. There is a correlation between grain structure and detectability.

As a conclusion, the phased array TRL ultrasonic testing technique shows higher detectability and accuracy compared with conventional TRL ultrasonic testing technique. And the detectability is affected by metallographic characteristic of reference blocks.

Fig. 1 Conventional UT probes

Fig. 2 PA UT probes

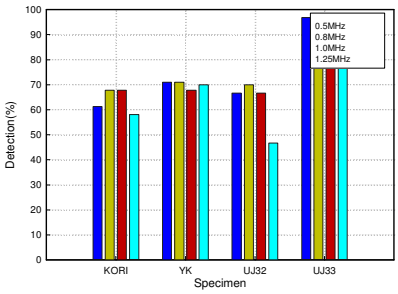

Fig. 3 PA experimental results

Keywords: Cast austenitic stainless steel, Phased Array Ultrasonic Testing, Nuclear power plant.

On-line Monitoring of Pipe Wall Thinning for Flow Accelerated Corrosion in a Piping at High Temperature

Yong-Moo Cheong [1], Dong-Jin Kim,[1] and Duck-Hyun Lee[1]
[1]Korea Atomic Energy Research Institute, 111, Daedeok-daero, 989-beon-gil, Yuseong-gu, Daejeon, 305-353, Korea

E-mail address(corresponding author) : ymcheong@kaeri.re.kr

An accurate ultrasonic thickness measurement technique at high temperature for monitoring the FAC (Flow Accelerated Corrosion) in a pipe was developed. Currently, a manual ultrasonic thickness measurement was carried out during the shutdown period in a nuclear power plant. Based on the accumulated thickness data of several hundred points for many years, the FAC of the curved region of the secondary piping are analyzed for the FAC phenomena occurring in the piping. There are some uncertainties in the measurement accuracy because the thickness variation is quite small, such as a few tens of micrometers after a year of operation, and errors might be introduced by manual ultrasonic measurements. In addition, conventional ultrasonic methods cannot be applied to the pipe at an elevated temperature because of the depolarization of piezoelectric-ceramic at temperatures above the Curie temperature, the differential thermal expansion of the substrate, inappropriate contact between the transducer and test piece, etc. To monitor the FAC phenomena in the pipe, we developed a high-temperature pipe thickness monitoring system. A couple of strip waveguides with optimized ultrasonic energy transfer at high temperature are fabricated. Also, a clamping device was designed and fabricated for stable contact between the waveguides and high-temperature pipe. This on-line pipe thickness monitoring system shows a very stable operation in a robust environment, such as a frequent temperature variation of RT to 300°C for several months of operation.

Keywords: FAC monitoring, pipe wall thickness monitoring, ultrasonic waveguide, high temperature ultrasound.

Sizing of Pipe Wall Thinning using Pulsed Eddy Current Signals

Shejuan Xie[1], Zhenmao Chen[1], Toshiyuki Takagi[2], Tetsuya Uchimoto[2]
[1]State Key Lab. for Strength and Vibration of Mechanical Structures, Xi'an Jiaotong University, Xi'an 710049, China
[2]Institute of Fluid Science, Tohoku University, Katahira 2-1-1, Aoba-ku, Sendai, Japan

E-mail address(corresponding author): Zhenmao Chen, chenzm@mail.xjtu.edu.cn

In nuclear power plants (NPPs), periodical quantitative nondestructive testing (QNDT) to evaluate the wall thinning caused by the flow accelerated corrosion and/or liquid droplet impingement in the inner side of the coolant pipes is very important to guarantee the integrity of NPPs. Pulsed eddy current testing (PECT), due to its rich frequency components and applicability of large excitation, is considered as a powerful candidate for the QNDT of wall thinning. In this study, an inverse analysis scheme has been proposed and validated based on a fast PECT signal simulator developed by authors and a deterministic optimization strategy.

In PECT, the transient response due to the pulsed excitation can be obtained through a summation of response signals due to excitations of a series of single harmonic frequency. Hence, to simulate PECT signal, the response of single frequency excitation has to be obtained in advance. In this work, the database approach for fast simulation of ECT signals has been imported for the simulation of the single frequency signals. In order to deal with wall thinning of 3 dimension geometry, the conventional fast simulator for 2D defect has been upgraded with help of an interpolation strategy. The comparison results show that the proposed fast simulation scheme is of high accuracy and over 100 times faster.

Sizing of wall thinning is conducted based on the inverse analysis strategy, which converts the sizing process to an optimization problem of minimizing the objective function. The local wall thinning is modelled as a group of planar slit defects of given width but with different length and depth, which are the defect shape parameters to be reconstructed. 2D PECT signals scanned over the wall thinning are used for the reconstruction. In case that the defect length and depth are close to 0 in some layers after reconstruction, this layer will be treated as unflaw region. In this way, the width information of the wall thinning can also be properly reconstructed.

The conjugate gradient based reconstruction scheme is employed to predict the lengths and depths of each layer. In this study, Eq. (1) is adopted for the direct calculation of gradient vector from the calculated electric fields for the TR type PECT probe.

$$\frac{\partial B(\boldsymbol{r},t)}{\partial c_{w,i}} = -\sigma_0 \sum_{n=1}^{N} F_n \left(\alpha \int_S \boldsymbol{E}_p^u \cdot (\boldsymbol{E}_e^u + \boldsymbol{E}_e^f) \frac{\partial s_w(\boldsymbol{c},\boldsymbol{r})}{\partial c_{w,i}} ds \right) e^{j\omega_n t}, \quad (1)$$

where, σ_0 is the conductivity of specimen in unflaw region, $\boldsymbol{E}_p^u$ is the unflawed electric field generated by unit current in the pickup coil, $\boldsymbol{E}_e^u + \boldsymbol{E}_e^f$ is the flawed electric field generated by excitation coil (including unflawed and perturbed field), is a coefficient to correspond the output of pickup coil and the PECT signal, $c_{w,i}$ is the *i*-th wall thinning shape parameter at the *w*-th planar layer in width direction and $s_w(\boldsymbol{c},\boldsymbol{r}) = 0$ is the equation of the defect boundary surface in *w*-th layer.

According to above theory, a reconstruction program has been developed. The detailed reconstruction results will be presented in the presentation.

The authors would like to thank the China ITER Program (2013GB113005), NSFC (51277139, 11321062, 51407132) and the 973 Program of China (2011CB610303).

Keywords: Quantitative NDT, Pipe wall thinning, Pulsed ECT, Inversion sizing

Model based simulation of Liquid Level Measurement using Ultrasonic Lamb wave

Ziqiao Tang, Maodan Yuan, Hakjoon Kim and Sungjin Song*
School of Mechanical Engineering, Sungkyunkwan University, Suwon 440-746, Korea
E-mail address(corresponding author) : sjsong@skku.edu

The paper examines the possibility of using an ultrasonic guided wave system for liquid level sensing. The system consists of an Aluminum plate which is partly immersed in water whose level is to be determined. When a wave guide is immersed in water, guided wave in the waveguide will be attenuated due to the leakage of waves into surrounding water. The rate of leakage depends on the material properties of Aluminum waveguide and that of water. The propagation characteristics of waves can be predicted using software like ABAQUS 6.12. With these predictions it is possible to relate measured characteristics to liquid level. Previous research shows that the various modes of Lamb waves are influenced by the presence of liquids. Thereby, the change in the characteristic of the lamb waves can be used as a function of liquid level. This effect has been investigated using Finite Element (FE) modelling. Finite Element Analysis is carried out using ABAQUS 6.12 to analysis the behavior of lamb waves in isotropic Aluminum plate immersed in water.

Keywords: liquid level sensor, ultrasonic lamb wave, waveguide, Finite Element Analysis

Evaluations of various scan-images with ultrasonic NDE simulator.

Yasushi Ikegami and Yukihiro Sakai

ITOCHU Techno-Solutions Corporation, Japan

Abstract

We have added two functions to ComWAVE[1-13], which is developed by ITOCHU Techno Solutions Corporation as below. These functions are effective to evaluate the various scan-images for array testing.

- Function of high-speed imaging with array testing.
  This function is for B-scan and aperture synthesis method using phased-array or matrix-array testing.
- Function of automatic report creation.
  This function is for generating images and movies from a result calculated by simulation automatically, and outputting a report in an HTML form to a database.

In this paper, we show the simulation results of various images (a slit or side-drill hole etc.) by B-scan and aperture synthesis method, and the characteristics of image evaluation for array testing. In addition, we show that the real inspection with a highly precise scan-image is enabled by building the database of the various scan-images using a simulation result.

Keywords : scan-images, linear-scan, sector-scan, aperture synthesis, simulator, phased array, matrix array.

1. Introduction

The array testing can inspect various directions from the small accessible region because it can change an incident angle and a transmission and reception position electronically.

In addition, an array testing can inspect a wide area in a short time in order to evaluate a defect with scan-image. However, the evaluation of scan images may be difficult because scan-images are changed widely depending on the conditions of angle or testing direction of a defect.

The simulator can create various inspection bodies and defects with easily and precisely. We believe that I can evaluate the validity of scan-images at the real inspection by comparing it with the simulation scan-images that was calculated various inspections bodies and assumed defects beforehand[14-15].

2. Hight speed method for array imaging

In this section, we explain the function of high-speed imaging for ComWAVE new feature. We show the procedure of high-speed imaging technique of array testing as below and figure 1.

1. Repeating FEM calculation of 1 element transmission and all elements reception till N times of total element numbers.
2. Calculating a high-speed imaging of B-scan and aperture synthesis method for various inspection conditions (a focus position and scan method etc.) by only post-processing with results of FEM.

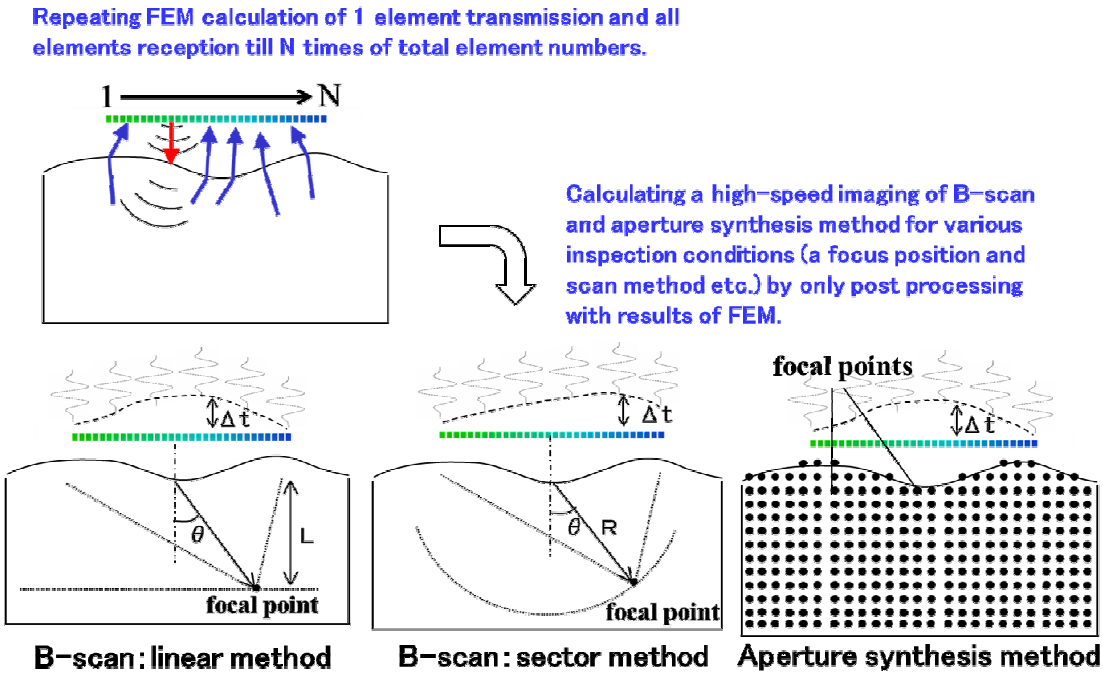

Figure 1. The calculation method for B-scan and Aperture synthesis images.

3. Evaluations

In this section, we show the simulation result of B-scan imaging using a high-speed imaging function of array testing. Here, we explain the influence that a defect angle and a testing surface shape give to scan-images. In addition, we explain the simulation of a three-dimensional image of aperture synthesis method using matrix array whose calculation load is high. Also, we evaluate an effect of the function of high-speed imaging with array testing. Furthermore, we introduce the function of automatic report creation and explain the characteristic.

3.1 The imaging simulation of array testing:

We show the model of simulation in figure 2[16]. Here, we evaluate the influence that a defect angle and a testing surface shape give to a scan-images (linear scan, aperture synthesis method) using the array probe for submersion.

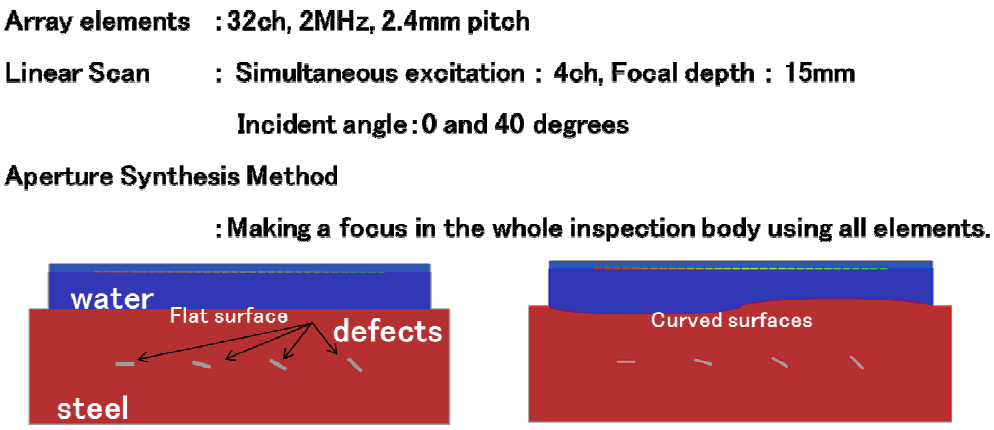

Figure 2. The model of scan-image analysis with phased-array.

We show various scan-images calculated by simulation in figure 3. Here, figure 3(a) is the B-scan image for flatted testing surface. Figure 3(b) is the B-scan image for a curved testing surface. Here, the echo of defect that is perpendicular to the scan direction becomes strong. Therefore, each scan-image of normal beam and angle beam testing relatively makes a great difference. On the other hand, there is little difference of images whether testing surface is flat or not. This phenomenon shows an inspection of a specimen with a complicated testing surface becomes possible using an array-scan testing.

In addition, figure 3(c) shows the result of an aperture synthesis method. The image of not only horizontal defect but also declined defect shows relatively clear in comparison with B-scan images. Even if the form of the testing surface varies, this tendency is similar. However, the echo strength by the aperture synthesis method was weaker than B-scan. We summarized the characteristics of these scan-images simulation in Table 1.

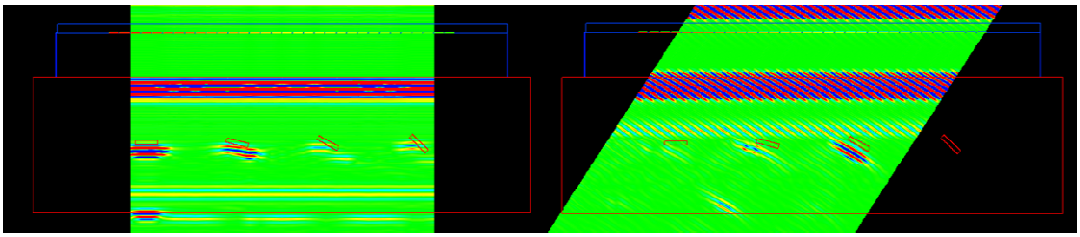

(a) B-scan image : flatted testing surface, linear scan, incident angle 0degree(left),40degree(right)

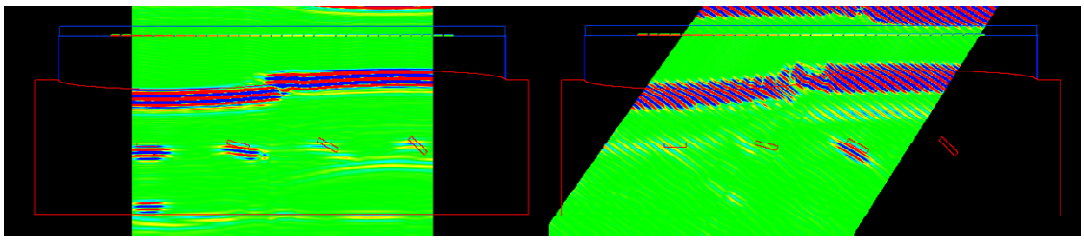

(b) B-scan image : curved testing surface, linear scan, incident angle 0degree(left),40degree(right)

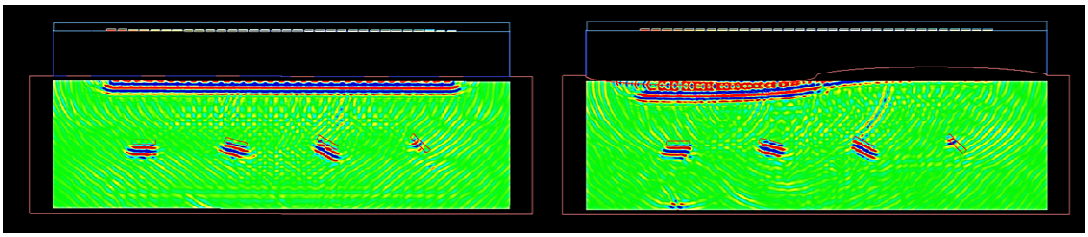

(c) aperture synthesis image : flatted testing surface (left), curved testing surface (right)

Figure 3. Image examples for several scan methods and testing surface(Flatted and curved).

Table 2. Characteristics of scan-images simulation.

	B-scan image with incident angle 0 degree.	B-scan image with incident angle 40 degree.	Aperture synthesis image
Flatted scan-surface	Defect echo with declined angle 0 and 10 degree (about perpendicular to the scan direction) becomes strong.	Defect echo with declined angle 20 degree (about perpendicular to the scan direction) becomes strong.	The image from declined defect shows relatively clear in comparison with B-scan images. However, the echo strength by the aperture synthesis method was weaker than B-scan.
Curved scan-surface	The tendency is similar as flatted scan-surface.	The tendency is similar as flatted scan-surface.	The tendency is similar as flatted scan-surface.

Then, we explain the simulation of three-dimensional aperture synthesis image using the matrix array that needs high calculation load. Figure 4 shows calculation model. Here, The specimen has Φ3mm side drill hole. That is inspected by ultrasonic matrix array probe of 4x8ch with transmit/receive separation type.

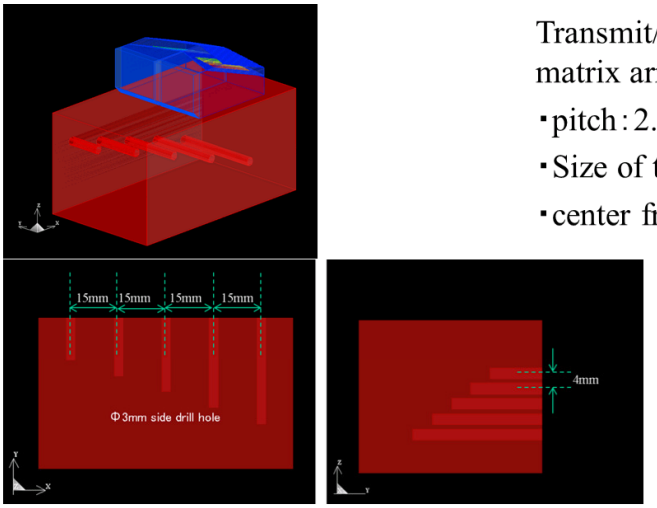

Transmit/receive separation type ultrasonic matrix array probe(4×8ch)

- pitch:2.5mm
- Size of transducer 2.4×2.4mm
- center frequency 2MHz

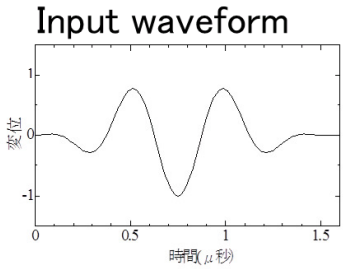

Material parameters

	Vp(m/s)	Vs(m/s)	Dens.(kg/m^3)
Wedge	2,730	1,430	1,180
Steel	5,900	3,200	7,800

Figure 4. FEM model of aperture synthesis method using matrix array.

First, we repeat FEM calculation of 1 element transmission and all elements reception till N times of total element numbers, then using the result of waveforms, we calculated aperture synthesis image by post-processing afterward. Figure 5(a) shows the three-dimensional aperture synthesis image. Figure 5(b) shows the ultrasonic wave propagation. In addition, we show the calculation time for 2D and 3D aperture synthesis image analysis in Table 2. We also show the analysis time for the three-dimensional aperture synthesis image by FEM calculation about all focus points. The image by all FEM and the image by post-processing become same image basically. However, we can see the calculation time by post-processing are 2,133 times for 2D and 280,000 times for 3D faster than calculated by all FEM.

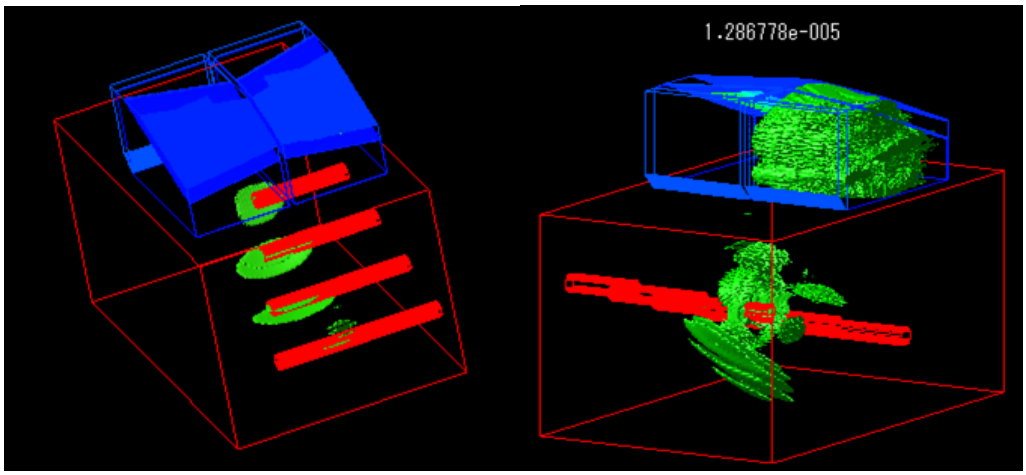

Figure 5. Three-dimensional aperture synthesis image (left) and snapshot of ultrasonic propagation (right).

Table 2. Simulation time of 2D and 3D aperture synthesis image.

	Calculated the images by post-processing.	Calculated the images by all FEM.
2D aperture synthesis image	**4,200sec.** **This is 2,133 times faster than calculated by all FEM.** (FEM+ Aperture synthesis image cal.) FEM:2,048×32ch/16jobs=4,096sec. Aperture synthesis image calculation: (pitch:0.2mm, focus points:70thousands) 20sec.(flatted testing surface) 93sec.(curved testing surface)	**8,960,000sec.** (FEM×focus points) FEM:2,048×70,000ch/16jobs
3D aperture synthesis image	**112,172sec.** **This is 280,000 times faster than calculated by all FEM.** (FEM+ Aperture synthesis image cal.) 32 times(32ch) FEM calculation: (225million element, 5,162steps) 13,860sec.×32ch/4jobs=110,880sec. Aperture synthesis image calculation: (pitch:0.2mm, focus points:9millions) 1,292sec.	**3.12×10^{10} sec.** (FEM×focus points) 13,860sec.×9 millions/4jobs

3.2 Function of automatic report creation:

We can generate an image and a movie automatically according to the procedure that we executed in the past by using this function. We showed the example of creating the movie of the three-dimensional aperture synthesis analysis with the procedure we executed in the past automatically. The merits of this function are as follows.

① The same procedure of post-process could be used again if you recorded its procedures. When there are many models, that should be made images and movies by using the same procedure, the time of post-processing can much decrease.

② We can prevent a mistake of input parameters because we can record correct parameters.

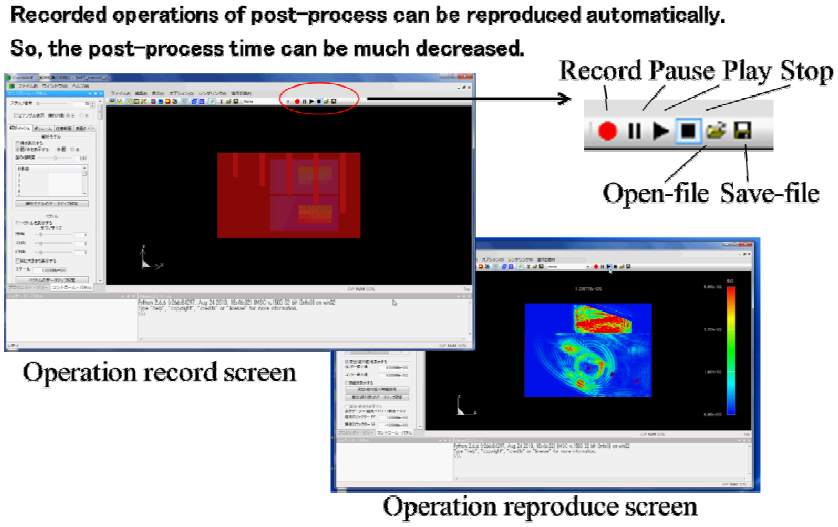

Figure 6. Function of operation recorded and reproduced at post-processer screen.

In addition, we introduce the function of output report in an HTML form to a database. Figure 7 shows a report creation window and example of output image for an HTML form. The merits of this function are as follows.

- The time to make a report becomes short by using wizard.
- It is easy to confirm the parameters errors with a report that writes automatically.
- We can confirm simulation results with web browser instantly if you have some mobile device.

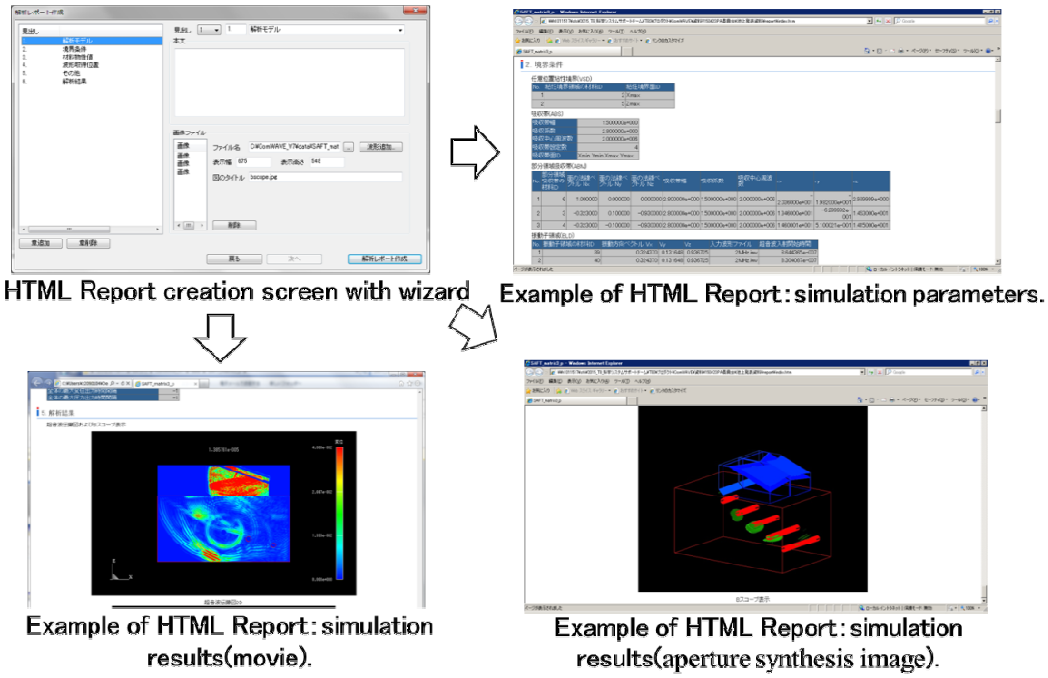

Figure 7. HTML report creation screen and examples of HTML reports.

4. Summary

We have added two functions to ComWAVE, which is developed by ITOCHU Techno Solutions Corporation. One is “high-speed imaging function of array testing”, another is “automatic report creation function”. These functions are effective to evaluate the various scan-images for array testing.

Using this function, we carried out the scan-image simulation of the array testing. As a result, this showed when we use array-scan, an inspection of a specimen with a complicated testing surface becomes possible. On the other hand, the difference of scan angle or scan methods relatively makes a great difference of scan-images. From these, the array testing was shown to need high know-how for the evaluation of the scan images even if the applicability to a complicated testing surface is high.

We can evaluate the result obtained from the array testing equipment by the function of high-speed imaging of simulation immediately. It becomes very important to highly precise inspection in future.

In addition, we can refer the database of simulation results at the real inspection immediately by using the function of automatic report creation. It can easy build the database of simulation results as shown in figure 8. Especially, we showed that the real inspection with a highly precise scan-image is enabled by building the database of the various scan-images using a simulation result.

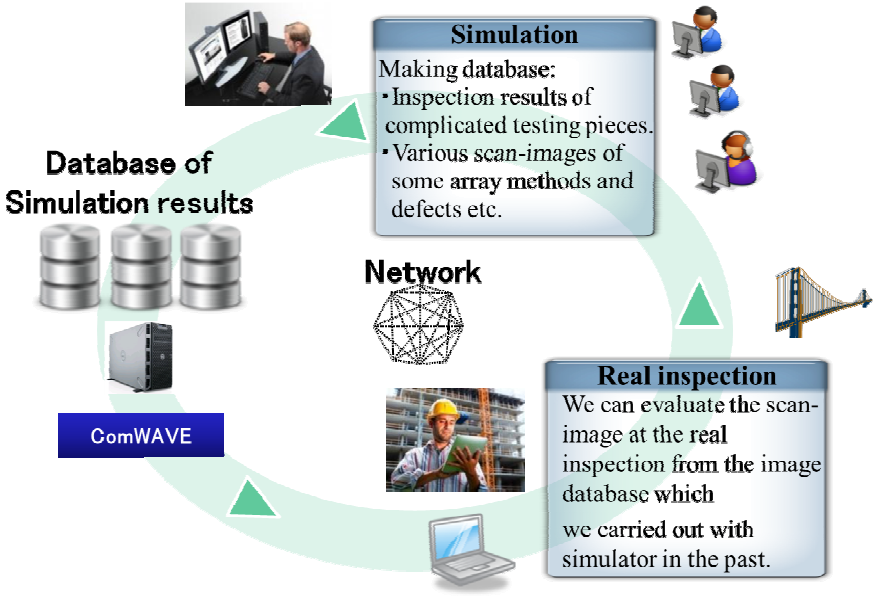

Figure 8. Effective utilization of simulation results database.

References

[1] Ikegami Y, Sakai Y, and Nakamura H, “Development of ultrasonic simulation software with FEM”, Proceedings of the 14th Symposium on Ultrasonic Testing, 2007.

[2] Ikegami Y, Sakai Y, and Nakamura H, “Large scale simulation of 3-D wave propagation”, Proceedings of the 12th Japan society for computational engineering and society, 2007.

[3] Tezuka K, Mori M, Wada S, Aritomi M, Kikura H and Sakai Y, ”Analysis of Ultrasound Propagation in High-Temperature Nuclear Reactor Feedwater to Investigate a Clamp-on Ultrasonic Pulse Doppler Flowmeter”, Journal of NUCLEAR SCIENCE and TECHNOLOGY, Vol.45,No.8,pp.752-762,2008.

[4] Ikegami Y, Sakai Y, and Nakamura H, "A Highly Accurate Ultrasonic Simulator Capable of Over One Billion Elements for Non-Destructive Evaluations”, 7th Int. Conf on NDE in Relation on Structural Integrity for Nuclear and Pressurized Components.

[5] Sakai Y and Ikegami Y, “Reducing the Computation Time of FEM Simulator for Ultrasonic Testing Using GPGPU”, 8th Int. Conf on NDE in Relation on Structural Integrity for Nuclear and Pressurized Components.

[6] Yoshiyasu Hirose, Miki Nagano, Yukihiro Sakai, Yoshikazu Iriya, and Yasushi Ikegami , “Accelerating Calculation for NDE Simulator of FEM by Using Multi-GPGPUs and its Procedures for Evaluation”, 38th Review of Progress in Quantitative Nondestructive Evaluation 2011.

[7] T. Mihara,Y. Ikegami and T. Furukawa,Subharmonic Wave Analysis in Cracks Using Developed FEM. QNDE 2011.

[8] Nagano, Hirose and Ikegami, High-accuracy analytical function for NDE simulation of FEM.,USE2011.

[9] Iriya, Sakai and Ikegami, Accelerating Calculation for Supersonic Vibration Analysis by Using MULTI-GPGPUs., Deformation processing and forming 53(618), 636-640, 2012.

[10] Hirose, Nagano and Ikegami, High-accuracy of ultrasonic propagation analysis with FEM., Ultrasonic Techno. 24(4),84-89,2012.

[11] Yasushi Ikegami, Ultrasonic propagation analysis in flow field using Finite Element Method.,USE2013.

[12] Ikegami, Sakai, Iriya and Hirose, The advice of the ultrasonic wave simulation., Piping engineering 56(4), 65-70,

2014.

[13] Yasushi Ikegami, Ultrasonic propagation analysis in flow field using Finite Element Method., Ultrasonic Techno.2014.

[14] Kimura, Hirose, Obara, Matsui, Kamiyama, Ikegami and Sakai, Study on characteristics of array angle probe for transverse wave using numerical simulation. Ultrasonic NDE sympo.2013.

[15] Furukawa etc., A study of phased array UT for austenitic stainless steel weld metal, Review of JAPEIC Vol.8, 2012.

[16] Dao Gavin, Braconnier Dominique and Gruber Matt, Full-matrix capture with a customizable phased array instrument, AIP Conference Proceedings, Volume 1650, Issue 1, p.1001-1006 03/2015.

Validation of an EMAT Code based on a Two-Dimensional FEM Coupled Electromechanical Formulation

D. Garcia Rodriguez[1], O. Mihalache[1], T. Yamamoto[2], W. Cheng[2]

[1] Japan Atomic Energy Agency (JAEA), Japan

[2] Japan Power Engineering and Inspection Corporation (JAPEIC), Japan

Abstract

This paper presents the validation of a previously introduced EMAT (Electro-Magnetic Acoustic Transducer) simulation code developed in-house at JAEA. The 2D (two dimensional) plane-parallel finite element code is based on a single coupled system including both the eddy currents and the wave propagation inside the metallic material. Validations are performed using both experimental measurements and 3D (three dimensional) numerical simulations done by JAPEIC. The experimental setup visualizes wave propagations along the vertical surface of a stainless steel plate using a piezoelectric sensor, while the 3D simulations were performed using an un-coupled model of EMAT based on two commercial codes: EMSolution for the eddy currents and COMWAVE for the wave propagation.

Keywords: EMAT, Ultrasonics, Finite Element, Eddy Currents, Electro-Magnetic Acoustic Transducer

1. Introduction

In previous work we had presented a novel JAEA developed Finite Element Method (FEM) approach to Electro-Magnetic Acoustic Transducer (EMAT) simulation in a two-dimensional (2D) plane-parallel approximation, in which for the first time both electromagnetic and mechanical phenomena are coupled in a single FEM equation system [1]. For comparison purposes, another code following the traditional uncoupled approach in three steps was also developed, in which the first step obtains the Lorentz forces in the test material, the second one calculates the resulting wave propagation, and the final one simulates the induced voltage in the pick-up coil. The uncoupled code is based on the same FEM architecture as the coupled one, but at that time no experimental validation was offered for either code.

In this paper we therefore compare the results obtained with both the coupled and uncoupled JAEA codes with experimental wave propagation measurements made by JAPEIC [2]. These measurements were carried on by scanning the free surface of a SUS316 austenitic stainless steel plate with a piezoelectric transducer, which allows visualization of the EMAT wave propagation along this surface. In the simulation, we start from the previous reference EMAT setup, and progress towards the JAPEIC experiment step by step, focusing on the effect of several approximations including, but not limited to, the magnet configuration, the coil type and positioning, and the EMAT lift-off distance. Finally, the JAEA simulation results are also compared with those from 2D and three-dimensional (3D) simulations performed by JAPEIC using a combination of two commercial simulations software in an uncoupled way.

For reference, additional details about EMAT theory/description and practical applications are described in [3].

2. Experimental visualization setup

The EMAT experimental setup was previously described in detail in [2], and is briefly summarized in Figure 1, where the sample and transmitter dimensions, measurement configuration, and the respective materials are shown. In comparison with the choices made during previous coupled EMAT work [1], the main differences are:

b) a single EMAT is used, and its elements are mounted without any additional shielding metal cage;

a) a double magnet structure is used vs. the previous single magnet design, and a circular coil is used vs. the previous meander coil with 5 turns;

c) the input signal is different, with less peaks/valleys and uses a higher main frequency (2GHz vs. 1GHz). Both are detailed later in paragraph 3.4 (see Figure 6);

d) the test sample is made from stainless steel SUS316, which is similar to the ANSI316, and different from the

previous aluminum plate.

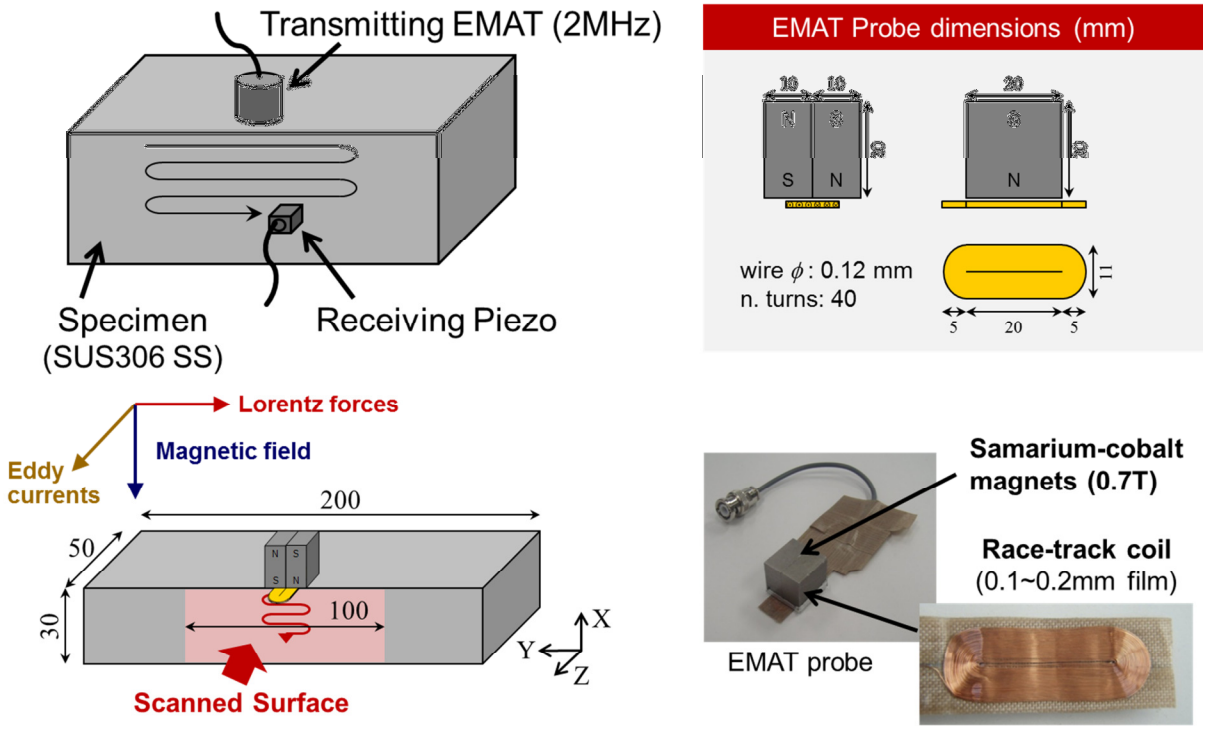

Figure 1. Description of the experimental EMAT visualization setup [2].

In the present paper, we analyze the effect of each of these differences individually, before heading to the ultimate goal of this study, the comparison between simulation results and experimental measurements shown in section 5.

It is also worth noting that in the original experiment done by JAPEIC [2] two sides (XY-plane and XZ-plane) of the sample were investigated, and the results were compared with simulations based on a combination of commercial 3D codes. Because of the 2D geometry limitations of the JAEA-developed coupled EMAT code, in this work we will only consider experimental data measured on the XY-plane to validate the numerical simulations, as detailed in Figure 1.

3. Simulations fundamentals

We describe below the fundamentals of the EMAT simulations carried out, from the domain and mesh considered to a brief introduction of the two different JAEA codes.

3.1. Simulation Codes

Three different approaches (four codes) are used in the present work to solve the time transient EMAT problem:

a) two EMAT-specific codes developed in-house by JAEA, 2DEMATc and 2DEMATu, which were previously presented in [1] and directly solve the EMAT coupled and uncoupled equations, respectively.

b) a combination of two commercially available software, which was previously used by JAPEIC to analyze their experimental results [2]: EMSolution [4], to simulate the eddy currents, and COMWAVE [5], to simulate the sound wave propagation inside the test material.

The uncoupled JAEA code, 2DEMATu, uses the conventional approach to solve the EMAT problem, by separating the electromagnetic and mechanical interactions in three distinct steps. From a physical point of view, the two first steps are therefore the same as those addressed by the commercial codes above:

a) Evaluation of the eddy currents induced in the test material, which are used to compute the Lorenz forces arising from its interaction with the permanent magnet field;

b) Propagation of the elastic sound-wave inside the test material and, also along the boundary air-material.

Contrary to the combination of commercial codes, however, the 2DEMATu code carries out the full EMAT calculation in a time-step by time-step basis, without requiring to store or read intermediate solutions, nor to adapt their respective meshes as in [2]. Moreover, the third and last step of the EMAT simulation, the receiver coil signal, can only be computed with the JAEA code:

c) Evaluation of the electromotive force induced in the receiver coil as a result of the sound wave-induced vibrations in the permanent magnetic field of the magnet.

The coupled code 2DEMATc is the first of its kind to solve the coupled electromagnetic-mechanical EMAT equations in a single FEM problem shown in equation (1). Here nodal values {C} represent the mix of both the electromagnetic vector potential and displacement solutions (**A**, **u**), while {F} is the force vector and [M], [Q], and [K] are the mass, damping and stiffness matrix, respectively. It is worth noting that, in order to reach this linear matrix system, a couple of approximations were introduced by taking advantage of the fact that the electromagnetic field due to the permanent magnet is much higher than that of the eddy currents involved. Both approximations were presented in detail and validated in previous work [1].

$$[\mathrm{K}]\{\mathrm{C}\} + [\mathrm{Q}]\frac{\partial}{\partial t}\{\mathrm{C}\} + [\mathrm{M}]\frac{\partial^2}{\partial t^2}\{\mathrm{C}\} = \{\mathrm{F}\} \tag{1}$$

Both of the codes above were developed in parallel at JAEA, and share a large part of the actual FEM code, the solver, the mesh, input data, etc. The only significant difference between both is the two different mathematical formulations.

3.2. Finite Elements Domain

The new simulation domain is shown in Figure 2, and it is an evolution from the one previously employed in [1], but adapted to follow the characteristics of the new experimental problem described above [2]. In Figure 3, the previous EMAT configuration is also given because it is used as a starting point reference in the analysis in section 4.

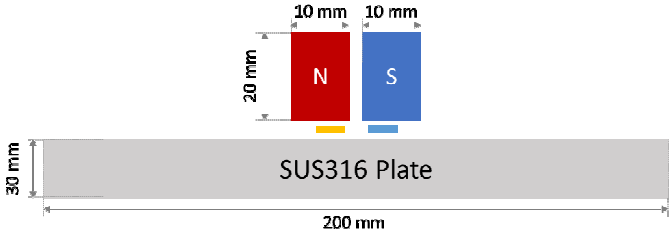

Property	SUS 316
σ (MS/m)	1.35
ρ (kg/m^3)	7980
μ_r	1
G (Gpa)	76.0
λ (Gpa)	89.2

Add. Dimensions (mm)	
coil track width	5
coil track sep.	1
magnet separation	0.250
magnet-coil sep.	0.125
coil height	0.125
coil liftoff	1

Figure 2. Simulation domain and test material properties corresponding to the experimental setup in Figure 1.

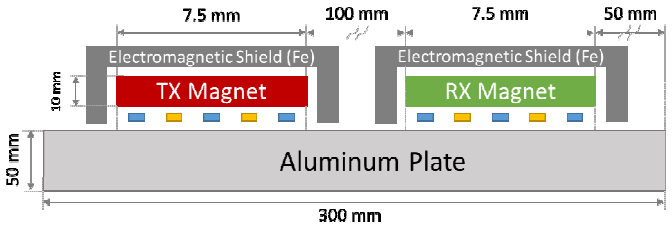

Property	Al	Fe
σ (MS/m)	35.5	10.4
ρ (kg/m^3)	2700	-
μ_r	1	1000
G (Gpa)	25.9	81.8
λ (Gpa)	52.0	112.9

Add. Dimensions (mm)	
coil spacing	1
coil-magnet sep.	0.25
coil liftoff	1
shield spacing	1
shield thickness	2

Figure 3. Simulation domain and material properties corresponding to the previous work reference setup [1].

3.3. Finite Element Mesh

Regarding the mesh, in [1] we already observed how, for this type of simulations, refinement in the test material surface was the key to prevent the appearance of large numerical instabilities on the edge. Before undertaking this work, where simulations are actually compared to experiments, we therefore pushed that idea further, and carried out the same simulation as in [1] with the most refined mesh (2-million elements, λ_S/ 50 pitch mesh M3), but this time employing 2nd

order triangular elements instead of 1st order ones. Those results are not directly showed here, but confirmed the hypothesis that the edge instabilities were due to the lack of edge mesh refinement.

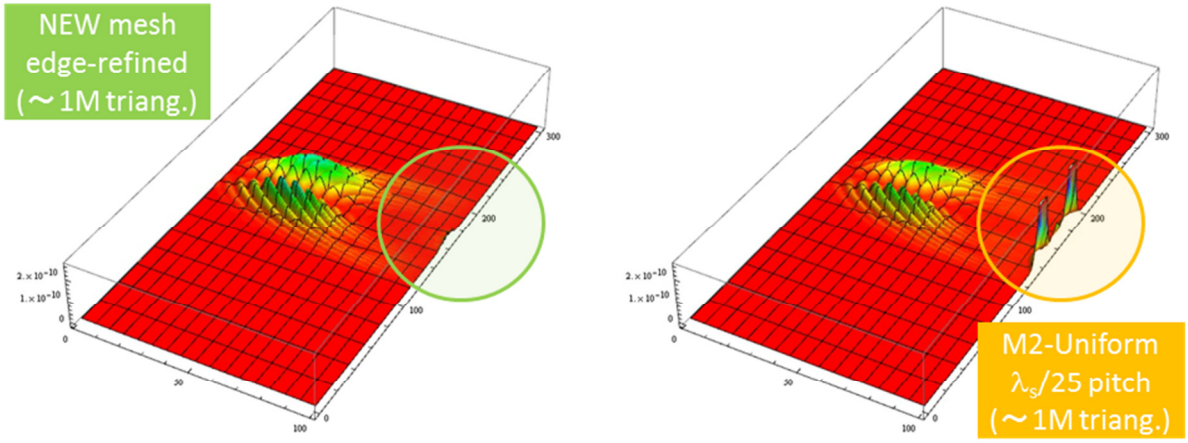

Figure 4. Effect of mesh refinement in the vicinity of the EMAT emitter. Using a uniform mesh large perturbations arise on the edge of the test material (right) [1], which totally disappear once the mesh is fine enough (left).

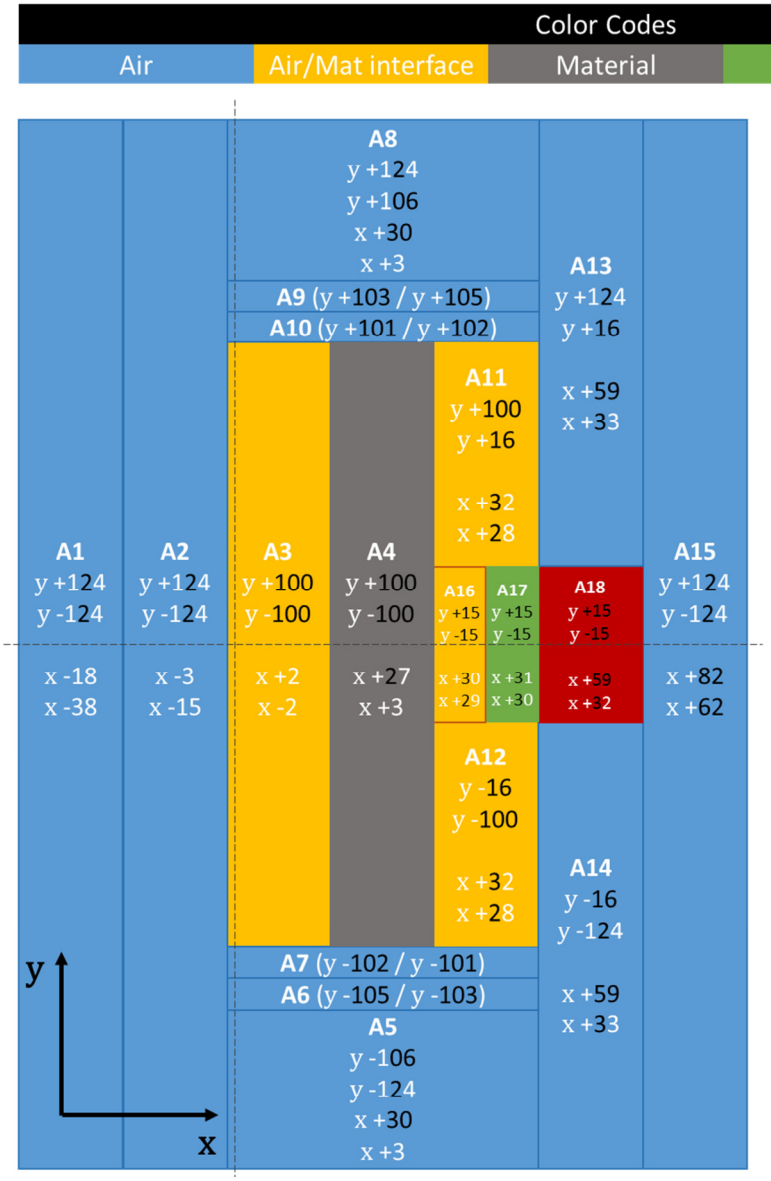

Area	High quality pitch (mm)	Standard pitch (mm)
1	5	5
2	3	3
3	0.125	0.25
4	0.125	0.25
5	3	3
6	1	1
7	0.5	0.5
8	3	3
9	1	1
10	0.5	0.5
11	0.125	0.125
12	0.125	0.125
13	3	3
14	3	3
15	5	5
16	0.0078125	0.0078125
17	0.125	0.125
18	0.125	0.125
N. nodes	900K	600K
N. elems	1.8M	1.2M

Figure 5. Schematic of the FEM mesh used for the simulation domain in Figure 2.

The 2-million 2nd order element mesh was however too large to be practical for running in a standard workstation, and further analysis was done to achieve similar results with a 1st order mesh. Focusing in the idea of refining the area in the vicinity of the EMAT coils, the maximum pitch resolution was increased to 7 μm, which for a 1MHz input EMAT signal corresponds to roughly λ_S / 800. Unsurprisingly, this spatial definition is of the same order of magnitude as the time discretization one we found to be good enough to reproduce all signal features during previous work [1]. A comparison with mesh M2, which has the same pitch inside the test material (λ_S / 50) but lacks the edge refinement, is shown in Figure 5 for the reference simulation in Figure 3 [1].

The same approach was therefore employed for the new experimental problem in Figure 2, with the final mesh using either 1.2 million (standard definition) or 1.8 million (high definition) 1st order triangles. The difference between both lies in the pitch inside the test material, which varies between 0.250mm (λ_S / 12.5) and 0.125mm (λ_S / 25), respectively. Both meshes are too dense to be represented directly, but a schematic of the different areas involved is shown in Figure 5. In the figure, for each area, both the X and Y ranges are indicated together with their respective base mesh pitches. The actual meshes are obtained by triangularization of the whole simulation domain while respecting these constraints, and using a minimum angle of 33 degrees to ensure adequate element geometrical quality.

3.4. Input Currents

Both, the newly adopted input current pulse [2] and that previously used in [1] are given in

Figure 6 left and right, respectively. As an example, here both are given when using the central frequency f_c of 1MHz, but several fundamental differences arise from their respective mathematical expressions:

a) While the new pulse becomes zero after the number of periods defined by the parameter n, the previous one has an infinite queue, slowly tending towards zero together with the exponential pre-factor.

b) While the central frequency effectively affects the duration of the new pulse (in the example 3µs because $n = 3$ and $f_c = 1$MHz), it controls the number of periods in the previous one (the duration of the pulse being fixed by the attenuation factor α in the pre-exponential term).

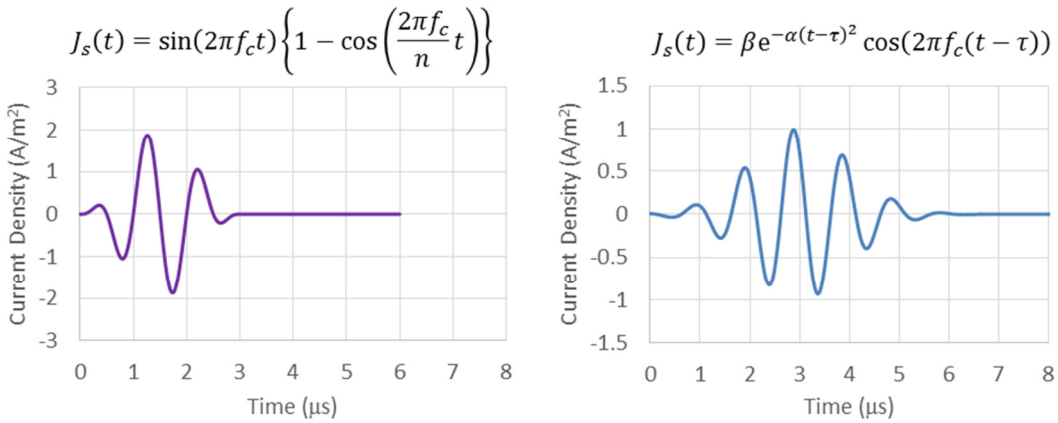

Figure 6. Newly adopted (left) and previously used (right) input current density pulses.

4. Analysis

4.1. Overview

One of the most noticeable differences between the new experimental setup and the previous one was the asymmetry of the EMAT-generated sound wave in the material [2]. At first, several hypotheses were made, but ultimately it was decided to follow a step by step approach, in which each of the configuration changes made when going from the previous model in Figure 3 to that in Figure 2 could be analyzed individually. The resulting full test matrix is presented in Figure 7, and includes a total of nine variables, four of which were tested using the previous setup configuration (Figure 3), and five others using the new setup (Figure 2). In the following, only the most relevant changes on each setup are detailed and compared qualitatively, since the experimental results only contain the displacement wave propagation figures.

Unless otherwise specified:

a) all the following 2D simulations were performed using the 2DEMATc coupled code, and display $\left(u_x^2 + u_y^2\right)^{0.5}$.

b) comparisons in paragraphs 4.2 to 4.4 are based in the ISEM'13 configuration in Figure 3, including the input signal from [1] in Figure 6 with a frequency of 1MHz.

c) comparisons in paragraphs 4.5 to 4.8 are based on the new JAPEIC configuration Figure 2, including the new input signal from [2] in Figure 6, and except that the EMAT was enclosed in a metallic box similar to those in Figure 3.

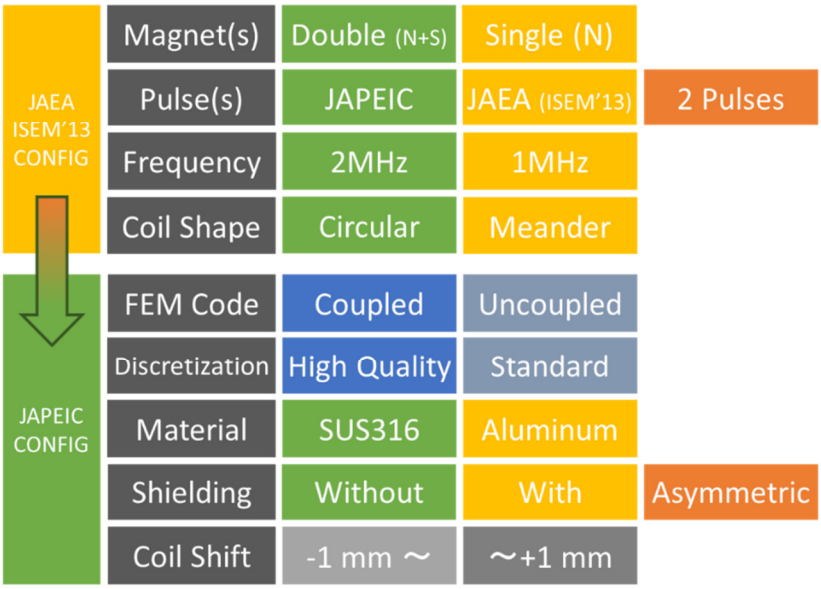

Figure 7. Analysis test matrix representing all the case-studies considered in the present work.

4.2. Magnet configuration effect

As seen in Figure 2, the magnet configuration was changed from a single magnet element to a couple of magnets with opposite polarization. The results are shown in Figure 8, where it is made clear that this was the change originating the asymmetry of the wave, arising from the magnetic field asymmetry of the EMAT in the vicinity of the test sample surface.

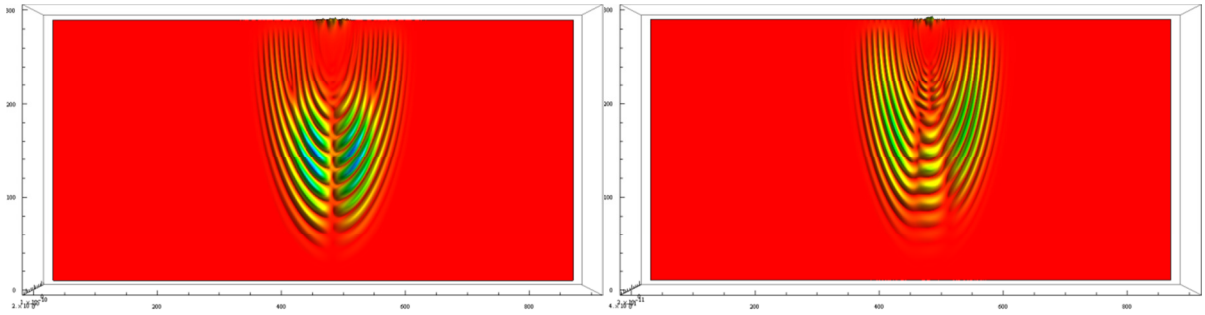

Figure 8. Sound wave comparison between the single magnet (left) and double magnet (right) configurations.

4.3. Input signal effect

Figure 9 shows how the differences between both input signals in

Figure 6 are well translated into the simulated sound-wave. In this particular single pulse configuration, the shorter new pulse (right) allows to clearly discern between the longitudinal (P) and shear (S) waves from the very beginning of the propagation, while the previous pulse is long enough for both to get mixed up in the early stages (left). Also, the new pulse seems to go ahead of the previous one, but that is only because its amplitude rises much faster as seen in

Figure 6. Comparing both of the time steps provided (top and down), it can be seen however that, after the initial rise, the wave propagation is identical in both cases, as one would expect since the input signal is the only difference between both simulations. This case was carried out starting with the overall ISEM'13 configuration in Figure 3, but using the circular coil from [2] (Figure 1) instead of the meander one [1].

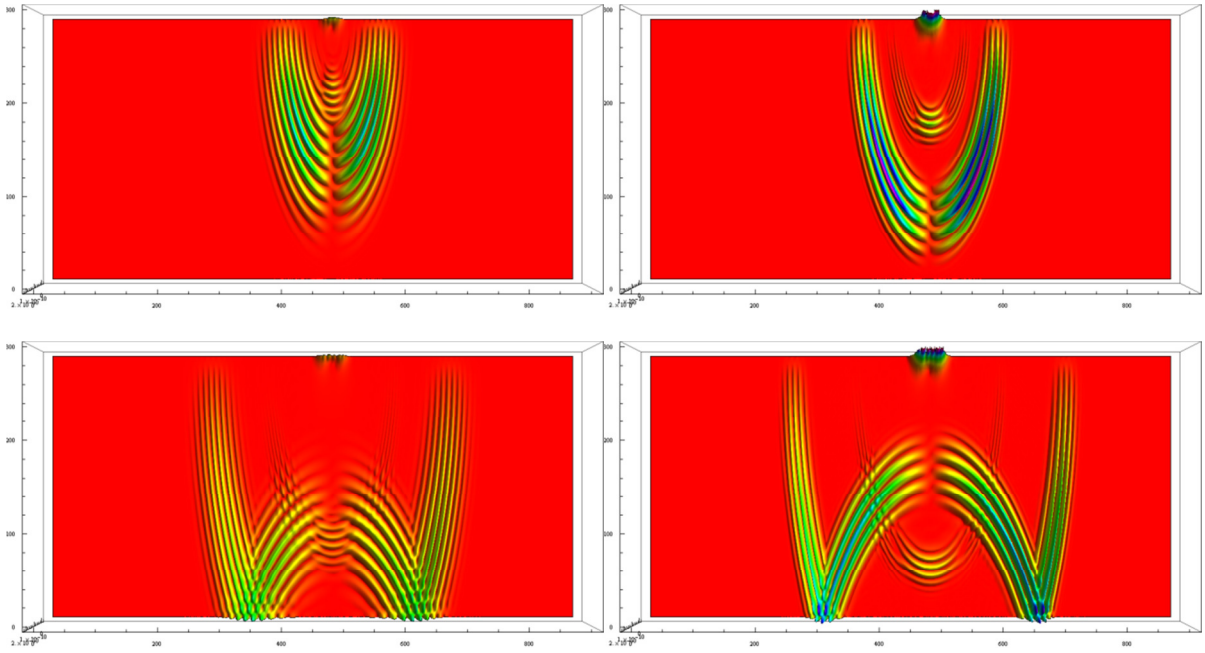

Figure 9. Sound wave comparison between the previous (left) and newly (right) adopted input density currents in

Figure 6.

4.4. Coil shape effect

Another one of the considerable changes between the two experimental configurations was going from a meander coil to a circular coil. The first direct effect was that of a much larger amplitude, due to the considerably larger section of the coil elements, so in Figure 10 below signals are actually scaled in order to better appreciate the other differences. As it can be seen, the overall propagation is very similar, but the shapes of both the shear-S and longitudinal-P waves are considerably altered, reflecting the coil setup geometry. Indeed, the asymmetry introduced by the double magnet configuration is considerably enhanced by the meander coil setup when compared with the perfectly symmetrical circular coil case. This

comparison was carried out starting with the overall ISEM'13 configuration in Figure 3 [1], but using the new pulse from [2] in

Figure 6.

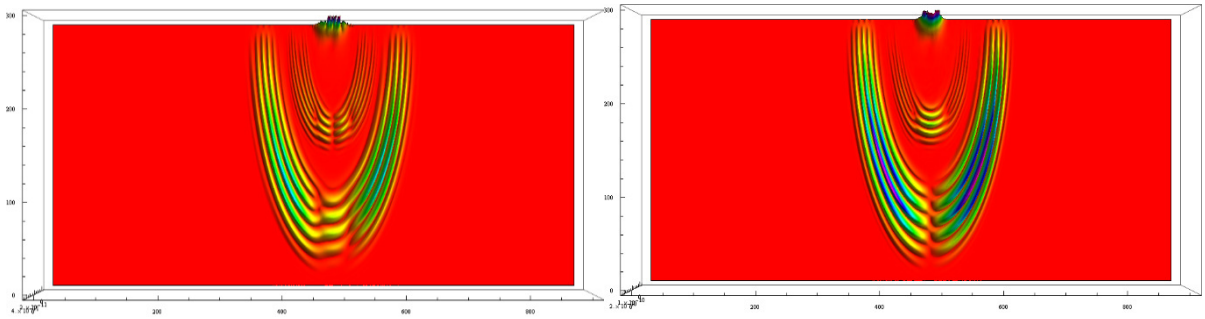

Figure 10. Sound wave comparison between the meander (left) and the circular (right) coil configurations.

4.5. FEM code effect

We had seen in previous work that the most noticeable difference between the coupled and uncoupled formulations of the EMAT problem was the decreased amplitude in the receiver-coil signal [1]. When looking at the propagated sound-wave in this new configuration, however, the differences are considerably smaller. Altogether, the most significant change in Figure 11 is the amplitude of the excited S-wave, which almost disappears when using the uncoupled code. It is worth noting here that in real life there is not such large amplitude difference between both, but our 2D setup can only properly reproduce the P-wave, as will be discussed later (section 5). This comparison was carried out with the new configuration from [2] in Figure 2, except that the EMAT was enclosed in a metallic box similar to those in Figure 3.

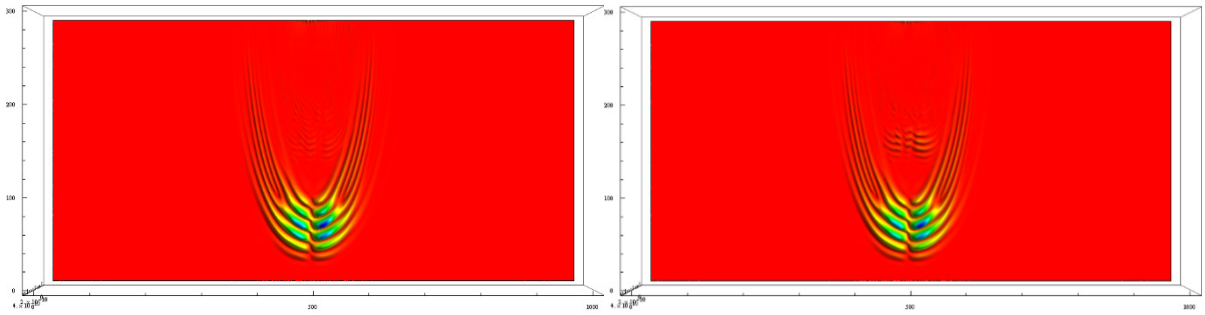

Figure 11. Sound wave comparison between the uncoupled (left) and the coupled (right) 2DECT codes.

4.6. Mesh refinement effect

As previously discussed (cf. 3.2), two meshes were tested with two different levels of refinement inside the test material bulk. As seen in Figure 12, the smaller mesh carries considerably more noise and some visible artifacts in the smallest details, for which the high-quality mesh is needed. If one is interested only in the main signal, however, the standard mesh with 1.2M elements remains reasonably good. This comparison was also carried out with the new configuration from [2] in Figure 2, except that the EMAT was enclosed in a metallic box similar to those in Figure 3.

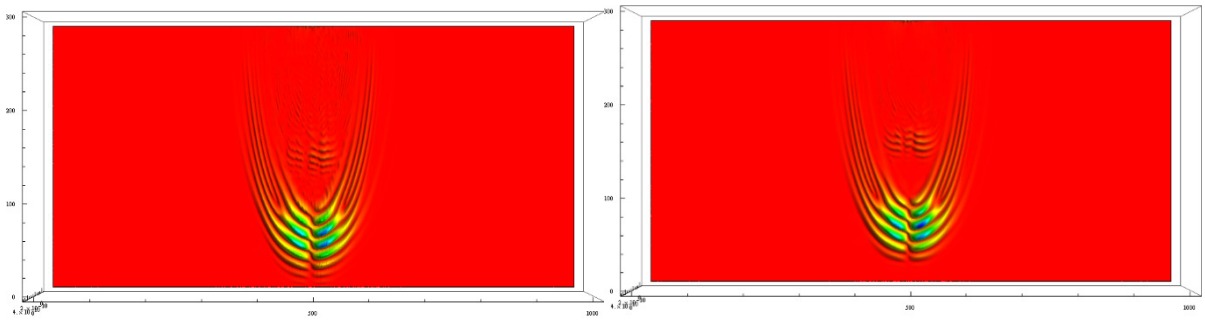

Figure 12. Sound wave comparison between the standard (left) and the high quality (right) meshes (cf. Figure 5).

4.7. Test material

As far as the test material is concerned, the main differences observed in Figure 13 correspond to the different wave velocities arising from the change in the material properties given in Figure 2 and Figure 3. Indeed, while the S-wave velocity is almost identical in both cases (～ 3.1 mm/μs), the P-wave is considerably slower in the SUS316 steel (5.5 mm/μs) vs. the Aluminum (6.2 mm/μs). Again, both of such changes are well rendered by the 2DEMATc coupled code. This comparison was also carried out with the new configuration from [2] in Figure 2, except that the EMAT was enclosed in a metallic box similar to those in Figure 3.

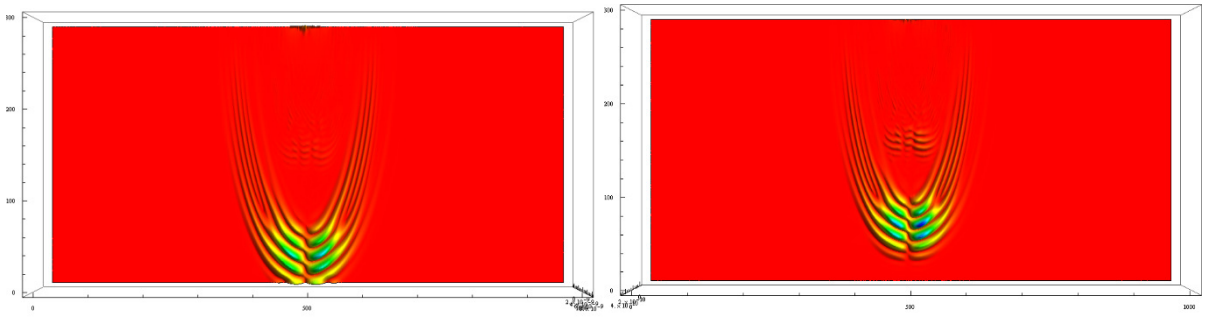

Figure 13. Sound wave comparison between the aluminum (left) and the SUS316 (right) test samples.

4.8. Coil misplacement effect

When considering the wave asymmetry observed in the experimental signal [2], an unnoticed shift in the coil position was among the possible causes. As seen in Figure 14 and Figure 15, however, this effect is noticeable when shifting the coils to the left (towards the N magnet), but only minor when shifting to the right (towards the S magnet). When comparing both the left and right shifts, however, it can be seen that differences remain relatively small up to 0.5mm [Figure 14], and only become truly significant if shifting 1mm [Figure 15], when a considerably loss of symmetry and signal amplitude can occur. This comparison was also carried out with the new configuration from [2] in Figure 2, except that the EMAT was enclosed in a metallic box similar to those in Figure 3.

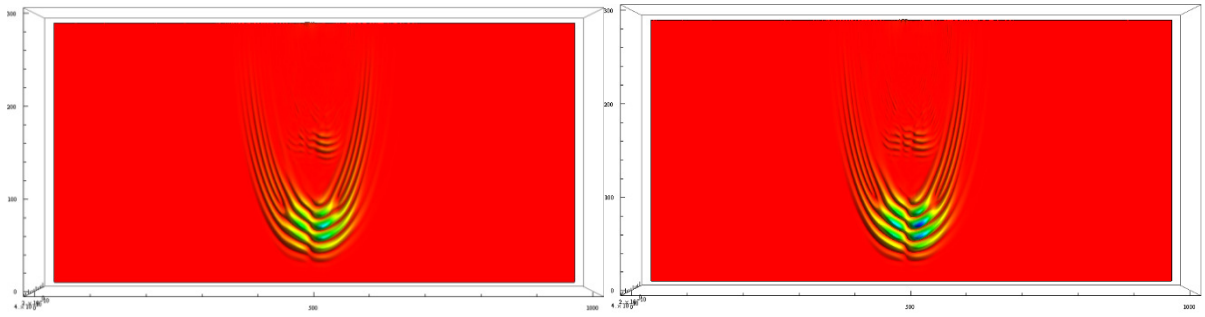

Figure 14. Sound wave comparison between the 0.5mm laterally shifted coils, towards N-magnet (left) or S-magnet (right).

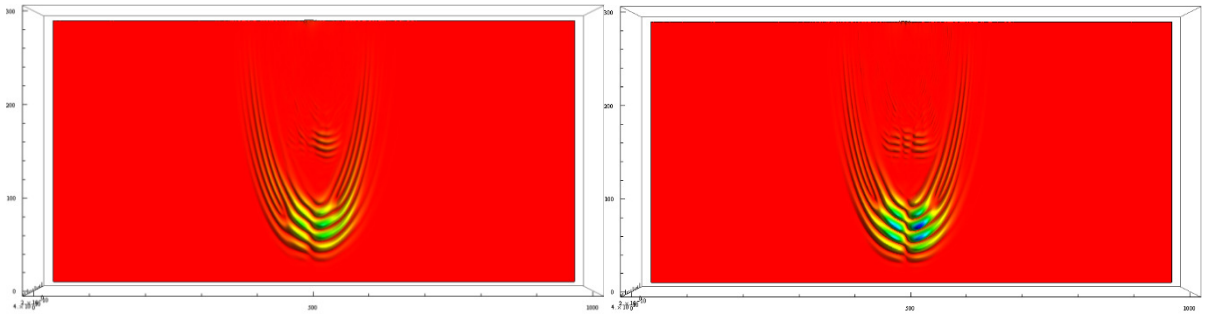

Figure 15. Sound wave comparison between the 1.0mm laterally shifted coils, towards N-magnet (left) or S-magnet (right).

5. Comparison between simulations and experimental data

The comparison between simulation and experimental results at three different time instants is shown in Figure 16. As seen in the figure, the initial longitudinal P-wave is well reproduced by the JAEA 2DEMATc code, both in amplitude and velocity, resulting in considerably similar figures. Other characteristic features such as the asymmetry of the experiment visualization could be also reproduced in the numerical simulation, which was confirmed to appear because of the asymmetry of the permanent magnets sources, creating an asymmetry in the Lorenz force inside the test material (cf. 4.2). In this case, the asymmetry is inverted left-right because the simulations were inadvertently run with the inverse polarity of the magnets. Other than that, there are some noticeable detail differences, which are thought to arise from the different magnitudes plotted. Indeed, while the computational plots are vector based ($u_x + u_y$) for the X and Y in-plane components together, the piezoelectric sensor experimental measurements might include also parts of the Z-perpendicular-plane component, as well as other 3D effects.

A cut-view for the 3D computational signal obtained by JAPEIC, and representing the amplitude of the displacement taking into account X, Y and Z components, is shown in Figure 17. It can be seen that, because of the 3D geometry, there is not only the main shear S-wave propagating in the volume of the material, but also additional waves that seem to result from other 3D effects in the simulation domain. None of them can be taken into account in the 2D geometry.

All in all, the results above highlight the limitations of the 2D plane-parallel code, into that only the longitudinal P-wave is excited. Indeed, the shear S-wave, which represents vibrations in the Z direction, perpendicular to the XY simulation domain, cannot be properly reproduced, because the Z-displacement component is ignored in the 2D approximation. This is even more clearly visible when comparing JAEA 2D coupled code (2DEMATc) results with those previously obtained by JAPEIC using a 3D version of COMWAVE, as seen in Figure 18 and Figure 19. The computational plot displays the absolute values of X and Y component with both FEM approaches.

Finally, as one could have expected from the analysis in paragraph 4.5, results obtained with JAEA 2D uncoupled code (2DEMATu) in Figure 20 show slightly smaller S-wave amplitude when compared with those obtained with 2DEMATc in Figure 18 and Figure 19.

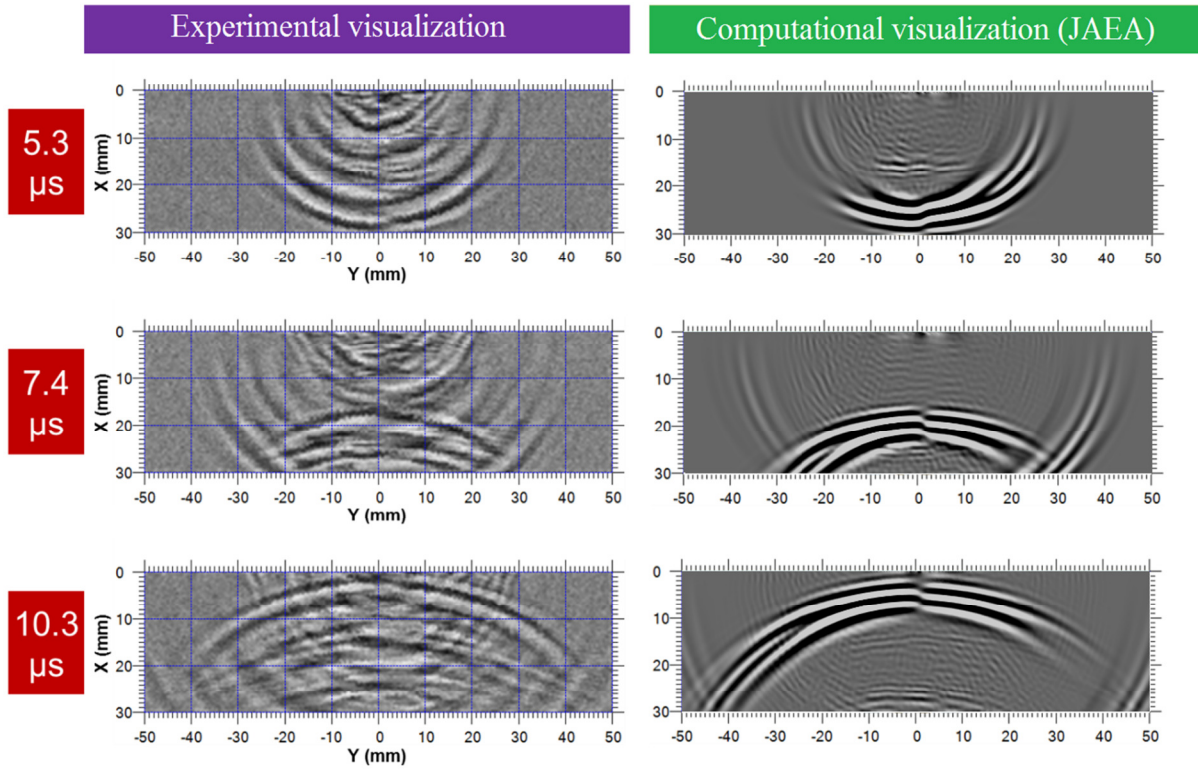

Figure 16. Comparison between experimental sound-wave measurements and JAEA's 2DEMATc simulations.

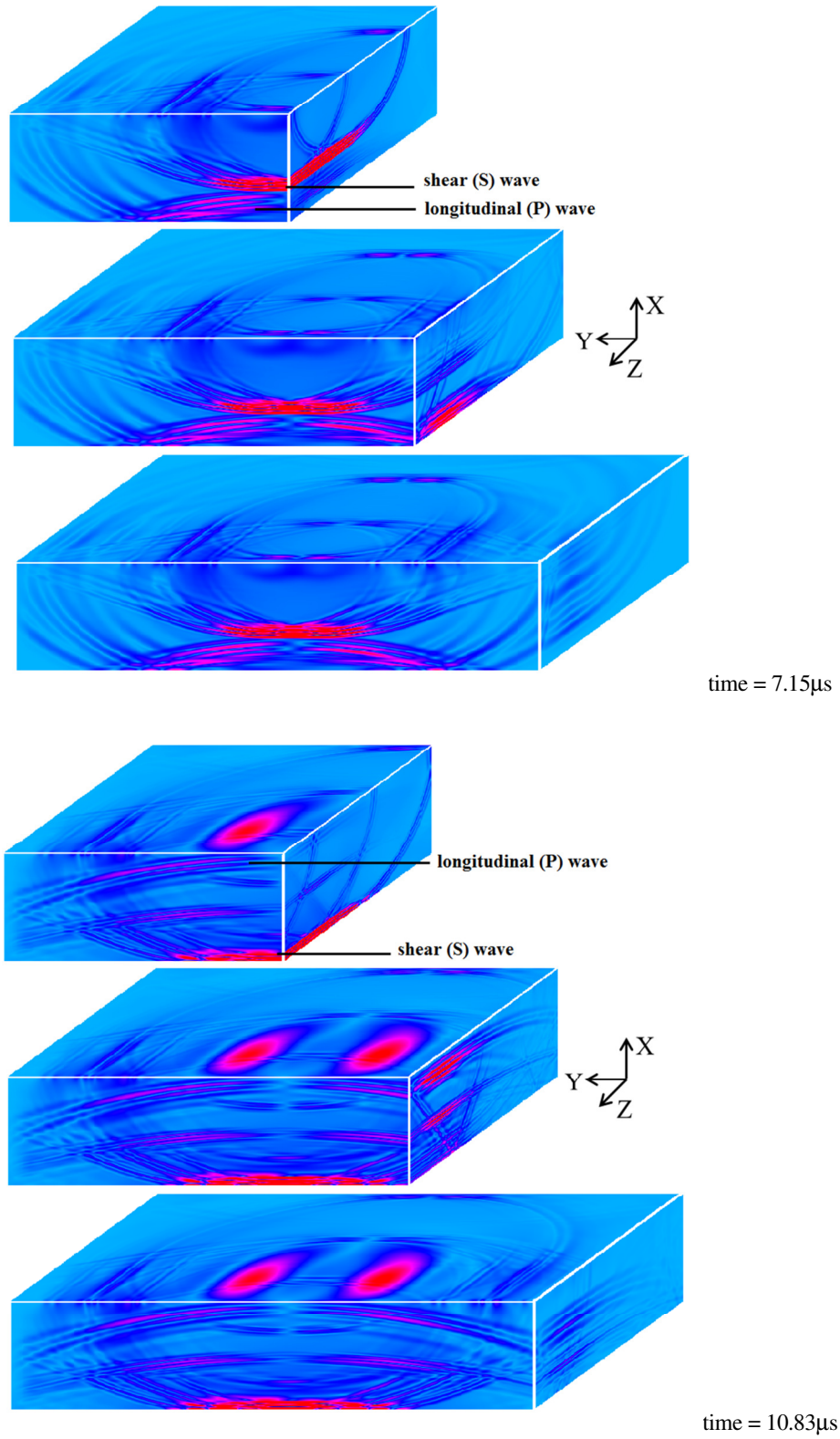

Figure 17. 3D cut-view at for positions at two time steps of the wave amplitude using 3D numerical simulations (JAPEIC)

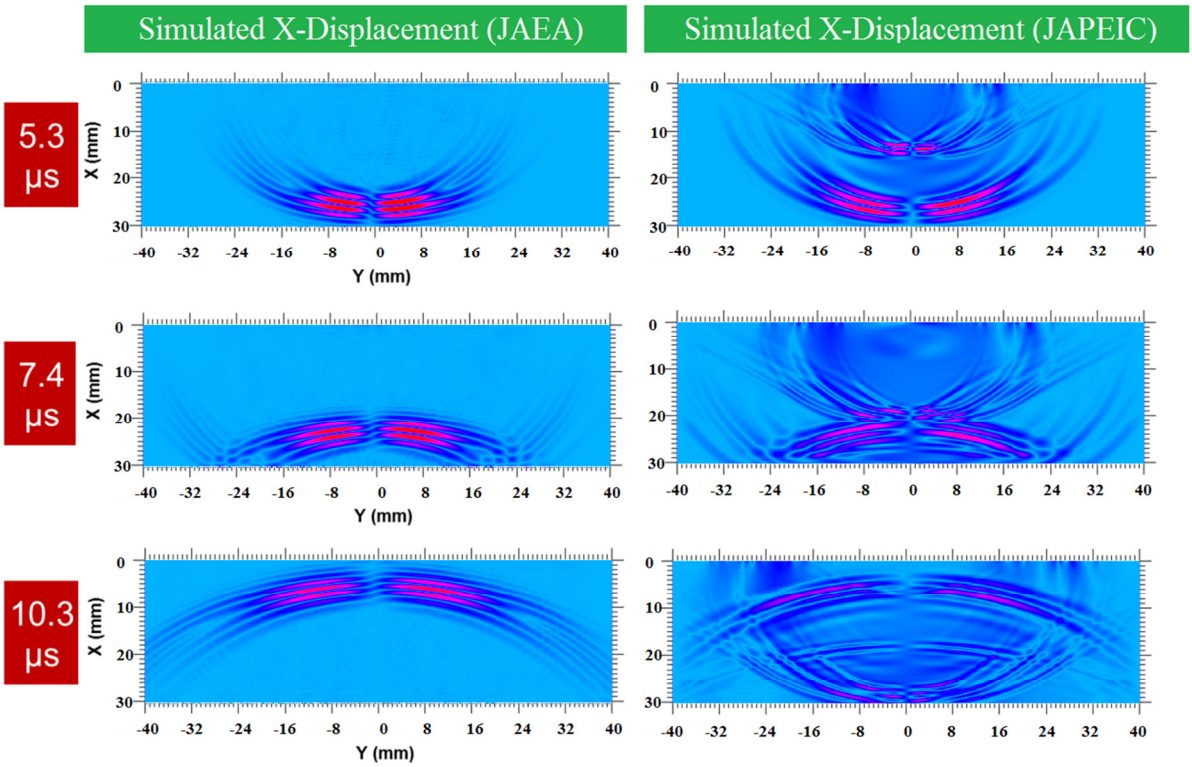

Figure 18. Sound-wave comparison for X-component between JAEA's 2DEMATc code and EMsolution/COMWAVE results.

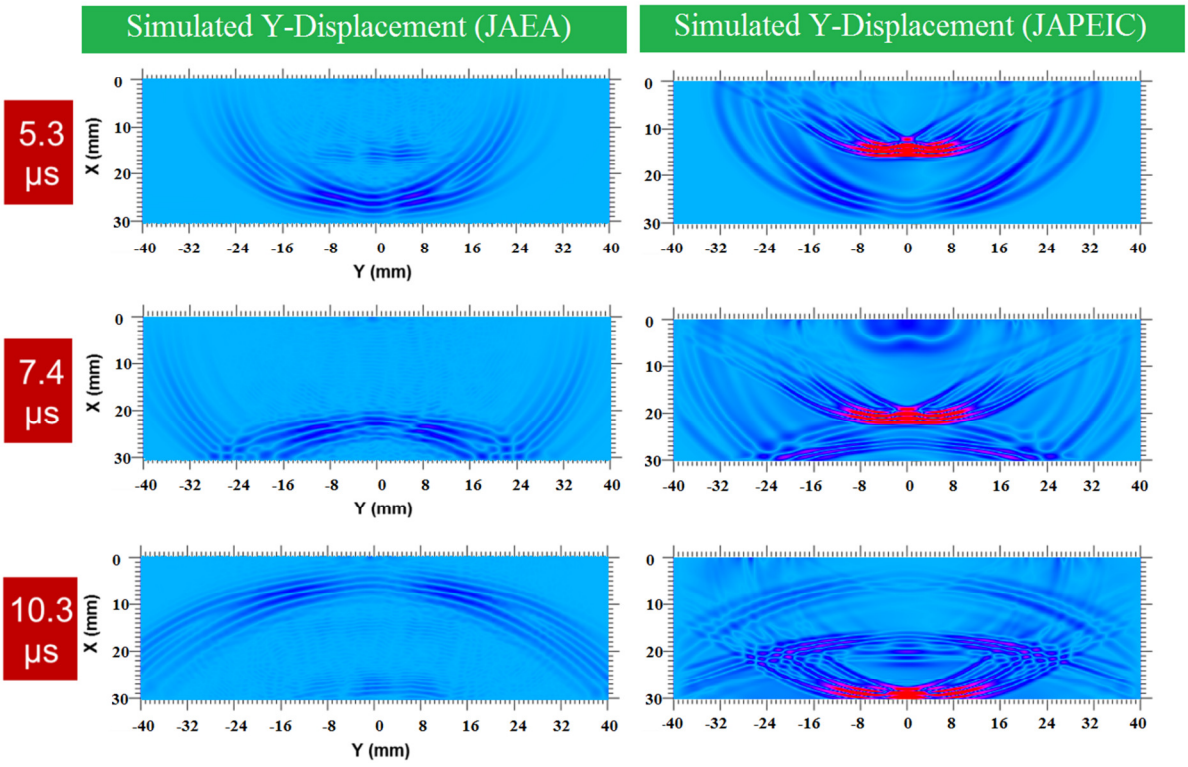

Figure 19. Sound-wave comparison for Y-component between JAEA's 2DEMATc code and EMsolution/COMWAVE results.

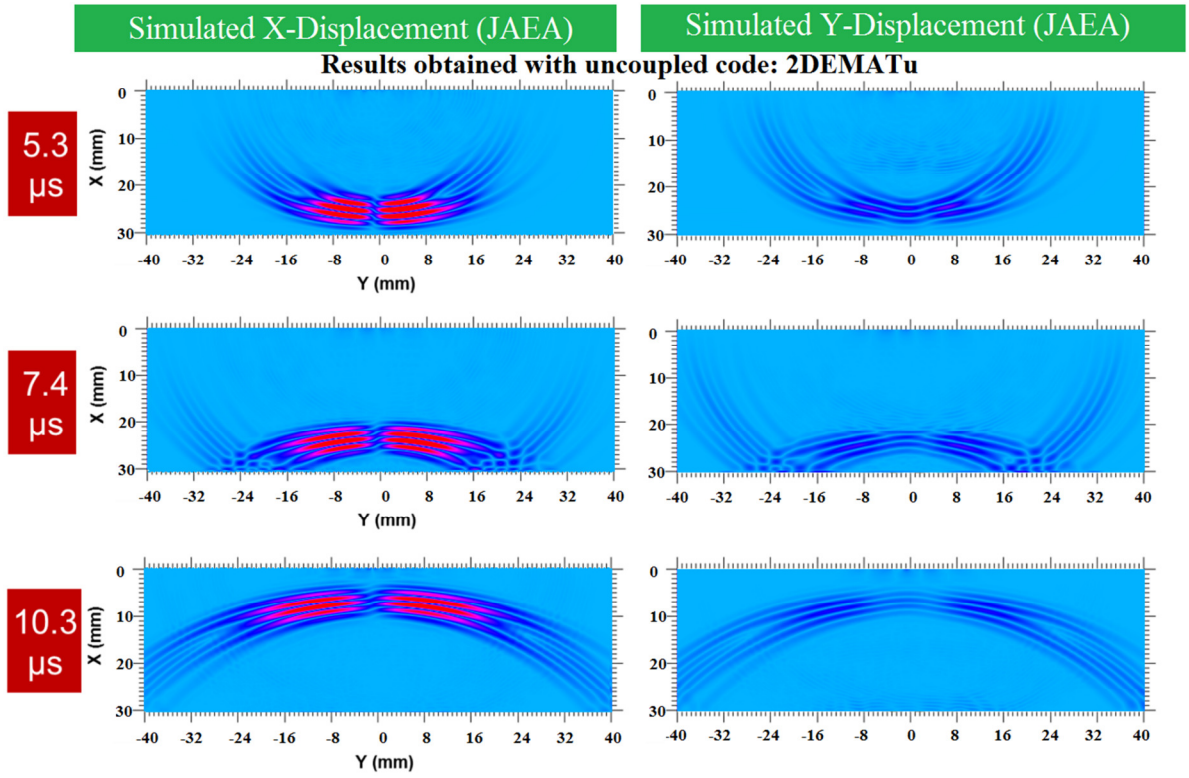

Figure 20. Sound-wave for X and Y-components computed with uncoupled JAEA's 2DEMATu code.

6. Conclusion

It was shown that the JAEA developed 2DEMAT codes accurately reproduce the EMAT sound-wave propagation characteristics, both in terms of overall wave-figures and velocities. Simulation results were shown to be in good agreement with the experimentally observed waves, but only within the 2D approximation limitations. Indeed, because the plane-parallel configuration assumes no field variations in the direction perpendicular to the plane, the shear wave cannot be adequately reproduced. Similarly, Rayleigh waves propagating along the surface of the material cannot be simulated in this 2D configuration. Finally, for the present EMAT configuration, it is seen that the wave propagation in the coupled and uncoupled approaches to EMAT result in relatively small differences. The main advantage of the coupled code thus remains its reduced computational time, which in practical applications is several times faster than the uncoupled code. That is not only because it is inherently simpler (we solve a single FEM problem instead of 3 consecutive ones in the uncoupled code), but also because it offers better scalability when parallelized on multi-core CPUs. This advantage is even greater when compared with the concatenation of several commercial codes, but the latter approach already allows for simulations of actual 3D configurations, which are required for many practical applications.

References

[1] Daniel Garcia-Rodriguez, Ovidiu Mihalache, Masashi Ueda, "EMAT Simulations based on a Two-Dimensional FEM Coupled Electro-Mechanical Formulation", International Journal of Applied Electromagnetism and Mechanics, Vol 45, pp. 543-549,2014.
[2] T. Yamamoto, T. Furukawa, I. Komura, R. Urayama, T. Uchimoto and T. Takagi, "Property study on EMATs with visualization of ultrasonic propagation", M. Bieth (Ed.), Proceedings of the 10th International Conference on NDE in Relation to Structural Integrity for Nuclear and Pressurized Components, pp. 902-909, European Union (2014).
[3] Hirao M and Ogi H, "EMATs for science and industry: Non-contacting ultrasonic measurements", Boston / Dordrecht / London, Kluwer Academic Publishers, 2003.
[4] EMSolution software (http://www.ssil.co.jp/em/EMSolution/ja/index.html), 2015.
[5] Y. Ikegami, Y. Sakai and H. Nakamura, "A Highly Accurate Ultrasonic Simulator Capable of Over One Billion Elements for Non-destructive Evaluations," Proceedings of the 7th International Conference on NDE in Relation to Structural Integrity for Nuclear and Pressurized Components, 177-190, (2009).

Conventional x-ray radiography versus image plates: a simulation and experimental performance comparison

D. Tisseur[1], B. Rattoni[1],G. Cattiaux[2], T. Sollier[2]

[1]CEA LIST, CEA Saclay 91191 Gif sur Yvette Cedex, France
[2]Institut de Radioprotection et de Sûreté Nucléaire, B.P.17 92262 Fontenay-Aux-Roses, France

ABSTRACT.X-ray/gamma ray radiography is a commonly used non-destructive evaluation method. For several years, a research program funded by the French Institute for Radioprotection and Nuclear Safety (IRSN), in partnership with CEA, studies gamma/X-ray simulation tools for evaluating NDE methods in the nuclear domain. In this context, IRSN has started in 2010 a program over several years for the validation of CIVA RT module. The aim of this paper is to present results of CIVA RT tools validation. The study consists in a cross comparison between classical X-ray films and image plates on experimental and simulation results. These have been carried out on very small openings (20 microns to 80 microns) notches. The study focuses on the case of homogeneous tube-tube and tube-elbow welds for iridium 192, selenium 75 and X-rays sources.
Keywords: Radiography, computed radiography, gamma source, validation, Monte Carlo simulation, CIVA
PACS: 28.41.Ak

INTRODUCTION

X-ray/gamma ray radiography is a commonly used non-destructive evaluation method. For several years, a research program funded by the French Institute for Radioprotection and Nuclear Safety (IRSN), in partnership with CEA, studies gamma/X-ray simulation tools for evaluating NDE methods in the nuclear domain. In this context, IRSN has started in 2010 a program over several years for the validation of CIVA RT module[1-3]. The aim of this paper is to present results of CIVA RT tools validation. The study consists in a cross comparison between classical X-ray films and computed radiography on experimental and simulation results. These have been carried out on very small openings notches (20 microns to 80 microns). The study focuses on the case of homogeneous tube-tube and tube-elbow welds for ^{192}Ir, ^{75}Se and X-rays sources.

MATERIALS AND METHODS

For this study, we used CIVA 11 version. Given the context of thick components, we usedthe fusion approach of scattered and transmitted images respectively fromMonte Carlo and analytical computations to simulate the final images [3,4,5]. For conventional radiography, we used the detector model (Gray model [8]) developed by EDF [7,9]. This model is based on the European standard EN 584-1 [6] and converts the incident dose into an optical density value.For computed radiography, we used the detector model named “generic detector” based on the transfer function between measured incident dose and grey level. For each incident dose, mean grey level and standard deviation is computed in a region of interest. The model converts the simulated incident dose into grey level via this transfer function. A Gaussian noise is added based on the standard deviation evaluated on experimental images.

Figure 1 presents the set up for dose versus grey level measurement. Figure 2 presents an example of “generic detector” transfer function for ^{192}Ir. These measures were performed for^{192}Ir, ^{75}Se and X-rays sources.

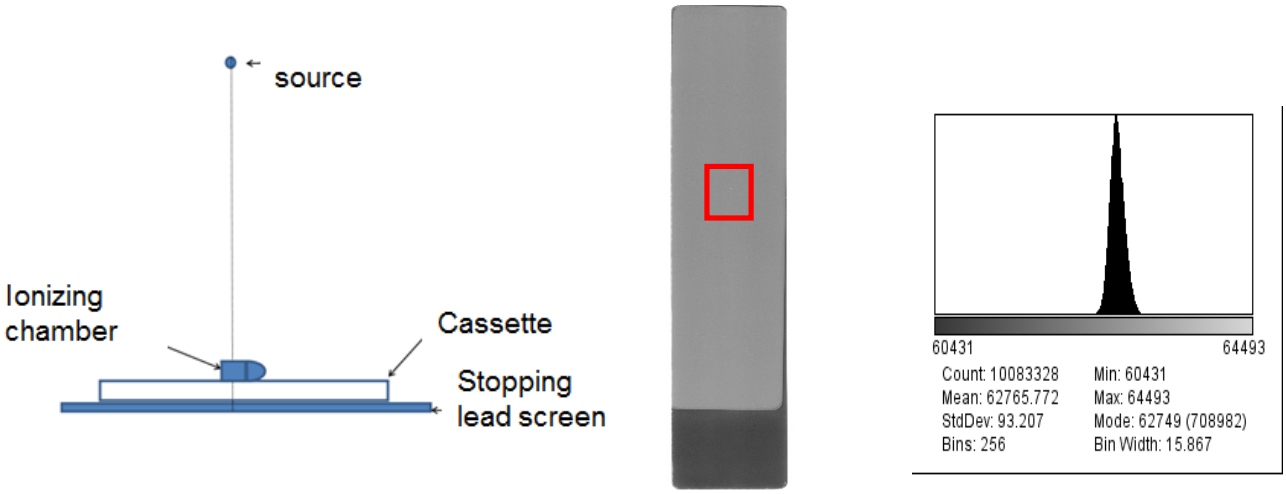

Figure 1: On the left, the experimental set up for dose measurement. On the middle, example of mean grey level and standard deviation in a region of interest.In the right, example of grey level histogram obtained with ImageJ [14].

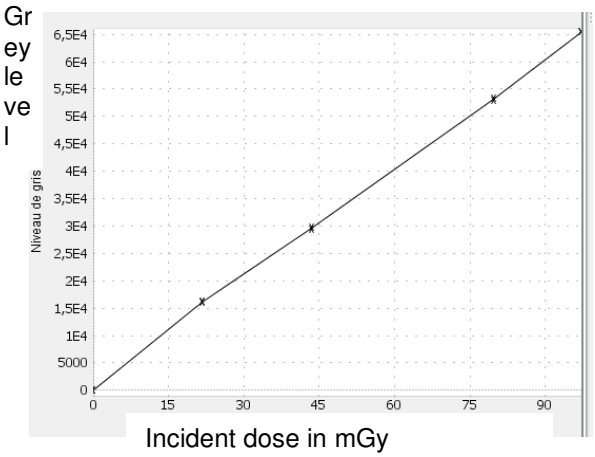

Figure 2: Example of transfer function.

In order to validate our detector modelling, we use ^{192}Ir source associate with Kodak HR and a step wedge:

- 7 steps between 4 and 18 mm thicknesses
- Ferritic steel
- Total length 272 mm (6*40 mm + 1*32 mm)

The following figure presents a cross comparison between CIVA and experimental results.

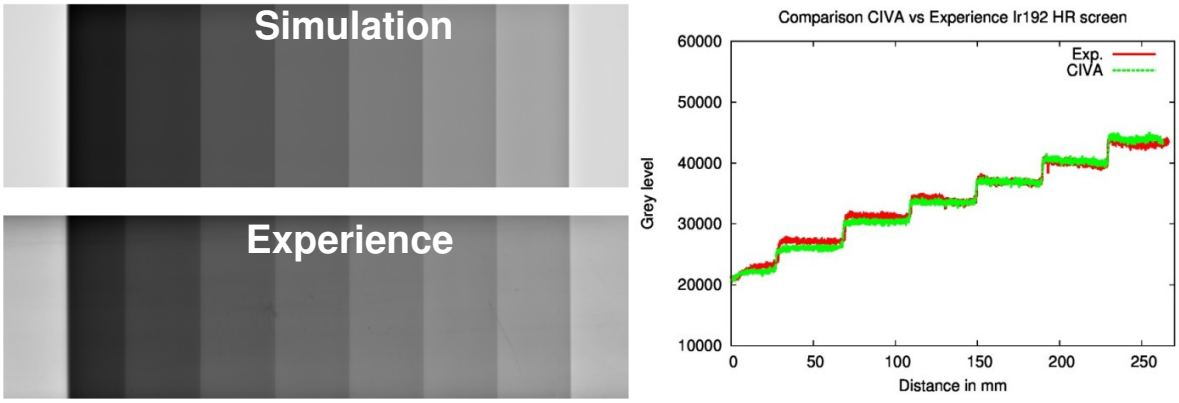

Figure 3: On the left, simulation and experimental image of the step wedge obtained with ^{192}Ir gamma source. On the right, grey level profiles (extracted along the step wedge) comparison between simulation and experimental data.

The X-ray source spectrum was measured experimentally by the National Laboratory Henri Becquerel (LNHB) using a highly collimated CdTe spectrometer. The following figure shows the spectrum measured at 1 m in the axis of the X-ray tube window.

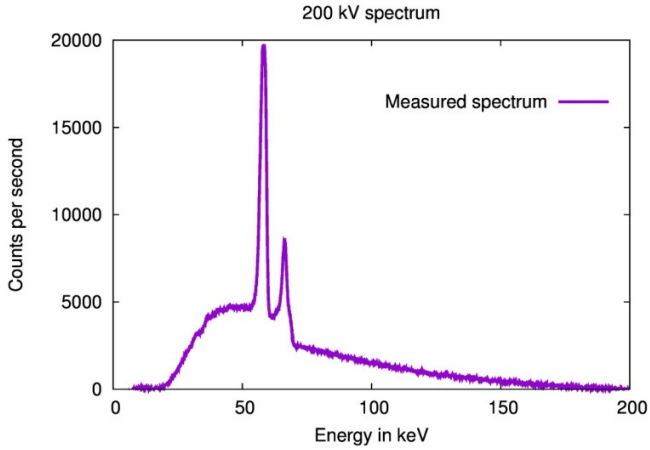

Figure 4: X-ray tube spectrum measurement at 200kV.

We used a homogeneous weld mock-up representative of auxiliary piping of main primary system. This mock-up is composed on one side of a straight part with a tube-tube weldand on the other side of anelbow part with tube-elbow weld (see figure 5). Pipe thickness is 8.56 mm, inside weld bead is 0.75 mm and outside weld bead is 2 mm.

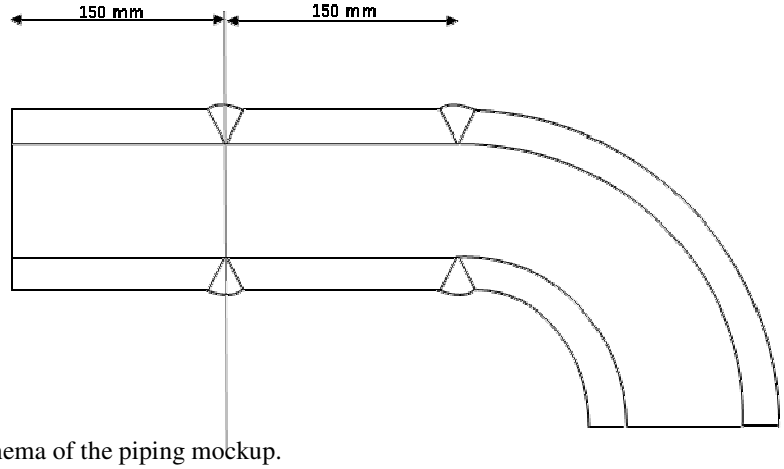

Figure 5: Schema of the piping mockup.

Four notches with several sizes (a height of 2.5 mm and an opening from 20 µm to 80 µm), orientations (axial or circumferential) and positions have been superimposed to the weld thanks to a manufactured insert (see figure 6 and table 1).

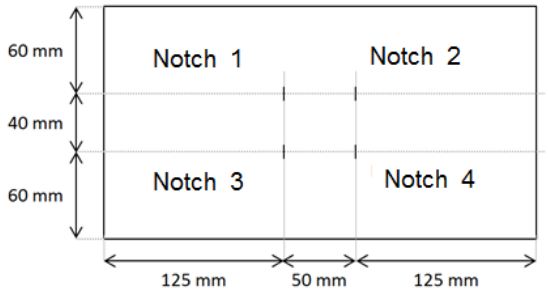

Figure 6: Schema of the insert with the four notches.

Reference	Name	Length (mm)	Heigth (mm)	Opening(mm)
Notch 1	EN-20	15	2.5	0.020
Notch 2	EN-40	15	2.5	0.040
Notch 3	EN-60	15	2.5	0.060
Notch 4	EN-80	15	2.5	0.080

Table 1:Description of the four notches.

For this validation, the notches are positioned in a circumferential and a longitudinal configurationin the middle of the weld (see figure 7 for straight part and figure 8 for elbow part) and the sources are axed on the weld.The distance from the source to the mock-up is 0.725 m.

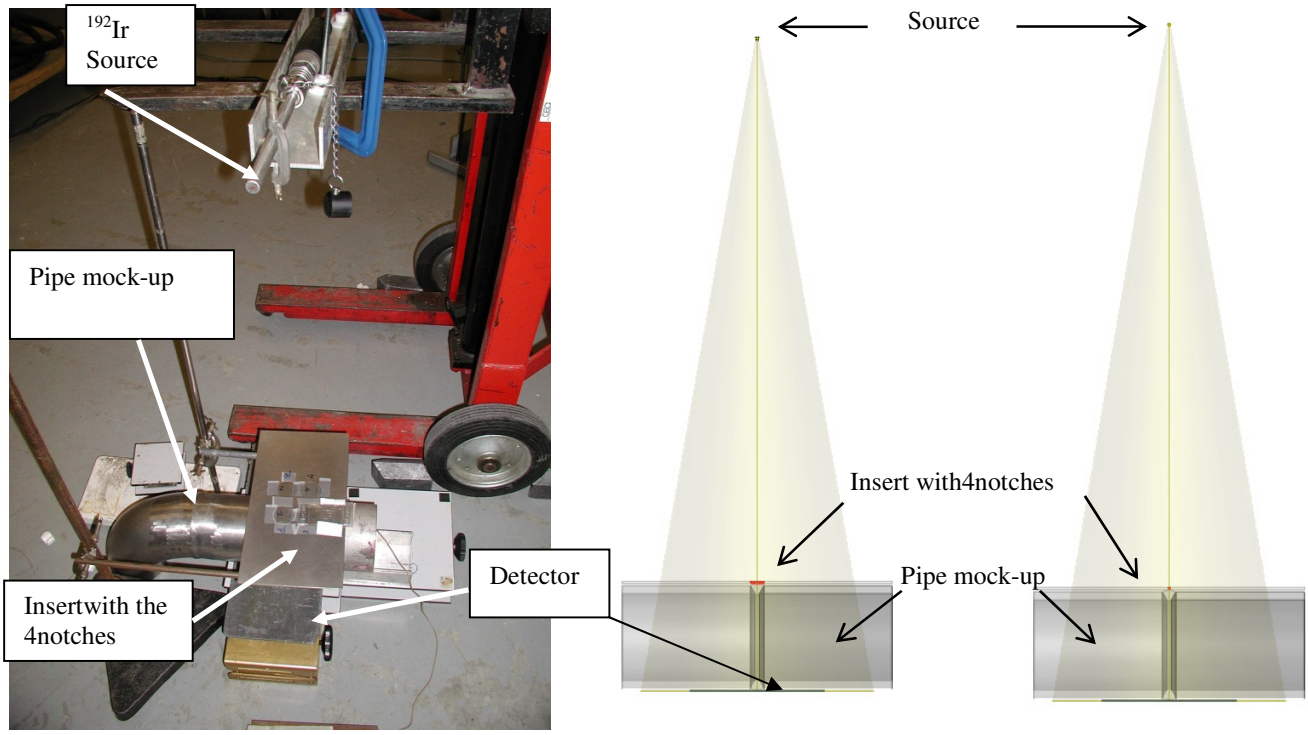

Figure 7: On the left, straight part experimental set-up. On the right, straight part simulation set-up with axial and circumferential notch configuration.

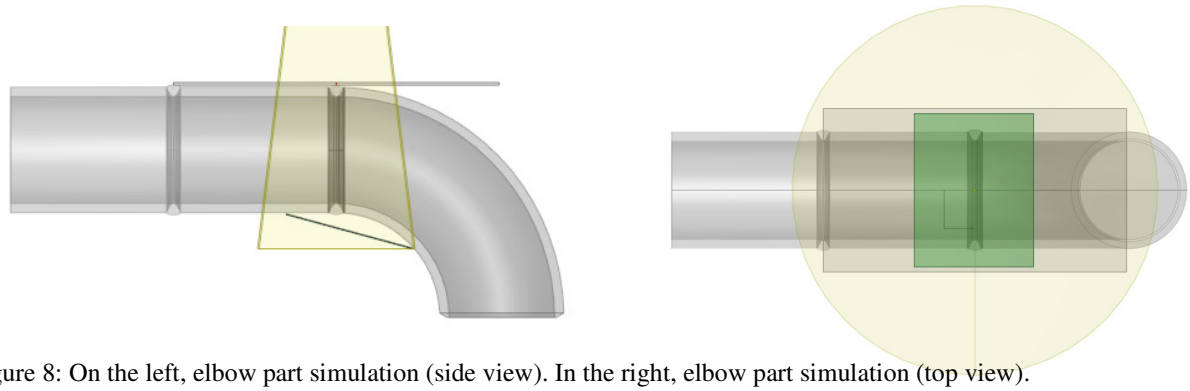

Figure 8: On the left, elbow part simulation (side view). In the right, elbow part simulation (top view).

We used a ^{192}Irand ^{75}Segamma source with a diameterof 3 mm and a height of 3 mm and an YXLON 225 kV X-ray tube at 200 kV (spot size 1 mm diameter). For conventional radiography, we used M100 Kodak X-ray films, manually developed in accordance with Kodak recommendations. Filters and reinforced used screens are in conformity with the Rules for Design and Fabrication of NPP Mechanical Components (RCC-M) and European standard [10,11,12]. For computed radiography, we used Kodak HR image plate associated with a HD CR35 DURR NDT scanner.Computed radiography cassette composition is in conformity with ISO17636 standard [13]. Image plates were scanned with 50 µm pixel size.

RESULTS AND DISCUSSIONS

Example of validation with ^{192}Ir gamma source with computed radiography on the straight part

Due to limited size of the paper, we only show a part of the results obtained for computed radiography with ^{192}Ir gamma source on the straight part.Grey level profiles have been extracted from the several images on the different notches (see figure 9). Amplitude and width at middle height have been measured on each notch on experimental and simulated images.

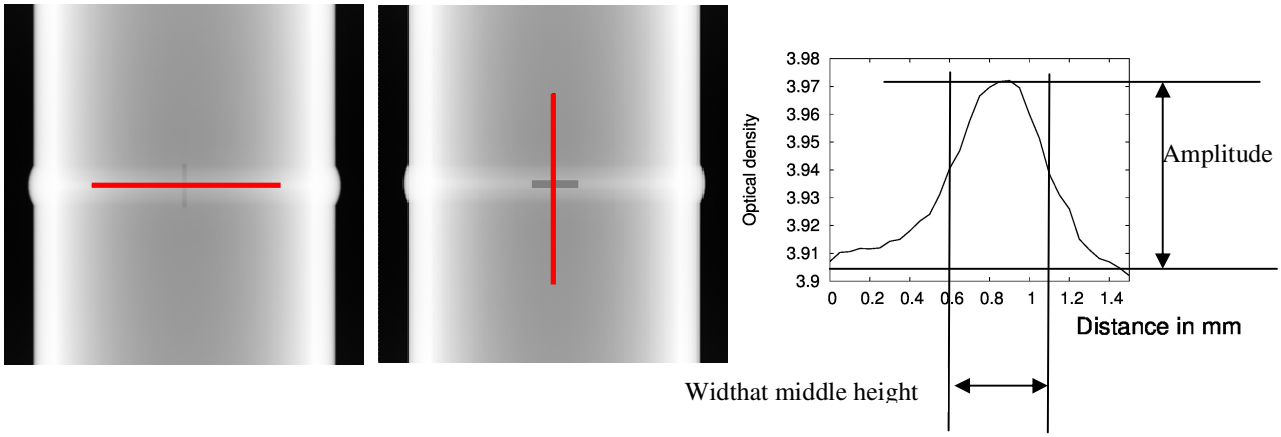

Figure 9: On the left, grey level profile extraction along the red line on axial notch. In the middle, grey level profile extractionalong the red line on circumferential notch. On the right, amplitude and width at middle height measurement example.

Figure 10 presents grey profiles comparison between CIVA and experimental film perpendicularly to the weld. The simulated data agrees with the experimental data.

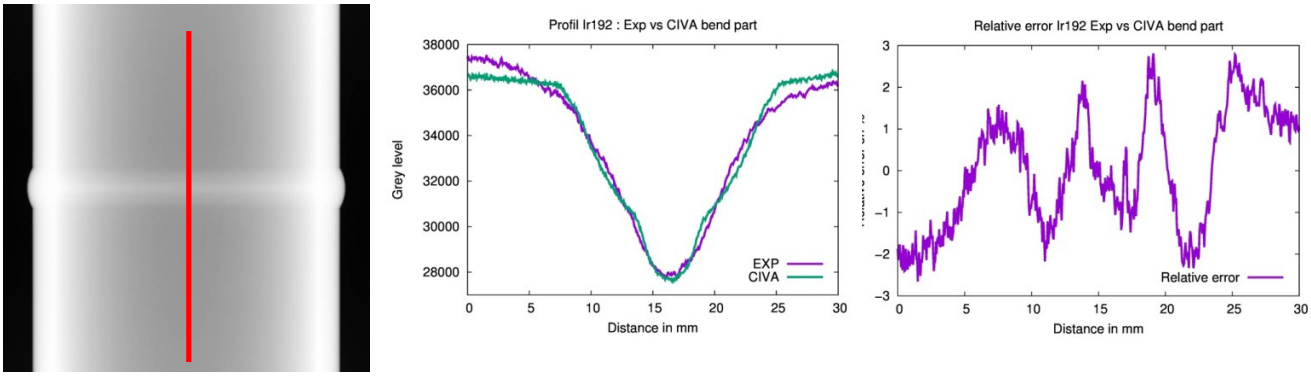

Figure 10: On the left, grey level profile extraction along the red line on a simulated image.In the middle, grey level profile comparison between CIVA and experimental data. On the right, relative error between CIVA and experimental data

Figure 11 presents grey level profiles comparison between CIVA and experimental data with circumferential notch.

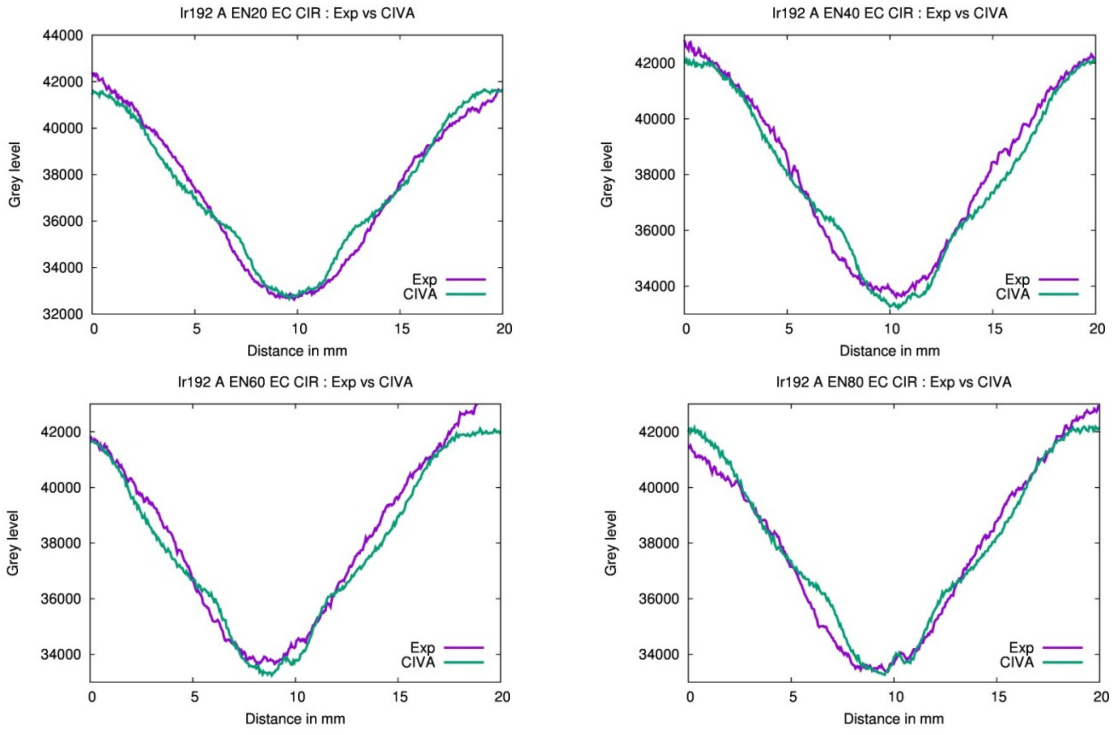

Figure 11: On the top left, grey level profile comparison between CIVA and the experimental image for EN20 notch. On the top right, grey level profile comparison between CIVA and the experimental image for EN40 notch. On the bottom left, grey level profile comparison between CIVA and the experimental image for EN60 notch. On the bottom right, grey level profile comparison between CIVA and the experimental image for EN80 notch.

The following table shows the results (note that ND= none detected) for ^{192}Ir gamma source with computed radiography for circumferential and axial flaw.

	Flaw	Measured amplitude	Simulated amplitude	Measured width at middle height in mm	Simulated width at middle height in mm
circumferentialflaw	EN80	321	397	0,38	0,43
	EN60	302	395	0,41	0,39
	EN40	188	180	0,39	0,44
	EN20	ND	ND	ND	ND
axial flaw	EN80	424	474	0,6	0,54
	EN60	406	452	0,46	0,48
	EN40	292	263	0,31	0,34
	EN20	ND	ND	ND	ND

Table 2:Amplitude and width comparison between CIVA and experimental data on the four notches for circumferential and longitudinal positionsfor computed radiography with ^{192}Ir gamma source.

The comparisons between CIVA and experimental data show a good adequacy. EN20 notch is never detected on the simulation and on the experimental data.

These comparisons have been performed for the 3 sources on the straight and elbow. The following tables show a result synthesis.

	Ir-192 circumferential position			Se-75 circumferential position			200 kV X-ray circumferential position		
notch	Measured amplitude (grey level) (Exp)	Simulated amplitude (grey level) (CIVA)	Relative error experience / simulation on amplitude in %	Measured amplitude (grey level) (Exp)	Simulated amplitude (grey level) (CIVA)	Relative error experience / simulation on amplitude in %	Measured amplitude (grey level) (Exp)	Simulated amplitude (grey level) (CIVA)	Relative error experience / simulation on amplitude in %
EN80	321	397	23.7	348	473	35.9	755	854	13.1
EN60	302	395	30.8	339	320	-5.6	735	647	-12.0
EN40	188	180	-4.3	242	236	-2.5	646	463	-28.3
EN20	ND	ND	-	ND	ND	-	ND	ND	-
Mean			16.7			9.3			-9.1

Table 3: Amplitude and width comparison between CIVA and experimental data on the four notches for circumferential positions for the straight part for computed radiography with ^{192}Ir and ^{75}Se gamma source and X-ray source.

	Ir-192 axial position			Se-75 axial position			200 kV X-ray axial position		
notch	Measured amplitude (grey level) (Exp)	Simulated amplitude (grey level) (CIVA)	Relative error experience / simulation on amplitude in %	Measured amplitude (grey level) (Exp)	Simulated amplitude (grey level) (CIVA)	Relative error experience / simulation on amplitude in %	Measured amplitude (grey level) (Exp)	Simulated amplitude (grey level) (CIVA)	Relative error experience / simulation on amplitude in %
EN80	424	474	11.8	415	499	20.2	955	1081	13.2
EN60	406	452	11.3	380	394	3.7	765	820	7.2
EN40	292	263	-9.9	230	263	14.3	724	653	-9.8
EN20	ND	ND	-	ND	ND	-	ND	ND	-
Mean			4.4			12.8			3.5

Table 4: Amplitude and width comparison between CIVA and experimental data on the four notches for axial positions for the straight part for computed radiography with ^{192}Ir and ^{75}Se gamma source and X-ray source.

	Ir-192 circumferential position			Se-75 circumferential position			200 kV X-ray circumferential position		
notch	Measured amplitude (grey level) (Exp)	Simulated amplitude (grey level) (CIVA)	Relative error experience / simulation on amplitude in %	Measured amplitude (grey level) (Exp)	Simulated amplitude (grey level) (CIVA)	Relative error experience / simulation on amplitude in %	Measured amplitude (grey level) (Exp)	Simulated amplitude (grey level) (CIVA)	Relative error experience / simulation on amplitude in %
EN80	324	366	13.0	254	336	32.3	760	968	27.4
EN60	167	230	37.7	280	329	17.5	450	669	48.7
EN40	121	164	35.5	201	148	-26.4	416	563	35.3
EN20	ND	ND	-	ND	ND	-	ND	ND	-
Mean			28.7			7.8			37.1

Table 5: Amplitude and width comparison between CIVA and experimental data on the four notches for circumferential positions for the elbow part for computed radiography with ^{192}Ir and ^{75}Se gamma source and X-ray source.

	Ir-192 axial position			Se-75 axial position			200 kV X-ray axial position		
notch	Measured amplitude (grey level) (Exp)	Simulated amplitude (grey level) (CIVA)	Relative error experience / simulation on amplitude in %	Measured amplitude (grey level) (Exp)	Simulated amplitude (grey level) (CIVA)	Relative error experience / simulation on amplitude in %	Measured amplitude (grey level) (Exp)	Simulated amplitude (grey level) (CIVA)	Relative error experience / simulation on amplitude in %
EN80	333	460	38.1	362	457	26.2	942	968	2.8
EN60	330	310	-6.1	286	253	-11.5	754	741	-1.7
EN40	282	266	-5.7	229	236	3.1	703	621	-11.7
EN20	ND	ND	-	ND	ND	-	ND	ND	-
Mean			8.8			5.9			-3.5

Table 6: Amplitude and width comparison between CIVA and experimental data on the four notches for axial positions for the elbow part for computed radiography with ^{192}Ir and ^{75}Se gamma source and X-ray source.

Same procedures have been applied for conventional radiography on the same setup with the three sources. Comparisons show a good agreement between simulation and experimental data for computed and conventional radiography.Due to the limited size of the paper, we only show a synthetic detection comparison between conventional and computed radiography in table 7.

Straight part

	Conventional radiography	Computed radiography
	Visual interpretation	Visual interpretation
Ir192 source		
IR A EC CIR		
EN 80	DETECTED	DETECTED
EN 60	DETECTED	DETECTED
EN 40	DETECTED	DETECTED
EN 20	DETECTED	NOT DETECTED
IR A EC AX		
EN 80	DETECTED	DETECTED
EN 60	DETECTED	DETECTED
EN 40	DETECTED	DETECTED
EN 20	NOT DETECTED	NOT DETECTED
Se75 Source		
SE A EC CIR		
EN 80	DETECTED	DETECTED
EN 60	DETECTED	DETECTED
EN 40	DETECTED	DETECTED
EN 20	DETECTED	NOT DETECTED
SE A EC AX		
EN 80	DETECTED	DETECTED
EN 60	DETECTED	DETECTED
EN 40	DETECTED	DETECTED
EN 20	DETECTED	NOT DETECTED
200kV RX		
RX A EC CIR		
EN 80	DETECTED	DETECTED
EN 60	DETECTED	DETECTED
EN 40	DETECTED	DETECTED
EN 20	DETECTED	NOT DETECTED
RX A EC AX		
EN 80	DETECTED	DETECTED
EN 60	DETECTED	DETECTED
EN 40	DETECTED	DETECTED
EN 20	DETECTED	NOT DETECTED

Elbow part

	Conventional radiography	Computed radiography
	Visual interpretation	Visual interpretation
IR ZC A EC CIR		
EN 80	DETECTED	DETECTED
EN 60	DETECTED	DETECTED
EN 40	DETECTED	DETECTED
EN 20	DETECTED	NOT DETECTED
IR ZC A EC AX		
EN 80	DETECTED	DETECTED
EN 60	DETECTED	DETECTED
EN 40	DETECTED	DETECTED
EN 20	NOT DETECTED	NOT DETECTED
SE ZC A EC CIR		
EN 80	DETECTED	DETECTED
EN 60	DETECTED	DETECTED
EN 40	DETECTED	DETECTED
EN 20	NOT DETECTED	NOT DETECTED
SE ZC A EC AX		
EN 80	DETECTED	DETECTED
EN 60	DETECTED	DETECTED
EN 40	DETECTED	DETECTED
EN 20	NOT DETECTED	NOT DETECTED
RX ZC A EC CIR		
EN 80	DETECTED	DETECTED
EN 60	DETECTED	DETECTED
EN 40	DETECTED	DETECTED
EN 20	DETECTED	NOT DETECTED
RX ZC A EC AX		
EN 80	DETECTED	DETECTED
EN 60	DETECTED	DETECTED
EN 40	DETECTED	DETECTED
EN 20	DETECTED	NOT DETECTED

Table 7: Detection comparison between conventional and computed radiography on the straight and elbow part for the three different sources.

CONCLUSIONS AND PERSPECTIVES

In terms of performance, testing on the straight and elbow part show a lower level of detectability with computed radiography (EN20 is never seen with computed radiography). Conventional radiography is able to detect EN20 notch in all scenarios tested with an X-ray source. Conventional radiography is able to detect EN20 notch in the straight part with a Se75 source.

If we take into account the signal amplitude of the defect (the results synthesis with conventional radiography are not presented due to the limited size of the paper). For the straight and elbow part, the ^{75}Se source and X-ray tube provides no gain in sensitivity with respect to the source ^{192}Irwith computed radiography contrary to what has been demonstrated with conventional radiography. The interpretation of the image is much easy with conventional radiography.

These first tries for computed radiography have been performed with respect to the ISO17636 standard but the cassette composition can be improved to enhance image quality.

REFERENCES

1. http://www-civa.cea.fr
2. R. Fernandez, A. Schumm, J. Tabary, P. Hugonnard, “Simulation studies of radiographic inspections with CIVA”, in 17th WCNDT, Shanghai (2008).
3. J. Tabary, P. Hugonnard, A. Schumm, R. Fernandez “Simulation studies of radiographic inspections with Civa", in COFREND 2008
4. R. Guillemaud, J. Tabary, P. Hugonnard, F. Mathy, A. Koenig, A. Glière, "SINDBAD: a multipurpose and scalable X-Ray simulation tool for NDE and medical imaging", in PSIP 2003, Grenoble, France(2003).
5. J. Tabary, F. Mathy, P. Hugonnard "New Functionalities in “SINDBAD” Software for Realistic X-Ray Simulation Devoted to Complex Parts Inspection" , in ECNDT 2006
6. EN 584-1:2006, "Non-destructive testing – Industrial radiographic film – Part 1: Classification of film systems for industrial radiography", European standard for non-destructive evaluation
7. A. Schumm, U. Zscherpel, “The EN584 standard for the classification of industrial radiography films and its use in radiographic modeling”, in Proceedings of the Sixth International Conference on NDE in relation to structural integrity for nuclear and pressurized components (2007).
8. T.Jensen, T.Aljundi, J.N.Gray, and R.Wallingford, “A model of X-ray film response”, in Review of progress in Quantitative Nondestructive Evaluation, edited by D. O. Thompson and D. E. Chimenti, AIP Conference Proceedings, American Institute of Physics, Melville, NY Vol 15, pp441-448(1996).
9. A. Schumm, U. Zscherpel, “Radiographic film modeling according to EN584”, in *COFREND 2008*
10. EN 444:1994, “Non-destructive testing — General principles for Radiographic examination of metallic materials by X- and gamma-rays”, European standard for non-destructive evaluation
11. RCC-M:2007, “Regulatory requirements and design code”, AFCEN publication
12. NF EN 13068-1:2000, “Radioscopic testing - Part 1 : quantitative measurement of imaging properties.”, European standard for non-destructive testing
13. ISO 17636, “Non-destructive testing of welds. Radiographic testing. X- and gamma-ray techniques with film” ISO standard, 2013.
14. W.S Rasband, ImageJ, U. S. National Institutes of Health, Bethesda, Maryland, USA, http://imagej.nih.gov/ij/, 1997-2014.
15. J. Plagnard, “Comparison of measured and calculated spectra emitted by the X-ray tube used at the Gustave Roussy radiobiological service”, X-ray spectrometry,volume 43, pp 298–304, 2014.

Simulation based design of Eddy Current sensor for thickness change measurement of Multi-layer

Seul-Gi Lee[1], Hak-Joon Kim[1], Sung-Jin Song[1] and Chang-Sung Seok[2]

[1, 2] Department of Mechanical Eng., Sungkyunkwan University, 300 Chunchon-dong, Changan-gu, Suwon, Kyunggi-do 440-746, Korea

Corresponding Author Sung-Jin Song / E-mail: sjsong@skku.edu, TEL: +82-31-290-7451, FAX: +82-31-290-5276

Abstract

In case of gas turbine engine, it usually works on extreme environment like ultra-high temperature and pressure. So, multi-layer spray coating method is applied in order to prevent failure of turbine components such as turbine blade. This micro failure could be propagated in multi-layer coating and finally these micro cracks changed into possibility of delamination. Thus, it is important to detect the micro failure crack before turns into the delamination. To detect these, NDE methods like Ultrasonic Testing (UT) and Eddy Current Testing (ECT) can be applied. But, UT can detect delamination but is hard to detect micro failure of surface because top coat of multi-layer coating is ceramic. Therefore, it is recommended that ECT is more effective to evaluate inside failure because ECT is useful to detect the micro failure of surface and delamination. In order to inspection of damaged multi-layer coating, magnetic shield eddy current probe to measure thickness of damaged layer are used since it shows focusing magnetic flux density on the coats. We have investigate relation between Eddy current signal (impedance, phase angle) and thickness of damaged layer using FEM simulation and by experiments results. In this presentation, we will discussed designed eddy current sensor and analytical and experimental results.

Keywords : multi-layer coating, micro failure, eddy current testing, FEM simulation

1. Introduction

Gas turbine power generation occupied approximately 30% of domestic power plant has increased steadily because it's useful to energy efficiency ratio, environmental affinity and power load control since 1990s[1]. So, to satisfy its performance and service life of key components under extreme environment, it is important to overcome its limitations of heat resistance, corrosion resistant anti-oxidation. There are some methods to solve this problem, TBC (Thermal Barrier Coating) technic attracts attention because TBC technic can get large effect with relatively low investment [2, 3].

TBC is composed by top coat and bond coat so those protect the substrate from environment of high temperature. TBC can be failure by repetitive thermal stress during operating gas turbine [4]. Failure of turbine Blade is generated from damage of TBC such as top coat delamination and difference of coefficient thermal conductivity therefore it's important to diagnosis the damage and predict remaining service life before generating safety problem. When between top coat and bond coat is exposed at high temperature, TGO (Thermally Grown Oxide) can be grown in two layers. Thermal stress is one of main reason of top coat delamination and changed because of TGO growth so this effects TBC durability [5]. In this study, used structure of TBC specimen and problems of each layer are shown in Fig. 1.

To detect this, non-destructive evaluation methods like Ultrasonic Testing (UT), Thermography, Impedance Spectroscopy, Eddy Current Testing (ECT) and Pulsed Eddy Current Testing (PECT) can be applied each suitable layer. When measuring TGO layer, ECT is used, existing research was applied coil with air core. Experiment results were not that clear and stable at each degradation hour of TBC specimen [6]. In this research, therefore ferrite core and magnetic shield are used to focus magnetic flux density into TBC specimen. Eddy current signal (impedance, phase angle) and thickness of damaged layer are investigated using FEM simulation and by experiments results. Finally, decided designed eddy current sensor through discussion of the results of both FEM simulation and experiments.

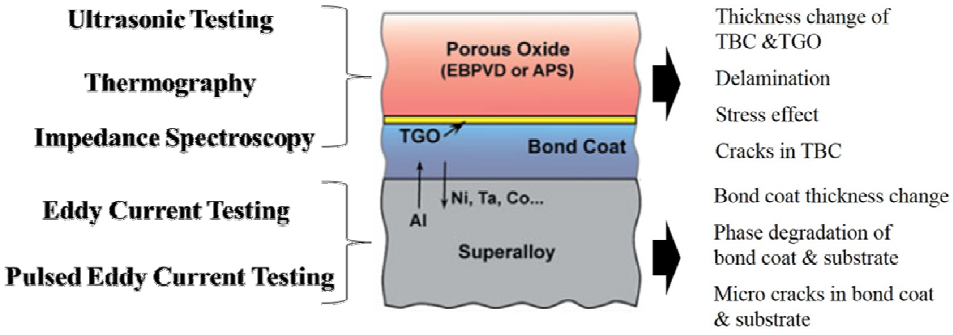

Figure 1. Structure and problems of TBC with suitable NDE methods[7]

2. Used TBC Specimens

There are two kinds of main TBC coating system, APS and EDC. Both coating system are shown as Fig. 2 (a), (b). APS has bulking when it is degraded but EDC shows less bulking and residual stress because of inserted vertical cracks even though EDC has thicker TGO layer. In this study, so we used EDC specimen. Micro-structure analysis results of used TBC specimens are shown as Table 1. TBC specimen was degraded at each temperature and degradation hours. Specific point is top coat was totally delaminated at 1100℃ both 200 hours and 400 hours. From those micro-structure analysis results, TGO thickness was adopted to the simulation.

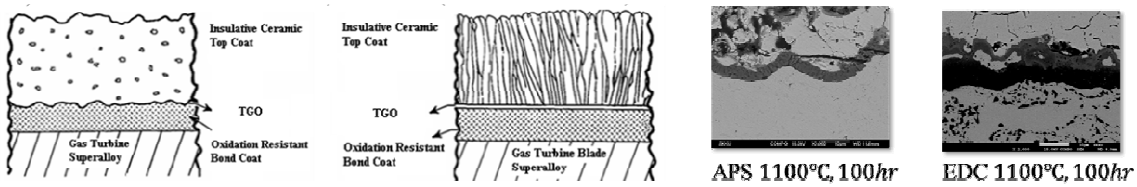

(a) APS (b) EDC (c) Micro-structure analysis of TBC specimen

Figure 2. (a), (b) Structure of APS & EDC[8], (c) Micro-structure analysis of APS & EDC

	25hr	50hr	100hr	200hr	400hr
900°C		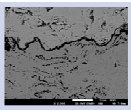	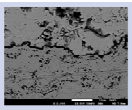	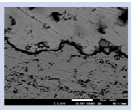	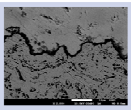
		1.70μm	1.84μm	1.87μm	2.22μm
1000°C		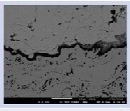	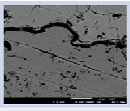	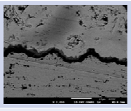	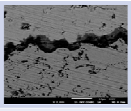
		2.58μm	3.30μm	3.55μm	4.69μm
1100°C	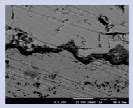	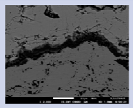	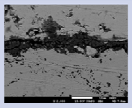	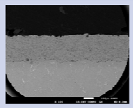	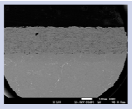
	4.01μm	6.53μm	8.14μm	10μm (delamination)	15μm (delamination)

Table 1. Micro-structure analysis results

3. Simulation of ECT

3.1 Simulation setup of ECT

Used simulation commercial program is COMSOL Multiphysics 4.4. Two kinds of simulation setup are about ECT probe for ‘with magnetic shield’ and ‘without (W/O) magnetic shield’. Ferrite core was used both setup and probe is placed

in the center of TBC specimen. Those are shown in Fig. 3 and minimum lift off was 0.5mm. Thickness of TGO layer is applied differently according to each degradation hour and temperature as shown in Table. 1. Operating Frequency range is 0Hz to 15MHz and coil impedance was measured in air for reference value.

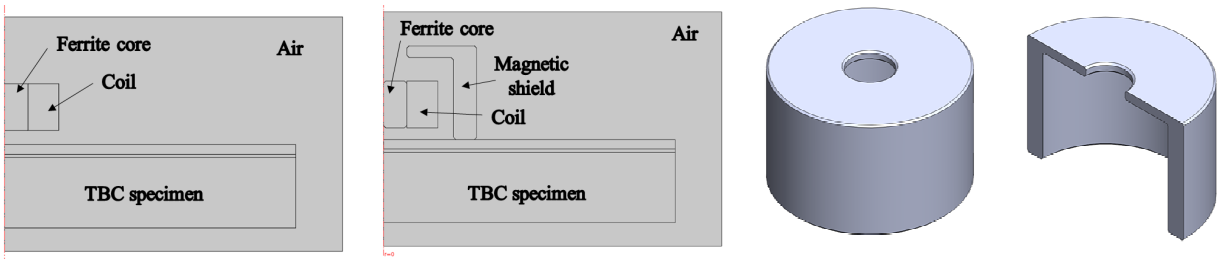

(a) APS (b) EDC (c) Micro-structure analysis of TBC specimen

Figure 2. (a),(b) Structure of APS & EDC, (c) Micro-structure analysis of APS & EDC

3.2 Simulation results

Obtained simulation results are coil resistance and reactance for coil impedance finally. The coil impedance of lift-off change can be adopted to measure the bond coat thickness, because the electrical properties of the top coat are same as those of air. The design lift-of the coil is constant, so the coil impedance of lift-off change can be adopted to measure the bond coat thickness. Normalized each part of coil impedance change and the results show at 9.3MHz were changed bigger when increasing degradation hour of TBC system. Simulation results of W/O magnetic shield are as shown in figure 3. In these results, both were changed bigger when degradation hour of TBC system is increased. 1100℃ shows the biggest change than other two temperature. In Figure 3. (a), resistance changes almost 0.3 and in Figure 3. (b), reactance changes as 2.5. Simulation results of with magnetic shield are also as shown in Figure 4. Both resistance and reactance change have similar trend with W/O magnetic shield. Therefore 1100℃ shows the biggest change, therefore resistance as shown in Fig 4. (a), changes approximately 0.4 and reactance as shown in Figure 4. (b), changes as 3.1.

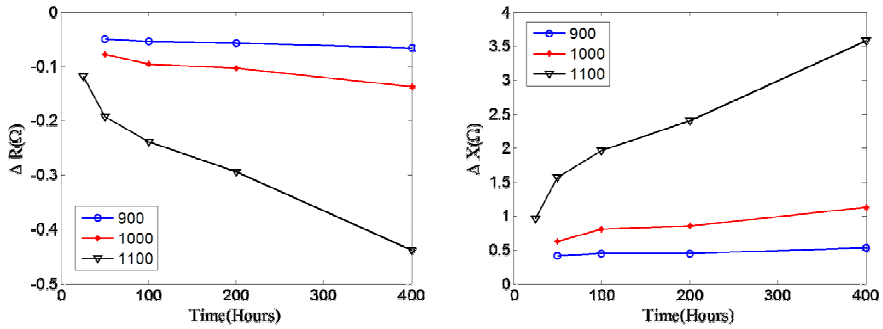

(a) resistance change (b) reactance change

Figure 3. Simulation results of W/O magnetic shield

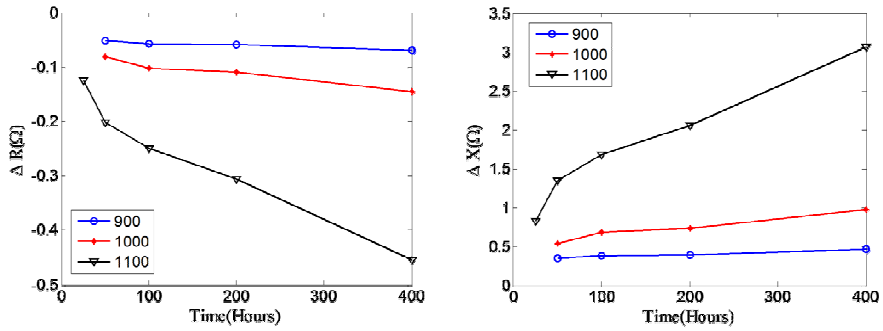

(a) resistance change (b) reactance change

Figure 4. Simulation results of with magnetic shield

So from those results, comparison of simulation result of W/O magnetic shield and with magnetic shield is as follow Figure 5. As shown in magnetic flux density, magnetic flux density can be compared with 'W/O magnetic shield' and 'with magnetic shield'. Magnetic flux density does not spread out more around because of magnetic shield. So magnetic flux density can be more focused to multi-layer and penetrated more deeply. By comparison with impedance change, with magnetic shield shows slightly bigger than which is not.

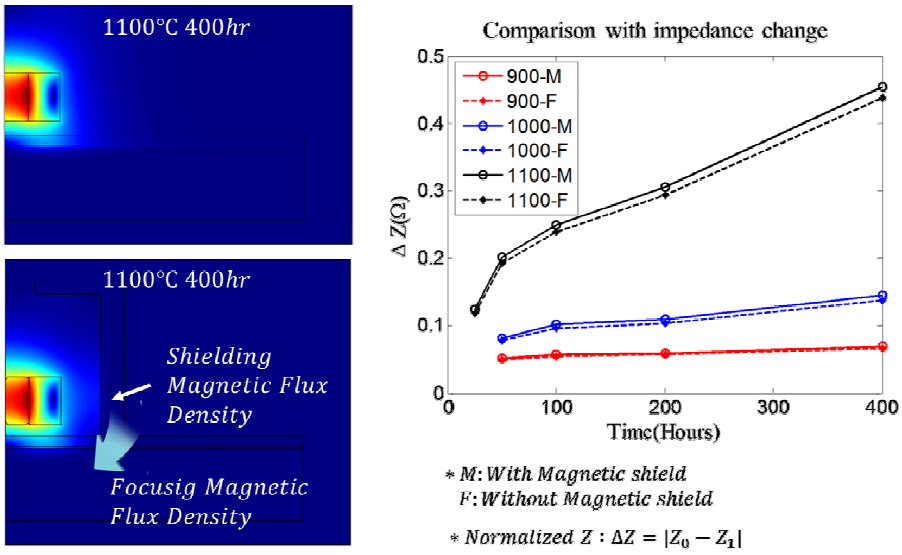

(a) Magnetic flux density (T) (b) Comparison with impedance change

Figure 5. Comparison with simulation results

4. Experiments of ECT

4.1 Experimental setup of ECT

Eddy current testing system for bond coat thickness measurement is as shown in Figure 6. Impedance analyzer is used for measuring impedance of eddy current probe. It can be used for finding resonance frequency of ECT probe and applied the frequency under resonance frequency when measuring the impedance. For the experiments, coil size and magnetic shield case size are same with simulation geometry size. Probe is placed in the center of TBC specimens as simulation did. Thickness of magnetic shield case is designed as same as simulation results and this is enough to shield magnetic flux.

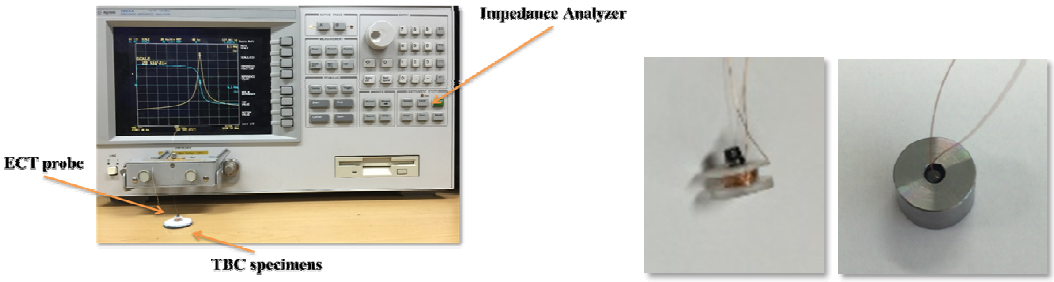

(a) Experimental setup of eddy current testing (b) Probe W/O magnetic shield (left), Probe with magnetic shield (right)

Figure 6. Experimental setup and used two types of ECT probe

4.2 Experiments results of ECT

Using impedance analyzer, coil impedance can get directly. When operating frequency is 9.3MHz, 'W/O magnetic

shield' and 'with magnetic shield' are also conducted 900℃, 1000℃, and 1100℃ degraded TBC specimens for every degradation hours. When compared at each degradation temperature and hours for W/O magnetic shield as shown in Figure. 7 (a), difference of impedance change at 1100℃ shows much bigger than others. Results of 900℃ and 1000℃ are not stable and show steady trend. As shown in Figure. 7 (b), difference of impedance changes steadily at each temperature and its value is getting bigger according to thermal degradation hours. This result is more easy to assort degradation temperature and hours relatively.

5. Summary

1) By simulation results, resistance and reactance of coil parameter change the difference of each degradation temperature and hours. When degradation temperature and hours are getting higher, each impedance change is also higher. So 'with magnetic shield' shows slightly higher than 'W/O magnetic shield'.

2) By experiment results, impedance change is getting bigger as simulation results did. From both simulation and experiment results, comparison of impedance change when magnetic shield case is applied or not.

3) Impedance change has been much bigger when TBC thermal degradation temperature is at 1100℃ and hours are higher.

4) Simulation and experiment results both show same trend when 'with magnetic shield' has been changed bigger than 'W/O magnetic shield'.

Acknowledgements

This paper was supported by Basic Science Research Program through the National Research Foundation of Korea (NRF) funded by the Ministry of Science, ICT & Future Planning (No. 2011-002024).

References

[1] Moon Young Kim et al., "Analysis of Damage Trend for Gas Turbine 1st Bucket Related to the Change of Models", Korean Soc. Mech. Eng. A, Vol. 31, No. 6, pp. 718~724 (2007)
[2] H. I. Kim et al., "Study on the Integrity Recovery according to Manual Overlay and Pre- & Post- welding Treatment of Nickel-based Superalloy for Gas Turbine Blade", Korean Soc. Precis. Eng., Vol. 26, No. 3, pp. 11~18 (2009)
[3] D. J. Kim, "Thermal Fatigue Test Methods for Thermal Barrier Coatings of Gas Turbine Blade", Korean Soc. Precis. Eng., Vol. 26, No. 2, pp. 7~15 (2009)
[4] Quadakkers, W.J., Shemet, V., Sebold, D., Anton, R., Wessel, E. and Singhesier, L., "Oxidation Characteristics of a plainized MCrAlY Bond Coat for TBC Systems During Cyclic Oxidation at 1000", Surface & Coatings Technology, Vol. 199, pp. **77**~82 (2005)
[5] Hyun Woo Song, Byung Woo Moon, Jae Gu Choi, Won Suk Choi, Dongju Song, Jae-Mean Koo and Chang-Sung Seok, "Durability Evaluation of Thermal Barrier Coating (TBC) According to Growth of Thermally Grown Oxide (TGO)", Korean Soc. Mech. Eng. A, Vol. 38, No. 12, pp. 1431~1434 (2014)
[6] Zhang Jianhai, "Electrical impedance based nondestructive evaluation of thermal barrier coating system", Thesis(PH.D.), Sungkwunkwan university : Department of Mechanical Eng., (2015)
[7] David R. Clarke, Matthias Oechsner and Nitin P. padture, "Thermal-barrier coatings for more efficient gas-turbine engines", MRS Bulletin, Cambridge univ., Vol. 37, (2012)
[8] Abdullah Cahit Karaoglanli, Kazuhiro Ogawa, Ahmet Turk and Ismail Ozdemir, "Thermal Shock and Cycling Behavior of Thermal Barrier Coatings (TBCs) Used in Gas Turbines", Ernesto Benini, ISBN 978-953-51-1166-5 (2013)

Technical Support Developing Performance Demonstration Programs in Japan

P. Ashwin, C. Latiolais, L. Esp, R.Grizzi, J. Langevin

Electric Power Research Institute (EPRI), Charlotte NC, USA

E-mail address: pashwin@epri.com

Following the discovery of intergranular stress corrosion cracks (IGSCC) in the 316L low-carbon stainless steel primary loop recirculation piping of a Japanese boiling water reactor (BWR), it was determined the ultrasonic technique to measure the through-wall depth of these cracks was unreliable.

The Japanese utilities responded and set about improving the reliability of the ultrasonic depth sizing techniques used for IGSCC. A key element was the development of their own performance demonstration (PD) program for depth sizing of IGSCC. By 2005, the 10 Japanese utilities with operating nuclear plants had joined EPRI's Nondestructive Evaluation (NDE) Program and had begun meeting with EPRI and other stakeholders to develop the Japanese Performance Demonstration (JPD) program. The first JPD qualification examination was carried out during 2006. Since then there have been many qualifications and the ultrasonic techniques now used in Japan to measure the through-wall depth of IGSCC have been demonstrated to meet the acceptance criteria.

Building on the success of the IGSCC depth sizing PD program, the Japanese utilities have set about introducing performance demonstration requirements for additional applications into National codes and standards. These applications include weld overlay and dissimilar metal weld examinations. The EPRI NDE Program continues to work closely with the Japanese team responsible for these actions and this paper will summarize the technical support provided by EPRI, this includes:

- Benchmarking Japanese PD requirements against U.S. requirements
- Participating in two pilot studies to improve the understanding of information readily available for typical dissimilar metal weld configurations in BWR and pressurized water reactor (PWR) plants
- Jointly developing a technical basis to use alternative flaw types for PD
- Fabricating additional test specimens to address differences in Japan and U.S. configurations
- Aligning Japanese PD instructions and U.S. instructions

Moving forward, the Japanese Utilities are now evaluating various technologies to support performance demonstration. Again EPRI are working closely with the Japanese utilities and other stakeholders. This joint research work includes developing training programs for NDE technicians and introducing the use of simulation technology to training, maintaining NDE technician proficiency and qualification.

Keywords: Performance Demonstration; Reliability; Qualification; Ultrasonic

The Progressive Statistical Analysis Results of Performance Demonstration for Piping Welds

Hung-Fa Shyu
Institute of Nuclear Energy Research, 1000 Wenhua Rd., Longtan, Taoyuan City, Taiwan ROC

E-mail Address: hfshyu@iner.gov.tw

A performance demonstration program has been implemented by the Institute of Nuclear Energy Research since 2002. This program followed the criteria of ASME Boiler and Pressure Vessel Code Section XI, Appendix VIII to prepare demonstration sessions in Taiwan and gained meaningful data during the past twelve years. In this paper, historical demonstration results on the similar metal pipe welds were analyzed and the statistical data showed the overall qualification rate, accuracy rate, and detection rate were about 59%, 93%, and 92% respectively. The length sizing errors depended on the piping material and flaw orientation, and the average relative error of qualified examinees was 59.1%±4.3%. This program can provide a good screening function for ultrasonic inspection personnel, and the statistical results can also provide both regulatory authorities and utilities with a conservative evaluation of the confidence level of realistic ultrasonic testing results in nuclear power plants.

Keywords: Performance Demonstration, Ultrasonic Testing, Piping Welds

Current Status of Japanese Performance Demonstration in FY 2014

Keiji WATANABE[1], Hajime SHOHJI[1], Koichiro HIDE[1], and Joji OHTA[1]

[1]PD center, Central Research Institute of Electric Power Industry, Japan

Abstract

The Performance Demonstration (PD) Center of the Central Research Institute of the Electric Power Industry (CRIEPI) commenced PD examinations for the depth sizing of intergranular stress corrosion cracking (IGSCC) in austenitic stainless steel pipes in March 2006. By the end of the 2014 fiscal year, 42 examination sessions had been completed, and 53 candidates had passed the examination. A total of 99 candidates had been administered exams, including re-tests and re-certification. Candidates who passed the examination can perform depth sizing of IGSCC flaws with a high level of accuracy. For the final determination of IGSCC crack depths in Japanese PD examinations, phased-array ultrasonic testing technology is used more often than conventional ultrasonic testing or other technologies. A statistical analysis shows that the average depth sizing error is 0.32 mm with a standard deviation of 1.87 mm for the successful applicant. From the PD examination results, the correct answer rate will decrease when the ultrasonic testing time concerning a test answer requires 2.5 hours or more.

Keywords: PD qualification examination, Ultrasonic testing, Nuclear power plant, Inservice inspection, PLR piping, Intergranular stress corrosion cracking

1. Introduction

The Japan Society of Mechanical Engineers (JSME) issued the first edition of a fitness-for-service code (FFS code) for nuclear power plants in 2000 [1]. The FFS code was endorsed by the Nuclear and Industrial Safety Agency (NISA) and has been in effect since October 2003 [1]. The Japanese performance demonstration (PD) standard, NDIS 0603, "Qualification and certification of personnel for performance demonstration of ultrasonic testing systems," was issued in 2005 [2]. The NDIS 0603 standard is essentially the same as Appendix VIII and Section XI of the American Society of Mechanical Engineers (ASME) Code, having the same fundamental content with some modifications reflecting Japanese technical expertise on IGSCC in austenitic stainless steel welds. The first Japanese PD qualification examination for the depth sizing of IGSCC flaws was administered in March 2006 [3], and as of January, 2015, 42 examinations have been conducted. In December 2010, the first PD recertification candidate took an examination. As of the end of the 2014 fiscal year (FY), 53 out of a total of 99 candidates passed the examination.

2. PD Certification System in Japan

2.1 Operating organization

Figure 1 shows the organizations involved in the Japanese PD qualification examination for crack depth sizing in austenitic stainless steel pipe welds in nuclear power plants [5]. The PD advisory committee oversees the PD qualification system. The PD advisory committee reviews the activities of the PD-related organizations (PD qualification activities, PD examination center, and PD training center) and makes recommendations. The Japanese Society for Non-destructive Inspection (JSNDI) certifies PD-related organizations. The PD qualification body of JSNDI consists of two committees: a PD certification committee to manage the PD certification system and a PD scheme committee to design future PD systems. The PD qualification body organizes the qualification examinations, preparing and maintaining the test specimens, test facility, and quality control documents. The PD examination center conducts PD qualification examinations under the direction of the PD qualification body. In particular, the PD Center of CRIEPI serves as both the authorized PD qualification body and the PD examination center. Finally, the PD training center serves two functions in the PD system: (1) the training of personnel who fail their first PD examination and desire to take a re-examination within 30 days and (2) annual training for license renewal. Both the Japan Power

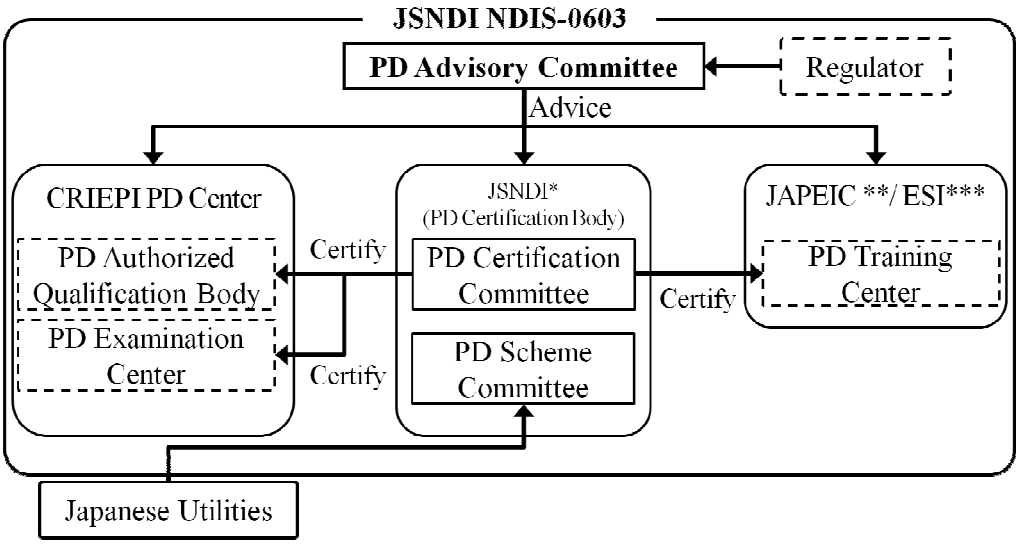

JSNDI: The Japanese Society for Non-Destructive Inspection
JAPEIC: JAPAN Power Engineering and Inspection Corporation ESI: Electron Science Institute

Engineering and Inspection Corporation (JAPEIC) and the Electron Science Institute (ESI) have been qualified as PD training centers.

2.2 Outline of qualification examination

Although the Japanese PD standard NDIS 0603 is similar to the ASME Code Section XI and Appendix VIII, some adaptations have been incorporated to reflect our findings on IGSCC in austenitic stainless steel welds [4]. The following adaptations have been incorporated:

(1) All cracks in the test sample should be IGSCC.
(2) At least one IGSCC should be deeper than 15 mm.
(3) At least one IGSCC should penetrate into the weld material.
(4) No undervalue of more than -4.4 mm should be permitted

The Japanese PD qualification test specimens are butt-welded austenitic stainless steel pipes with artificially introduced IGSCC. The weld crowns are ground flush. Ten IGSCC must be tested in pipes of the following three sizes:

- Nominal diameter of 600 mm with 35 mm wall thickness.
- Nominal diameter of 350 mm with 25 mm wall thickness.
- Nominal diameter of 150 mm with 10 mm wall thickness.

The distribution of the IGSCC crack depth introduced into the Japanese PD qualification test specimens is given in Table 1.

Table 1. Distribution of crack depth

Crack depth h (% wall thickness)	Minimum number of IGSCC (Test specimen)
$0 < h \leq 30\%$	2
$30 < h \leq 60\%$	2
$60 < h < 100\%$	2

For each candidate, the allowable examination time is five days for 10 samples with up to 8 h per specimen. One test specimen is examined at a time, and the examinee is not permitted to carryover a specimen to the following day. The acceptance criteria are as given follows:

A) Root-mean-square error (RMSE) must be less than 3.2 mm.
B) Critical mistake must be less than -4.4 mm.

The RMSE is derived from the following formula:

$$\text{RMSE} = \left[\frac{\sum_{i=1}^{n}(m_i - t_i)^2}{n}\right]^{\frac{1}{2}}$$

where m_i is the measured IGSCC depth, t_i is the true IGSCC depth, and n is the number of test specimens.

The PD certification is valid for one year and can be extended for up to five years if the qualified personnel receive PD training at a PD training center.

3. PD Qualification Examination Results

The first PD qualification examination was conducted in March 2006. Over the next nine years, 53 candidates applied for the examination, and 49 candidates were qualified. The total number of examinees during that nine-year period, including those who took the recertification test, was 99. Figure 2 shows the change in the number of candidates as well as the successful applicants from March 2006 to the end of FY 2014. The number of candidates in each period has decreased gradually over the past eight years. However, looking at the results from a different point of view, the required number of qualified personnel to support the Japanese nuclear industry was almost satisfied within the first three years of the PD qualification examination process. After this period, the number of candidates performing the qualification examination during each period stabilized as candidates was primarily performing the examinations to support future activities within their organizations. Since then, the number of candidates in each period has been stable. The PD-qualified persons took the examination considering their futures in their organizations. Although the pass rate has fluctuated, the overall pass rate has gradually improved. Information obtained though

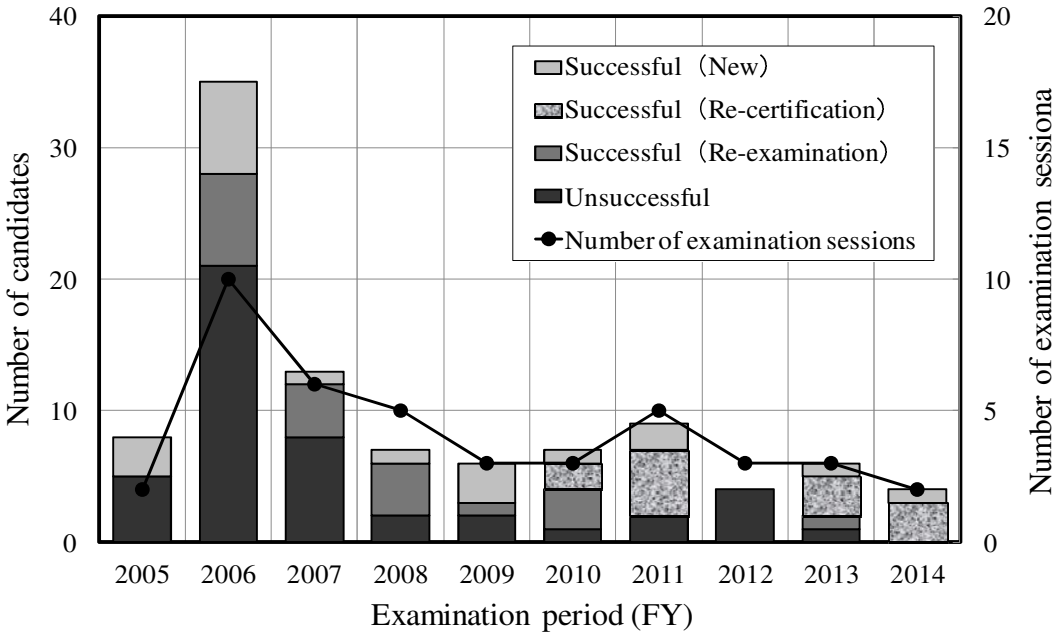

Figure 2 Number of candidates and successful applicants per year

candidate interviews suggests that this improvement is the result of education and training at independent companies.

3.1 Variation in Candidate Performance

Table 2 Statistical analysis of PD result candidates

Candidate group	Mean Error (mm)	Standard Deviation (mm)
Successful	0.32	1.87
Unsuccessful	1.02	4.84

To clarify the depth sizing reliability, the PD Center conducted a statistical analysis of all accumulated test data. Table 2 shows the statistical results of the IGSCC depth sizing errors. The mean error and standard deviation for successful candidates were 0.32 mm and 1.87 mm, respectively, whereas the mean error and standard deviation for

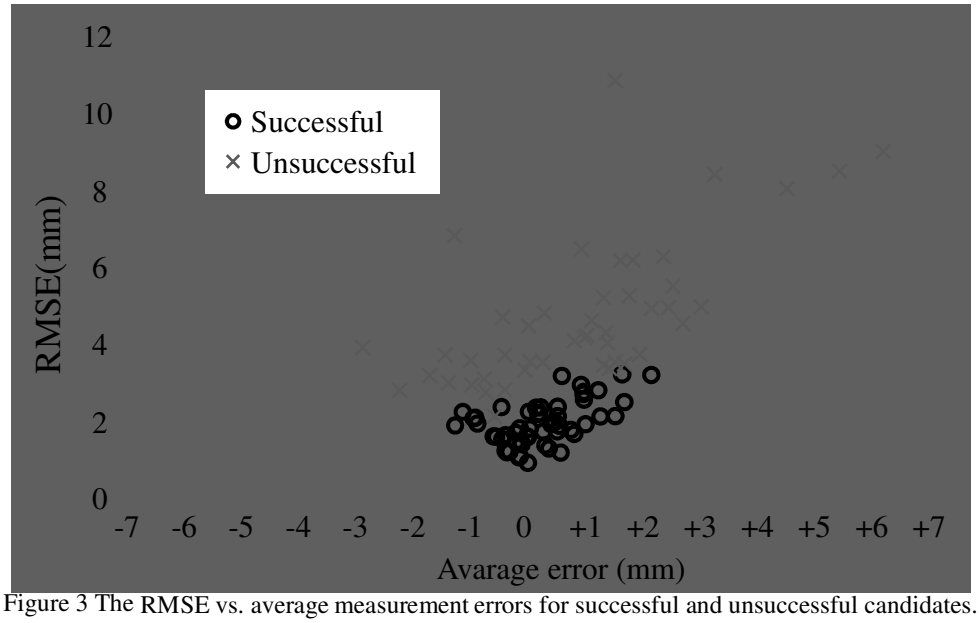

Figure 3 The RMSE vs. average measurement errors for successful and unsuccessful candidates.

unsuccessful candidates were 1.02 mm and 4.84 mm, respectively.

Figure 3 shows the relationship between the RMSE and the average measurement errors of the successful and unsuccessful candidates. The majority of successful candidates performed IGSCC depth measurements with average errors of 1 mm or less. This shows that depth sizing of IGSCC flaws can be performed with a high level of accuracy.

Figure 4 shows the change in the standard deviation and average error for candidates who successfully passed the PD certification examination. The mean error lies below 1 mm, while the standard deviation fluctuates between 1.5 to 2 mm. Thus, the candidates who pass the Japanese PD certification examination have the skill to determine crack depth sizing with high accuracy.

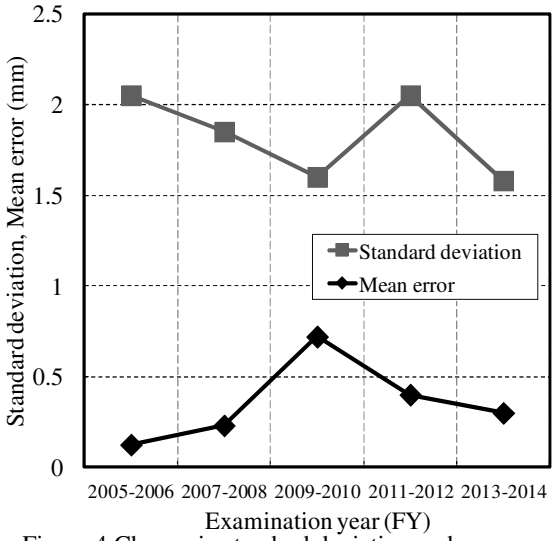

Figure 4 Change in standard deviation and mean error for the PD certification examination

3.2 Sizing Procedure

Figure 5 shows the number of candidates utilizing various crack depth sizing procedures in PD qualification examinations. In the figure, “PA” refers to a phased-array examination using either linear or matrix phased-array transducers with encoded or automated scanning systems. As shown in Figure 5, the combination of PA with conventional ultrasonic testing (UT) (“PA + conventional UT”) is the most successful procedure. The number of PD candidates using only “PA” is almost the same as those using only “Conventional UT”; however, the number of successful candidates using PA is higher than those using conventional UT.

Figure 6 shows the number of measurements for various crack depth sizing procedures used in PD

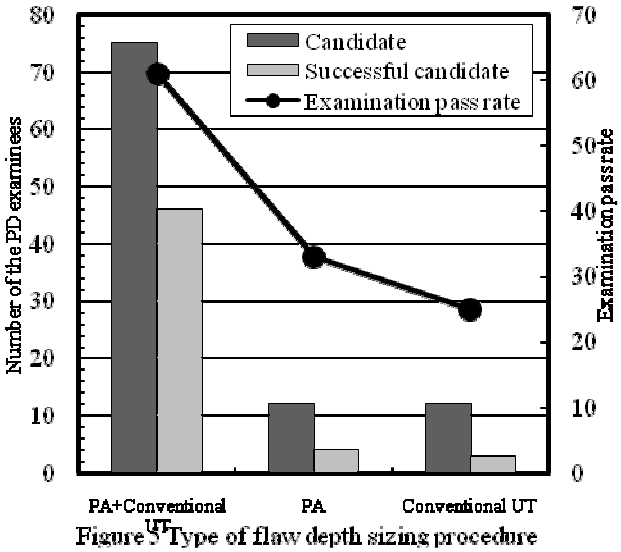

Figure 5 Type of flaw depth sizing procedure

certification examinations. In this figure, “Others” refers to normal beam method and tandem probe technique. The results shown in Figure 6 indicate that more successful candidates use PA for the final specification of IGSCC depth than unsuccessful candidates. On the other hand, when conventional UT or other technologies are used for the final specification of a crack depth, there are more unsuccessful candidates than successful candidates.

Figure 7 shows the rate of the errors for various crack depth sizing procedures used in PD certification examinations. The error criterion adopted here is whether the difference between the true and measured value was less than ±3.2 mm. The results shown in Figure 4 indicate that the PA technique, which yielded the lowest error percentage, was the most successful technique. The error rate associated with the PA technology was slightly lower than that associated with the conventional UT technology and other technologies. The results suggest that the highest percentage of correct answers is associated with skillful utilization of the PA technology, and the second highest percentage is associated with the use of conventional UT technologies.

Figure 8 shows the relationship between the rate of errors and the average UT time for all candidates. When the inspection time for one test specimen is less than 2 hours, there are a high percentage of correct answers. In contrast, when the UT time for one test specimen exceeds 2.5 hours, the percentage of correct answers decreases. This trend suggests that longer UT times result in a higher percentage of errors, possibly due to hesitation by the examinee.

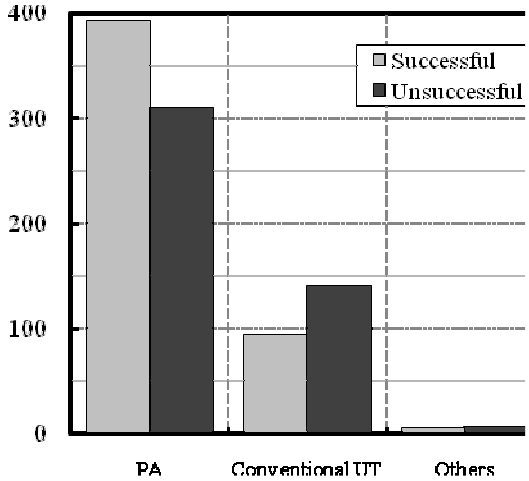

Figure 6 Final specific techniques for depth sizing of IGSCC

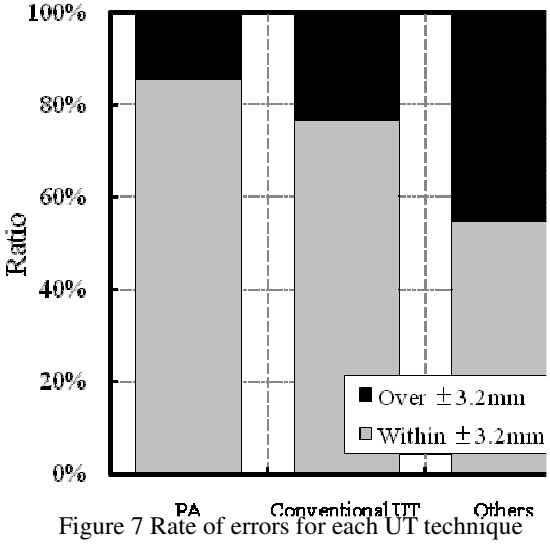

Figure 7 Rate of errors for each UT technique

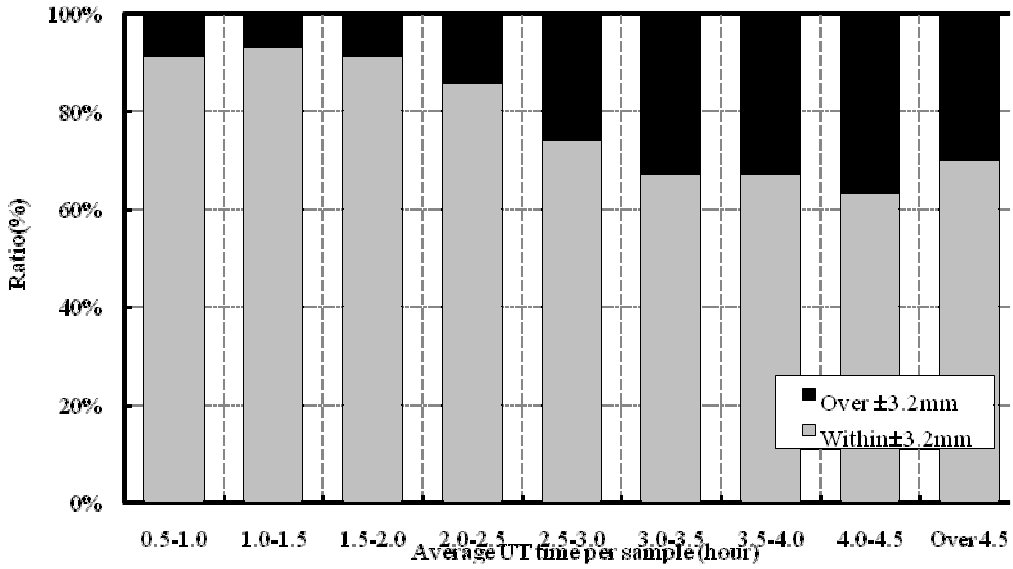

Figure 8 Relationship between the average UT time and the percentage of correct answers

3.3 Trends for PD Certification Examinees

Figure 9 shows the PD examination results (numbers of successful and unsuccessful candidates and pass rates) with respect to candidate age. Although many candidates were between 30–40 years of age, there was no substantial difference in the examination pass rates among the different age groups.

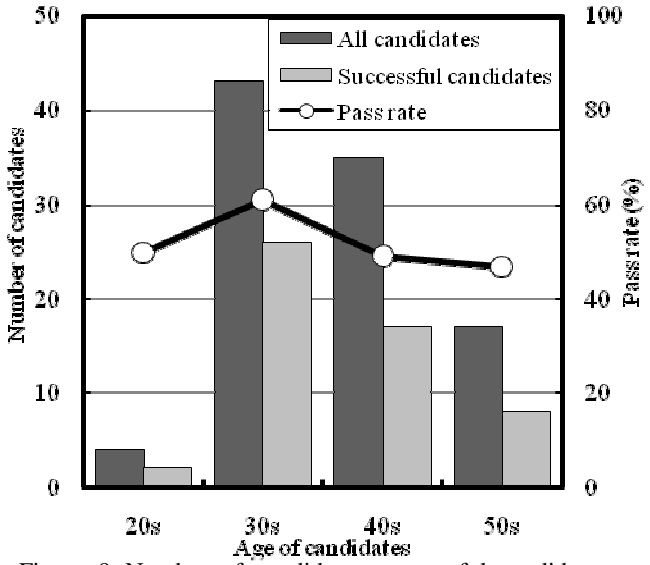

Figure 9 Number of candidates, successful candidates, and examination pass rate by age

4. Conclusion

The CRIEPI PD center has been conducting Japanese PD certification examinations since March 2006. The results of the Japanese PD examinations through FY 2014 can be summarized as follows:

1. Successful candidates for the Japanese PD certification examination have a high level of proficiency in measuring crack depth sizing.
2. Successful candidates are capable of skillfully applying phased-array technologies as well as the supplemental utilization of conventional UT or other technologies for identifying IGSCC.
3. Based on the RMSE, standard deviation, and mean error, the reason for the rejection of PD certification examinations should be identified to successfully clear the re-examination.
4. When the UT time for one test specimen exceeds 2.5 hours, the percentage of correct answers decreases, suggesting that longer UT times result in a higher percentage of errors.

References

[1] K. Kashima, T. Nomura, and K. Koyama, "Current status of Japanese Code on Fitness-for-Service for Nuclear Power Plants," Pressure Vessel and Piping Codes and Standards, PVP-Vol. 480 (2004).

[2] T. Sasahara, T. Yamashita, and T. Nomura, "UT Performance Demonstration in Japan," Fifth Int. Conf. on NDE in Relation to Structural Integrity for Nuclear and Pressurized Components (2006).

[3] H. Shohji, K. Hide, and K. Watanabe, "Trends Identified Between Successful and Unsuccessful Candidates that have Participated in the Japanese Stress Corrosion Cracking (SCC) Depth Sizing Performance Demonstration (PD) Program," E-Journal of Advanced Maintenance, Vol. 4, p. 125–132 (2013).

[4] T. Sasahara, T. Jikimoto, K. Hide, and H. Inoue, "Evaluation of SCC Depth Sizing Candidate and Performance," Maintenology, Vol. 9, No. 1, p. 44 (2010).

[5] H. Shohji, K. Hide, and K. Watanabe, "Current Status of Japanese Performance Demonstration in FY 2012," Proceedings of Twelfth International Conference on NDE in Relation to Structural Integrity for Nuclear and Pressurized Components, Cannes, p. 436–441 (2013)

Development of Virtual Ultrasonic Testing System

Hajime SHOHJI [1] and Koichiro HIDE [1]

[1] Central Research Institute of Electric Power Industry, JAPAN

Abstract

The reliability of inspection results is affected by the skill of examination personnel, in particular with regard to manual ultrasonic testing (UT). The number and design of test specimens are among the most important points to be considered during training or assessing the qualification of UT examination personnel. For training, a simulated UT system using a computer mouse or touch sensor was proposed. However, this system proved to be inadequate as a replacement for actual UT work. In this study, we have developed a novel virtual UT system that simulates actual UT work for piping welds.
This system (the Tool for Realistic UltraSound Testing) comprises a dummy UT probe, dummy piping, a computer system, and a 3D position detection system. It can detect the state of the dummy probe (3D position and skewing angle) and displays recorded A-scan data corresponding to the dummy probe status with random noise. Furthermore, it does not display A-scan data if the dummy probe is not in contact with the pipe. In this way, the system simulates actual UT work. Using this system, it is possible to significantly reduce the number of test specimens utilized for training or assessing the qualification of UT examination personnel. In addition, highly efficient training and certification will be achieved through this system.

Keywords: Ultrasonic, Virtual System, Training, Qualification, Simulator, Piping

1. Introduction

In Japan, ultrasonic testing (UT) for in-service inspection (ISI) has been performed by UT engineers with a great deal of experience. However, most Japanese nuclear power plants (NPP) have ceased operation, and periodic ISI is not performed regularly. Most UT engineers are now working in nonnuclear fields. Moreover, after the NPPs are restarted, most of these highly skilled UT engineers will not return to nuclear field. Conversely, performance demonstration systems such as PDI programs are currently only being applied to crack depth sizing and Weld Overlay (WOL) inspection, rather than crack detection in Japan. This is based on a national research project [1] that reports that good inspection results and reliability are achieved with general examination procedures and highly skilled UT engineers. In addition, Japanese inspection companies have been operating their own training programs. For these reasons, a highly efficient, highly effective training program is needed for high reliability UT examination.

However, this training program needs to use test specimens, which should be fabricated by the same process as used on parts of actual plants, and have realistic defects. But these realistic test specimens are very expensive and take much time to fabricate. Thus, one idea is to use virtual UT system as a part of training or PD examination.

In this study, we fabricate a prototype realistic virtual UT examination system (the Tool for Realistic UltraSound Testing) and confirm the viability of this system for training UT engineers.

2. Feasibility Study

In Japan, ISI-UT procedure is based on the standard JEAC4207 code[2]. This code is based on the previous ASME Code in terms of its use of DAC evaluation and conventional UT techniques. Japanese inspection companies use their own examination procedure, but these are based on JEAC4207 closely enough that there is no noticeable difference. The reliability of these procedures was confirmed through a national research project [1]. Therefore, the key to the reliability of examination results is the skill of the UT engineers involved.

UT examination for ISI is performed using automated scanning tools, especially for vessel inspection. However, some piping inspection is still performed manually, especially at old plants. In addition, IGSCC has been detected at piping welds. Therefore, the priority of training and/or PD testing for piping inspection for UT engineers is high. Thus, this virtual system is focused on manual inspection of piping welds.

Generally, commercially available UT simulation systems use a computer mouse as a dummy UT probe. This kind of

system is useful for determining wave characteristics. However, it is insufficient for training engineers totally for the inspection process. We extract the points simulating a realistic UT examination process as follows:

- ✓ Realistic shape, Piping shape
- ✓ The waveform should be displayed, and it should
  - depend on the absolute position of the dummy probe.
  - depend on the skew angle of the dummy probe
  - have a real-time response
  - be accompanied by random noise
- ✓ Record scanning tracks for feedback training

3. System Design

3.1 Waveform data

It is possible to calculate the ultrasonic waveform using an FEM code or lay trace calculation. However, its calculation time is generally too long for "real-time response" [3]. Conversely, human perception should be within a time lag no greater than 40–50 ms [4]. Therefore, this system uses data from pre-recorded or pre-calculated waveforms.

3.2 Position detection system

This system should detect the absolute position and skew angle of a dummy probe with a "real-time response." To simulate realistic flaw detection, the dummy probe should require no wires or special equipment having cables. We examined various position detection systems, including CCD cameras, pressure sensors, touch sensors, and lasers. Ultimately, a 3D electromagnetic position detection system was selected for this purpose. This 3D system can detect sensor position and angle with high accuracy, and the slave sensor is as small as a UT probe. However, this system cannot detect whether the dummy probe is in contact with the dummy pipe surface or not. Thus, a small pressure sensor needs to be added to this system.

3.3 System Design

Figure 1 shows the basic system design for the Virtual UT system. The master sensor of the 3D position system is set on the dummy pipe, and a UT engineer moves the dummy UT probe, which includes a slave sensor and a small pressure sensor. The 3D position system detects the position and skew angle of dummy probe, whereas its touching power is detected through the pressure sensor.

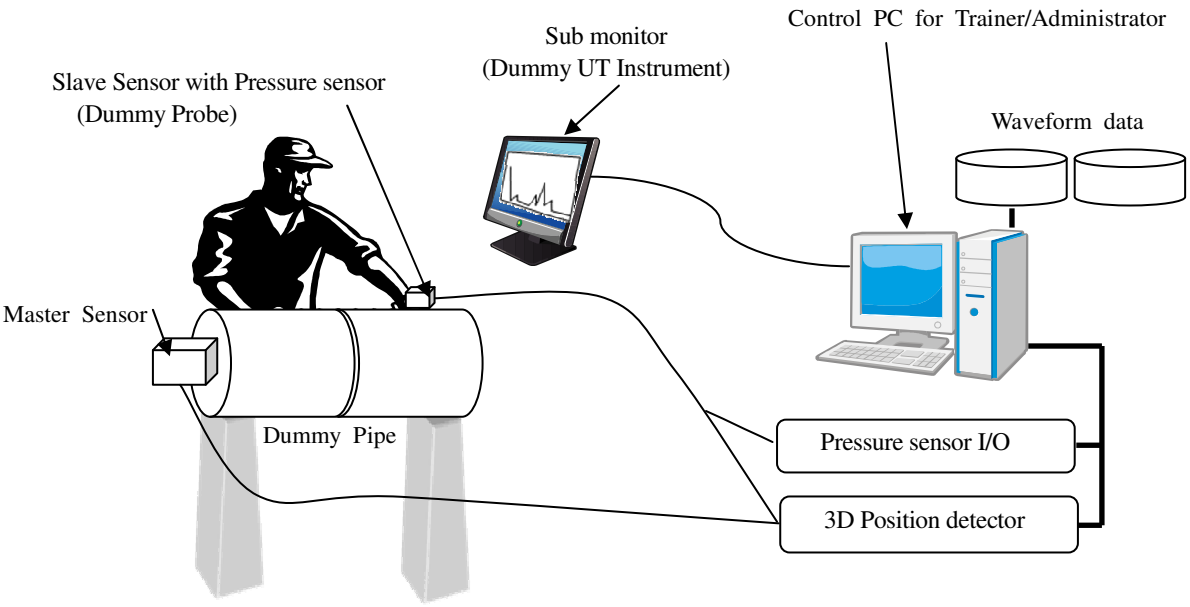

Figure 1 Virtual UT system

Pressure sensor output and dummy probe 3D position and skew angle are sent to a control PC via the USB port. When one starts up the software and loads the waveform data, they move to the cash memory of the PC. The control PC displays the waveform depending on the dummy probe position, angle, and contact with the dummy pipe. The same waveform is displayed on the sub monitor (Dummy UT instrument).

3.4 Waveform data

We collect UT data from small segmented test specimens (Figure 2). One segment includes a shallow IGSCC on the butt weld line and the other does not include IGSCC. We use an automated scanner and special probe holder. The special probe holder can be used to adjust control the skew angle of the conventional probe. We collect UT data from the upstream and downstream sides at various skewing angles. In this case, the skewing angle is set between −10° to +10° and 170° to 190° with 2° pitch.

We copy the data several times and merge these data, in the form: “"Blank data"+"Blank data"+"IGSCC data"+"Blank data"+"IGSCC data"+ *+*+*+. Then we generate waveform data for a whole pipe with data from several IGSCC-bearing specimens.

In addition, we calculate sample waveform data using an FEM code.

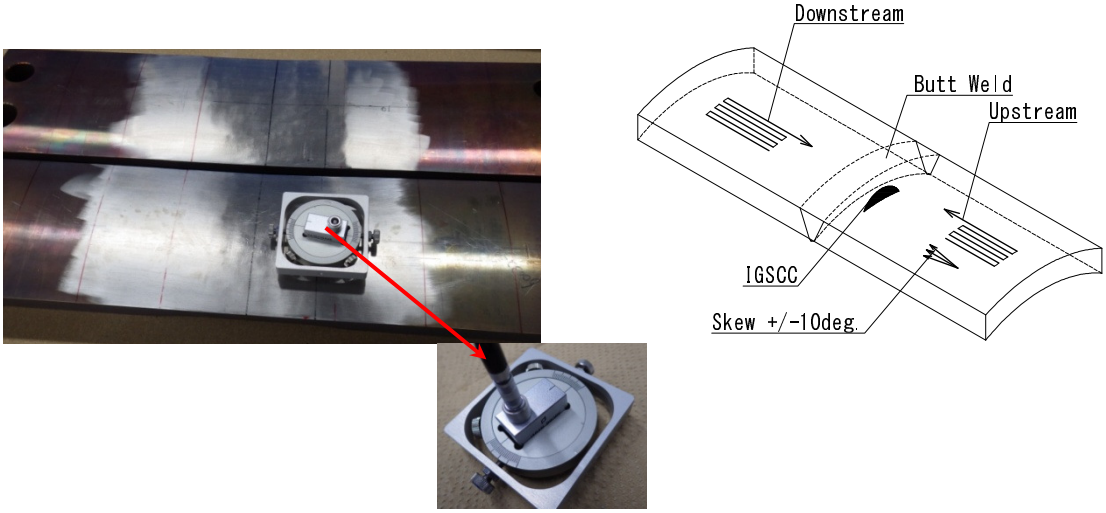

Figure 2 IGSCC specimens and special probe holder

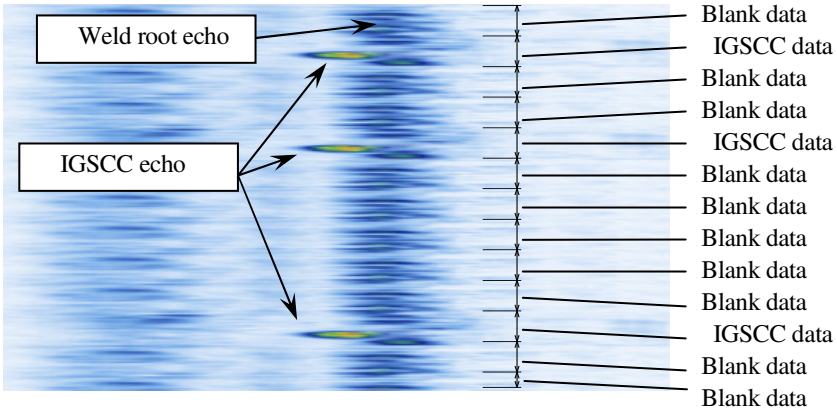

Figure 3. C-scan display of merged sample data

5. Prototype Model

5.1 Prototype Model

Figure 4 shows the prototype model of the Virtual UT system (Tool for Realistic UltraSound testing). The specifications of the prototype model are as follows:

- Waveform display function depending on the position and skew angle of the dummy probe without time lag
- Measurement of position and skew angle of the dummy probe within +/– 1 mm or +/– 2°.
- Functionality for detecting contact status; if no contact with the dummy pipe surface, do not display waveform
- Functionality for adding random noise to the displayed waveform
- Gain control of the displayed waveform (for both main control monitor and sub monitor with pressure sensor)
- Display DAC curve on the waveform display
- Accept 8-bit and 16-bit waveform data
- Maximum waveform data: approximately 7 GB (extending the memory is allowable if necessary)
- Functionality for creating a scanning log (record of scanning trajectory and skew angle)
- Piping diameter of 350 mm (9 in)

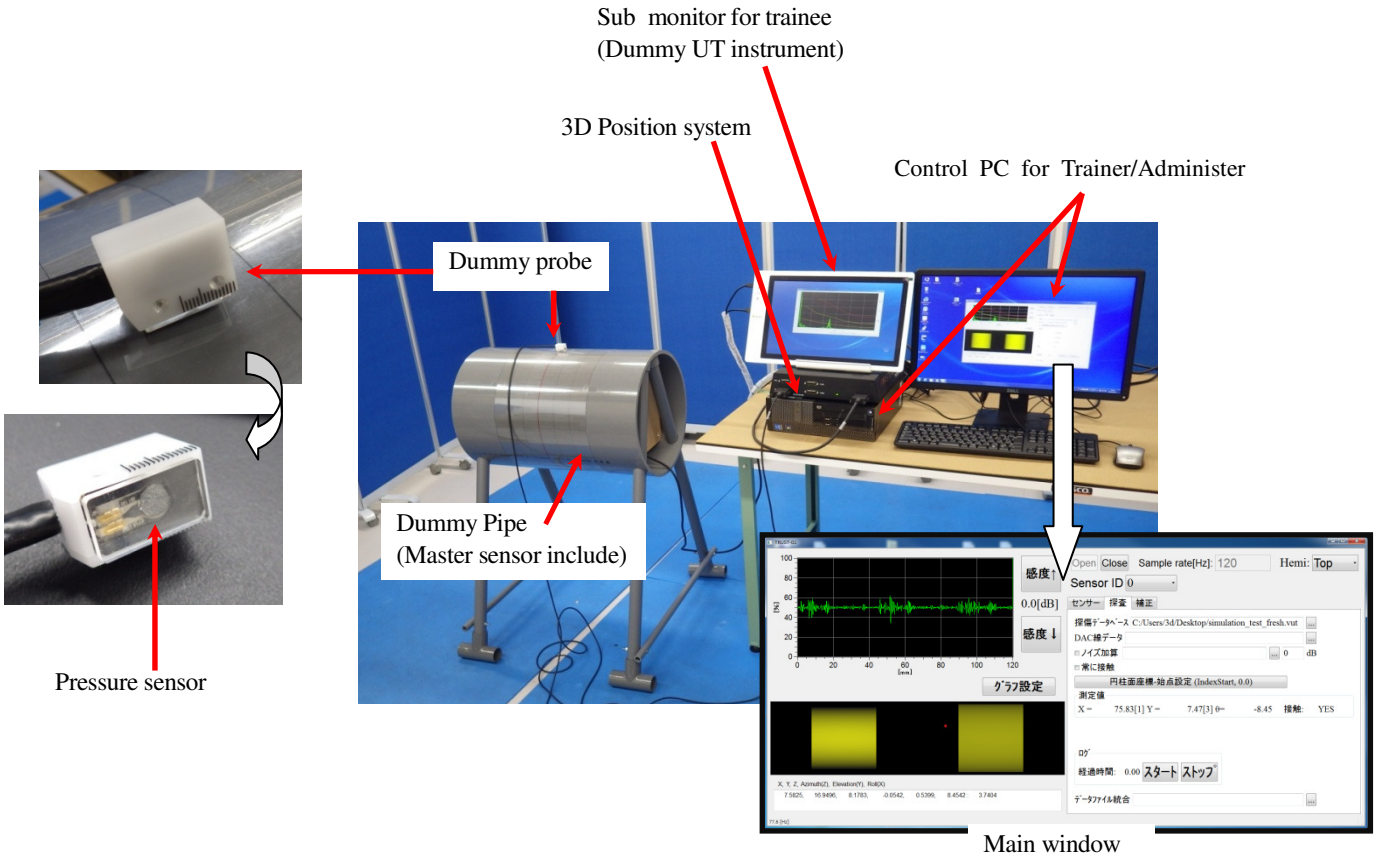

Figure 4. Virtual UT system prototype

5.2 Verification of the Prototype Model

We verify the virtual UT system and confirm that the prototype model has a sufficiently high performance. The system has the following properties:

- Positioning error: less than +/– 1 mm (with position calibration)
- Skew angle error: less than +/– 1.5°
- Can record a scanning log, as in Figure 5.
- Verification by UT engineers certified as level 2 or more (Figure 6)
  - +Cannot feel waveform display time lag
  - +Can perform in a manner similar to the actual work
  - +Same difficulties as in field UT examination

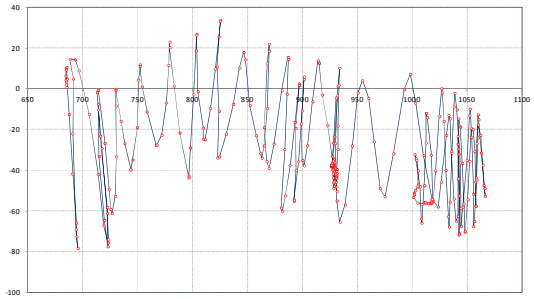

Figure 5 Sample of the scanning log result

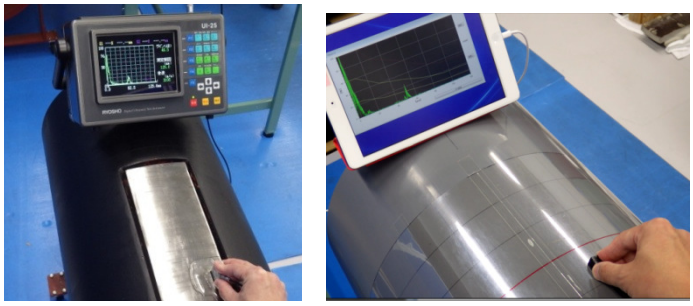

(a) UT work with specimen (b) UT work using virtual UT system

Figure 6 Virtual UT system prototype

6. Conclusion and Future plan

We have clarified the required functionality of the virtual UT system for training or qualification purposes. We have fabricated a prototype of the virtual UT system based on the required specifications. Its prototype was confirmed to have sufficiently high performance for use in actual inspection training.

We are now fabricating the first complete, commercial system based on this prototype, including large and small diameter piping, and we are still improving sample data. We plan to perform the training or qualification tests using this system to confirm the difference between actual and virtual training. In the future, the training program can be enhanced especially for rare defects and can reduce the number of actual specimens by replacing part of the training or qualification tests with this system.

Acknowledgment

The authors wish to thank to Japanese utilities for their assistance.

References

[1] Japan Nuclear Energy Safety Organization, “Report of on Development Standards and Guides for Formati on of Upgraded Inspection System on NPP (Ultrasonic Test & Evaluation for Maintenance Standards,” 20 05. (in Japanese)

[2] Japan Electric Association, “JEAC 4207 Ultrasonic examination for in-service inspection of light water cooled nuclear power plant components”, 2008. (in Japanese)

[3] S.Lin, H.Yamada, H.Fukutomi, T.Ogata, “Development of Simulation Tools for Improvement of Measurement Accuracy and Efficiency in Ultrasonic Testing Part 1: Development of Hybrid Approach for Accurate Simulation Based on the Combination of Analytic Solution and Finite Element Method,” CRIEPI report Q07004 (2007)

[4] S.Okamoto, M.Konyo, S.Saga, S.Tadokoro, “Identification of Cutaneous Detection Thresholds against Time-Delay and its Effects on Subjective Feelings,” proceedings of 13th Robotics Symposia, pp.153-158 (2008)

Austenitic Weld Inspection for Long-Term Fuel Storage Canisters

A Brockett[1], J M Dagen[2] and R Hague[3]
[1,2,3] Doosan Babcock Ltd, Renfrew, PA4 8DJ, Scotland

E-mail address (corresponding author): andrew.brockett@doosan.com

As part of the long term strategy to manage spent irradiated fuel from UK reactors, a dedicated facility has been constructed housing modular storage units. Central to these modules is a stainless steel canister, designed specifically to accommodate spent fuel for a period of up to 100 years. These canisters comprise a rolled shell and a forged lid which are welded to form closure of the canister.

Qualified inspection of the austenitic lid to shell weld is required. The inspection is performed immediately after the spent fuel has been seal welded into the canister.

Doosan Babcock has designed, and is in the process of qualifying, a unique, 3 probe phased-array inspection with a bespoke automated scanning system to meet the rigorous inspection requirements.

The project presents a number of technical challenges, for example, ENIQ qualification, highly reliable defect detection and characterization, remote operation, high temperature operation and variable surface condition.

This paper examines the technical challenges, and how they were overcome through design studies, modelling, technical justification, practical trials to deliver a complete solution for the ongoing inspection needs.

Keywords: Austenitic, Ultrasonic, Weld, Storage, Fuel

Ultrasonic phased array technique for check valve evaluation in comparison with magnetic flux and acoustic method

H. Calás, B. de la Fuente, V. Barcenilla, R. Martínez-Oña and F. Fernández

Tecnatom Group, Avda. de Montes de Oca 1, 28703 San Sebastián de los Reyes, Spain

Abstract

The non destructive evaluation of check valves has received a considerable attention by the nuclear power industry because these devices are used extensively in nuclear plant safety systems. The most common technique for check valve inspection includes radiography, acoustic and magnetic flux.

Tecnatom has the VITER-2.0 system with magnetic and acoustic sensors for the non destructive evaluation of check valves. On the other hand, Tecnatom has developed a new ultrasonic technique for diagnosis of check valves using the phased array hardware FPA-128M. This technique provides qualitative information on the operation of the valve, the state of the internal components and can be considered an important complement to the VITER-2.0 system.

In the present work the results obtained for check valve diagnosis with the new integrated system VITER-2.0 + FPA-128M are presented and analyzed considering different internal components problems.

Keywords: Ultrasonic technique, Check valves, nuclear industry

1. Introduction

Check valves plays as security elements allowing flow path on one direction preventing the opposite direction. These valves are on work by the flow passing through them. Their main functionalities are: as an isolation of the containment building at Nuclear power plant, to separate systems that work under different pressures and to preserve turbo pumps or motor pumps at industrial facilities. Due to the inherent features of its performance, failures or malfunction can be hidden during the plants operation, affecting to Security, so they have to be regularly inspected. Most common techniques used so far, are magnetic flow and Sound emission.

For the check valves diagnosis it is desirable to determine: fixing conditions, movement and status of the joint, disc, hinge ping, and hinge arm (internals of the check valves from now on).

This has motivated the implementation of Phased Array ultrasonic techniques (PAUT) [2] for the diagnosis of check valves, due to their ability to provide direct information about the location and movement status of the internals. Figure 1 shows the pattern for internals movement in the standard check valve.

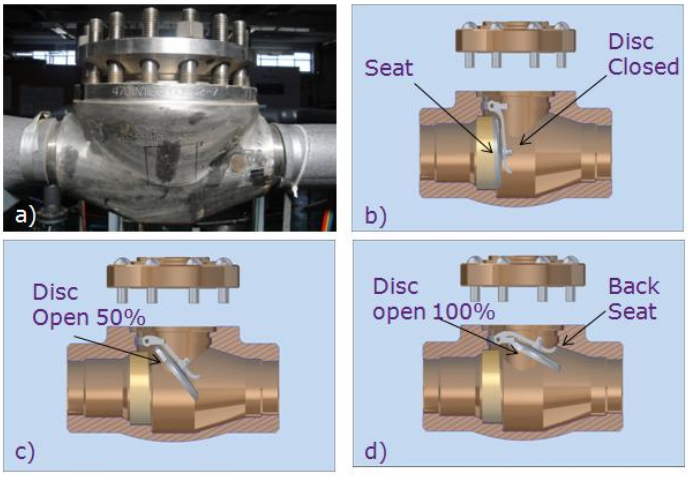

Figure 1. a) Stainless Steel Valve, b) Pattern of closed disc, c) Pattern of 50% opened disc, and d) Pattern of 100% opened disc.

Tecnatom has developed a new technique for check valves diagnosis, based in Ultrasonic phased array. On it, the ultrasounds are expanded inside the valve, sweeping up all the internals position and the trajectory where the valves once, activated must run. The PAUT technique, provides main information about the productivity of the valve and about the status of the internals. Its implementation can be considered a main complement to the current system VITE-R 2.0.

VITE-R 2.0. System of check valves diagnosis, developed by Tecnatom, enables to analyze 2 valves at the same time, for that, it has 5 channels per valve: 3 channels of accelerometer, one magnetic sensor channel and a subsidiary channel that can be used to fix the system to a displacement sensor. Thanks to modularity, adaptability and flexibility of the Electronics of Tecnatom SONIA + FPA-128M, integration of the new technique Phased Array into the system VITE-R 2.0 is achieved.

Fixing and status of internals within the valve can be or not the adequate, due to the running erosion and/or poor maintenance and this can generate strange signals that will be difficult to read if they are not duly studied. For this it's been realized and study of the PAUT Technique behavior faced to the different anomalies in fixing and the internals statement.

The current work shows the results obtained for the diagnosis of check valves with the integrated system VITER-2.0 + FPA128M. Different types of problems on the internal components are been considered and there has been analyzed the ultrasonic response in comparison with the rest of the sensors of the system.

2. VITE-R 2.0 System + PAUT

New system integrates accelerometer, magnetic sensors and PAUT probe, is being controlled by a computer connected via Ethernet to the equipment VITE-R 2.0 (accelerometer, magnetic sensor and displacement sensor) and to the SONIA COMPACT equipment. Cables for this connection will be 50 meters large as maximum. For each valve to be analyzed one FPA-128M (PAUT) will be used, which is connected to the SONIA COMPACT system via optical fibre, being approximately 10 meters length. PA Probes are connected to the FPA-128M modules with a cable of 5 meters (see Figure 2). With this configuration valves to be inspected can be separated by 20 meters maximum to each other.

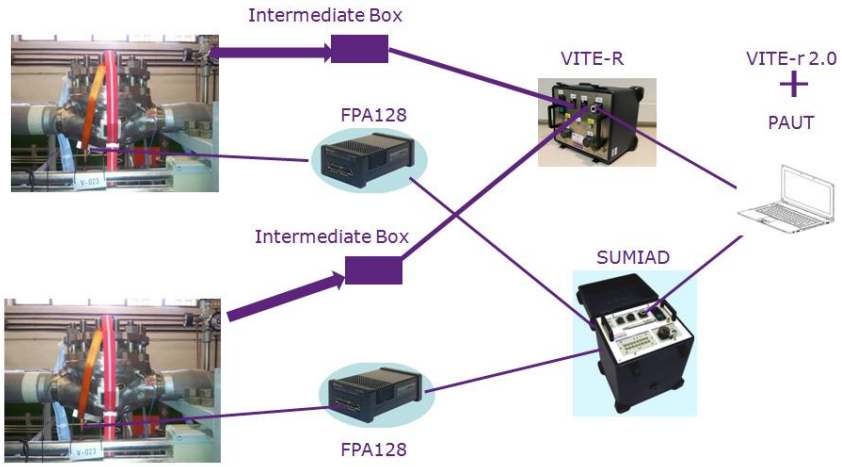

Figure 2. Scheme of the electronic configuration of valve diagnosis system

Acquisition Software VITE-R + PAUT, developed by Tecnatom, offer the possibility to realize the inspection of two valves simultaneously and manage the diagnosis for accelerometers, magnetic sensors and with ultrasounds. In this work, we are focused on the ultrasonic part of the inspection and will use the rest of the sensors as a reference only. Figures 3 & 4 show the acquisition interfaces and the evaluation respectively for the ultrasonic part of the developed software.

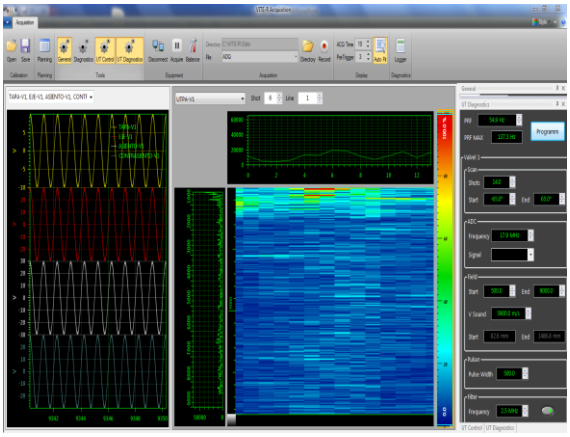

Figure 3. Acquisition software

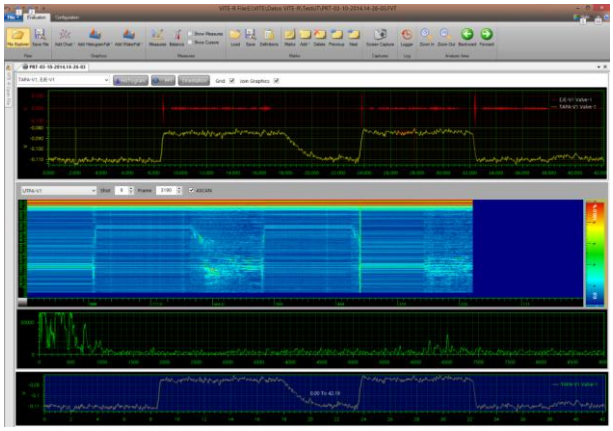

Figure 4. Evaluation Software

Ultrasonic technique is based on pulse-echo with a phased array transducer. The transducer is located directly on the valve surface and the focal rules are defined to obtain a sector scan with the appropriate aperture according to the size of the valve to be inspected. Beams generated for the focal laws have to cover the position of the internals and the path where they have to move. Figure 5 shows CIVA Simulation of the acoustic field generated within the check valve for three focal laws.

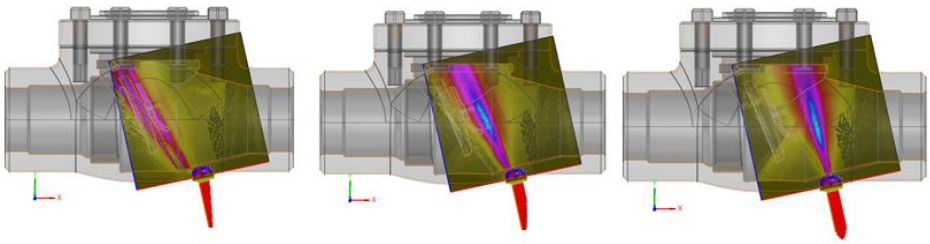

Figure 5. Focal laws modelling

Focal laws and the inspection area must be defined according to the geometry and the size of the valve to be inspected. As higher will be the number of focal laws, and higher will be the inspection area, the optimal PRF will be lower. This creates a compromise between accuracy that will be in depth and the accuracy that will be in time to determine the position of the internals. When activated the valve, echoes coming from the internals will be moved through the focal law or from one focal to the other. Figure 6 shows the trail left by internals in a Scroll View for a focal law and its corresponding position in a S-Scan view non corrected.

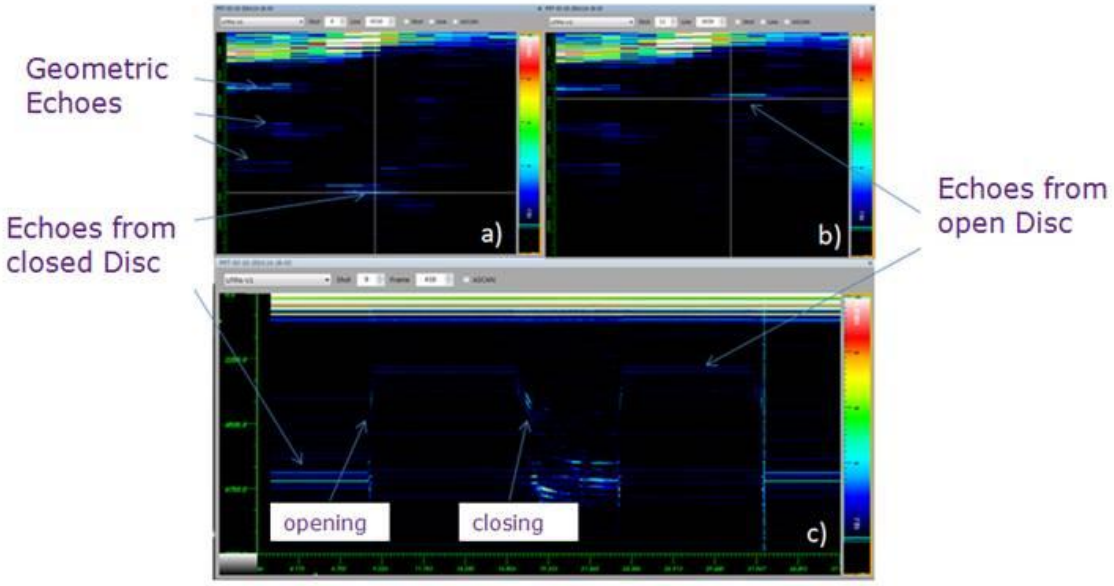

Figure 6. Evaluation View: a) S-Scan before activation, b) S Scan with opened disc, and c) Scroll View of the focal law where it is appreciated the temporal evolution of the internals.

Configuration of focal laws must be done according to the following factors:

- Size of Valve
- Geometry of valve
- Access point for ultrasound sensor (effective area for probe position)

Potential points of access will be the following:

- Bottom side
- Inclined bottom side
- Perpendicular side

Figure 7 shows these points, in the access to the lateral, parallel and perpendicular positions; they are referred to the relative position between the scanning direction and the initial position of the disc

Technique was approved with satisfactory results in the testing loop of Tecnatom, in 3 inch valves, and field tests were made in operative valves.

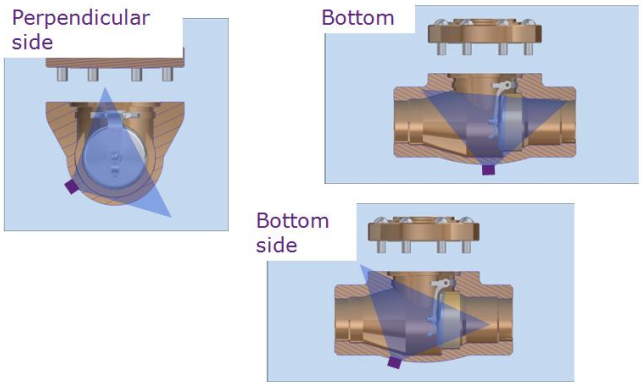

Figure 7. Access points to position the ultrasonic probe on valve.

2. Testing made

Testing made had an objective of verifying the effects on the PAUT views of some anomalies in the placement of the internals of the valve. Internal Parts that can generate reflections are the following (see figure 8): disc, hinge ping, hinge ping caps, hinge arm, disc stud.

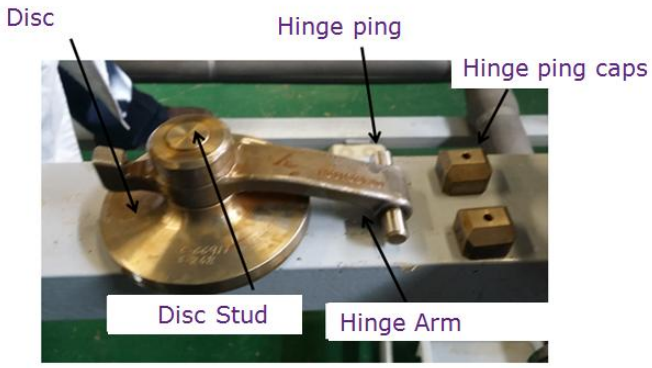

Figure 8. Internals in valve.

Some issues that can be found while carrying out a valve diagnosis are the following:

-Non appropriate placement or lack of caps of the turning hinge ping that can induce to a continuous clap along the flow path and a henceforth wear of the internal of the valve, driving failures of action and the possibility of excessive leaks, so the valve could not fulfil its functionality.

- Clearance at the hinge ping.

- Shaft hinge ping break, so the disc will be lost within the body of the valve and this valve will not fulfil its functionality.

- Shaft hinge arm break, so the part of internals will be lost in the body of the valve, with random movements during the path flow, so the valve will not fulfil its functionality.

- Fixing clearance of the disc to the hinge arm can induce to twist and swing movements of the disc.

In this work, we are limited to compare the response of the internals duly located with the response of the internals out of seat, which is equivalent to the hinge arm break (Figure 9).

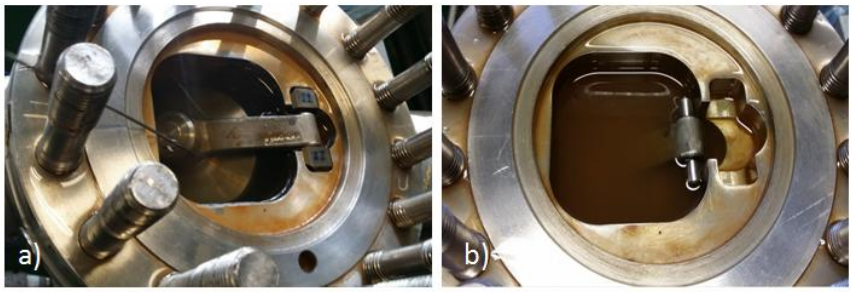

Figure 9. Internals location: a) Internals duly placed, and b) internals out of seat.

4. Results

For the case of the internal well placed the response obtained is shown on figure 9. On this it can be appreciated clearly the different status of the disc, closed and opened, timing for opening-closing, and the recovery of the echoes had before auctioning the valve, what implies that the internals have come back to their original position. As well as it can be appreciated the coincidence on the closing and opening moments with the indications of the rest of sensors.

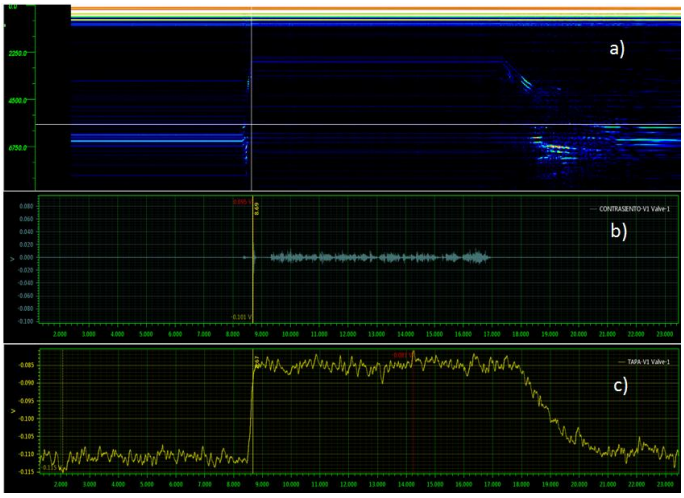

Figure 9. Response of the valve with internals well placed. a) Sensor PAUT, b) accelerometer in the back seat, and c) magnetic sensor on top

In the case the internals are out of the support, it may happen that these move in a chaotic way within the valve or that they can be fixed in a non desirable way due to the flow strength. Figure 10 shows both cases, both pictures were taken when opening the valve after one each driving.

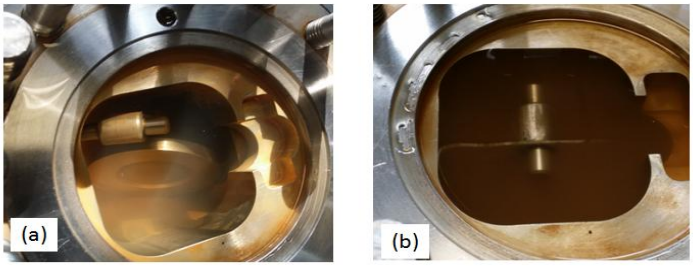

Figure 10. Status of the internals after operating with the internals out of seat: a) Disc moving inside the valve, and b) Disc fixed in the exit tube with little movement

Answer to Figure 10b case, is shown on Figure 11. Action moments for aperture and closing are clearly appreciate in the three types of sensors, but both at PAUT sensor and at Magnetic Sensor, behaviour doesn't mean the valve aperture and doesn't exist a recovering of the initial echoes. There seem to be some fixed PAUT echoes in the sensor that were not present before the action. This clearly shows that the internals have taken the fixed position due to the flow strength.

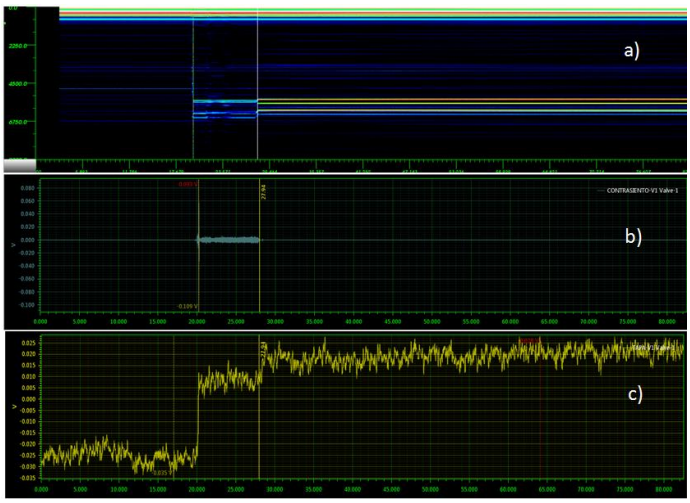

Figure 11. Valve response with internals located out of the seat. a) PAUT sensor, b) Accelerometer against-seat and c) Magnetic sensor

5. Conclusions

Tecnatom has developed a PAUT technique for the diagnosis of check valves. The same has been integrated into the VITE-R 2.0 System, using the electronics Phased Array of Tecnatom (FPA-128M). Through a software development that controls both electronics at the same time it is able to synchronize on time all the sensors. This new technique has the advantage to give a direct reference of the position of the internals in every moment through the reflection of the ultrasonic beams and it constitutes a high value complement to the diagnosis system of valves based in accelerometers and magnetic sensors. Diagnosis of operative valves has been done in plants that ratify the performance of the presented technique.

References

[1] H. D. Haynes, “Aging and service Wear of Check Valves Used in Engineered Safety-Feature Systems of Nuclear Power Plants”, NUREG/CR-4302, ORNL-6193. Vol. 2. 1991

[2] EPRI Project Manager D. Kull, “Nondestructive Evaluation: Check Valve Evaluation Using Phased Array Ultrasonics”. Final Report, December 2014

Detection of Artificial Defects at Storage Vessels for Liquefied Hydrogen by Ultrasonic Guided Wave

Mu-Kyung Seo[1,2], Ki-Bok Kim[2*], Geonwoo Kim[2,3], Hak-Joon Kim[1], Chi-Hwan Oh[4], Sung-Jin Song[1], Minsu Park[5] and Yong Sang Cho[6]

[1]Dept. of Mechanical Engineering, Sungkyunkwan Univ., 2066, Seobu-ro, Jangan-gu, Suwon-si, Gyeonggi-do, Republic of Korea

[2]Center for Safety Measurement, Korea Research Institute of Science and Technology, 267, Gajeong-ro, Yuseong-gu, Daejeon, Republic of Korea

[3] Dept. of Science of Measurement, University of Science and Technology, 217, Gajeong-ro, Yuseong-gu, Daejeon, Republic of Korea

[4] Daum Energy Co., Ltd, 830, Yeonsam-ro, Jeju-si, JeJu-do, Republic of Korea

[5] Technology Research & Development Institute Robotics Lab, KEPCO plant service & Engineering Co., LTD, 211, Munhwa-ro, Jeollanam-do, Republic of Korea

[6] Mechanical Engineering Group, Korea Electric Power Corporation Research Institute, 105, Munji-ro, Yuseong-gu, Daejeon, Republic of Korea

E-mail address(*corresponding author) : kimkibok@kriss.re.kr

Recently, many researches on hydrogen have been carried out as one of the alternative energy sources. The hydrogen is stored at a storage vessel in liquefied state for maximum efficiency of its storage. The safety of pressurized hydrogen storage vessel is very important because of explosive characteristics of liquefied hydrogen. As a material for the storage vessel, the stainless steel 304 (SUS304) has been used. At the former research to apply the ultrasonic guided wave (UGW) technique to the storage vessel for liquefied hydrogen, we presented the STFT technique to detect defects at the metal plate (SUS304) for the storage vessel. In this paper, based on the former research results, we tried to detect the artificial defects at the storage vessels and hence the artificial defects could be detected by combination of STFT and UGW techniques.

Keywords: Pressurized hydrogen storage vessel, Ultrasonic guided wave (UGW), Short time Fourier transform (STFT), Artificial defects

Development of sizing techniques of SCC height in dissimilar metal welds of vessel nozzle safe-end by means of Phased Array TOFD technique with asymmetrical ultrasonic beams and Multi-Angle Synthesis technique

K. Endoh[1], J. Kitasaka[1] and H. Ishida[2]

[1] Non-Destructive Inspection Co., Ltd., Japan

[2] Institute of Nuclear Safety System, Inc., Japan

Abstract

TOFD technique with asymmetric ultrasonic beams between a transmitter and a receiver, and the multi-angle synthesis technique which synthesizes test results with different conditions have been developed. Ni base alloy is included in a dissimilar metal weld of an outlet nozzle of a reactor vessel in a nuclear power plant. The measurement for defect height of SCC in a direction perpendicular to a Ni base alloy weld line was difficult due to an acoustic anisotropy and high attenuation. Therefore, examinations of mock-up test specimens using this technique were carried out. As a result of this study, developed techniques were applicable to height measurement method of SCC on the inner surface by examining from the inner surface or outer surface of the vessel nozzle.

Keywords: Phased array technique, TOFD technique, Ni based alloy weldment, SCC, Image processing

1. Introduction

A stress corrosion cracking (SCC) was found on an inner surface of a dissimilar metal weld of an outlet nozzle of a reactor vessel in Japan in 2008. Dimensions of this SCC measured by cross-sectional observation were 13mm in length and 21mm in depth. Flaw height of SCC is conventionally measured by tip echo technique and/or Time of Flight Diffraction (TOFD) technique of ultrasonic testing. However, the dissimilar metal weld of the outlet nozzle of the reactor vessel had coarse-grained structures, thus it was difficult to distinguish tip echoes from scattering noises due to an acoustic anisotropy and high attenuation caused by coarse grain.

The following techniques which were conventionally based on phased array TOFD have been developed.

(1)To measure the height of SCC with different conditions of refraction angles and focal depth, TOFD technique using asymmetrical ultrasonic beams by means of a phased array probe (hereafter the phased array asymmetric TOFD technique) was developed. In this technique, a transmitter emits ultrasound with various refraction angles to a receiver which handles different beam paths from each refraction angle.

(2)To improve the signal-to-noise ratio, the image processing synthesized scanning data of (1) with different refraction angles and beam paths (hereafter the multi-angle synthesis technique) was developed.

By combining techniques (1) and (2), examinations of plate specimens were carried out. [1] Examinations of pipe specimens were also carried out by these techniques from aperture side of crack or the other side.

This study presents evaluation results of crack depth measurement using these techniques from inner and outer side of pipe specimen.

2. Measurement techniques

2.1 Phased array asymmetric TOFD technique

Figure 1 (a) shows a schematic drawing of a conventional phased array TOFD technique with symmetrical ultrasonic beams between a transmitter and a receiver. On the other hand, in the figure using phased array asymmetric TOFD technique, refraction angles from a transmitter are different from those of a receiver. Both transmitter and receiver are focused on the intersection (figure 1 (b)). Matrix phased array probes for a transmitter and a receiver were moved in a constant distance.

"Steering angle" is defined as the angle formed by the line from the center of transmitter and receiver to the

focal point and a normal to the surface of test specimen, because refraction angles of transmitted wave is different from those of received wave.

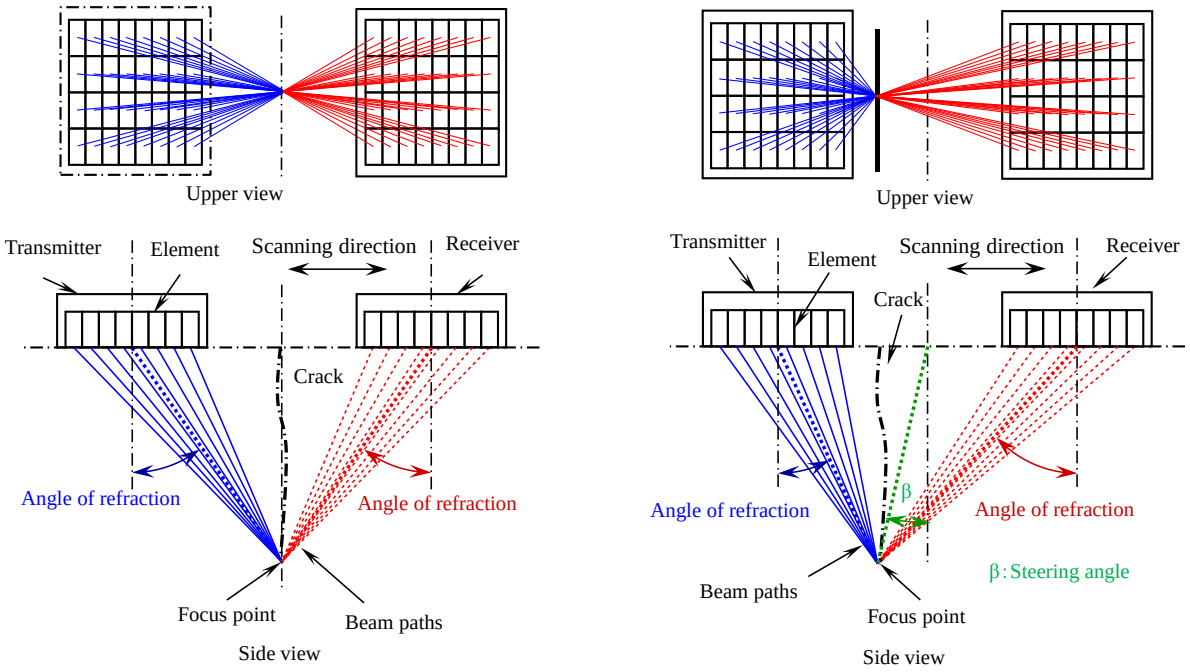

(a) Phased array TOFD technique (b) Phased array asymmetric TOFD technique

Figure1. Schematic drawing of phased array TOFD technique

2.2 Multi-angle synthesis technique

This technique is a method of synthesizing results from the different steering angles. Received signal of ultrasonic testing consists of not only signals from a defect but also scattering noise from microstructure of steel.
This Multi-angle synthesis technique is used to average some signals which refraction angles and beam paths are different from each other. After the signals averaging, the tip echoes from a defect appear clearly, and structural noises are reduced.

Figure2 shows schematic drawing of Multi-angle synthesis technique. Some tip echoes from a defect can be obtained from different steering angle at the same focus depth. These echoes which also include some structural noises randomly are averaged to clarify the tip echoes and reduce the structural noise. In this case, the tip echoes which refract around the focal depth are emphasized. The tip echoes from different focal depths are synthesized to make the cross sectional image of test specimen as a result of the examination.

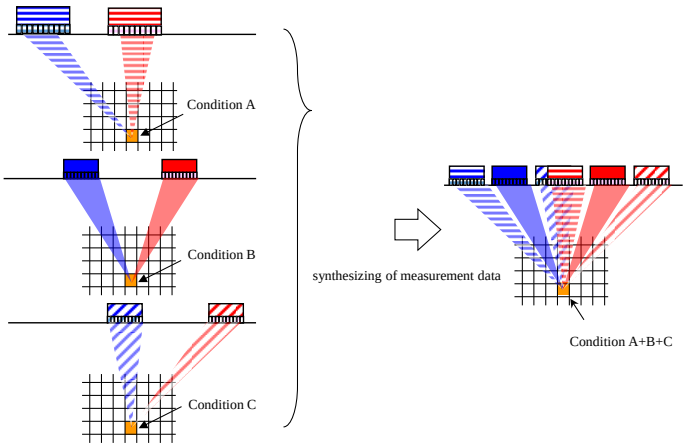

Figure2. Multi-angle synthesis method

3. Testing method

3.1 Test Specimen

Figure 3 shows a test specimen. The vessel nozzles and the safe-ends are fabricated from carbon steel and stainless steel respectively. INCONEL 600 was used for a dissimilar metal welded joint connected the safe-end to the vessel nozzle by butt welding method. SCC and an electric discharge machining slit (hereafter EDM slit) were fabricated at right angle to the weld line. First, high carbon INCONEL 600 filler metal was used for welding overlay. Then EDM slit was fabricated. Finally SCC was grown by tensile testing with immersing the test specimen in solution of tetrathionic acid.

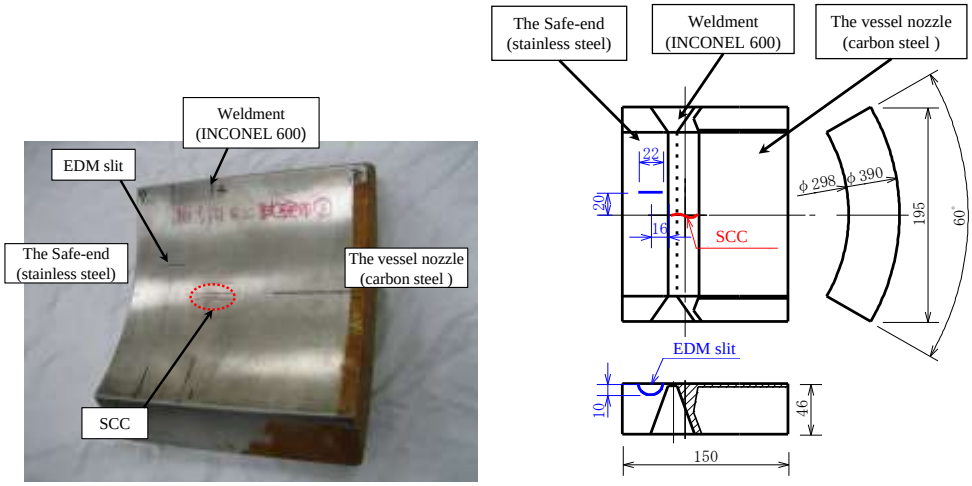

Figure3. Test specimen

3.2 Test system

Table 1 shows the specification of the phased array probes. Figure 4 shows pictures of the phased array probes and the wedges. Array probes used for examinations from inner side or outer side consist of 8x4(32) elements or 32x8 (256) elements respectively. Each probe is installed on a transmitter or a receiver, and both of them are attached to the wedge for measuring the defect on the test specimen. Wedges surfaces are machined to add curve based on the surface shape of the test specimen. 'Dynaray' and 'Ultra Vision' made by Zetec, Inc. are used for phased array system.

Table1. Specification of the phased array probes

	inner	outer
Frequency(MHz)	2.25	1
Number of elements	32	256
Element array(length×width)	8×4	32×8
Aperture dimension(mm×mm)	15.8×15.8	71.8×25.0

(a) 8x4 matrix probes and wedge (b) 32x8 matrix probes and wedge

Figure 4. Phased array probes and the wedges

3.3 Testing conditions

In case of examination from inside, focus depth are from 4mm to 24mm with a pitch of 4mm, steering angles are from -42 degree to 42 degree with a pitch of 1 degree. On the other hand, in case of examination from outside focus depth are from 30mm to 46mm with a pitch of 4mm, steering angles are from -26 degree to 26 degree with a pitch of 1 degree.

4. Result

4.1 Examination from inner side

Figure 5 shows result of the examination from inner side to EDM slit and SCC by phased array asymmetric TOFD technique. B-scope displays with focus depth of 4mm, 8mm and 12mm and steering angle of - 31, -15, 0, 15 and 31 degree are shown in the figure. Tip echoes from EDM slit with 10mm in depth were detected clearly when focus depth was 8mm or 12mm. Tip echoes from SCC were also detected when focus depth was 8mm or 12mm. However, signal-to-noise ratio of tip echoes from SCC was lower than those from EDM slit. This result was influenced by characteristics of weld because SCC was grown into the INCONEL weld but EDM slit was machined into the stainless steel base metal.

Figure 6 shows an example of the result of synthesized data of different steering angle condition of 8, 12, 16, 20 or 24mm in focus depth. In case of 8mm and 12mm in focus depth, tip echoes from EDM appears clearly by synthesizing data. However, the phased array asymmetric TOFD technique can be influenced by scattering noises from the weld; tip echoes from SCC appear in synthesized data when focus depth is 8mm or 12mm.

Figure 7 shows the result of synthesized data of different focus depth. An examination result can be seen in a cross-sectional image. The height of EDM slit and SCC measured 14mm and 6mm respectively. The multi-angle synthesis technique was confirmed to be applicable to examine pipes in a nuclear power plant.

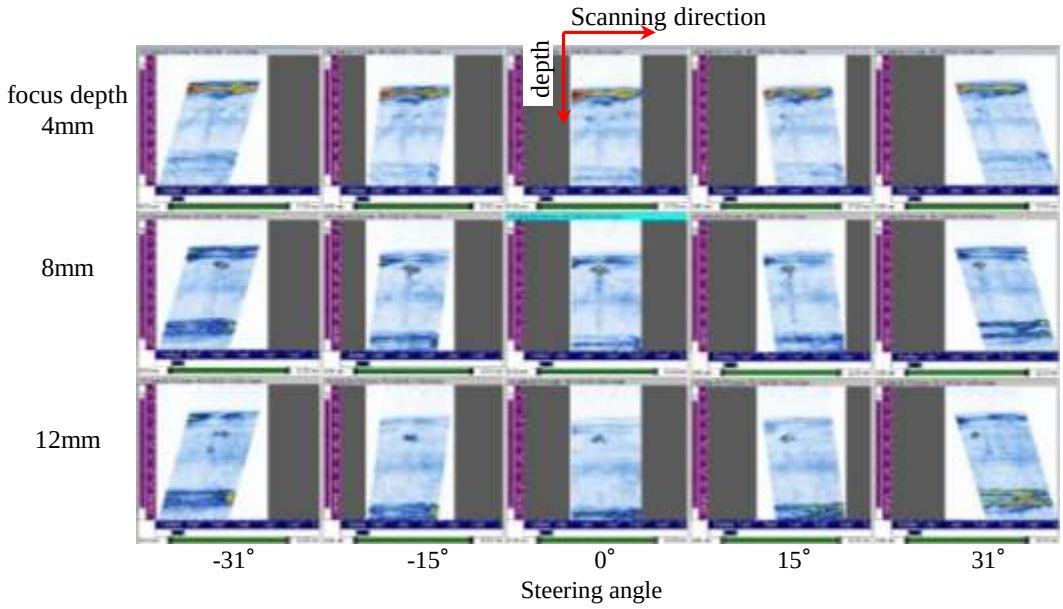

(a) EDM slit

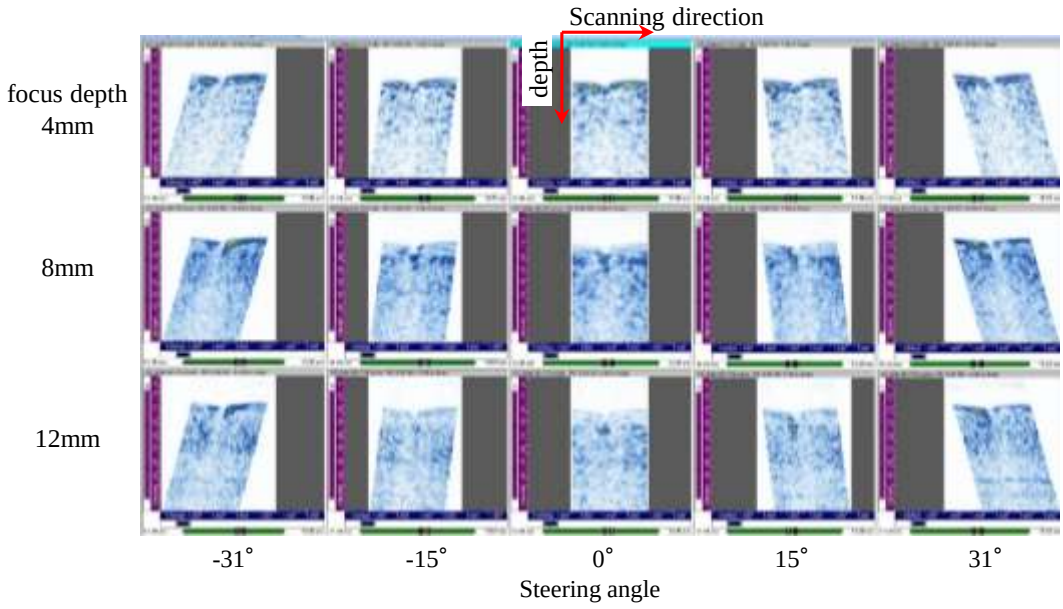

(b) SCC

Figure 5. Result of the examination from inner side by the phased array asymmetric TOFD technique

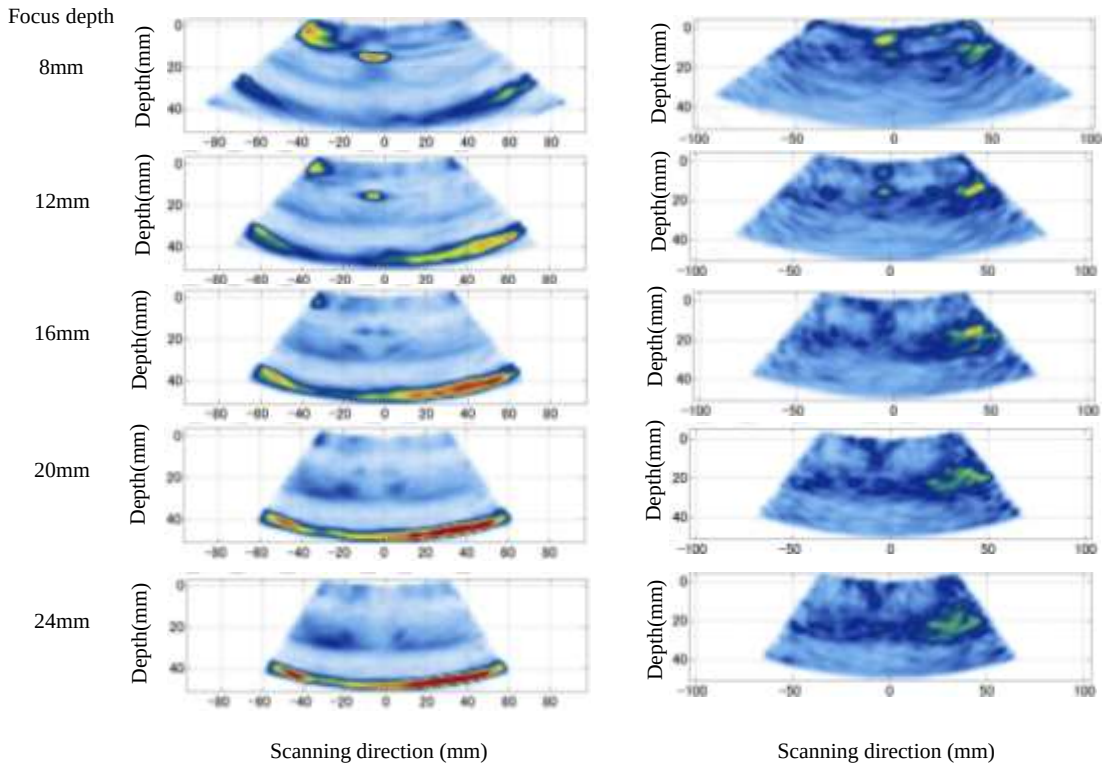

(a) EDM slit (b) SCC

Figure 6. The result of synthesizing data of different steering angle condition

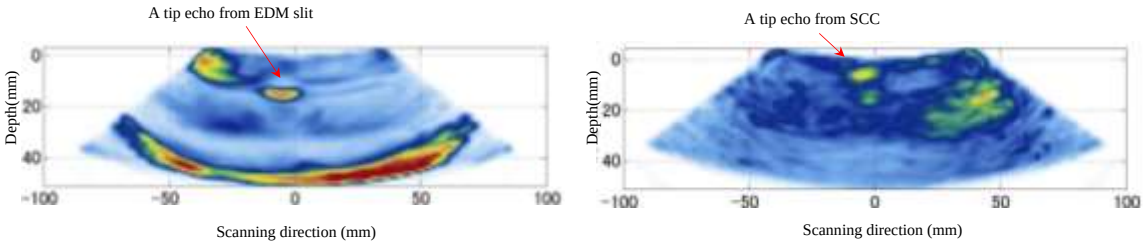

(a) EDM slit (b) SCC

Figure 7. The result of synthesizing data of different focus depth condition

4.2 Examination from outer side

Figure 8 shows result of the examination from outer side to EDM slit and SCC by the phased array asymmetric TOFD technique. B-scope displays with focus depth of 30mm, 34mm and 38mm and steering angle of -24, -12, 0, 12 and 24 degree are shown in the figure. Tip echoes from EDM slit with 10mm in depth were detected clearly when focus depth was 34mm or 38mm. Tip echoes from SCC were also detected when focus depth was 30mm. However, signal-to-noise ratio of tip echoes from SCC was lower than that from EDM slit. This result was also influenced by characteristics of weld because SCC was grown into the INCONEL weld but EDM slit was machined into the stainless steel base metal.

Figure 9 shows an example of the result of synthesized data of different steering angle condition of 30, 34, 38, 42 or 46mm in focus depth. In case of 34mm or 38mm in focus depth, tip echoes from EDM appears clearly by synthesizing data. However, the phased array asymmetric TOFD technique can be influenced by scattering noises

from the weld; tip echoes from SCC appears in synthesized data when focus depth is 30mm.

Figure 10 shows the result of synthesized data of different focus depth. An examination result can also be seen in a cross-sectional image. The height of EDM slit and SCC measured 6mm and 16mm respectively. The multi-angle synthesis technique was confirmed to be applicable to examination from outside of pipe.

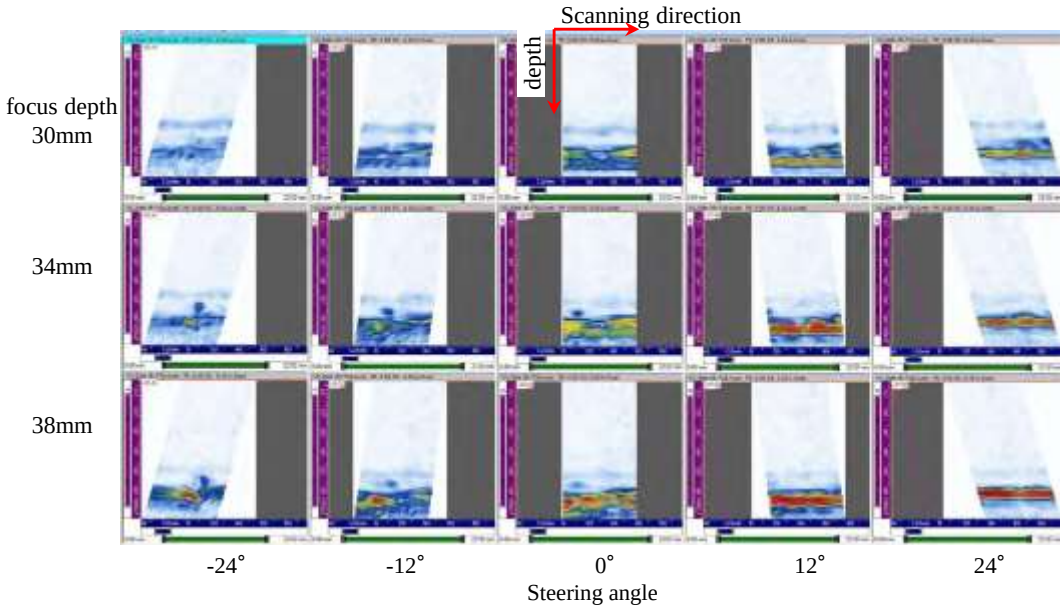

(a) EDM slit

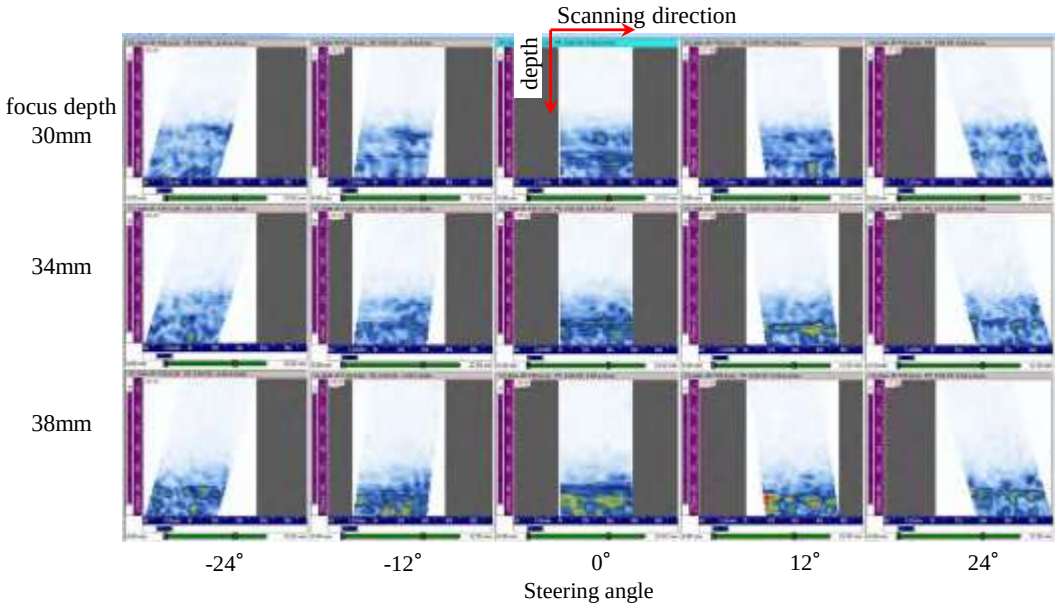

(b) SCC

Figure 8. Result of the examination from outer side by the phased array asymmetric TOFD technique

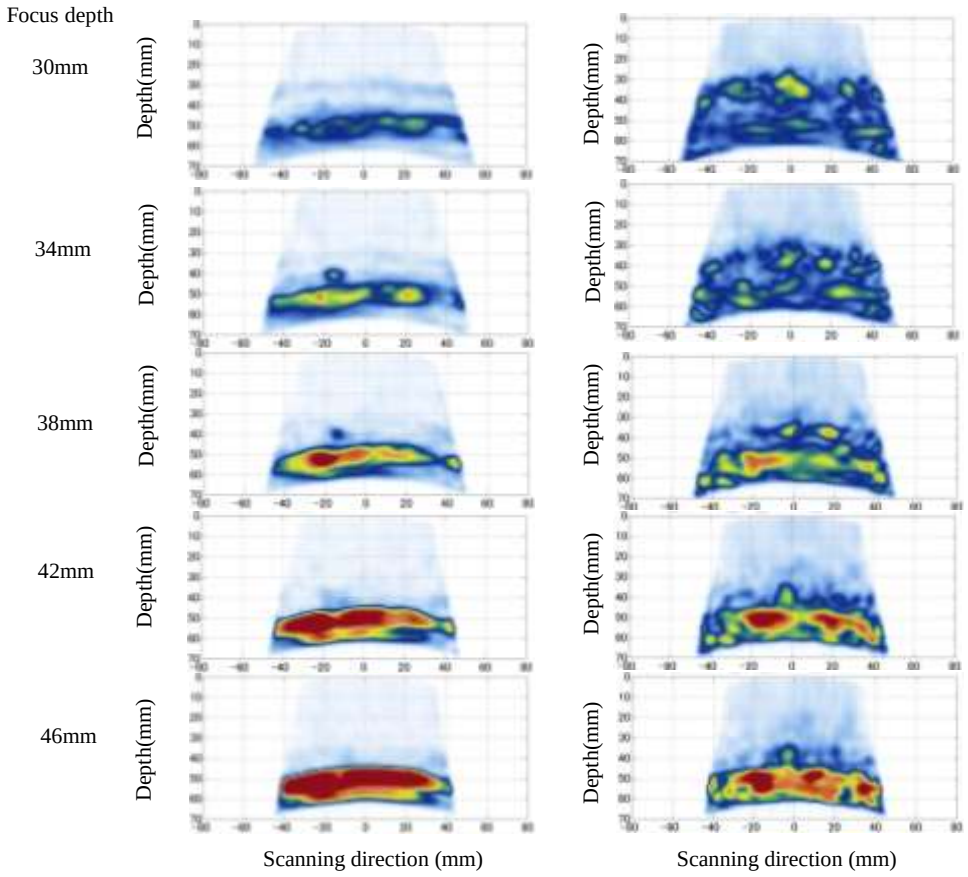

(a) EDM slit (b) SCC

Figure 9. The result of synthesizing data of different steering angle condition

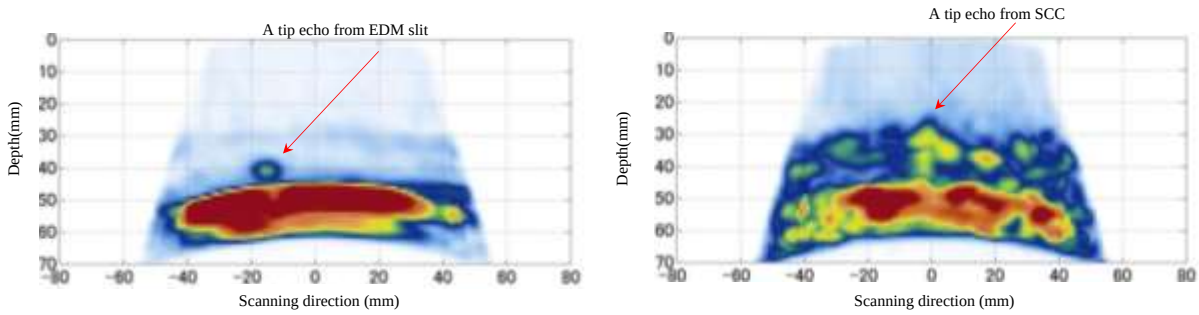

(a) EDM slit (b) SCC

Figure 10. The result of synthesizing data of different focus depth condition

5. Conclusion

In this study, with phased array asymmetric TOFD technique, Multi-angle synthesis technique and combined those techniques, examination was carried out from an aperture side of crack and an opposite side of pipe.

As a result, these techniques were confirmed to be applicable to measurement of the height of SCC on inner surface by examining from the inner surface or outer surface of the vessel nozzle.

These below are the points that we set as the next goals.

(1)Improve to optimize conditions for detecting defect and measure its depth more accuracy.

(2) Collect many other measurement data.

(3) Evaluate by the Multi-angle synthesis technique in different cross-sections.

References

[1]H.Ishida, J. Kitasaka, "Development of a Phased Array TOFD UT Method to Measure Depth of SCCs in Dissimilar Welds", 9th International Conference on NDE in Relation to Structural Integrity for Nuclear and Pressurized Components, pp.754-762 (2012)

Development of the improved PECT system to evaluate thermal degradation of thermal barrier coatings

Zhang Jianhai[1], Hak-Joon Kim[1], Sung-Jin Song[1] and Chang-Sung Seok[1]
[1]Sungkyunkwan University, Korea

E-mail address(jhzh1986@gmail.com) :

Thermal barrier coatings (TBCs) are applied to protect hot section components, such as gas turbines for aircraft propulsion and power generation, from high temperature. Major failure mechanisms of the TBCs include thermal stress developed by the mismatch of the thermal expansion coefficients between each of the coating layers. The thermal grown oxide (TGO) layer formation resulting from bond coating (BC) oxidation is known as the most influential cause of failure in the TBCs. To evaluate the phase degradation of BC layer due to thermal oxidation, a pulsed eddy current testing (PECT) using a differential probe is proposed. Firstly, an improved PECT experimental system are developed and verified. Then, PECT technique is utilized to measure the remaining life of TBCs. Secondly, the basic theory of finite element model of PECT using a differential probe is presented. Then, the phenomena of phase degradation of BC are theoretical studied. The PECT experimental results are analyzed by the proposed model. Finally, the rates of β-NiAl depletion zone and β-NiAl zone of BC are analyzed through the experimental results and simulation results.

Keywords: Pulsed eddy current testing, thermal barrier coating, phase degradation, finite element modelling.

Effects of Metallic Diaphragm on Sensitivity Characteristics of Optical Ultrasonic Sensor for Under-Sodium Inspection

Koichi Saruta, Toshihiko Yamaguchi, and Masashi Ueda

Japan Atomic Energy Agency, Japan

Abstract

The paper evaluates experimentally the effects of the metallic diaphragm on the sensitivity characteristics of an optical ultrasonic sensor used in the under-sodium inspection. The diaphragm is set in a water tank to have direct contact with water on one side and air on the other side. Ultrasonic pulse propagating through water impinges on the diaphragm, on which vibration induced by the ultrasonic pulse is detected by a heterodyne interferometer. The sensitivity of the diaphragm is then evaluated based on the detected amplitude. On the diaphragm two waves are generated. The first wave is initiated by the ultrasonic pulse that impinges directly on the diaphragm. The second wave, on the other hand, results from the interference of lamb waves that propagates from the edge of the diaphragm. We have found that the amplitudes of both waves increase with decreasing thickness of the diaphragm. Thus, the sensitivity can be improved by using a thinner diaphragm. Moreover, the second wave has larger amplitude than the first wave because the lamb waves meet in phase, resulting in constructive interference at the center of the diaphragm. The experimental results show that the sensitivity for the second wave is by a factor of 5 to 6 higher than that for the first wave. This suggests that the weak ultrasonic wave can be amplified and detected with a higher sensitivity by using the second wave.

Keywords : Optical ultrasonic sensor, Optical pressure sensor, Under-sodium inspection, Fast reactor

1. Introduction

In a fast reactor power plant, visual inspection is being planned to be introduced in order to further enhance the safety and reliability. Standard optical instruments such as an optical fiber scope and a charge-couple device camera have been commonly used in a light water reactor for this purpose, while ultrasonic imaging devices are employed in a sodium-cooled fast reactor on account of the liquid metal coolant [1, 2]. Piezoelectric sensors have been widely used as the sensor to detect ultrasonic wave, though optical ultrasonic sensors are considered as an attractive alternative because they offer unique advantages such as small dimensions, multiplexing capability, and immunity to electromagnetic interference, thereby enabling us to develop a compact sensor array with a high spatial resolution and to realize long-haul signal transmission without additional signal conditioning devices. The acoustic pressure sensitivity of the optical probe, however, is lower than that of the piezoelectric probe. The optical ultrasonic sensor employed in under-sodium inspection consists of a metallic diaphragm and a laser interferometer [3, 4], where mechanical vibration is induced on the diaphragm as a result of the incidence of ultrasonic wave, which is then detected by the interferometer. Among the key factors that determine the sensitivity are the properties of the diaphragm.

In this paper we report the effects of the metallic diaphragm on the sensitivity characteristics of the optical ultrasonic sensor for under-sodium inspection. The diameter and thickness of the diaphragm are used as parameters in order to evaluate the sensitivity. The diaphragm is set in a tank filled with water instead of liquid sodium so that one side has direct contact with water and the other side with air. A heterodyne interferometer is employed to detect the wave induced on the diaphragm as a result of the incidence of ultrasonic wave, which is emitted from a piezoelectric transducer placed in the water tank. In addition to experimental evaluation of the sensitivity, we also describe the mechanism of the wave observed on the diaphragm.

2. Experimental setup

Shown in Fig. 1 is the diaphragm used in the experiment, which is fabricated by bonding a sheet of metallic foil on one side of a substrate with circular apertures by means of diffusion bonding technique. The metallic foil and the substrate are made of stainless steel (SUS304). The thicknesses of the foil are 5, 10, and 20 μm. The aperture sizes are 3, 5, 7, and 10

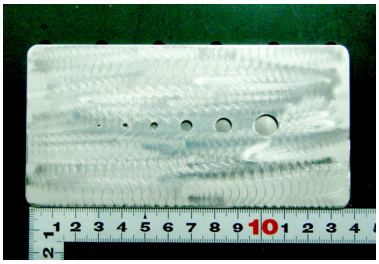

Figure 1. Diaphragm.

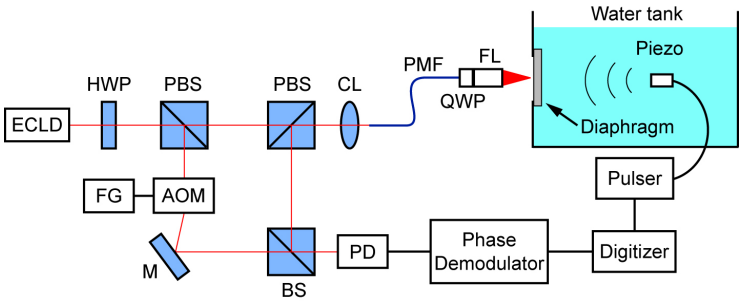

Figure 2. Experimental setup to evaluate the sensitivity of the diaphragm. ECLD, external cavity laser diode; HWP, half-wave plate; PBS, polarization maintaining beam splitter; AOM, acousto-optic modulator; FG, function generator; M, mirror; BS, beam splitter; CL, coupling lens; PMF, polarization maintaining fiber; QWP, quarter-wave plate; FL, focusing lens; PD, photodiode.

mm in diameter, which in turn define the diameter of the diaphragm. The experimental setup to evaluate the sensitivity is illustrated in Fig. 2. In the laboratory experiments water is used in place of liquid sodium. The diaphragm is set on the sidewall of a water tank and receives the ultrasonic pulse emitted from a piezoelectric transducer with a center frequency of 5 MHz. The center of the transducer is adjusted to a line that perpendicularly passes through the center of the diaphragm, and the distance between the transducer and the diaphragm is set at z = 30 cm. A heterodyne interferometer configured in Mach-Zehnder arrangement is employed to measure the displacement of the diaphragm. The light source is an external cavity laser diode (ECLD), the lasing wavelength of which is stabilized at λ = 780 nm. The output beam is divided into two orthogonally polarized beams by a polarizing beam splitter (PBS), where the reflected beam is vertically polarized and the transmitted beam is horizontally polarized. The splitting ratio is adjusted by rotating a half- wave plate (HWP) in order to obtain the maximum visibility in the interference signal. In the reference path the beam is given a frequency shift f_b by passage through an acousto-optic modulator (AOM). In the measurement path the beam is launched into a polarization maintaining fiber (PMF), transmitted through a quarter-wave plate (QWP), and then focused onto the diaphragm with a focusing lens (FL). The use of the PMF in measurement path allows us to scan the measurement beam over the diaphragm and to produce a diffraction limited beam spot owing to spatial filtering effect of the narrow mode field diameter of the PMF. A spot size of approximately 5 µm can be obtained on the diaphragm. A part of the measurement beam reflected by the diaphragm is coupled into the PMF and travels back the same path as the forward propagation. Since the polarization of the measurement beam emerging from the PMF is flipped to vertical as a result of passing twice through the QWP, the measurement beam is reflected at the PBS and goes toward the beam splitter (BS). The measurement and the reference beam are recombined at the BS, and the resulting interference signal is then converted into electrical signal by a photodiode (PD). This interference signal is a sinusoid oscillating at a frequency *fb* with a time varying phase term, which is proportional to the displacement of the diaphragm. The displacement of the diaphragm is in turn obtained by means of in-phase/quadrature measurement of the interference signal using a phase demodulator.

3. Results and discussions

In order to compare the waveform detected on the diaphragm, the ultrasonic pulse excited by the transducer is measured with the use of a needle hydrophone, which is placed in the same plane as the diaphragm. The result is shown in Fig. 3, where the time is referenced to the trigger signal generated by the pulser. Several cycles of 5 MHz waves with decreasing amplitude compose the whole ultrasonic pulse, the duration of which is roughly 1.5 µs. The first cycle of the ultrasonic pulse appears around 200 µs, which is consistent with the propagation time of the acoustic wave from the transducer to the

hydrophone in water at room temperature. The peak-to-peak output voltage is approximately 3.77 mV, which can be converted into an acoustic pressure of 94.3 kPa using the conversion factor of 40 nV/Pa at 5 MHz.

The effect of the thickness of the diaphragm on the detection of ultrasonic pulse is examined using the 10-mm-diameter diaphragm with thicknesses t of 5, 10, and 20 μm. Figure 4 shows the response of each diaphragm to the incidence of the ultrasonic pulse shown in Fig. 3, when the measurement beam is adjusted on the center of the diaphragm by means of a translation stage. One can see that there are two distinct waves that are separated in time. The first wave is similar in both shape and duration to the ultrasonic pulse measured by the hydrophone and appears around 200 μs. We confirmed that the waveform does not change and the amplitude is maintained almost constant over the diaphragm except for the region close to the edge. It follows from these facts that the first wave results from the translational motion of the diaphragm, which is induced by the ultrasonic pulse that impinges directly on it. In contrast, the shape of the second wave is different from that of the incident ultrasonic pulse and appears behind the first wave with a delay that depends on the thickness of the diaphragm. In other words, the group velocity of the second wave increases with increasing thickness of the diaphragm, indicating that the second wave is a lamb wave propagating over the diaphragm. For both the first and the second wave, the amplitude increases as the thickness of the diaphragm is reduced. This can be explained as follows. Because of the same aperture size D = 10 mm, the diaphragms receive the same amount of energy from the ultrasonic pulse while the weight becomes lighter for the thinner diaphragms. As a result the amplitude of the first wave increases with decreasing thickness of the diaphragm. The decrease in the thickness also causes a reduction of the flexural rigidity, leading to an increase in the amplitude of the second wave.

Shown in Fig. 5 are the waveforms detected on the 5-μm-thickness diaphragms with diameters D of 3, 5, 7, and 10 mm. As with the waveforms shown in Fig. 4, the first wave is followed by the second wave with a delay, but which is proportional to the diameter D. This implies that the second wave propagates from the edge of the diaphragm; that is, it can be considered that the boundary of the metallic film and the substrate serves as the source of the lamb wave. Notice that the amplitude of the first wave is independent of the diameter, whereas the second wave increases in amplitude with

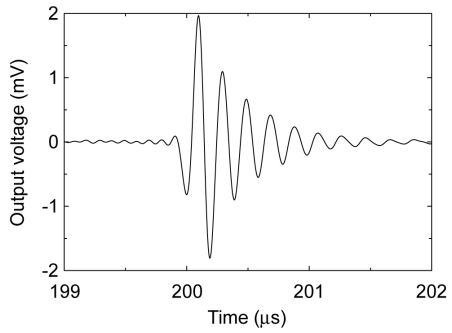

Figure 3. Ultrasonic pulse measured by a needle hydrophone in the plane of the diaphragm.

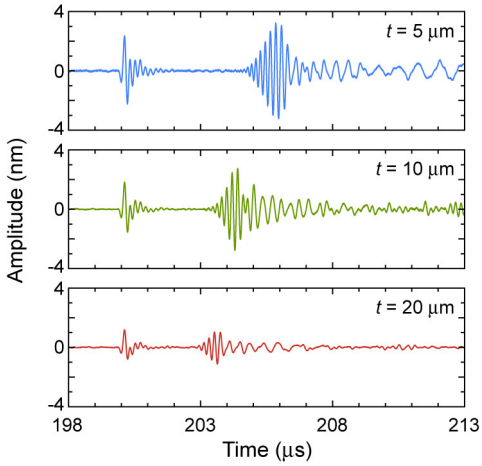

Figure 4. Waveforms detected on the diaphragm with the diameter of 10 mm. The delay between the first and the second wave depends on the thickness t of the diaphragm.

decreasing diameter. To account for the difference in behavior of two waves, the lateral profile of the acoustic pressure filed measured in the plane of the diaphragm is plotted in Fig. 6, where the output voltage of the hydrophone is normalized to the maximum value. The deviation of the acoustic pressure is expected over the diaphragm, ranging from 2 to 10%, depending on the diameter. However, as far as the first wave is concerned, a uniform pressure field p may be assumed over the diaphragm except for the vicinity of the edge because we observed the almost constant amplitude when the measurement beam was swept over the diaphragm, in which case the force applied on the diaphragm is given by $p\pi(D/2)^2$. The weight of the diaphragm m is given by $\sigma t\pi(D/2)^2$, where σ and t are the density and the thickness of the diaphragm, respectively. To calculate the force exerted on the diaphragm of a unit area per unit weight, we have $p/\sigma t$. Thus, the amplitude of the first wave becomes independent of the diameter. On the other hand, the acoustic pressure at the edge of the diaphragm is likely to play a critical role in the generation of the second wave because the lamb waves appear to emerge at the boundary between the metallic film and the substrate. As can be expected from Fig. 6, the diaphragm with smaller diameter can receive higher pressure at the edge; therefore, it is considered that the amplitude increases as the diameter is decreased. It is also important to mention here that as opposed to the first wave, the second wave drastically changes shape and the amplitude alternates between local extrema before reaching the maximum value at the center of the diaphragm when the measurement beam is scanned along the diameter. Such behavior of the second wave can be attributed to the interference of lamb waves. At the center of the diaphragm, constructive interference takes place because all lamb waves propagating from the circumference meet in phase due to the circular aperture. Therefore, we consider that the second wave has a larger amplitude compared with the first wave. In fact, the amplitude of the second

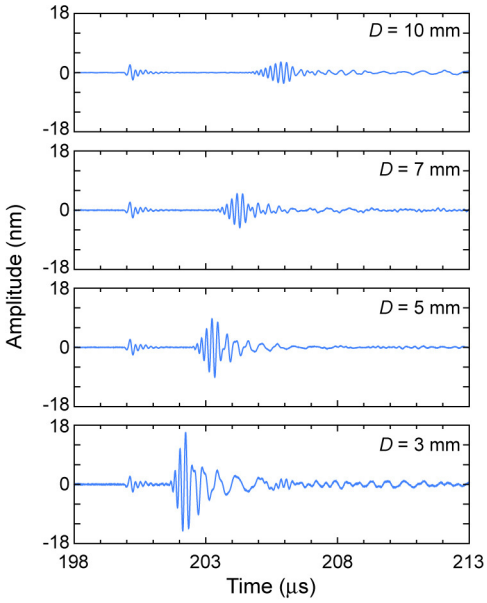

Figure 5. Waveforms detected on the diaphragm with the thickness of 5 μm. The delay between the first and the second wave depends on the diameter D of the diaphragm.

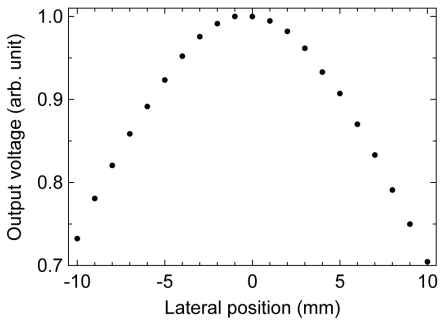

Figure 6. Lateral profile of the acoustic pressure field in the plane of the diaphragm.

wave becomes significantly larger than that for the first wave for the case of D = 3 mm, even though the pressure field is almost flat over the aperture (see Fig. 6).

Figure 7 shows the amplitude of the first wave as a function of acoustic pressure applied on the diaphragm. As described above, the first wave depends solely on the thickness of the diaphragm. The amplitude linearly increases with increasing applied pressure with slopes of 0.050, 0.036, and 0.021 nm/kPa for the thicknesses t of 5, 10, and 20 μm, respectively. A comparison between these slopes indicates that the pressure sensitivity can be improved by reducing the thickness of the diaphragm. The second wave, however, depends not only on the thickness but also on the diameter of the diaphragm as shown in Fig. 8, where the data taken from the 5-μm-thickness diaphragm is plotted as a function of applied acoustic pressure. As the diameter is decreased the slope of the curve becomes steeper; that is, the pressure sensitivity is improved. The pressure sensitivities obtained from the first and the second wave are summarized in Table 1. One can see that the sensitivities for the second wave are by a factor of 5 to 6 higher than those for the first wave when the diaphragm with the diameter of 3 mm is employed regardless of the thickness. It follows from these results that in addition to reducing the thickness of the diaphragm, the use of the second wave can more effectively improve the sensitivity.

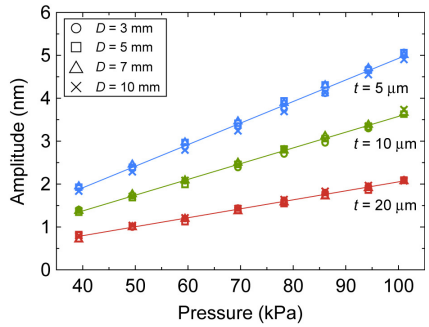

Figure 7. Amplitude of the first wave as a function of applied acoustic pressure.

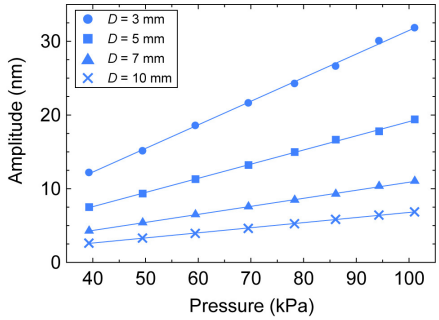

Figure 8. Amplitude of the second wave as a function of applied acoustic pressure. Data taken from the diaphragm with the thickness of 5 μm are shown.

Table 1. Sensitivity of the diaphragms for the first and the second wave.

		Sensitivity (nm/kPa)		
Wave	Diameter (mm)	t = 5 μm	t = 10 μm	t = 20 μm
First	3-10	0.050	0.036	0.021
Second	3	0.320	0.179	0.139
	5	0.192	0.127	0.085
	6	0.109	0.084	0.034
	10	0.069	0.061	0.023

4. Summary

We have experimentally evaluated the effects of the metallic diaphragm on the sensitivity characteristics of the optical ultrasonic sensor for under-sodium inspection. Incident ultrasonic pulse produces two distinct waves on the diaphragm: the first wave and the second wave. The former is initiated by the ultrasonic pulse that impinges directly on the diaphragm, and depends only on the thickness, while the latter results from the interference of lamb waves that propagates from the edge of the diaphragm, and depends both on the thickness and on the diameter. We have found that the amplitudes of both waves increase with decreasing the thickness of the diaphragm. Thus, the sensitivity can be improved by use of a thinner diaphragm. Moreover the second wave has larger amplitude than the first wave due to constructive interference at the center of the diaphragm. The experimental results show that the sensitivity for the second wave is by a factor of 5 to 6 higher than that for the first wave. This suggests that the weak ultrasonic wave can be amplified and detected with a higher sensitivity by using the second wave.

References

[1] H. Kawahara, M. Izumi, T. Suzuki, S. Nagai, M. Tamura, and S. Fujimori, “Development of Under-so dium Three-dimensional Visual Inspection Technique Using Matrix-arrayed Ultrasonic Transducer,” J. N ucl. Sci. Technol., Vol. 37, No. 9, pp. 769-779 (2000).

[2] A. Tagawa and T. Yamashita, “Development of Real Time Sensor for Under Sodium Viewer,” Proc. 1 9th Int. Conf. on Nuclear Engineering, ICONE19-43187 (2011).

[3] R. Mezrich, D. Vilkomerson, and K. Etzold, “Ultrasonic waves; their interferometric measurement and display,” Appl. Opt. Vol. 15, No. 6, pp. 1499-1505 (1976).

[4] M. Takeishi, F. Tsuri, Y. Koketsu, T. Kobayashi, H. Ito, H. Nishikawa, S. Sasaki, and J. Uchi, “Devel opment of Multiple Ultrasonic Transducer for Under Sodium Visual Observation,” Proc. 5th Int. Conf. Nuclear Engineering, ICONE5-2334 (1997).

Liquid sodium test results of an 8 element phased array EMAT probe for nuclear applications

Florian LE BOURDAIS[1], Thierry LE POLLÈS[1]
[1]CEA non destructive testing department, CEA LIST, Digiteo Labs, Bât. 565, PC 120, F-91191 Gif-sur-Yvette, France

E-mail address (corresponding author): florian.lebourdais@cea.fr

Sodium fast reactors pose a significant challenge to conventional non-destructive testing means. The high temperature, the liquid metal environment and the opacity of liquid sodium prevent inspections by optical means and make it necessary to design inspection devices and methods specifically for these conditions. During the last years, CEA LIST has been developing EMAT probes to close the gap with conventional ultrasonic probe performance dedicated to under-sodium ultrasound applications, thanks to the advantages of EMAT wave generation. The potential applications include: telemetry, defect detection in sodium immersed welds, defect sizing, and more recently using phased array probes, beam forming images and synthetic focusing.
In this paper we will present an 8 element phased array probe that was developed for use in liquid sodium. The design process for this probe will be presented, along with laboratory tests showing the probe's performances on aluminium blocks. Liquid sodium test results will also be presented, including beam steering imaging results. These results are compared to simulation results obtained with the dedicated EMAT computation module included in the CIVA software.

Keywords: Sodium fast reactors, ultrasonic testing, electromagnetic acoustic transducers, phased array, liquid sodium testing

Open Phased Array Ultrasonic Instrument for Advanced Applications and Full-Matrix Capture

Gavin Dao[1]
[1]*Advanced OEM Solutions, Cincinnati, USA*
Gavin.Dao@aos-ndt.com

Dominique Braconnier[2]
[1]*The Phased Array Company, West Chester, USA*
dominique@thephasedarraycompany.com

Abstract: Full-Matrix Capture (FMC) is a data acquisition technique used to collect valuable ultrasonic information that can be processed real-time using a popular method like Total Focus Method (TFM). Furthermore, combining such advanced techniques with a small and open platform phased array (PA) ultrasonic module provides new opportunities for both industry and research. Industrial applications benefit by creating custom solutions. A small form factor advanced PA module allows mounting the instrument on a scanner or robotic arm, shortening the transducer cable, which provides better signal quality, better integration, avoids cable failures and reduces cost. An open instrument allows customization of the software to create a dedicated software that can simplify user operation. Researchers benefit with an instrument that allows access to low-level parameters, raw waveforms and the freedom to control and interface to instrumentation with their choice software language.

Keywords: Non Destructive Testing; Phased Array; Ultrasound; Full –Matrix Caputre

High performance Equipment for the Steam Generator Tubes Inspections

Hervé GAC, and Rock Samson,
SG NDT Sarl
190 Route de la croix d'évieu
38110 St Clair de la tour
FRANCE

hgac@sgndt.com :

- Steam generator tubes of pressurized water reactors are designed as a pressure boundary between the Nuclear Power Plant Primary and Secondary sides. Unanticipated tubes degradations can cause some tubes leakages during the plant operation with the consequences of the plant shutdown.
- It's therefore mandatory to perform the steam generator tubes inspection in a regular basis with a reliable and high performances inspection equipment.
- In the last years the French Canadian Company **SG NDT** has developed a sophisticated equipment which allow the tubes inspection with high reliability.
- **SG NDT** is specialized in the development of Eddy Current Instrument, software and probes.
- **SG NDT**'s innovative solutions have been used in a variety of applications such as steam generators and standard tubes inspections;
- The technical staff at **SG NDT** pioneered the development of digital Eddy Current equipment. The heart of the product range are the Eddy Current equipment, the software and both standards and multicoils probes. The high probes sensitivity allows the detection and the follow up of all kind of tube degradations.
- The innovative probe design leads to a high life time which consequently leads to a reduction of the total occupation time of the Steam Generators during the outage.
- The first aim of this report is to describe a new Eddy Current method applied for the Steam generator tubes inspection.
- The second is to describe the equipment and probes technical features and to summarize their high performances.

Keywords: Eddy Current inspection, quality insurance, maintenance, nuclear safety.

Effect of NDE Signal Variation by Chemical Cleaning on the Steam Generator Tube Integrity for Axial Cracks

Yong Seok Kang[1], In Chul Kim[1] and Jai Hak Park[2]

[1,2]KHNP Central Research Institute, Daejeon, Korea

[3]Chung Buk National University, Cheongju, Korea

Abstract

Axial out diameter stress corrosion cracking (ODSCC) is one of the main degradation mechanisms in Korean nuclear steam generators. Eddy current testing is the most common non-destructive examination (NDE) technique used to inspect steam generator tubes. An extensive number of stress corrosion cracking was detected by the eddy current testing after chemical cleaning with alloy 600 mill annealed steam generator tubes. In the process of root cause analysis for the increased number of cracking, NDE signal variation of bobbin coil and rotating pancake coil signal are observed. It was found out that voltage amplitude and phase angle are slightly changed after chemical cleaning. Bobbin coil probability of detection is improved. Crack depth and length are became deepen and shorter but their change is not noticeable. Therefore, it seems reasonable to conclude that eddy current signal variation by the chemical cleaning is not affects directly to the structural integrity of steam generator tubes but affects to probability of detection of NDE technique.

Keywords: Axial ODSCC, Chemical cleaning, Eddy current testing, Probability of detection, Steam generator tube integrity

1. Introduction

The thin-walled steam generator tubing is an important part of a major barrier of the pressure boundary of reactor coolant system. Failure of steam generator tubes, which can be caused by cracking, will release radioactive materials to the secondary coolant system [1]. An axial out diameter stress corrosion cracking (ODSCC) is one of the main degradation mechanisms in steam generator tubes of Korean nuclear fleets. Hard chemical cleaning technique was performed to prevent progression of ODSCC by removing tube support plate deposit to one of the CE type steam generators with alloy 600 mill annealed tubes. After an application of steam generator chemical cleaning (SGCC), extensive number of axial ODSCC was observed at the tube support plate contact area. In the process of investigation for the root cause of the increased number of the ODSCC, NDE signal variation was observed. This paper discussed the effect of NDE signal variation by chemical cleaning on the steam generator tube integrity for axial out diameter stress corrosion cracking.

2. NDE Signal Variation Analysis

2.1 NDE system performance

Eddy current testing (ECT) is the most widely utilized NDE technique for determining the extent and location of steam generator tube defects and it has provided valuable information on tube defects. An electrically conducting nature of the inspected Alloy 600 tube will influence the voltage and current relationships in the coil. If some anomaly occurs in the tube then the electrical parameters will change in a characteristic manner [2]. Total system NDE performance uncertainties include technique and analyst variability and shall be established for detection and sizing. A probability of detection (POD) is a functional measure of the ability of an NDE system to detect degradation remaining in-service after an eddy current examination of the tube bundle. Various structural parameters such as maximum depth, average depth, length, voltage can be used as the independent variable depending on the needs of the tube integrity engineer [3].

2.2 Bobbin Coil Signal Variation

In order to compare the POD performance between before and after SGCC to axial ODSCC data sample of more than 500 tubes were obtained during in-service inspection to one of CE type steam generators with alloy 600 mill annealed tubes. From the comparison results of the bobbin coil inspection signals to axial ODSCC at tube support plates, variation of voltage amplitude and phase angle are observed. Fig.1 shows comparison results of bobbin voltage amplitude between before and after SGCC. After chemical cleaning bobbin peak to peak voltage amplitude, Vpp, is increased from 0.29 volts to 0.37 volts and maximum voltage amplitude, Vmax, also increased from 0.15 volts to 0.23 volts. Phase angle signals which were located within 0~20 degree and 140~180 degree are moved to 40~100 degree. Therefore the signal is change from horizontal to vertical direction. Both changes are influenced to improve bobbin POD.

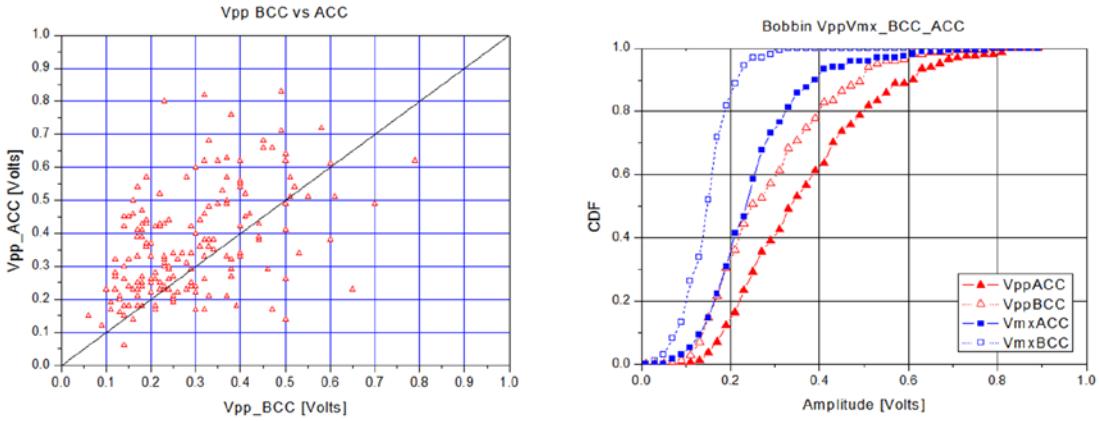

Figure 1 Bobbin voltage amplitude between before and after SGCC to axial cracks

2.3 RPC Signal Variation

Some sample of rotating pancake coils (RPC) data, which confirmed as an axial crack, was analyzed correlation phase angle and amplitude between before and after SGCC. Comparison result is shown in figure 2. Phase angle and amplitude shows subtle changes. Amplitude median increased from 0.19 volts to 0.21 volts. RPC amplitude is connected to crack depth. Figure 3 shows measure NDE maximum depth and length distribution of the axial ODSCC. After chemical cleaning, NDE measured maximum depth is increased about 2.1% of tube through wall. In the other hand, the maximum length is decreased. The extent reduction is just 0.28mm (0.011 inch). Even though the shape of crack became deeper and shorter after chemical cleaning, the extent change is negligible.

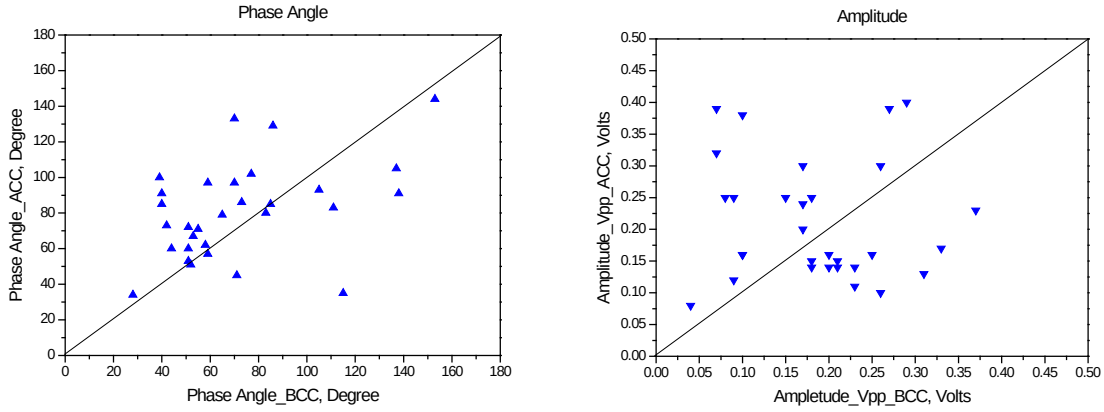

Figure 2 RPC phase angle and voltage amplitude between before and after SGCC to axial cracks

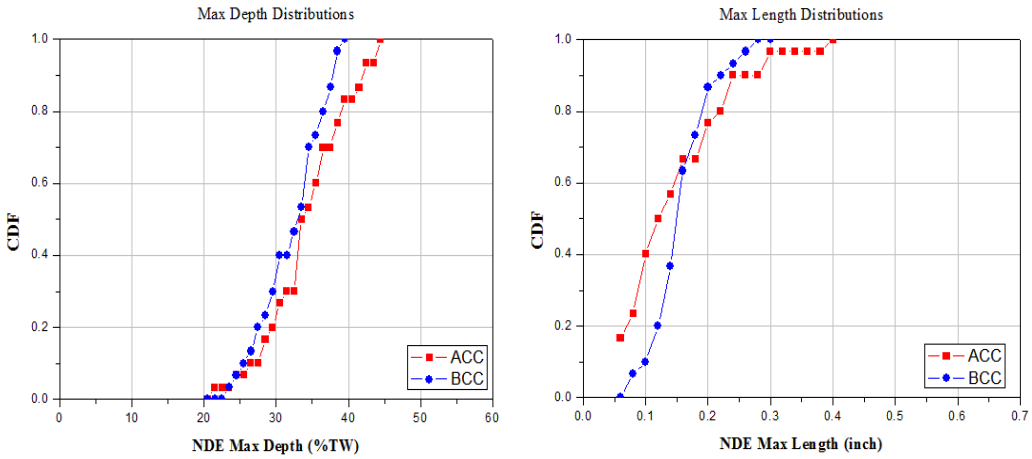

Figure 3 Maximum depth and length distribution between before and after SGCC to axial cracks

3. Discussion

From the investigation on bobbin and RPC signals for both of before and after chemical cleaning to axial ODSCC, variation of amplitude and phase angle was observed. It is well known that bobbin voltage amplitude and phase angle variation influence on probability of detection (POD). The POD provides an estimate of undetected tube degradation left in-service after steam generator examination and is used as an input to deterministic or probabilistic tube bundle integrity models to establish tube bundle burst probabilities and leak rate [4]. The flaw sizing is also used as an input to steam generator tube bundle integrity models for quantitative tube burst and leakage assessments. Even though crack shape became shorter and deeper by the NDE signal variation, their extent change is not noticeable. It seems reasonable to conclude that eddy current signal variation by SGCC is not directly affected to structural integrity performance criteria but it is influenced to improve POD. The increased detectability of cracks reduces the potential for ODSCC to lead to failure of structural performance criteria. Therefore it will be helpful to ensure condition monitoring structural performance criteria will not be affected from signal variation with the chemical cleaning but it will be affect to the over the length of the upcoming operating interval due to the improvement of POD.

4. Conclusion

Hard chemical cleaning technique is performed to one of CE type steam generators with alloy 600 MA tubing in Korean nuclear fleet. Variation of eddy current signal was observed from the comparison of both before and after chemical cleaning to the sample tubes. Increase of bobbin voltage amplitude and erection of phase angle were observed and it is influenced to improve POD. Crack shape such as maximum depth and length became deepen and shorter after chemical cleaning but their extent change is negligible. This goes to the conclusion that the variation of NDE signal by steam generator chemical cleaning affects to the system POD but may not have a strong correlation with the structural integrity margin requirements.

References

[1] US NRC Regulatory Guide 1.83,"Inservice inspection of pressurized water reactor steam generator tubes",(1975)

[2] E.E. Chick, "NDE and Mechanical removal of sludge in PWR steam generators", Vol. 1, EPRI NP-5563, pp.2-10~2-11 (1988)

[3] H. Cothron,"Steam generator integrity assessment guidelines", EPRI 1019038, pp.4-1 (2009)

[4] S. Swilley, "Pressurized Water Reactor Steam Generator Examination Guidelines", EPRI 1013706, pp.I-9 (2007)

Advanced Inspection Technique for Tube Seal Welds of Steam Generators

H. Yonemura, N. Kawai, M. Morikawa, H. Murakami, T. Hanaoka, T. Tsuruta, K. Kawata, M. Kurokawa

Mitsubishi Heavy Industries, Ltd., 1-1, Wadasaki-cho 1-chome, Hyogo-ku, Kobe JAPAN

E-mail address: takayoshi_tsuruta@mhi.co.jp

Keywords: Eddy Current Testing, Radiography, Steam Generator, Tube Seal Weld

Mitsubishi Heavy Industries (MHI) has total inspection techniques for Steam Generators (SG) during SG fabrication process and each of them is optimized according to characteristics of applicable objective based on careful consideration and broad experience. In this presentation, MHI proposes our new solution for inspection of SG tube seal welds which is consist of the important boundary between primary and secondary sides in Pressurized Water Reactor (PWR) with advanced inspection technique.

In general, Penetrant Testing (PT) and Helium Leak Testing (HLT) are applied for SG tube seal welds during SG fabrication process. These techniques are effective to detect surface breaking defects or leak pass, but not effective to detect sub-surface defects in seal welds. Therefore, MHI has developed Advanced Inspection Technique combined with Eddy Current Testing (ECT) and Radiography (RT) in order to achieve higher quality of SG tube seal welds.

ECT Technique makes it possible to examine many seal welds in a short time and to detect not only surface breaking defects but also sub-surface volumetric defects. Actually, some noise caused by geometry change of SG tube seal welds is observed. The configuration of ECT coils was optimized and The state-of-art filtering technique was developed in order to reduce noise signals and improve Signal to Noise Ratio. In addition, MHI has developed accurate RT technique to detect volumetric defects and support ECT evaluation. After careful consideration, MHI decided to adopt X-Ray technique because of more suitable image and more simple operation compared with gamma ray technique. MHI also considered possibility of applying Digital Radiography Technique.

As mentioned above, MHI has developed Advanced Total Imaging System for SG tube seal welds by combination of ECT and RT. MHI has already applied this state –of-art technique to actual inspection during SG fabrication process and MHI achieved higher quality of SG seal weld. This technique can be applicable to In-Service Inspection (ISI) and contributes safety operation of nuclear power plants.

AUTOMATED CORRELATION OF HISTORICAL WITH PRESENT EDDY CURRENT INSPECTION DATA USING HDC® FOR UNDERSTANDING CHANGE IN STEAM GENERATOR TUBING CONDITIONS AND VISUAL FLAW MORPHOLOGY

Tom O'Dell[1], Tom Bipes[1], Kevin Newell[1]
[1]Zetec Inc. , Snoqualmie Wa, USA

E-mail address: todell@zetec.com

In nuclear power plant primary loop steam generator tubing inspections current data is compared with historical data to understand change in signals. This historical comparison process has been a manual effort requiring the analysis to independently recall both sets of data and compare results. Due to the time consuming effort required to manually compare, this action could only be partially performed on the data and the analysis of the change limited to measurement values only.

A new technology called HDC has been developed where three independent data files acquired during different inspections can be automatically correlated, displayed and compared for change analysis. This correlation is applied to all active frequency channels of bobbin data allowing analysis of change to be performed on any available frequencies as well as process channels. Typically the data files represent the current inspection, prior inspection, and baseline inspection data. All three data files are overlaid in a commonly calibrated to provide the analyst a visual to see morphology of change and make comparative measurements.

In addition, HDC can process a "delta channel" of change for each of the reference inspections compared to the current inspection. This delta channel provides a strong visual of change, suppressing common signals and allowing the analyst to focus on change signals only. This approach does not depend on applying different analysis methodologies based on regions of interest as the correlation process is only concerned in the basic signals in the available channels used in the comparison. This delta channels can also be used in an automated process for analysis such as RevospECT® where the delta signals can be automatically analysis and reported on.

The HDC technology can provide value to the inspection at multiple levels. In Manual Production HDC provides the analyst with additional tools to understand change and morphology of signals. In Automated Production, the delta channel can be used for detection and reporting of change, including new anomalies. In the Resolution process, the analysts can use the correlated overlaid signals to address history and/or determine the resolution of signals based on morphology. In the Independent Review process, the analyst can use the correlated overlaid data channels to confirm the reporting and/or use the delta channel to scan for potentially missed indications.

This paper will provide greater detail on these topics as well as examples of field data showing the strong visual perspective available.

Keywords: Eddy Current, Steam Generator, Inspection, Analysis, Automated Analysis.

Effect of vibration reflection on vibrothermography

Wonjae Choi[1*], Manyong Choi[1] and Jeounghak Park1

[1]Center for Safety Measurement, KRISS, 267 Gajeong-Ro, Yuseong-Gu, Daejeon 305-340, Rep. of Korea

* E-mail address(corresponding author) : w.choi@kriss.re.kr

Vibrothermography has been increasingly studied for Non-Destructive Evaluation. In this method, vibration energy is given to a structure, which is transferred into heat energy at defects, and infra-red camera is used for detecting the heat from the defects. Laboratory experiments are often conducted with samples sizing a few times input wavelength, and then the wave reflection from the sample boundaries inevitably influences the heat generation mechanism. However, what is inspected in a real industrial field is often a large structure sizing in the order of ten times the wavelength or more, and then the inspection results will be different from the experimental ones in laboratory. This paper studies the effect of sample size on vibrothermography. Numerical simulations are conducted with a group of sample sizes and their differences are discussed.

Keywords: Vibrothermography, sample size, numerical simulation.

Comparison of PZT and PMN-PT based sensors for detection of partial discharge at electric transformer

Geonwoo Kim[1,2], Mu-Kyung Seo[3], Namkyoung Choi[1,2],Ki-Bok Kim[1*], Jae-Ki Jeong[4], Hong-Sung Kim[4] and Minsu Park[5]
[1]Korea Research Institute of Science and Standards, 267 Gajeong-ro, Yuseong-gu, Daejeon 305-340, Republic of Korea
[2]Dept. of Science of Measurement, University of Science & Technology, 217 Gajeong-ro, Yuseong-gu, Daejeon, 305-350, Republic of Korea
[3]Dept. of Mechanical Engineering,Sungkyunkwan Univ., 2066, Seobu-ro, Jangan-gu, Suwon-si, Gyeonggi-do, Republic of Korea
[4]Hanbit EDS. CO., Ltd , 44-10, Techno 10-ro, yuseong-gu, DaeJeon, Republic of Korea
[5]Kepco plant service & Engineering Co.,Ltd, 211, Munhwa-ro, Naju-si, Jeollanam-do, Republic of Korea

E-mail address(corresponding author) : kimkibok@kriss.re.kr

This paper describes the fabrication and comparison of PZT and PMN-PT basedsensors to detectPD (partial discharge)signalatelectric transformer. As a front matching material for ultrasonic PD detecting sensor between a surface of external metal wall ofelectrictransformer and piezoelectric materials (PZT and PMN-PT), the alumina ceramic (Al_2CO_3) was selected. Because ofthe wideband characteristics of PD, optimal back acoustic materials of both sensors were fabricated. To compare the performance of the developed both PD sensors, experimental setup consisted of the developed sensors, high voltage supplier generating the PD within test block and oscilloscope. From the experimental results, PMN-PT based sensor showed better performance than PZT based sensor.

Keywords:Partial discharge, PZT, PMN-PT, Electric transformer

New improved piezoelectric detection method to measure ultrasonic nonlinearity parameters for incipient damages in nuclear engineering materials

To Kang[1,2], Jeong K. Na[3], Sung-Jin Song [2], and Jin-Ho Park [1]
[1]Korea Atomic Energy Research Institute, 111, Daedeok-daero 989beon-gil, Yuseong-gu, Daejeon, 305-353 Rep. of Korea; [2]Dept. of Mechanical Engineering, Sungkyunkwan Univ., 2066, Seobu-ro, Jangan-gu, Suwon-si, Gyoenggi-do, 440-746, Rep. of Korea; [3]Wyle Laboratories Inc., 2700 Indian Ripple Road, Beavercreek, OH 45440, USA

E-mail address (corresponding author): tkang@kaeri.re.kr

When ultrasonic nonlinearity parameter values are measured to determine incipient damage levels in an engineering metal alloy, a conventional piezoelectric detection method is commonly used. Piezoelectric detection methods are simple and can be adopted for an industrial field measurement during which data needs to be collected at a high rate of speed due to restrictions on accessibility and availability of components or structures at sites. Despite of the simplicity with the measurement procedure, one of the biggest drawbacks of conventional piezoelectric detection methods is the possibility of getting a high level of measurement uncertainty caused by receiving transducer's low sensitivity to the second harmonic component of received signals. In this paper, a newly developed piezoelectric detection method is introduced to overcome the intrinsic weakness of conventional piezoelectric detection methods. This improved system employing a couple of additional high Q-value band-pass filters and low-noise preamplifiers is demonstrated to show a significantly lower uncertainty in the nonlinearity parameter measurement. It is also demonstrated that absolute nonlinearity parameter values can be determined without having a tedious calibration procedure otherwise required with the capacitive detection or laser interferometry method. In order to validate the effectiveness of new improved piezoelectric detection method, nonlinearity parameter measurements have been made on a titanium alloy that is widely used for components of nuclear power plant condenser tubes and heat exchangers due to its high corrosion resistance and light weight.

Keywords: Nonlinearity parameter, Second harmonic signals, Improved piezoelectric detection, Titanium alloy

Application of Fiber-optic Sensors to CFRP Pressure Tanks for Internal Strain Monitoring

Donghoon Kang[1]

[1]Advanced Materials Research Team, Korea Railroad Research Institute, 176, Cheoldo Bangmulgwan-ro, Uiwang-si, Gyeonggi-do, 437-757, Republic of Korea

Abstract

There are growing concerns on carbon fiber reinforced plastics (CFRP) due to their high specific strength and light weight for applications on many kinds of structures including aerospace structures like satellites, infrastructures like bridges, and special purpose structures requesting high level of engineering performances. Among those structures, CFRP pressure tanks are recently promising as an alternative of metal based pressure tanks that are being widely applied to many types of gas tanks for decades. In this paper, fiber-optic sensors, fiber Bragg grating (FBG) sensors in particular, are applied to a CFRP pressure tank with embedment in order to measure internal strains during its in-situ operation. The tank is fabricated using filament winding processes and the pressurizing test is conducted with water up to 1,000 psi. All data from embedded FBG sensors and attached electric strain gauges (ESGs) are acquired to a laptop computer in real-time. Through the test, the applicability and validity of FBG sensors on CFRP pressure tanks are evaluated by comparing the experimental results from FBG sensors with those from both ESGs and FEM analysis. In conclusion, FBG sensors embedded into CFRP pressure tanks can successfully measure internal strains at both domes and cylinders and the results show good agreements with those from FEM analysis as well as ESGs. This means that FBG sensors can be one of good solutions to monitor internal strains of many kinds of pressure tanks, which are generally under severe environmental conditions like very high internal pressures and ultra-low temperatures, including CFRP pressure tanks by embedment.

Keywords : Pressure tanks, CFRP, Fiber-optic sensors, FBG, Internal strain

1. Introduction

Recently, the use of filament wound pressure tanks is increasingly prevalent because of high specific strength and specific stiffness over their metal counterparts, as well as excellent corrosion and fatigue resistance. The main applications of filament wound pressure tanks are fuel tanks that are a kind of composite structures and so have the complexity in damage mechanisms and failure modes. Most of the conventional damage assessment and nondestructive inspection methods are time-consuming and are often difficult to implement on hard-to-reach parts of the structure. For these reasons, a built-in assessment system must be developed to monitor the structural integrity of critical components constantly.

Fiber optic sensors (FOSs) have shown a potential to serve as real time health monitoring of the structures. They can be easily embedded or attached to the structures and are not affected by the electro-magnetic field. Also, they have not only the flexibility in the selection of the sensor size but also high sensitiveness. Recently, fiber optic sensors have been introduced to composite structures (Kang et al. 2000, Park et al. 2000). Among many fiber optic sensors, FBG sensors based on wavelength-division-multiplexing technology are attracting considerable research interest and appear to be ideally suitable for structural health monitoring of smart composite structures. FBG sensors are easily multiplexed and have many advantages such as linear response, absolute measurement, and etc. Among many researches on filament wound pressure tanks, only a few were performed using FBG sensors.

The temperature and strains were measured during the cure and ingress/egress methods for a standard testing and evaluation bottle (STEB) were investigated using FBG sensors. Through a water-pressurizing test, experimental data were compared with the results of ESGs and finite element analysis results (Foedinger et al. 1999). The unbalanced strain was calculated from the wavelength difference of a pair of FBG sensors during a water-pressurizing test (Lo et al. 2000). However, it was impossible to measure absolute strains at each sensor position. An FBG sensor was embedded between the hoop layers and used for measuring the internal pressure of the tank through a water-pressurizing test form the wavelength shift of an FBG sensor (Degrieck et al. 2001). The lack of sensors limited strain measurements onto local positions. In addition, they conducted a 3-point bending test of carbon/epoxy composite laminate. Using attached 32 FBG sensors on the filament wound pressure tank as 4 channels, the strains of a filament wound pressure tank were measured through a water-pressurizing test (Kang et al. 2002). From the above literatures, it can be found out that only a few FBG sensors were used when embedding sensors into the pressure tank and relatively a large number of FBG sensors were used when attaching sensors on the surface. Moreover, problems on FBG sensor signals, especially peak split induced by

birefringence and strain gradients occurred in a dome part during a water-pressurizing test. Therefore, it is necessary to monitor the strains of a filament wound pressure tank using a number of embedded FBG sensors in real time without peak split problems.

In this paper, the strains of a filament wound pressure tank were monitored using a number of embedded FBG sensors in real time during the water-pressurizing test and the strain results measured by FBG sensors were compared with those by ESGs and FEM analyses.

2. Fabrication of filament wound pressure tanks

2.1 Fabrication of FBG sensor lines

Among several fabrications of FBG sensors, fabrication using a phase mask, devised by (Hill et al. 1993), is currently the most prevalently employed approach because it is suitable for mass production and is simple to handle. However, the grating parts of an FBG sensor can be easily broken by transverse stress applied on the optical fiber. Due to the reason, FBG sensors embedded into a filament wound pressure tank are easy to fail because of the applied tension in reinforcing fibers. In this paper, a revised fabrication process of FBG sensors that is focused on the improvement of sensor survivability during the embedment of FBG sensors is introduced. For this purpose, several processes concerning the fabrication and the embedment are revised.

First, an optical fiber used for fabricating an FBG was substituted to a photosensitive optical fiber (PS1250/1500, Fibercore) because the hydrogen loading process of optical fibers decreased the mechanical strength of them. Second, a sensor line with multiple sensors was fabricated not by the splicing between FBG sensors, but by a simultaneous fabrication of FBG sensors in single optical fiber. Generally, optical fibers connected by arc-fusion splicing showed strength degradation to the transverse stress. Third, as a reinforcement of FBG sensors during the embedment, the protection with an adhesive film was conducted as a 2nd protection process after recoating with acrylate. Lastly, optical fibers were extracted from a filament wound pressure tank towards both directions of a sensor line. It was because optical fiber lines were the weakest at the ingress/egress point after the end of curing process. Figure 1 shows an FBG sensor line fabricated by a revised fabrication process mentioned in the above paragraph.

Figure 1. An FBG sensor line protected with a revised process

2.2 Filament wound pressure tank with embedded FBG sensor lines

A filament wound pressure tank consists of a forward dome, an aft dome, a cylinder, and a skirt for joining with other structures. In this paper, a tank is fabricated by the wet winding process using a 4-axis filament winding machine controlled by a computer. The winding tension was 1.5kg/end and the bandwidth of hoop and helical layer was 10.0, 10.5(*mm*) for 5-ends, respectively. The cylinder part includes a 3-body helical layers and 7-body hoop layers so that the sequence is $[(\pm 27.5)_3]_T$ for helical layers and $[90_2/(\pm 45)_2/90_3]_T$ for hoop layers denoting from inner to outer layers. Figure 2 shows the embedded sensor lines during the fabrication process.

Seven channels of FBG sensors were embedded into a tank. The channel 1(Ch1) and channel 2(Ch2), each has 3 FBG sensors, were embedded between the layer 1 and 2 at aft dome and the layer 2 and 3 at forward dome, respectively. The channel 3(Ch3), which has 3 FBG sensors, was embedded into axis direction of a cylinder part and 3 more lines were used as spare channels (Ch5, 6, 7) because FBG sensors are the weakest when they are embedded perpendicular to the reinforcing fiber like the case of a Ch3. The channel 4(Ch4), which has 4 FBG sensors, was embedded into hoop direction of a cylinder part.

After embedding each sensor line, embedded positions of FBG sensors were measured accurately using a laser pointer. The filament wound pressure tank with embedded FBG sensor lines were cured under rotating condition in the curing cycle ; 80°C(1hr)→120°C(1hr)→150°C(3hrs) in an oven.

Figure 3 shows the configurations of a tank including sensor positions. From the Fig. 3, ‘F’ denotes FBG sensor and ‘E’ denotes ESG. And, the figure following ‘F’ means the channel number.

(a) aft dome – Ch1 (b) forward dome – Ch2

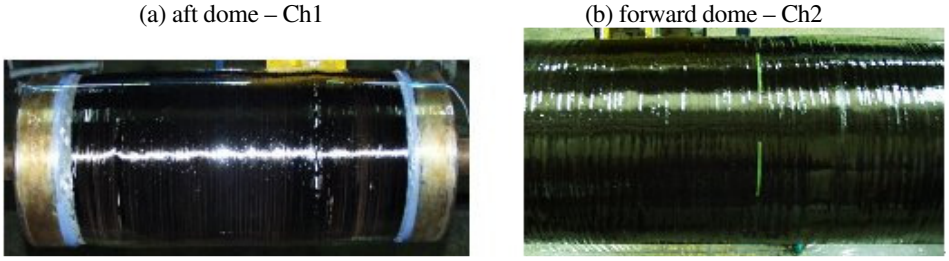

(c) cylinder : axis dir. – Ch3, 5, 6, 7 (d) cylinder : hoop dir. – Ch4

Figure 2. Embedded FBG sensor lines during the fabrication

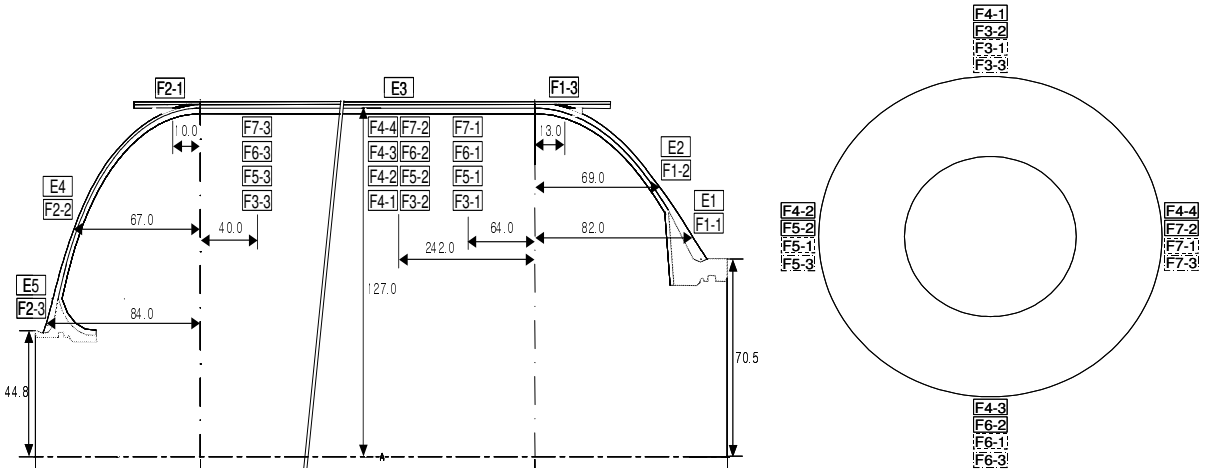

Unit : [mm]

Figure 3. Configurations and sensor positions

When embedding FBG sensors into a filament wound pressure tank, especially a dome part, the signal stability of FBG sensors is very important for the strain measurement because there exists a strain gradient in a dome part due to its geometric shape during the water-pressurizing. However, the effects of strain gradient decrease as the grating length of an FBG sensor decreases (Kang et al. 2005). In addition, FBG sensors with shorter grating lengths are more effective when they are embedded perpendicular to the reinforcing fibers. For the reason, two kinds of grating lengths were used such as 10*mm* and 5*mm*. All sensors except those of a Ch4 were fabricated as FBG sensors with gage length of 5*mm*.

When the STEB was completely fabricated, 100% (22 of 22) of sensors survived through the whole fabrication processes such as embedding, curing, and mandrel separation.

3. Water-pressurizing test

After fabricating a pressure tank, a water pressurizing test of STEB was performed to verify the tank itself. Figure 4 depicts the experimental setup for the strain monitoring of a filament wound pressure tank during hydrostatic pressurization. The tank was pressurized at intervals of 100 psi up to 1,000 psi using a rotary pump. The strain data from the FBG sensors, ESGs, and a pressure transducer were acquired and processed by a laptop computer in real time.

As shown in Fig. 3, 4 ESGs were attached on the dome surfaces at the same locations of embedded FBG sensors, aligned to the helical winding direction. On the cylinder, only 1 ESG (E3) was attached in the hoop winding direction, i.e., the circumferential direction of cylinder. The signals of the FBG sensors, strain gauges, and a pressure transducer were

acquired simultaneously by computers, processed and displayed by a signal-processing program written in LabVIEW® software. The specifications of used FBG sensor systems are shown in Table 1.

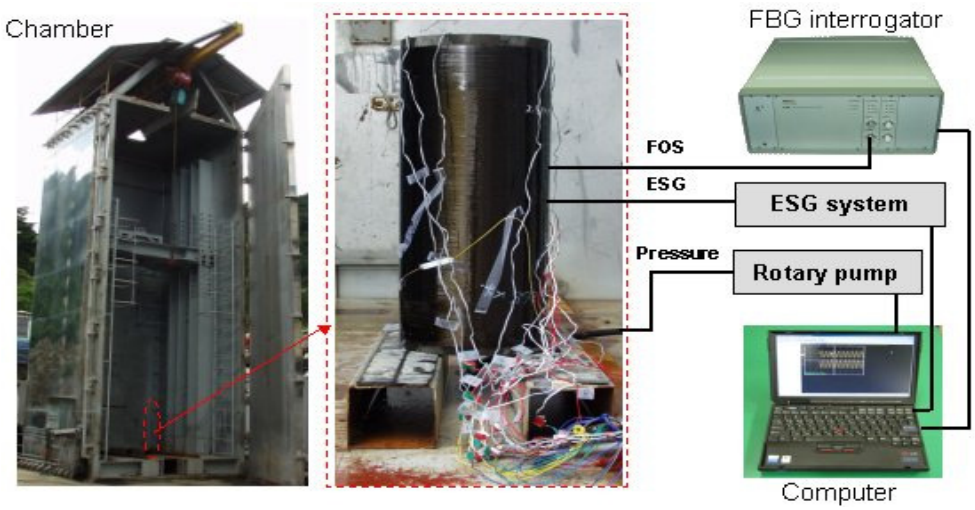

Figure 4. Experimental setup of water-pressurizing test

Table 2. Specifications of an FBG interrogator

LS-7000 FBG Interrogator (FiberPro Co.)	
Wavelength range	35 nm (1530 ~ 1565 nm)
Average output power	3 mW
Resolution	< 2 pm
Measurement speed	200 Hz
# of channels	8
Temperature range	10 ~ 40 °C

4. Finite element modeling

To compare the strain results measured by FBG sensors and ESGs, finite element analyses on STEB were done by a commercial code, ABAQUS. In this research, the 3-D layered solid element was utilized and the boundary condition was considered as cyclic symmetric. Figure 5 shows the detailed FEA model of STEB realized by a commercial code, PATRAN, and the material properties of T700/Epoxy used in the analysis are as follows.

$$E_1 = 134.6\ \text{GPa},\ E_2 = 7.65\ \text{GPa},\ G_{12} = 3.68\ \text{GPa},\ \nu_{12} = 0.3,\ \sigma_f = 2290\ \text{MPa},\ \sigma_t = 31.8\ \text{MPa},\ S = 75.8\ \text{MPa}$$

The modified Hashin's failure criterion was selected and applied to progressive failure analysis. For the purpose of failure analysis, a subroutine, USDFLD of ABAQUS ver 6.3 was coded to define the change of mechanical properties due to failure.

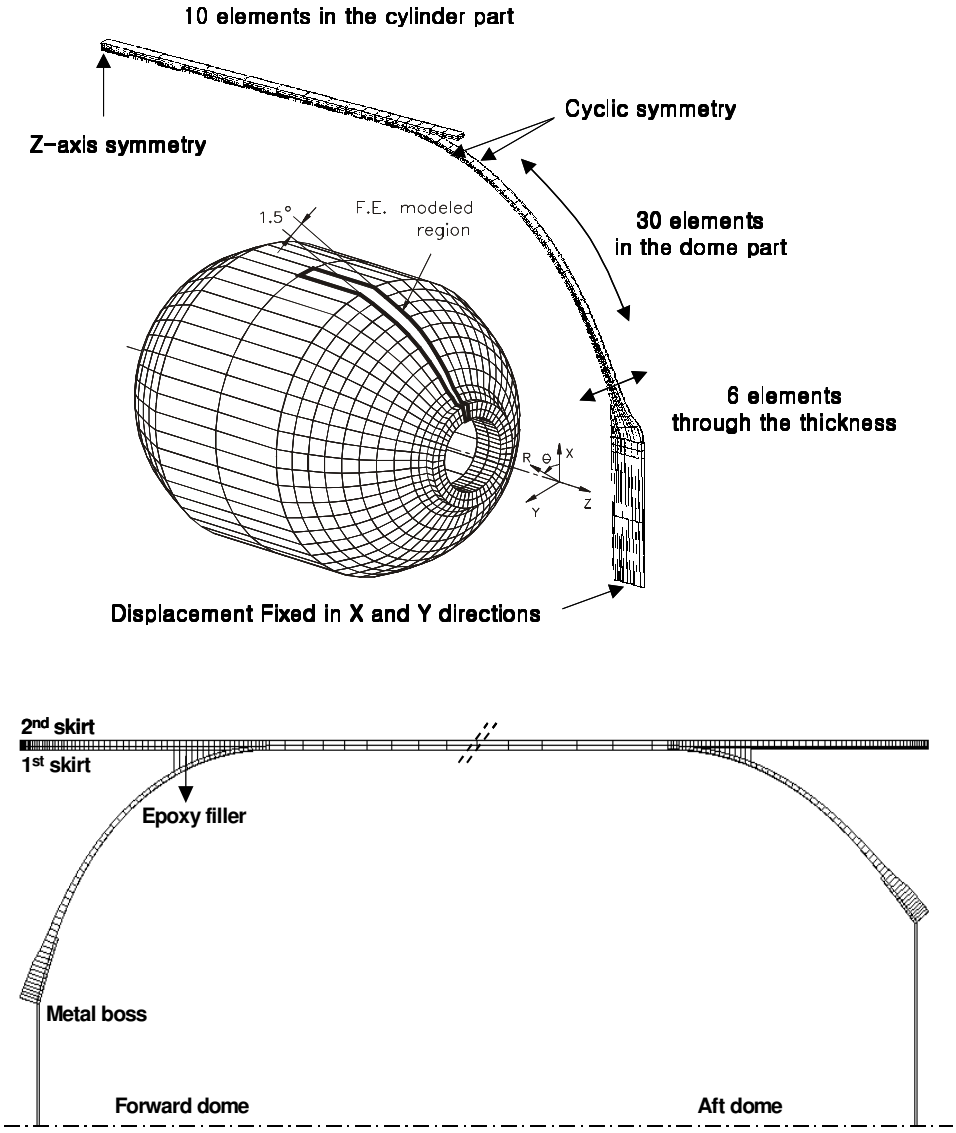

Figure 5. The FEA model of STEB

5. Results and discussions

Figure 6 shows strain results measured by FBGs and ESGs in an aft dome. Strains measured by two FBG sensors showed a good agreement with those by ESGs and the strain measured by each FBG sensor showed a good linearity with the increase of pressure.

In case of a forward dome, as shown in Fig 7, strains measured by two sensors showed a little higher difference than the case of an aft dome. The differences in strains measured by FBG sensors and ESGs may be occurred by a mismatch of attaching angles and locations between them. Also, these differences may be caused by the slippage of an embedded FBG sensor line during the curing process due to resin flow. This can be occurred more easily in a forward dome than in an aft dome because the gradient of a forward dome is steeper.

Figure 8 shows the strain results of FBGs and an ESG (E3) in a cylinder part. Compared with an ESG, two FBG sensors showed a little higher strains and the others lower strains though all sensors showed a good linearity. The reason seems that there occurred a small angle between optical fiber and reinforcing fiber during embedding the Ch4.

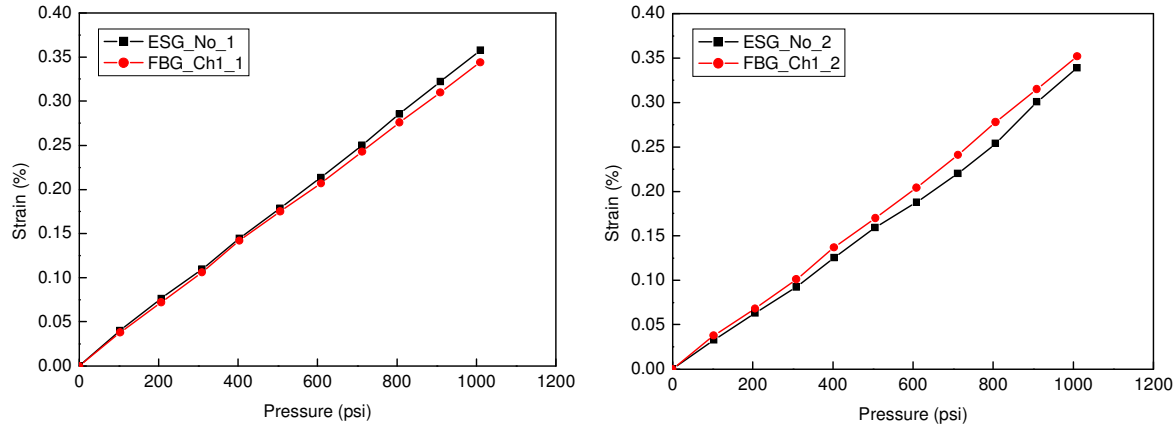

Figure 6. Strain results of FBG and ESG – aft dome

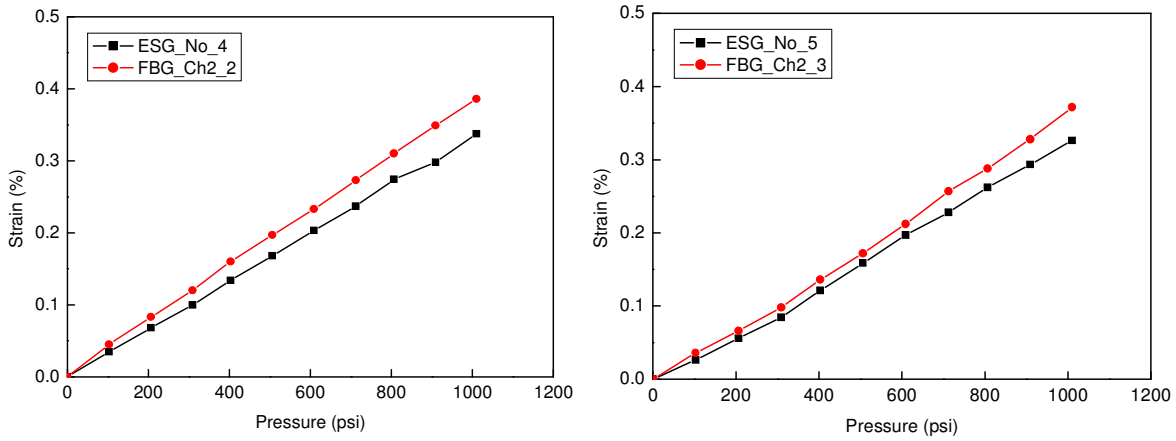

Figure 7. Strain results of FBG and ESG – forward dome

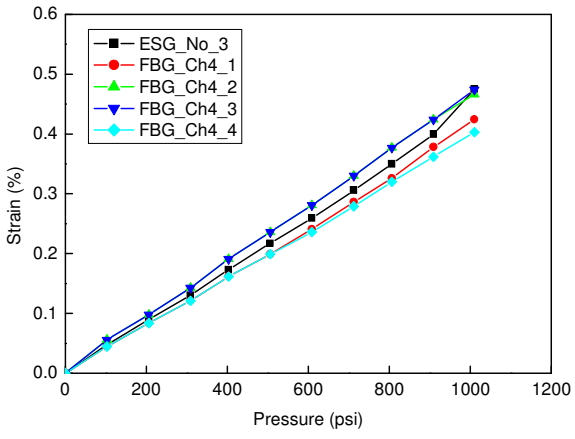

Figure 8. Strain results of FBG and ESG – cylinder part

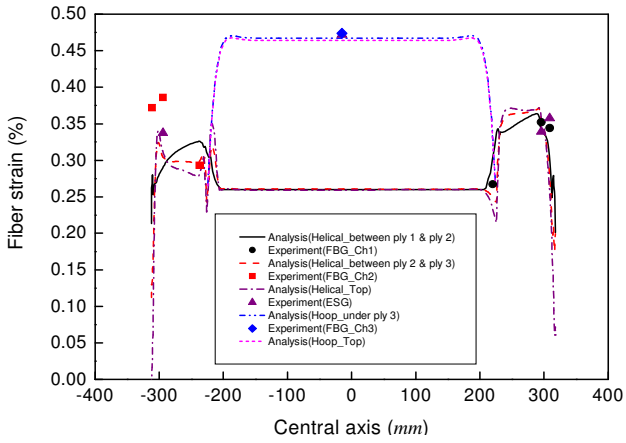

Figure 9. Strain results of FBGs, ESGs and FEA at 1,000 psi

Figure 9 shows the strain results measured FBGs, ESGs, and FEA simultaneously at 1,000 psi. The results from FBG sensors were compared with those from ESGs that were attached at the same longitudinal locations with FBG sensors. Both strain results were also compared with those of FEM analyses, which were indicated as lines in Figure 9.

Considering only the FEA results, helical layers of forward dome and aft dome showed a large difference in strains between inner and outer layers. However, there was little difference in strains between inner and outer layers at cylinder part.

In Figure 9, the strains measured by FBGs and ESGs were similar at hoop layers of cylinder part and also showed a good agreement with the FEA results, while the results from FBGs and ESGs at both domes showed a little large difference with each other. As shown in Figure 9, strain changes in both dome parts are very steep in axis direction. Thus, a small error in sensor position can cause large difference in strain results. Nevertheless, the tendency of strain results seems to be agreeable. The errors occurred in this research can be decreased if FBG sensors can be embedded more accurately without any slippage.

Nevertheless, in Figure 9, it is very noticeable that FBG sensors can measure the strain at the positions where the measurement is impossible with ESGs, for example, between the layers of dome and cylinder, the junction part. And, this is very important advantage of FBG sensors, especially in a filament wound pressure tank because it has a severe change in strains between layers of dome part.

6. Conclusions

FBG sensors totaled 22 in 7 channels were embedded into the domes and cylinder parts of a filament wound pressure tank in order to measure the strains in real time during hydrostatic pressurization. When embedding multiplexed FBG sensor lines into a filament wound pressure tank, some fabrication steps with sensor line protection were introduced to increase the survivability of FBG sensors.

From the experiment, the strain data from FBGs showed close agreement with the data from ESGs and the results were also verified by the finite element analyses. Through the results, it was successfully demonstrated that the FBG sensors could be useful for the internal strain monitoring of filament wound structures that require a large number of sensor arrays.

References

[1] H. K. Kang, J. W. Park, C. Y. Ryu, C. S. Hong, and C. G. Kim, "Development of fibre optic ingress/egress methods for smart composite structures," Smart Materials and Structures, 9(2): 149-156 (2000)

[2] J. W. Park, C. Y. Ryu, H. K. Kang, and C. S. Hong, "Detection of buckling and crack growth in the delaminated composites using fiber optic sensor," Journal of Composite Materials, 34(19): 1602-1623 (2000)

[3] R. C. Foedinger, D. L. Rea, J. S. Sirkis, C. S. Baldwin, J. R. Troll, R. Grande, C. S. Davis, and T. L. VanDiver, "Embedded fiber optic sensor arrays for structural health monitoring of filament wound composite pressure vessels," Proc. Of SPIE, 3670: 289-301 (1999)

[4] Y. L. Lo, P. H. Sung, H. J. Wang, and L. W. Chen, "Pressure vessel wall thinning detection using multiple pairs of fiber Bragg gratings for unbalanced strain measurements," Journal of Nondestructive Evaluation, 19(3): 105-113 (2000)

[5] J. Degrieck, W. De Waele, P. Verleysen, "Monitoring of fibre reinforced composites with embedded optical fibre Bragg sensors, with application to filament wound pressure vessels," NDT&E International, 34: 289-296 (2001)

[6] H. K. Kang, J. S. Park, D. H. Kang, C. U. Kim, C. S. Hong, and C. G. Kim, "Strain Monitoring of Filament Wound Composite Tank Using Fiber Bragg Grating Sensors," Smart Materials and Structures, 11(6): 848-853 (2002)

[7] K. O. Hill, "Bragg gratings fabricated in monomode photosensitive optical fiber by UV exposure through a phase mask," Applied Physics Letters, 62(10): 1035-1037 (1993)

[8] D. H. Kang, S. O. Park, C. S. Hong, and C. G. Kim, "The signal characteristics of reflected spectra of fiber Bragg grating sensors with strain gradients and grating lengths," NDT&E International 38(8): 712-718 (2005)

Computation of inspection parameters for complex component using CIVA simulation tools

Arnaud VANHOYE[1], Sébastien BEY[1],Séverine PAILLARD [1] and Stéphane LE BERRE [1]

[1]Commissariat à l'Energie Atomique,Saclay, France
Phone: +331 69 08 19 30, Fax: +33 1 69 08 75 97; e-mail: arnaud.vanhoye@cea.fr

Abstract

The inspection of complex component assumes the choice of an adapted transducer, and its supervision along an adequate trajectory. Flexible probes are generally the most suited probes for this application, since they can fit the wavy surface of the component and perform an electronic drive of the acoustic beam. However, their supervision requires the computation of proper delay laws that directly arise from the trajectory and focusing parameters. In case of complex component, this number of delay laws can considerably increase and become difficult to manage, especially for data analysis.

The CEA has developed several inspection tools that take advantage of CIVA modeling capacity to determine the most suited trajectory for a given transducer, and minimize the number of delay laws to embed. On one hand, probe positioning maps and sensitivity maps can be computed to help in determining the best probe location on the surface, in regards to the resulting sensitivity to the researched flaw and positioning constraints. On the other hand, the tools enable the computation of delays laws validity and coverage domain onto a probe positioning area. A trajectory can then be set with the minimal combination of delay laws and scans that ensures the entire zone coverage.

Considering the example of a nozzle inspection for ortho-radially oriented flaw detection, the article presents the use of the tools described.

Keywords: Inspection, Optimization, Flexible Phased Array, Trajectory, Nozzle

1. Introduction

The inspection of complex component requires the use of an adapted transducer in order to overcome the coupling problematic caused by the surface geometry. Good results can be achieved locally with conventional TRL wedge, but as long as a trajectory is needed, the use of a flexible transducer becomes necessary. Indeed, such transducers allow proper fitting of the component surface and enable an electronic drive of the acoustic beam.

However, unlike TRL wedge, the relative position of the flexible probe elements depends on the deformation undergone by the transducer. Therefore, for a given set of acoustic parameters, the corresponding delay laws will directly be function of the probe positioning on component surface. This may imply to compute and manage a large number of delay laws in order to cover an entire inspection trajectory, which can quickly become tedious, especially for data analyzing. Indeed, it is impossible for most acquisition devices to trigger a delay law considering the current probe position: All delay laws must be fired on each position, and then sorted during the data processing. The CEA has thus developed several tools that enable to plan an inspection with the minimum set of delay laws, and provide the proper way to analyze acquired data.

At first, the tools consider the component geometry to help in determining the best probe positioning area in regards of accessibility constraints and sensitivity to the researched flaw. Probe positioning map and probe sensitivity map are computed for several inspection configurations, for the user to be likely to decide the most adequate one.

On this basis, the tools evaluate the delays laws validity and coverage domain and a trajectory is subsequently set with the minimal combination of delay laws that ensures the entire zone coverage. The data acquiredusing the computed delay laws can then be treated and sorted according to the model.

Considering the robotized inspection of a nozzle weld,the study presents the methodology of the developedinspection planning tools in order to compute an inspection trajectory and its associated delay laws.

2. Probe optimal positioning area

The computation of needed delay lawsarises from the use ofthe developed probe positioning tool, which first helps in defining the optimalconfiguration in regards of component accessibility and sensitivity to the researched flaw. Its operation is detailed here.

2.1 Geometric definitions

The tool first requires a geometric definition of the component, researched flaw and region of interest.A parametric definition was used to depict the nozzle of our study,its characteristics are describedinFigure 1. The researched flaw consists in a 10x60mm (h x l) radially oriented notch around the secondary nozzle cylinder. The cylindrical coordinate system centered on the secondary cylinder axis was retained in order to describe transducer or flaw position. All following results will be presented within this coordinate system.

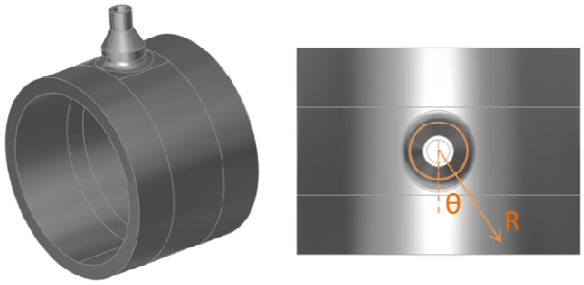

Nozzle geometrical characteristics	
Primary cylinder ext. diameter	820.4 mm
Primary cylinder thickness	61 mm
Secondary cylinder ext. diameter	88.9 mm
Saddle curvature radius	33 mm

Figure 1. Geometrical characteristics of the nozzle and coordinate system definition

The study will consider a region of interest which spreads from -10° to +10° around the secondary cylinder with an extension of 60mm, that is to say the extension of the researched flaw.

2.2 Determination of probe optimal positioning area

The researched flaw and region of interest specified geometries can lead to several probe positioning areas on the component surface, depending on the manner in which the flaw is hit. Generally, the optimum of detection is obtained when the acoustic beam hits specularly the bottom of the flaw with an angle of 45° (Figure 2.a).

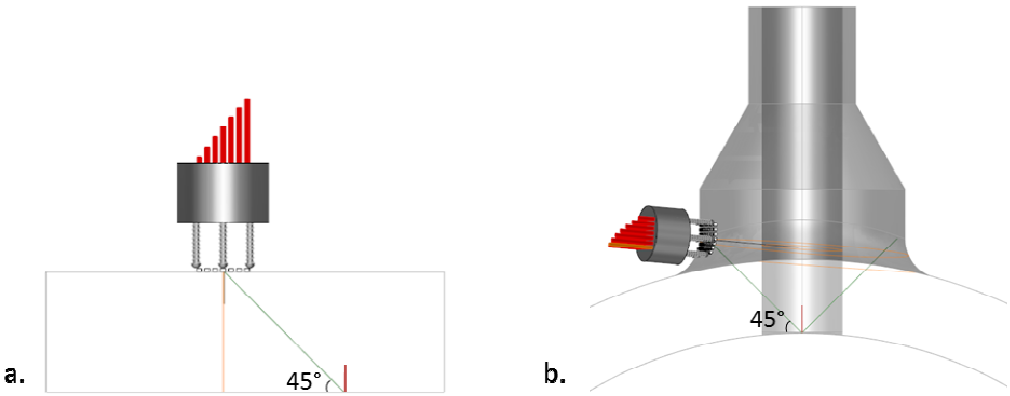

Figure 2. Optimal flaw attack configuration resulting in favorable probe positioning (a), Optimal flaw attack configuration resulting in unfavorable probe positioning (b)

However, due to complex surface geometry, such configuration can lead to unfavorable probe positioning (Figure 2.b). Indeed, positioning the probe within the saddle or cone may be incompatible with the robotized probe positioning device. Furthermore, such positioning might be less effective for proper acoustic wave generation, resulting in a loss of sensitivity.
In order to evaluate these two aspects, the probe positioning tool generates, for different attack angles, a probe positioning map and its associated sensitivity map.

2.2.1 Probe positioning map

The probe positioning information is obtained by firing a ray oriented with the considered attack angle, from the bottom of the flaw to the component surface. Depending from where the ray is fired within the region of interest, the probe can be positioned in different areas on the nozzle surface: primary cylinder, nozzle saddle, cone, etc...

Two positioning map can be obtained for a given attack angle, whether the flaw is hit on one side or the other. The user can also choose to consider the bottom or the top of the notch, whether a corner or a diffraction echo is more suited to its application.

CIVA positioning tool associates a specific color for each area in order to easily differentiate favorable from unfavorable configurations (Figure 4).

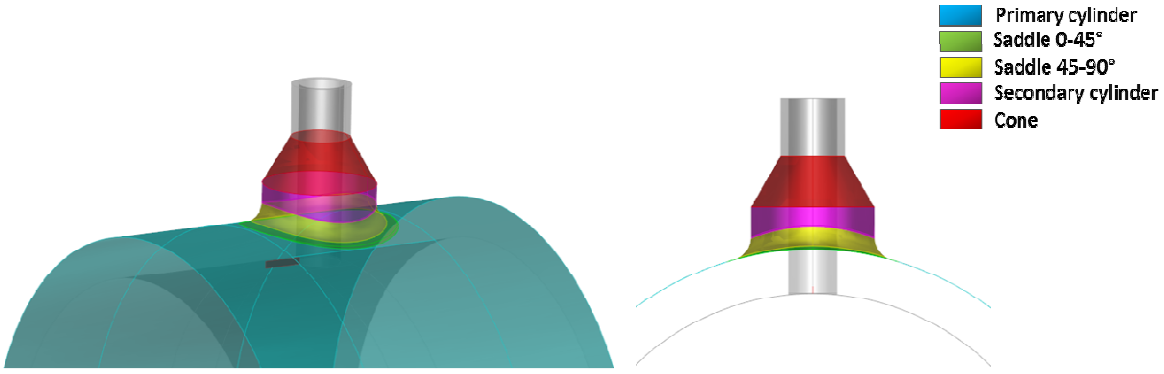

Figure 3. Colormap for the different nozzle surface areas

On our application, the two sides of the flaw are equivalent since the problem is symmetrical. Only one side will be considered. We used the bottom of the notch for the generation of probe positioning maps, for this application targets the maximization of corner echoes.

The probe positioning tool was used to generate the positioning maps for a 25°, 30°, 35°, 40°, and 45° attack angle. Figure 4below illustrates the results obtained and an example, within the 3D view.

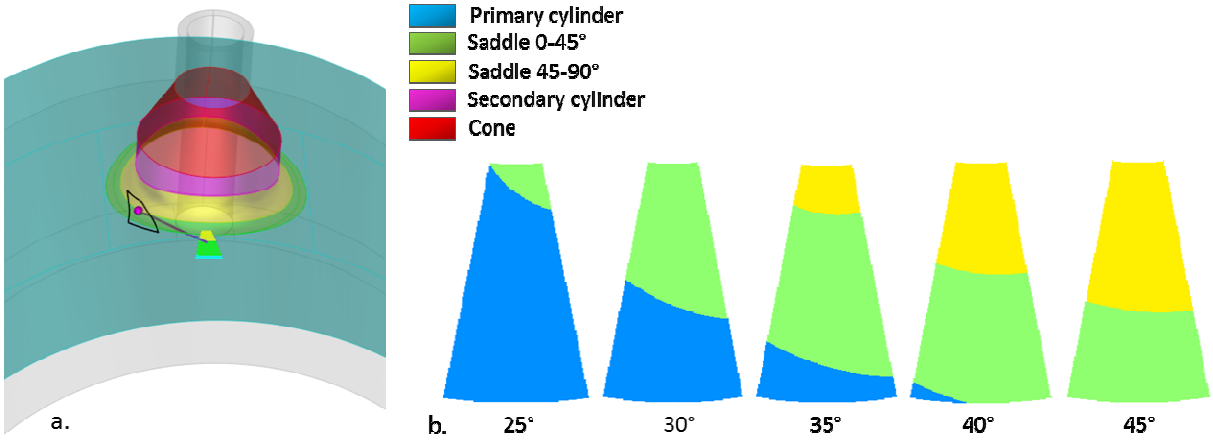

Figure 4. Example of probe positioning map generated by the tool, displayed within the region of interest on the internal surface of the nozzle (a). Probe positioning maps obtained for various attack angles (b).

Since the nozzle saddle is considered as an unfavorable positioning area, the positioning map reveals a more favorable positioning configuration for small attack angles. Indeed, inspecting the region of interest with a 25° attack angle hardly require to impinge the saddle while a 45° attack angle always require to position the probe on the saddle.
However, this result is obtained without any acoustical consideration and attack angles which deviate from the optimum 45° may lead to less effective sensitivity. In order to determine the best compromise, the probe sensitivity mapsmust be computed.

2.2.2 Probe sensitivity map

The probe sensitivity map renders the manner in which a considered probe will be sensitive to a flaw located in the region of interest, in regards of its position. Depending on the probe and its focusing parameters used for the inspection, it can reveal low sensitive area where the detection of the researched flaw might be uneasy.
For the sensitivity map to be computed, the region of interest is divided into a high number of points. At each point, a modelling is performed thanks to CIVA modelling tool:

- A flaw with characteristics identical to researched flaw is positioned atthe point.
- Then, the considered probe is positioned on the surface in regards of the focusing parameters to assess.
- CIVA performs a flaw response modelling in this configuration

From each single flaw response, the maximum Ascan response amplitude is extracted and plotted to form the sensitivity map on the considered region of interest.

In order to evaluate the best fitted attack angle for our application, the sensitivity maps were computed for the 25°, 30°, 35°, 40° and 45° angles. The considered probe is a 84 (12x7)elements transducer, working at 2MHz with a global aperture of 32.6x26.5mm². The resultsof the sensitivity map computing are presented in Figure 5below:

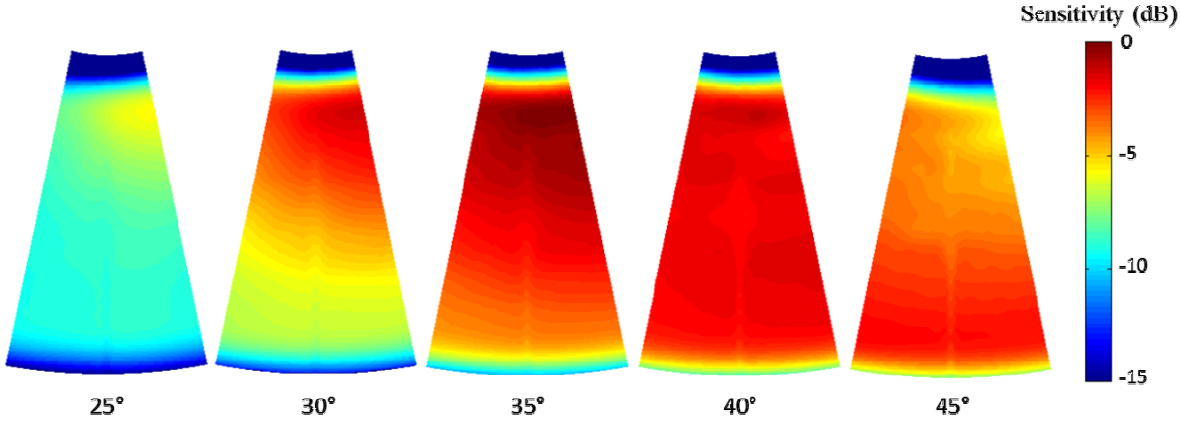

Figure 5. Sensitivity map obtained for various attack angles. Reference (0 dB) is defined as the maximum of all combined map

The results show an enhancement of the sensitivity with higher attack angle, even if an area remains less sensitive whatever considered angle. This reveals an unfavorablezone within the region of interest where inspection might be difficult to achieve anyhow, independently of the attack angle.

Furthermore, 45° does not appear to be the optimum since an attack angle of 40° givesa more homogeneous sensitivity on the region of interest. This assumes unfavorable positioning configurations for proper acoustic wave emission arising from the 45° attack angle.

The comparison of the probe positioning maps and probe sensitivity maps highlights the 40° attack angle as the best compromise between unfavorable probe positioning and best acoustical performance. This angle was thus retained for the computation of the inspection trajectory.

3. Trajectory and delay laws computation

The sensitivity maps computed previously gives thetheoretical ideal sensitivityfor an inspection performed within our region of interest. It assumes that the inspection is performed at each point of the probe positioning surface and that perfectly adapted delays laws are always used. This is obviously not the case in practice.

The purpose of CIVA trajectory computation tool is to determine a trajectory with the minimum number of scans and minimum number of delay lawswhich sensitivity to the flaw is as close as possible to the theoretical ideal sensitivity maps. CIVA thus introduces the notion of sensitivity loss tolerance, which defines the maximum loss of sensitivity to the ideal acceptable for the application. On this basis, the trajectory computation process begins.

3.1 Computation of trajectory potential scanning paths

The ideal sensitivity is obtained with a trajectory made of an infinite number of scans, which is not realistic. The user is thus first asked to define the maximum number of scans the trajectory should consist of. Obviously, the computing time depends on this parameter.
The region of interest is then divided in as many regularly spaced scans as specified by the user. In fact, this amounts to consider regularly spaced flaws within the region of interest, and an optimal inspection pathfor each of them, according to the specified attack angle (here, 40°).Figure 6illustrates the principle with a maximum of 5 scans trajectory.

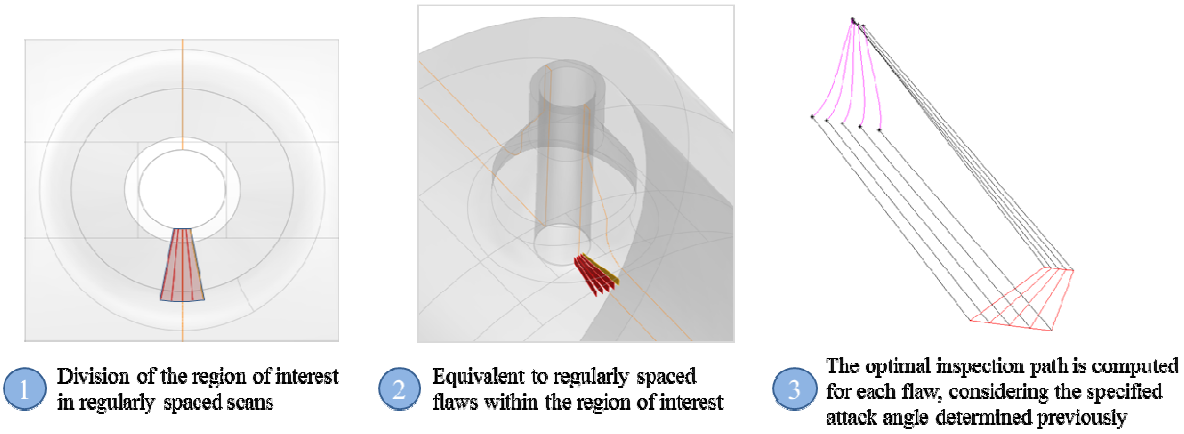

Figure 6. Illustration of the computation principle of final trajectory potential scanning paths

The purpose of the tool is to determine which of theses potentials paths are mandatory to ensure the entire coverage and which aren't. The combination of the kept paths forms the final inspection trajectory.

The assessment of a path consists in evaluating its resulting coverage onto the region of interest. However, this operation cannot be achieved without considering the delay laws used along it. In the case of the ideal sensitivity map, perfectly adapted delays laws are used at each point. Since our purpose is also to minimize the number of delay laws to embed, a selection operation must be performed.

3.2 Delay laws selection along a potential scanning path

To select which delay laws to keep, the potential path is first divided into a high number of test points. On each of theses test points, the considered probe (cf. 2.2.2) is positioned and proper delay laws are computed. The purpose is then to evaluate the domain along which the delay laws are still valid for flaw detection, with a reasonable loss of performance (equal to the sensitivity loss tolerance specified previously).

3.2.1 Delays laws validity and coverage domain computation

For each delay laws computed, the probe is moved along the scanning path and a flaw response simulation is performed without re-computing the delays law. The loss of performance compared to flaw response obtained with the perfectly adapted delays law is evaluated and the limit of validity established, according to the acceptable loss of sensitivity.Figure 7 below illustrates the principle.

At this point, the flaw considered in the simulation is located at the exact angular position from where the scanning path was determined (cf.Figure 6). Though, in order to evaluate the capacity of the delay laws to detect a flaw located slightly apart, the same simulations are performed with the flaw moved to different angular positions.This enables to get a 2D coverage domain for the delay laws, which refers to the area covered on the region of interest when the transducer evolves on the delays law validity domain. The principle is illustrated in Figure 8.

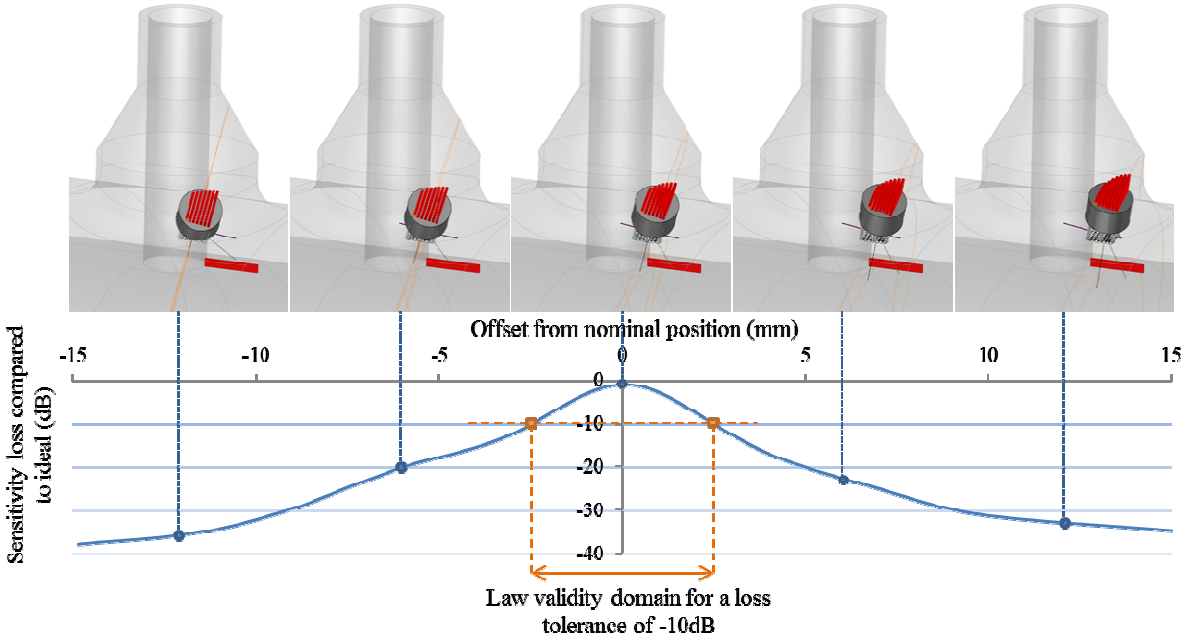

Figure 7. Illustration of a delay law validity domain computation. The delay law is computed at its nominal position, and the sensitivity loss evaluated while moving the transducer along the scan without changing the laws. The validity domain refers to the part of the scan within which the transducer can evolve without changing its delays law.

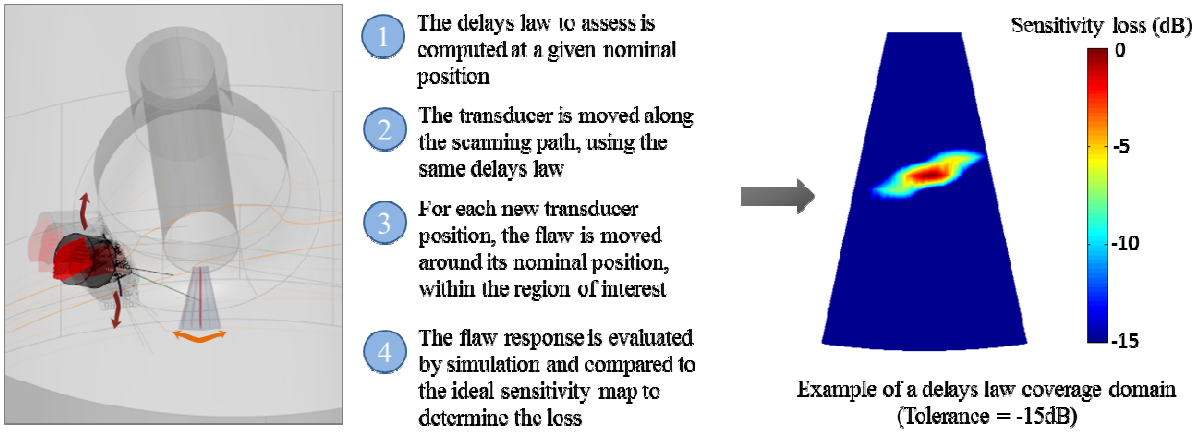

Figure 8. Illustration of a delays law coverage domain computation. The delays law coverage domain refers to the area covered on the region of interest when the transducer evolves on the delays law validity domain.

3.2.2 Delays laws sorting

Delays laws coverage computation is performed for eachtest point constituting the scanning path, providing a set of domains. The high number of test points leads to an overlap of successive domains, that enables the sorting process.This process consists in removing the domains, thus the delays laws, that aren't needed to ensure the overall coverage of the scanning path.The remaining delays laws form the minimal set needed for the inspection along the considered scanning path, according to the specified loss tolerance. The results of the process for the middle scanning path are presentedinthe figure below.

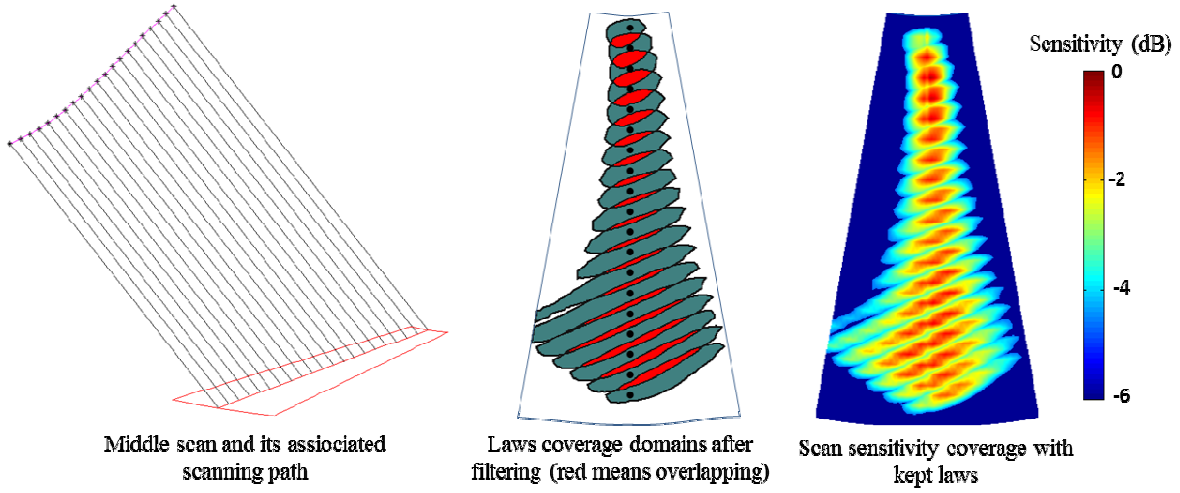

Figure 9. Illustration of a delays law selection for the middle path and its results in terms of sensitivity. The loss tolerance was set at 6dB.

3.3 Scanning path selection and trajectory parameters computation

The previous step enables the determination of the minimal set of delays laws to perform an inspection with the target sensitivity. Concurrently, the coverage in sensitivity provided by each scanning path is computed. The objective of selecting a scanning path among all those considered can then be fulfilled using the same methodology as laws selection.Indeed, the coverage in sensitivity of successive scans can also overlap and some of them become useless.

Figure 10 below presents the results of the scanning path filtering onto our region of interest. It indicates that a loss tolerance of 6dB on sensitivity enables to consider a trajectory of only three scans, and a total of 57 delays laws.

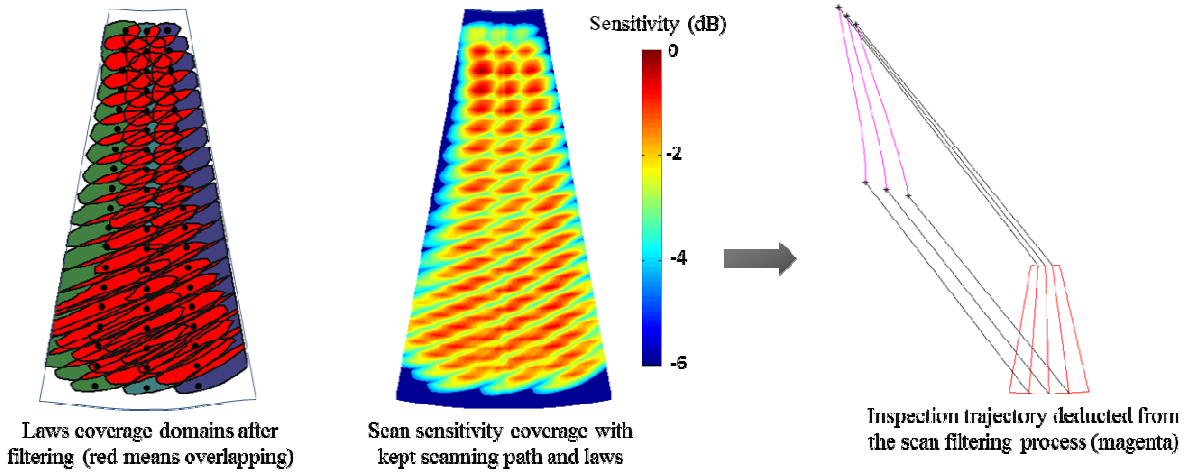

Figure 10. Results of scan filtering process with a loss tolerance set at 6dB. Sensitivity coverage map and deducted inspection trajectory are presented.

The resulting inspection trajectory can directly be exported by CIVA to a robot interpretable file, as well as delays laws to an acquisition device. CIVA also enables to perform further simulation on this computed trajectory and delay laws. Thesesimulations can help in corroborate the validity of the inspection parameters in some specific configurations.

Moreover, the user is able to add an angular sweep to each delays laws, in order to perform flaw characterization. The study of the corner echoes and diffraction echoes on these simulations will enable to evaluate the characterization performance of the trajectory.

Below is an example of such a simulation, performed on our application case with the flaw located at 0° within our region of interest.

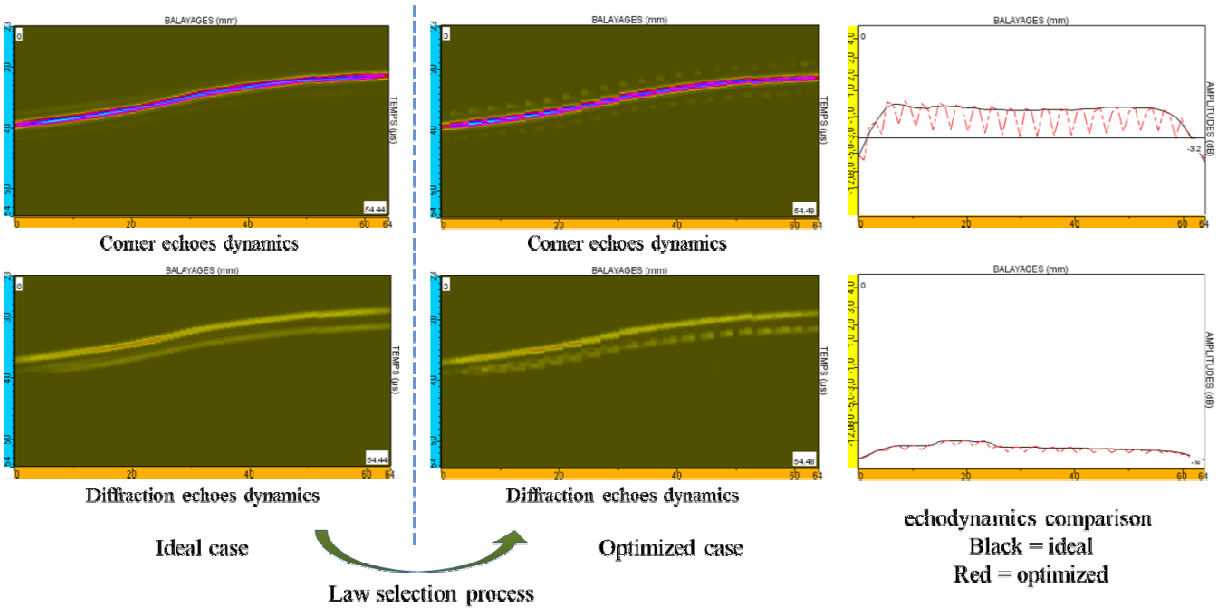

Figure 11. Results of a simulation performed on the trajectory for a flaw located at 0°. The figure illustrates the degradation induced by the laws selection process on the corner echoes and diffraction echoes dynamics. The resulting detection and characterization performance can then be evaluated.

The results of the simulation presented above give good confidence in the selection process performance. The loss of sensitivity induced by the laws selection remains limited and still enables to properly detect the flaw and characterize it.

5. Conclusion

Considering the example of a nozzle, this study presented the use of CIVA tools in order to properly define an optimized inspection trajectory, with the minimum number of scans and minimum number of delays laws to embed.

The first steptakes advantage of CIVA probe positioning tool in order to determine the optimal inspection settings. The computation of probe positioning maps depicts the different possible probe configurations on the component and are useful to identify unfavorable conformation in respect of robotized positioning device. On the other hand, the computation of sensitivity maps informs the manner in which a given configuration will be sensitive or not to the researched flaw. The comparison of the two maps gives the best compromise and thus the optimal inspection settings to use.

The second step aims at determining an optimized trajectory according to the inspection settingsset previously. It first computes a panel of potential scanning path and then performs acoustic simulations in order to evaluate the coverage in sensitivity they provide.The strategy is to build a trajectory with the minimum number of scanning paths that ensure an entire coverage of the region of interest. This coverage is meant to ensure a target sensitivity, according to a loss tolerance compared to the optimal coverage obtained with an infinite number of scans.

This loss tolerance is also an input criteria for the delays laws selection. For each potential scans, divided into test points, the adapted delays laws are determined and their coverage computed. The overlapping of the different domains obtained enables to remove a considerable number of delays laws and to come out with the minimal set that ensure the zone coverage. The same methodology is used for the scanning paths selection.

The combination of the two processes gives the optimal trajectory parameters: scanning path, delays laws and their domain of validity, which are directly exportable to a robot and acquisition device. CIVA also enables to add an angular sweep to the computed delays laws in order to perform flaw characterization. The performance of the methodology can be assessed by simulation, to confirm the validity of the parameters in specific configurations. The results obtained for our case of application gives good confidence in the obtained inspection parameters, which remains to be experimentally validated.

References

[1] A Vanhoye, SBey, TDesrez, 'Phased Array Transducer Instrumentation for Complex Geometry Component Inspection', ECNDT, Prague, 2014.
[2] A Vanhoye, O Casula, D Moussebois, 'Phased array transducer optimization for complex nuclear component inspection', ICNDT, Cannes, 2013.
[3] A Vanhoye, O Casula, D Moussebois, 'Design by simulation of the UT array inspection of a nozzle with a flexible probe: Definition of 3D trajectories and focusing parameters', QNDE, Denver, 2012.
[4] O Casula, G Toullelan, L Doudet, A Le Brun, N Etchegaray, 'Flexible multi-elements transducers, new applications in NDT', SFEN-COFREND, Paris, 2009.
[5] G Maes, S Turgeon, D Reilly, 'Advanced phased array UT inspection through complex surfaces', 7th Int. Conf. on NDE in relation to Structural Integrity for Nuclear and Pressurized Components, Yokohama, 2009.
[6] D Richard, G Maes, D Reilly, J Berlanger, 'Advanced software tools for design and implementation of phased array UT inspection techniques on complex components', 8th Int. Conf. on NDE in relation to Structural Integrity for Nuclear and Pressurized Components, Berlin, 2010.

Numerical Study of Ultrasonic Nonlinearity Parameter in Solids with Rough Surfaces

Maodan Yuan[1], Jianhai Zhang[1], Sung-Jin Song[1] and Hak-Joon Kim[1]

[1]School of Mechanical Engineering, Sungkyunkwan University, Suwon, 440-746, Korea

Abstract

In nonlinear ultrasonic methods, the surface preparation of specimen is of great concern to provide an accurate value of nonlinearity parameter. To investigate the influence of the rough surface on the nonlinearity parameter and give a correction to the practical measurement for arbitrary surfaces, an effective FE model is desirable to model the higher harmonic generation and recover the nonlinearity parameter. At first, a verification model using plane wave is built and the calculated nonlinearity parameter agrees with analytical result. Then solids with rough surfaces of sinusoidal profile are studied and different roughness values are taken into consideration. Transmission coefficients and nonlinearity parameters generally decrease with surface roughness, while the nonlinearity parameter shows much higher sensitivity than transmission coefficient. The FE model can provide a good guidance and give corrections for the nonlinear ultrasonic measurement for practical specimens.

Keywords : Higher Harmonic Generation; Nonlinearity Parameter; FE Model; Surface Roughness.

1. Introduction

It becomes of greater significance and more urgent demand to track the onset of early-stage damage in the safety-critical fields, such as the nuclear industry. In the early stage, the formation and accumulation of dislocations or the microcrack initiation lead to tiny and ignorable changes in the bulk properties of the material, before the materialization of macrocracks or voids [1]. The new challenge to acquire quantitative early-stage information about inspected materials is thus presented as a difficult task to the NDT community. Therefore, it is required to determine microstructural properties such as grain size, texture and porosity and characterize failure mechanisms including fatigue, creep, and fracture. However, the material properties variations at early stage have subtle influence on the linear parameters, making the conventional ultrasonic methods insensitive to indicate the early-stage damage. Based on the nonlinear response due to the nonlinear interaction between the elastic wave and the specimen under test, nonlinear ultrasonic is proposed and developed to evaluate early damage. The nonlinear interaction can distort the incident wave form and generate higher harmonics. An example of the nonlinear effects of wave distortion is shown in Fig.1. Comparing a nonlinear and a linear solution, the time-varying waveform distortion from sine harmonic wave into sawtooth-like wave is apparently shown as Fig.1 (a). The physical background lies in that the peaks of the wave travel faster than the valleys, due to the dependence of local wave speed on the pressure or particle velocity [2]. Morever, the higher harmonics generation of incident fundamental frequency along with waveform distortion is shown in Fig.1 (b). The further the ultrasonic wave propagates away from the source position, the severer waveform is distorted and the more energy of higher harmonic is generated.

The physical nonlinearity resulting from the nonlinear stress-strain relationship is a global and homogenous effect in the material. In 1963, Breazeale et al. firstly provided second order harmonic generation from anharmonic lattices in solids using polycrystalline aluminum [3]. Later the experimental evidences of the contributions of dislocation monopoles and diopoles under plastic deformation were reported by Hikata et al. [4] and Cantrell et al. [5] for the first time. Cantrell et al. also investigated the influence of the crystalline structure and precipitates to the acoustic nonlinearity [6]. Commonly, the

second-order nonlinearity parameter is calculated using the following expression based on the plane-wave theory [7]

$$\beta = \frac{8}{xk^2}\left(\frac{A_2}{A_1^2}\right) \qquad (1)$$

where x is the propagation distance or the specimen length in the experiment; $k = 2\pi/\lambda$ and λ is the wave length of the specimen. Therefore, once the amplitudes of fundamental A_1 and second harmonic A_2 are obtained, the nonlinearity parameter β can be calculated as a material property indicator. This is a simplified way to calculate the nonlinearity parameter and does not fully take the real behavior of the ultrasonic propagation in solids. Numerical models are the effective way to handle the complex combined boundary effects and compare with various experimental conditions. Drewry et al. [8] developed one-dimensional time-domain finite element (FE) model achieves accurate quantitative modeling of ultrasonic wave propagation and provide modeling guidelines concerning various model parameters. Based on a quasi-linear assumption, Best et al. [9] described a three-dimensional numerical model designed to accurately predict the axial variation of nonlinearity parameter and compared with experiments as well. Therefore, it is a good choice to account for the real ultrasonic wave propagation using such numerical methods as FE method in the accurate calculation of ultrasonic nonlinearity parameter.

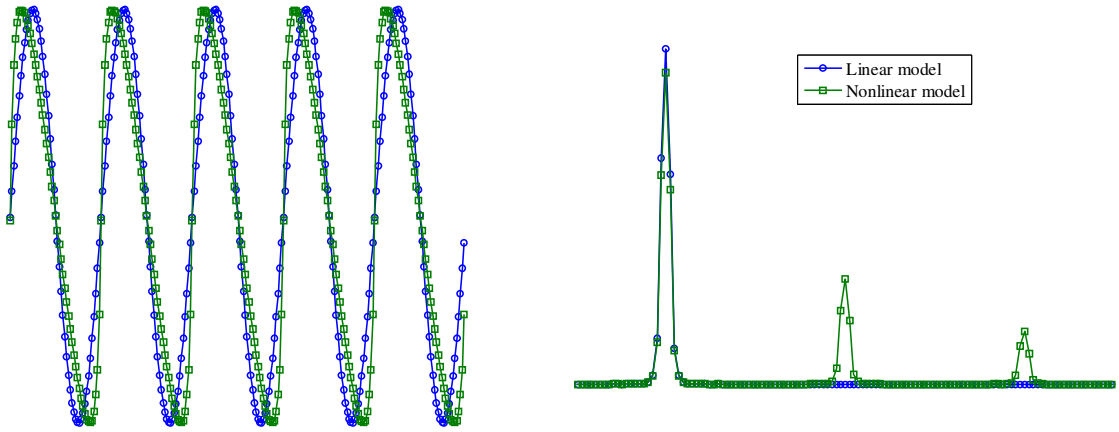

(a) (b)

Fig. 1. Nonlinear effects in ultrasonic wave propagation: (a) wave distortion and (b) high harmonics generation.

In the nonlinear ultrasonic measurement, surface treatment of the specimen is usually strict to ensure the measurement accurate. Therefore, a lot of efforts should be done on the surface treatment prior to the experiment. This kind of stringent requirement limits the in-situ application of the nonlinear ultrasonic method, since the actual surfaces usually appear with various features such as curvature and roughness. When ultrasonic wave is incident on these kinds of surfaces, part of the wave will be scattered at these surface irregularities. This kind of scattering phenomenon results in serious energy losses which can render an internal defect undetectable and especially changes the sensitive nonlinearity parameter unpredictable, since the nonlinearity parameter measurement relies on the measuring amplitudes of the fundamental and second harmonic signals, which can be affected by scattering and phase cancellations due to rough and nonparallel surfaces [10]. Therefore, a thorough study on the surface irregularity is desirable, which not only proposes a new method for the characterization of irregular surface, but also provides the correction term for the absolute nonlinearity parameter measurements. In this study, a unit cell FE model will be built to simulate the higher harmonic generation in solid and extended to investigate the influence of the rough surface with different roughness value.

2. FE Model for Rough Surface

2.1 Unit Cell FE Model

A FE model of plane wave is firstly built and validated by comparing with the analytical values. The hyperelastic materials models calculate stresses based on a strain energy density function and are often used to simulate materials

like rubber, but also used in acoustic. The Murnaghan model is adopted to simulate the hyperelastic material. The specimen is Al-1200 and its material properties are shown in Table 1. The third-order elastic constants come from the experiment data of Smith et al.[11].

Table 1. The material property of Al-1200 [11].

Density	Lame Coefficients		Murnaghan Constants		
ρ	λ	μ	l	m	n
2737 kg/m^3	57.0 GPa	27.6 GPa	-311 GPa	-401 GPa	-408 GPa

To avoid the scattering from the side boundaries, large geometry size with non-reflecting boundaries in the irrelevant directions is usually used to simulate the wave scattering from rough surfaces. However, the non-reflection element may also produce unpredictable numerical errors and make the model complicated. Unit cell models, calculating only a represent domain, have been proposed and proved to be effective to model the wave propagation in infinite periodic boundaries [12]. The size of the unit cell size is usually set as one period of the surface and proper boundary conditions $\mathbf{n} \cdot \mathbf{u} = 0$ are given to both sides to model the periodic boundaries. The geometry model is shown as Fig. 2 and the incident wave is $p = A\sin(2\pi f_c t)$. Wave propagation from the FE simulation is obtained at a certain time and an example of wave scattering from the rough surface can be seen, shown as in Fig. 3.

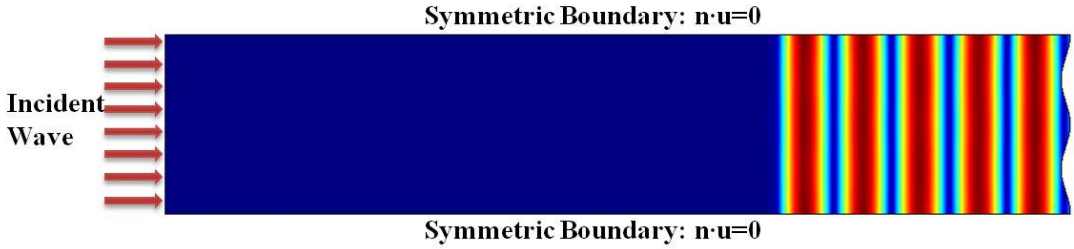

Fig. 2. Unit cell FE model for ultrasonic wave interaction with rough surfaces.

The corresponding A-scan signals for transmitted waves and their FFT results are shown in Fig. 3. Although the time-varying signal seems to be not distorted, higher harmonics, especially the second harmonic, are clearly generated in the spectrum, which demonstrates it is possible to simulate generate higher harmonics effectively using the Murnaghan hyperelastic material model.

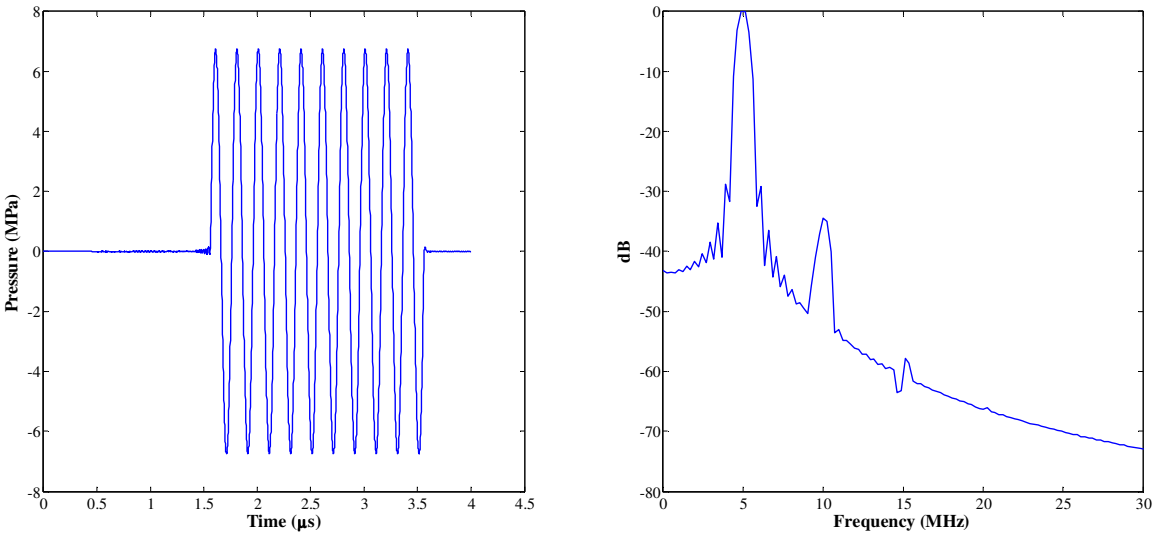

(a) (b)

Fig. 3. The received signals of plane wave model: (a) A-scan signal and (b) its FFT result.

Using Eqn. (1), the convergence value of ultrasonic nonlinearity can be calculated to be β=17.16. Also the explicit expression for the nonlinearity parameter can be calculated with Murnaghan constants [13].

$$\beta = -\frac{3(\lambda+2\mu)+2(l+2m)}{\lambda+2\mu} = 16.84 \qquad (2)$$

Although there is a little difference from both values (relative error is 1.9%) due to the FE numerical error and also the input sinusoid signal with finite cycles, the nonlinearity parameters calculated from FE simulation and analytical solution are considered to be agreed very well. Therefore, this FE model is effective for modeling harmonic generation in a Murnaghan material.

2.2 Rough Surface Profiles

Easy-to-implement regular surfaces are introduced and corresponding unit cell FE model is shown in Fig. 3. The simplest sinusoidal surface with the same peak height R_p is investigated here. The periodic length of the surface is kept the same and roughness value R_p varies from 0 to 200 μm. The nonlinearity parameters are calculated as Eqn. (1), as well as the transmission coefficient for different surface roughness R_p, shown as Fig. 4. From the results, generally, transmission coefficient and nonlinearity parameter decrease in an exponential fashion with the increasing surface roughness R_p for the sinusoidal surface profiles. With this result, the nonlinearity parameter can be recovered with a proper correction term using FE model. Moreover, with increasing roughness value, the change rate of nonlinearity parameter is much larger than that of transmission coefficient. Therefore, the nonlinearity parameter is much more sensitive to the surface roughness than transmission coefficient and can be adopted as an effective indicator to evaluate the surface roughness.

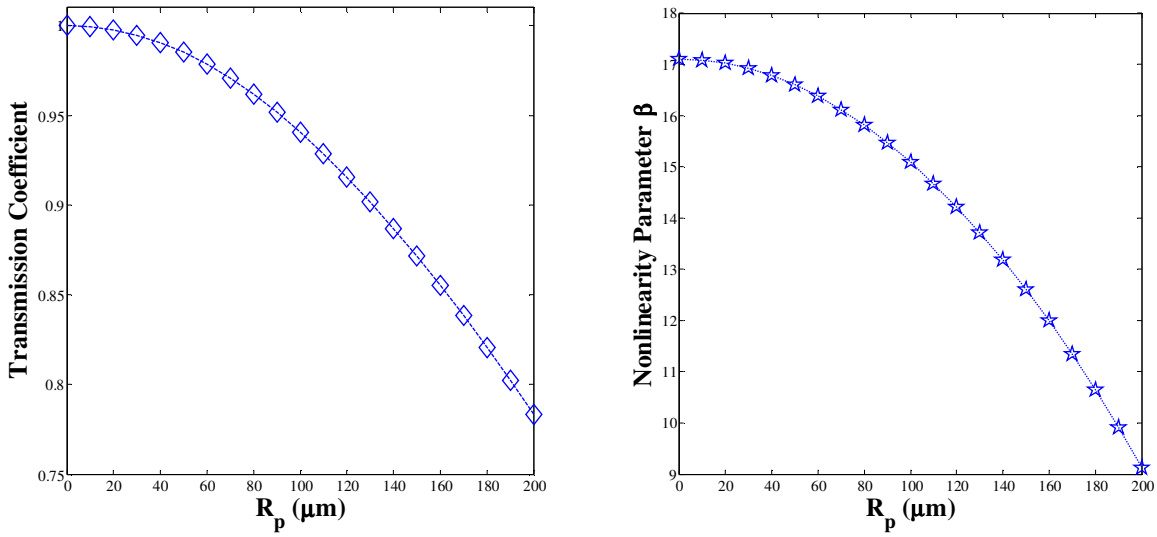

(a) (b)

Fig. 4. Variations with roughness values R_p for sine profile: (a) transmission coefficient and (b) nonlinearity parameter.

3. Conclusion Remarks

Unit cell FE model is built to simulate the higher harmonic generation in solids based on Murnaghan hyperelastic material model and calculate the absolute nonlinearity parameter. The nonlinearity parameter from FE simulation agrees with the analytical calculation, providing a effective tool to analyze the nonlinear ultrasonic wave propagation with complicated geometries including rough surfaces. Sine surface profile decreases transmission coefficient and the nonlinearity parameter monotonically. Moreover, a higher decreasing rate of the nonlinearity parameter as a function with the roughness demonstrates that the nonlinear ultrasonic is much more sensitive and nonlinearity parameter can be proposed as an effective indicator to the surface roughness measurement.

Acknowledgements

This work was supported by Basic Science Research Program through the National Research Foundation of Korea (NRF) funded by the Ministry of Science, ICT and Future Planning (No. 2011-0020024).

References

[1] S. I. Rokhlin, and J. Y. Kim, "In situ ultrasonic monitoring of surface fatigue crack initiation and growth from surface cavity," International journal of fatigue, Vol. 25, No. 1, pp. 41-49, (2003).

[2] M. F. Hamilton, and D. T. Blackstock, Nonlinear acoustics: Academic press San Diego, (1998).

[3] M. Breazeale, and D. Thompson, "Finite-Amplitude Ultrasonic Waves in Aluminum," Applied Physics Letters, Vol. 3, No. 5, pp. 77-78, (1963).

[4] A. Hikata, B. B. Chick, and C. Elbaum, "Dislocation Contribution to the Second Harmonic Generation of Ultrasonic Waves," Journal of Applied Physics, Vol. 36, No. 1, pp. 229, (1965).

[5] J. H. Cantrell, and W. T. Yost, "Acoustic harmonic generation from fatigue-induced dislocation dipoles,"

Philosophical magazine A, Vol. 69, No. 2, pp. 315-326, (1994).
[6] J. H. Cantrell, “Crystalline structure and symmetry dependence of acoustic nonlinearity parameters,” Journal of Applied Physics, Vol. 76, No. 6, pp. 3372-3380, (1994).
[7] J. K. Na, “Ultrasonic measurement of the linear and the nonlinear elastic properties of PZT ceramics,” The Univeristy of Tennessee, 1994.
[8] M. A. Drewry, and P. D. Wilcox, “One-dimensional time-domain finite-element modelling of nonlinear wave propagation for non-destructive evaluation,” NDT & E International, Vol. 61, pp. 45-52, (2014).
[9] S. R. Best, A. J. Croxford, and S. A. Neild, “Modelling harmonic generation measurements in solids,” Ultrasonics, Vol. 54, No. 2, pp. 442-50, Feb, (2014).
[10] J. K. Na, W. T. Yost, J. H. Cantrell *et al.*, “Effects of Surface Roughness and Nonparallelism on the Measurement of the Acoustic Nonlinearity Parameter in Steam Turbine Blades,” in Review of Progress in Quantitative Nondestructive Evaluation(2000).
[11] R. Smith, R. Stern, and R. Stephens, “Third‐Order Elastic Moduli of Polycrystalline Metals from Ultrasonic Velocity Measurements,” The Journal of the Acoustical Society of America, Vol. 40, No. 5, pp. 1002-1008, (1966).
[12] W. Choi, E. Skelton, M. Lowe *et al.*, "Unit cell finite element modelling for ultrasonic scattering from periodic surfaces." pp. 83-90, (2013).
[13] F. D. Murnaghan, “Finite deformations of an elastic solid,” American Journal of Mathematics, Vol. 59, No. 2, pp. 235-260, (1937).

Eddy-current non destructive testing with the finite element tool Code_Carmel3D

P. Thomas [1], B. Goursaud [1], L. Maurice [2] and S. Cordeiro [2]

(1) EDF R&D / THEMIS, 1, avenue du Général de Gaulle, 92141 Clamart Cedex, France.
(2) EDF CEIDRE, 2 rue Ampère, 93206 Saint Denis, France.

Abstract

The numerical modeling is increasingly involved in the performance demonstration of NDT processes of French PWR. In that context, EDF commonly uses simulation tools dedicated to eddy currents testing (ET), ultrasonic testing (UT) and radiographic testing (RT). All of them include realistic models of probes and flaws, but the rest of the domain is somewhat simplified. For its part, the tri-dimensional finite element method (3D-FEM) allows any complex configuration but it is sometimes very expensive to operate. However, since the computational resources have dramatically increased, the 3D-FEM today proves to be effective in many NDT configurations. To illustrate, we present the enhancements carried out in Code_Carmel3D, a finite element tool developed by EDF and L2EP for electrotechnics, to simulate EC NDT for steam generators tubes of french PWR. We detail the fundamental pros and cons of the 3D-FEM when applied to electromagnetism, and through experiences with Code_Carmel3D, we give limitations and cost of EC NDT simulation by 3D-FEM.

Keywords : eddy current, finite element method, numerical simulation

1. Introduction

The use of numerical simulation is more and more important in the framework of the non destructive testing [1]. More precisely, the numerical modeling helps the demonstration of performance of NDT applications for the purpose of their qualification, and particularly, it allows an efficient analysis of the influence of any environmental parameter likely to degrade the performance of the control. These parameters often are tri-dimensionnal and bring a numerical challenge. Occasionally, the simulation can aid the interpretation of unusual signals or contribute to the design of innovating probes.

Since the mid 1970's, EDF-R&D has developed powerful simulation codes for solving the tri-dimensional (3D) problems in thermal-hydraulics (Saturn/Syrthes), thermal-mechanics (Aster) and electromagnetism (Trifou). In addition to these 3D codes, EDF more recently have developed with the CEA (Comissariat à l'Energie Atomique) a common graphical user interface (GUI) platform SALOME providing all the computer aided design (CAD) resources for the meshing and the visualization as well as some multi-physic inter-operability for these 3D codes. All these developments profit of an high power computing (HPC) environment which is increasing every year.

In that favourable numerical context, EDF-R&D has developed during the last ten years, in partnership with the L2EP (Laboratoire d'Electronique et d'Electrotechnique de Lille), a research finite element 3D tool named "code_Carmel", in order to address the electrotechnic problems. More recently, EDF decided to derive a new branch from that academic code in order to fulfil the two main requirements of the simulation for NDT: accuracy and robustness. We present here this new version named "Code_Carmel3D" (C3D). We first present the fundamentals, then the main difficulties to face with when modelling NDT problems with the finite element method. We give some examples on the validation and the quality of the results, to finish with few computational skills of the software.

2. The fundamentals of Code_Carmel3D

2.1 The Physics

Most of the finite element codes are based on a physical power balance. For C3D this balance is written in time harmonic with the two equivalent following forms:

- the "ELECTRIC" form: $P_{\mathrm{B,E}}(\mathbf{B},\mathbf{E}) = i\omega\int_{V_\mu}\frac{1}{\mu}\mathbf{B}^2 dV_\mu + \int_{V_\sigma}\sigma\mathbf{E}^2 dV_\sigma \quad + 2\int_{V_I}\mathbf{E}\cdot\mathbf{J}_I dV_I \quad + \int_{S_\mu}\frac{1}{\mu}\mathbf{E}\times\mathbf{B}\cdot\mathbf{n}dS_\mu$
- the "MAGNETIC" form: $P_{\mathrm{H,J}}(\mathbf{H},\mathbf{J}) = i\omega\int_{V_\mu}\mu\mathbf{H}^2 dV_\mu + \int_{V_\sigma}\frac{1}{\sigma}\mathbf{J}^2 dV_\sigma + 2i\omega\int_{V_I}\mu\mathbf{H}\cdot\mathbf{H}_I dV_I + \int_{S_\mu}\frac{1}{\sigma}\mathbf{J}\times\mathbf{H}\cdot\mathbf{n}dS_\mu$

The first integral is the magnetic power in V_μ (the whole domain), the second one is the electric losses in the conductor V_σ (included in V_μ), the third one is the source imposed in the inductors V_I : the current $\mathbf{J}_I$ in ELECTRIC form and the equivalent magnetic field $\mathbf{H}_I$ such as $\mathbf{J}_I = curl(\mathbf{H}_I)$ in MAGNETIC form. The last term (Poynting vector) imposes on the surface S_μ one of the two following boundary conditions: the "wall" condition: $\mathbf{H}\times\mathbf{n} = 0$ or $\mathbf{E}\times\mathbf{n} = 0$, and the "impedance" condition: $\mathbf{E}\times\mathbf{H}\cdot\mathbf{n} = \sigma\lambda\,\mathbf{E}^2$ in ELECTRIC form and $\mathbf{E}\times\mathbf{H}\cdot\mathbf{n} = i\omega\mu\lambda\mathbf{H}^2$ in MAGNETIC form. All these boundary conditions reduce the surface integrals.

We perform the resolution in minimizing each form with respect to an appropriate couple of potentials unknowns (one vector and one scalar). These new unknowns are chosen to exactly satisfy two of the Maxwell equations, the other two are satisfied approximately after resolution, following the scheme:

Choice of the potential:		exactly satisfy:	and by minimization of:	weakly satisfy:
$(\mathbf{A},\varphi)$	such as : $\begin{cases}\mathbf{B} = curl\mathbf{A}\\ \mathbf{E} = -i\omega\mathbf{A} - \mathbf{grad}\,\varphi\end{cases}$	$\begin{cases}div(\mathbf{B}) = 0\\ Faraday's\ Eq.\end{cases}$	$P_{E,B}(\mathbf{A},\varphi)$	$\begin{cases}div(\mathbf{J}) = 0\\ Ampere's\ Eq.\end{cases}$
$(\mathbf{T},\Omega)$	such as : $\begin{cases}\mathbf{J} = curl\mathbf{T}\\ \mathbf{H} = \mathbf{T} - \mathbf{grad}\Omega\end{cases}$	$\begin{cases}div(\mathbf{J}) = 0\\ Ampere's\ Eq.\end{cases}$	$P_{H,J}(\mathbf{T},\Omega)$	$\begin{cases}div(\mathbf{B}) = 0\\ Faraday's\ Eq.\end{cases}$

So, for one given physical problem, C3D provides two sets of equations which have a “dual” structure, that is to say, what is strongly satisfied in one set of equations, is weakly satisfied in the other.

2.1 The Numerics

The finite element interpolation of the two above forms is performed with linear volume elements, based on edge degrees of freedom (DoF) for the vector potential (Whitney elements) and on node DoF for the scalar potential. The consequence is a space linear variation in each volume for $\mathbf{E}$ in ELECTRIC form and for $\mathbf{H}$ in MAGNETIC form (other fields are constant). Another consequence is that unfortunately, the required physical continuities at interfaces, which are tangent $\mathbf{E}$, $\mathbf{H}$ and normal $\mathbf{B}$, $\mathbf{J}$ are not all satisfied: for example, in ELECTRIC form, we have the only continuity of tangent $\mathbf{E}$ and normal $\mathbf{B}$, and in MAGNETIC form, we have the only continuity of tangent $\mathbf{H}$ and normal $\mathbf{J}$. The respect of the other two conditions, because they are obtained by the resolution, depends on the quality of the mesh.

So, we actually get two different solutions for one given problem. For example, in NDT problems, one should choose the ELECTRIC form for best accounting the reluctance in modelling the ferrite core of probes, and on the contrary, the MAGNETIC form for the best accounting of defects in the tubes. Since the difference between the both forms decreases with mesh refinement, we shall use that difference as a mesh quality criterion.

3. EC-NDT finite element modelling issues

3-1. Probe modelling

Thanks to the finite element method, there is no principled limitation in modelling any probe, neither in the geometry nor in the electrical or magnetic properties of its components. The only problem is the availability of the data, and when we have to assume any missing parameter, we first must evaluate its sensitivity (accounting the signal calibration process).

The four models of probe already available in C3D are [4], [5], [6] and [7]:

- Two axial probes, with a couple of coils ("AXP") or with two rings of transverse coils ("MXP"),

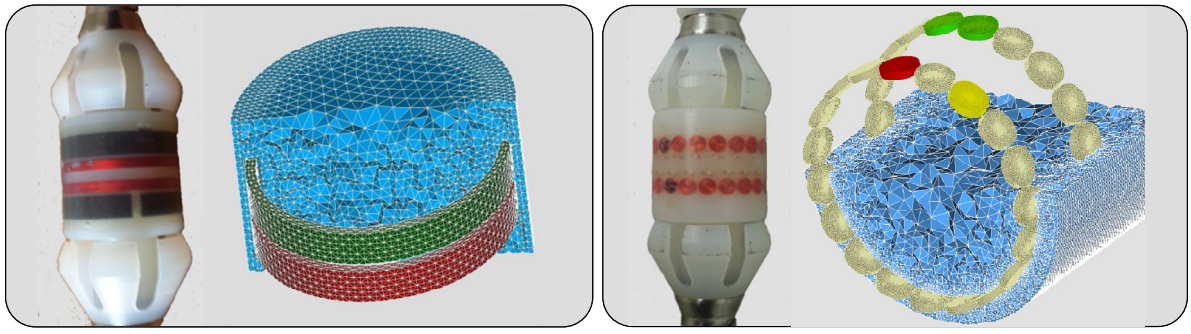

Figure 1. Axial probes: AXP (left) and MXP (right)

- Two rotating probes, much more difficult to modelize because of the magnetic core of the "LRP" (long rotating probe or the a copper ring around the ferrite pot of the "TRP" (transverse rotating probe).

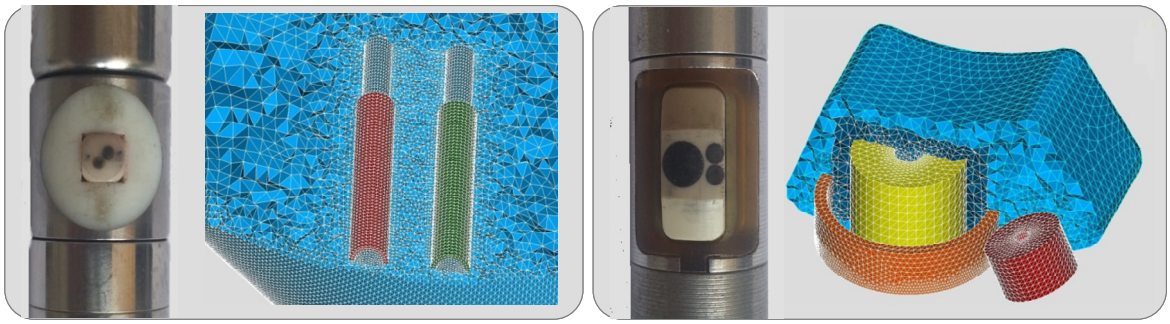

Figure 2. Rotating probes: LRP (left) and TRP (right)

Since the finite element domain has finite dimensions, the field emitted by the probe must be compatible with the size of that domain. There are two options for that:

- Option 1: put on the boundary an appropriate non-reflecting model, such as the “infinite box” model or “perfectly matched” layer,
- Option 2: extend the mesh of the box far from the probe, so that the emitting field is negligible on its boundary, then apply the wall condition seen above.

In C3D, we adopt the second option because it is more simple and also we have a good meshing tool with Salome. Furthermore, the probe signal is obtained by summing the solution field over the volume of the coils. As probes often operate in differential mode, the two coil integrals may be very close in value for small defects, so the coil meshes have to be as symmetric as possible and the computation must be accurate. Moreover, in case of small lift-of or in presence of a ferrite core, the gradient of the solution field may be strong at the end of the coil, so the mesh must be fine enough to catch this gradient.

Finally, the key words for the probe model are: realism of geometry and properties, fineness and symmetry of mesh.

3-2. Eddy current modelling

The first question arising in modelling the eddy current by the finite element method is the discretization of the skin depth. In C3D, we adopted the rule of about 5 elements in the Conventional Penetration Depth (CPD). If that is not possible because the CPD is too small (high frequency of permeability), we can use the surface impedance elements, allowing to limit the meshing to the surface of conductors, but without exempting to refine that surface mesh in the corners. The simplified case of the figure 3 illustrates the current in the volume of a tube (CPD = 1mm), and on the surface of the surrounding support plate (CPD = 70µm).

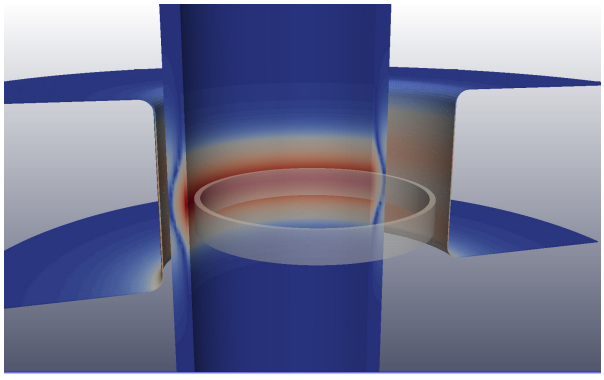

Figure 3. eddy currents in tube volume and on plate surface

The second question is the meshing of the thin layers without producing distorted elements. A thin layer is a flat volume with thickness small before the CPD. We verified that in that case, we can mesh the layer with only one volume in the thickness (pentaedron or hexahedron is recommended). If the layer is very thin (less than 1µm), we can arbitrarily thicken it in keeping the same effective conductance (it is the product of the conductance by the thickness).

The left figure 4 left shows the eddy currents in a tube volume and in the 20 µm thick chromium coating of an anti-vibration bar (AVB). We note a slight shielding effect and a concentration of current at the corners of the AVB, that both have a strong effect on the signal (they produce secondary loops). The figure 4 right shows the eddy current in the volume of a tube and on the surface of a 20 µm thick copper outer square deposit, showing that the deposit diverts the current from the tube, thus clearly degrading the detection of a potential outer flaw located under the deposit.

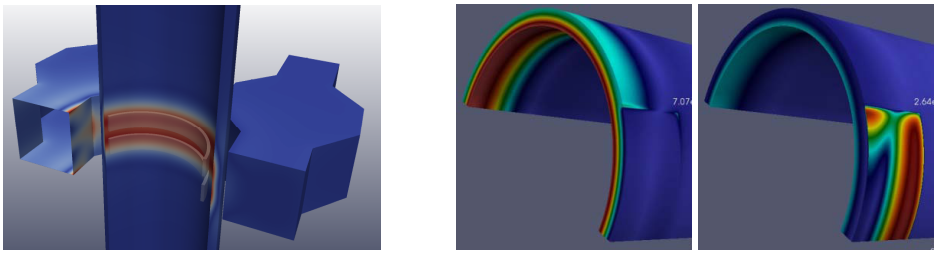

Figure 4. eddy currents in an AVB coating (left) and in a copper deposit (right)

3-3. Notch modelling

In C3D, we can modelize a fine notch with a "null normal current" surface condition or with a thin volume of air that we can mesh like the above thin layer. The figure 5 illustrates the current lines transversally impacting a through-the-wall notch. We note that with ELECTRIC form (figure 5 left), a part of current crosses the notch end, which results in a small error on the flaw signal, so we should refine the conductor at the surface of the notch to ensure a good insulating effect (despite the wall condition is weak in ELECTRIC form). For MAGNETIC form, all the lines by-pass the end of the notch (figure 5 right), producing a higher current concentration, which is physically relevant.

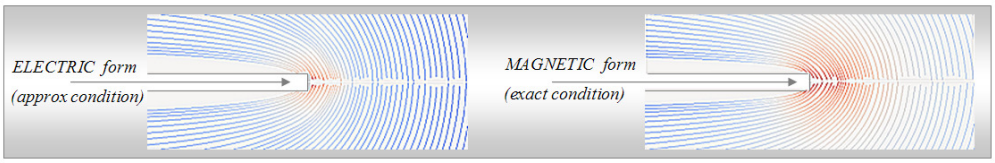

Figure 5. current lines around the end of a notch

Since the two refined faces of the notch have roughly the same fineness, we can put only one element in the thickness as said for the thin layers (figure 6 left). But we still need to refine the mesh in the surrounding volume of the conductor, because of the concentration of the current at the ends and corners of the notch (figure 6 right).

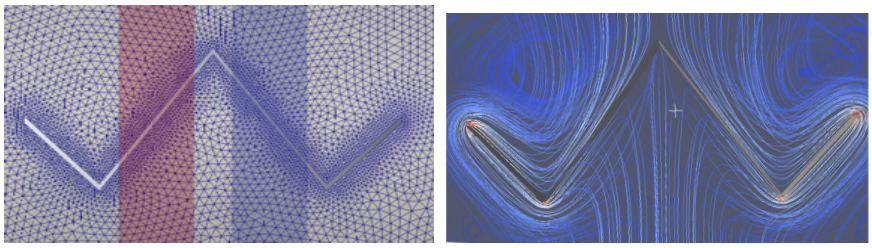

Figure 6. meshing refinement and current concentration around a notch

3-4. Moving the probe

In C3D, we have two techniques to move the probe for the simulation of a scan, based on two pre-meshed parts of the global domain: the "static mesh" and the "moving mesh".

The "sliding mesh" technique: in this technique, the mobile mesh contains the probe and the static mesh contains the tube and defect, the external air and potential components. Both are connected via a "sliding grid" (cylindrical or plane), composed with identical quadrangles (distorted if the scan is helical). To move the probe, we just have to shift the mobile mesh in translation and/or rotation with a round number of quadrangles. The advantage of this technique is its robustness (no numerical noise) and simplicity of implementation, the drawback is its lack of generality in movement and its heavy numerical cost when the sliding grid is fine (that is the red surface of the figure 7).

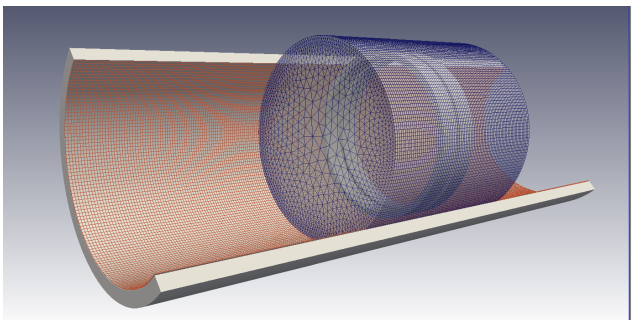

Figure 7: box, tube and sliding grid of the “sliding mesh” technique

The “re-meshing” technique: in this technique, the mobile mesh is reduced to the only probe, which releases the regular surface contact between the mobile mesh and the static mesh so that the meshing of the probe and that of the defect become totally independent. That provides a very low cost because the two meshes are refined separately only where it is useful. The drawback is that when moving the probe, the air volume between the probe and the tube must be totally re-meshed for each position of the probe. That is quite easy with the free-meshing tool of Salome, but the random-like dependence of the free-meshed zone to the probe displacement induces a so-called “mesh noise” in the signal. Two improvements have been implemented in C3D to solve that:

1- Include the probe mesh in a pre-meshed “probe box” such as on figure 8 left, in order to drive away the free-meshed zone, thus preserving a clean symmetric air mesh in the vicinity of the coils. The benefic effect on the signal is tremendous : on figure 8 right, the red signal is without the box, the black one is with the box.

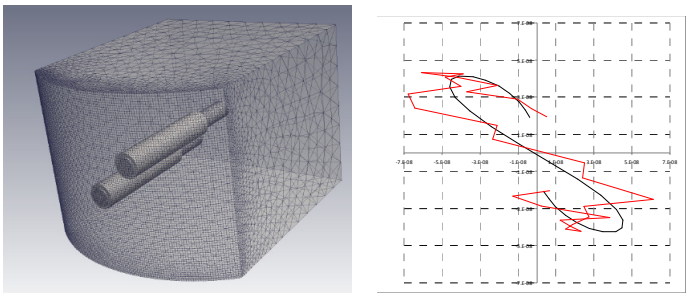

Figure 8. The LRP probe box and signal with (black) and without (red) the probe box

2- Add a so-called “refinement box” (read boundary on the figure 9 left), attached to the probe box (black on the figure 10 left), and refine the static mesh only included in it. The consequence is that the probe box and the static mesh facing it have always the same fineness (figure 9 right), and we verified that this property strongly reduces the mesh noise.

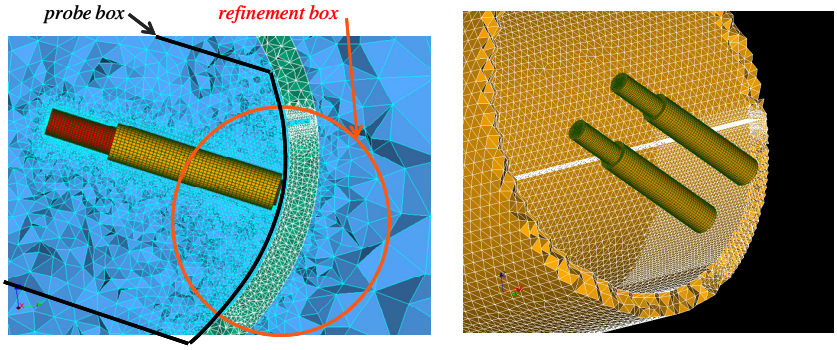

Figure 9. The LRP probe box (red), the refinement box (black) and the refined static mesh (right)

4. Validation and quality

4-1 Three levels of validation test

-1: the verification tests consist in checking individually any elementary function of the code. It implies the availability of theoretical documentation and a good software mastering. The figure 10 shows the 3D mesh (left) used to test the 1D problem of the skin effect. Indeed on this simple test, the agreement of the two C3D forms with the analytic solution is excellent (figure 10 right), what is normally the case if there is no bug in the coding of the function.

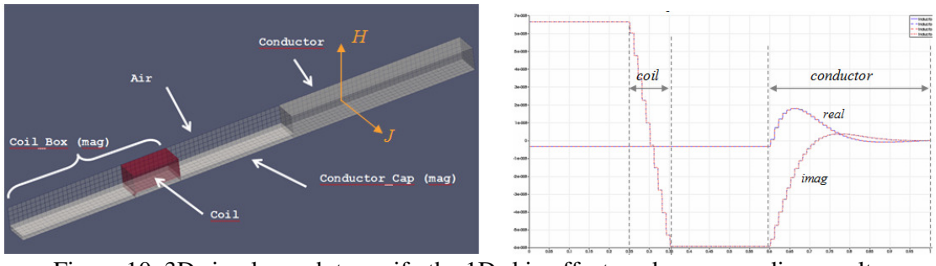

Figure 10. 3D simple mesh to verify the 1D skin effect, and corresponding results

-2: the benchmarking tests consist in comparing several numerical models with each other and with experimental data, in order to evaluate the relevance of the hypothesis assumed in each model. We show below the case#1 of the Benchmark B#9 of the COFREND Working Group « EC–NDT modelling » [2]. The case#1 deals with a coil in emitting-receiving mode (1 kHz) moving along the axis of a thin plate with a hole and an axial notch (figure 11 left). The scan is performed by C3D with the "sliding mesh" technique (figure 11 right).

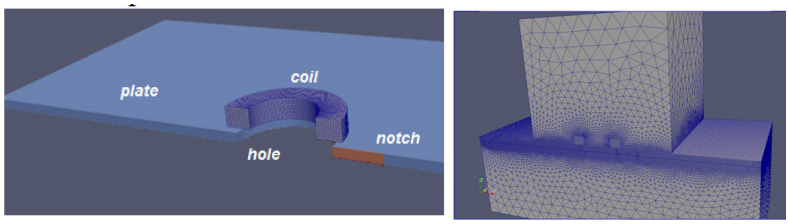

Figure 11. the Cofrend B#9 case#1 (left), and the corresponding "sliding mesh" (right)

We see on figure 12 left that the two C3D forms are in very good agreement except near the boundary of the static mesh, which is predictable. On figure 12 right, the comparison of the MAGNETIC form with the experiment is satisfying for the notch signal (the thickness of the large loop) and for the hole signal (the angle of the small loop).

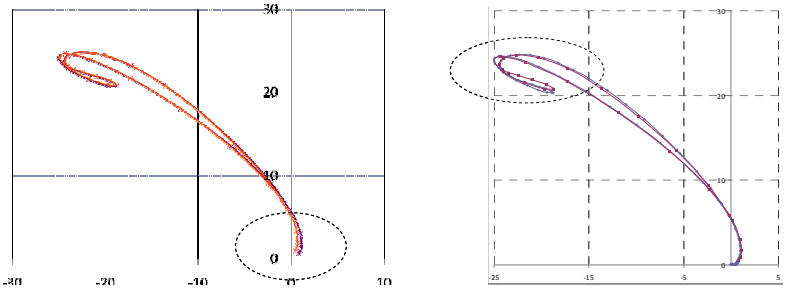

Figure 12. the two C3D forms compared (left) and the hole and notch signals compared to measure (right)

-3: the full-scale tests check the capability of the entire simulation process to account a complex phenomena. In the example illustrated of figure 13, we validate the re-meshing technique for the TRP scanning of the expansion zone (EZ) of a tube. In that case, the displacement of the TRP is driven by a 2 parameters tilting model (figure 13 left) taking the inner tube radius in input. We compare the C3D signal with measurements (figure 13 right) for the absolute real channel generated by a simple axial scan. That test proves that the TRP model properly « see » the EZ.

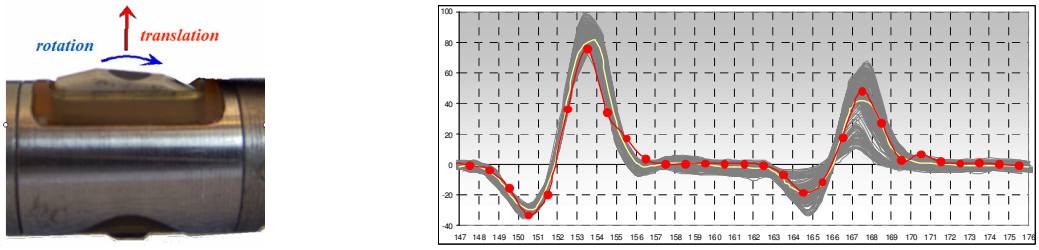

Figure 13. tilting parameters and comparison of C3D re-meshing computed signal (red) with measurements (yellow)

4-2 Quality

We have seen that the agreement of the two forms of C3D is obtained by the mesh refinement. We verified that in the case of an external 50% 40 mm longitudinal flaw, with the long rotating probe (LRP). For that purpose, we considered 2 meshes of the ferrite (coarse and fine) and 3 tunings of the refinement box: X1, X2, X4. We see on the figure 14 that the effect of the refinement differs with the refined component: on the left, the refining of the magnetic core of the probe only improves the offset of the signal, since the refinement of the tube (and defect) only improves its amplitude.

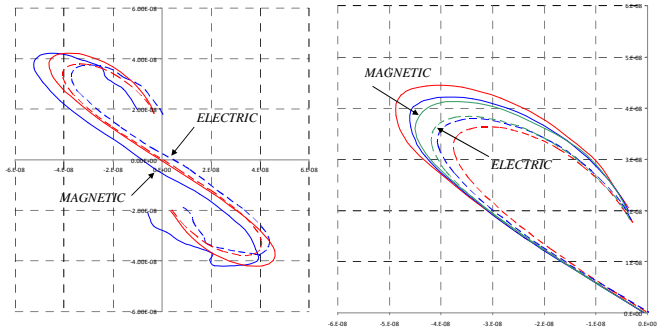

Figure 14. refinement of the probe (left) and of the tube (right)

The conclusion is that to better fit the two C3D forms, one should have to refine everywhere, but that is very expensive. A solution is the use of a local error estimator, such as that developed by the L2EP in code_Carmel, wich is reliable (it majorates the global error) and efficient (it minorates the local error). This estimator already has been validated in magneto-harmonics [3], and it is easily implementable in C3D. The global error is derived from the results $\mathbf{B}_{\mathrm{B,E}}, \mathbf{E}_{\mathrm{B,E}}$ of the ELECTRIC form and $\mathbf{H}_{\mathrm{H,J}}, \mathbf{J}_{\mathrm{H,J}}$ of the MAGNETIC form via the following formula:

$$\eta^2 = \omega \int_{V_\mu} \mu \left(\mathbf{H}_{\mathrm{H,J}} - \frac{1}{\mu} \mathbf{B}_{\mathrm{B,E}} \right)^2 dV_\mu + \int_{V_\sigma} \sigma \left(\mathbf{E}_{\mathrm{B,E}} - \frac{1}{\sigma} \mathbf{J}_{\mathrm{H,J}} \right)^2 dV_\sigma$$

which clearly discriminates two local error maps, magnetic and electric. So, the simple example of figure 15 illustrates the region to be refined to improve the coil meshing (middle) and to improve the defect meshing (right).

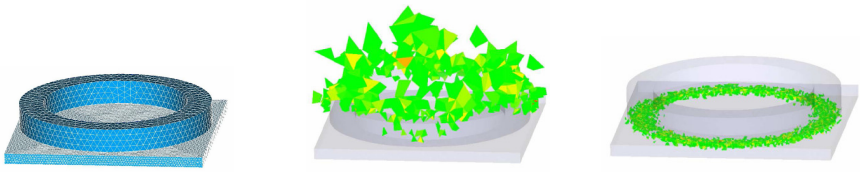

Figure 15: the test-case of a coil above a plate (left), and magnetic (middle) and electric (right) error maps

5. Software features

5.1. NDT oriented interface

Following all the precautions seen above, the meshes are developed thanks to the CAD resources of the Salome platform and once finalized are stored as Python scripts. Salome is supplemented by dedicated windows to:

- assign physical properties to the mesh components (figure 16 left),
- choose the scan technique and define the probe trajectory,
- launch the computation of the entire scan (on a cluster generally),
- repatriate and display the results (coil fluxes).

The post-processing of the coils fluxes are performed with a specific tool dedicated to the NDT indicators, which provides the Y Channel, C-Scan (figure 16 middle) and the Amplitude and Phase of the defect (figure 16 right).

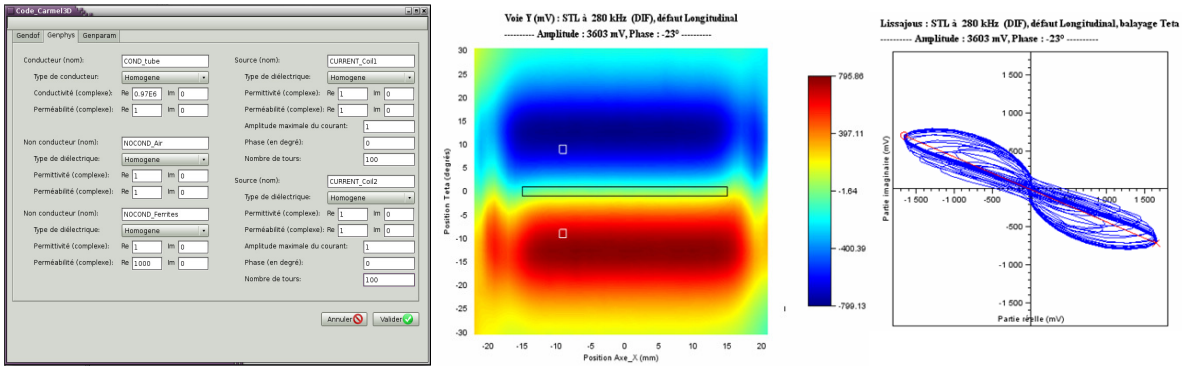

Figure 16. pre-processing window (left), Cscan of the signal (middle) and defect indicators in the phase plane (right)

5.2. Some computational skills

The HPC resources of EDF-R&D grows every year, for example, the cumulated power was around 1200 Tflops in 2012, 1600 Tflops in 2013 and 2200 Tflops in 2014. The last cluster entered in 2015, named PORTHOS, provides us 14532 Haswell cores.

Given that the both scanning techniques of C3D allow the distributed computing (one position of the probe for one core of the cluster), and because the total number of available cores is huge for our needs, we can say that the total time of the simulation of a complete scan never will exceed that of one resolution for one position.

In Table 1, we compare the computational parameters for the simulation of one position of a standard configuration, obtained with the two forms and the two scanning techniques (with the same result accuracy required for all options). We note that the "re-meshing" technique is 5 times faster than the "sliding mesh" technique, and we suppose that this ratio could be improved with the future scanning methods, since the ratio of 2 between both forms probably will not change. Finally, for a standard study, because we need for both forms to check the quality of the mesh, we can state today that the total time is about 20 min for any scan, using a cluster.

Table 17: Computational figures for one position of the probe

	« Sliding mesh » technique		« Re-meshing » technique	
	ELECTRIC	MAGNETIC	ELECTRIC	MAGNETIC
total number of DoF	6.8 millions	3.8 millions	3.4 millions	0.62 millions
CPU time for FE tasks	1min 50 sec	1min 30 sec	35 sec	1 min 8 sec
RAM needed (store the system)	**3.2 GO**	**2.7 GO**	**2.2 GO**	**1.9 GO**
CPU time per step of resolution	1.3 sec	0.75 sec	0.41 sec	0.17 sec
number of steps (error < 10^{-9})	3011	2896	1446	1563
total time	**65 min**	**37 min**	**13 min**	**6 min**

Note that the Table 1 only deals with the standard case, but we happened to solve with C3D exceptional cases about 10 times bigger in memory and time.

6. Conclusion

The finite element method (FEM) can account, without any limitation, a large panel of realistic 3D geometry (probes, flaws, influential parameters…), or electromagnetic properties (ferrites, plates and bars, deposit...) at least in the linear domain, but it involves a significant effort in meshing the skin effect, the thin layers and the defects, and particularly, the probe displacement in avoiding numerical noise. These problems often lead to refine the finite element meshes and consequently, they imply a high numerical cost.

To cope with that, Code_Carmel3D profits of advantages: a powerful CAD platform Salome, allowing the fine meshing of complex configurations, the ability to control the quality of the mesh, thanks to the specific dual formulations implemented in the code, and a high performance computing environment (clusters) available for EDF. Thanks these resources, the numerical simulation of various EC-NDT configurations today seems to be ready-to-hand. The main potential future improvement of Code_Carmel3D is the increasing of the ratio accuracy/cost.

References

[1] ENIQ, ENIQ Recommended Practice 6: the Use of Modeling in Inspection Qualification, ENIQ report No. 45, vol. 6, 2nd issue, 2011A

[2] Foucher, F., Maurice, L., Sollier, T. Reboud, C., Deneuville, F., Trillon, A., Thomas, P., "Working Group COFREND « Eddy Current NDT modeling »: Benchmarks for validating and improving simulation codes acceptation", 11th ECNDT, 2014

[3] E. Creuse, S. Nicaise, R. Tittarelli, A guaranteed equilibrated error estimator for the A - j and T - W magnetodynamic harmonic formulations of the Maxwell system, https://hal.archives-ouvertes.fr/hal-01110258,

[4] C. Gilles-Pascaud, A. Skarlatos, G. Pichenot, G. Cattiaux, T. Sollier, "Modelling of Steam Generator Tubes Inspection in the Proximity of Support Plates Area via a Coupled Finite Elements – Volume Integral Method Approach", Proceedings of the 7th ICNDE, Yokohama, 2009, May 12-14.

[5] Mistral, Q., Charret, T., "Array probe implementation (SMX) on EDF Steam Generator tubes", 10th ICNDE, Cannes, 2013, October 1-3.

[6] Ducreux, J.-P., Lepaul, S., Vérité, J.-C. , "Modelling of NDT in tubes of heat exchanger", 9th ICEM, San Fransisco, 2005, September 3-8.

[7] Moreau, O., Reboud, C., Buvat, F., Gilles-Pascaud, C., and Pichenot, G., “Experimental validations of eddy current testing models: case of multiple flaws affecting a steam generator tube”, 10th ECNDT, Moscow, 2010, June 7-11.

Modelling Ultrasonic Image Degradation due to Beam-Steering Effects in Austenitic Steel Welds

O. Nowers[1,2], D. J. Duxbury[1] and B. W. Drinkwater[2]

[1]NDE Research, Rolls-Royce, Derby, PO BOX 2000, DE21 7XX, UK

[2]Dept. of Mechanical Engineering, University Walk, University of Bristol, Bristol, BS8 1TR, UK

Abstract

Ultrasonic inspection of austenitic welds is challenging due to their highly anisotropic and heterogeneous structure. Epitaxial growth of grains across adjacent weld beads drives the formation of elongated and preferentially oriented grains within the weld region. The anisotropy causes a steering of the ultrasonic beam and the heterogeneity causes highback-scatter of energy due to the macroscopic granular structure of the weld. However, the specific impact and dependencies of these phenomena on ultrasonic imaging is not well understood.A semi-analytical simulation frameworkis developed to allow the analysis and evaluation of beam-steering effects in austenitic welds. Ray-tracing is performed using an efficient path-finding algorithm and coupled with a beam simulation and imaging routineto observe the impact of weld anisotropy on ultrasonic imaging. Representative anisotropy weld-maps are supplied by a model of the welding process. To provide an example of the operation of the model, the magnitude and behaviour of defect mislocation and amplitude as a function of the weld anisotropy is presented.

Keywords : Ultrasonics, austenitics, ray-tracing, inspections, welds

1.Introduction

Within the UK nuclear power generation industry, ultrasonic Non-Destructive Evaluation (NDE) is employed as a means to verify the structural integrity of a given component at the manufacturing stage and at various points throughout its operational life. Due to the safety-critical nature of the industry, the ability to accurately detect, characterize and size defects is of paramount importance. Ultrasonic NDE of austenitic welds is particularly challenging due to the highly anisotropic and heterogeneous microstructures exhibited. This is due to a number of mechanisms. Firstly, austenitic steel does not undergo a change in crystal structure during the weld solidification process leading to the formation of large grains [1]. With the majority of other metals, a change in crystal structure during solidification would help to 'break-up' the grain structure leading to a more refined microstructure. Secondly, re-melting of previous weld passes by the current weld pass leads to the epitaxial growth of grains along the local temperature gradient, in turn leading to an elongated grain morphology. Furthermore, favorably oriented grains i.e. grains with a <100> crystallographic direction parallel to the heat flow direction, dominate the crystal structure during solidification in a process known as selective growth. As a result, a typical austenitic weld microstructure is composed of large, preferentially oriented grains and exhibits a high degree of anisotropy.

Due to the highly anisotropic and heterogeneous microstructure exhibited by typical austenitic welds, ultrasound passing through a weld is 'bent' in a process known as 'beam-steering'. This causes a variety of problems during ultrasonic inspection, including the mislocation of defects and aberration of the ultrasonic beam. This leads to a reduced Probability of Detection (POD) and an increased Probability of False Alarm (PFA), impacting upon both the quality of the inspection and the confidence placed in its results. The ability to model this beam-steering and its impact upon ultrasonic imaging allows a qualitative and quantitative assessment of the severity of anisotropy of a particular weld, and more importantly, the potential to optimize an inspection through parametric analysis.

Fundamental to the ability to model beam-steering is the use of a ray-tracing algorithm. A ray-tracing algorithm, as applied to ultrasonic NDE, is designed to predict the path of a wave during propagation through an arbitrary medium. Ray-tracing algorithms are particularly useful for the prediction of wave propagation in inhomogeneous and anisotropic materials, where the path of a ray is 'steered' due to the characteristic directional dependence of the wave velocity. Typically, the wave is 'traced' in the direction of maximum group velocity i.e. the energy flow. Historically, ray-tracing algorithms as applied to austenitic weld inspection have fulfilled a number of applications, including the modelling of

wave paths to determine weld inspection coverage [2,3,4,5], analysis of reflection properties of defects within welds [6], and the correction of degraded images due to wave propagation through austenitic welds [7,8]. This paper, however, concerns the novel use of ray-tracing algorithms to simulate degraded ultrasonic images due to propagation through austenitic weld material, and analysis of the characteristics of the degradation when key inspection parameters are varied through parametric analysis.

There are generally two types of ray-tracing algorithm as applied to ultrasonic NDE: 'marching' algorithms and 'minimisation' algorithms. The former generally relies upon the principle of 'stepping' a ray a through a fixed time or distance interval coupled with iterative solution of the wave properties at each increment. If $\Psi(t)$ is the ray-state at time, t, and $\Psi(t+dt)$ is the ray state at a later time, $t + dt$, then:

$$\Psi(t + dt) = F(\Psi(t)) \quad [1]$$

where$F$ is a necessary operation on the current ray state to calculate the next ray state. For example, this may include the creation of an imaginary interface and consideration of refractive properties such that the on-going ray may be calculated.

One of the principal marching methods was developed by Ogilvy [2]and packaged into softwarecalled RAYTRAIM. A ray is launched at a specific angle and discrete distance steps are taken along the ray trajectory. At each step, an imaginary interface is created and the local material properties are analyzed to solve for the on-going ray. Both the wave amplitude and direction are predicted, however this can lead to lengthy computation times should a ray be required to propagate a long distance or to a specific termination point. The latter limitation was addressed by Connolly et al. who implemented a procedure to iteratively adjust the 'launch' angle of a ray until the ray terminates at the desired point in a trial-and-error approach [5]. This is particularly useful for imaging where a specific ray creation and ray termination point are required. However, the algorithm can suffer from extended computation times due to the potential need for hundreds of trial solutions before the correct termination point is achieved to a given accuracy.

Minimisation algorithms operate through the minimization of a particular function descriptive of the material heterogeneity and anisotropy. Their operation is founded upon Fermat's principle of minimum time stating that a wave will propagate between two arbitrary points in space such that the time of propagation between the two is a minimum. A common example is the beam-bending method [9], which relies upon the iterative 'bending' of a spline curve between two points such that the total time-of-flight along the spline is minimized. The algorithm does not explicitly involve the calculation of wave properties (e.g. amplitude, polarization e.t.c.), however this allows a dramatically reduced computation time as compared to typical marching methods. Another class of minimization algorithms is the field of path-finding algorithms, predominantly used within computer science applications but which have seen increased uptake into the field of NDE in recent years [8,10]. The A* algorithm is a rapid nodal-based path-finding algorithm and enables ray-tracing between two specified points. Unique to its operation is the use of 'heuristics', whereby knowledge of the termination point is used to inform the progression of the algorithm. This may be exploited to yield a solution for a given ray-trace in a very short amount of time, making the algorithm ideal for the current array modelling requirements, where many thousands of ray-traces may be required for a parametric study or optimization attempt. The algorithm does, however, assume a ray-trace will always exist between the specified creation and termination points and therefore does not account for the potential existence of dead-zones i.e. regions where ultrasound does not propagate. The operation of the A* algorithm is discussed in further detail in Section 2.2.

This paper details the development of a beam-steering simulation framework that draws upon an efficient ray-tracing algorithm, the A* algorithm, to simulate both the propagation of ultrasound through anisotropic and heterogeneous austenitic welds, and to analyse the subsequent impact upon ultrasonic imaging. Crucial to the model is the ability to rapidly and accurately simulate propagation through anisotropic weld material such that parametric analysis or optimization methods may be undertaken, where many thousands of ray-traces may be required.

2. Methodology

The beam-steering modelling framework consists of four major parts: (1) weld simulation, (2) ray-tracing, (3) defect simulation and (4) beam-simulation and imaging. The weld simulation step concerns the specification of the weld anisotropy, and its material parameters such that the velocity of propagation may be calculated. Ray-tracing is performed using the A* algorithm [11] as detailed in Section 2.2, to obtain the time-of-flight for each array element combination to and from the defect. The scattering behaviour of the defect is encapsulated through use of the scattering matrix (or S-matrix) associated with the defect, describing the far-field scattering amplitude as a function of the incident and scattered angles, and the ultrasonic wavelength [12]. Finally, the full matrix of transmit-receive data is created in the beam simulation step, and an imaging algorithm applied to allow analysis of defect mislocation and aberration due to weld anisotropy.

2.1 Weld simulation

The beam-steering simulation framework relies upon the initial specification of the weld anisotropy, such that the velocity of wave propagation may be calculated and ray-tracing performed. A 'weld-map' is a useful descriptor of material anisotropy, and indicates the local anisotropic orientation as a function of position in the weld. A number of models exist for the description of anisotropy in austenitic welds [2, 6, 13, 14, 15]. The MINA model (Modelling anIsotropy through the Notebook of Arc-welding) described by Moysan et al. [15]can be tailored towards a specific weld and draws upon measurements made from a macrograph of the weld and knowledge of welding parameters to predict the weld anisotropy. As such, the model is able to account for anisotropy variation on a weld-by-weld basis. There are five key inputs to the MINA model. The re-melting rates govern the extent to which one weld-pass re-melts a previous weld-pass and includes the lateral re-melting rate, R_L, defined as the ratio of the re-melted width of the current weld-pass due to deposition of the next weld-pass and its total width, and the vertical re-melting rate, R_V, defined as the ratio of the re-melted height of the current weld-pass due to deposition of the weld-pass above, and its total height. The inclination angles govern the tilt of each weld-pass with respect to a given parameter, and include the chamfer inclination, θ_B, and the weld-pass inclination, θ_C, defined as the angles of inclination of the symmetry axis of the weld-pass to the vertical when the weld-pass is against the edge of the chamfer, or another weld-pass, respectively. Finally, the sequencing order of weld-passes must be included to account for variation induced by differing welding procedures. In this way the MINA model can be used to predict the weld anisotropy on a case-by-case basis.

Since ray-tracing is performed using a time-minimisation approach, knowledge of the associated propagation velocities of each section of the weld is crucial to the accuracy of the final ray-trace. As such, once the weld anisotropy has been specified, the Christoffel equations may be used to calculate the velocity variation associated with the particular anisotropic orientation and incident angle of the wave [16].Ray-tracing may then be performed as detailed in Section 2.2.

2.2 Ray-tracing algorithms

The A* algorithm is chosen to perform ray-tracing for the given weld anisotropy input. The A* algorithm [11] is a modified version of Dijkstra's algorithm [17], which was originally conceived in 1958 as a solution to the 'Travelling Salesman Problem' [18].Dijkstra's algorithm operates on a nodal basis, whereby a ray-trace is calculated through the connection of a number of nodes that form the shape of the ray, with the properties of each node dependent upon its location within the anisotropic region. The algorithm performs a 'weighted' breadth-first search and obeys the general search rules as follows to determine the minimum propagation time from a given start node to every node in the system.

1) Assign every node an infinite propagation time except start node (zero propagation time).
2) Mark all nodes unvisited and allocate all to the unvisited set.
3) Consider all neighbor nodes to current node and update propagation time dependent on local propagation velocity and distance from current node, overwriting previous propagation time if less.
4) Save minimum propagation time taken to node under consideration.
5) Once all neighbor nodes considered, remove current node from unvisited set.
6) Set current node as the unvisited node with the minimum propagation time and repeat steps 3-5.
7) Repeat until unvisited set is empty at which point terminate algorithm.

Nodes may be allocated to an imaging area in a regular arrangement or randomly distributed. Previous work by the authors[10] recommends the use of a random nodal distribution, and includes the optimization of various parameters associated with the accurate operation of the Dijkstra and A* algorithms.

Fundamental to the concept of the A* algorithm, is the concept of the 'weighted time', $T(n)$, defined as:

$$T(n) = g(n) + h(n) \quad [2]$$

where n is the node under consideration, $g(n)$ is the nodal cost and $h(n)$ is the heuristic cost. The nodal cost describes the propagation time between the current node and the desired propagation node. The heuristic cost is composed of two parts:

the heuristic time, t_h, and the heuristic weight, η, and is given as:

$$h(n) = \eta t_h \quad [3]$$

The heuristic time describes the propagation time from the node under consideration to the finish node and is given as the Euclidean distance divided by a reference velocity, c, as:

$$t_h = \frac{\sqrt{(x - x_g)^2 + (z - z_g)^2}}{c} \quad [4]$$

where x, z are the co-ordinates of the node under consideration, and x_g, z_g are the co-ordinates of the finish node. The reference velocity may either be chosen as the base material velocity or an average velocity attributed to all propagation directions within the weld. The heuristic weight is able to strengthen or weaken the influence of the heuristic calculation on the progression of the algorithm and varies from 0 i.e. nodal-dominated with no consideration of heuristic costs (i.e. Dijkstra's algorithm), to infinity i.e. heuristic-dominated with no consideration of nodal costs (i.e. a weighted depth-first search). Contrary to Dijkstra's algorithm, the A* algorithm can terminate before all nodes have been visited, and therefore a globally optimal solution cannot be guaranteed unless the choice of heuristic is admissible i.e. it never over-estimates the cost of reaching the finish node. With the correct choice of heuristic and a carefully chosen weight to ensure its admissibility, the literature indicates that the A* algorithm can reduce computational time with no impact upon accuracy as compared to Dijkstra's algorithm [10,19].

2.3 Defect simulation

To simulate defect scattering events, the beam-steering simulation framework uses Finite-Element Method (FEM) generated Scattering matrices (or S-matrices). This has been developed by Velichko et al. [20, 21, 22] and allows the computation of the scattered amplitude and phase for a given incident and scattered angle, from a scatterer of arbitrary size and shape at a given frequency. The method draws upon a numerical implementation of the integral representation formula for an elastic solid along a surface that bounds the scatterer and can be implemented in both 2D and 3D domains. As such, S-matrices provide a robust and efficient method to obtain the complete scattering behaviour of an arbitrary scatterer.

2.4 Beam-simulation and imaging

The beam-steering simulation framework is built in a semi-analytical environment [23] and thus benefits from a high degree of flexibility with regards to both the type and geometry of the component to be inspected, and the probe to be used (e.g. single-element or contact/wedge-mounted phased array). Considering the phased array inspection of a weld and accounting for the interaction of longitudinal waves only, the frequency domain response for an arbitrary scatterer, $F(\omega)$, is given as:

$$F(\omega) = \left| \frac{\sqrt{\lambda}}{r_{tx} r_{rx}} e^{-i\omega(t_{tx}+t_{rx})} D(\omega, \theta_{tx}) D(\omega, \theta_{rx}) I(\omega)^2 A_{LL}(\omega, \theta_{inc}, \theta_{scat}) \right| \quad [5]$$

where λ is the wavelength, r_{tx} and r_{rx} are the propagation distances from the transmitting and receiving element to the defect, respectively,t_{tx} and t_{rx} are the times-of-flight from the transmitting and receiving element to the defect, respectively, ω is the angular frequency, D is the directivity function of the array element, θ_{tx} and θ_{rx} are the ray angles as taken from the normal to the transmitting and receiving elements, respectively, $I(\omega)$ is the impulse response function of the element, A_{LL} is the longitudinal-longitudinal far-field defect scattered amplitude component as given by the corresponding S-matrix and θ_{inc} and θ_{scat} are the incident and scattering angles from the defect, respectively.

The beam-steering simulation framework collects the full FMC of data for a given inspection scenario and can therefore support any imaging algorithm in a post-processing environment. For all scenarios considered in this paper, the Total Focusing Method (TFM) is used for imaging as developed by Holmes et al. [24]due to its ability to produce a fully focused image. To calculate the mislocation and amplitude decrease of the defect response, firstly the isotropic equivalent simulation is run and then the anisotropic ray-tracing simulation is run. The defect mislocation is equivalent to the distance between the locations of the maxima of each simulation, while the defect amplitude decrease is equivalent to the difference between the peak amplitudes of each simulation (in *dB*).

3. Validation

Previous work by the author has involved the validation of the Dijkstra and A* algorithms against the beam-bending method [10]. To provide validation of the entire beam-steering simulation framework, a methodology was used whereby perturbation of an array-generated focal spot was measured in experiment, and then recreated in simulation and compared. Figure 1 details the validation experimental arrangement indicating two linear contact 64 element 2 *MHz*ultrasonic phased arrays; array A and array B. Both arrays were held a fixed lateral distance apart, x_{sep} = 90 *mm*, and placed firstly over 55 mm thick isotropic 304 stainless steel parent material (position 1) and then asymmetrically over a 55 mm thick anisotropic 308 stainless steel V-weld (position 2) so as to maximise the distance of propagation through the weld. Note that the test-piece in Figure 1 has been 'split' into separate sections for illustrative purposes. FMC data was captured at both positions and array A focused onto the surface of array B at each element location in post-processing for both data-sets. For each focal spot position, the absolute amplitude across array B was measured at each element such that the position of the focal maxima could be extracted. The difference between the position of the focal maxima during isotropic propagation and that obtained for anisotropic weld propagation was then calculated to give the 'focal-spot shift', *S*, due to the presence of weld anisotropy. Note that *S* can be either positive or negative dependent on whether the focal-spot movement was to the right or to the left, respectively. This procedure was conducted in experiment, and an equivalent arrangement built in the beam-steering simulation framework.

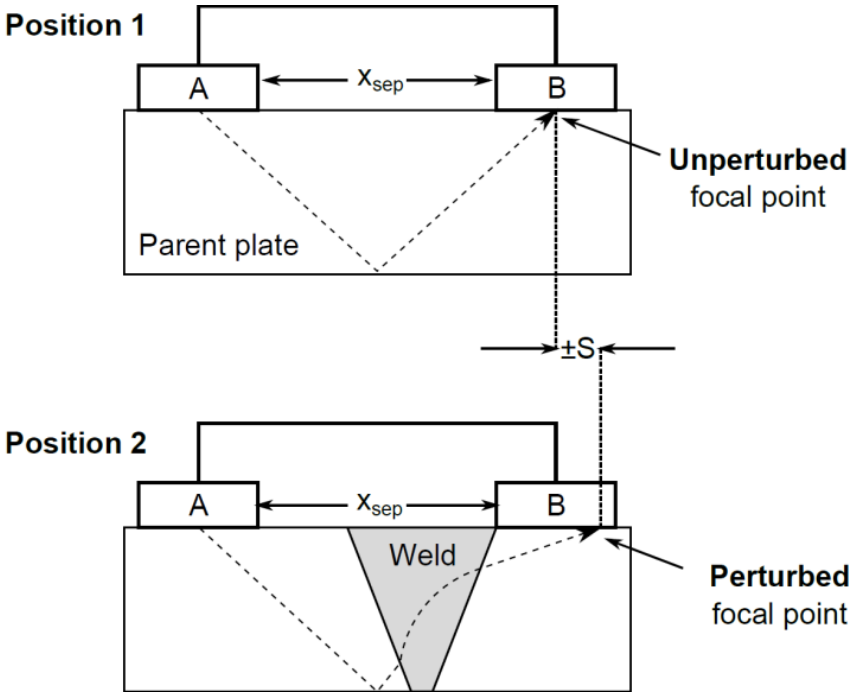

Figure 1. Schematic showing the positioning of the rig so as to allow measurement of the focal spot perturbation due to weld anisotropy.

Fundamental to the accuracy of the validation was the recreation of the experimental weld in simulation. With knowledge of the welding parameters, and analysis of a macrograph of the weld, the MINA weld-map was produced and used to describe the anisotropy of the weld as given in Table 1. An anisotropy sub-region size of 1 mm^2 was used to approximate to the typical grain sizes observed within the weld.

MINA Parameter	Value
R_L	0.165
R_V	0.311
θ_B	17.08°
θ_C	0.82°

Table 1.MINA parameters for the validation weld test-piece

Figure 2 details the focal spot movement as a function of the focal element position on array B. Both simulated and experimentaldata show excellent trend agreement as the focal element is adjusted, with a negative *S* shift at lower focal elements and a positive *S* shift at higher focal elements. For example, at a focal element of 27, a 3 *mm* positive *S* shift is recorded in both simulation and experiment. Results do, however, observe a degree of fluctuation that can be attributed to the inherent variation of the weld microstructure and the errors associated with weld recreation in simulation using the MINA model. Larger discrepancy between results above a focal element of 28 may be attributed to the reduced ability of the array to focus at higher beam angles. Results below a focal element of 15 have been excluded such that a sufficiently large amplitude profile across array B could be analyzed and a focal spot maximum extracted.

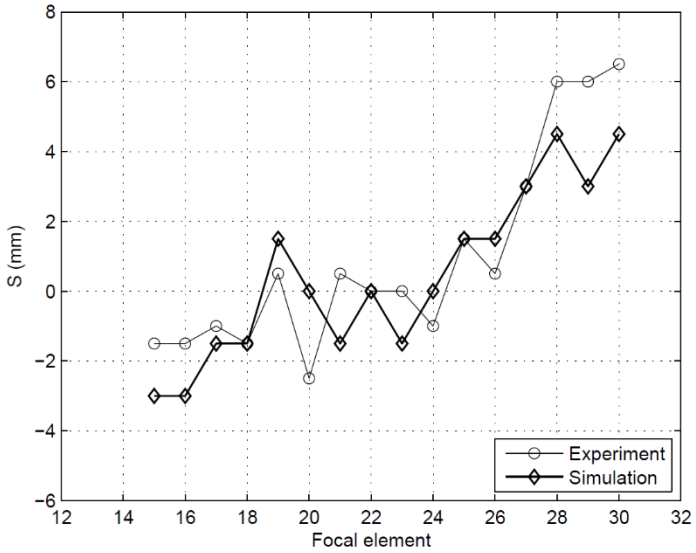

Figure 2. Focal spot movement as a function of the focal element on array B for simulated and experimental data.

4. Parametric studies

To provide an example of the operation of the beam-steering simulation framework, aparametric study is described. This was chosen to reflect the flexibility of the individual components of the model, with particular reference given to the corresponding computation time and the ability to conduct parametric studies on a reasonable timescale. The primary purpose of the model is to allow optimization of a given austenitic weld inspection. For this reason, there is significant future potential to encapsulate the model within an inversion framework.

4.1Variation of anisotropy distribution

Due to the fact that grain formation is an inherently random process during weld solidification (albeit subject to mechanisms that influence the size, shape and orientation of the grains), the grain structure at different circumferential positions along a weld cannot be assumed to be identical. Moreover, due to the variation in weld microstructure, the

subsequent impact upon ultrasonic imaging cannot be assumed to remain constant. As such, it is useful to perform statistical analysis of variation in the weld microstructure and the associated impact upon mislocation and aberration of a defect response as compared to an equivalent isotropic inspection. Averaging metrics may then be produced, such as the mean mislocation or mean amplitude decrease, and used to inform an inspection development process. Furthermore, worst-case scenarios may be extracted should a statistically sufficient number of weld-map variations be run.

Figure 3 details the simulated inspection setup for analysis of the impact of anisotropy distribution upon imaging. All simulations were performed using a 32 element 0.78 *mm* pitch 2 *MHz* phased array mounted on a rexolite wedge with a wedge angle of 16°. A 4 mm planar smooth lack of fusion crack is located on the right-hand fusion-face of a 308 austenitic steel weld at (x,z) = (10.88,27.5)*mm*. Table 2 details the bounds of variation of the MINA parameters to simulate variation of the weld anisotropy due to the inherently random grain formation process.Note that variation in the weld microstructure due to gravitational effects, for example, if the welding head is moved around a fixed pipe, has not been considered. Instead, the welding head is considered to be fixed while the pipe is rotated. The chosen weld is intended to simulate the experimental weld used for validation in Section 3 due to its industrial applicability.

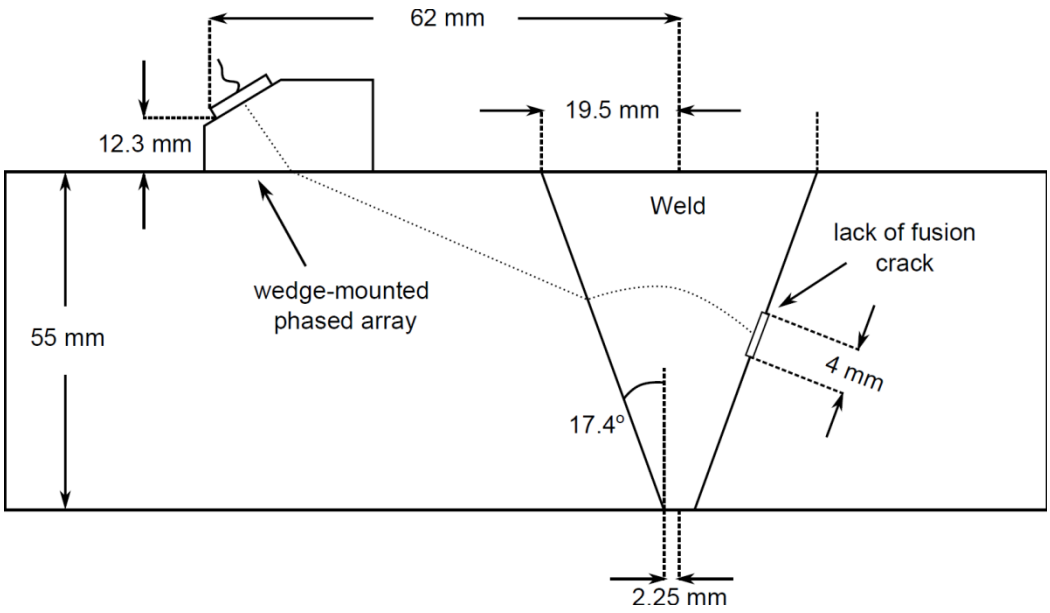

Figure 3. Simulated inspection setup for the anisotropy distribution parametric study.

MINA Parameter	± Variation	Minimum Value	Actual Value	Maximum Value
R_L	0.15	0.015	0.165	0.315
R_V	0.15	0.161	0.311	0.461
θ_B	10°	7.08°	17.08°	27.08°
θ_C	10°	0°	0.82°	10.82°

Table 2.Variation of MINA parameters for the anisotropy distribution parametric study.

Figure 4 illustrates one iteration of the beam-steering simulation framework indicating both the isotropic material case (Figure 4a) and the anisotropic material case (Figure 4b). For isotropic material, the lack of fusion crack is easily located and exhibits a smooth response from the crack face. The anisotropic material image is normalized against the peak amplitude of the isotropic image and exhibits an amplitude decrease of around -3 dB, including a mislocation of around 5 mm. The direction of mislocation towards the upper part of the weld would be of particular concern in a real

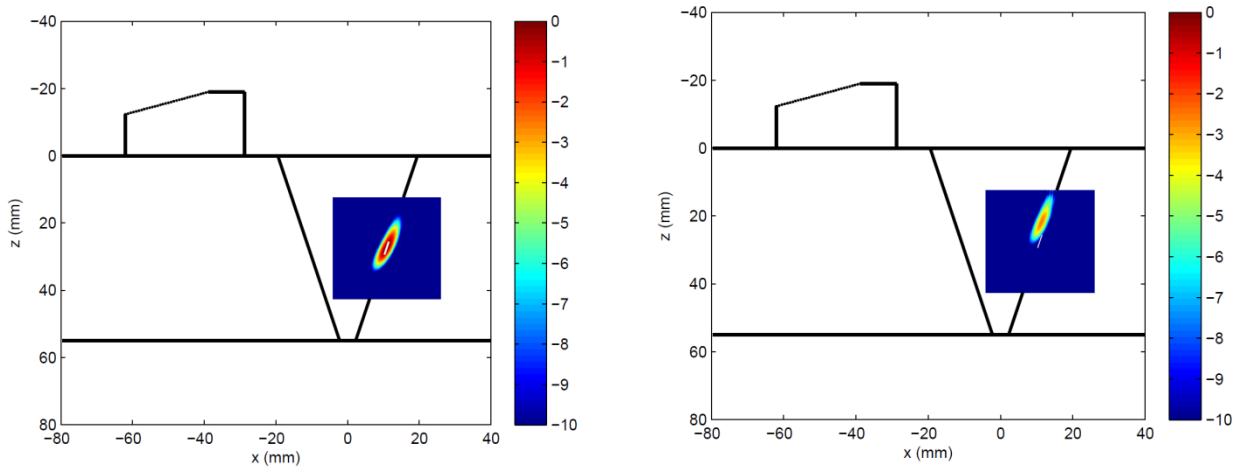

(a) (b)

inspection, as the defect to inner-diameter measurement is of critical importance from a structural integrity point of view.

Figure 4. Example TFM images (in dB) assuming material isotropy for (a) isotropic material and (b) anisotropic material, indicating the corresponding defect mislocation and degradation.

Figure 5 details the corresponding histograms for defect mislocation (Figure 5a) and defect peak amplitude decrease (Figure 5b) for 200 iterations of the beam-steering simulation framework. Each iteration of the model (i.e. collection of 32x32 FMC data and imaging) took a total of 3 minutes to run. A mean defect mislocation of (3.7 ± 1.2) *mm* was obtained, where the error is equal to the standard deviation of the results. Analysis of Figure 5a indicates a distribution skewed to a lower mislocation and the presence of 'gaps' in the histogram, for example at a mislocation of 5.75 *mm*. This may be due to the presence of preferential ray-traces for the set of MINA parameter distributions leading to highly unlikely mis-located defect positions. A mean defect peak amplitude decrease (Figure 5b) of (-4.4 ± 1.8) *dB* was obtained, where the error is equal to the standard deviation of the results. However, analysis of Figure 5b indicates a bimodal distributionwith two distinct peaks at -2 and -6 *dB*, respectively. Such a result highlights the importance of a model of this nature, and the added insight that can be provided with regards to potential defect degradation during inspection of a weld.

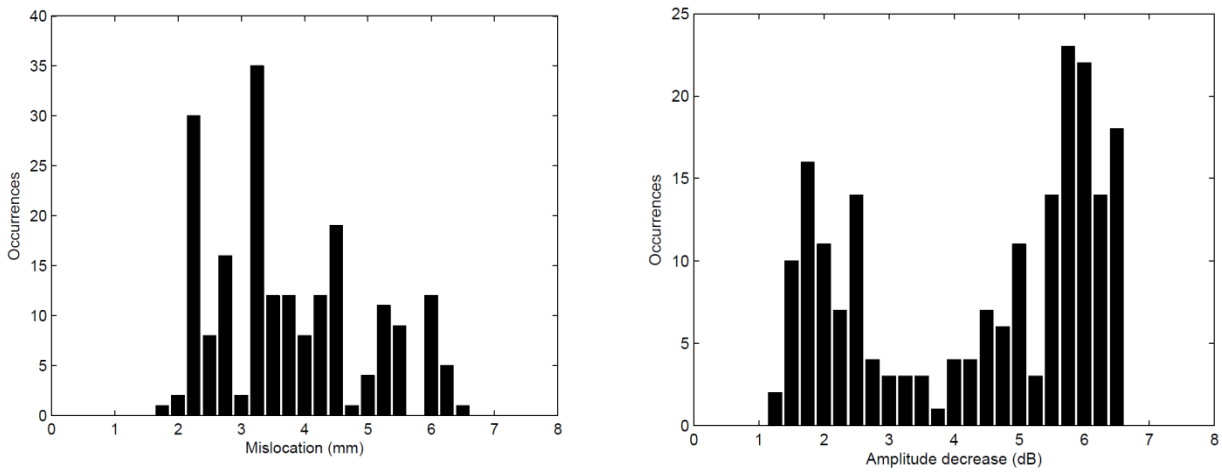

(a) (b)

Figure 5. (a) Mislocation and (b) amplitude decrease histograms for 200 iterations of the beam-steering simulation framework

4. Conclusions

This paper has detailed the development and operation of a semi-analytical beam-steering simulation framework for the analysis of defect mislocation and aberration due to anisotropic austenitic weld material. The model draws upon a rapid ray-tracing algorithm, the A* algorithm to calculate the path of ultrasound through a predetermined weld anisotropy distribution and calculates the scattered response from a given defect using an efficient FEM method. This is then compared to the isotropic equivalent and metrics such as defect mis-location and aberration due to the presence of weld anisotropy extracted. An example parametricstudy was presented to simulate the ultrasonic inspection of a typical austenitic weld, and to exhibit the potential for use of such an algorithm in an industrial environment. Crucial to this was the speed of execution of the model, requiring only 3 minutes to collect and image a 32x32 FMC data-set.

Acknowledgements

This work was jointly funded by the Engineering and Physical Sciences Research Council (EPSRC) and the Research Centre in Non-Destructive Evaluation (RCNDE).

References

[1] R. J. Hudgell and B. S. Gray, "The ultrasonic inspection of austenitic materials – State of the Art Report", Technical Report, Risley Nuclear Power Development Laboratories, pp.1-29 (1985)

[2] J. A. Ogilvy, "Computerized ultrasonic ray-tracing in austenitic steel", NDT International, Vol.18, pp67-77 (1985)

[3]J. A. Ogilvy, "Ultrasonic beam profiles and beam propagation in an austenitic weld using a theoretical ray-tracing model", Ultrasonics, Vol.24, pp337-347 (1986)

[4]A. Harker, J. A. Ogilvy and J. A. G. Temple, "Modelling ultrasonic inspection of austenitic welds", Journal of Non-Destructive Evaluation, Vol.9, pp155-165 (1990)

[5]G. D. Connolly, "Modelling of the propagation of ultrasound through austenitic steel welds", PhD thesis, Imperial College London (2009)

[6]J. A. Ogilvy, "The ultrasonic reflection properties of planar defects within austenitic welds", Ultrasonics, Vol.26, pp318-327 (1986)

[7]G. D. Connolly, M. J. S. Lowe, J. A. G. Temple and S. I. Rokhlin, "Correction of ultrasonic array images to improve reflector sizing and location in inhomogeneous materials using a ray-tracing model", Acoustical Society of America, Vol.127, pp2802-2812 (2010)

[8]J. Zhang, B. W. Drinkwater and P. Wilcox, "Monte-Carlo inversion of ultrasonic array data to map anisotropic weld properties", IEEE Transactions on Ultrasonics, Ferroelectrics and Frequency Control, Vol.59, pp2487-2497 (2012)

[9]B. R. Julian and D. Gubbins, "Three-dimensional seismic ray-tracing", Journal of Geophysics, Vol.43, pp95-114 (1977)

[10]O. Nowers, D. J. Duxbury, J. Zhang and B. W. Drinkwater, "Novel ray-tracing algorithms in NDE: Application of Dijkstra and A* algorithms to the inspection of an anisotropic austenitic steel weld",NDT&E International, Vol.61, pp58-66 (2014)

[11]P. E. Hart, N. J. Nilsson and B. Raphael, "A formal basis for the heuristic determination of minimum cost paths", IEEE Transactions on Systems Science and Cybernetics, Vol.4, pp100-107 (1968)

[12]A. Velichko and P. Wilcox, "A generalized approach for efficient finite element modelling of elastodynamic scattering in two and three dimensions", Journal of the Acoustical Society of America, Vol.128, pp1004-1014 (2010)

[13]M. G. Silk, "Computer model for ultrasonic propagation in complex orthotropic structures", Ultrasonics, Vol.19, pp208-212 (1981)

[14] V. Schmitz, F. Walte and S. V. Chakhlov, "3D ray-tracing in austenite materials", NDT&E International, Vol.32, pp201-213 (1999)

[15] J. Moysan, A. Apfel, G. Corneloup and B. Chassignole, "Modelling the grain orientation of austenitic stainless steel multipass welds to improve ultrasonic assessment of structural integrity", International Journal of Pressure Vessels and Piping, Vol.80, pp77-85 (2003)

[16] B. A. Auld, "Acoustic fields and waves in solids", Wiley (1973)

[17]E. Dijkstra, "A note on two problems in connexion with graphs", Numerische Mathematik, Vol.1, pp269-271 (1959)

[18]G. Gutin and A. P. Punnen, "The travelling salesman problem and its variations", Springer (2006)

[19]I. Chabini and S. Lan, "Adaptations of the A* algorithm for the computation of fastest paths in deterministic discrete-time dynamic networks", IEEE Transactions on Intelligent Transportation Systems, Vol.3, pp60-74 (2002)

[20] A. Velichko and P. Wilcox, "A generalized approach for efficient finite element modeling of elastodynamic scattering in two and three dimensions", Journal of the Acoustical Society of America, Vol.128, pp1004-1014 (2010)

[21] P. Wilcox and A. Velichko, "Efficient frequency-domain finite element modeling of two-dimensional elastodynamic scattering", Journal of the Acoustical Society of America, Vol.127, pp155-165 (2010)

[22] A. Velichko and P. Wilcox, "Efficient finite element modeling of elastodynamic scattering with non-reflecting boundary conditions", Review of Progress in Quantitative Nondestructive Evaluation Proceedings, Vol.1430, pp142-149 (2012)

[23] MatLab R2012a, The Mathworks Inc.

[24] C. Holmes, B. W. Drinkwater and P. Wilcox, "Post-processing of the full matrix of ultrasonic transmit-receive array data for non-destructive evaluation", NDT&E International, Vol.38, pp701-711 (2005)

Overview and Status of the International Program to Assess the Reliability of Emerging Nondestructive Techniques

Ryan M. Meyer[1], Ichiro Komura[2], Kyung-cho Kim[3], Tommy Zetterwall[4], Stephen E. Cumblidge[5], and Iouri Prokofiev[5]

[1]Pacific Northwest National Laboratory, Richland, WA, USA

[2]Japan Power Engineering and Inspection Corporation, Yokohama, Japan

[3]Korea Institute of Nuclear Safety, Daejeon, South Korea

[4]Swedish Qualification Center, Täby, Sweden

[5]Nuclear Regulatory Commission, Washington D.C., USA

Abstract

The Program to Assess the Reliability of Emerging Nondestructive Techniques (PARENT) was established to follow on from the international Program for the Inspection of Nickel alloy Components (PINC). The goals of PARENT are to conduct a confirmatory assessment of the reliability of nondestructive evaluation (NDE) techniques for detecting and sizing primary water stress corrosion cracks and apply the lessons learned from PINC to a series of round-robin tests. Testing was performed on a set of typical pressure boundary components including dissimilar metal welds (DMWs), bottom-mounted instrumentation (BMI) penetrations, and weld over-lay (WOL) components. Testing is split into blind and open tests with the aim of blind testing to assess the performance of more established technologies and procedures applied by qualified teams. Open testing engaged participants from industry, academia, and national research laboratories in participating countries with the goal of assessing the capability of emerging and less mature technologies. This paper provides an overview of the PARENT program including some results obtained from DMW test blocks in blind testing and a brief description of the Atlas information tool under development for open test data.

Keywords: Nondestructive Examination, Dissimilar Metal Weld, Bottom-Mounted Instrumentation, Stress Corrosion Cracking, Round Robin Test

1.Introduction

The U.S. Nuclear Regulatory Commission (NRC) has established the Program to Assess the Reliability of Emerging Nondestructive Techniques (PARENT) whose goal is to investigate the effectiveness of current emerging and perspective novel nondestructive examination (NDE) procedures and techniques to find flaws in nickel-alloy welds and base materials. This is done by conducting a series of open and blind international round-robin tests on a set of piping components that include large-bore dissimilar metal welds (LBDMW), small-bore dissimilar metal welds (SBDMW), and bottom-mounted instrumentation (BMI) penetration welds.

The PARENT is a follow-on to the Program for Inspection of Nickel Allow Components (PINC) [1] based on the Bilateral International Agreements with participants and the in-kind contribution of resources from organizations of Finland, Japan, Republic of Korea, Sweden, and the United States of America to evaluate several nondestructive techniques for detection and characterization of primary water stress corrosion cracking (PWSCC) in SBDMW and BMI components. In February 2012, the NRC executed new agreements with VTT Technical Research Centre of Finland, Nuclear Regulatory Authority of Japan (NRA, former JNES), Korea Institute of Nuclear Safety (KINS), Swedish Radiation Safety Authority (SSM), and Swiss Federal Nuclear Safety Inspectorate (ENSI) to establish PARENT to conduct a series of round-robin tests on SBDMWs, BMIs, and LBDMWs.

The PARENT was divided into blind and open testing portions, whose objectives are described below:

(1) Blind Round-Robin Testing: The objective of the blind testing is to evaluate the latest commercially employed NDE inspection techniques to determine the effectiveness for reliably detecting and accurately sizing PWSCC in SBDMWs, LBDMWs, and BMIs. Only qualified inspectors and qualified procedures participated in blind testing.

(2) Open Round-Robin Testing: The objective of the open testing is to evaluate novel and emerging NDE inspection techniques to determine which ones show the most promise for inspecting SBDMWs, LBDMWs, and BMIs. The

tests are designed to learn how a variety of advanced techniques being developed by universities and new techniques being developed by industry respond to realistically simulated PWSCC in components that have realistic geometries.

Final reports for PARENT blind and open testing are anticipated to be published in the final quarter of 2015. This paper will provide an overview of the blind and open testing portions of PARENT including a presentation of current status of both efforts. For the blind testing, substantial data analysis has been completed and results obtained from this data analysis will be presented. For the open testing effort, data analysis is in a much earlier phase. Therefore, a description of the status of open testing will focus more on the description of the Atlas information tool, which is an electronic database for organizing open test data.

During the course of planning for the PARENT blind testing, the opportunity arose to inspect some LBDMW test blocks with laboratory-grown stress corrosion cracking (SCC) flaws, contributed by Japan. However, the test blocks were scheduled to undergo a destructive evaluation before most of the blind testing could be completed so a decision was made to conduct a "Quick" blind (referred to hereafter as "Quickblind") study on these test blocks on a separate schedule than the rest of the blind testing. The Quickblind test results have been analyzed and are documented in a report [2]. In Section 3, results from the Quickblind portion of testing are presented separately from the rest of the blind testing results.

The next section (Section 2) will provide a general overview of the blind and open testing methodologies. This is followed by a presentation of some results from blind testing and a discussion of those results in Section 3. The next section will present the status of open testing, which includes a discussion of the development of the Atlas information tool. Finally, the paper will conclude with a discussion on future efforts and some conclusions from PARENT.

2. Testing Overview

Both the blind and open testing portions of PARENT include BMI nozzle test blocks and dissimilar metal weld (DMW) test blocks. The DMW specimens could be further classified as small bore (SBDMW) and large bore (LBDMW) test blocks. In addition, one weld overlay (WOL) test block was included in blind testing. Test blocks contained a variety of simulated flaws including laboratory-grown stress corrosion cracking (SCC), thermal fatigue cracks, weld solidification cracks, welding defects, and electrical discharge machining (EDM) notches. An overview of blind and open test blocks and the techniques applied in blind and open testing has been presented by Prokofiev et al. [3]. Information on flaw true states for each test block were documented on test block drawings based on information documented in the flaw fabrication process, by fingerprinting of test blocks, and by destructive analysis of a few test blocks. A total of 15 test blocks were contributed for the blind testing, while 19 test blocks were contributed to the open testing. Four of the test blocks contributed to the blind testing portion of PARENT were inspected as part of the Quickblind testing. A breakdown of test blocks by category included in the blind and open tests is provided in Table 1.

Table 1.Number of Test Blocks for Each Category in Open and Blind Testing

Category	All Blind Testing	Quickblind Testing	Open Testing
BMI	5	0	4
SBDMW	2	0	11
LBDMW	6	4	4
WOL	1	0	0

Results from individual examinations were recorded on datasheets, which included entries for coordinates of cuboids bounding each indication. This information was input to a database that also included flaw true-state information for the purpose of evaluating "hits" (an indication volume that intersects a flaw true-state volume), "false calls" (an indication volume that does not intersect any flaw true-state volumes), and "misses" (flaw true-state volumes that are not intersected by any indication volumes). A tolerance of 10 mm was provided on all sides of the flaw true-state bounding rectangle to avoid penalizing minor positioning errors. The data can be represented visually by mapping the coordinates for bounding indication and flaw cuboids onto two-dimensional indication plots. Two such plots are used to represent the data in two separate views. Following a Cartesian coordinate system definition, these views include an X-Y view (seeFigure 1) and Y-Z view (seeFigure 2). Figure 1provides an illustration of a "miss," "false call," and "hits" while Figure 2illustrates how flaw heights and recorded indication heights can be used to quantify depth-sizing accuracy. Length-sizing accuracy can be quantified based on similar data in the X or Y dimension. It should be noted that the 10-mm tolerance is not represented in Figures 1and2.

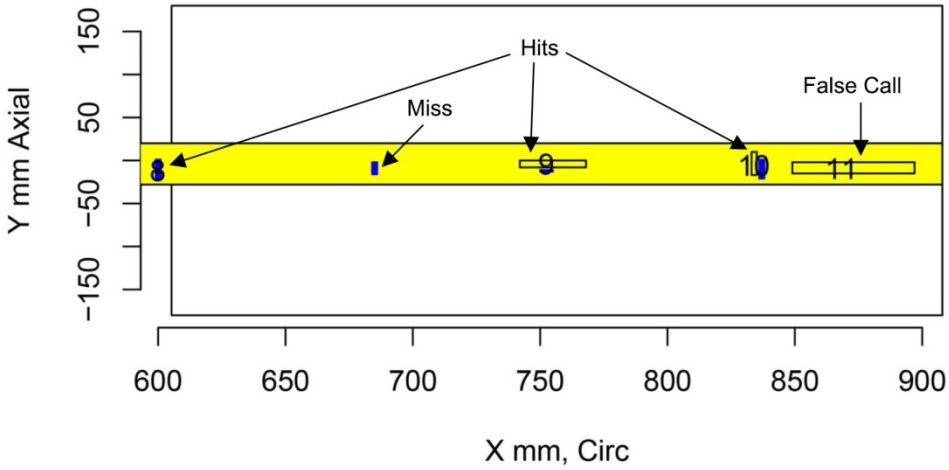

Figure 1. Example of a 2-D indication plot (X-Y view) illustrating a miss, false call, and hits. Blue rectangles represent true state (flaws) while the transparent rectangles represent recorded indications. The yellow shaded region is the reported region of examination.

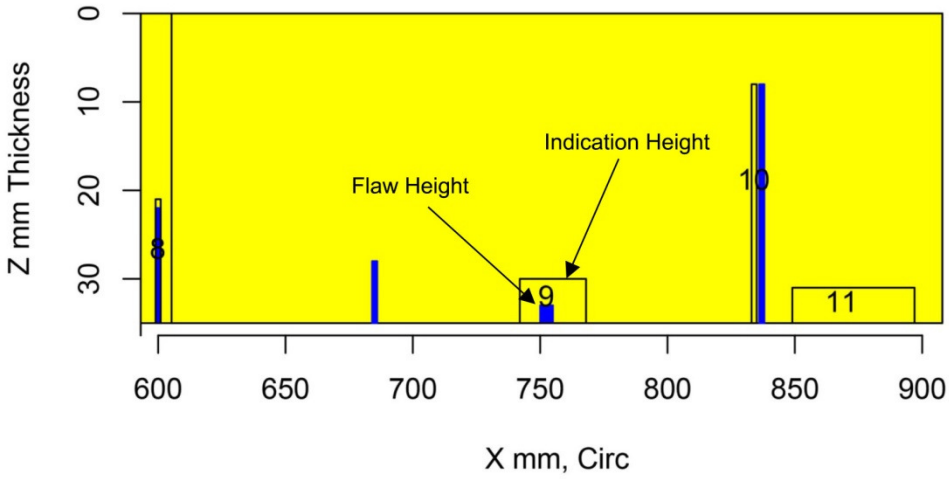

Figure 2. Example of a 2-D indication plot (X-Z view) illustrating flaw height and indication height.Blue rectangles represent true state (flaws) while the transparent rectangles represent recorded indications. The yellow shaded region is the reported region of examination.

Detection performance can be evaluated through probability-of-detection (POD) and false-call-probability (FCP) metrics. Because POD is significantly influenced by flaw dimensions, POD is often expressed as a curve with respect to flaw dimension of interest (i.e., depth or length). For open test data, however, this traditional approach to performance assessment is not suitable as teams are provided with the flaw information prior to inspection, significantly biasing the results. Further, open inspections were approached in different ways, with some teams intending only to evaluate sizing capability of a particular technique, while other teams approached open testing similarly to the way they would approach a blind inspection. Sizing performance analysis for blind and open testing can be performed in a similar fashion—by applying regression analysis to fit a curve to sizing data and computing the root mean squared error (RMSE) of estimated indication depths relative to flaw depths.

The NDE techniques applied in blind testing could be classified as conventional UT (UT), phased-array UT (PAUT), time-of-flight diffraction UT (TOFD), or eddy current testing (ECT). Test procedures could include one or more of these techniques and a unique procedure identifier can be constructed by concatenation of techniques applied and the team identifier. A total of 23procedures were applied in the blind testing by a total of 14 teams. In all, 71 inspections were performed in blind testing for a total of 421 flaw observations on DMWs, 77 flaw observations on BMIs, and 20 flaw observations on WOLs. In the Quickblind portion of testing, a total of 6 procedures were applied by 6 teams for a total of 24 inspections and 18 flaw observations (one test block was blank). A summary of Quickblind test procedures and inspections performed is included inTable 2, while a summary of test procedures and inspections performed in “Normal” blind testing is included in Table 3.

Table 2.Number of Inspections Performed for Each Procedure in PARENT Quickblind Testing

Procedure	BMI	DMW	WOL
PAUT.132	0	4	0
UT.134.1	0	4	0
UT.ECT.106	0	4	0
UT.PAUT.108	0	4	0
UT.PAUT.113	0	4	0
UT.PAUT.126	0	4	0
TOTAL	0	24	0

Table 3.Number of Inspections Performed for Each Procedure in PARENT "Normal" Blind Testing

Procedure	BMI	DMW	WOL
ECT.108	5	0	0
ECT.124	5	0	0
ECT.135	0	1	0
PAUT.108.1	0	4	0
PAUT.108.2	0	0	1
PAUT.115	0	2	0
PAUT.126.1	0	4	0
PAUT.126.2	0	0	1
PAUT.128	0	2	0
TOFD.ECT.126	2	0	0
UT.108	0	4	0
UT.126	0	4	0
UT.134.2	0	4	0
UT.25	0	1	0
UT.ECT.144	0	2	0
UT.PAUT.113	0	1	0
UT.TOFD.117	0	2	0
UT.TOFD.ECT.101	0	2	0
TOTAL	12	33	2

Open testing included inspections by unqualified teams and unqualified procedures. A greater diversity of techniques was employed in terms of type, maturity, and capability in the open testing. A detailed summary of techniques employed in open testing will be provided in the final open testing report.Motivations for exploring many of the NDE techniques in open testing can be characterized as addressing one or more of the following challenges: (1) to more accurately characterize large defects, (2) to enable inspections of difficult-to-access regions, and (3) to improve detectability of small defects. Moreover, the techniques employed in open testing can largely be associated with one of two categories: i) established techniques or novel techniques that represent an incremental advancement of established techniques currently deployed in the field, and ii) novel techniques that are significantly different than any technique that has been field-deployed. One can expect that techniques in the former category should provide data with a high degree of fidelity. With the latter category, however, greater uncertainty is associated with anticipated performance. Examples of techniques that would fall in the former category include PAUT, ECT, and UT. Examples that would fall into the latter category include some techniques based on nonlinear acoustic phenomena such as higher harmonic UT (HHUT) and nonlinear resonant ultrasound spectroscopy (NRUS). A summary of procedures implemented in open testing and number of inspection records collected for each procedure is included inTable 4.

Table 4.Number of Inspections Performed for EachProcedure in PARENT Open Testing

Procedure	BMI	DMW
CEECT.5.1	1	2
CEECT.5.2	0	1
ECT.7	4	0
PECT.11	0	3
ECT.16	2	11
AECT.33	2	11
PAUT.114	0	10
PAUT.122.1	0	7
PAUT.122.2	0	7
PAUT.131.1	0	7
PAUT.131.2	0	3
PAUT.131.4	0	1
PAUT.150	0	2
PAUT.20	0	7
PAUT.7	0	2
PAATOFD.29.0	0	6
PATP.29	0	6
PAATOFD.29.1	0	20
PAATOFD.29.2	0	17
SAFT.17	0	14
PATRT.22	0	1
UT.104	0	9
SHPA.6.1	0	2
SHPA.6.2	0	1
SHPA.6.3	0	4
NRUS.11	0	3
HHUT.30	0	3
LASH.18	0	7
HHUT.27.1	0	2
HHUT.27.2	0	8
MM.28.1	1	6
MM.28.2	0	5
RT.109	0	6
RT.112	0	4
UIR.20	0	6
GW.21	1	1
LUV.170	6	4
TOTAL	17	209

3. Blind Testing Results

This section presents some of the blind testing results including results from the Quickblind testing and results obtained from DMW test blocks in the “Normal” blind testing. The results from Quickblind testing are presented next, including results of the detection performance analysis by procedure, flaw depth, and flaw length, expressed as overall POD values and POD curves. Depth and length sizing results are also included and expressed as root-mean-squared-error (RMSE) by procedure.

3.1 Quickblind Testing Results

Figures 3 and 4provide POD curves as a function of flaw depth and length, respectively. These were developed from the combined detection and false call data of the six test teams. The dashed red lines represent the 95% confidence bounds. The wide confidence interval is a result of the limited number of data points available. The black circles near the origin of

both figures are representative of the false call probability. The black circles at the top of Figures 3and 4represent the POD data for each of the flaws. Three flaws were included in Quickblind testing (one in each test block), and all flaws were inspected by each team (total of six teams). All the teams detected all flaws in all test blocks.

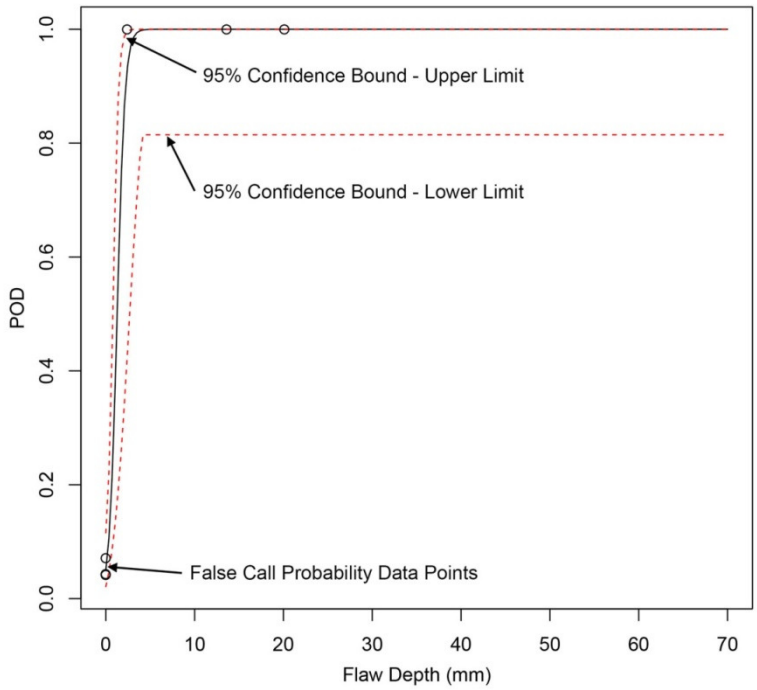

Figure 3. Probability of detection versus flaw depth

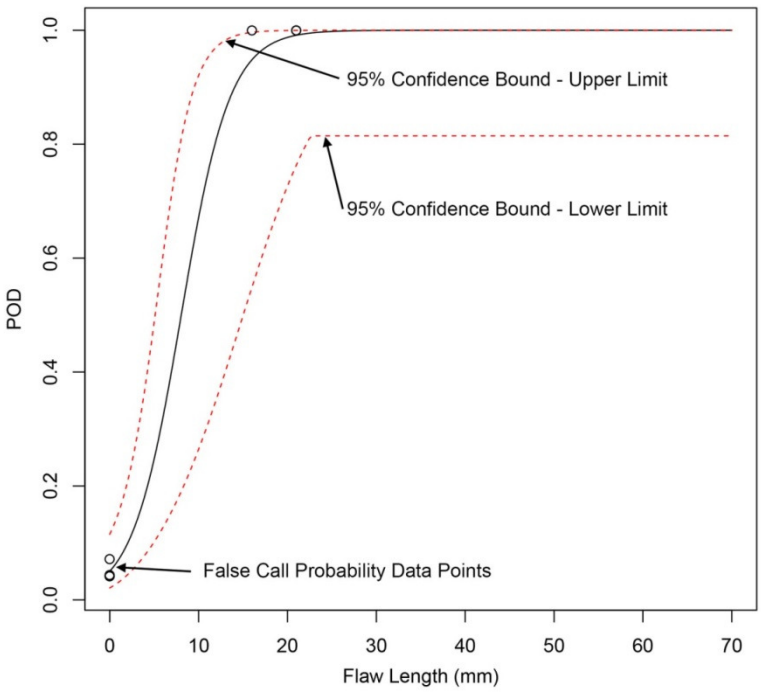

Figure 4. Probability of detection versus flaw length

Table 5 shows the depth sizing error by test team and by ID or OD access for combined data taken on Quickblind test blocks. Teams 113 and 106 had the lowest RMSE, both having accessed the test block from the ID. Table 6 provides a summary of the depth sizing errors for all of the Quickblind inspections. Based on the –4.3-mm sizing error for flaw depth, it can be concluded that overall, teams tended to undersize the depth.

Table 5. Flaw Depth Sizing Error by Procedure

Procedure	Access	Bias (mm)	RMSE (mm)
UT.134.1	OD	−6.5	11.3
PAUT.132	ID	−7.5	9.4
UT.PAUT.108	OD	−9.1	12.4
UT.PAUT.126	OD	−3.5	7.1
UT.PAUT.113	ID	0.9	1.3
UT.ECT.106	ID	0.0	4.1

Table 6. Flaw Depth Sizing Error Summary

Flaw Dimension	Bias (mm)	RMSE (mm)
Depth (mm)	−4.3	7.9

Table 7 shows how the depth sizing error differs for ID and OD access. The RMSE values indicate that those procedures that accessed the test block from the ID outperformed procedures that accessed from the OD.Table 8 shows the length sizing error by test team for data collected from Quickblind test blocks.

Table 9 provides a summary of the length sizing errors for all of the inspections performed on Quickblind test blocks.

Table 7. Flaw Depth Sizing Error by ID/OD Access

Access	Bias	RMSE
ID	−2.2	5.8
OD	−6.4	28.4

Table 8. Flaw Axial Length Sizing Error by Procedure

Procedure	Bias	RMSE
UT.134.1	−5.0	8.2
PAUT.132	26.4	26.9
UT.PAUT.108	−5.0	7.3
UT.PAUT.126	4.7	8.1
UT.PAUT.113	−8.0	9.4
UT.ECT.106	−10.7	11.4

Table 9. Flaw Axial Length Sizing Error Summary

Flaw Dimension	Bias	RMSE
Length (mm)	0.4	13.7

3.2 “Regular” Blind Testing Results

This section presents the results of the regular portion of Blind testing. The POD, as a function of depth, is tabulated for procedures applied to LBDMWs in Table 10 and for procedure types for LBDMWs in Table 11. For SBDMWs, the POD as a function of depth is tabulated for procedures in Table 12 and procedure types in Table 13. A review of Tables 11 and 13indicates that PAUT procedure types performed better than UT procedure types for both LBDMW and SBDMW test blocks, although the difference is smaller for LBDMWs. As expected, PAUT procedure types and UT procedure types exhibit better performance for a given flaw size in SBDMW test blocks. For LBDMW test blocks, in particular, several multi-technique procedures have been applied. The multi-technique procedures were applied to the inner diameter (ID) surface as opposed to the outer diameter (OD) surface.Comparison of the detection performances of PAUT and UT

procedure types in Tables 11 and 13indicates significantly greater PODs on SBDMWs versus LBDMWs, as expected. Tables 10 and 11 also indicate that ID procedures perform better than OD procedures, overall, as expected. However, many of the ID procedures are also multiple technique procedures, making it difficult to separate the effects of access and combination of techniques.

Table 10. Summary of POD versus Depth for Procedures Applied to LBDMWs

	# Obs.	5mm	10mm	15mm	30mm	FCP	Access
ECT.135	16	22	72	96	100	3	ID
PAUT.108.1	19	8	15	29	82	4	OD
PAUT.126.1	19	14	25	39	83	8	OD
UT.108	19	8	15	29	82	4	OD
UT.126	19	11	15	20	42	8	OD
UT.134.2	19	14	27	47	92	6	OD
UT.ECT.144	19	17	29	45	86	9	ID
UT.PAUT.113	18	37	91	99	100	3	ID
UT.TOFD.ECT.101	19	21	46	74	99	8	ID

Table 11.Summary of POD versus Depth for Procedure Typesfor LBDMWs

	# Obs.	5mm	10mm	15mm	30mm	FCP	Access
ECT	16	22	72	96	100	3	ID
PAUT	38	11	21	36	85	5	OD
UT	57	11	19	32	78	6	OD
UT.ECT	19	17	29	45	86	9	ID
UT.PAUT	18	37	91	99	100	3	ID
UT.TOFD.ECT	19	21	46	74	99	8	ID

Table 12. Summary of POD versus Depth for Procedures Applied to SBDMWs

	# Obs.	5mm	10mm	15mm	30mm	FCP	Access
PAUT.108.1	28	35	84	98	100	5	OD
PAUT.115	28	58	97	100	100	6	OD
PAUT.126.1	28	12	33	65	99	3	OD
PAUT.128	28	51	89	99	100	11	OD
UT.108	28	33	81	97	100	6	OD
UT.126	28	14	23	35	76	8	OD
UT.134.2	28	28	59	84	100	9	OD
UT.25	12	17	26	37	74	11	OD
UT.TOFD.117	28	37	90	99	100	4	OD

Table 13. Summary of POD versus Depth for Procedure Types for SBDMWs

	# Obs.	5mm	10mm	15mm	30mm	FCP	Access
PAUT	112	39	87	99	100	6	OD
UT	96	20	43	69	98	8	OD
UT.TOFD	28	37	90	99	100	4	OD

Summaries of sizing errors including depth sizing errors for LBDMWs and SBDMWs and length sizing errors for all test blocks are included in Tables 14 through20.Depth sizing performance is tabulated for procedures and procedure types in Tables 14 and 15 for LBDMWs and for procedures and procedure types applied to SBDMWs in Tables 16 and 17. Length sizing performance is tabulated for all procedures in Table 18 and for procedure types in Tables 19 and 20 for LBDMWs and SBDMWs, respectively.Table 15 seems to clearly indicate that ID procedures exhibit much better depth sizing performance than OD procedures. However, the ID procedures are also multiple technique procedures, so it is not clear the extent to which each factor may be contributing to the improved depth sizing performance on LBDMWs. A review of Tables 15 and 17indicates that PAUT and UT procedures exhibit better depth sizing performance on SBDMWs

compared to LBDMWs. In the case of LBDMWs, the depth sizing RMSEs of PAUT and UT procedure types are equivalent. For SBDMWs, The depth sizing RMSE for PAUT procedure types is smaller than the depth sizing RMSE for UT procedure types. A review of the "Bias" columns in Tables 15 and 17indicate an overall tendency of UT procedure types to undersize flaws while PAUT procedure types exhibit a slight overall oversizing tendency.

Tables 19 and 20indicate it is difficult to draw strong conclusions regarding length sizing trends. While it appears that better length sizing performance is observed for PAUT procedure types applied to LBDMWs relative to SBDMWs, this is not true for UT procedure types. Also, several of the ID procedure types exhibit better length sizing performance than OD procedure types, with the exception of procedure type UT.PAUT.

Table 14. Summary of Depth Sizing Errors for Procedures on LBDMWs

	# Obs.	Bias	RMSE	Access
PAUT.108.1	7	−2.8	5.3	OD
PAUT.126.1	8	2.6	13.3	OD
UT.108	4	−0.3	10.3	OD
UT.126	4	0.6	7.8	OD
UT.134.2	8	−8.9	11.7	OD
UT.ECT.144	9	0.7	2.3	ID
UT.PAUT.113	15	2.0	3.0	ID
UT.TOFD.ECT.101	15	−1.0	3.5	ID

Table 15. Summary of Depth Sizing Errors for Procedures Types on LBDMWs

	# Obs.	Bias	RMSE	Access
PAUT	15	0.1	10.1	OD
UT	16	−4.4	10.1	OD
UT.ECT	9	0.7	2.3	ID
UT.PAUT	15	2.0	3.0	ID
UT.TOFD.ECT	15	−1.0	3.5	ID

Table 16. Summary of Depth Sizing Errors for Procedures on SBDMWs

	# Obs.	Bias	RMSE	Access
PAUT.108.1	23	−0.3	5.2	OD
PAUT.115	27	1.0	5.1	OD
PAUT.126.1	16	−2.5	8.0	OD
PAUT.128	26	3.0	7.6	OD
UT.108	22	0.5	6.6	OD
UT.126	12	−0.5	10.3	OD
UT.134.2	23	−3.5	10.0	OD
UT25	3	−8.8	15.9	OD
UT.TOFD.117	18	0.6	4.4	OD

Table 17. Summary of Depth Sizing Errors for Procedures Types on SBDMWs

	# Obs.	Bias	RMSE	Access
PAUT	92	0.6	6.4	OD
UT	60	−1.7	9.1	OD
UT.TOFD	18	0.6	4.4	OD

Table 18. Summary of Length Sizing Errors for Procedures Applied to SBDMWs and LBDMWs.

	# Obs.	Bias	RMSE	Access
ECT.135	12	–2.5	7.4	ID
PAUT.108.1	30	3.5	13.8	OD
PAUT.115	27	12.4	20.6	OD
PAUT.126.1	23	9.2	16.5	OD
PAUT.128	26	14.7	20.7	OD
UT.108	29	7.8	15.0	OD
UT.126	15	23.6	29.3	OD
UT.134.2	31	6.3	19.2	OD
UT.25	3	15.3	18.0	OD
UT.ECT.144	11	3.3	4.7	ID
UT.PAUT.113	15	11.6	14.1	ID
UT.TOFD.117	21	3.5	15.9	OD
UT.TOFD.ECT.101	15	1.4	6.6	ID

Table 19. Summary of Length Sizing Errors for Procedure Types Applied to LBDMWs.

	# Obs.	Bias	RMSE	Access
ECT	12	–2.5	7.4	ID
PAUT	14	4.8	12.1	OD
UT	18	9.1	20.5	OD
UT.ECT	11	3.3	4.7	ID
UT.PAUT	15	11.6	14.1	ID
UT.TOFD.ECT	15	1.4	6.6	ID

Table 20. Summary of Length Sizing Errors for Procedure Types Applied to SBDMWs.

	# Obs.	Bias	RMSE	Access
PAUT	92	10.5	18.7	OD
UT	60	10.9	19.9	OD
UT.TOFD	21	3.5	15.9	OD

3.3 Comparison of Quickblind and “Regular” Blind Testing Results

The only procedure applied in both Quickblind and the rest of blind testing was UT.PAUT.113. A comparison of the depth and length sizing results for UT.PAUT.113 from these two portions of blind testing is provided in Table 21. The table indicates that somewhat better depth sizing performance was obtained in the Quickblind testing, although the sample for Quickblind testing only includedthree flaw observations. Interesting results are indicated in the length sizing summary for UT.PAUT.113. Whereas Table 21 indicates a strong under-sizing tendency in Quickblind testing, a strong over-sizing tendency is indicated for regular blind testing.

Table 21.Comparison of QuickblindTest Results and Blind Test Results for Procedure UT.PAUT.113.

Depth Sizing		
	Bias	RMSE
Quickblind	0.9	1.3
Blind	2.0	3.0
Length Sizing		
	Bias	RMSE
Quickblind	–8.0	9.4
Blind	11.6	14.1

4. The PARENT Atlas Information Tool

The PARENT Atlas information tool is under development to document the open testing data and results as well as relevant data from field experience. The main tab for the open data is shown inFigure 5 and allows users to filter through data by technique, team, or test block. Multiple selections can be made so that the results of multiple inspections can be compared. The selections appear on the right-hand side of the main Open Data interface where data regarding the selected inspections can be accessed. An expanded view of one of the menu items from the right-hand side is shown in Figure 6and shows that the information that may be accessed for an inspection includes procedure information, data images, inspection record sheets, and flaw information for the flaws in the inspected test blocks.

Efforts are currently underway to develop hitograms in the PARENT Atlas tool and to incorporate field experience into the PARENT Atlas. The hitograms allow simultaneous display of hits, misses, and false calls for multiple selected inspections relative to true flaw state for the inspections.

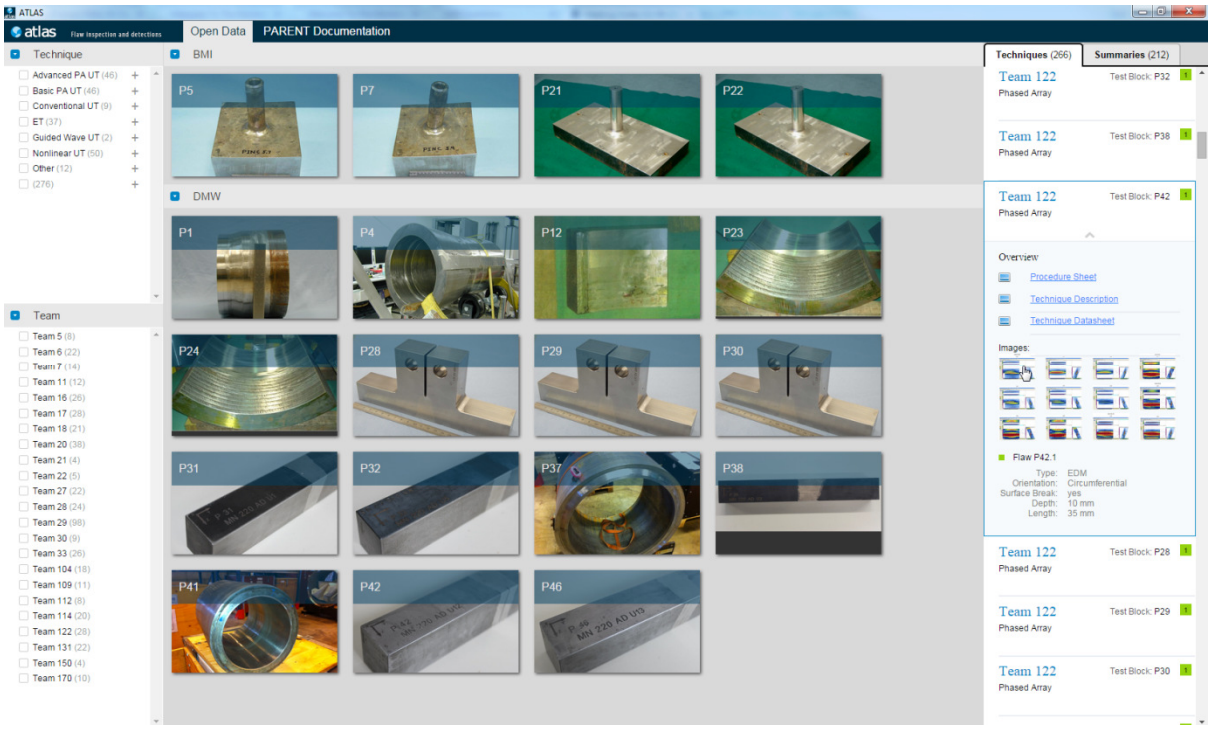

Figure 5. Screenshot of the PARENT Atlas information tool Open Data tab display

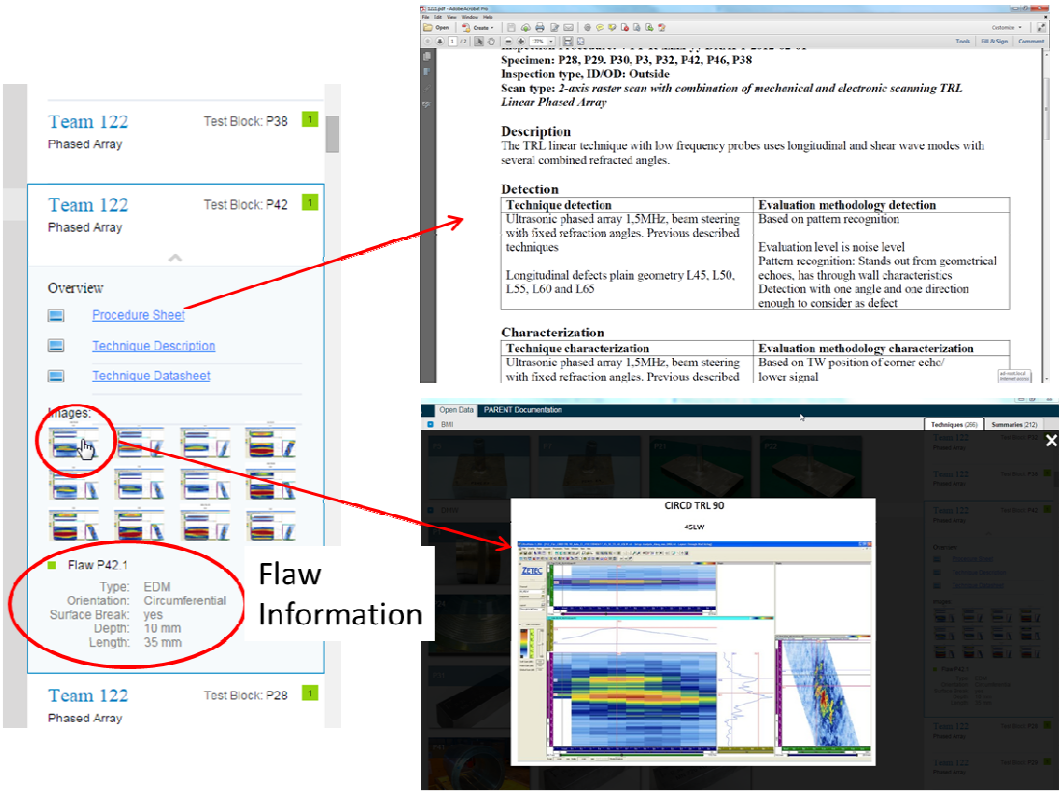

Figure 6. Expanded view of the right-hand side of the Open Data interface illustrating information accessible for each selected inspection

5. Conclusions

This paper presents some of the blind data results for DMW test blocks from the PARENT program and status of the PARENT Atlas information tool for open testing. Final reports for PARENT blind and open testing are anticipated to be published in the final quarter of 2015. Although not all of the blind testing analysis and results could be included in this paper, the results that are provided illustrate some significant trends. For instance, the detection and depth sizing performances of PAUT and UT procedure types are better for SBDMW test blocks than LBDMW test blocks. Also, the performance of PAUT procedure types is generally better than the performance of UT procedure types, but the difference in performance appears to be somewhat diminished for LBDMW test blocks. Further, whereas the sizing performances of PAUT procedure types appears to be significantly different between LBDMW and SBDMW test blocks, the sizing performances of UT procedure types are consistent between block types. Finally, several of the ID procedures applied to LBDMW test blocks were also multiple technique procedures. The ID procedure exhibited much better depth sizing performance than the OD procedures and the detection and length sizing performances of ID procedures were better than OD procedures, as well. Only OD procedures were applied to SBDMW test blocks in PARENT.

Acknowledgements

This work is being conducted by U.S. Nuclear Regulatory Commission and Pacific Northwest National Laboratory in partnership with ; IHI Southwest Technologies; AlphaSense; Nuclear Regulatory Authority of Japan; Japan Power Engineering and Inspection Corporation; Tohoku University; Mitsubishi Heavy Industries, Ltd.;Institute of Nuclear Safety System, Incorporated ; Ultrasonic Materials Diagnosis Laboratory; Nagoya University; Toyama University; Kansai Electric Power Company; Korea Institute of Nuclear Safety; Korea Atomic Energy Research Institute; Doosan Heavy Industries; Korea Hydro & Nuclear Power; Korea Plant Service & Engineering;; Korea Research Institute of Standards and Science; Korea Inservice Inspection; Sungkunkwan University; Hanyunag University; Pusan National University; Swedish Radiation Safety Authority; Swedish Qualification Centre; VTT Technical Research Centre of Finland; Aalto University; Swiss Federal Nuclear Safety Inspectorate; Paul Scherrer Institute; Swiss Association for Technical Inspections, Nuclear Inspectorate; Swiss Federal Laboratories for Materials Science and Technology; Alstom; DEKRA; Chalmers Institute of Technology, FORCE Technology; and NRG.

References

[1] Cumblidge, S.E., et al., *Results of the Program for the Inspection of Nickel Alloy Components*. 2010, U.S. Nuclear Regulatory Commission: Washington, D.C.

[2] Braatz, B.G., P.G. Heasler, and R.M. Meyer, *PARENT Quick Blind Round-Robin Test Report*. 2014, Pacific Northwest National Laboratory: Richland, Washington.

[3] Prokofiev, I., et al., *New International Program to Assess the Reliability of Emerging Nondestructive Techniques (PARENT)*, in *Review of Progress in Quantitative Nondestructive Evaluation, Vol. 32, AIP Conference Proceedings Vol. 1511*, D.O. Thompson and D.E. Chimenti, Editors. 2013, American Institute of Physics, Melville, New York: Denver, Colorado. p. 1097-1103.

Challenge for the Detection of Crack in Dissimilar Weld Region Using PECT (Pulsed Eddy Current Technology)

Duck-Gun Park[1], M.B Kishore
Nuclear Materials Safety Research Division , Korea Atomic Energy Research Institute, Daejeon, South Korea -305-353,

Abstract

Pulsed Eddy Current (PEC) technique uses multiple frequency current pulse to drive the excitation coil of PEC probes unlike conventional single frequency eddy current methods. In the present study, we make an effort to detect the crack in dissimilar weld region using PEC technique. The test samples were prepared by welding two base metals, the composition of base metal is SA508 cl.2 and that of welding metal is alloy 182. The defect region was positioned in the weld metal, and the types of defect are stress corrosion cracking, fatigue cracks having the width of several micrometers. A rectangular pulse having 10ms pulse width and 15A current is applied to the exciting coil of PEC probe to inspect the sample cracks. The peak amplitude of the detected PEC pulse was chosen as a measure to estimate the cracks under the sample surface. The PEC signal amplitude detected in the defect region (welded part) showed lower value than that of base material. The crack is positioned in the middle of dissimilar weld region, which shows the minimum PEC signal amplitude. In time domain analysis, the peak amplitude of the detected pulse is decreased, with an increase in the crack depth. The experimental results indicated that the proposed system using PEC technique has the potential to detect the sub surface cracks in dissimilar weld region.

Keywords— pulsed eddy current, dissimilar weld, crack, PEC probe, hall sensor, peak amplitude

1. Introduction

Eddy current testing is a non destructive testing (NDT) method used for metals and includes the detecting and sizing of defects, identifying composition, structure and measuring thicknesses. Among the available conventional NDT methods, eddy current testing (ECT) is the most promising technique to detect flaws in conductive materials. The conventional ECT uses a single-frequency sinusoidal excitation for the detection of defects or flaws as a function of changes in voltage, impedance, or phase. Because of limited depths of penetration and complexity in signal analysis ECT was confined to limited applications [1]. Unlike a conventional ECT, PEC uses a multiple frequency sinusoidal excitation of the electric current resulting from the broad band nature of the pulse; hence it has the ability to penetrate different depths in a conductive material and provides the depth information of the defects [2, 3] located at different depths. PEC testing has been demonstrated to be one of the most effective methods, and is capable of performing different inspection tasks, such as sub-surface defect detection in complex structures, wall thinning detection, crack detection, coating thickness detection etc. [4,5]. Moreover, PEC is more economical than other NDT methods such as low power consumption owing to short pulse excitation and it doesn't need any complex electronic circuitry. Even though the use of PEC has long been considered for the testing of materials, in recent decades, PEC testing has become the subject of wide spread interests in NDT because of its advancement in technologies such as computer data acquisition and digital signal processing. Because of the potential advantages of the PEC, prevalent investigations on this technique have been made, such as for detection of wall thinning and corrosion in aircraft multilayer structures [9, 10]. Especially, it is efficient to detect the subsurface crack of thick

plate often used in the nuclear industry. The thickness of tubes and nozzle used in the nuclear power plant is up to several tenth of millimeter, which is made of stainless steel and/or Inconel alloy to protect the corrosion. The crack detecting sensitivity using PEC probes depends on several parameters such as pulse width, coil size, coil diameter. To achieve this, it is necessary to increase the flux through the circular coil, which can be described by the following equation.

$$\emptyset = B\pi r^2$$

Where B is the magnitude of the magnetic flux density perpendicular to the surface defined by the coil of radius (r). Therefore, if larger size coil is used for the detection purposes, a low resolution and sensitivity would be achieved. The reason is that they respond to all magnetic flux line passing through the coil winding, regardless of their spatial direction and orientation. This characteristic together with the size of the coil can impact the sensitivity of this sensor. Using smaller coil would provide a better sensitivity but would limit eddy current penetration within the test object. Therefore, in order to detect the deep crack buried under thick sample, we have to design PEC probe considering many parameters such as skin depth, coil inductance, and detection sensor. In the present study, a new PEC probe to detect a very thin cracks made by stress corrosion cracking phenomena in the dissimilar weld region was made by considering special resolution and sensitivity of detecting element. For this purpose, specially designed probe was used, and the performance of the new designed probe was tested with a PEC system designed and developed for this purpose

2. Experimental Setup

The block diagram of the PEC system design is shown in Figure 1. The system consists of a rectangular waveform generator, a probe integrated with an excitation coil and a pickup Hall-sensor to detect the induced field from test specimen, an amplifier to process the signal obtained from Hall-sensor for further steps as the sensor output is too low in magnitude, a data acquisition card connected to PC using signal processing software to digitize the obtained data and to record the PEC data. The operational flow of the PEC system is as follows; the waveform generator produces a rectangular pulse with variable frequency and duty cycle. The pulse is fed to a coil driver circuit which excites the driving coil of the PEC probe. When the probe is mounted on the metal structure, the pick-up hall sensor will measure the vertical resultant magnetic field, which is the vector sum of the field generated by the excitation coil and the opposing magnetic field generated by the induced eddy currents in the test sample (Primary flux Φ1 created by driving coil induces EC in the conducting medium, induced EC produces counter flux Φ2. Now pick-up sensor measures total flux Φ = Φ1 + Φ2.). The signal obtained from the pick-up sensor is amplified by a voltage amplifier with variable gain. The A/D card will convert the analog input signal into digital data which can be used for further signal analysis by the end user. A software program is used to Signal pre-processing, feature extraction, defect categorization, and the presentation of the results on the PC monitor.

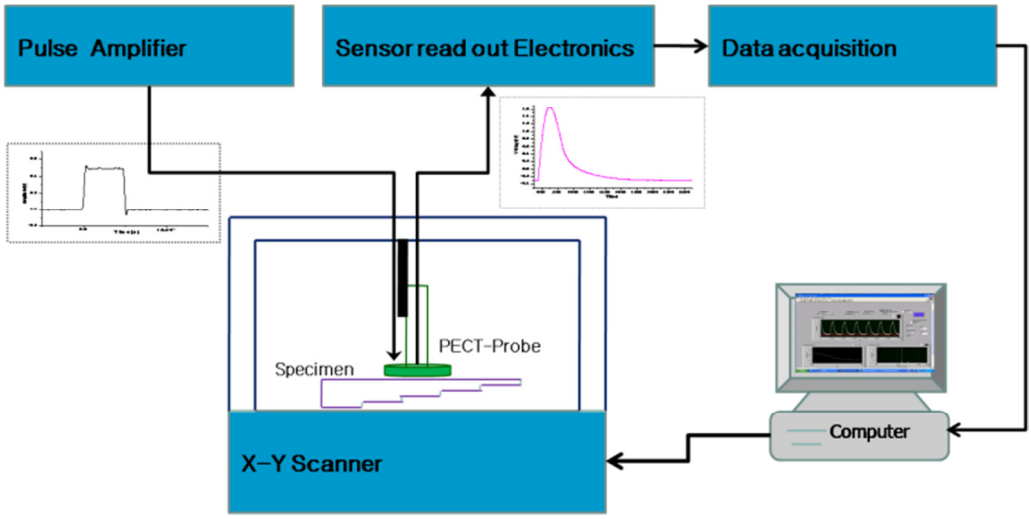

Figure 1.The block diagram of the PEC system.

The pulse amplifier supplies a high current pulse to the Driving Coil or exciting coil. The pulse width, pulse amplitude and duty cycle can be controlled and selected by considering the skin depth of sample. The excitation coil is a 1x3 mm rectangular cross sectional copper wire wound on the cylindrical ferrite core, the number of turns are made to be 132 turns having total resistance 0.192 Ω . To obtain good special resolution, the probe has a 60mm height and 9mm inner diameter, and the Hall-sensor was positioned in the center of probe to detect the induced signal from defects. The cylindrical type ferrite core not only reduces the magnetic leakage but also improves the detection sensitivity by sustaining adequate excitation intensity. The Hall-sensor gives ~~the~~ frequency independent sensitivity from DC to 100 KHz, high spatial resolution, less power consumption with increased sensitivity and simple readout circuitry. When the probe was placed in close proximity to the conducting plate, the steep exciting pulse induces eddy currents and its associated magnetic field dissipates exponentially to approach its steady state. The induced eddy current field ~~flow~~ is in the opposite direction to primary exciting field, hence when the probe is placed on the conducting plate, the detected field rises slowly to the maximum peak value.

3. PEC signal measurement and Tested Sample

A 10ms pulse width and 15A excitation current is applied to exciting coil of the probe to test the sample. figure 2(a) shows the experimental setup, The PEC probe is fixed to the X-Y scanner to perform the manual scanning on the defect free side of the tested sample. Initially the probe is placed on the sample such that the hall sensor positions at the center in vertical direction i.e. about x axis and continued to be at its center position as the scanning process continues along the y axis i.e. along the length of the test sample, the probe used in this experiment and the test specimen can be observed in figure 2(b) . A LabView based data acquisition program shown in figure 2(c) was developed to continuously monitor the variation in the thickness of the sample and is observed on the computer screen. The time domain feature, peak amplitude of the detected pulse is used to detect the sub-surface cracks

in the tested sample. in order to reduce the experimental error, average of 5 pulses is considered as the resultant PEC pulse. The three kinds of test blocks with ID 28, 29, and 30 provided by ENSI were tested. the flaw types of these test blocks are BWR/NWC SCC Crack, Fatigue Crack, and PWR SCC crack, respectively. The samples were composed by the welding of two base metals, and the composition of base metal is SA508 cl.2, and the welding metal is alloy 182 as shown in the figure 2(d).

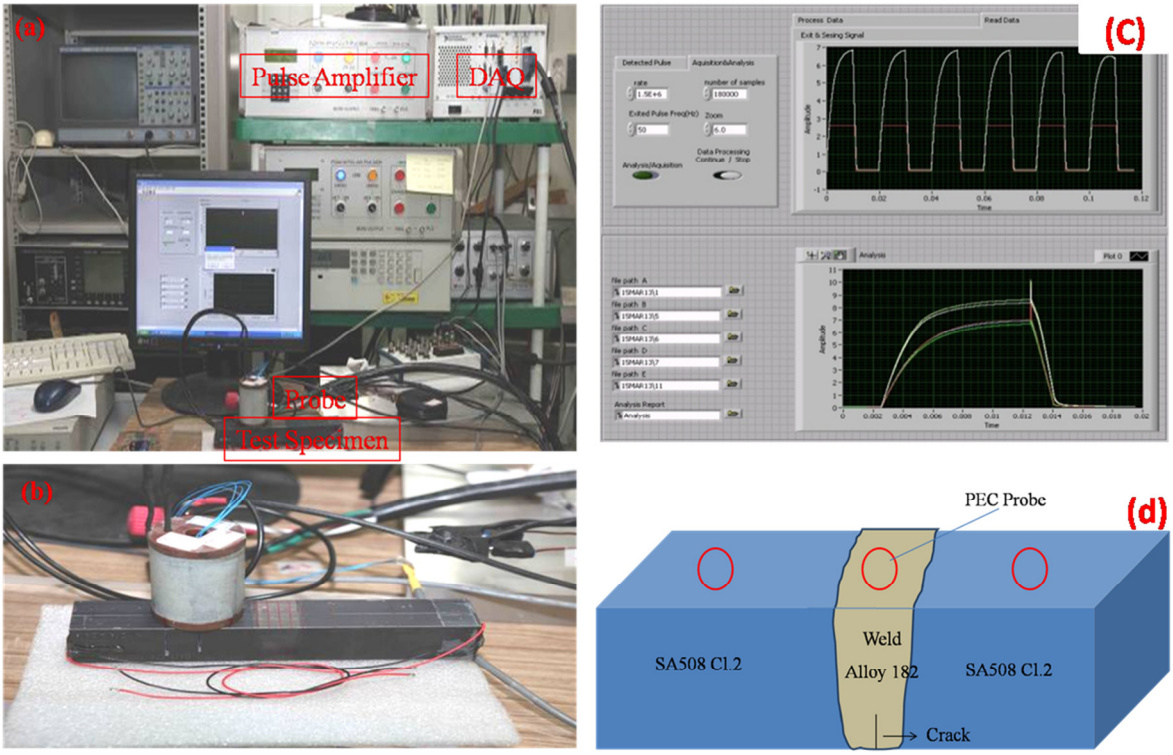

Figure 2(a).Experimental Setup. (b) closed view of Probe and Test specimen. (c) Lab VIEW based application to read and process PEC data. (d) Schematic of PARENT Test Specimen, PECT probe is located on the opposite side of crack surface

5. Experimental results and feature extraction

when the probe is placed on the test specimen, the excitation pulse will generate a primary magnetic field which can penetrate into the test sample resulting into eddy currents to generate and pass through the sample, these small eddy currents will generate secondary magnetic field which can oppose the primary magnetic field will be detected by the hall element. since the secondary field is opposite to the primary magnetic field, the detected pulse tends to change depending on the test specimen and portrayed as the defect information. A typical response signal from PEC probe when placed on the test sample in such a position is shown in Fig. 3. Calibration of PEC signal with standard specimen is essential to obtain a reliable experimental result. Because of no calibration sample is prepared, the validity of experiment was verified using the difference of the PEC peak amplitude obtained in the crack and opposite side (Fig. 4). The base metal of sample block SA508 Cl.2 is ferromagnetic and

welding material alloy 182 which is nonmagnetic material. Therefore, the PEC amplitude measured in the ferromagnetic part is higher than that of the nonmagnetic part. The y coordinate 10 and 12 cm neighborhood is the interface region between ferromagnetic and nonmagnetic material. The crack is positioned in the neighborhood of y coordinate 11 cm, which shows the minimum PEC signal amplitude.

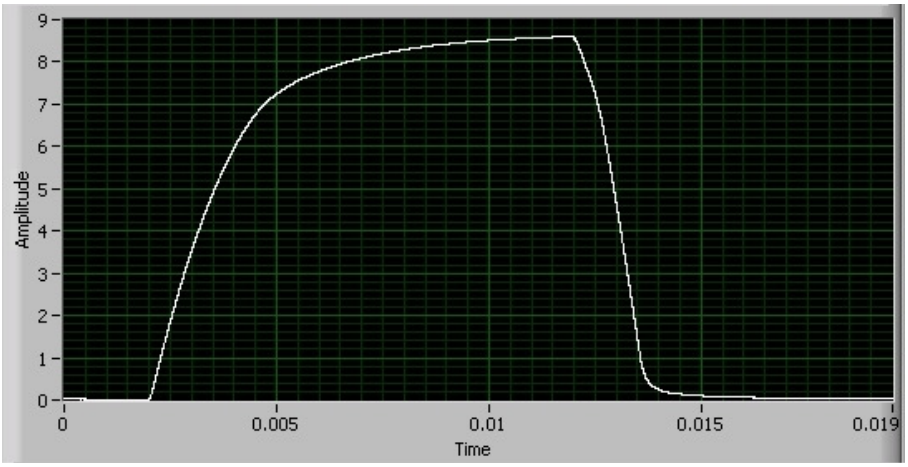

Figure 3. Typical PEC signal induced in the Hall-sensor from the test block.

The important characteristic of detected signal to interpret the results is the peak value of the pulse. The measuring points were selected as a x-y coordinate, the x points were fixed at the center of transverse direction and y points were selected along the longitudinal direction.
Fig. 5 show the change of PEC peak amplitude along the coordinate and shows minimum value at the defect position.

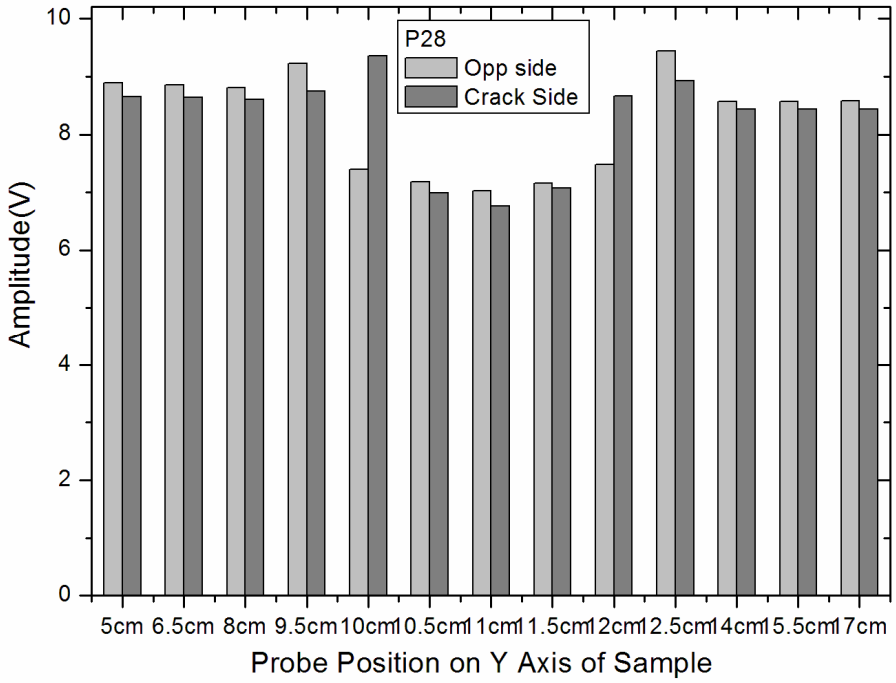

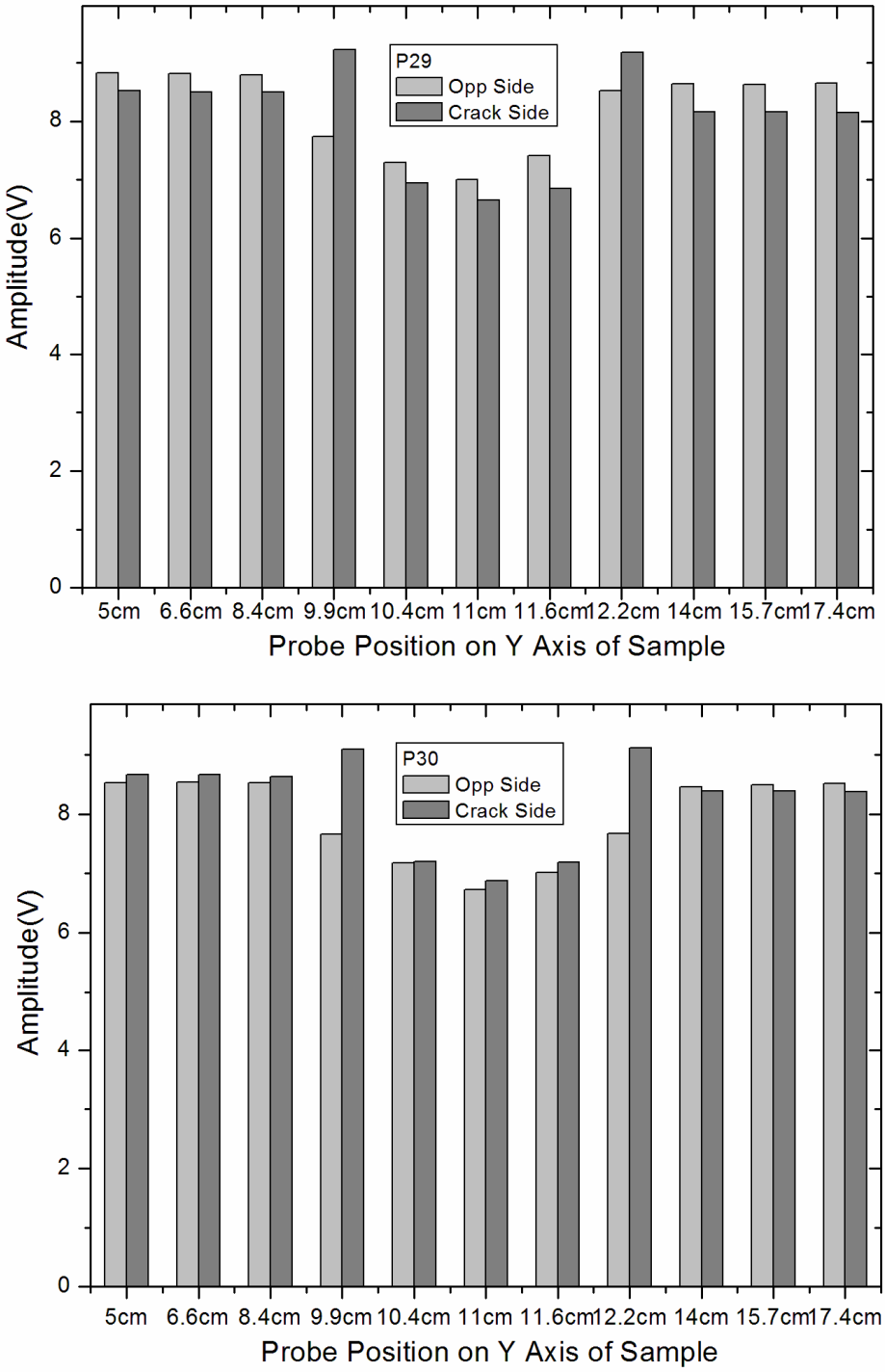

Figure 4.The difference of the PEC peak amplitude obtained in the crack and opposite side for P28, P29 and P30.

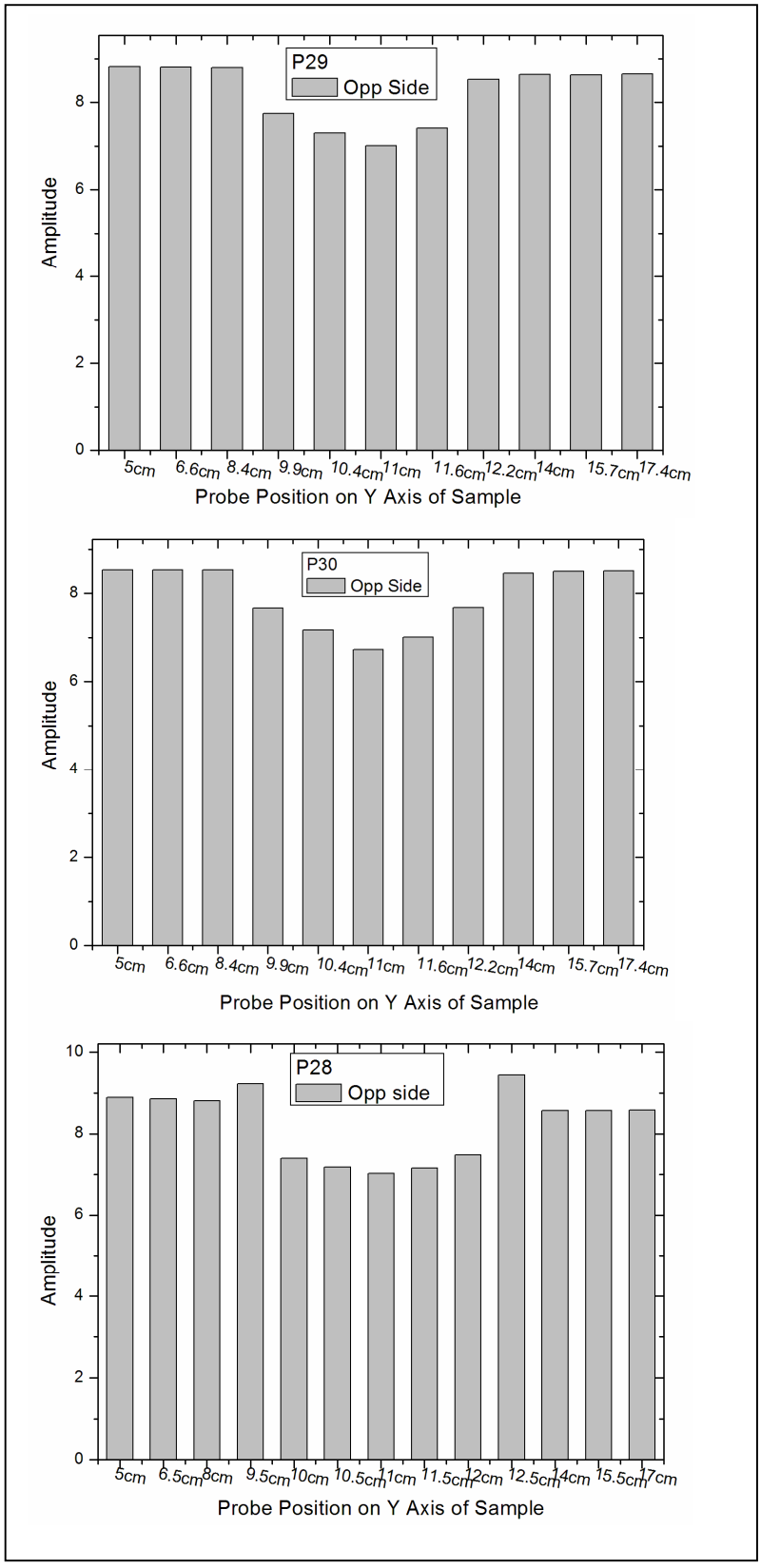

Figure 7.The difference of the PEC peak amplitude obtained in the crack and opposite side for P28, P29 and P30

6. Summary

1) The nondestructive evaluation (NDE) using PECT to detect the sub surface crack under the thick plate has been performed on the PARENT round robin sample. Three classes of round robin sample for P28, P29 and P30 have been tested, each class has dissmilar weld region between two ferromagnetic base materials.
2The PEC amplitude detected in the defect region (welded part) showed lower value than that of base material. The y coordinate 10 and 12 cm neighborhood is the interface region between ferromagnetic and nonmagnetic material. The crack is positioned in the neighborhood of y coordinate 11 cm, which shows the minimum PEC signal amplitude.
3) The base material is made of ferromagnetic materials, and dissimilar weld region is made of nonmagnetic materials. Considering the ferromagnetic materials induce a high magnetic signal, it is not certain that the decrements of amplitude are attributed to the defects or nonmagnetic part.

4) The PEC technology showed potential possibility detecting the subsurface crack in the nonmagnetic stainless steel plate, but the signals are largely depend on the appearance of ferromagnetic substance. Therefore the PECT technique requires further assessment and improvement in order to apply in the dissimilar weld region.

References

[1] G. Y. Tian, Z. X. Zhao, and R. W. Baines, “The research of inhomogeneity in eddy current sensors”, Sens. Act. A., vol. 69, pp 148–151, 1998.
[2] E. E. Kriezis, Theodoros D. Tsiboukis, Stavros M. Panas and John A. Tegopoulos, “Eddy currents: Theory and applications”, Proceedings of IEEE, Vol. 80, No. 10, pp 1559- 1589, Oct 1992.
[3] B.P.C. Rao, B. Raj, T. Jayakumar and P. Kalyanasundaram, “An Artificial neural network for eddy current testing of austenitic stainless steel welds”, NDT&E Internationl, Vol. 35,pp 393-398, 2002.
[4] Y. He, F. Luo, M. Pan, “Defect characterisation based on pulsed eddy current imaging technique”, Sensors and Actuators A, Vol 164, pp 1-7, 2010.
[5] J.C. Moulder, J.A. Bieber, W.W. Ward III, J.H. Rose, “Scanned pulsed eddy current instrument for non-destructive inspection of aging aircraft”, SPIE 2945, pp 2–13,1996.
[6] B.P.C. Rao, B. Raj, T. Jayakumar and P. Kalyanasundaram, “An Artificial neural network for eddy current testing of austenitic stainless steel welds”, NDT&E Internationl, Vol. 35,pp 393-398, 2002.
[7] Y. He, M. Pan, F. Luo, G.Ti, “Pulsed eddy current imaging and frequency spectrum analysis for hidden defect nondestructive testing and evaluation”, NDT& Int., Vol 44, pp 344-352, 2011.
[8] H. C. Yang, C.C. Tai, “Pulsed eddy current measurement of a conducting coating on a magnetic metal plate”, Meas Sci Techno.l, Vol 13, pp 1259-1265, 2002.

[9] M. A. Robers, R. Scottini, "Pulsed eddy current in corrosion detection", *NDT.net The e-Journal of Nondestructive Testing*, Vol.7, Oct. 2002.
[10] A. Smith, G. R. Hugo, "Transient Eddy-current NDE for aging aircraft capabilities and limitations", *Insight: Non-Des. Testing and Condition Monitoring,* Vol.43, pp. 14-25, Jan. 2001.

TOFD Technique and field application in Korean nuclear plants

Euisoon DOH, Jae-yoon KIM, Chang-ho Song, Tack-su LEE
KEPCO KPS, Busan, Korea

E-mail :dohes@kps.co.kr

TOFD(Time of Flight Diffraction) technique is a very useful method to detect a very tight crack caused by PWSCC(Primary Water Stress Corrosion Crack) in nuclear power plant. A Lateral wave and Tip signals are used to detect and size a flaw in TOFD technique. And one of the most important factor for TOFD technique is a proper spacing between two paired probes to maximize the detect ability and accuracy of sizing flaw considering the thickness of examined material.
We are applying this TOFD technique to Reactor vessel upper and bottom head penetration inspection in Korean plants. We also have participated in the Blind Round Robin test for the PARENT to detect flaws at BMI(Bottom Mounted Instrumentation Nozzle) mock up specimens.
We have found the first several PWSCC flaws at upper Reactor vessel head penetrations in Korean nuclear plants. And this event has played a main role in reducing the inspection interval of Reactor upper head penetration inspection, which designed with alloy 600 materials in Korean nuclear plants.
I will describe the characteristics of TOFD technique and the detection of PWSCC flaws in the field examination in Korean nuclear plants in this paper.

Keywords: Reactor vessel, Reactor vessel Head Penetration Examination, RVHP Inspection, RVHPI, ISI.

Nonlinear Ultrasonic Technique for Assessment of Thermal Aging

Jongbeom Kim[1] and Kyung-Young Jhang[2†]

[1]Department of Mechanical Convergence Engineering, Hanyang University, 222 Wangsimni-ro, Seongdong-gu, Seoul, Republic of Korea 133-791

[2]School of Mechanical Engineering, Hanyang University, 222 Wangsimni-ro, Seongdong-gu, Seoul, Republic of Korea 133-791

[†]Corresponding Author/ E-mail: kyjhang@hanyang.ac.kr,

TEL: +82-2220-0434, FAX: +82 -2299-7207

Abstract:

The second-order ultrasonic nonlinear parameter β has been studied for the evaluation of material degradation. However, there are some limits to the assessment of thermal aging in aluminum alloys due to the fluctuation in the nonlinear parameter with the aging time. This is because the nonlinear parameter strongly depends on the behavior of the precipitate when exposed to high temperatures. That is, the nonlinear parameter does not one-sidedly increase with the thermal aging. In such cases, it is difficult to evaluate the damage level from the nonlinear parameter. In order to overcome such limitations, we propose a cumulative nonlinear parameter β_c defined by the accumulation of variation in the nonlinear parameter over the aging time. In order to verify the usefulness of the proposed parameter, the nonlinear parameters were measured in aluminum alloy specimens heat-treated with different aging temperatures and aging times, and accumulated values of their variation were obtained as a function of the aging time. Tensile tests were conducted to estimate the altered strength of the Al alloy specimens due to thermal aging from the stress–strain curves. Results showed that the nonlinear parameter β varied in directions of both increase and decrease, but the strength decreased one-sidedly with aging. Thus, the parameter β could not be used as a direct index of strength degradation. On the other hand, the proposed parameter β_c one-sidedly increased and agreed well with the reduction in the strength.

Key words: Cumulative ultrasonic nonlinear parameter; Ultrasonic nonlinear parameter; Thermal aging; Aluminum Alloy; Precipitation

A Feasibility Study on Detection and Sizing of Defects in the Reference Block Specimen by Using Ultrasonic Infrared Thermography

Hee-Sang Park[2], Jeong-Hak Park[1], Dong-Jin Yoon[1*], Kyung-cho Kim[3], Won-Tae Kim[4] and Man-Yong Choi[1]

[1] Center for Safety Measurement, Korea Research Institute of Standards and Science, Korea,
[2] Korea Research Institute of Smart Material and Structures System Association, Korea
[3] Dept. of Mechanical & Materials Engineering, Korea Institute of Nuclear Safety, Korea
[4] Dept. of Mechanical Engineering, Kongju National University, Cheonan, Korea
* djyoon@kriss.re.kr

Ultrasonic infrared thermography (UIRT) is based on the detection of thermal energy generated when elastic energy is absorbed by a defect and converted to thermal energy through thermos-elastic effects. The advantage of UIRT is that it potentially enables more rapid examination of large areas based on camera images in contrast to other techniques that would require a point-by-point raster scan. Especially, with lock-in phased method, the amplitude and phase information about the thermal waves emitted from the specimen is preserved for several frequencies. Therefore it enables characterizing the depth of a source of thermal emissions in the test component inside.

This study describes a part of the results of open round robin test for PARENT by using ultrasonic infrared thermography technology. We used several types of specimen which is fabricated as reference block including several kinds of defects inside. In this preliminary study, all indications produced by infrared thermal image and lock-in phase image with temperature difference within the volume to be examined shall be considered as defect indications. This procedure was conducted after exciting the basic material near the welds by using ultrasonic guided horn for a certain amount of time. And also, a defect indication was discriminated by a healthy image to show temperature difference (< 0.15°C) along the position of component. In case of the evaluation of length sizing, defect size was correlated with the spatial resolution of pixel image. And the lock-in phase images was used for evaluating the temperature distribution through the temperature difference. Finally hot spot image indications produced by infrared thermal image and lock-in phase image were evaluated by comparing with defect size.

Keywords: Detection of defects, Ultrasonic infrared thermography, Dissimillar metal weld, PWSCC, NDE

Experimental Visualization of Ultrasonic Wave Propagation in Dissimilar Metal Welds

Masaki NAGAI[1], Shan LIN[1], Audrey GARDAHAUT[2], Hugues LOURME[2] and Frédéric JENSON[2]

[1]Central Research Institute of Electric Power Industry, Japan

[2]CEA, LIST, France

Abstract

In nuclear power plants, a number of surface cracks attributed to stress corrosion cracking (SCC) have been detected in dissimilar metal welds (DMWs) between austenitic stainless and low alloy steels. When a crack is detected in a component of a nuclear power plant during an in-service inspection, fitness-for-service codes require that a flaw evaluation has to be conducted. Detection and sizing of such cracks with high accuracy are necessary for accurate flaw evaluation. Although ultrasonic testing (UT) is widely used in nondestructive inspection techniques for components in nuclear power plants, it is difficult to be applied to DMWs because coarse grains in DMWs scatter and attenuate ultrasonic waves severely. Moreover, anisotropic and heterogeneous properties in DMWs result in beam splitting and skewing, which reduce the detection capability and the sizing accuracy of UT. For improvement of UT capability, CEA and CRIEPI both agree to have a collaborative research program focusing on deep understanding of wave propagation within DMWs. In this program, CEA performed a simulation of wave propagation and defect response regarding DMWs by using CIVA software. And CRIEPI conducted experimental visualization of wave propagation in DMWs and ultrasonic examination by phased array technology, which is the content of this paper.

Keywords: Ultrasonic Testing, Dissimilar Metal Welds, Phased Array Technology, Wave Visualization

1. Introduction

In nuclear power plants, nickel alloys have been used for dissimilar metal welds (DMWs) between austenitic stainless and low alloy ferritic steels. In recent years, a number of surface cracks attributed to stress corrosion cracking (SCC) have been detected in DMWs. In Japan, for instance, a crack was found in a weld in a reactor pressure vessel nozzle at the Ohi-3 pressurized water reactor (PWR) power plant [1], and cracks were detected in a shroud support weld at the Tsuruga-1 boiling water reactor (BWR) power plant [2]. When a crack is detected in a component of a nuclear power plant during an in-service inspection, fitness-for-service codes require that a flaw evaluation be conducted. Detection and sizing of such cracks with high accuracy are necessary for accurate flaw evaluation. Although ultrasonic testing (UT) is widely used to detect components of nuclear power plants, it is difficult to be applied to DMWs due to (1) ultrasonic waves are scattered and attenuated by coarse grains in DMWs, and (2) anisotropic and heterogeneous properties in DMWs result in beam splitting and skewing. These reasons reduce the detection capability and the sizing accuracy of UT.

In order to improve UT capability, experimental investigation by means of mock-up is useful, but it is time-consuming and costly. Instead of experiments, the CIVA developed by CEA/LIST is a proven software that it is effective for the optimization of inspection conditions. Nevertheless, it is necessary to ascertain whether the CIVA software can be used to model UT inspections in DMWs with severe anisotropic and heterogeneous properties. Therefore, CEA and CRIEPI both agree to have a collaborative research program focusing on (1) deep understanding of wave propagation within DMWs by means of simulation and experiment, (2) the evaluation of applicability of CIVA to DMWs with anisotropic and heterogeneous properties. In this paper, experimental visualization of wave propagation in DMWs and UT results using phased array method are shown.

2. Overview of collaborative research program

In this research, as shown in figure 1, a specimen made of austenitic stainless and ferritic steels with a nickel ally weld has been prepared and its crystallographic orientation of grains in weld is observed by macrograph. Three electrical discharge machining (EDM) notches with the same dimensions and shape are introduced into buttering, weld and stainless

steel base metal, respectively. In order to deeply understand how waves propagate within DMWs, the propagation of waves which are excited on surfaces of ferritic steel, buttering, weld metal and stainless steel, are visualized experimentally. Several linear array transducers with different frequencies are used to detect notches by pulse-echo and pitch-catch techniques. UT results predicted by the CIVA are compared to experimental results to evaluate the applicability of the model developed in the software. This collaborative research program started in April 2012 and ended in March 2014.

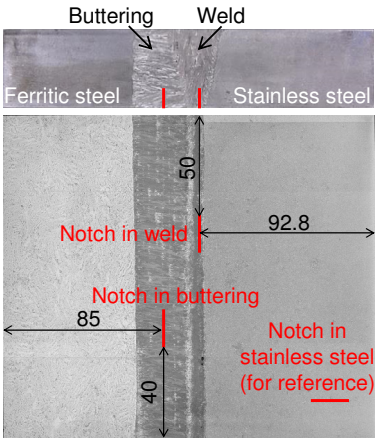

Figure 1 Specimen with dissimilar metal weld

3. Experimental visualization of wave propagation

3.1 Measurement method

Figure 2 shows the system used for measuring wave propagation. This system consists of a pulser / receiver, an oscilloscope, a transmitter, a receiver, a computer and a scanner. A voltage pulse is sent to the transmitter, which is an angle beam transducer, and is located on the top surface. The transmitter generates waves propagating within a specimen. As the waves propagate within the specimen, they are probed by the receiver which is a normal incidence transducer. The diameter of vibrator in the receiver is 1 mm. Received waves are digitized by the oscilloscope and are inputted to the computer. The measurement is performed on an area so that wave propagation is not disturbed by notches introduced. The scanner moves the normal incidence transducer over 80 mm in *x*-direction and 35 mm in y-direction with a resolution of 0.2 mm on the side surface. The computer acquires data sent by the oscilloscope, controls the scanner and processes acquired data to view wave propagation. The transmitter and the receiver have the same nominate frequency of 2 MHz. A longitudinal angle beam transducer with a refraction angle of 49 degrees is used.

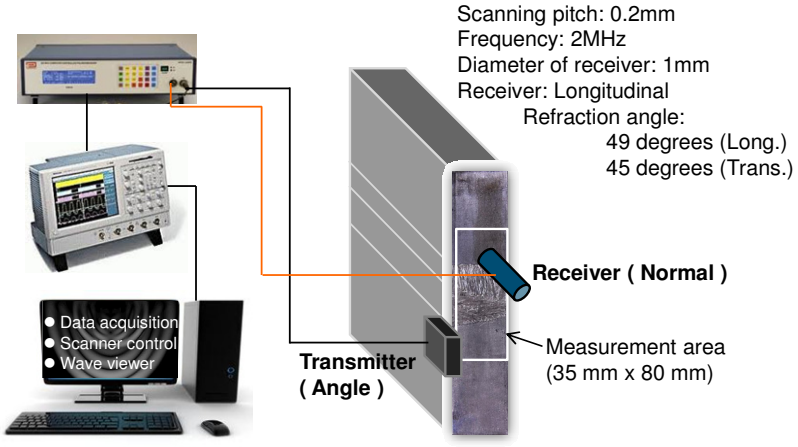

Figure 2 System for wave propagation visualization

3.2 Visualization results and discussion

Figure 3 shows waves excited by a longitudinal angle beam transducer on the ferritic steel, where L and T represent longitudinal and transverse waves, respectively. Color code represents the amplitude of waves. As shown in this figure, longitudinal and transverse waves are excited at the same time. Longitudinal waves are scattered in the buttering, but this scattering is so weak that it does not prevent longitudinal waves from traveling through the buttering. Figure 4 depicts longitudinal and transverse waves excited on the buttering. As shown in this figure, longitudinal waves can travel through the buttering and the weld while it is difficult for transverse waves to do so because they are severely scattered. Figure 5 and 6 are results of wave propagation observed on the opposite side of those shown in Figures 3 and 4. As shown in Figure 5, the weld scatters and attenuates longitudinal waves to some degree, but longitudinal waves propagate through it. Moreover, as shown in Figure 6, for longitudinal and transverse waves excited on the weld, longitudinal waves propagate through the buttering and the weld without difficulty. On the other hand, the weld scatters and attenuates transverse waves much more seriously than longitudinal waves, which implies that transverse waves propagate difficulty through the weld and the buttering. However, as shown in Figure 6, the wave front of transverse waves can be observed in some degree in the weld, but not in the buttering in figure 4. This is probably because the angle between grain axis and incident direction of ultrasonic waves in the buttering is much larger than that in the weld. This fact suggests that the buttering affects the propagation of transverse waves more than the weld. From results shown in figures 3-6, longitudinal waves have sufficient capability to travel through DMWs.

4. Ultrasonic examination by phased array technology

4.1 Examination conditions

Four kinds of ultrasonic examinations are performed using three different types of linear array transducers. Nominal frequency, the number of elements, pitch, length and width of respective transducer are shown in Table 1. Main examination conditions corresponding to respective examination are shown in Table 2, where PE and P/C mean pulse-echo and pitch-catch techniques, respectively. All examinations are carried out under longitudinal mode by raster scan.

4.2 Examination results and discussion

In this paper, only results of Examination 3, in which pulse-echo technique was applied with 1 MHz, are presented due to limitations of space. Figures 7 and 8 show results corresponding to the refraction angle of 45 degrees. T1 and C1 are indications in regard to tip and corner echoes of notch in weld metal, respectively. T2 and C2 mean tip and corner echoes of notch in buttering, respectively. WB is the indication of echo from the boundary between the weld and the buttering. Values shown in dB are echo intensities of notches introduced in the weld and the buttering normalized with respect to that of notch in stainless steel. Except for notch in the weld when waves are emitted from the stainless steel side, the decrease level for corner echoes is much larger than that for tip echoes. This is probably resulted from anisotropic and heterogeneous properties in the weld and buttering.

As shown in Figures 7 and 8, noise echoes resulting from scattering in the weld and buttering are observed. It is easy to detect notches introduced in weld and buttering when waves are emitted from the ferritic steel side. However, it is not easy to identify echoes associated to notches, especially for a notch in buttering, because of strong boundary echoes when waves are emitted from the stainless steel side.

5. Conclusions

In order to improve UT capability regarding DMWs, the specimen made of austenitic stainless and ferritic steels with a nickel alloy weld was prepared. Wave propagation in DMWs was visualized experimentally to understand how waves propagate within DMWs. Longitudinal waves have sufficient capability to travel through DMWs. Moreover, UT inspections were performed using several linear array transducers. Due to strong boundary echoes between weld and buttering, it is difficult to identify echoes associated to a notch in the buttering when waves are emitted from the stainless steel side.

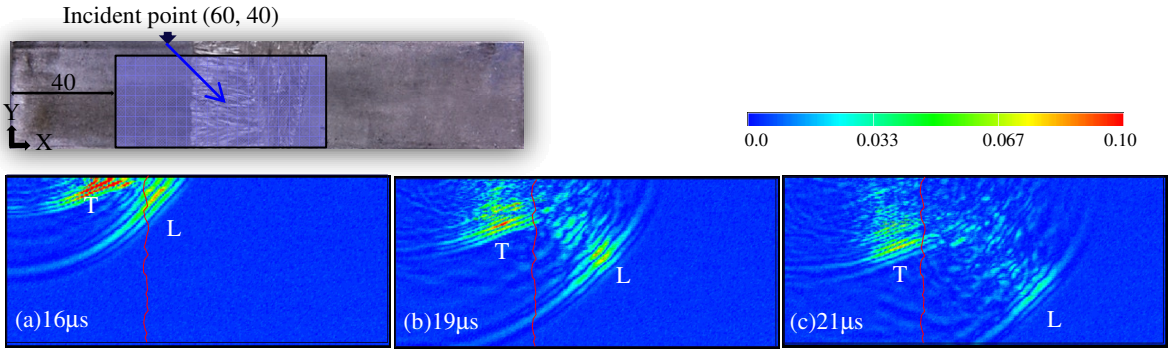

Figure 3 Waves excited by a longitudinal angle transducer located on ferritic steel

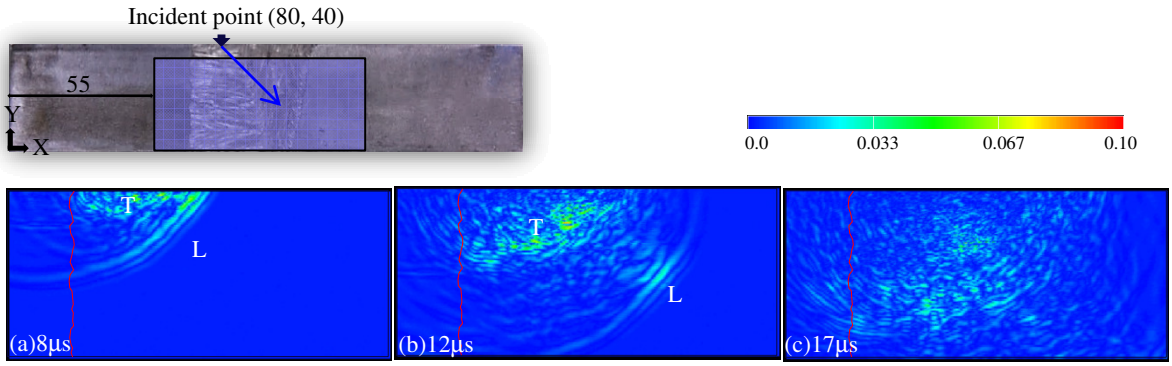

Figure 4 Waves excited by a longitudinal angle transducer located on buttering

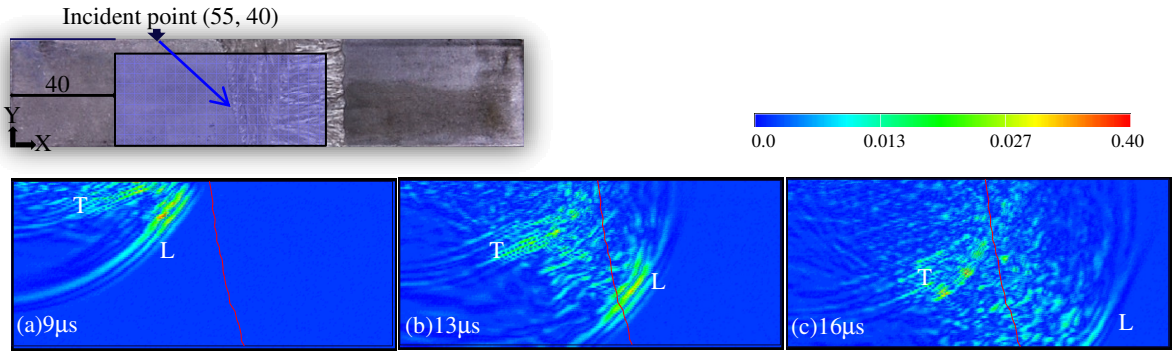

Figure 5 Waves excited by a longitudinal angle transducer located on austenitic stainless steel

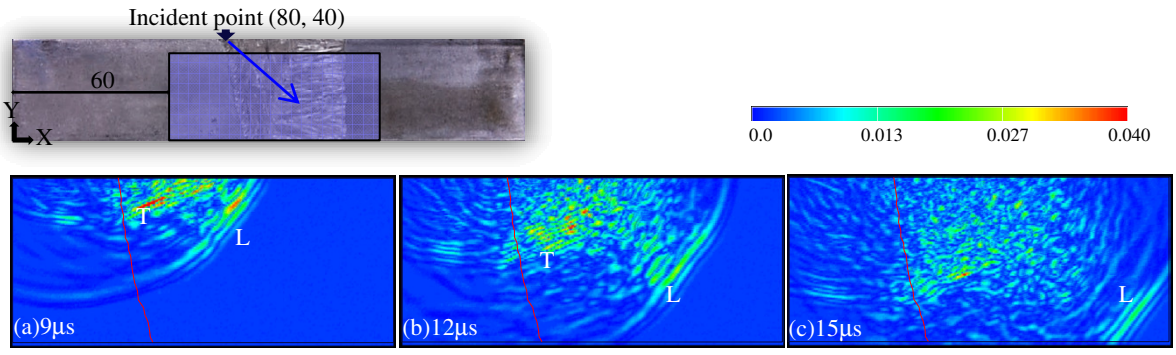

Figure 6 Waves excited by a longitudinal angle transducer located on weld metal

Table 1 Main specifications of transducer

	Nominal frequency (MHz)	Num. of elements	Pitch (mm)	Length (mm)	Width (mm)
Transducer 1	2	32	0.8	0.7	10
Transducer 2	2	64	0.6	0.5	20
Transducer 3	1	64	0.6	0.5	20

Table 2 Main examination conditions

	Technique	Transducer	Wave type	Num. of active elements	Emission depth (mm)
Examination 1	PE	Transducer 1	Longitudinal	32	20
Examination 2	PE	Transducer 2	Longitudinal	64	20
Examination 3	PE	Transducer 3	Longitudinal	64	20
Examination 4	P/C	Transducer 1	Longitudinal	32	32

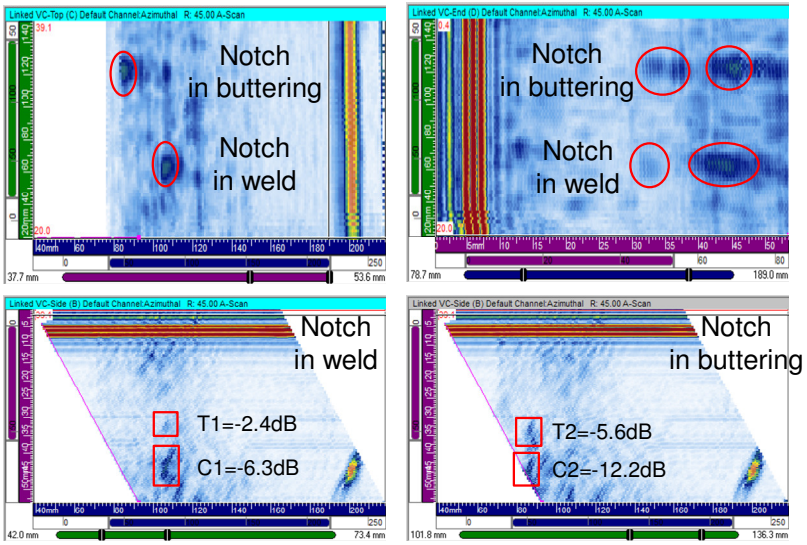

Figure 7 Results performed from ferritic steel side for examination 3

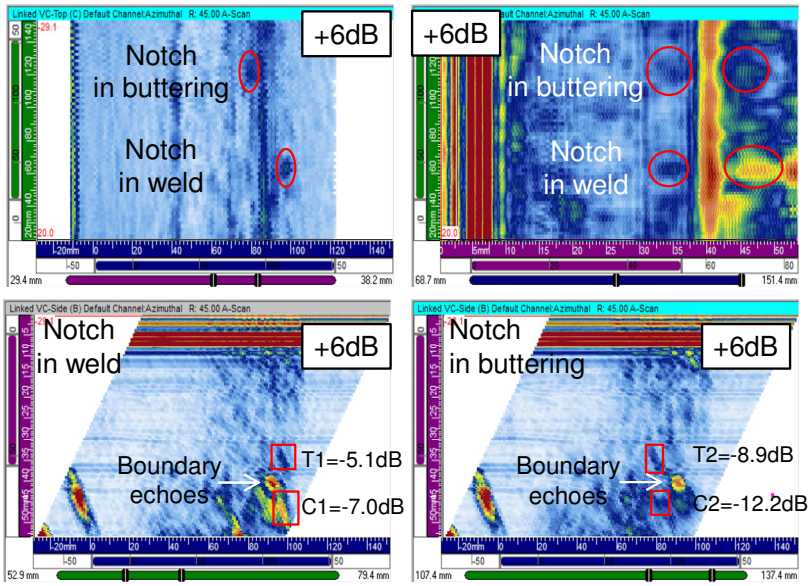

Figure 8 Results performed from stainless steel side for examination 3

References

[1] Nakamura T., Taniguchi, K., Hirano, S., Narita M., Sato T., “Stress Corrosion Cracking in Welds of Reactor Vessel Nozzle at Ohi-3 and of Other Vessel’s Nozzle at Japan’s PWR Plants”, PVP2009-77344, pp. 1-9 (2009)

[2] Aoki T., Shimizu S., Miyazaki K., Hayashi M., Kobayashi, H., “Evaluation on Crack Growth Analysis Model based on the Knowledge obtained from Stress Corrosion Cracking in Ni-Based Alloy used for a Long Time in a BWR”, Maintenology, 5, pp. 46-53. (2006)

Application of a 3D ray tracing model to the study of ultrasonic wave propagation in Dissimilar Metal Welds

Audrey GARDAHAUT[1], Hugues LOURME[1], Frédéric JENSON[1], Shan LIN[2] and Masaki NAGAI[2]

[1]CEA, LIST, Bât. 565, PC 120, F-91191 Gif-sur-Yvette, France

[2]Materials Science Research Laboratory, Central Research Institute of Electric Power Industry, 2-6-1 Nagasaka, Yokohama-Shi, Kanagawa-ken 240-0196, Japan

Abstract

The primary circuit of Nuclear Power Plants (NPP) is inspected using Ultrasonic NonDestructive Testing (NDT) techniques in order to maintain the integrity of its structure and detect eventual defects such as Stress Corrosion Cracking (SCC). Nevertheless in some components as Dissimilar Metal Welds (DMW), the interpretation of inspection results is difficult due to the appearance of beam disturbances as well as splitting and skewing. Those physical phenomena, occurring due to the anisotropic and inhomogeneous properties of the media, affect the detection and the characterization of possible discontinuities located inside or in the vicinity of the welds. In this context, numerical simulation tools are really useful to understand these disruptions and optimize the ultrasonic NTD methods. An analytical model, based on a ray theory, has been recently developed by CEA-LIST and implemented in the CIVA software to evaluate the propagation of elastic waves in anisotropic and inhomogeneous media. It allows the evaluation of the ray trajectories and travel-time and the computation of the amplitude along the ray tube in a medium described thanks to a continuously varying description of its physical properties. This paper presents the work made as a part of a collaborative program between CRIEPI and CEA. The ray-based model has been applied to the study of a DMW described by a smooth representation of the crystallographic orientation. Comparisons of the transmitted beam and the detection of notches, located in the weld and the buttering, obtained by simulations and experiments performed on this mock-up have been presented.

Keywords: Ultrasonic Testing, Ray-based Model, Dissimilar Metal Weld.

1. Introduction

Nickel-based alloys have been widely used in Nuclear Power Plants (NPP) to facilitate the welding of stainless steel cooling line pipes and instrumentation components to the ferritic steel vessels. Leaks have appeared in Dissimilar Metal Welds (DMW) of the primary circuit of NPPs [1-6] due to the formation and the growth of Stress Corrosion Cracking (SCC). Accurate detection and depth sizing of such cracks is a serious issue regarding the reliability and the safety of NPPs. Ultrasonic Testing (UT) techniques are commonly apply for DMWs inspection and difficult to interpret due to disturbances of the ultrasonic beam. Splitting and skewing [7], resulting from the anisotropy and heterogeneity of the materials [8], and scattering and attenuation, due to the coarse grain structure, may indeed affect the detection capabilities and sizing accuracy of UT. In this context, simulation tools are quite useful to understand those complex phenomena observed on inspection results.

Finite differences [9], finite elements [10-11] and ray tracing [12] models have been used to simulate the propagation of ultrasonic wave. Semi-analytical propagation models [13], based on a ray theory, have been implemented in the CIVA software [14-15], developed by CEA-LIST, and applied to the inspection of weld. The welds are described as a set of several anisotropic and homogeneous domains with a given crystallographic orientation. However, for domains with small dimensions compared to the wavelength, the simulated results are valid only if the contrast of impedance is small between two neighbouring domains [16]. A new approach has been considered to take into account the inhomogeneity in such anisotropic media. Based on the Dynamic Ray Tracing (DRT) model, it is applied to a weld described as a continuously variable description of the crystallographic orientation [17].

A collaborative research program has been set up between CRIEPI and CEA-LIST to understand the propagation of ultrasonic wave in DMWs. It focuses on the realization of simulations and experiments, the evaluation of applicability of CIVA for the study of material with complex structures and the evaluation of phased array techniques for DMWs inspections.

2. Dynamic Ray Tracing model for the simulation of ultrasonic propagation

Usually applied in Geophysics [18], the Dynamic Ray Tracing (DRT) model is based on the solving of two equations in anisotropic and inhomogeneous media [17].
The solving of the first equation, the *eikonal equation*, gives the following system called axial ray system [18]:

$$\begin{cases} \dfrac{dx_i}{dT} = a_{ijkl}\, p_l\, g_j^{(m)} g_k^{(m)} = V_i^{e(m)}, \\ \dfrac{dp_i}{dT} = -\dfrac{1}{2}\dfrac{\partial a_{ijkl}}{\partial x_i}\, p_k\, p_n\, g_j^{(m)} g_l^{(m)}. \end{cases} \tag{1}$$

Composed of two coupled ordinary differential equations, this system describes the variations of the position x_i and the slowness p_i with respect to the travel-time $T(x)$. It is expressed in function of the elastic constants of the material a_{ijkl}, the density ρ and the components of the slowness vector p_i. $g_j^{(m)}$ are the eigenvectors of the Christoffel tensor corresponding to the polarization vectors and $V_i^{e(m)}$ is the energy velocity for the *m*-mode. The solutions of this system give the ray trajectories and the travel-time in the weld.

A second system called the paraxial ray system is obtained by solving the *transport equation*. Composed of ordinary linear differential equations of the first order of the paraxial quantities Q_i and P_i, it expresses the variations of the position x_i and the slowness p_i in function of the travel-time $T(x)$ and the parameter γ:

$$\begin{cases} \dfrac{d}{dT}\left(\dfrac{dx_i}{d\gamma}\right) = \dfrac{dQ_i}{dT} = \dfrac{1}{2}\dfrac{\partial^2 G}{\partial p_i^{(x)} \partial \gamma}, \\ \dfrac{d}{dT}\left(\dfrac{dp_i^{(x)}}{d\gamma}\right) = \dfrac{dP_i}{dT} = \dfrac{1}{2}\dfrac{\partial^2 G}{\partial x_i \partial \gamma}. \end{cases} \tag{2}$$

γ is any parameter of a ray Ω and is chosen as a take-off angle between a reference axis and the initial slowness vector and G_m, expressed as $G_m = a_{ijkl}\, p_j\, p_l\, g_i^{(m)} g_k^{(m)}$, are the normalized eigenvalues of the Christoffel tensor. Through the solving of this system, the evolution of the ray tube during the propagation is obtained and its amplitude, assuming the conservation of the energy across a ray tube section, is evaluated.

These two systems are solved simultaneously by using numerical techniques such as the Euler method in this example.

3. Description of the physical properties of a dissimilar metal weld

The mock-up considered in this study (cf. Figure 1) connects a SM490 ferritic steel pipe to a SUS316L stainless steel pipe. This dissimilar V-butt weld and the buttering are made with alloy 600.

Figure 1. Macrograph of a V-butt DMW.

This weld is characterized by an anisotropic and inhomogeneous structure and a strong attenuation. Responsible for the splitting and skewing of the ultrasonic beam along the propagation, these characteristics have to be known and used as input data in the simulations.

The anisotropy of the material, expressed through the elastic constants, results of the dependence of the ultrasonic velocity to the direction of propagation. The chosen set of parameters is presented in Table 1. These properties of alloy 182 are representative of the anisotropy of the studied V-butt weld made of alloy 600.

	C_{11}	C_{22}	C_{33}	C_{23}	C_{13}	C_{12}	C_{44}	C_{55}	C_{66}	ρ
Alloy 182 [19]	255.8	255.8	236	135.4	137.9	130.5	111.4	111.9	81.4	8260

Table 1. Input parameters in CIVA for alloy 182. Elastic constants in GPa and density in $kg.m^{-3}$.

The ultrasonic attenuation during the propagation is caused by two phenomena: the wave scattering on the constitutive macroscopic grains and the absorption linked to the material viscosity. This energy loss has been evaluated at 2 MHz for a 316L sample in function of the orientation between the ultrasonic beam and the grain [19]. It is given in Table 2.

	0°	15°	30°	45°	60°	75°	90°
Attenuation coefficient (in $dB.mm^{-1}$) [19]	0.037	0.036	0.048	0.068	0.087	0.115	0.175

Table 2. Attenuation coefficient for a L-wave at 2 MHz in 316L material.

These values are used in the CIVA software to express the attenuation law of the longitudinal wave in function of the angle between the incident beam and the grain.

As the DRT model relies on a high frequency approximation, the weld has to be described as a continuously varying description of the grain orientation. This representation of the inhomogeneity of the medium can be made through an analytical law [12] expressed as:

$$\theta = \begin{cases} \arctan\left(\dfrac{T(D + z\tan\alpha)}{x^{\eta}}\right), & for\ x > 0, \\ -\pi/2, & for\ x = 0, \\ -\arctan\left(\dfrac{T(D + z\tan\alpha)}{(-x)^{\eta}}\right), & for\ x < 0. \end{cases} \tag{3}$$

T and η represent the evolution of the grain orientation and D and α express the geometry of the V-butt weld. The macrograph presented previously highlights two distinct domains in the mock-up. The buttering is then considered as a homogeneous medium with a grain orientation of 78° and the weld is described as symmetrical with the closed-form expression. This description is presented in Figure 2.

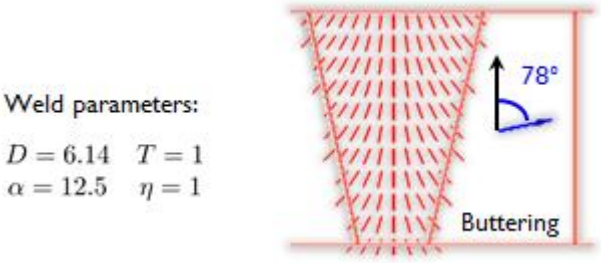

Figure 2. Representation of the weld orientation in the V-butt DMW.

4. Ultrasonic wave propagation

4.1 Experimental set up

The aim of this first experiment is to measure the transmitted beam of longitudinal wave through the mock-up (cf. Figure 3). A first transducer emits a longitudinal wave at 2 MHz with a refraction angle equal to 49° in the weld. It is located on the top of the weld while a second 2 MHz normal incidence probe with a 1 mm diameter vibrator is positioned on a side of the mock-up.

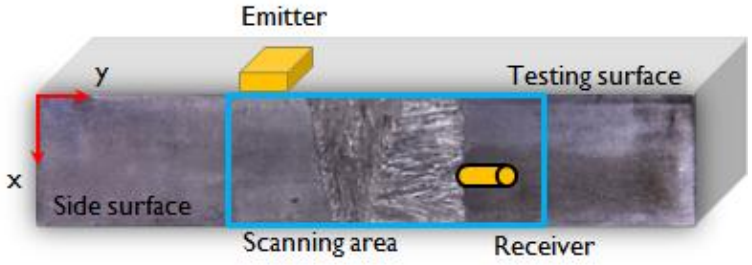

Figure 3. Experimental set up for the ultrasonic wave propagation visualization.

4.2 Comparison of simulation and experiments

The first application of the DMW modelling is the simulation of the wave propagation through the weld. Figure 4 presents the simulated and experimental results obtained for an emission in the buttering and propagation from the ferritic to the stainless steel part across the buttering and the weld.

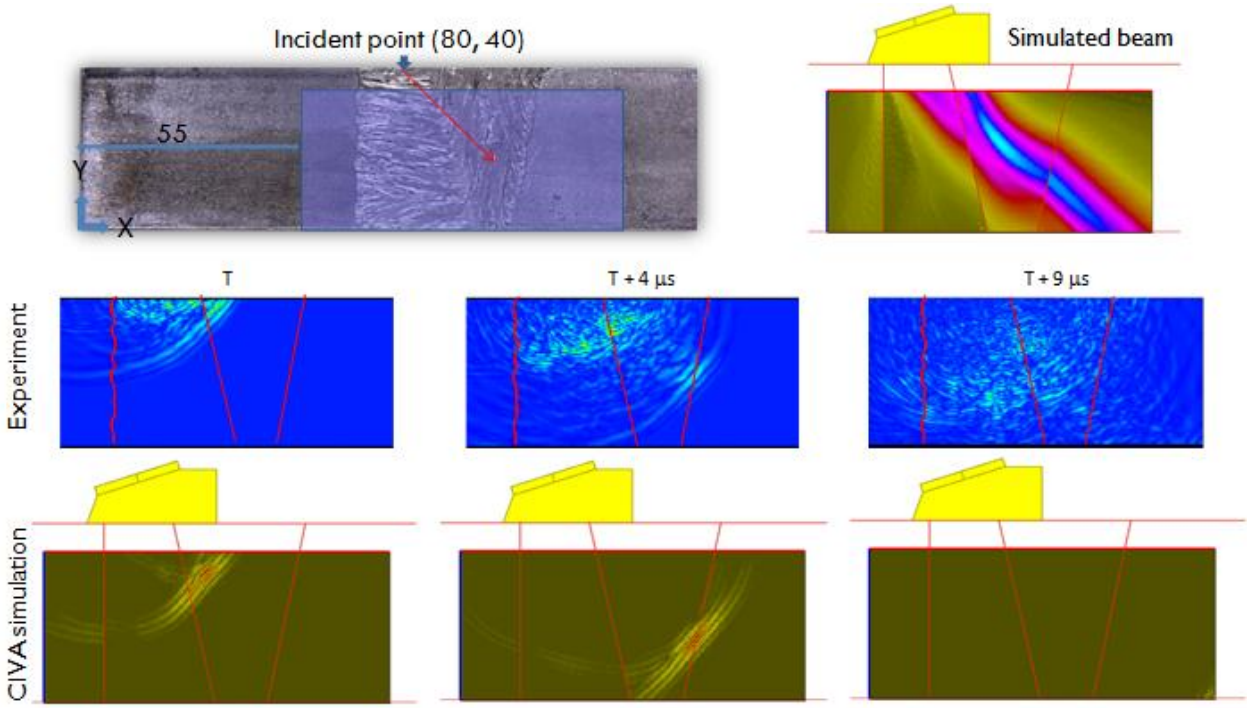

Figure 4. Experimental and simulated beam of a L49° wave emitted on the top of the buttering.

At this position, the deviation of the ultrasonic beam during its propagation through the buttering and the weld is well represented in the simulation. Furthermore, the wave front of the longitudinal wave propagating in this mock-up is observed. The experimental and simulated snapshots are in good agreement at different propagation time. Even so, the wave field perturbation is not represented as the shear wave has not been taken into account in the simulations. The scattering of the elastic wave due to the constitutive grains of the DMW is not simulated either.

Figure 5 shows the results obtained for a second position, where the emitting probe is located at the interface of the stainless steel and the weld and for propagation from the stainless to the ferritic steel part.

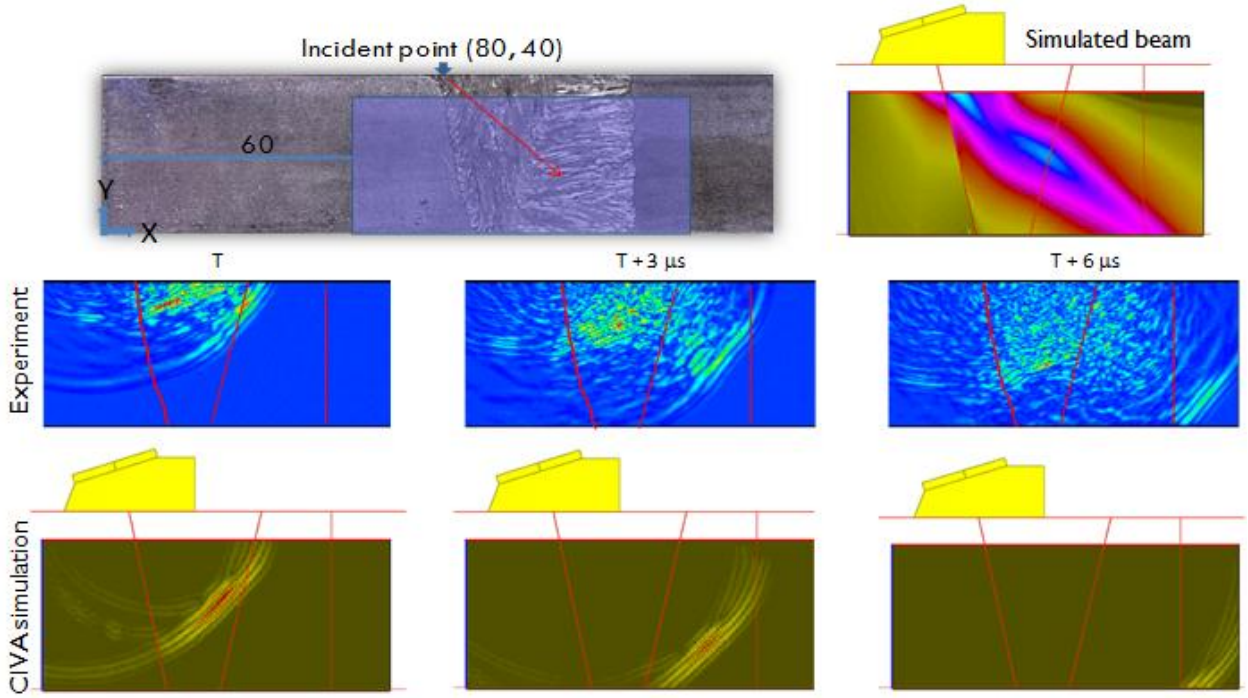

Figure 5. Experiment and simulation of a L49° wave emitted at the interface of the weld and the stainless steel part.

At this position, the wave propagates in the weld and the buttering, and the simulation shows its deviation. As for the first direction of propagation, the wave front is well simulated compared to the experiment but the positions of the maximal amplitude are slightly different.

5. Ultrasonic inspection

As the ultrasonic beam is well evaluated, the simulated and experimental results of a defect response are then compared.

5.1 Experimental set up

Three 10 mm height notches are considered here. As shown in Figure 6, one is in the buttering (S1), one in the weld (S2) and another one in the stainless steel (S3). A 1 MHz linear array transducer of 64 elements (length = 0.5 mm, pitch = 0.6 mm) is used in pulse echo technique and emits a longitudinal wave at 49°. The simulations, performed in a development version of the CIVA software, are compared to the experimental results.

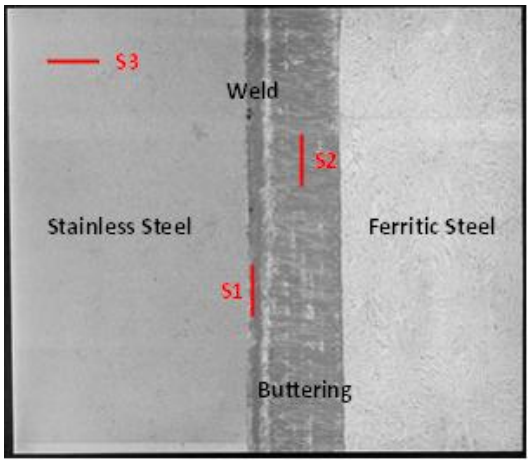

Figure 6. Location of the three considered 10 mm height notches in the mock-up.

In the following section, T and C indicate the tip diffraction and corner echoes of the notches and the S3 defect is chosen as the reference.

5.2 Simulated and experimental results

Figure 7 shows the simulated and experimental detection of the notches located in the weld and the buttering for an inspection made from the ferritic steel to the stainless steel part while Figure 8 is the comparison for propagation from the stainless steel to the ferritic steel.

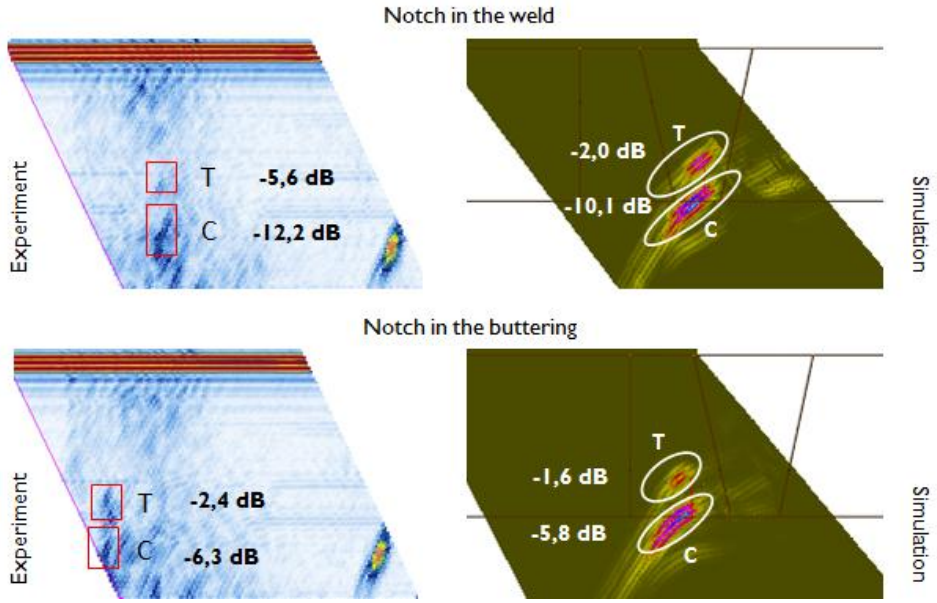

Figure 7. Simulated and experimental inspection from the ferritic to the stainless steel part of notches located in the weld and the buttering.

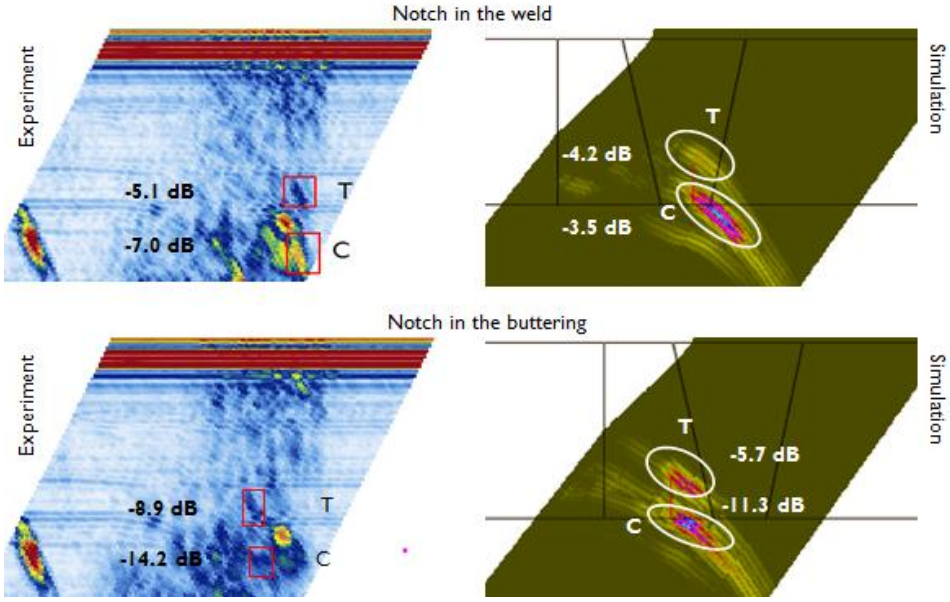

Figure 8. Simulated and experimental inspection from the stainless to the ferritic part of notches located in the buttering and the weld.

For an inspection from the ferritic to the stainless steel part, the tip diffraction and corner echoes are well detected in experiments for both notches and well reproduced by simulation. Furthermore, the amplitude of each echo is in good

agreement between simulation and experiment. The maximal difference is obtained for the tip diffraction of the S2 notch located in the weld. It corresponds to a wave that propagates across the buttering and the weld zone.

In the second direction of propagation, the tip diffraction and corner echoes are well detected in simulation but not in experiment. Indeed, the inspection interpretation is difficult due to the noise caused by the internal structure organization of the weld. Nevertheless, the amplitude evaluated from the simulated and experimental results are in a very good agreement.

6. Conclusion and perspectives

Simulations and experiments of the ultrasonic propagation and defect response, performed on a V-butt weld, have been presented in this paper. The aim was to evaluate the applicability of the DRT model developed in CIVA to study the propagation of ultrasonic wave in anisotropic inhomogeneous media. The weld considered in this study has been described with a continuously variable representation of the crystallographic orientation obtained thanks to an analytical law from the observation of the macrograph.

Simulations of the transmitted beam through the mock-up have been compared to experimental studies. The snapshots made of the wave front are in good agreement at different time. Moreover, the amplitude of defects located in the weld and the buttering are also well evaluated with the model in comparison to the experimental UT inspection.

Nevertheless, slight differences have been highlighted. A new description of the weld is planned to be used to improve the evaluation of the defect response. It is considered to represent the entire weld with a continuously variable description of the crystallographic orientation to avoid the creation of a straight separation between the buttering and the welded zone. Furthermore, the amplitude is overestimated in simulation. The attenuation used in this work is maybe lower than the real attenuation of the considered material. The scattering coefficient on the defect is currently evaluated by considering that the defect is located in a homogeneous media. The variations of physical properties of the material on its edges are not considered at this point which can explain discrepancies observed for the evaluation of the amplitude of the notches.

This collaboration has been extended to study the ultrasonic inspection of a real stress corrosion cracking defect implanted in a dissimilar metal weld whose physical properties are well-known.

References

[1] B. G. Braatz *et al.*, "Primary Water Stress Corrosion Cracks in Nickel Alloy Dissimilar Metal Welds: Detection and Sizing Using Established and Emerging Nondestructive Examination Techniques", IAEA-CN-194-025, pp.1-9 (2012)

[2] W. H. Bamford *et al.*, "Integrity Evaluation for Future Operation: Virgil C. Summer Nuclear Power Plant Reactor Vessel Nozzle to Pipe Weld Regions", WCAP-15615, Rev. 0, Westinghouse Engineering (2000)

[3] W. H. Bamford *et al.*, "Alloy 182 Crack Growth and its Impact on Service-Induced Cracking in PWR Plant Piping", (Proc. 10th International Conference on Environmental Degradation of Materials in Nuclear Power Systems – Water Reactors, Houston, Texas), NACE , Paper 34 (2002)

[4] A. Jenssen *et al.*, "Assessment of Cracking in Dissimilar Metal Welds", (Proc. 10th International Conference on Environmental Degradation of Materials in Nuclear Power Systems – Water Reactors, Houston, Texas), NACE (2002)

[5] A. Jenssen *et al.*, "Structural Assessment of Defected Nozzle to Safe-End Welds in Ringhals-3 and -4", (Proc. Fontevraud V International Symposium), SFEN (2000)

[6] S. E. Cumblidge *et al.*, "Nondestructive and Destructive Examination Studies on Removed from-Service Control Rod Drive Mechanism Penetrations", NUREG/CR-6996, PNNL-18372, U.S. Nuclear Regulatory Commission, Washington, D.C. (2009)

[7] B. Chassignole *et al.*, "Ultrasonic Examination of Austenitic Weld: Illustration of the Disturbances of the Ultrasonic Beam", 35th Review of Progress in Quantitative Nondestructive Evaluation, Vol. 28, pp. 1886-1893 (2009)

[8] D. S. Kupperman and K. J. Reimann, "Ultrasonic Wave Propagation and Anisotropy in Austenitic Stainless Steel Weld Metal", IEEE Transactions on Sonics and Ultrasonics, Vol. SU-27, No. 1, pp. 7-15 (1980)

[9] P. Fellinger *et al.*, "Numerical Modeling of Elastic Wave Propagation and Scattering with EFIT – Elastodynamic Finite Integration Technique", Wave Motion, Vol. 21, pp. 47-66 (1995)

[10] A. Apfel *et al.*, "Coupling an Ultrasonic Propagation Code with a Model of the Heterogeneity of Multipass Welds to Simulate Ultrasonic Testing", Ultrasonics, Vol. 43, pp. 447-456 (2005)

[11] B. Chassignole *et al.*, "Modelling the Attenuation in the ATHENA Finite Elements Code for the Ultrasonic Testing of Austenitic Stainless Steel Welds", Ultrasonics, Vol. 49, pp. 653-658 (2009)

[12] J. A. Ogilvy, "Computerized ultrasonic Ray Tracing in Austenitic Steel", NDT International, Vol. 18, No. 2, pp. 67-77 (1985)

[13] N. Gengembre and A. Lhémery, "Pencil Method in Elastodynamics: Application to Ultrasonic Field Computation", Ultrasonics, Vol. 38, pp. 495-499 (2000)

[14] CIVA software platform for simulating NDT techniques (UT, EC, RT) http://www-civa.cea.fr

[15] A. Lhémery *et al.*, "Modeling Tools for Ultrasonic Inspection of Welds", NDT&E International, Vol. 37, pp. 499-513 (2000)

[16] A. Gardahaut *et al.*, "Evaluation of Ray-Based Methods for the Simulation of UT Welds Inspection", 39th Review of Progress in Quantitative Nondestructive Evaluation, Vol. 32B, pp. 1073-1080 (2013)

[17] A. Gardahaut *et al.*, "Paraxial Ray-Tracing Approach for the Simulation of Ultrasonic Inspection of Welds", 40th Review of Progress in Quantitative Nondestructive Evaluation, Vol. 33A, pp. 529-536 (2014)

[18] V. Červený, "Seismic Ray Theory", Cambridge: Cambridge University Press (2001)

[19] B. Chassignole *et al.*, "Ultrasonic and Metallurgical Examination of an alloy 182 Welding Mold", 7th International Conference on NDE in Relation to Structural Integrity of Nuclear and Pressurized Components, 12-15 May, Yokohama, Japan (2009)

Comparison of Artificial flaws in Austenitic Steel Welds with NDE Methods

Ari Koskinen[1] and Esa Leskelä[1]
[1]VTT Technical Research Centre of Finland; Kemistintie 3, 02150 Espoo, Finland

Abstract

Qualification of non-destructive examination (NDE) procedures for in-service inspections (ISI) of nuclear power plant (NPP) components is performed using different types of artificial flaws. The assessment of the reliability of a procedure requires representative flaws compared to the real service-induced flaws.

Fatigue cracks can nowadays be produced artificially as thermal fatigue or mechanical fatigue cracks. Thermal fatigue crack production is very well controlled in matter of size and opening. That kind of cracks are very realistic option compared to the real service-induced cracks. Mechanical fatigue crack production is well known and widely used method and can produce very realistic cracks as well. The aim of the study is to get a wider perspective to the differences in similar size of flaws from different manufacturers.

Ultrasonic indications are highly dependent on defect characteristics like roughness, crack opening, tilt and branching. This work studies the influence of different reflector properties on flaw indications. Two kinds of artificially produced cracks from different manufactures and one electric discharge machining (EDM) reference notch were made in two welded austenitic stainless steel test blocks. Flaws were examined using conventional ultrasonic testing (UT), phased array ultrasonic testing (PAUT) and computed tomography (CT). The flaws were sized with different techniques and those results are compared to the true state flaw dimensions as determined by destructive analysis.

This study was made as a part of Finnish national research program on NPP safety 2010-2014 (SAFIR2014), Monitoring of the structural integrity of materials and components in reactor circuit, MAKOMON project.

Keywords : ultrasonic testing (UT), phased array, computed tomography, mechanical fatigue crack, thermal fatigue crack, indication, flaw, flaw sizing

1. Introduction

Qualification of non-destructive examination (NDE) procedures for in-service inspections (ISI) of nuclear power plant (NPP) components is performed using different types of artificial flaws. The assessment of the reliability of a procedure requires representative flaws compared to the real service-induced flaws.

Fatigue cracks can nowadays be produced artificially as thermal fatigue or mechanical fatigue cracks. Thermal fatigue crack production is very well controlled in matter of size and opening. That kind of cracks are very realistic option compared to the real service-induced cracks. Mechanical fatigue crack production is well-known and widely used method and can produce very realistic cracks as well.

Ultrasonic indications are highly dependent on defect characteristics like roughness, crack opening, tilt and branching as well as any additional disturbances of the material caused for example by the flaw manufacturing process. This work studies the influence of different reflector properties on flaw indications. This study was made as a part of Finnish national research program on NPP safety 2010-2014 (SAFIR2014), Monitoring of the structural integrity of materials and components in reactor circuit, MAKOMON project. The aim of the study is to get a wider perspective to the differences of two different types of fatigue cracks from different manufacturers [1].

2. Goal

The goal of the study was to compare NDE indications of different kinds of artificial flaws. Another objective was to evaluate the accuracy of various ultrasonic techniques – both conventional ultrasonic testing (UT) and phased array ultrasonic testing (PAUT) – in flaw sizing. Also the effect of flaw type on sizing accuracy was compared. The crack characterization and sizing accuracy with computed x-ray tomography (CT) was also studied.

The goal of destructive examination was to measure the dimensions of the flaws, to characterise the fracture surface as well as the crack path in the materials. Another objective was to evaluate how well the characteristics of the flaws mimic

real cracks in NPP primary system piping.

3. Test samples

Two different fatigue samples were studied. Both samples were made of austenitic stainless steel 316L (ASTM) plate with a thickness of 25 mm. Samples were butt welded of two pieces and both weld face and root sides were ground to allow full scanning access and to exclude geometrical indications. The cracks were produced on the weld root side along the fusion line (Figure 1 a) to simulate inside surface breaking service-induced stress corrosion cracks (SCC). One of the samples contained one thermal fatigue (TF) crack and electric discharge machining (EDM) reference notch and the other contained two mechanical fatigue (MF) cracks [2].

Liquid penetrant indications of both thermal and mechanical fatigue cracks are shown in Figure 1 b and c. The branching shape of the TF crack is well visible whereas the shape of the MF crack seems to be rather smooth. The dimensions of the cracks in both samples were targeted to be 15 mm in length and 5 mm in height. The true dimensions were determined by destructive investigation as a part of SAFIR2014, Environmental influence on cracking susceptibility and ageing of nuclear materials, ENVIS project [3].

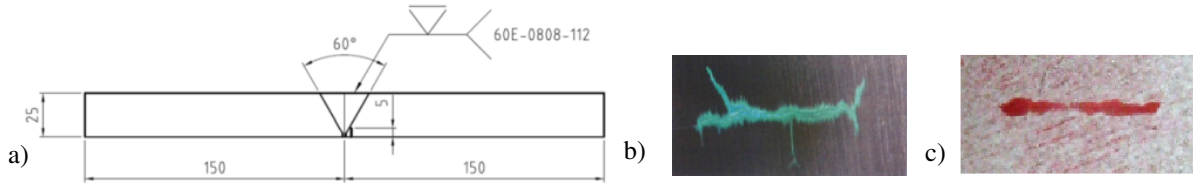

Figure 1. a) Schematic picture of the sample and liquid penetrant indications of b) thermal fatigue crack and c) mechanical fatigue crack.

4. Methods

4.1 Destructive examination

The three plate samples, named MF A, MF B and TF were received for destructive examinations after thorough NDE investigations which are presented in detail in the following chapters. First, the locations of the defects in the plates were identified and then about 30 x 80 mm sized samples were cut out, containing the defects.

The surfaces with the cracks were investigated using scanning electron microscopy (SEM), and the length was measured from the SEM-pictures in the two cases, where the cracks were visible on the surfaces. The cracks were then opened and the sizes (length and height) were measured from stereo microscope pictures. One of each fracture surface was investigated using SEM, and the typical features were documented.

A cross-section was prepared from each flaw by cutting a slice across the crack. As the crack was opened, the cut was performed separately from each half at the same location. This will, however, never result in a perfect match of the two fracture surfaces. If the cutting would have been performed before opening of the flaws, the dimensions would have been less accurate, and this was considered more important. The cross-sections were investigated in polished and etched condition using an optical microscope.

4.2 Ultrasonic examination

The ultrasonic inspections were performed on the two test blocks containing flaws. Scanning was performed on the top surface of the blocks from both sides of the weld. PAUT and conventional UT were both used with multiple setups. With conventional UT eight different setups and with PAUT six different setups were used for height sizing for each flaw. In length sizing with conventional UT 12 setups and with PAUT eight setups were used for each flaw. The PAUT TRS (transmit-receive shear wave) and TRL (transmit-receive longitudinal wave) techniques are included in a procedure qualified through the Performance Demonstration Initiative (PDI) program administered by Electric Power Research Institute (EPRI). The procedure which is later referred as ‘PDI technique’ is not qualified for height sizing but only for length sizing.

4.3 X-ray tomography examination

Digital radiography was used to gather more information on the crack size, tilting, possible branching etc. [4]. Digital radiography examinations were done at Federal Institute of Material Research and Testing (BAM), Division 8.3, Radiological Methods in Berlin. The used methods included Vidisco RayzorX flat panel detector and TomoCAR which is equipment for x-ray tomography. TomoCAR results are included in this article.

The TomoCAR equipment has an ENIQ certification for detecting cracks in the tube with 25 mm wall thickness, the total penetration thickness 50 mm. The certified crack opening is min. 100 µm and the tolerance in crack height sizing is ± 1 mm. In the equipment the x-ray tube moves along a straight bar over the examined specimen taking 400 images. The Cadmium telluride detector is made by AJAT Finland. The size of the detector is 100 mm x 25 mm with 0.1 mm pixel size. Tomographic data was processed and analysed using Analytical RT Inspection Simulation Tool (aRtist) [5].

4.4 Flaw sizing in ultrasonic examination

Height sizing was primarily based on crack tip diffraction method: height of a flaw is the distance between flaw base and the maximum amplitude of tip diffraction signal. In the case that this signal was not detected or clearly separated, the estimation of height was based on 6 dB maximum amplitude drop sizing method: height is the distance between flaw base and the position where the flaw amplitude decreases 50 % (6 dB drop) of the maximum amplitude of the flaw.

Length sizing was done according to full amplitude drop technique: length of a flaw is the distance between two end points where the flaw signal drops on the average noise level of the surrounding area.

According to ASME Code, Section XI, Appendix VIII acceptance criterion, to pass a typical weld qualification examination, the maximum difference between indicated and true state values for flaw height and length is 3.18 mm and 19.05 mm, respectively [6].

4.5 Evaluation of sizing performance of ultrasonic examination

Some statistical analysis of flaw length and height characterization was done to make conclusions concerning flaw sizing capability and to compare the flaws and UT techniques. The statistical analysis presented in this article is limited to calculations of the root mean square error (RMSE). Also measurement error, mean error and standard deviation were calculated [1], but are not presented in this article.

RMSE is computed according to the formula shown below:

$$RMSE = \sqrt{\frac{1}{n}\sum_{i=1}^{n}(M_i - T_i)^2} \quad (1)$$

5. Results

In the destructive analyses the study included the surface examination, dimensioning, fracture surface examination and 3D-profiling (in Figure 2), followed by the results from the microscopical analyses. In this article a short conclusion of the destructive results is presented. The dimensions of the cracks were determined after opening from stereomicroscope pictures and the results are presented in Table 1. As can be seen from the table, there is a difference between the length measurements from the surface and from the fracture surface. The measurements from the fracture surfaces are considered more accurate. The height measurements are projections, and do not take the inclination into account.

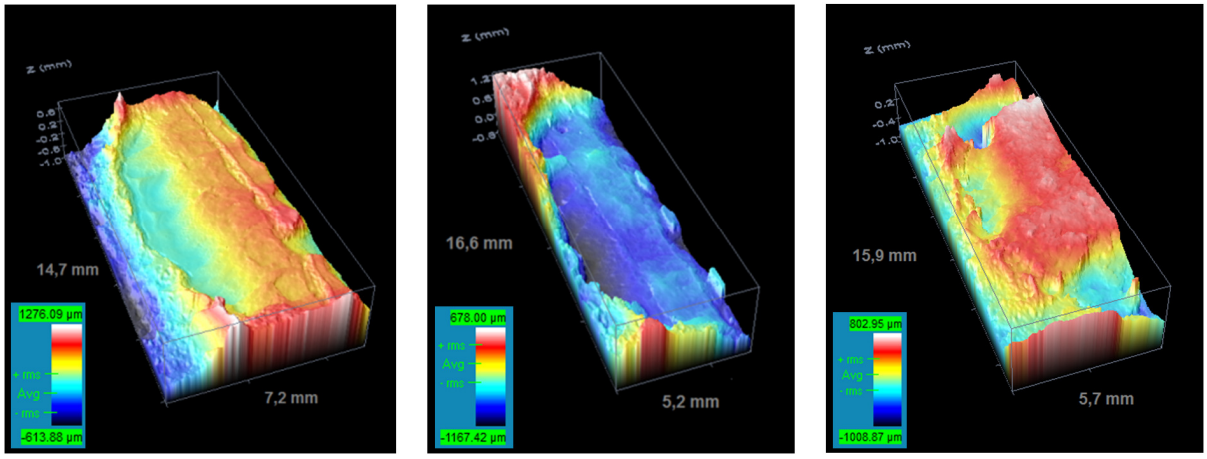

Figure 2. 3D-profimetric picture of the fracture surface in samples. From the left MF A, MF B and TF.

Table 1. Summary of dimensions for samples MF A, MF B and TF.

Sample	Length measured from surface (mm)	Maximum length measured from fracture surface (mm)	Maximum height measured from fracture surface (mm)	Length/height
MF A	(14.5)	13.1	6.2	2.11
MF B	-	14.3	5.0	2.86
TF	(12.8)	13.5	5.2	2.60

5.1 Height sizing results

It can be seen on the left hand side in Figure 3 that most of the techniques tend to undersize crack MF A except the conventional UT techniques with longitudinal wave (LW) mode which oversized the crack. The height sizing error was smallest with shear wave SW55 PAUT technique and the both PDI techniques.

All conventional UT techniques oversized crack MF B. PAUT techniques with lower frequencies (1.5–2.25 MHz) slightly undersized and PAUT techniques with higher frequency (5 MHz) slightly oversized the crack. The errors were smallest with MWK45-4 conventional UT and 45 SW PAUT techniques. The both PDI techniques slightly undersized the crack.

It can also be seen on the right hand side in Figure 3 that most of the conventional UT techniques oversized TF crack but all the PAUT techniques undersized the crack. Error was smallest with TRL 45-2 technique.

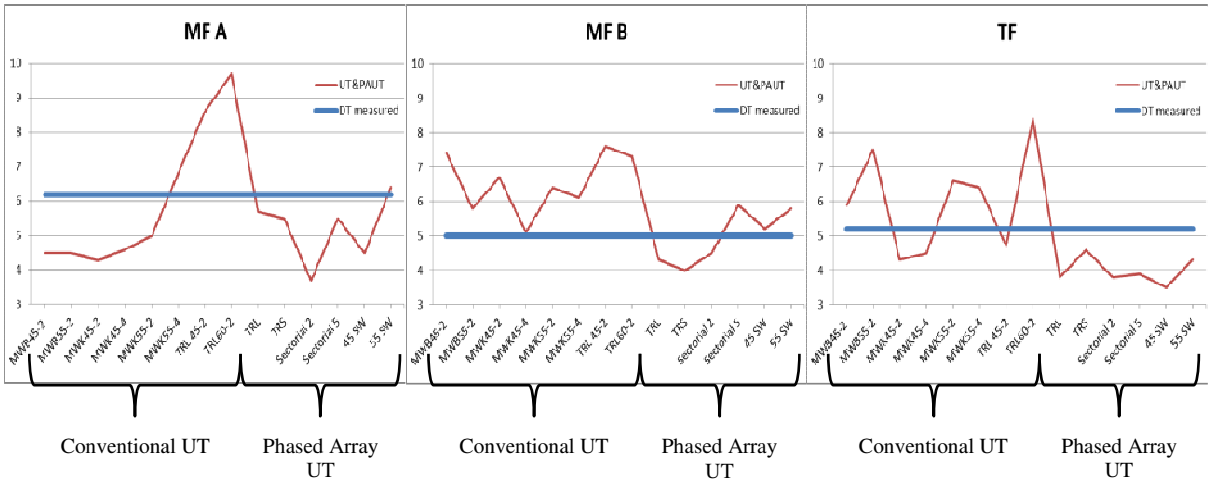

Figure 3. Comparison of the ultrasonic measurement height from the near side and destructively measured height.

5.2 Height sizing results

Only PAUT was performed for EDM notch. All the techniques were able to height size the notch both from near side (sounding from defect side) and far side (sounding through the weld). Half of the techniques undersized the notch when scanned from near side and all the techniques except TRS technique undersized the flaw when scanned from far side of the weld. The maximum error was –1.5 mm with 45 SW technique.

Reliable flaw height sizing of mechanical fatigue cracks was not possible from far side. This was due to the strong structural noise and metallurgical indication on the crack tip area. Half of the techniques were able to height size the thermal fatigue crack also from far side.

In the study all test techniques fulfilled the RMSE requirement of 3.2 mm in height sizing. The lowest RMSE values were calculated for MWK 45-4, MWK 55-4, 55 SW, TRL and TRS techniques. The highest RMSE value was calculated for TRL 60-2 technique.

The highest RMSE value with both conventional UT and PAUT was calculated for crack MF A. The lowest RMSE value with conventional UT was calculated for TF crack and with PAUT for crack MF B. There was a clear difference between the two mechanical fatigue cracks with both conventional UT and PAUT. All RMSE values were lower with PAUT than with conventional UT and unexpectedly the far side RMSE values were lower than the near side RMSE values.

Results showed lower RMSE values for PAUT than with conventional UT and highest RMSE values for crack MF A. It was also seen that the combined RMSE values were lowest for EDM notch and highest for crack MF A. There was a difference between the two mechanical fatigue cracks. The combined RMSE value for height sizing in this study was approximately 1.4 mm.

5.3 Length sizing results

According to results the greatest flaw undersizing for crack MF A occured with conventional UT techniques MWB55-2 and MWK55-2 together with the PAUT TRS technique when scanned from far side as can be seen on the left hand side in Figure 4. The TRL70-2 undersized the crack both from near and far side. Techniques MWB45-2, MWB70-2, MWK70-2, Sectorial 2 and 70 SW oversized the crack in near side scanning.

As can be seen in the middle of Figure 4, with crack MF B the TRL70-2, TRS and sectorial 2 techniques undersized the crack when scanned from far side. Techniques MWB45-2, Sectorial 2, 45 SW and 55 SW oversized the crack in near side scanning.

Comparison of length measurement results of MF A and MF B indicated the difference between the results of two similarly targeted mechanical fatigue cracks. The common observation was that all undersizing was done when scanned from far side with one exception (TRL70-2) and all oversizing was done when scanned from near side.

The results of length sizing of crack TF showed that all PAUT techniques except TRL and MC well oversized the crack when scanned from far side as can be seen on the right hand side in Figure 4. That was likely a consequence of noise due to

weld metal causing difficulties to define the actual end points of a flaw indication. Despite of that, only two conventional techniques, MWK55-2 and MWK55-4, oversized the crack. Several techniques undersized the crack in near side inspection and TRL technique in both scanning directions. The results differ from those of mechanical fatigue cracks.

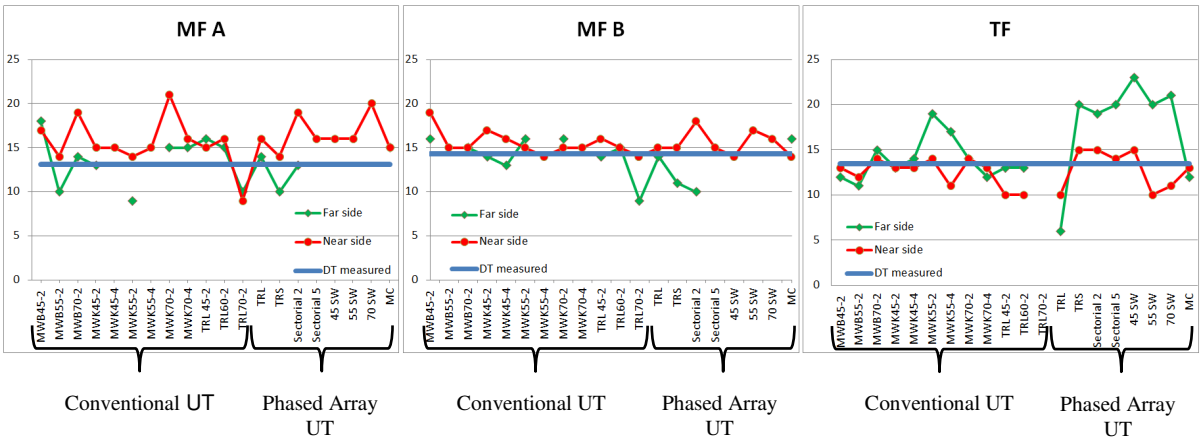

Figure 4. Comparison of the ultrasonic measurement length and destructively measured length.

Results showed that all PAUT techniques used in the inspection of EDM notch oversized the flaw except 55 SW and MC techniques.

It was also seen that the highest RMSE values with conventional UT were calculated for techniques MWK55-2 from far side and MWK70-2 from near side. All PAUT RMSE values were rather high. The highest values were calculated for TRS and Sectorial 2 techniques from both scanning directions ranging from 4.0 mm to 5.0 mm. Also the RMSE of 70 SW from near side and with TRL from far side were among the highest values. A combination of near and far side inspection results indicated the higher RMSE of PAUT (except MC) compared to those of conventional UT.

Clearly higher RMSE was calculated for crack MF A than for other cracks with conventional UT. With PAUT, the RMSE for crack TF scanned from far side and EDM notch scanned from near side were clearly higher than the others.

Comparison of conventional UT and PAUT showed that RMSE of TF crack and EDM notch with PAUT were clearly the highest and there was no difference between the techniques with crack MF A.

The highest length sizing RMSE values were calculated for TF crack when scanned through the weld (4.7 mm) and for EDM notch in both scanning directions (far side 4.0 mm and near side 5.5 mm). The RMSE of crack MF A was clearly higher when scanned from near side. Combination of near and far side inspection data showed that there was a difference between the two mechanical fatigue cracks and the highest RMSE was measured for EDM notch and secondly highest for TF crack.

Results indicated that the length RMSE values of the studied flaws were higher in far side inspection with PAUT. With conventional UT, there was only a minor difference between near and far side inspection. The combined RMSE value of all length sizing data in this study was 3.3 mm.

5.4 X-ray tomography results

The results of tomographic x-ray imaging are presented in more detail in VTT research report VTT-R-05649-14 [1]. The length and the height measurements of the tomographic imaging are shown in Table 2 and visualisation of the cracks can be seen in **Figure 5**. According to these results tomographic imaging seems to be good method for sizing fatigue flaws. The TF length measure differs more from the destructive results than MF A and MF B lengths. It can be concluded that the true branching of the both ends of the TF crack is not fully visible in tomographic x-ray imaging and this can affect on the accuracy of the length measurement done using tomographic results. It seems that tomographic imaging results are showing the shape of the flaws quite nicely near the surface area. Although the height measurement is relatively accurate, the shape of the flaw tip does not represent the actual flaw shape described in the destructive results.

Table 2. Dimensions measured using x-ray tomography.

Sample	Maximum length measured from tomographic x-ray imaging (mm)	Difference to length measured from fracture surface (mm)	Maximum height measured from tomographic x-ray imaging (mm)	Difference to height measured from fracture surface (mm)
MF A	13.0	-0.1	6.3	0.1
MF B	14.5	0.2	5.0	0.0
TF	12.5	-1.0	5.2	0.0

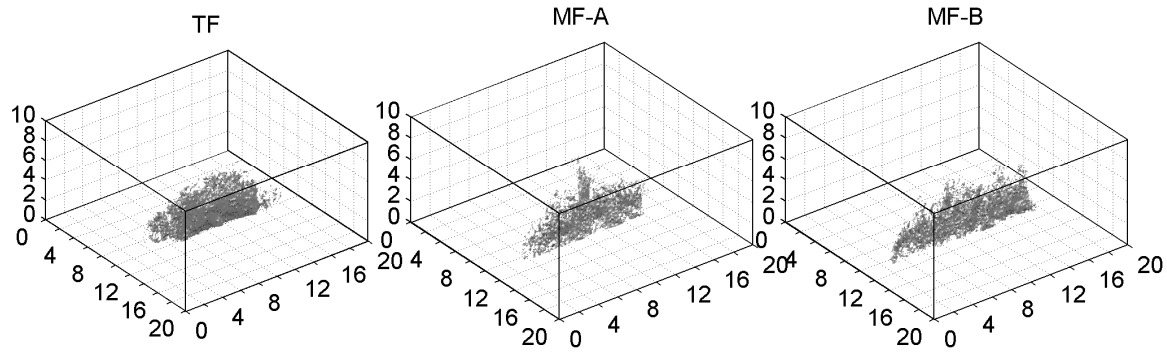

Figure 5. Visualisation of the tomographic x-ray inspection results.

6. Summary and conclusions

In this study two kinds of artificial cracks from different manufactures and one reference notch were made in austenitic stainless steel test blocks. Flaws were examined using conventional UT, PAUT, computed x-ray tomography and digital radiography. The flaws were sized with different techniques and those results were compared to the true state flaw dimensions as determined by destructive analysis.

Typically flaw detection and especially flaw height sizing is considered challenging in ultrasonic inspection done from far side as the sound beam must penetrate through the weld material distorting and attenuating the sound waves. This study showed that mechanical fatigue cracks were not possible to reliably height size from far side but in most of the cases both TF crack and EDM notch could be height sized also from far side. That may be a consequence of the branching shape of the TF crack and wider opening of both TF crack (surface area) and EDM notch. This indicates the flaw type chosen may have a significant influence in the evaluation of the performance of the technique in that case. On the other hand, the strong structural noise and metallurgical indications on the crack tip area affected the results.

To draw some conclusions of the performance of the techniques, RMSE values were compared. According to RMSE, EDM notch was height sized most accurately. PAUT performed better in height sizing than conventional UT and far side access was better than near side access. With conventional UT, TF crack was height sized most accurately and with PAUT, crack MF B was height sized most accurately. This study indicated slight height undersizing for PAUT techniques. Still, all PAUT techniques fulfilled the requirement of sizing accuracy stated by ASME [6].

Best performing conventional UT techniques for height sizing were techniques utilizing composite probes and angles of 45 and 55 degrees shear wave. The poorest conventional UT techniques for height sizing were the techniques utilizing longitudinal waves. Best performing PAUT technique for height sizing was 55 SW. This indicates that rather high frequency can be used for austenitic weld inspection with thickness of at least 25 mm. However, both side access is required to ensure the detection. The poorest PAUT techniques for height sizing were Sectorial 2 and 45 SW techniques which both undersized the flaws. Comparison between 45 SW and 55 SW – both utilizing 5 MHz frequency with linear scanning – indicates that a higher angle performs better in height sizing.

Crack MF B was length sized most accurately. Conventional UT performed better in length sizing than PAUT and near side access was slightly better than far side access. With conventional UT, both MF B and TF crack were length sized with smallest error and with PAUT, crack MF B was length sized most accurately.

Conventional UT techniques MWK45-2 and MWK45-4 were both performing best in length sizing. The poorest

conventional UT techniques for length sizing were MWB45-2, MWK70-2 and TRL70-2. PAUT technique performing best in length sizing was MC technique utilizing inside surface creeping wave. The poorest PAUT techniques for length sizing were 45 SW and 70 SW both oversizing the flaws.

The size of the two mechanical fatigue cracks differed from each other. Also there was a difference in length/height ratio of the two similarly targeted flaws. All the flaws were reliably detected with all techniques when scanned from near side and with all techniques with frequency of 4 MHz or lower when scanned from far side.

X-ray tomography seems to be very accurate NDT method for length and height measurements of fatigue cracks with the setup and samples used in this research. There is some deviation in thermal fatigue crack length measurement but this is probably due to branching of the thermal fatigue crack is not fully visible with x-ray tomography. As a conclusion, x-ray tomography is a potential method for NDT inspections of crack like defects in austenitic stainless steels and welds. As seen in the x-ray tomography results section, the shape of the flaw is not entirely representative, especially the flaw tip area seems to be more or less incomplete compared to destructive analysis. Verifying the full potential of the method would need more research with different types and sizes of flaws as well as different materials and material thicknesses. X-ray tomography is relatively slow inspection method and therefore the use of the method requires careful planning in advance. The best option for in-service inspections with x-ray tomography would be the use of the method for verification and sizing the indications detected with other NDT methods.

The destructive investigations revealed that the cracks, in the investigated cross-sections, located in the weld metals, close to the fusion line. The cracks were unbranched and in two cross-sections, i.e., from samples MF A and MF B, small weld pores were observed. The cracks resembles fatigue cracks, although typical fatigue (corrosion fatigue and mechanical fatigue) are even straighter that these flaws. Intergranular stress-corrosion cracks in sensitized austenitic stainless steels are typically only slightly branched and the resemblance to the flaws is thus good. Also intergranular stress corrosion cracks in non-sensitized stainless steels are unbranched and resemble those of the flaws. They locate very close to the fusion line, within the few first grains from the fusion line. Transgranular stress corrosion cracks are, however, typically much more branched than the flaws.

In the future, more data from flaws of different sizes is needed to extend the knowledge of different reflector properties and the performance of different techniques. Also real geometries (pipe) shall be used. The presence of weld cap can also be studied by limiting the scanning area. As flaw manufacturing is expensive, destructive testing cannot be always done so data and knowledge gathered from this study is very important for future research work.

References

[1] Leskelä, E.; Koskinen, A.; Haapalainen, J.; Ehrnsten, U.; Autio, J.-M. 2014. Comparison of artificial flaws in austenitic steel welds with NDE methods, VTT. 51 p. Research Report ; VTT-R-05649-14

[2] Jäppinen, T.; Koskinen, A.; Leskelä, E.; Tuhti, A.; Haapalainen, J.; Sandlin, S. 2013. Monitoring of the structural integrity of materials and components in reactor circuit (MAKOMON). In: SAFIR2014. The Finnish Research Programme on Nuclear Power Plant Safety 2011-2014. Interim Report. Simola, Kaisa (ed.). VTT Technology 80. VTT, pp. 292 – 301 http://www.vtt.fi/inf/pdf/technology/2013/T80.pdf

[3] Ehrnsten, U.; Pakarinen, J.; Karlsen, W.; Hänninen, H.; Mouginot, R.; Soinila, E.; Ahonen, M.; Autio, J.-M., Aaltonen, P.; Saukkonen, T. 2013. Environmental influence on cracking susceptibility and ageing of nuclear materials (ENVIS). In: SAFIR2014. The Finnish Research Programme on Nuclear Power Plant Safety 2011-2014. Interim Report. Simola, Kaisa (ed.). VTT Technology 80. VTT, pp. 268 – 282 http://www.vtt.fi/inf/pdf/technology/2013/T80.pdf

[4] Koskinen, A.; Leskelä, E. 2013. Differences in indications of different artificially produced flaws in non-destructive examination. The 10th International Conference on NDE in Relation to Structural Integrity for Nuclear and Pressurized Components, Cannes, France, 1 – 3 October 2013. COFREND (Confédération Française pour les Essais Non Destructifs)

[5] Leskelä, E. and Koskinen, A. Comparison of mechanical and thermal fatigue cracks by ultrasonic examination. VTT, Espoo 2014. 65 p. Research Report; VTT-R-00626-14

[6] ASME. 2004. "Rules for Inservice Inspection of Nuclear Power Plant Components, Section XI." In ASME Boiler and Pressure Vessel Code – An International Code. American Society of Mechanical Engineers, New York.

Manufacturing of a new type of NDE test samples with laboratory-grown intergranular SCC cracks in a Nickel base weld – Comparison of various NDE techniques applied to a challenging crack morphology

Klaus GERMERDONK[1], Hans-Peter SEIFERT[2], Hardy ERNST[3], Alex FLISCH[4] and Dominik NUSSBAUM[5]

[1]ENSI – Swiss Federal Nuclear Safety Inspectorate, Industriestrasse 19, Brugg, Switzerland
[2]PSI – Paul Scherrer Institute (PSI), Nuclear Energy and Safety Research Department, Laboratory for Nuclear Materials, Villigen, Switzerland
[3]SVTI – Swiss Association for Technical Inspections – Nuclear Inspectorate, Wallisellen; and QuaNDT GmbH, Switzerland
[4]EMPA – Swiss Federal Laboratories for Materials Science and Technology, Dübendorf, Switzerland
[5]ALSTOM – ALSTOM Power Products, NDT METHODOLOGIES, Baden, Switzerland

E-mail address (corresponding author): klaus.germerdonk@ensi.ch

In order to produce NDE-test samples with a crack morphology close to PWSCC/IDSCC-cracks found in the field, a modified fracture mechanic specimen was designed. Several test samples were produced containing different crack morphologies (PWSCC/IDSCC-cracks as well as fatigue-cracks and EDM-notches for comparison purposes).
The specimen fit into the autoclave test facilities at PSI. The specimens were loaded under typical PWR und BWR water chemistry conditions at 290 °C. It took several months until sufficient IDSCC crack growth was achieved, afterwards the NDE-specimen were machined to the final geometry for later NDE-testing.
In order to validate the new test samples for further utilization, several organizations in Switzerland performed evaluations by advanced NDE-techniques on those test samples including X-ray testing as well as UT-techniques. Furthermore, metallographic analysis of a laboratory grown IDSCC-crack completed the investigations.
The UT-measurements seem to indicate that the existing tip diffraction technique reaches its limit for the challenging crack morphology ensuing from the newly developed NDE-test samples.

Keywords: laboratory-grown SCC, PWSCC/IDSCC, tip diffraction technique

Advanced ultrasonic technologies applied to the inspection of HDPE piping fusion welds

Andre Lamarre
Olympus NDT Canada, Quebec City, Canada

E-mail address(corresponding author) : andre.lamarre@olympus-ossa.com

High-density polyethylene (HDPE) piping is known for its exceptional corrosion and erosion resistance. Over time, its use has spread to a variety of industries, such as petrochemical, power generation, and mining.

Drawing on years of experience and expertise in advanced ultrasonic technology (AUT) for metal weld inspection, Olympus has adapted its AUT tools to ensure full coverage of HDPE piping fusion joints. An instrument featuring time-of-flight diffraction and ultrasonic phased array technology equipped with a semi-automated scanner is the method of choice for performing a reliable inspection.

The main issues to overcome when inspecting HDPE with ultrasound are the low sound velocity and high attenuation of the material. To benefit from the refraction phenomena, it is preferable to use a wedge with a lower sound velocity than plastic. As the velocity of sound in water is much lower than that in HDPE, and the signal attenuation is practically nonexistent, specially designed water wedges are well suited to resolve these issues.

Keywords: HDPE, ultrasonic phased-array, TOFD

New Magnetic Crawler Inspection Manipulators

Mats Wendel, Torbjörn Sjö, David Eriksson
DEKRA Industrial AB, Stockholm, Sweden

E-mail address: mats.wendel@dekra.com, torbjorn.sjo@dekra.com, david.eriksson@dekra.com

ABSTRACT
Small, independent and possible for use on different objects has been the key function for the development of these new magnetic crawler systems for PWR and BWR vessels.
By using magnets as attachment and base for the traction system we have realized the combined manipulator system for both RPV and Core Shroud in the same lightweight solution.
This new manipulator concept has been developed mainly for BWRs with their complicated internal structures and confined spaces. The development have been performed in two steps, first with a simple but very effective and position accurate crawler manipulator for the RPV outer surface, where the challenge mainly where the positioning.
The second step was to develop this concept further into a magnetic crawler for submersed use. Here was the challenge to achieve sufficient attachment through a non-ferrite stainless steel cladding maintaining the position accuracy.
Our goal was also to minimize the time in the reactor containment with the possibility to prepare the equipment in only a few hours for a full RPV or CS exam.
Furthermore, the manipulator is neutrally buoyant in water and is intended for parallel operations together with identical manipulators to minimize the total inspection time. With its small size and simple functions it is really a “direct out of the box” operating equipment totally independent of other systems. No pre-installations in the vessel are needed.

The NDE techniques are being qualified according to the ENIQ and respective Swedish rules. The qualifications are valid for detection, characterization and sizing.

Keywords: Magnetic Crawler Inspection Manipulator, BWR, PWR, Scanner, Submersed Magnetic Crawler

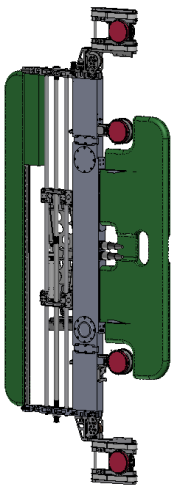

Background

DEKRA Industrial has designed manipulators for several types of nuclear power plants as well as for conventional plants. This includes development of scanners and manipulators for the inspection of the RPV Shell Welds, Nozzle Welds and BMI Welds (Bottom Mounted Instrumentation nozzles) as well as visual testing of internals in PWRs.

Fig. 1 The nozzle tool during set up

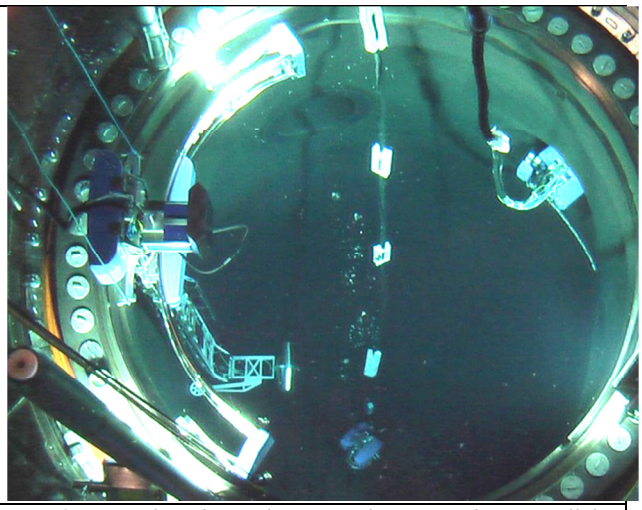

Fig. 2 Vessel and Nozzle manipulators used in parallel

The new set of manipulators will now address the inspection task of core shroud and vessel in BWR's.

Development of tooling

Small, independent and possible for use on different objects has been the key function for the development of these new magnetic crawler systems for PWR and BWR vessels.
By using magnets as attachment and base for the traction system we have realized the combined manipulator system for both RPV and Core Shroud in the same lightweight solution.

All manipulators have been designed to minimize the time in the reactor vessel and also in the reactor containment. The equipment can be prepared in only one shift for a full vessel exam. Furthermore, the equipment will work in parallel totally independent of each other and with minimum support from the crane and service bridge. No pre-installation in the vessel is needed.

This new manipulator concept has been developed mainly for BWRs with their complicated internal structures and confined spaces.

The development has been performed in two steps, first with a simple but very effective and position accurate crawler manipulator for the RPV outer surface, where the challenge mainly

were the positioning.
The second step was to develop this concept further into a magnetic crawler for submersed use. Here the challenge was to achieve sufficient attachment through a non-ferrite stainless steel cladding maintaining the position accuracy.

Furthermore, the manipulator is neutrally buoyant in water and is intended for parallel operations together with other manipulators to minimize the total inspection time. With its small size and simple functions it is really a “direct out of the box” operating equipment totally independent of other systems. No pre-installations in the vessel are needed.

The NDE technique has been qualified according to the ENIQ and the Swedish regulations. The data gathered will be sufficient for detection, characterization and sizing.

The personnel resources cover all needs for development of manipulators and NDT, as well as probe design. All equipment has been tested in a pool with mock-ups before the first outage performance.

The Equipment

Several new equipment has been designed with the focus to allow for inspection of the vessel and core shroud in hard to reach areas with the possibility to perform parallel inspections.

- **MJÖLNER,** Manipulator for Vessel OD
- **RINGHORNE,** Manipulator for Vessel ID and Core Shroud OD
- **GRISNE,** Manipulator for Core Shroud ID

The concept is based on the idea of lightweight and remotely operated vehicles, ROV-equipment, independent of cranes and platforms. The same type of controllers is used for all tooling.

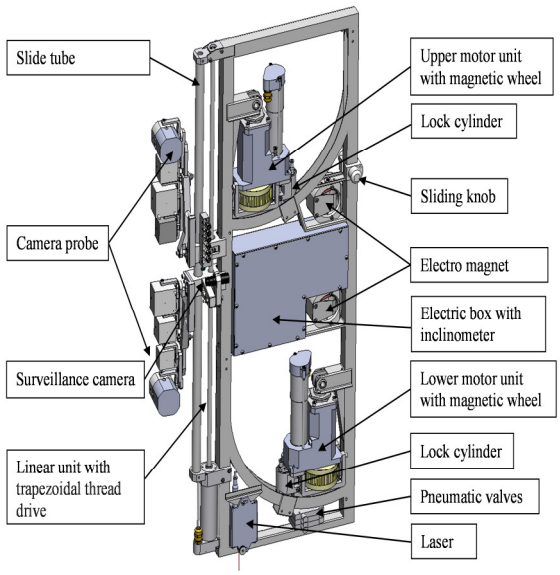

Fig. 3 The Vessel OD inspection manipulator Mjölner

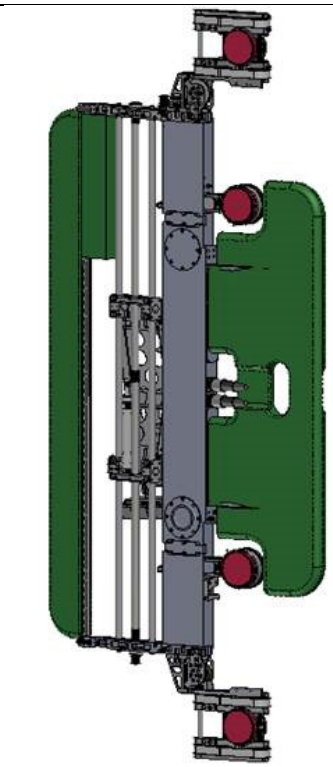

Fig. 4 The Vessel ID manipulator Ringhorne

Fig.5 The Vessel OD inspection manipulator Mjölner sc anning

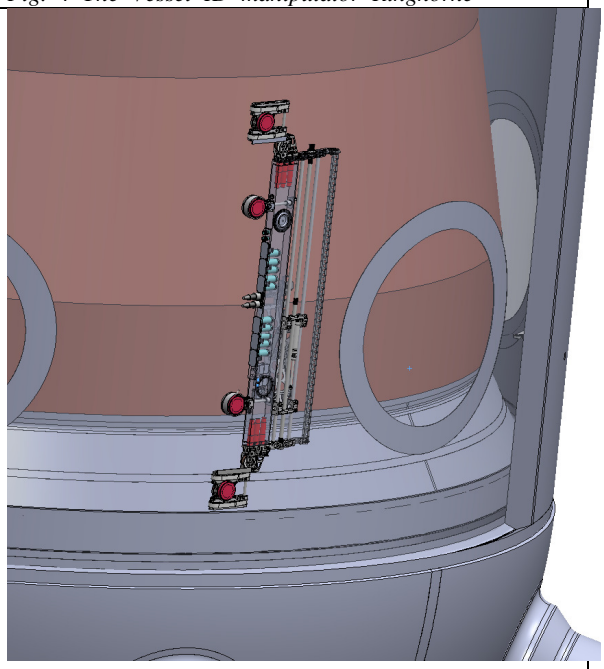

Fig. 6 The Vessel ID manipulator Ringhorne scanning

In figures 3-6 the new concept of magnetic wheel crawlers are shown. The crawlers can position on either inside or outside of reactor vessels. The wheels can be rotated 90 degrees to be able to scan with high accuracy in both vertical and circumferential direction. The concept is designed for access in tight spaces including the core shrouds. The Ringhorne manipulator is designed for gaps of 80 mm.

Fig. 7 The manipulator GRISNE, Configuration for Core Shroud ID scanning

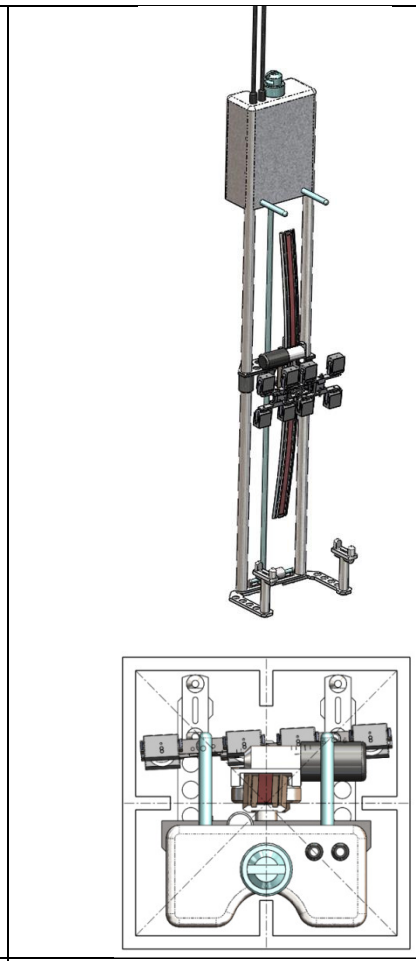

Fig. 8 The manipulator GRISNE, Configuration or introduction through the core grid

The Grisne manipulator includes a buoyancy tank to give the function of sinking down to the scanning area and the floatation force to give a firm fixation force on the core shroud bottom edge. The manipulator is installed with poles. The manipulator is then clamped under the core shroud bottom edge.

Scanning is possible on circular and vertical welds. The scanning rail rotates 90 degrees and has a manual emergency rotation possibility

The manipulator is installed through the core grid

All equipment are tested and the personnel are trained at our test facility which includes a test pool with demineralized water as well as a hot cell for contaminated manipulators.

Fig. 9 The test pool

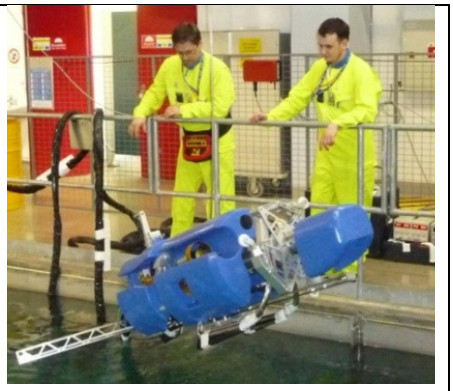

Fig. 10 Handling a nozzle ROV

Performance

The task is to perform a qualified inspection of BWR vessel welds and core shroud welds.

The first inspection was performed on the Oskarshamn 3 vessel OD with a very good result.

With its small size and simple functions it is really a “direct out of the box” operating equipment totally independent of other systems.

The ability to perform parallel activities results in less impact on critical path.

The next inspection projects with the manipulators will be the vessel, core shroud and nozzles in BWR’s in Oskarshamn and Ringhals, Sweden and the vessel and nozzles in the PWRs in Beznau, Switzerland. This includes qualified state-of-the-art phased array technique for lamination inspection.

CRONOS, An Advanced System for RCCA Inspection

A. Sola, F. Fernández

Tecnatom S. A., Avda. Montes de Oca, 1, 28703 San Sebastián de los Reyes (Madrid), Spain

Abstract

CRONOS is a system for the inspection of PWR NPP Rod Cluster Control Assemblies (RCCA) designed and developed entirely by Tecnatom. This system combines ultrasonic test (UT) and eddy current test (ET) methods to detect and characterize typical defects affecting the control rods, including wear caused by friction of the rods with the guide structures and swellings at the tips of the rods induced by the deformation of the irradiated absorbent.

The main components of CRONOS Inspection System (IS) are: a mechanical module with rotary UT transducers and encircling ET coils; SUMIAD F1 equipment and ETbox8i equipment as UT and ET data acquisition systems (DAS); INSPECTVIEW and TEDDY as UT and ET data acquisition and analysis Software; UMAC control of movements system, and SIRINET Data Base system.

Tecnatom currently have available a mechanical system for inspecting RCCA's of 17x17 fuel elements and is developing another mechanical system for rods assemblies of 16x16 fuel elements. CRONOS IS system has already made inspections at different NPPs in China and Spain.

1. Introduction

The Rod Cluster Control Assembly (RCCA) is critical for the safe operation of nuclear power plants since its main function is to control neutron activity inside the core. These assemblies have a spider-shaped structure and are made up of a set of rods filled with a neutron absorbent. They are usually partially inserted in the fuel assemblies (normally only the lower part during normal operation) and may be completely inserted when necessary.

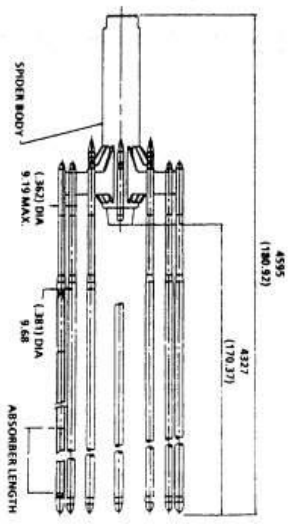

Fig. 1 - Rod Cluster Control Assembly

The degradation mechanisms that may typically occur during the operation of the rod cluster control assemblies are as follows:

- wear caused by friction of the rods against their guide structures;

- increase in the diameter of the tips of the rods caused by irradiation-induced swelling of the absorbent. This increase in diameter causes deformation of the rod, which may generate cracks in the material of the rod and eventually hinder its insertion in the fuel assemblies.

The RCCA's have traditionally been inspected with a view to verifying their correct status and guaranteeing their operability. Since the 1990's, Tecnatom has been performing eddy current inspections using systems based on different techniques (wrap-around, pancake and rotary probes).

The new CRONOS inspection system (IS) developed by Tecnatom combines the eddy current (ET) and ultrasonic (UT) methods, incorporating the capacity to detect and characterise all the possible degradations that affect the RCCA's. At present Tecnatom has a mechanical system applicable to RCCA's for 17x17 fuel assemblies and is developing a second unit for 16x16 assemblies.

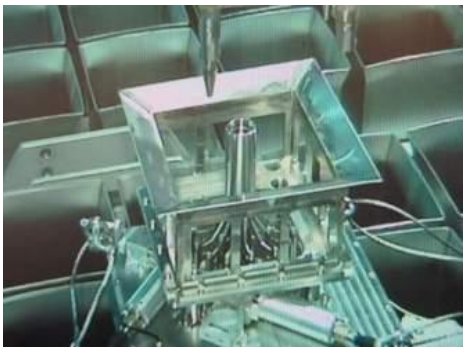

Fig. 2- CRONOS RCCA Inspection System

Development of the CRONOS IS began in 2011 and the system has been used successfully in three inspections at Spanish NPP's (2 at Vandellós 2 and 1 at Ascó 1) and one inspection in China (Ling Ao 2 NPP). The control cluster rods inspected are made of AISI304 or 316 stainless steel, with a chrome or nitride surface treatment, and have a nominal outer diameter of 9.68 mm and a thickness of between 0.47 and 0.98 mm.

2. CRONOS RCCA IS

The configuration of the IS contains 24 housings, 12 of them holding eddy current encircling bobbin probes and the other 12 locating 0º focussed rotary ultrasonic probes. This configuration allows 100% of the rods to be inspected using both methods in just two positions (it should be pointed out that the inspection is performed by inserting the RCCA rods through the housings in the IS main box). The system also includes an additional probe that allows for the instantaneous measurement/monitoring of the speed of the ultrasonic wave in water depending on temperature and the automatic correction of the calibration. The equipment is also fitted with a circumferential encoder and two axial resolvers (one redundant) that allow indications detected to be located circumferentially and axially.

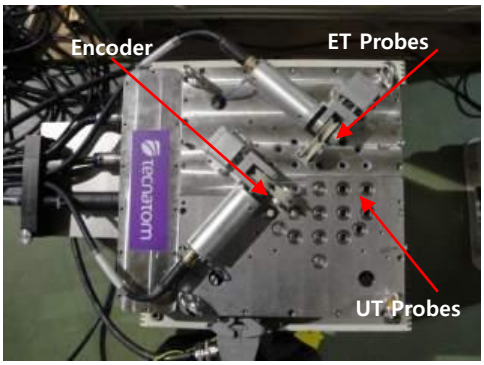

Fig. 3- UT&ET probe configurations

The main equipment drive box is fitted with a motor that provides the UT probes with a maximum rotation speed of 700 rpm. The inspection is carried out following a helicoidal trajectory, combining the rotation of the probes with the axial movement of the control rod imparted by the control rod handling tool. While other inspection systems for these components require low inspection speeds for acquisition of the UT data, the CRONOS system allows performing the inspection of the control rods at the normal operating speed of the rod handling tool, with remarkable axial resolution. As a reference, CRONOS carries out inspections at axial speeds of up to 58 mm/s, acquiring UT data with an acquisition mesh of 5 mm axial resolution and 1 mm circumferential resolution. These parameters allow the examination of an RCCA to be completed in approximately 10 minutes.

In the normal acquisition mode, the UT and ET data are registered simultaneously in the same insertion; in other words, while 12 rods are being inspected by UT, the other 12 are being acquired by ET. Subsequently, the acquisition of all the rods is completed using both methods in two insertions with an intermediate rotation of 180º.

Besides the mechanical system, the main components of the CRONOS inspection system are: the data acquisition systems (DAS), the SUMIAD F1 equipment with INSPECTVIEW acquisition and analysis SW for UT inspections and the ETbox8i equipment with TEDDY ACQ/EVA acquisition/evaluation SW for ET inspections; the SIROCO mechanical control that is based on UMAC technology and the specific SIRIO NET database application for the recording and management of the inspection registers obtained. The entire above make up a compact IS based fully on Tecnatom proprietary technology, covering all the areas of RCCA inspection from data acquisition to the drawing up of the final report, including registers, lists and tables of inspection results.

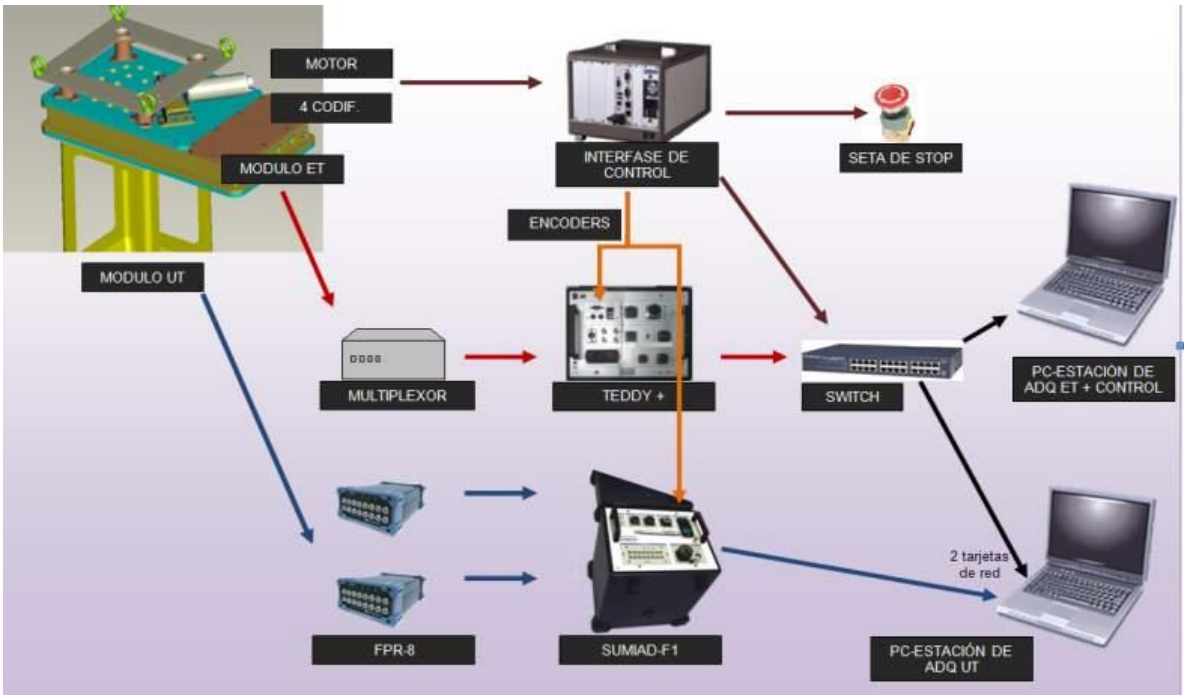

Fig. 4 – CRONOS RCCA IS

3. UT Data Acquisition System

The SUMIAD F1 UT data acquisition system is made up of two so-called FPR8 modules providing up to 16 channels. The product has an adequate industrial termination for field applications, with IP54 especially suitable for contaminated environment. With the current machine configuration, 12 of these channels are used for acquisition with 0º UT rotary probes. An additional channel is used to measure the speed of the ultrasonic wave in water and perform an automatic correction depending on temperature. Overall 13 channels are in use and three are left as spare. The acquisition configuration associates each of the UT channels with a given probe, and therefore a specific rod, depending on the data acquisition position. The UT data acquired via each channel are assigned a rod identification, which is pre-defined by each of the previously defined and programmed trajectories.

Fig. 5 – SUMIAD F1 UT DAS & 2 FR8 modules

A version of the Tecnatom INSPECTVIEW software specific for the inspection of control rods is used for UT data acquisition and analysis. This SW allows either simultaneous acquisition of the 12 channels or a selection of channels to be acquired. In all cases the progress of the acquisition may be displayed in real time. The digitalisation mode may be controlled depending on the configuration selected, registering data in coordination with the axial encoder signals or in accordance with a fixed frequency (by "pulse repetition frequency" or PRF).

While data acquisition is being performed, the system allows the operator to perform an on-line data quality verification, showing the "A-Scan" view registers of the 12 channels and the "C-Scan" view of each channel selected in a separate window. Furthermore, INSPECTVIEW is equipped with an alarms system that notifies the operator of any signal loss on any channel. The system has sufficient processing capacity to allow the operator to view the data recorded by each of the UT channels in order to be capable of validating the register before removing the rod inspected from the CRONOS manipulator.

The INSPECTVIEW analysis SW application has pre-programmed utilities for the control of critical control rod dimensions. Also incorporated is monitoring of the outer diameter of the rods in areas in which swelling might occur.

It is also possible to measure the remaining wall of the rods following wear arising as a result of fretting against the plates of the guide tubes, these being of two types depending on the geometry of the plate rubbing against the rod, as may be appreciated in figure 6. The application uses display and measuring tools based on the fast Fourier transform (FFT). Additionally, INSPECTVIEW also reports the distance between the probe and the surface of the rod (IG), this allowing wear measurement to be confirmed by two independent routes.

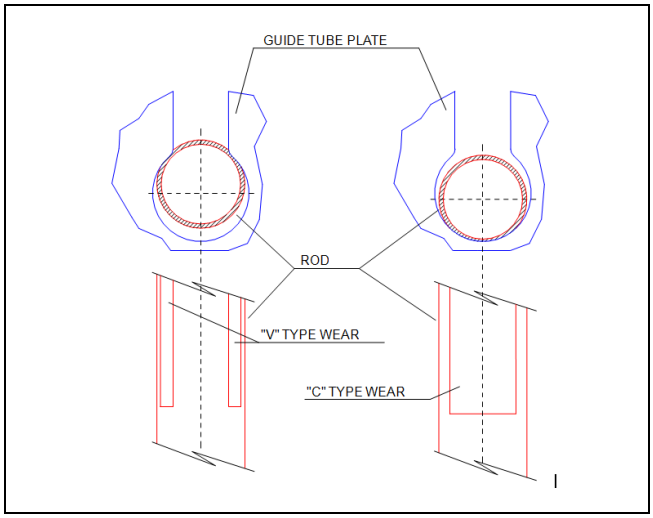

Fig. 6 Defect types

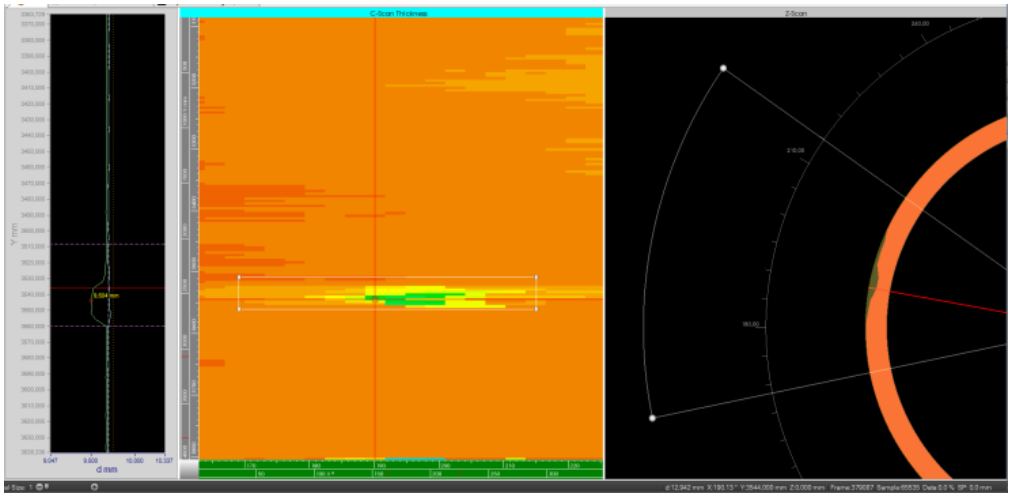

Fig. 7 – INSPECTVIEW TOOL – FFT wear measure

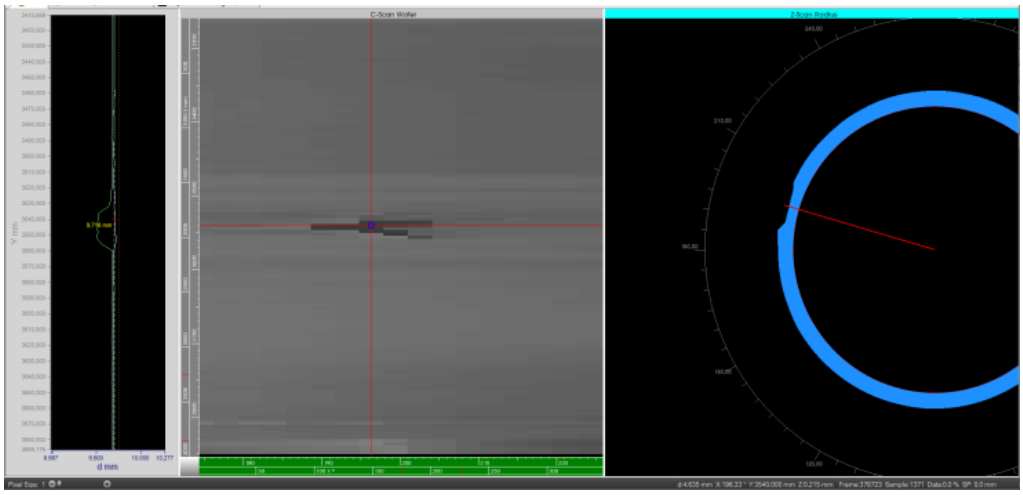

Fig. 8 – INSPECTVIEW TOOL – IG wear measure

Each of the indications detected may be appropriately characterised, specifying the remaining wall thickness in the case of wear and the outer diameter in the case of swelling, in addition to axial and circumferential location. INSPECTVIEW is equipped with a utility for the generation of inspection records, which includes the parameters most representative of the analysis of the indications detected. The analysis SW is capable of generating a file containing all the indications reported, attaching the main parameters, this being easily exported in database format for subsequent treatment.

The measurement uncertainties obtained by the CRONOS system applying the UT method are ± 0.03 mm for the characterisation of wear (measurement of remaining wall thickness) and the measurement of diameters (swelling) and ± 2mm for axial location.

4. ET Data Acquisition System

The ET data acquisition equipment used is the ETbox8i, this multi-channel and multi-frequency equipment developed by TECNATOM allows working with a wide range of probes (including multi-coil and array probes) and in reference simulation mode. In its basic configuration this state-of-the-art DAS has 8 inputs, for which reason for the CRONOS application, which uses 12 ET encircling bobbin probes, a 3x4 multiplexing device is used, allowing the 12 coils to be excited simultaneously when operating in absolute mode. Even when working with the external multiplexor, the sampling capacity of the ETBox8i equipment allows for high acquisition speeds, with a sampling by mm ratio far above the habitual sampling frequency for this type of ET tests (1.2 samples per mm).

Fig. 9 – TEDDY + ET DAS (change for ETBox 8i)

The ET data acquisition SW used is TEDDY ACQ, the general TECNATOM application for the acquisition of tube bundles. The ET data mesh includes information on the resolvers that allows detected indications to be located axially.

The ET analysis SW used is TEDDY EVA, which is the specific TECNATOM eddy current analysis SW application for the analysis of control rods. In RCCA inspections using the CRONOS system, the ET data are used to characterise wear on the basis of loss of rod cross-section (the system allows a loss of around 1% to be discriminated) and to detect and characterise axial cracks (capacity for the detection of realistic defects of up to 1mm minimum length).

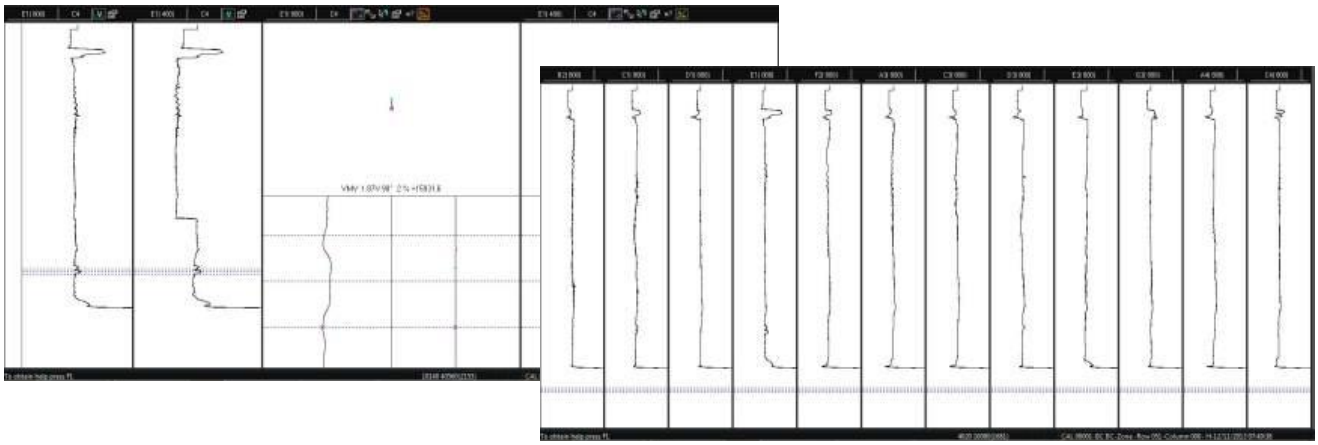

Fig. 10 – TEDDY EVA analysis windows for RCCA's

The TEDDY EVA analysis SW incorporates the tools required to generate independent report lines for each indication detected, identifying the control cluster, rod, axial location, nature of the indication (wear or cracking) and loss of cross-section due to wear.

5. Database

Based on the SIRIONET tube bundle database, developed by Tecnatom for the management of SG tube bundle inspections, the CRONOS IS includes a specific database for management of inspections and control of the results. This application allows for the transfer of the results from UT (INSPECTVIEW) and ET (TEDDY EVA) analysis applications. After the integration and structuring of all the results obtained, the database application allows for control and for the programming of queries concerning different inspection parameters (rod UT/ET analysis performed, rods pending analysis, duplicated indications, etc.). Also, on conclusion of the inspection, it is possible to perform comparisons on the results, either by comparing UT and ET results or by comparing the results of the current

inspection to those for the same rods in previous inspections.

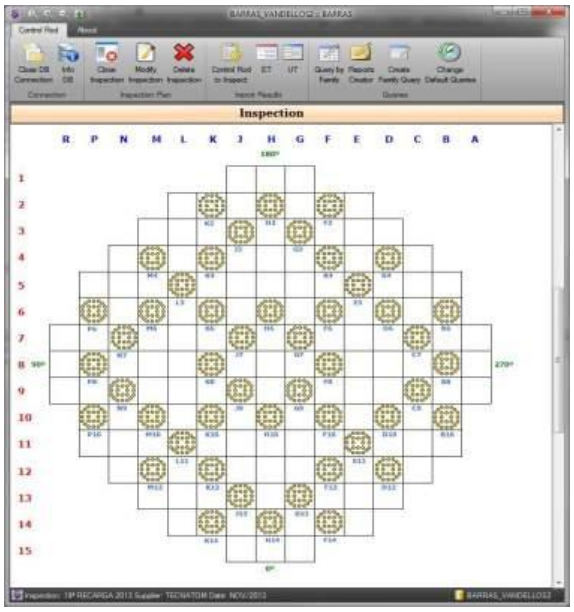

Fig. 11 –RCCA SIRIONET map in core

RCCA		UT RESULTS				ET RESULTS					
ID	ROD	TP	LOC.	THIN	% DPH.	TIP	LOC.	% L.S.	VOLTS	PH	CHANNEL
R-01	A4	V	149,5	0.931	5%	FRE	135	1	0.48	89	A4(800)
R-01	B6	V	149,5	0.796	18.7%	FRE	151	2	1.29	87	B6(800)
R-01	C1	V	130	0.865	11.7%	FRE	133,9	1	0.99	267	C1(800)
R-01	C1	V	149,5	0.855	12.8%	FRE	153,6	1	1.09	269	C1(800)
R-01	C4	V	3718	0.737	24.8%	FRE	3740	3	2.56	66	C4(800)
R-01	C7	V	2860	0.767	21.7%	FRE	2870	1	1.19	264	C7(800)
R-01	C7	V	3146	0.885	9.7%	NBD					
R-01	C7	V	3438,5	0.86	12.3%	NBD					
R-01	D3	V	3393	0.575	41.4%	FRE	3420	2	1.38	95	D3(800)
R-01	E1	V	130	0.802	18.2%	FRE	133	2	1.87	90	E1(800)
R-01	E1	V	149,5	0.776	20.8%	FRE	153,5	1	1.23	269	E1(800)
R-01	E1	V	3406	0.862	12.1%	FRE	3409	1	0.85	263	E1(800)
R-01	G5	V	110,5	0.871	11.1%	FRE	122	1	0.76	267	G5(800)
R-01	G5	V	149,5	0.794	18.9%	FRE	160	2	1.51	269	G5(800)

Fig. 12 – RCCA UT&ET wear results

The CRONOS DB allows all types of statistical calculations to be performed or tables to be presented with the results obtained from the inspection performed. The table included in Figure 13 shows the maximum diameter value measured for each of the cluster rods.

RCCA	G4	D3	B6	F2	C5	F6	A3	A4	E1	G5	E4	C1	D7	B2	E3	E7	E5	D5	C3	C7	A5	C4	G3	D1
R-01	9,673	9,767	9,727	9,796	9,716	9,709	9,738	9,719	9,693	9,755	9,687	9,738	9,74	9,73	9,727	9,671	9,672	9,699	9,708	9,758	9,686	9,732	9,714	9,743
R-02	9,676	9,69	9,723	9,729	9,687	9,695	9,69	9,688	9,776	9,708	9,724	9,682	9,746	9,677	9,732	9,706	9,738	9,686	9,725	9,701	9,679	9,718	9,674	9,682
R-03	9,728	9,744	9,722	9,741	9,701	9,664	9,729	9,704	9,768	9,683	9,67	9,72	9,753	9,725	9,724	9,688	9,701	9,718	9,707	9,743	9,766	9,721	9,757	9,715

Fig. 13 – RCCA UT results - OD diameters (swelling)

The following table shows the maximum loss of thickness value evaluated by UT for cases of wear, related to the remaining wall thickness of the rod measured.

G4	D3	B6	F2	C5	F6	A3	A4	E1	G5	E4	C1	D7	B2	E3	E7	E5	D5	C3	C7	A5	C4	G3	D1
	41	19					5	21	19		13								22		25		
		14							10	14		8			18		27					14	
						18		14		33				16					9	7			
	13							5	27	30				15	18	13	11		30	16	50	21	28
	14			19					14	23							35		11		35		
									7	17	3					14	34	11		9	2		
	18	10	5	17		18		11	14	44				29	17	8	19		22	18	24		
									17	19							8				26	44	
	10					19		19		16	30						25		24		17		
	31		1							13							18		15		29		
																	40						
																6	20						
														4					8		12		
					9																27		
																	27						
										36											17		
	38	3	4								4				18		16		8			15	
										14		13											
	14																						
						19				16		15								13			
										23													
								7															
										48	10				22					18	23		

Fig. 14 – RCCA UT results - % loss of thickness

Generically speaking, the CRONOS DB provides pre-configured consultations in which it is possible to show the results in map and list form, with outputs in "pdf", Word or Excel format. These files are subsequently the basis of the results that make up the inspection reports. In addition, it allows for the creation of specific tables, with the performance of specific selections and the application of a series of basic statistical and logic filters that are very simple to use.

6. Conclusions

In summary, TECNATOM possesses a CRONOS IS control rod inspection system whose SW and HW technology has been developed completely in house and that integrates both eddy current and ultrasonic inspections for the verification of control rod status.

The effectiveness of this system has been contrasted in three inspections at Spanish NPP's (2 at Vandellós 2 and 1 at Ascó 1) and one inspection carried out in China (Ling Ao 2 NPP), validation results of ±0.03mm being obtained, with inspection times of approximately 10 minutes per RCCA.

Nondestructive Testing of Ferromagnetic Heat Exchanger Tube Using Bobbin-Type Solid-State Hall Sensor Array with Low Exciting Frequency

Jung-Min Kim[1], Jong-Hyun Seo[1], Sol-A Kang[1] and Jinyi Lee[1,2]
[1]Departmet of Control and Instrumentation Engineering, Chosun University, Gwangju, Korea
[2]Departmet of Electronic Engineering, Chosun University, Gwangju, Korea

E-mail address(Jinyi Lee) : jinyilee@chosun.ac.kr

More than 70 % of heat exchangers, ferromagnetic tubes are used in the thermal power station and petrochemical plants. The remote field (RFECT), partial saturation (PSET) and pulsed eddy current techniques (PEC) are used for inspecting damages in the ferromagnetic heat exchanger instead of the conventional eddy current testing (ECT) because of high permeability and magnetic properties of specimen. However, the low sensitivity, complicated structure and big sensor size have to be improved to apply RFECT, PSET and PEC to inspect damages in the small bore-piping system with ferromagnetic material. In this paper, an advanced nondestructive testing (NDT) technology using bobbin coil and bobbin-type Hall sensor array is proposed. Low frequency alternative current was supplied to the bobbin coil. The induced current in the specimen was distorted because of fretting wear, and radial-directional time-varying magnetic field occurs. A solid-state bobbin-type linearly integrated Hall sensor array (BIHaS) is used to measure the distribution of time-varying magnetic field. To measure the amplitudes of the time-varying magnetic field, high-pass-filters (HPF), and amplifiers, root-mean-square circuits (RMSs), and AD converters were connected to output lines in parallel. By using this system the amplitudes of radial-directional magnetic fields due to outer diameter fretting wear were measured with high sensitivity, simple structure and compact size.

Keywords: ferromagnetic tube, heat exchanger, low frequency, Hall sensor array, magnetic image

Development of ROV systems for Narrow Environment Inspection

Satoshi OKADA and Ryosuke KOBAYASHI
Hitachi Research Laboratory, Hitachi, Ltd.
7-2-1 Omika-cho, Hitachi-shi, Ibaraki, 319-1221, Japan
E-mail address: satoshi.okada.nc@hitachi.com:

We have developed underwater ROV system for core internal inspections of nuclear power plants. In this paper, a compact type ROV is proposed to inspect narrow environment. The inspection area is to depth of the water 30m. Also ROV has to pass through the gap of 0.18m. The ROV has multiple thrusters and a buoyancy adjustment mechanism to move three-dimensionally. The buoyancy is adjusted by changing a cylinder volume. A pan-tilt camera unit is also mounted for visual testing. The pan and tilt mechanism can move in the range of 180 degrees. In addition, an installation launcher is equipped with a localization system, a stereo camera with wide-angle lens. LEDs mounted to the bottom of ROV are tracked by the localization system. Region-dividing distortion correction of the images is developed to improve measurement accuracy. Evaluation experiments of the proposed systems were implemented at mock-up environment. As a result, it was confirmed that visual testing was implemented with localizing the ROV position.

and localization method are
Keywords: ROV, narrow environment, visual testing, localization, stereo camera

HELIUM LEAK TEST IN-LINE: ENHANCED RELIABILITY FOR HEAT EXCHANGER TUBES

Mathieu Lheureux[1]
Pascal Gerard[1]
[1]Vallourec Heat Exchanger Tubes, ZI Rue Marthe Paris, 21150 Venarey-Les-Laumes, France

E-mail address:
mathieu.lheureux@vallourec.com
pascal.gerard@vallourec.com

Non Destructive Testing (NDT) techniques are vital to guarantee the delivery of dependable shell and tube heat exchangers. They are even more relevant when it comes to nuclear applications. This is critical not only in the nuclear island to prevent catastrophic issues, but the conventional island and the balance of plant also call for high quality product.. Among these issues is tube tightness which may be considered a basic quality but which can become a very challenging topic when the operator and/or the fabricator must choose the leak test method to be carried out on the tube. The optimal leak test method must be the best compromise between sensitivity, repeatability in industrial environment, cost evaluation and possible consequences in case of failure.

The current ASTM standard (A1016/A1016M) specifies pneumatic test using air under water or the air pressure differential method for welded tubes. This paper reviews these two leak testing methods and introduces an innovative in-line helium leak test method developed by Vallourec Heat Exchanger Tubes. The first results obtained by this method demonstrate its advantage to substitute and improve the current pneumatic tests with lower detection level and higher reliability. This innovative leak testing method not only reduces the potential of an undetected leak due to complex defect geometry, but it also closes the gap between the final testing methods used on assembled heat exchangers and the leak test performed during tube manufacturing process.

Keywords: Leak Test, Helium Test, Heat Exchangers Tubes

Effectiveness Evolution of DMW Inspection Techniques Assessed Through Three International RRT's

[1]Tommy Zettervall, [2]Steven R Doctor
[1]SQC Swedish Qualification Centre,
P.O.Box 519, 183 25 Täby, Sweden
[2]Pacific Northwest National Laboratory PNNL,
P.O. Box 999, MSIN K5-26, Richland, WA 99352, USA

E-mail address : tommy.zetterwall@sqc.se; steven.doctor@pnnl.gov;

Nickel-based alloy cracking of reactor pressure boundary components has been a worldwide concern for about 25 years. Increased inspection frequencies, improved inspection practices, and increased licensee vigilance continue to identify nickel-based alloy cracking in vessel penetrations and various components of the primary coolant loop.
To address the issue of quantifying the effectiveness of NDE, a number of international Round Robin Tests (RRT) have been conducted since 1986.

The first RRT was PISC III Action No. 3 which was initiated in 1986 with the objective to evaluate the non-destructive examination (NDE) performance capability of in-service inspection procedures used for structural integrity assessment of safe-end welds in power plants. A number of test pieces were manufactured with state of the art techniques at that time for implanting flaws simulating the NDE response expected from service degradation.

The next RRT was the PINC-project initiated in 2005 addressing the problem of primary water stress corrosion cracking (PWSCC/IDSCC), which is a form of degradation observed in some reactor piping and pressure vessel components. PINC was designed to understand the crack morphology and to assess the NDE evaluation of procedures/techniques for the detection, characterization and sizing of SCC. PINC provided data that enabled a quantitative assessment of both commercially available and evolving laboratory NDE techniques. Two types of nickel-alloy components were studied, bottom-mounted instrumentation penetrations (BMI) and dissimilar metal piping welds (DMWs).

An on-going RRT is PARENT that was initiated in 2010 as a follow-up to the PINC RRT and is planned to be finished in 2015. The PARENT RRT comprises a study of the efficiency of NDE techniques for detecting, characterizing and sizing SCC defect types in nickel based materials. Emerging techniques were demonstrated in open tests and commercial techniques in blind tests.

The objectives of this paper is to compare results, make conclusions and propose future activities based upon these three international RRT's conducted over the past 3 decades. The paper will also include a comparison of field experience from detected PWSCC/IDSCC at power plants in the USA and Sweden. One focus is the NDE signal responses versus the crack morphology that have been simulated in test pieces with respect to real crack morphologies.

Keywords: Ni-alloys, RRT, NDE

Integrity evaluation case subject to replacement & preventive maintenance for NPP Ni-alloy components

Changkuen Kim[1], Jooyoul Hong[1], Dongjin Lee[1]
[1]Doosan Heavy Industries & Construction 22, DoosanVolvo-ro, Changwon, 642-792, Korea

changkuen.kim@doosan.com (jooyoul.hong@doosan.com, dongjin.lee@doosan.com) :

DHIC has been participated PARENT(Program to Assess the Reliability of Emerging Nondestructive Techniques) that is an International collaboration to explore the NDE responses of cracks in nikel-alloy components. The objectives of PARENT participants are to pool available resources to cooperatively conduct research on emerging nondestructive evaluation (NDE) technologies to address detection and characterization issues for PWSCC in DMW.
Especially it shall be investigated that flexible ECT array probe has highly POD(probability of detection) and best practice form complex surface shape like J-weld of RPV BMI or penetration, because this probe has excellent resolution for near adjacent resolution.(refer to Fig.1)

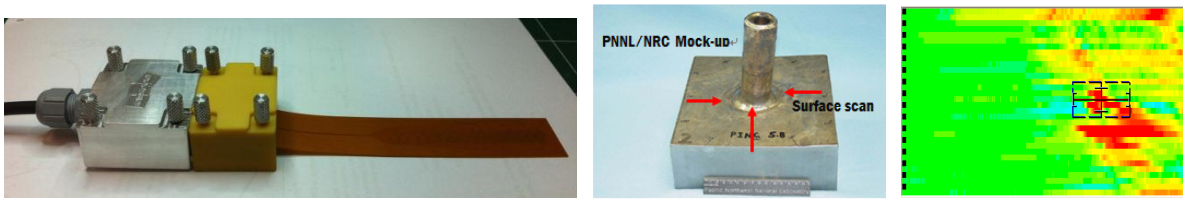

Fig.1 Application of flexible ECT array probe for PARENT round robin Mock-up

Activity of Ni-alloy component inspection being applied advanced techniques. Case of Fig. 2 had replaced from Inconel-6600 to Inconel-690 material for preventing of PWSCC. It performed semi-immersion UT technique and automated scanning for A-, B- and C-scan display which allowed image evaluation.

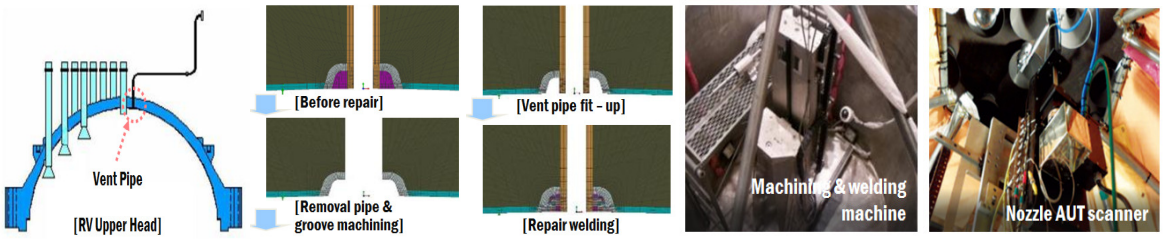

Fig.2 Repair and inspection of Ni-alloy J-weld of RPV Head vent line

Thus, in this article introduce the PARENT Activity of DHIC and component integrity case including Mock-up, Site-work & results.

Keywords: PARENT, Inconel-690, PAUT, TOFD, Replacement.

Simulation of inspection for dissimilar metal welds by phased array UT with focusing techniques

Young-In Hwang[1], Jae-Hyun Bae[1], Hak-Joon Kim[1], Sung-Jin Song[1], Kyung-Cho Kim[2], Yong-Buem Kim[2] and Hun-Hee Kim[3]

[1]Sungkyunkwan University, Republic of Korea

[2]Korea Institute of Nuclear Safety, Republic of Korea

[3]Doosan Heavy Industries & Construction, Republic of Korea

Abstract

Dissimilar metal welds (DMWs) are widely used as nozzles of major components in nuclear power plants, for example, control rod drive mechanism (CRDM), bottom-mounted instrumentation (BMI) and large bore pipe connecting reactor vessel and steam generator. These welds have caused significant reliability problem; leakage in the small bore piping, Primary Water Stress Corrosion Cracking (PWSCC) associated with safe end welds and etc. Especially, PWSCC is critical to the potential for large loss of coolant inventory or control rod ejection and loss of coolant accident. Inspection of dissimilar metal welds can be performed with ultrasonic testing. However, ultrasonic inspection of nickel-based dissimilar metal welds is difficult due to anisotropic and dendrite structure of DMWs and attenuation phenomena which propagates dendrite structure. So, phased array ultrasound is widely used to inspect surface break cracks and stress corrosion cracks in DMWs. Nevertheless, the inspection of dissimilar metal weld using phased array ultrasound has relatively low probability of detection of cracks due to high attenuation and noise caused by coarse grains and beam skewing due to anisotropy in material properties. Therefore, advanced focusing techniques of phased array ultrasound are needed for improvement in the probability of detection of flaws in DMWs. In this study, we had investigated focusing and steering phased array ultrasound in dissimilar metal welds with modeling crystalline structure and determination of time delays. And, compared focusing techniques to enhance SNR of phased array ultrasonic signals for optimal inspection setup of testing systems in DMWs.

Keywords : Dissimilar Metal Weld, Phased array ultrasonic testing, Adaptive focusing technique, Time Reversal Technique

1. Introduction

In nuclear power plants, PWSCC in dissimilar metal welds is critical as there is high potential for a serious loss of control rod ejection and coolant inventory. By tension residual stress and etc., corrosion damage can occur in nuclear power plant at BMI Nozzle RCS hot leg and CRDM, especially. Ultrasonic Testing of Dissimilar Metal Welds is a very difficult task due to grain noise and splitting by anisotropic / inhomogeneous structure and coarse grain. From those figures, we can see grain noise and splitting effect at austenitic weld area.

Phased array ultrasonic techniques are increasingly adapted as those can focus beams at desired locations. However, inspection of dissimilar metal welds using phased array ultrasound has relatively low probability of detection of cracks due to beam skewing in dissimilar metal welds and high attenuation and noise caused by coarse grain. So, advanced focusing techniques of phased array ultrasound are needed for improvement in the probability of detection of flaws in DMWs.

2. Objectives

Modeling crystalline structures of dissimilar metal welds, Determination of time delays for focusing and/or steering ultrasonic beams at desired position in the austenitic steel welds, Comparison of focusing techniques such as time reversal technique, adaptive focusing technique, and conventional focusing techniques to enhance SNR of phased array ultrasonic signals were performed to investigate a focusing techniques for optimal inspection setup of phased array ultrasonic testing systems in dissimilar metal welds.

3. Modeling of DMWs

Even though Ogilvy's model [1] is widely used in the austenitic stainless steel welds, it can describe just symmetric welds. In this study, we adopted the modified Ogilvy's model [2] that can describe asymmetric weld structures using Eqs. (1) and (2).

$$F(y,z) = \tan\theta_1 = \frac{\left(T_1(D_1 + z\tan\alpha_1)\right)}{y^{\eta}} \qquad y > 0 \tag{1}$$

$$F(y,z) = \tan\theta_2 = \frac{\left(T_2\left|(D_2 + z\tan\alpha_2)\right|\right)}{\left|y^{\eta}\right|} \qquad y < 0 \tag{2}$$

T_1 and T_2 are proportional to the tangents of the grain axes at the sloping edges. η is a parameter for determination of how fast the grain orientation falls with an increase in y. Figure 1. shows result of grain orientation in dissimilar metal welds based on the modified Ogilvy's model.

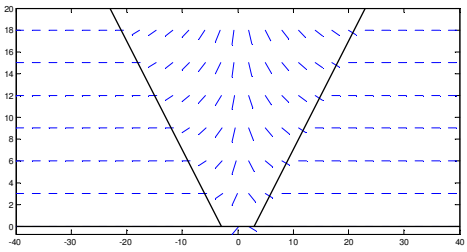

Figure 1. Grain orientation in dissimilar metal welds based on the modified Ogilvy's model

We applied rotation matrix to elastic constant of transversely isotropic austenitic weld metal, then we calculate applied elastic constant using this matrix. The center frequency of transducer 2.25 MHz and 16 elements of phased array transducer were used. The width and spacing of phased array transducer are 0.8mm and 1mm and bush shaped flaw image was extracted [3] and imported for the application of DMWs. Figure 2. shows the simulation setup for ultrasonic propagation in DMW. The calculations were carried out by a finite element modeling software, COMSOL Multiphysics.

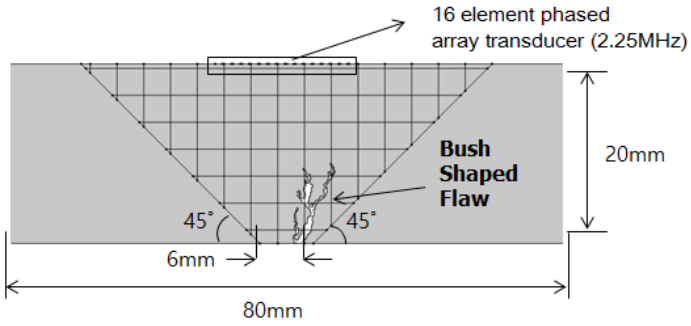

Figure 2. Simulation setup for ultrasonic propagation in DMW

To investigate the performance of three focusing techniques for phased array ultrasonic testing in dissimilar metal welds, firstly, we simulate the ultrasonic beam propagation without any time delay. As shown in Figure 3., due to the

complexity of grain orientation in weldments, there occurred beam distortion and skewing during ultrasonic beam propagation. One can see low signal-noise ratio from crack in weldments due to beam distortion and skewing. It is hard to discriminate flaw from the signals. For that reason, it is necessary to have enhanced focusing techniques to improve signal-noise ratio. So, we applied focusing techniques such as time reversal technique and adaptive focusing technique.

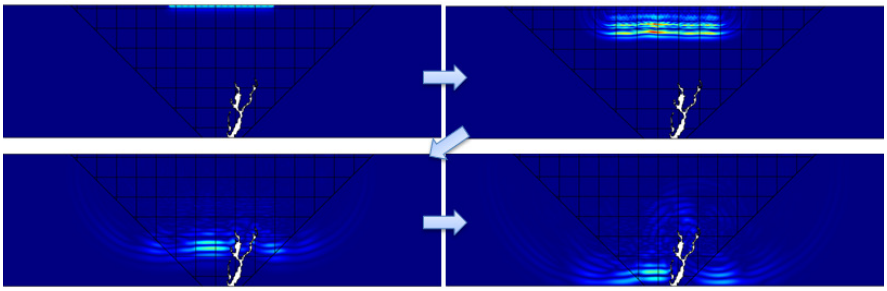

Figure 3. Simulation of phased array ultrasonic beam without time delay

4. Comparison of flaw signals with different ultrasonic focusing methods

We compared the performances of three focusing techniques to improve the probability of detection of flaws in the DMWs; phase matching method, adaptive focusing method and time reversal method.

To focus the phased array ultrasonic beam, time delays should be applied to the array elements. In order to determine the time delay to be applied, the distances of between individual elements to the focal point should be identified. Then, the time delay can be determined. For phase matching at focal point, we matched radiated sound pressure. Then, we matched radiated sound pressure. The adaptive focusing technique is a time delay estimation method based on the cross correlation. Time delay can be rapidly detected and quantified using a cross-correlation between each received signals. Time reversal technique was time delay estimation method that can be used in ultrasonic testing to improve flaw detection through anisotropy and inhomogeneous material such as dissimilar metal weld. Among the techniques, we applied DORT method.

Figure 4. shows simulation of ultrasonic beam propagation using phase matching method. Using the phase matching methods, the reflected beam from crack was weak and it still caused beam distortion and skewing during the ultrasonic beam propagation.

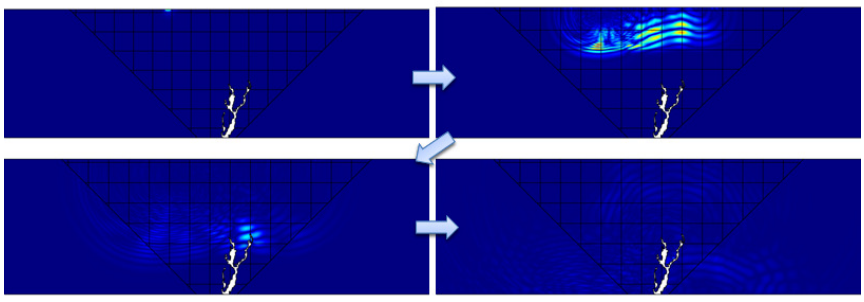

Figure 4. Simulation of phased array ultrasonic beam with time delay

For calculating the cross-correlation between each received signals, the maximum of the cross-correlation function indicates the point in time where the signals are best aligned[4]. Figure 5. shows the calculated time delay using adaptive focusing techniques. This figure shows the simulation results using the adaptive focusing method. The reflected beam from crack using adaptive focusing method was stronger than reflected beam using phase matching method. And, the beam distortion and skewing during ultrasonic beam propagation noticeably decreased, compared to phase matching method.

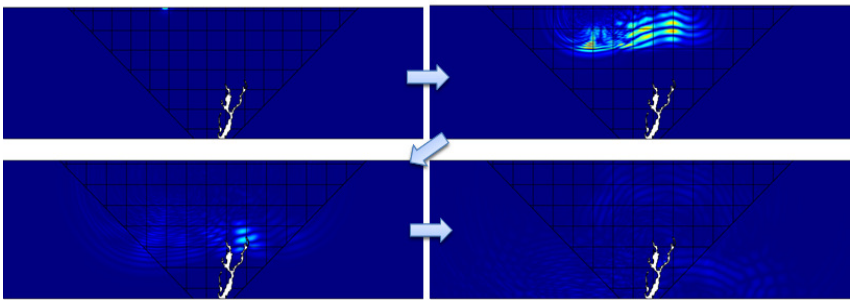

Figure 5. Simulation of phased array ultrasonic beam with adaptive focusing technique

For time reversal method, first, Acquired inter-element waveforms from crack without time-delay are measured by each of the elements. Then, we have converted from time-domain to frequency-domain. We used singular value decomposition (SVD) of the transfer matrix to obtain eigenvalue and eigenvector of acquired inter-element waveforms[5]. The number of significant eigenvalues is equal to the number of well resolved scatters. Each eigenvector provides phase and amplitude information that should be applied to the transducer array in order to focus on each scatterer. One high eigenvalue means that there is only one scatter exist in the sector. Figure 6. shows simulation of ultrasonic beam propagation using time reversal techniques. The reflected beam from crack using time reversal techniques was strongest among the focusing techniques. Using the time reversal technique, the beam distortion and skewing during the ultrasonic beam propagation noticeably decreased compared to the phase matching technique and the adaptive focusing technique.

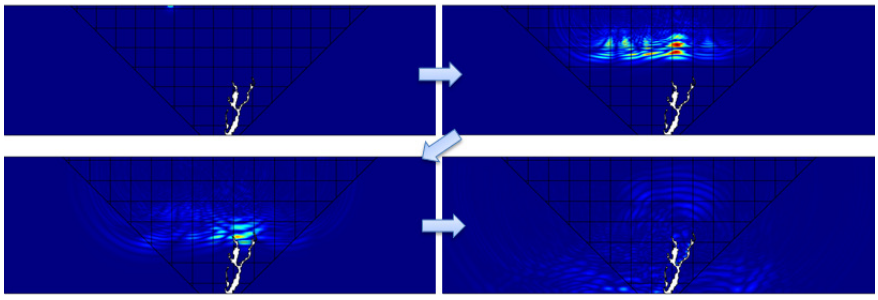

Figure 6. Simulation of phased array ultrasonic beam with time reversal technique

Figure 7. shows the comparison of A-scan signals obtained by using three different focusing techniques. When the time delay determined by the time reversal techniques, the signal amplitude is the highest, showing higher than that by the phase matching method. Time reversal techniques enhanced SNR of phased array ultrasonic signals most effectively compared to other techniques.

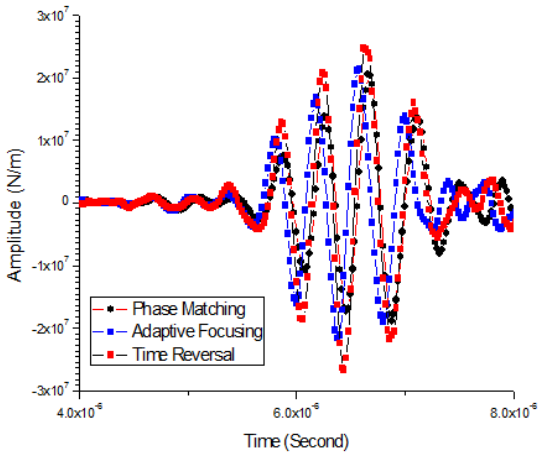

Figure 7. Comparison of A-scan signals obtained by using three different focusing techniques

5. Conclusion

Modeling crystalline structures of the austenitic steel welds was performed using Ogilvy's crystalline structure model. Time delays were calculated for focusing and/or steering ultrasonic beams at desired position in the austenitic steel welds, for phase matching focusing techniques, adaptive focusing techniques and time reversal technique. Comparison of focusing techniques such as time reversal technique, adaptive focusing technique, and etc. to enhance SNR of phased array ultrasonic signals were performed. Time reversal techniques enhanced SNR of phased array ultrasonic signals more than other techniques. However, in practical field, adaptive focusing techniques could be one of alternative method to improve SNR.

Acknowledgements

This work was supported by the National Research Foundation of Korea (NRF) grant funded by the Korea government (MEST) (No. 2012R1A1A2044423)

References

[1] JA Ogilvy, Computerized ultrasonic ray tracing in austenitic steel, NDT international, 18 pp. 66-67 (1985)

[2] J. Ye, H. J. Kim, S. J. Song, S. S. Kang, K. C. Kim, M. H. Song, Model-based simulation of focused beam fields produced by a phased array ultrasonic transducer in dissimilar metal welds, NDE&E International, 44, 3, pp. 290-296, 2011

[3] Heloisa CunhaFurtado, Iain Le May, High Temperature Degradation in Power Plants and Refineries, Materials Research, Vol. 7, No. 1, pp. 103-110, 2004

[4] Noor Shafiza Mohd Tamim, Farid Ghani, "Techniques for Optimization in Time Delay Estimation from Cross Correlation Function", International Journal of Engineering & Technology IJET-IJENS, Vol. 10, No.02

[5] C. Prada, etc, "Time reversal techniques in ultrasonic nondestructive testing of scattering media", Inverse Problems, Vol. 18, pp. 1761-1773, 2002.

Higher harmonic imaging of SCC in dissimilar metal weld with Ni-based alloy and fatigue crack in cast stainless steel

Hitoshi Ishida[1], Koichiro Kawashima[1,2]

[1]Institute of Nuclear Safety System, Inc., Mihama-cho, Mikata-gun,Fukui, 919-1205, Japan

[2]Ultrasonic Materials Diagnosis Laboratory Ltd., Showa-ku, Nagoya-shi, Aichi, 466-8555, Japan

1. Introduction

Ultrasonic testing is performed for welds of the reactor vessel and pipes,etc. in nuclear power plants as an in-service inspection.

Complex configurations and the possible occurrence of acoustic anisotropy in a dissimilar metal weld with Ni-based alloy in a nozzle of a reactor vessel and the main coolant pipe made of cast stainless steel necessitate that the inspection techniques be advanced and the inspectors be experienced. Many kinds of techniques have been developed including those that use a large aperture focused transducer and a phased array[1)].The ultrasonic testing method applied to an in-service inspection in nuclear plants is a pulse echo technique to detect an acoustic discontinuity based on the difference of acoustic impedance (product of density and propagation velocity of material).

On the other hand, the fitness rule requires sizing of flaws(cracks) with high accuracy to evaluate structural integrity in nuclear power plants.It is difficult to detect a closed crack in an acoustic continuous condition with contact of crack surfaces despite material discontinuity under the principle of the pulse echo technique.For the closed crack, the incident ultrasonic wave changes the contact condition of the crack surfaces causing distortion of the wave form of the ultrasonic wave. This wave form distortion generates a high harmonic wavewith a frequency that is a multiple of the incident wave frequency.Therefore it is expected that the closed crack, which cannot be detected by a conventional pulse echo method, can be detected by the high harmonic wave[2)].

In this paper, we report the test results obtained using the high harmonic ultrasonic wave method to detect, visualize and measure cracks, specifically caused by stress corrosion cracking(SCC) in the Ni-based alloy weld and fatigue cracks in the cast stainless steel.

2. Test method

2.1 Specimens

Figure 1 shows a Ni-based alloy weld specimen. This specimen simulated the weld on a nozzle (943mmOD, 77.5mm*t*) of an actual reactor vessel.The nozzle was made of carbon steel as the nozzle and it had stainless steel as a safe-end. The SCC and electrical discharge machining (EDM) slit were manufactured perpendicular to the nozzle weld line on the inner surface of the nozzle.The depths of the SCC of 5mm and 10mm were the target manufacturedsize.

Figure 2 shows a cast stainless steel specimen.The specimen was a block made froma centrifugal cast stainless steel pipe (65mm*t*) and the fatigue crack was manufactured on the inner surface of the pipe.The target depths of the fatigue cracks were 10, 20, 30, and 50% of the specimen thickness2.

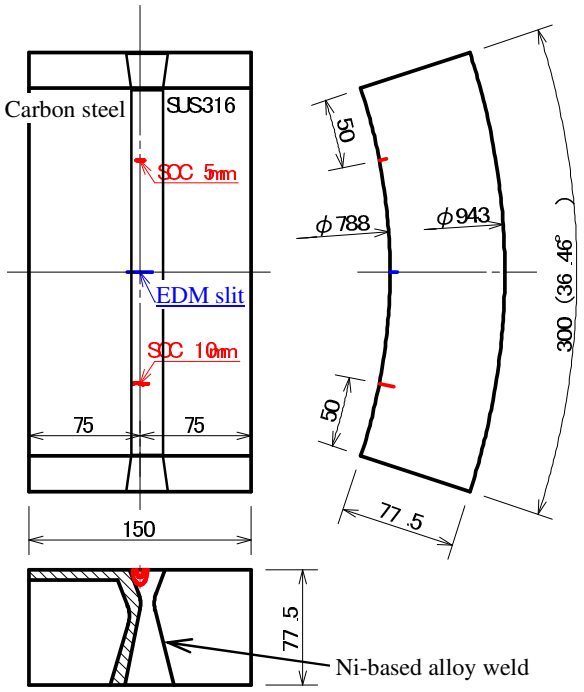

Fig.1 Ni-Based alloy weld specimen

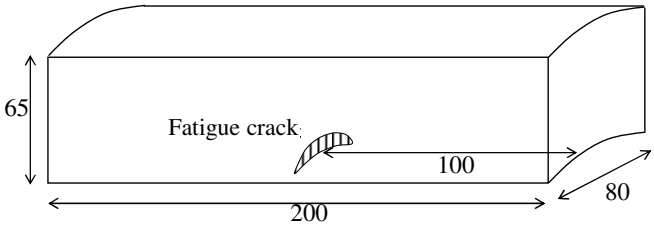

Fig.2 Cast stainless steel specimen

2.2 Measurement method

We visualized the cracks by normal incidence from the specimen inner surface and the angle beam incidence from the specimen outer surface using the immersion technique.

Figure 3 shows a schematic diagram of the testing system.We useda large amplitude continuous sine wave signal generator(RPR-4000,RITEC). We could sample a high harmonic wave arbitrarily by selection of a suitable cut-off frequency on the high-pass filter for the signal received by the transducer.

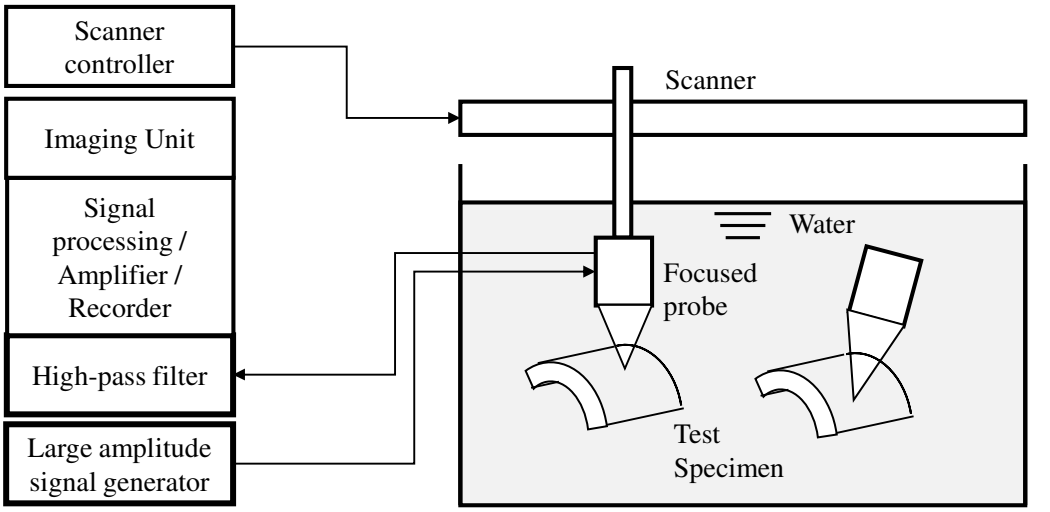

(a) Normal beam technique (b) Angle beam technique

Fig.3 Immersion higher harmonic imaging system

3. Test results

3.1 Ni-based alloy weld specimen

Figure 4 shows examples of images from the crack side (vessel nozzle inner surface) for the SCC of 5mm depth.We used the following conditions: 5MHz frequency, 9.6mm diameter element, 51mm focus length transducer with 194V applied voltage, 5MHz-2cycle sine wave by normal incidence, and the received echo with 10MHz high-pass filter.We could detect the SCC on the C-scope image clearly and we also recognized the surface of the SCC in the direction of the depth clearly on the B-scope images.We measured a depth of 4.2mm from the B-scope image for the 5mm depth of the manufactured SCC.

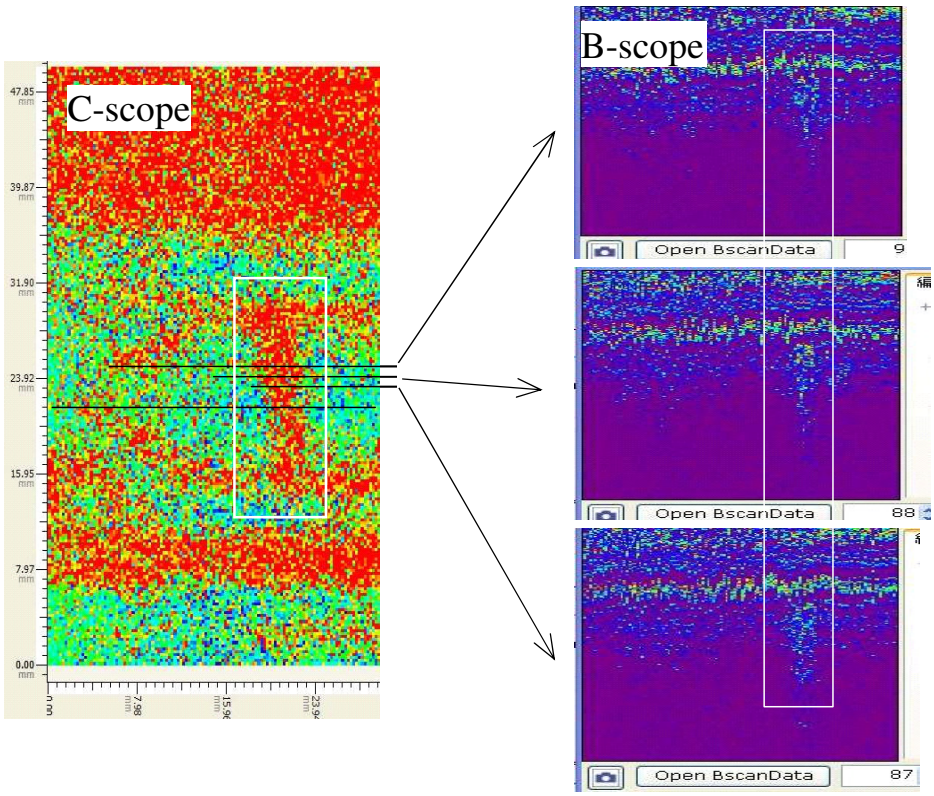

Fig.4 Scan image of SCC 5mm in the Ni-based alloy weld specimen

3.2 Cast stainless steel specimen

Figure 5 shows examples of images from the crack side (pipe inner surface) for the fatigue crack of 50% thickness depth.We used the following conditions: 2.25MHz frequency, 25mm diameter element, 152mm focus length transducer with 240V applied voltage, 2MHz-3cycle sine wave by angle incidence of 10 degrees, and the received echo with 4MHz high-pass filter.On the B-scope image, the surface (thickness direction) was drawn with an angle due to drawing the vertical direction in the direction of the angle beam path.We could detect the fatigue crack on the C-scope image clearly and we could also recognize the surface of the SCC in the direction of the depth clearly on the B-scope images.We measured a depth of 31mm from the B-scope image for the for the fatigue crack of 50％thickness depth.

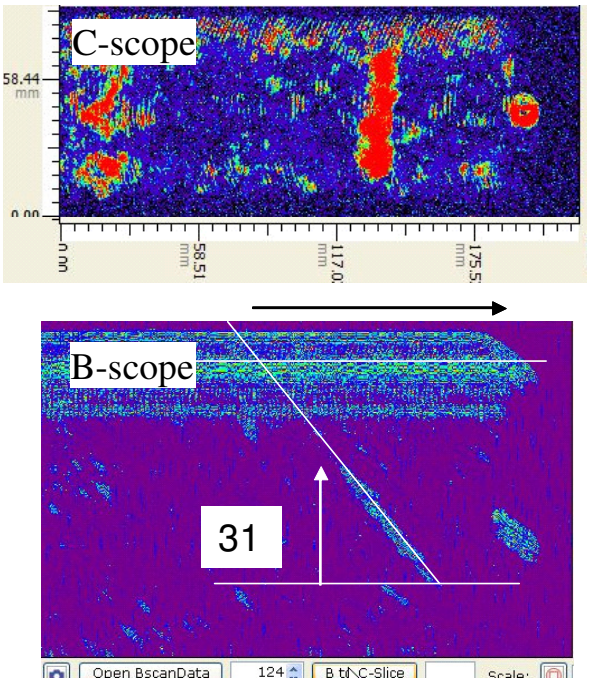

Fig.5 Scan image of fatigue crack 50%t in the cast stainless steel specimen

4. Conclusion

We visualized the flaws (cracks) in the Ni-based alloy weld and cast stainless steel specimens by a high harmonic ultrasonic method. We could detect the flaws on the images and measure their depth with good accuracy. In particular, recognition of the flaw and its surface on the image is a distinctive feature of the high harmonic method, and something thatthe pulse echo method does not have.

Next, we are going to evaluate testing conditions and the procedure to apply the high harmonic ultrasonic method in the field.

References

1) H. Ishida, J. Kitasaka, “Development of a Phased Array TOFD UT Method to measure the Depth of SCCs in Dissimilar Metal Weld,”the 9th International conference on NDE in Relation to Structural Integrity for Nuclear and Pressurized Components, pp. 754-762, (2012).

2) K.Kawashima, R. Imanishi, “Harmonic Imaging of Inter-Granular Stress Corrosion Cracking in Ni-Based Alloy Welds,” Journal of JSNDI, 60(12), pp.713-719, (2011).(in Japanese)

Automated Ultrasonic Nondestructive Evaluation of High Density Polyethylene Mitered Joints and Butt Fusion Welds

Jeff Milligan[1], Cliff Searfass[2], and Joseph Agnew[1]
[1]Structural Integrity Associates, 11515 Vanstory Drive, Huntersville, NC, USA
[2]Structural Integrity Associates, 1951 Pine Hall Rd, State College, PA, USA

jagnew@structint.com (Joseph Agnew):

High density polyethylene (HDPE) is being increasingly used for buried and aboveground piping in the marine, septic, highway, and nuclear energy industries due to its low cost, lightweight, and corrosion resistant properties. Traditional ultrasonic nondestructive evaluation (NDE) techniques that are commonly applied to metallic structures cannot be directly applied to HDPE materials due to their viscoelastic material properties and new or modified inspection techniques are needed. The paper will review the review the special consideration that must be made when applying ultrasonic (UT) inspection techniques to HDPE materials and will present several Phased Array UT (PAUT) inspection techniques for the inspection of butt fusion and mitered joints. Numerical modeling results will also be presented that justify the inspection methods employed and experimental results will be presented for several HDPE joint configurations and flaw types and geometries.

Keywords: HDPE; high density polyethylene; fusion joints; PAUT; Phased Array UT.

Developments of Portable Pulsed Eddy Current Equipment for the Detection of Wall Thinning in the Insulated Carbon Steel Pipe

Duck-Gun Park [a], M.B. Kishore[a], D.H. Lee [a].

[a] Nuclear Materials Development Division, Korea Atomic Energy Research Institute, Daejeon, South Korea -305-353.

Abstract

Non Destructive Technique (NDT) methods that are capable of detecting the wall thinning and defects without removing the insulation are necessary. In this study we developed a Pulsed Eddy Current (PEC) technique to detect wall thinning of Ferro magnetic steel pipes covered with fiber glass thermal insulator and shielded with Aluminum plate. The developed system is capable of detecting the wall thickness change through an insulation of thickness 9.5cm and 0.4mm Aluminum (Al) shielding. In order to confirm the thickness change due to wall thinning, two different sensors, a hall sensor and a coil sensor were used as a detecting element. In both the cases, results show a very good change corresponding to the sample thickness variation. To simulate the wall thinning, two kinds of tube samples are tested with different defects configurations and depth using experimental setup portable equipment.

Keywords: wall thinning, Eddy Currents, Carbon steel, portable PEC equipment, hall sensor and Coil

1. Introduction

The pipelines of power plants and heat exchangers are covered with a thermal insulator to decrease the heat loss. During the long-term services, corrosion might occur on the outer side of the pipe as corrosion under insulation (CUI), or on the inner side of a pipe as flow accelerated corrosion (FAC) and develops into wall thinning of the pipelines is a real threat for the reliability of carbon steel equipment, which may finally results into a catastrophic failure. Therefore, local wall thinning is a point of concern in almost all steel structures. Usually, thermal insulators used for the purpose of covering the pipelines is made up of materials with low thermal conductivity (fiberglass or mineral wool); hence, NDT methods that are capable of detecting the wall thinning and defects without removing the insulation or through this insulation are necessary. PEC nondestructive testing is widely used for the characterization of deep flaw in ferromagnetic materials. The conventional ECT which operates with a single frequency sinusoidal excitation has gained wide acceptance in the field of NDT [1]; yet, this technique suffers from a limitation, i.e., penetration depth or skin depth. The penetration depth δ depends on excitation frequency f [2]. In contrast to the traditional ECT, the PEC employs a non sinusoidal excitation, such as a pulse or square wave, instead of a single frequency sinusoidal excitation Because the Fourier transform of a pulse contains multiple frequency components [3, 4], a rectangular pulse can provide the depth profile of a material under test [5, 6]. The usage of short current pulse excitation reduces the power consumption, which is the most desired specification for the development of portable instruments. Due to the potential advantages of the PEC, prevalent investigations on this technique have been conducted, such as detection of wall thinning and corrosion in aircraft multilayer structures [7, 8].The developed PEC system is optimized for the detection of thickness change as well as sub surface crack detection on the Ferro magnetic samples. A LabView based program is used to record the data and to analyze the recorded data. We developed two kinds of PEC equipment, one is laboratory setup and another is portable equipment. Both the results give a concrete change in the thickness of the sample

2. System Designing

The PEC system consists of a pulse amplifier, a probe with a driving coil and a magnetic field detecting sensor, a sensitive PEC differential amplifier with variable gain to amplify the output voltage from the magnetic field detection sensor, a A/D converter, and a computer with signal processing software. A schematic of the PEC system is shown in Fig. 1(a). From this figure it is clear that the pulse amplifier drives the excitation coil and the sensor electronic reads the output from magnetic sensor used in probe and conditions the detected signal, the proper conditioned signal is recorded in computer using some software application. The PEC probe characteristics are determined by a combination of measuring environments and a PEC probe consisting of an exciting coil and a field detection sensor. The excitation coil is made by wounding a copper wire, and detection coil is wounded around the excitation coil. A commercially available hall sensor with proper connections was placed in the middle of the excited coil to detect the response from eddy currents. A real-time LabView program was developed for the data acquisition and for scanning the probe on the insulated and shielded sample. The scanning and analyzed results were displayed on the computer monitor.

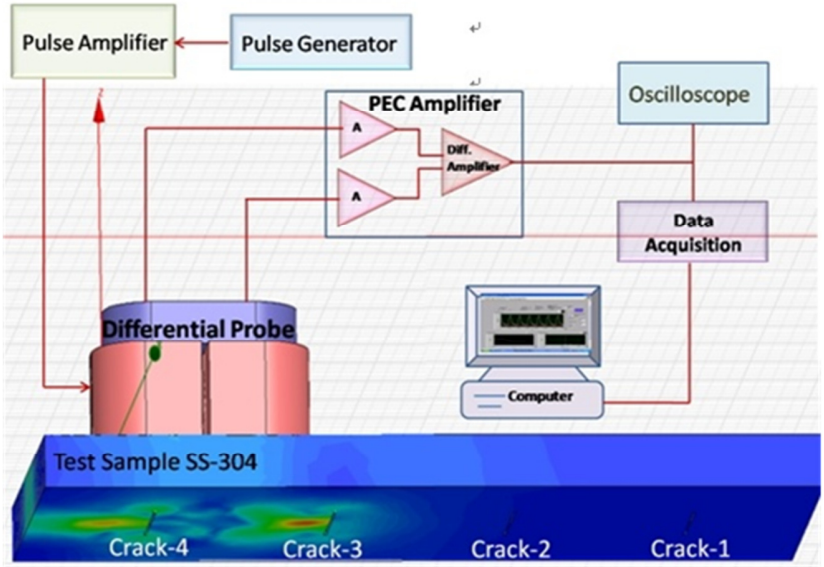

Fig 1 Schematic Diagram of the PEC System

3. Experimental Setup

The PEC system to simulate the wall thinning of a steel pipe, a mock-up of During these experiments a Ferro magnetic steel tube of diameter 210mm and a length of 620mm, which is covered with insulator of 95mm thickness was used a wall thinned pipe with various thickness regions 2.5mm, 5mm and 8mm respectively was shown in Fig. 1 (a, b, c). A 95mm thick insulator with galvanized cladding of 0.4 mm thickness covers the pipeline to simulate real time environment as shown in the Fig. 2(b). The test specimen also consists of three similar cracks of 5mm width, 1mm depth on 2.5mm thick region and same quantity of 5mm width, 2mm deeper cracks on 5mm thick region. Fig. 2(c) clearly depicts the inner cross section of the tube covered with insulation and shielded with Al plate, three similar cracks also can be observed on 2.5mm and 5mm thick regions. A bipolar rectangular current pulse generated from Pulse Amplifier was used to excite the driving coil and the detected sensor output is fed to the PEC amplifier for signal conditioning and then connected to a computer through DAQ equipment as shown in the Fig. 2(a). While placing the probe great care was taken to avoid the cracked region not to come under the probe area in order to avoid the ambiguity in the results of thickness change. The probe was scanned along the different thickness step of pipe, and the excited pulse is repeated for five times and the average of the response is recorded as the resultant detected pulse corresponding to a thickness of the

test sample which leads to reduce the percentage of error as less as possible. After finishing the measurement, the probe is moved to 5 mm thick region of the sample and repeated the same process to record the detected signal corresponding to 5mm thickness. Finally, the probe is moved to 8mm thickness region and its corresponding detected pulse is recorded in same fashion. All the data recording process has been developed in Lab VIEW environment also the data analysis and processing can be done by using this program. Once after completing the data recording process all the data is analyzed and displayed on the computer. The system applied in the mock-up can distinguish a wall thickness of 2.5, 5, and 8 mm under 95 mm insulation covered with 0.4 mm of stainless cladding**.**

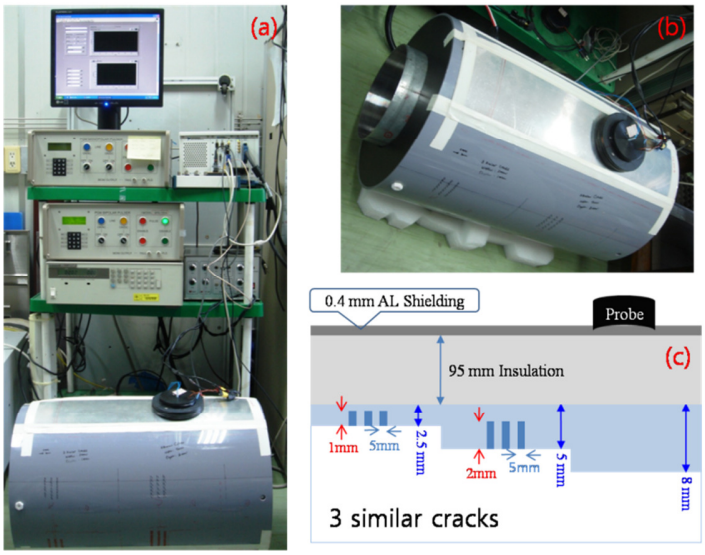

Fig 2.a) Experimental Setup of PEC system b) Test Specimen c) Inner Cross sectional view of the test specimen

4. Results and Analysis

When a high-level current is applied to the exciting coil, the coil makes a static magnetic field (primary magnetic field) into the sample; when there is a sudden transition in the exciting current, eddy currents are induced into the sample. The time-varying magnetic fields (secondary magnetic field) generated by the decaying eddy currents are captured by the Hall-sensor as a voltage signal. The strength and duration of induced pulse signal resembles the average wall thickness that can be measured. The duration of the eddy currents will have an effect on the transition period of the detected pulse. Form the Fig. 2(a) it is clearly observed that the transition time gradually increases as the thickness of the sample increases during the rising of the detected pulse. In other words the rising edge of the detected pulse is delayed more as the thickness of the sample increases, during its falling edge the delay is decreasing as the thickness increases also the magnitude of the detected pulse gradually decreases with increasing sample thickness. When the insulation over the test specimen is covered with 0.4mm Aluminum plate, same phenomenon is observed i.e. the transition period gradually increases as the thickness of the sample increases during the rising of the detected pulse, also the magnitude of the detected pulse gradually decreases with increasing sample thickness in the detected pulse. The detected pulse is further reduced compared to the previous case i.e. without aluminum plate on the insulation as shown in Fig 2(b). The slope of rising pulse in the Al shielded

one increased compared to that of unshielded one, which is attributed to the damping of the eddy current by Al shield.

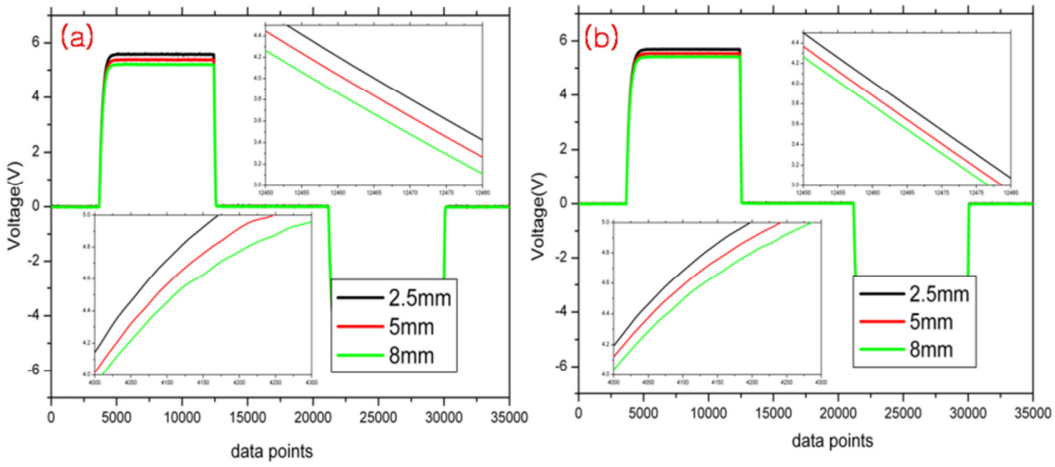

Fig 3. a) Hall Sensor output with 95mm Insulation and not Aluminum shielding b) Hall Sensor output when the sample insulated with 95mm Insulation and shielded with 0.4mm Aluminum plate

When the insulation on the sample is shielded with Aluminum plate the magnitude of the detected pulse considerably decreased since the penetration of the excited magnetic fields are limited by the aluminum shielding as shown in Fig. 4(b). For conformations of the experiments, the coil sensor results are also analyzed which concludes the same as that of hall sensor detection method. Since both the experiments are conducted in a single instant all the experimental conditions are exactly same as the prior experiment which is clearly shown in Fig 4(a). From this figure it is clear that the peak of the sensing signal gradually increases as the thickness of the tube decreases, it is observed that the decaying of the eddy currents increases as the thickness decreases which is a clear identification of the change in the sample thickness. When the insulation on the sample is shielded with Aluminium plate the magnitude of the detected pulse considerably decreases since the penetration of the excited magnetic fields are limited by the aluminium shielding.

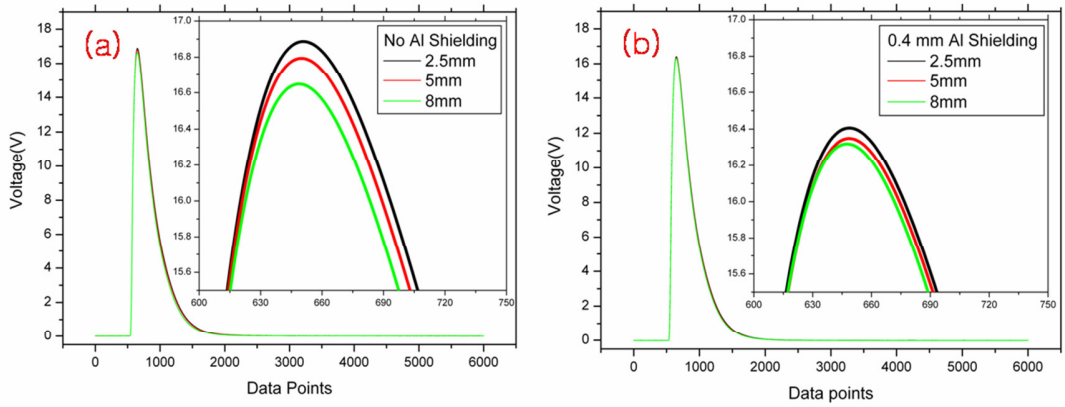

Fig 4. a) Coil Sensor output with 95mm Insulation and not Aluminum shielding b) Coil Sensor output when the sample insulated with 95mm Insulation and shielded with 0.4mm Aluminum plate

Fig. 5(a) and (b) shows the portable PEC equipment and tested tube sample. The portable equipment was manufactured in order to apply for the field test, and the constructions are same as the laboratory setup. The sample in Fig 5(b) sample was machined considering the defects created in the pipe of oil refining company. The tube was covered with silica insulation with 60mm thickness, and the insulation was protected with 0.5mm thickness Al shield, which is the same environment of the pipe in oil industry.

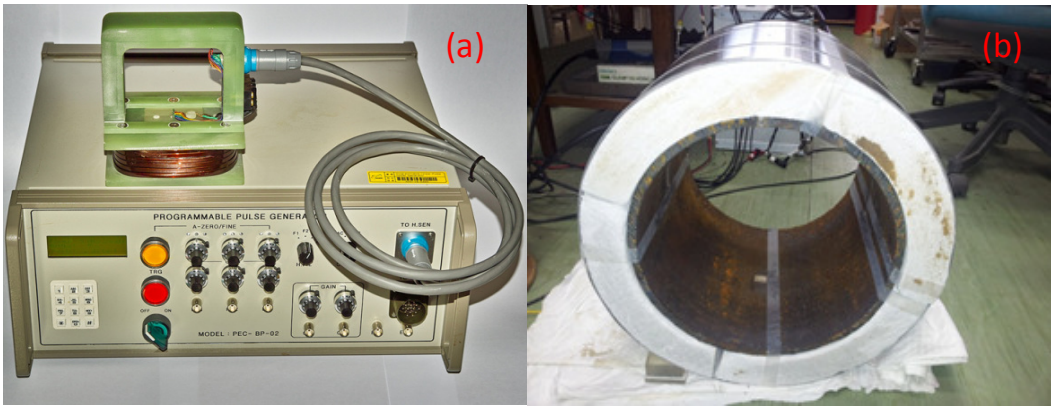

Fig. 5. The portable PEC equipment (a) and tested tube sample (b).

Four different kinds of defects are machined in the tube wall with the angle of 0, 90, 270, and 360degree. The depth of defects are 20%, 40%, 60%, of the tube wall thickness, and the widths are 20x20, 40x40, and 60x60mm, respectively, which are positioned in the 0, 90, and 270 degree from the arbitrary reference line in the axial direction. Last one defect in the 360 degree direction is the combination of three defects configuration having same width, but the depth is 100, 40, and 20% of the wall thickness. The defects configurations and tested results are shown in Fig. 6(a), (b), and (c).

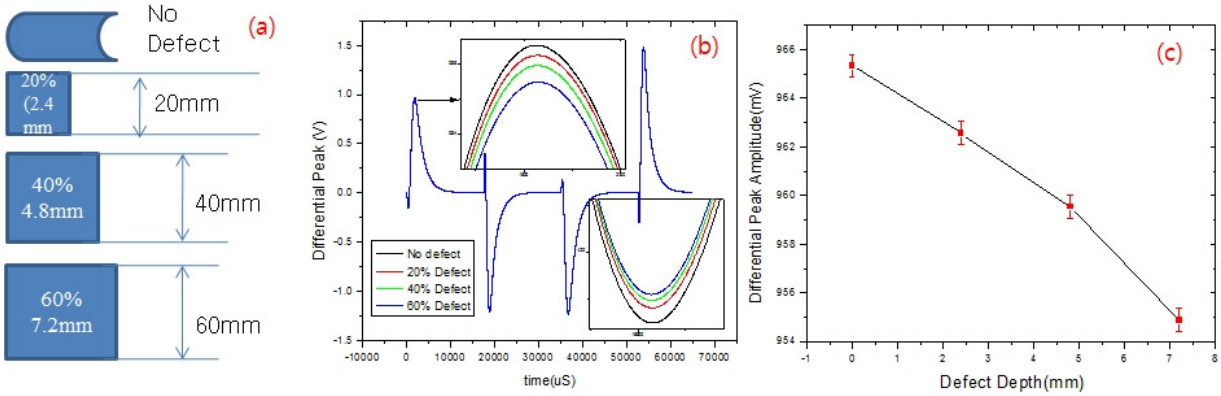

Fig. 6(a) defect sizes and configuration, (b) induced Hall sensor signal at each defect, (c) differential peak amplitude with defect depth.

Fig. 6(b) shows the induced signal by differential Hall sensor at each defect. The upper convex part of induced signal is come from the decreasing transition region of driving pulse, and lower concave part is that of increasing transition region of the negative to positive pulse. As shown in Fig.6(c) the peak amplitude of induced differential pulse signal decrease with increasing defects depth, which attributed to the decaying of eddy current with increasing depth. Fig. 7 shows the signal variation obtained from step

like defects positioned at 360 degree from the reference line. The measurements were conducted at each probe position on the Al shielding corresponding to the defect position. The peak amplitude decreases with increasing defect depth as shown in Fig. 7(c).

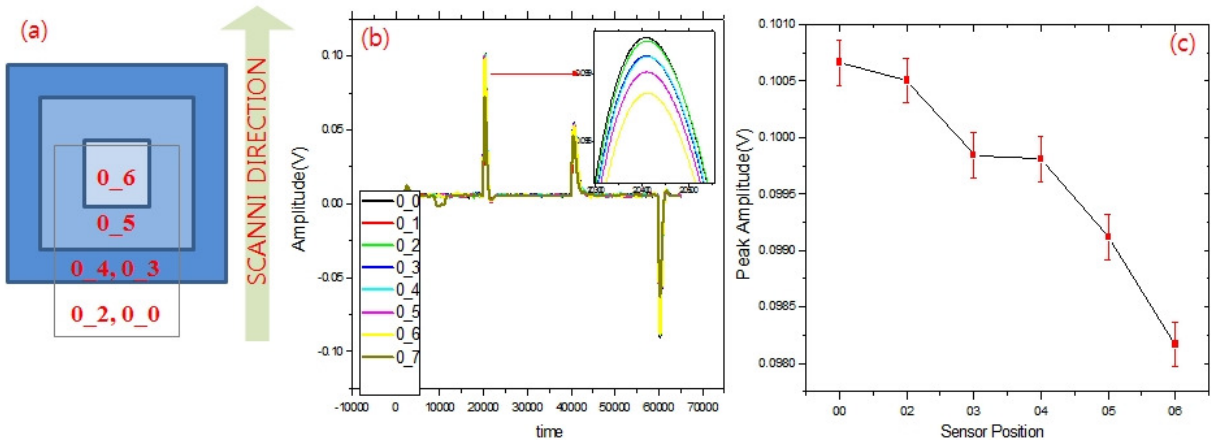

Fig. 7(a) defect sizes and configuration, (b) induced coil sensor signal at each defect step, (c) differential peak amplitude with defect step. The number in Fig. 7(a) represent the sensor positions (points 0_0 and 0_2 are the without defect positions in the base of tube sample, points 0_3 and 0_4 are the position of 20% defect with size of 60x60mm, point 0_5 is the position of 40% defect with size of 40x40mm, point 0_6 is the position of through hole defect with size of 20x20mm. (b) signal induced at each defects position, and (c) represent the variation of peak amplitude at each sensor position.

5. Conclusion

The PEC technique which can detects wall thinning of pipelines covered with thick insulation and shielded with thick metal sheets was developed using a Hall sensor and coil sensor. The probe performance was tested using the wall thinning pipe covered with95 mm insulation covered with 0.4 mm of Aluminum cladding. The results obtained from Hall-sensor show better resolution than that of coil sensor. The detected pulse is further reduced compared without aluminum plate on the insulation. The slope of rising pulse in the Al shielded one increased compared to that of unshielded one, which is attributed to the damping of the eddy current by Al shield. The results obtained from portable equipment also showed are well accorded with that measured at laboratory equipment. The eddy currents decays at a faster rate as the thickness increases, which means that the energy of the detected pulse for higher thickness region is small compared to that of lower thickness regions.

REFERENCES

[1] N.Nair, V.Melapudi, J. Hector, X. Liu, Y. Deng, Z. Zang, L. Udpa, J. M. Thomas and S. Udpa, A GMR based eddy current system for NDE of aircraft structures, IEEE Trans. Magn.42, 3312 (2006).

[2] R. Griberg, L. Udpa, A. Savin, R. Steigmann, V. Palihovic and S. S. Udpa, “2D eddy current sensor array”, NDT&E Int. 39, 264 (2006).

[3] Sophian, G. Y.Tian, D.Taylor, J. Rudlin, A feature extraction technique based on the principal component analysis for pulsed eddy current NDT, NDT & E int., Vol. 36, 37, (2003).

[4] Zhang Gang, Zhao Liang, Research on thickness of metallic layers from pulsed eddy current nondestructive measurements, Transducer and Microsystems Technologies, 25(4), 35 (2006).

[5] C.J.Renken. The use of personal computer to extract information from Pulsed eddy currents, Materials Evaluation, 59(3), 356 (2001).

[6] J. Blitz, Electrical and magnetic Methods of nondestructive testing, Chapman & Hall (London). 1997.
[7] M. A. Robers, R. S. Scottini, Proc. of 8th ECNDT conf, ndt.net, 7(10), Barcelona, June (2002).
[8] R. A. Smith, G.R. Hugo, Transient Eddy-current NDE for aging aircraft capabilities and limitations, Insight, 43(1), 14 (2001).

New developments in the use of flexible PCB-based eddy current array probes for the surface inspection of welds and pipes

Andre Lamarre[1], Tommy Bourgelas[1] and Benoit Lepage[1]
[1]Olympus NDT Canada, Quebec City, Canada

E-mail address(corresponding author) : andre.lamarre@olympus-ossa.com

The use of eddy current arrays (ECA) is already known to increase the inspection speed and the reliability of the inspection process. One practical limitation of the ECA technology is each ECA probes have to conform to the shape of the inspected components making its use expensive and limited. Recently, Olympus NDT has overcome these limitations by introducing the flexible PCB-based ECA probe technology. This paper will present the contribution of this technology for the surface inspection of weld. Detection and sizing of stress corrosion cracking (SCC) on pipes will also be presented.

Keywords: eddy current array, flexible, pipe

A Study on Development of RFECT System for Inspection of Ferromagnetic Pipelines

Jae-Ha Park[1], Hak-Joon Kim[1], Sung-Jin Song[1], Dae-Kwang Kim[2], Hui-Ryong Yoo[2], Sung-Ho Cho[2]

[1]School of Mechanical Engineering, Sungkyunkwan university, South Korea

[2]R&D Division, Korea Gas Coporation, South Korea

Abstract

The RFECT(Remote-field Eddy Current Testing) is one of the non-contact and non-destructive testing method inspects both external and internal flaws of pipelines. Also it does not require a great traction force. Due to these advantages some countries have tried the RFECT in pipeline inspection. However, there are lack of discussion about optimal exciting and pick-up coil design and accurate understanding of measurement signal depend on variation of parameters for the evaluation of flaw. In this work, discussion about acquired signal focusing on parameters such as dipole magnetic moment, induced electromotive force, lift-off and orientation was presented. The 3-bed RFECT system was fabricated to verify performance of RFECT system. Also experimental results showed detectability to flaw in 8 inch ferromagnetic pipeline.

Keywords : Remote-field, Eddy current, In-line inspection, RFECT

1. Introduction

The RFECT is based on a phenomenon that takes place in the vicinity of a solenoid exciting coil in a conductive material. There exists the direct field and remote field in conductive material. Measurements are made in the remote field region of the magnetic circuit, some distance away from the exciting coil where the induced eddy current fields are decaying inwards from the outside wall [1]. RFECT phenomenon is based on skin depth of ECT. While conventional reflected impedance eddy current testing techniques are limited by skin depth, RFECT technique is a through-wall inspection because RFECT operates below the cut-off frequency to pass through double-wall of pipe[2-3]. The electromagnetic waves by eddy current can travel inside and outside of the pipe. Inside of the pipe, direct electromagnetic waves in the vicinity of exciting coil are rapidly attenuated because of permeability of ferromagnetic material. This section is called the direct coupled field. Outside of pipe, indirect electromagnetic waves flow from backward to inside of pipe. These two direct and indirect waves are coupled at some distance away from exciting coil along the pipe, then transition zone occurs and then indirect electromagnetic waves are stronger than direct wave. This section is called remote eddy current field. In the remote-field, electromagnetic waves are gradually attenuated. Generally remote field in the pipeline is formed in 2 diameter or over. So a sensor placed in this remote-field, is able to be pick up magnetic flux from currents through the pipe wall. The magnitude and phase of sensed voltage depending on the wall thickness is presented for evaluation of discontinuity.

RFECT has advantage that can detect the flaws on the interior and exterior of the pipe wall with approximately equal sensitivity[4]. Also the RFECT can inspect both ferromagnetic conducting pipelines. RFECT has low traction force compared to Conventional in-line inspection tools such as MFL(Magnetic Flux Leakage), EMAT(Electromagnetic-acoustic Transducer). So it is advantageous to configure integrating any other tracking system. Despite these advantages, RFECT has not been applied much in industrial application. Because there is lack of accurate understanding and discussion about RFECT phenomenon. So in this work, to develop an applicable RFECT in ferromagnetic pipeline for in-line inspection, we studied on the optimization of exciting and pick-up coil for efficient transmission and receiving. And sensitivity of coils was considered in order to improve the efficiency. Also 3-bed RFECT system is developed in order to verify the performance of RFECT system. Detectability of flaws was

confirmed in 8 inch ferromagnetic pipeline.

2. Design for RFECT

To develop the applicable RFECT system for in-line inspection of ferromagnetic pipeline it is important to design optimal exciting and pick-up coil suitable to use in the measurement target. RFECT using the electromagnetic wave with solenoid coils could estimate the sensitivity of coils. So, to increase the receiving sensitivity we have considered configuration of high resolution type pick-up coil. And exciting coil was designed to maximize the dipole magnetic moment. Operational frequency for exciting in 8 inch pipe is 50 Hz that can be applied with skin depth equation. To confirm the sensitivity, we decided to look at the signal one might get from a typical defect by carrying out the pull-out test.

2.1 Exciting coil design

To optimize the exciting coil in 8inch pipe, we considered the performance of coil which can have higher magnetic moment contrast with lower power consumption. So calculation model considering the coil parameters was applied to performance evaluation. And dissipating transient current was set to 1 A per hour. Maximum outer diameter of exciting coil is 92 mm approximately 50% of pipe inner diameter and input voltage is $12V_{pp}$. So some cases are selected by considering the geometric condition. Also space factor of winding coil was considered to be 75%. Parameters and equations for calculation are presented in table 1. Where R is resistance and L is inductance, respectively. I and J are current and current density. Also P and M are power consumption and magnetic moment. To increase the excitation efficiency, an impedance dominated by resistance and inductance could be key parameters determining the performance of the coil. Allowable currents to coil diameter can differ by cross-sectional area of each coil. So Increased allowable power consumption for system will compensate the decrease in coil diameter. Thus, three models are selected and fabricated by calculation of parameters near the targeted applied current 1A. Amplitude and phase angle are measured by pull-out test and imperfection sensitivity was evaluated for same defect. As a result, exciter number 3 showed a highest sensitivity among three cases. The measurement results of current applied to the coil are similar to calculation results. As shown table 2, dipole magnetic moment of number 3 is largest because the current applied to the coil is proportional to magnetic moment. On the other hand, power consumption is smallest. The more current is applied to the coil, the larger magnetic moment can be generated. However we always consider a compromise between geometrical design and system capacity. The acquired signal of the selected models is shown in figure 1. Figure 1(c) shows the sensitivity of each coils. The magnitude variation from base line to peak point of amplitude and phase shown in figure 1(a) and 1(b) is largest in exciter 3. So exciting efficiency is well evaluated by increasing magnetic moment contrast with lower power consumption.

Parameter	Turns [Times]	R [Ω]	L [H]	I [A]	J [A/m^2]	P [W]	M [Am^2]
Equation	$\frac{D\times l_{coil}\times S_f}{0.25\times {d_{wire}}^2\times\pi}$	$\frac{l_{wire}}{\sigma_{copper}\times S_{wire}}$	$\mu_r \frac{0.8{r_{coil}}^2\times Turn^2}{6r_{coil}+9l_{coil}+10D}$	$\frac{V}{Z}$	$\frac{I}{S_{wire}}$	I^2R	μNIS_{coil}

Table. 1 Parameters and equation for calculation model

Parameter	Coil Diameter [mm]	Turns [Times]		I [A]		P [W]	M [Am^2]
		Calculation	Measurement	Calculation	Measurement		
Exciter #1	0.75	611	607	0.850	0.694	4.502	2.733
Exciter #2	0.85	657	651	0.803	0.709	3.455	2.814
Exciter #3	1.1	726	715	0.995	0.994	3.299	3.677

Table. 2 Comparison with calculation and measurement model

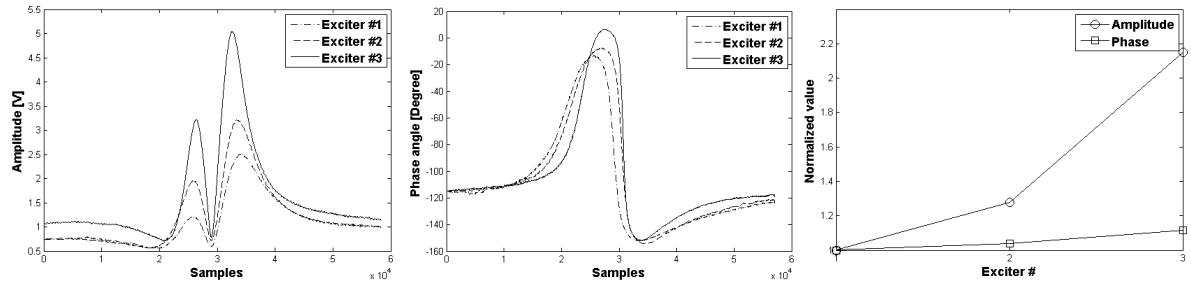

(a) (b) (c)

Figure. 1 The acquired (a) amplitude and (b) phase variation with exciting coils and it's (c) sensitivities comparison

2.2 Pick-up coil design

To increase the receiving efficiency, we considered following points: The first is coil turns and size, second is orientation of sensor on the pipe and third is lift-off. Performance of pick-up coil is proportional to magnetic flux through unit area and number of turns of coil. This relation is represented by Maxwell-Faraday' law as equation 2. So, to increase the induced electromotive force of pick-up coil, it is good to wind the coil as many times as possible. However sensor size of high resolution type for full coverage of pipe is limited by number of sensors. In this study, arrangement of pick-up coils is 36 channel for 8 inch ferromagnetic pipeline. We wound the coil to 40000 turns with 0.02mm coil diameter and maximum diameter is 16∅.

$$\varepsilon = -\mathrm{N}\frac{d\emptyset}{dt} \tag{2}$$

To investigate the effect of orientation of pick-up coil on the pipe, experiment with 2 configuration of pick-up coil by radial and axial direction was performed. Amplitude and phase angle were measured by pull-out test and imperfection sensitivity was evaluated for same defect. Signal pattern and sensitivity are different by orientation of pick-up coil. Assuming that the pattern of signal with B_r and B_z component of magnetic field leaking in the vicinity of flaw, signal pattern has a mono-peak by axial direction and bipole-peak by radial direction. So to verify the signal pattern and it's sensitivity, pull-out test was carried out on the test pipe as shown figure 2. Acquired signals have a same pattern as shown figure 3. And the variation of peak magnitude with radial direction is larger than axial direction. Amplitude variation is 4.7 times greater and phase angle variation is 2.6 times greater in radial direction. Also radial scan signal has better stability than the axial scan. In figure 3(a), radial amplitude has presented as positive bipole-peak unlike assumption because the amplitude is represented square root of in-phase and quadrature component. So orientation of pick-up coil with radial direction is good for sensitivity.

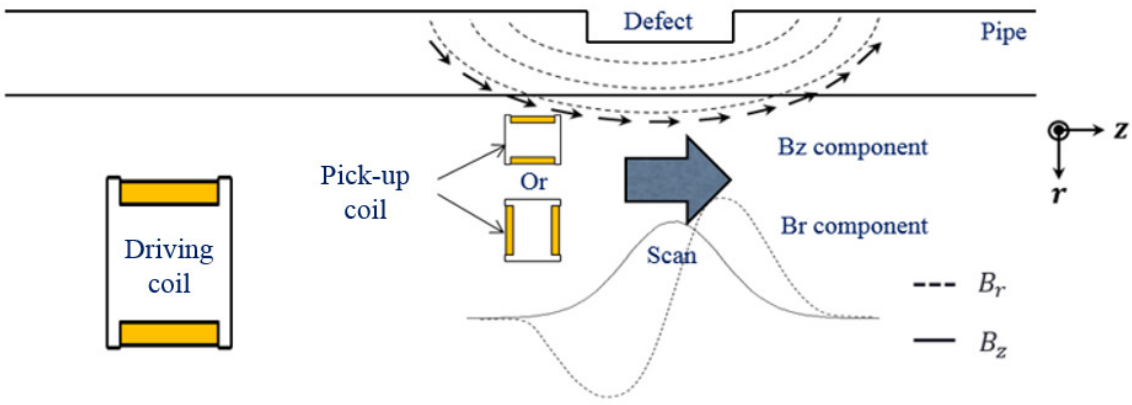

Figure. 2 Configuration of sensor orientation

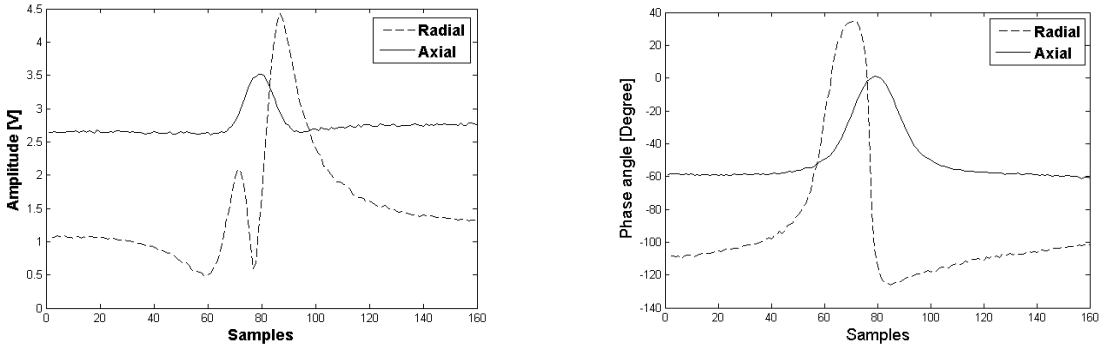

(a) (b)

Figure. 3 Acquired signals depending on the orientation of pick-up coil; (a) amplitude and (b) phase

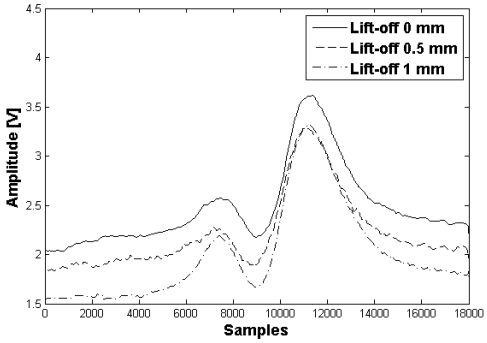

Figure. 4 Acquired signals depending on lift-off between pick-up coil and pipe wall

Generally in non-contact method, the lift-off has significant effect on receiving efficiency. The contact condition between pick-up coil and pipe wall is unstable because pipe wall is not smooth and including any local irregularity. Also stability of sensor in dynamic environment such as in-line inspection is more unstable. Attenuation of acquired signal could be severed even a little off the pipe wall. So, to investigate the sensitivity depending on the lift-off of pick-up coil on the pipe, we test the effect of lift-off by increasing the distance of 0.5mm. The orientation of pick-up coil was placed in radial direction. Figure 4 shows acquired signal by increasing lift-off. The amplitude of base-line has decrease by increasing lift-off. However variation of amplitude by flaw are similar to each of them. The sensitivity is best of the 1mm lift-off. So, lift-off does not affect significantly to 1mm.

3. 3-bed RFECT system

To verify the performance of fabricated exciting and pick-up coils, 3-bed RFECT system which can drive inside the pipe by pull-rig test was fabricated for in-line inspection. Test specimen was 8 inch pipeline. And distance between exciting and pick-up coils is 480mm for remote zone in 8inch pipeline. The chosen exciting coil was model number 3, which has wound 715 turns with 1.1mm copper wire on 80mm wide of 700mm diameter spool. Pick-up coil has wound 40000 turns with 0.02mm copper wire on 6mm wide of 4mm diameter spool. And pick-up coil was placed in radial direction. Lift-off was considered 1mm. Function generator(Agilent 33220A) was used for excitation of 50Hz continuous sine wave, and amplify the excitation signal using amplifier(Kepco BOP 36-6D). Lock-in amplifier(Femto LIA-MV-200D) receives the signal by pick-up coil for real time acquisition. An odometer which has 1.5mm pitch is applied for data sampling. Figure 5 shows the fabricated 3-bed RFECT system. It designed to enable running in one direction. Flaw can be detected by pull-rig test as shown figure 4.

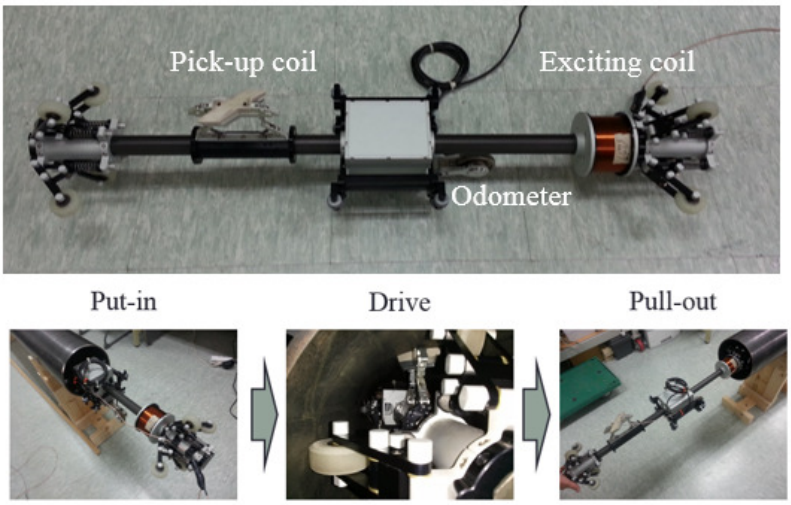

Figure. 5 The fabricated 3-bed RFECT system and pull-rig test

4. Flaw detection and evaluation

The main purpose of in-line inspection is the characterization of external flaws. For this work, data analysis method is important. The available data using lock-in amplifier are in-phase(X) and quadrature(Y) component. The relation of this two components is represented the amplitude and phase angle. The variation of magnetic field leaking in the vicinity of flaw present variation of amplitude and phase. So we can estimate the size of flaw using variation of amplitude and phase. Equation 3 and 4 are calculation of amplitude and phase.

$$\text{Amplitude(R)} = \sqrt{X^2 + Y^2} \tag{3}$$

$$\text{Phase}(\theta) = tan^{-1}\frac{Y}{X} \tag{4}$$

To verify the detectability of flaw, we has machined the artificial flaws which has length of 17.55mm and depth of 20~80% thickness of 8 inch pipeline. Thickness of 8 inch pipe wall is 5.8mm. The pull-rig test has performed in test pipe. Figure 6 show the scan data in the vicinity of the flaw. The amplitude and phase angle have increased depending on increasing depth. The distance between peaks represents length. And phase angle represents depth. This results show that depth are affected in both amplitude and phase angle. Figure 7 shows the relation of amplitude and phase angle depending on depth variation. The relations have a tendency with linearly increasing depending on increasing depth. The 20 % and 80% depth of flaw has evaluated in each of 33.46 degree and 71.48 degree. The phase angle is a difference of 6.33degree when the depth is increased 10%. So we can estimate the flaw size using a variation of amplitude and phase.

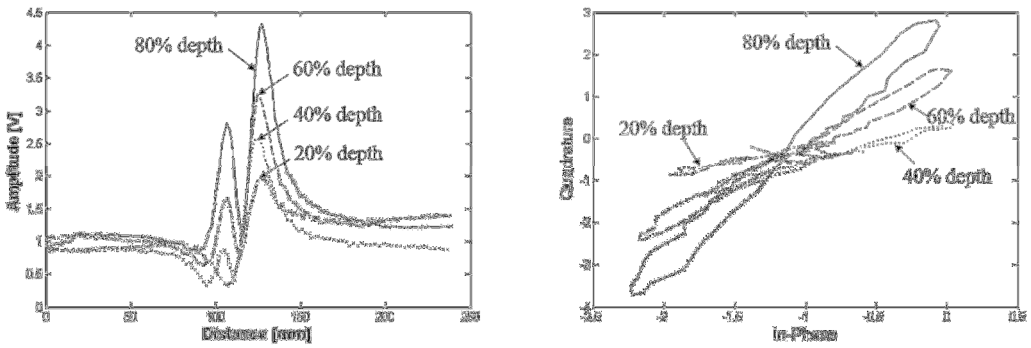

Figure. 6 Acquired signals of (a) amplitude and (b) phase depending on depth variation

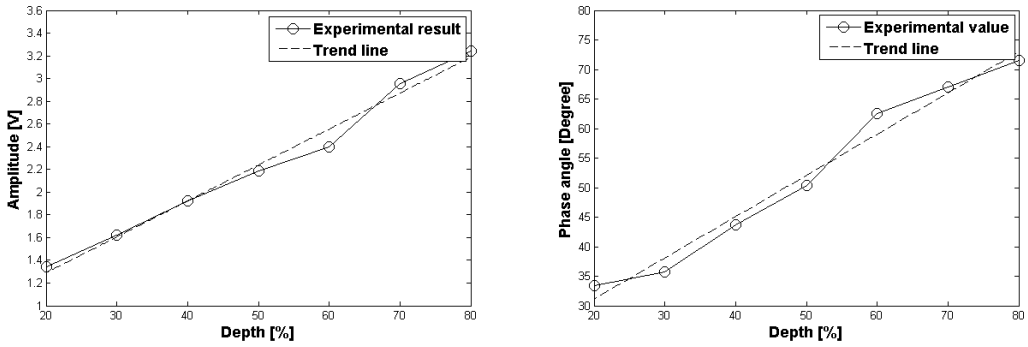

Figure. 7 The relation between (a) amplitude and (b) phase depending on depth variation

5. Conclusion

In this work, we focused on parameter study to develop the RFECT for inspection of ferromagnetic pipeline, to optimize the exciting and pick-up coils applied in 8 inch pipe. The exciting coil which can have higher magnetic moment contrast with lower power consumption was designed. Also pick-up coil was considered as high resolution type sensor and designed by increasing the induced electromotive force. The signal pattern and sensitivity depending on pick-up coil orientation was confirmed by pull-out test. Consequently detectability of flaw was verified using fabricated 3-bed system. Also characterization of the flaw by applying the relation between amplitude and phase angle was presented.

Acknowledgements

Research supported by ministry of knowledge economy in 2014 as South Korea's economic resources.

References

[1] W. Lord, S. Sun, S.S. Udpa, S. Nath, ″A finite element study of the remote field eddy current phenomenon,″ IEEE Transactions on Magnetics, Vol. 24, No. 1, pp. 435-438, 1988.

[2] David D. Mackintosh, David L. Atherton, and Sean P. Sullivan, ″Remote-field Eddy Current Signal Analysis in Small-bore Ferromagnetic tubes,″ Materials Evaluation, vol. 51, No. 4, pp. 492-495, 1993.

[3] Atherton, D. L, ″Remote Field Eddy Current Inspection,″ IEEE Transactions on Magnetics, vol. 31, pp. 4142-4147, 1995.

[4] David Atherton, David Mackintosh, Sean Sullivan, J. M. S. Dobois, and Thomas Schmidt, ″Remote-field Eddy Current Signal Representation,″ Materials Evaluation, vol. 51, No. 7, pp. 782-789, 1993.

Evaluation of Effect of the magnetic field on the Exciter tilting of RFECT System Module in pipeline.

Jeong-won Park[1], Jae-ha park[1] , Sung-jin Song[1] Hak-joon Kim[1]
School of Mechanical Engineering, Sungkyunkwan Univ., 300 chunchun-dong, Jangan-gu Suwon 440-746, Requblic of Korea

E-mail address (corresponding author): sjsong@skku.edu

In order to ensure structural integrity in domestic industrial facilities, various researches have been performed actively. Especially in storage tank or gas pipe, thinning and corrosion occurred by external environmental factors may one of major defect affect those structural integrity. In General, defect inspection methods of thinning and corrosion are Ultrasonic(include EMAT), Eddy Current (include Pulsed ECT and RFECT) and etc.

Among them, Eddy Current methods have great potential to rapid inspection of gas pipe or gas storage tank. These methods do not require coupling materials and, especially, RFECT used for inspection of pipe with ferromagnetic.

Thus, in this study, we studied tilting, misalign, distance between exciter and receiver, receiver shape and orientation to RFECT signal when driving the pipeline based on FEM simulation and experiment.

Keywords: RFECT, Exciter tilting, Receiver.

Improvements to Surface Detection Algorithm for the TFM Beam Former

R.L. ten Grotenhuis[1], R. Fernandez-Gonzalez[2], N. Saeed[1, 3], M. Wang[2], T. Zulueta[2], A. Hong[1], and Y. Verma[1]

[1]Ontario Power Generation, Inspection & Maintenance Division, 800 Kipling Ave. Toronto, Canada; E-mail (corresponding author): ray.tengrotenhuis@opg.com

[2]University of Toronto, Institute of Biomaterials and Biomedical Engineering, Canada

[3]University of Toronto, Division of Engineering Science, Canada

Abstract

Ontario Power Generation's (OPG) Matrix Inspection Technique (MIT) is based upon the combination of the Full Matrix Capture (FMC) UT acquisition technique with the Total Focusing Method (TFM) beamformer. This recent development has yielded outstanding results in several CANDU field inspection campaigns from 2010 to present. The inspection coverage and resolution of pressure boundary fitting to fitting weld geometries is unsurpassed in the TFM derived intensity images. Current work directed towards the Inspection Qualification of the MIT system has provided an opportunity to re-examine the surface detection strategy applied to the TFM images. Previous versions of the TFM beamformer employed the Canny edge detector. The Canny detector is acknowledged as an excellent general-purpose algorithm however requires judicious selection of operating parameters as well as carefully constructed 'wrapper' logic to provide stable results in the MIT application. Unique characteristics and specific features are typically observed in high quality TFM images. It is believed these characteristics could be exploited by a bespoke edge detector in a way that affords greater robustness in the final result. The new strategy was implemented to address several challenging scenarios highlighted in field based OPEX. Rejection of grating lobe artefacts, suppression of ring-down noise and identification of isolated discontinuities are issues specifically addressed by the new edge detector. Modification of the wrapper logic also permitted isolation of features of the weld pool ripple, the constituent data provided by contributions across the elevation direction of the transducer. Isolation of these features in turn enables superior imaging of the weld volume. This paper describes the development of an enhanced edge detector and the resultant performance on data sets obtained from the field.

Keywords : Total Focus Method (TFM), Beam Former, Surface Detection, Edge Detection, Image Analysis

1. Introduction

The CANDU nuclear units operated by Ontario Power Generation (OPG) have experienced Flow Accelerated Corrosion (FAC) in carbon steel piping of the Primary Heat Transport (PHT) system (Figure 1). Areas located at the weld root and immediately downstream are particularly prone to highly localized FAC. These locations are particularly challenging to inspect due to the confluence of complicating factors. The factors include: constrained access, small diameter pipes, fitting to fitting configurations, presence of unground weld caps, and a demanding inspection specification.

NDE Projects Department devised a novel inspection system in response to this inspection challenge, called the Matrix Inspection Technique or MIT. The system developed employs the Full Matrix Capture (FMC) data acquisition method in combination with a proprietary version of a two media Total Focussing Method (TFM) beam former [1]. It was first deployed in 2010 and since that time has been used in four inspection campaigns.

MIT has evolved and several changes have been made to address deficiencies, enhance productivity and improve overall capabilities. A sufficient body of inspection Operating Experience (OPEX) has been established to facilitate an Inspection Qualification (IQ) exercise. At OPG the IQ of the MIT system is proceeding on facets of the system that are accepted as appropriate and hence not subject to change. The schedule for the IQ activity has given impetus to

assess the MIT system for potential modifications prior to completion of the IQ exercise. One of the areas identified as a candidate for improvement is the TFM beam former algorithm.

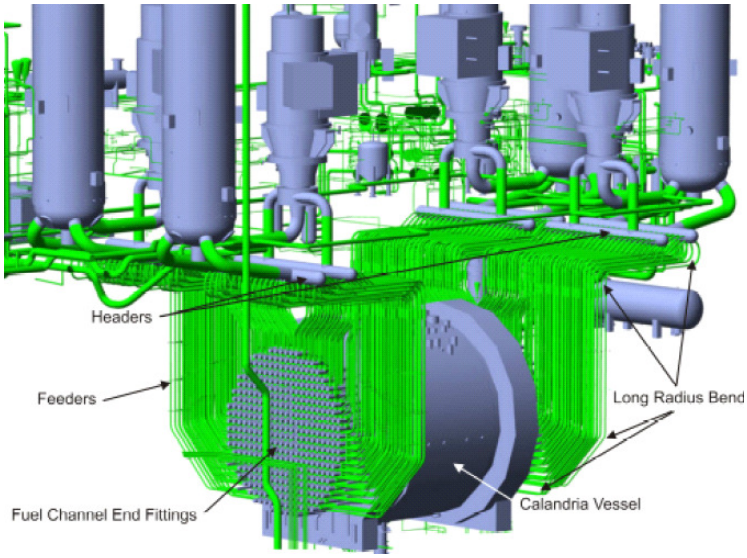

Figure 1. CANDU PHT General Configuration

2. TFM Beamforming and Imaging

2.1 TFM Overview

A description of the TFM beam former follows from Figure 2. First, pre-processing is applied to the raw data, including zero-phase bandpass filtering, up-sampling and formation of the analytic waveform. The outside diameter (OD) or exterior surface of the inspection sample is imaged using a series of sub-apertures, calculating the flight times for transducer element pairs within the aperture to each point in the region imaged. The size of the sub-aperture is optimized based on the distance to the focal point. The arrival time of the interface signal in the linear electronic B scan is used to set the centre of the zone to be imaged. An intensity image is rendered as the signal envelopes of the analytic waveforms are summed for the collection of points in the image zone. Once the OD intensity image is successfully formed, coordinates of the OD surface are obtained by applying an edge detection algorithm.

Imaging of the interior volume essentially follows the same algorithm as defined for the OD however has the added complication of solving for the correct flight time from the transducer element to the desired focal point through the edge-detected OD surface. This is accomplished by sequentially evaluating the flight times through the OD to isolate the path of least time, otherwise known as the Fermat's principle. The coordinates of the inside diameter (ID) or interior surface are obtained by again applying an edge detection algorithm. OD and ID surfaces are created for FMC data acquired at each specific, circumferential location on the specimen, called a *frame*. These are evaluated for the minimum distance between the two surfaces, and finally compiled into a 3D rendering of the inspected specimen.

2.2 Canny Edge Detector

Edge detection plays a central role in the overall performance of the MIT imaging method. The edge detector chosen for this application is the Canny operator, which is a member of operators known as first order or gradient edge detectors. Other members of this category include Prewitt, Sobel, and Phase Congruency. Canny is widely acknowledged as an optimal, general purpose, first order edge detector, defined by a series of steps [2]:

1. Image smoothing using a Gaussian filter to reduce noise that gives rise to spurious gradients. Key parameters include the standard deviation, σ, which determines the degree of smoothing and the size of the Gaussian kernel which specifies the number of pixels to sample while filtering (Figure 3).

2. Finding gradient magnitudes (or *edge strength*) and directions to mark pixels that meet the gradient criteria

as possible edge points.

3. Non-maximum suppression to ‘thin’ the edges, preserving only the local maximum gradients.

4. Edge tracking by hysteresis to connect maximum gradient points with weaker maxima in adjacent regions to form segments of a detected edge.

5. Geometric dilation and erosion to link segments into a continuous surface where possible.

The OPG implementation of the edge detector includes additional logic to reject non-relevant edges, address aberrations, and interpolate in regions of weak image intensity where no edges were detected. Since only the leading OD and ID surfaces are desired, the trailing or lower sides of closed edges are non-relevant and aberrations include curved edges wrapping around the ends of the imaged region.

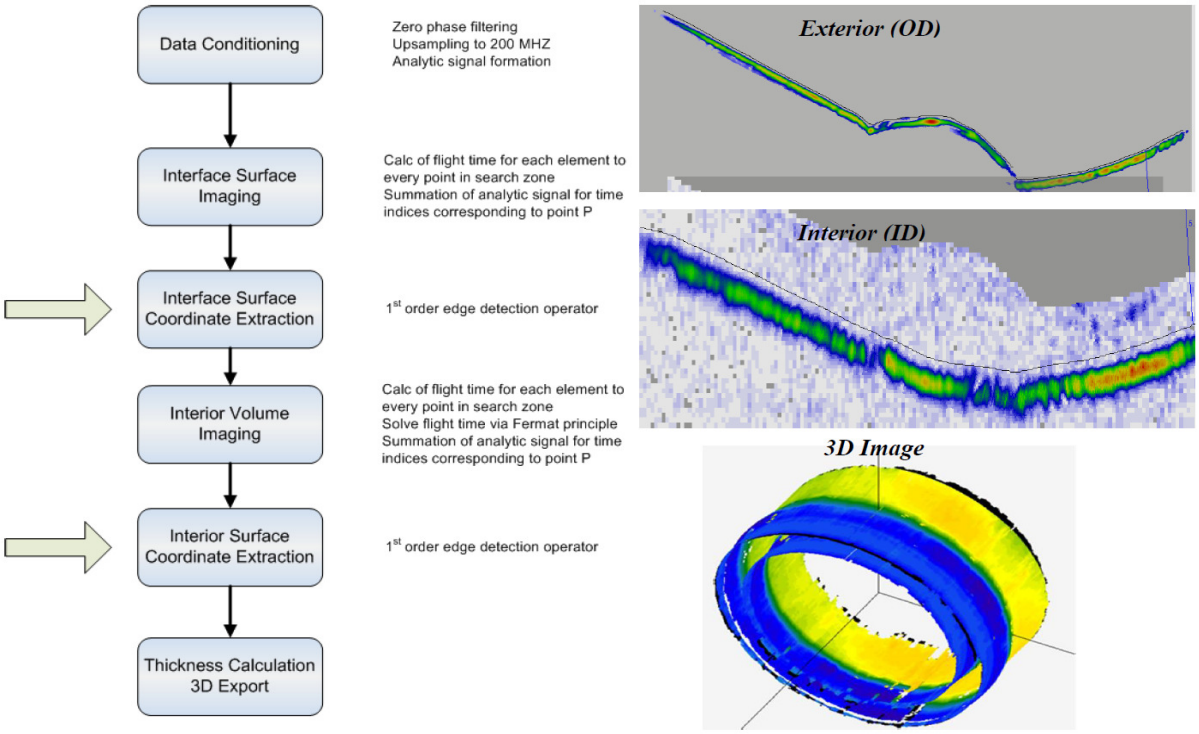

Figure 2. High level functions within the dual media TFM imaging method.

Figure 3. *(Left)* The 'LENA' benchmark image. *(Centre)* Canny edge detection with σ = 0.15. *(Right)* Canny edge detection with σ = 0.28.

3. Field Images

Parameters associated with the TFM beamformer and the Canny algorithm were established through trials on reference samples and spool pieces, for which the performance yielded accurate, consistent results. When applied in the field, similar performance was obtained in the majority of cases. These inspection campaigns presented some cases where the performance of the edge detection method was observed to be degraded. These conditions, discussed in detail in this section, briefly included:

- False detection of non-relevant surfaces on the OD, including grating lobe artefacts and the crest of air bubbles
- Inaccurate interpolation of missing surface regions
- Inappropriate detection of interior volume pulse ring-down artefacts
- Over-smoothing of ID in presence of rapid contour changes or attenuated (weak intensity) regions

3.1 Outer Surface Edge Detection

OD images compose of 2 main regions, the parent material and the weld cap. These can be further subdivided into local features with unique properties (Figure 4A):

Parent Material

Canny generally performs reasonably well detecting smooth edges of the OD parent material. However, parent material can have texture (variations in the vertical direction with short duration in the circumferential direction) which is currently undetected.

Weld Cap

The single, continuous surface assumption used for a parent material cannot be applied to the weld cap. This is because surfaces of the weld cap consist of fine ripples, overlaps, ridges and valleys all of which become manifest in the TFM intensity images (Figure 4B). The peaks and troughs of the weld pool ripples may segment the weld into individual entities/bodies or multiple surfaces lying on top of one another. These features can be easily delineated visually by observing the intensity patterns on the images. Observations of adjacent frames show that as one surface builds in, the other fades out with steps in the circumferential direction (Figure 4C).

Weld Toe

A third critical feature of the weld is the weld toe, defined as the junction between the weld and the parent material. In some cases, the weld cap is flat enough that the contour between the parent material and the cap will be continuous. In cases of a higher weld cap, the image will have a discontinuity due to the directivity of the transducer elements restricting the transducer from ‘seeing’ surfaces at large angles. Currently, linear interpolation is applied but results in a poor approximation of the missing surface (Figure 4C).

3.2 Inner Surface Edge Detection

ID images consist primarily of horizontal surfaces, but can vary in intensity considerably through the regions of the parent material, under the weld cap to the parent material on the remaining side. Highly localized wall loss may result in rapid contour changes in the circumferential direction which the edge detector must accurately delineate. Noisy features of the ID volume, including speckles and anomalous ring-down artefacts from decaying pulses of the transducer interrupt the current edge detector.

3.3 Effects of Gaussian Smoothing

Canny performs reasonably well outlining the overall OD and ID surfaces at the expense of local features due to the Gaussian blurring. Mathematically, applying a Gaussian filter reduces the image’s high frequency components which removes noise and makes the edges smoother. However, besides noise, details such as fine contours and underlying weld surfaces are also smoothed out (Figure 5).

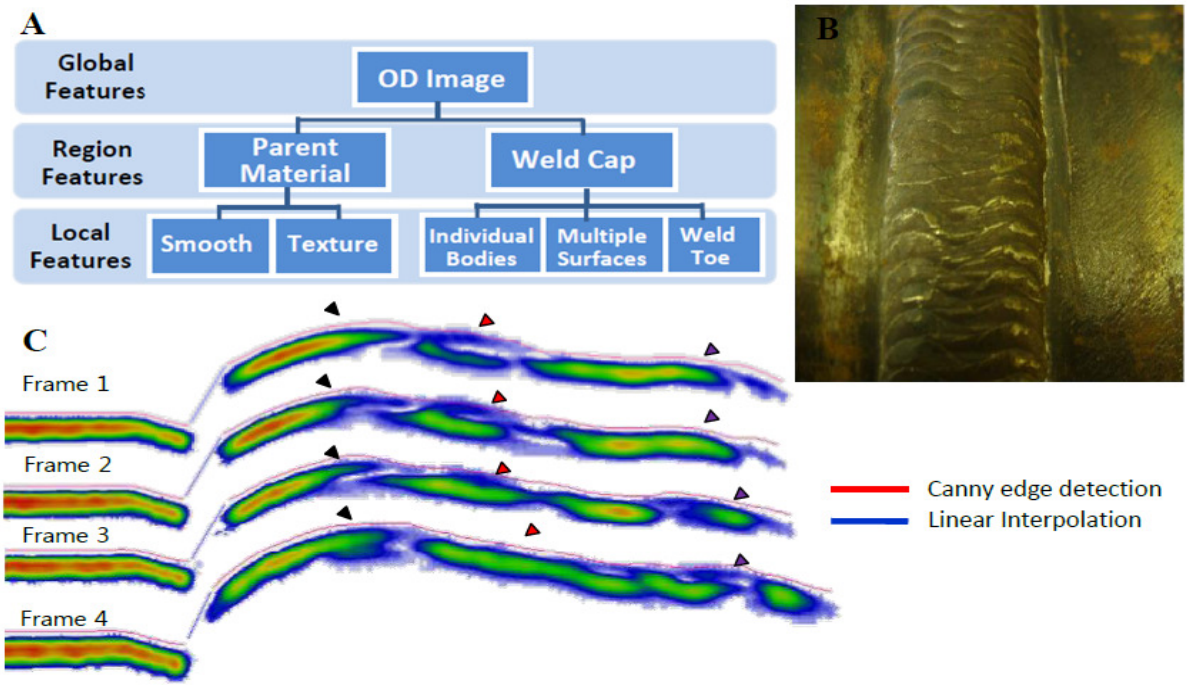

Figure 4. (A) Features of OD Images. (B) Weld cap ripples on a piece of pipe. (C) OD Intensity Images showing building in and fading out of peaks and troughs of a ripple pool in adjacent frames. Canny edge detection and linear interpolation at the weld toe are shown.

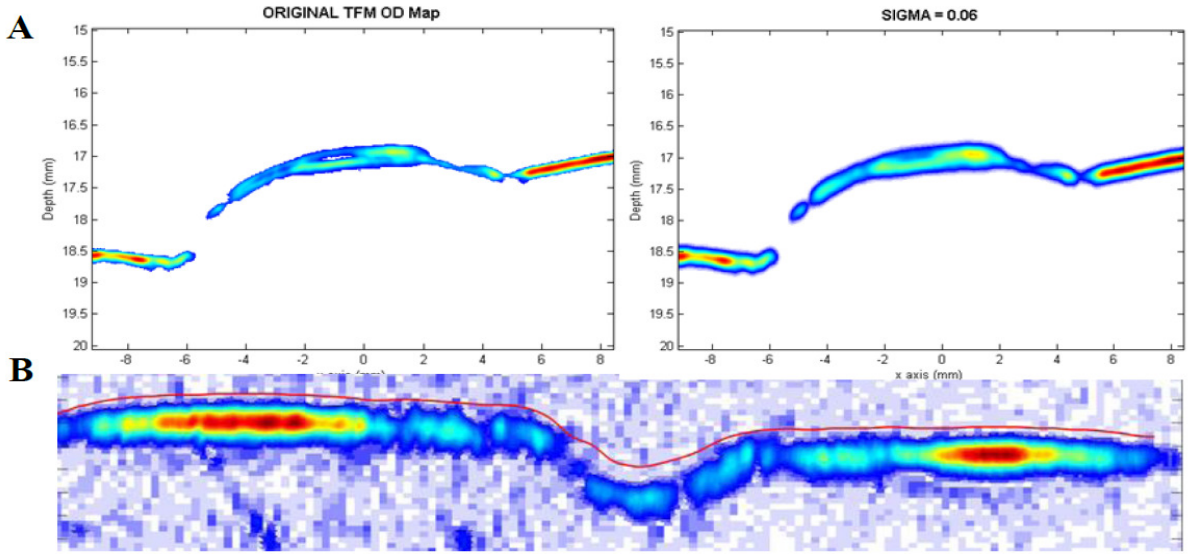

Figure 5. Effect of Gaussian Smoothing. (A) Loss of OD features (B) Improper ID contour following.

Use of conventional edge detection strategies is challenged by the results of TFM imaging. Underlying reasons for reduced performance are:

- Inherently wide dynamic intensity range of relevant features in the image
- Variable signal to noise ratio from image to image
- Resolution mismatch arising from fine resolution available in the time-denoted direction in contrast to the pixel resolution limit imposed by element geometry

Some of the above issues could be addressed by applying even more sophisticated wrapper logic to the Canny algorithm; however, a re-evaluation of the edge detection approach was undertaken instead.

3. Improved Algorithm

The proposed algorithm comprises of comprehensive techniques implemented in MATLAB 2012 [3], described as follows:

Step 1: Triangle Thresholding

The intensity image is binarized using a Triangle Threshold to separate foreground and background pixels [4]. Thresholding is a simple technique where intensity values greater than a threshold are set as foreground (objects of interest) and all other pixels are voided as background. Unlike conventional fixed thresholding, triangle method investigates the histogram (or *intensity range*) of each image to automatically determine the optimum threshold value (Figure 6A). Since OD and ID features can have relatively weak intensities in the histogram, this method is particularly effective.

Step 2: Morphological Opening

A morphological opening is applied to erode the binary image in order to separate objects in close proximity to each other. The technique facilitates the identification of multiple weld surfaces which sometimes blend into each other and hence can be difficult to distinguish.

Step 3: Connected Component Labeling

The binary image from Step 1 is 'grouped' into connected components based on pixel connectivity. The process enables extraction and labeling of various features such as the parent material, individual weld cap entities, and objects representing noise.

Step 4: Identification of Valid Objects

Conditions related to object size, long-to-short axis ratio, and angle with respect to horizontal are tested for each labeled object to identify valid objects and eliminate specific artifacts including grating lobes, ring down, and interior volume noise.

Step 5: Surface Detection

The labeled image containing only valid objects is scanned column-by-column to detect the upper surfaces. For every column, the position of the surface is determined as the first non-zero (non-background) pixel. Scanning continues beyond the surface, and subsequent non-zero pixels encountered after a background pixel are determined to be underlying surfaces.

Step 6: Upper Surface Interpolation

Missing surface segments are then connected using Piecewise Cubic Hermite Interpolating Polynomials (PCHIP), which are piecewise cubic polynomial functions [5]. PCHIP interpolation connects a number of predefined points ensuring that their first derivatives are continuous, and that monotonicity of the data is preserved. PCHIP-based interpolation creates smooth edges in regions where edge detection had failed, particularly the weld toe and weak ID regions beneath the weld cap.

Step 7: Multiple Surfaces Interpolation

Underlying surface pixels are connected using *Dijkstra's* minimum cost path search algorithm [6]. The blending and spatial proximity of weld features make polynomial interpolation ineffective here. *Dijkstra's* algorithm identifies the "cheapest" path based on intensity values between the ends of disconnected surface segments, such that the reconstructed boundary would follow the most intense set of pixels between both segments (Figure 6B).

Step 8: Smoothing

Edges are filtered and smoothed using local regression methods in MATLAB to decrease influence of outliers as well as jaggedness of final surfaces.

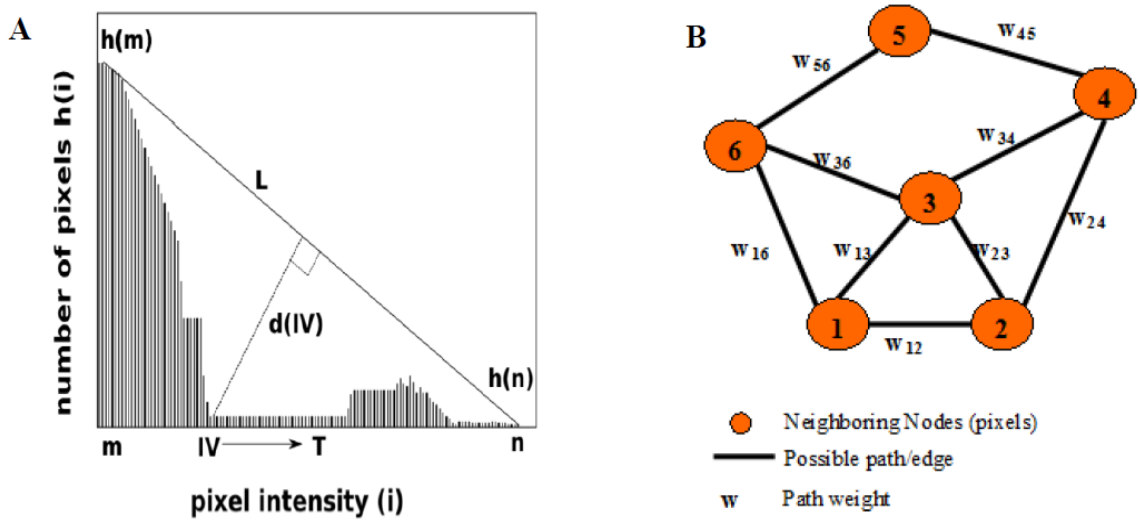

Figure 6. (A) Triangle Thresholding. Line *L* is constructed between the histogram maximum, *h(m)* and minimum, *h(n)*. Pixel value IV at which distance *d(IV)* normal to *L* is maximized is located, and then a fixed constant is added to determine threshold value, *T*. (B) Dijkstra's Search Algorithm. A bidirectional, weighted graph is built to find the 'cheapest' path between pixels based on intensity values.

4. Results

Improved results from the proposed edge detection algorithm are shown in Figures 7-10.

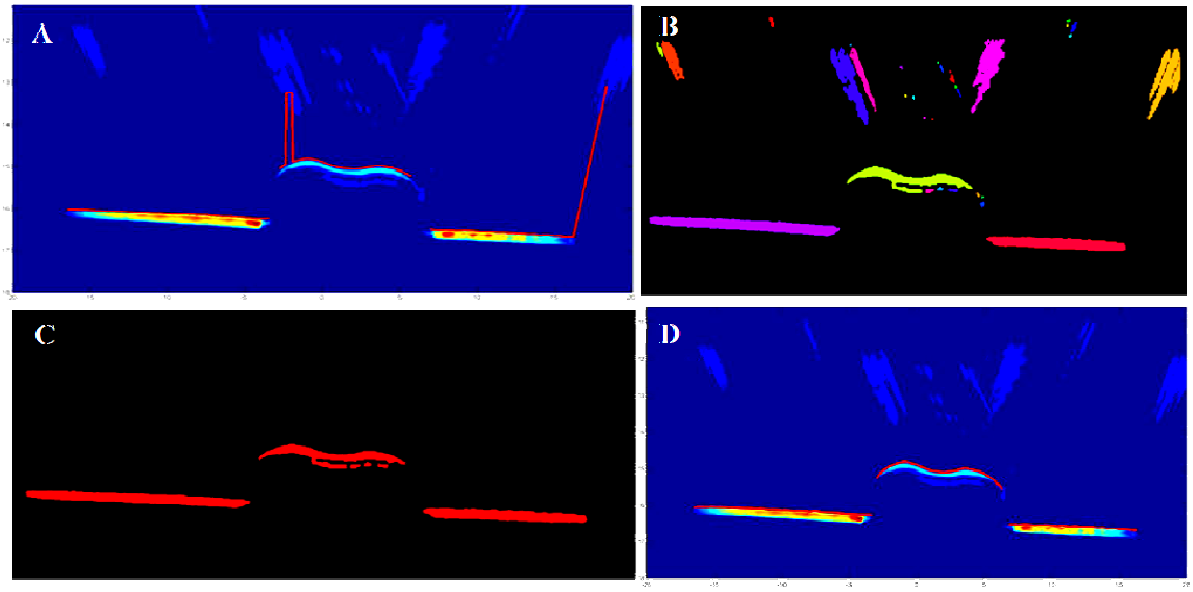

Figure 7. Artifacts Removal from Intensity Images. (A) Grating lobes being picked up by Canny gradient-based edge detector. (B) Thresholding and labeling of binary image. (C) Valid objects retained based on morphology, size, and orientation. (D) Edge detection result *without multiple surfaces and interpolation*.

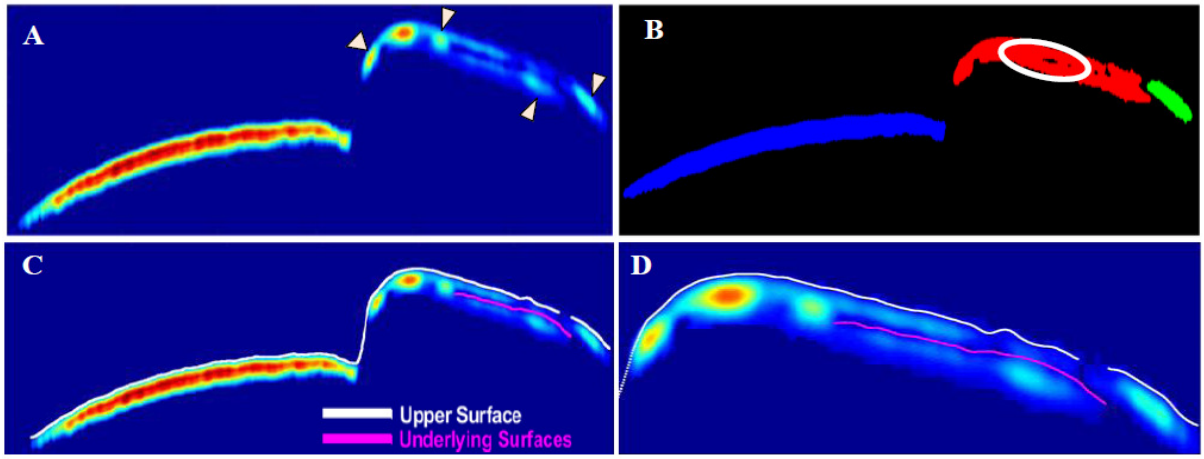

Figure 8. OD Feature Detection. (A) Individual entities of weld cap. (B) Thresholding, object labeling and morphological opening to distinguish between multiple surfaces. (C-D) Detection of multiple OD surfaces.

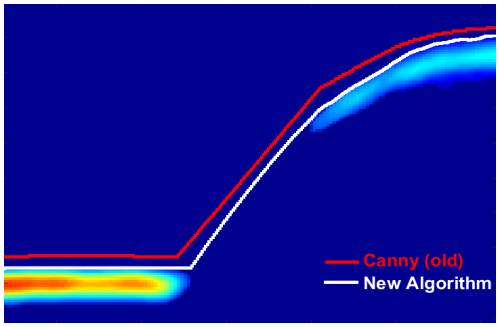

Figure 9. Weld Toe. Piecewise Cubic Hermite (white) versus Linear Interpolation (red).

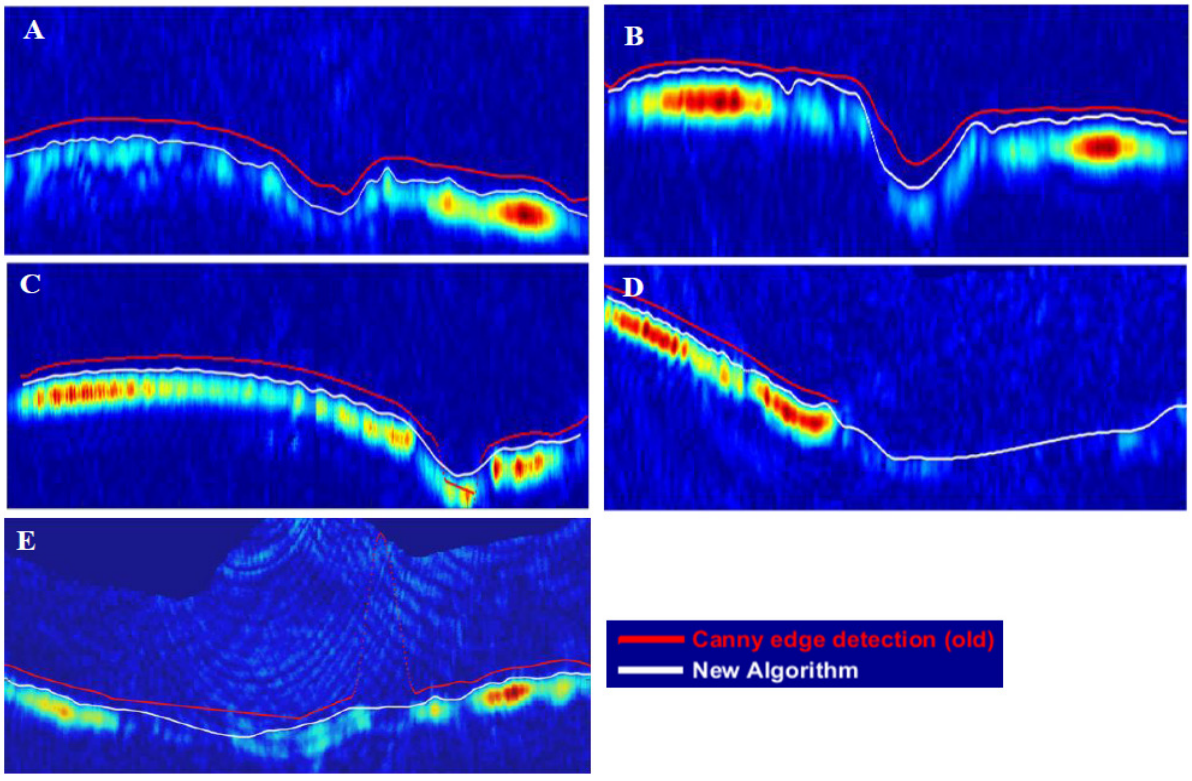

Figure 10. ID Edge Detection. (A-C) Improved texture and contour following. (D) Improved detection of weak surfaces. (E) Rejection of ring-down artifacts.

5. Quality Metric

The proposed algorithm detects surfaces scanning a binary image column-by-column. Ultrasonically, TFM beam forming and image formation occurs in a direction approximately normal to the surface. One way to assess the quality of surface detection is to 'walk along' the detected edge points, and evaluate the intensity profile normal (perpendicular) to the surface point based on a fit to a desired profile using Gaussian fitting. The normal intensity profile is fitted by a single Gaussian function (Figure 11A) or in case of multiple surfaces, the profile has two maxima and is fitted using a sum of Gaussians instead (Figure 11B). To perform the fitting, a Gaussian curve is defined as:

$$G(z) = \frac{s}{\sigma\sqrt{2\pi}} \cdot e^{-\frac{(z-\mu)^2}{2\sigma^2}} \quad \text{..... (1)}$$

where μ is the mean of the Gaussian, σ is the standard deviation, s is the amplitude, and z are the coordinates of the intensity profile along the line perpendicular to the edge. To evaluate the goodness-of-fit, a correlation coefficient, ρ, between the line intensity profile and the fitted function is calculated as:

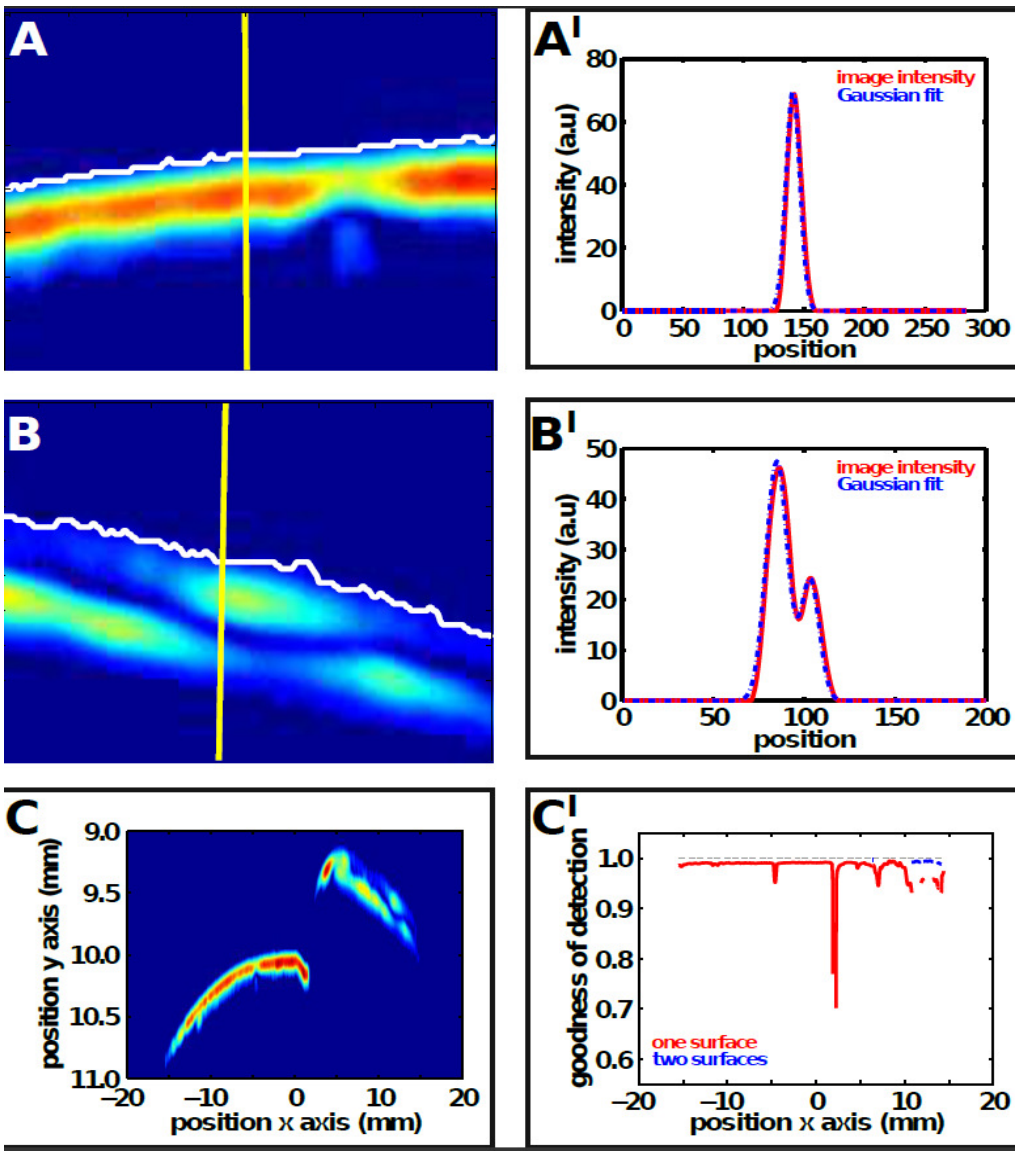

Figure 11. Surface Detection Quality Measure. (A-B) Normal line (yellow) to the detected edge (white) at different points along the surface. Fitting the normal intensity profile with a Gaussian function (A^I) or a sum of Gaussians (B^I). (C-C^I) Goodness of fit for upper (red) and second (blue) OD surfaces along the image horizontal. Missing image regions such as the weld toe cause a sharp drop in detection reliability.

$$\rho = \frac{cov(Y,G)}{\sigma_Y \sigma_G} \quad \text{.....(2)}$$

where $cov(Y,G)$ is the covariance between the intensity profile values, *Y,* and the Gaussian function, *G*, and σ_Y and σ_G are the respective standard deviations.

The correlation coefficient measures the dependence between the functions that are being evaluated, and varies from 1 to -1, with 1 indicating a perfect correlation, -1 a perfect anti-correlation, and 0 no correlation. In most cases, the goodness-of-fit is very close to 1 but provides a useful relative measure of surface detection reliability (Figure 11C). Regions of low fit *relative* to other regions of the image will suggest where edges may be less reliable.

6. Conclusions

A UT inspection system has been developed incorporating FMC data acquisition with a two media TFM beamforming and imaging strategy. Accurate, robust surface detection is central to the beamforming function. The Canny edge detector was originally selected for this application and has been proven to be suitable under most conditions encountered on the field. Performance of the edge detector is diminished as inspection conditions deteriorate or as surfaces present rapid changes in profile.

A revised edge detection strategy has been developed to address these shortcomings. The edge detection problem has been divided into unique regions that can be treated separately. Triangle thresholding has been introduced to accommodate changes in signal to noise ratio with morphological operators applied to the resulting binary image. Potential objects are filtered using a series of rules to reject non-relevant indications and isolate features of interest.

The new edge detection strategy has been applied to a series of test images representing weld pool ripple, weld toe area interpolation and rapid changes in interior contour. In all cases the new approach has outperformed the previous method based on the Canny detector.

A quality of fit metric was developed to evaluate the success of the edge detection process. This same metric can be leveraged to provide an overall confidence level for the surfaces detected in the different regions of the TFM image and hence the final results.

Acknowledgements

This study was funded by an engage grant from Natural Sciences and Engineering Research Council of Canada (NSERC).

References

[1] R. Ten Grotenhuis and A. Hong, "Imaging the Weld Volume Via the Total Focus Method", *4th International; CANDU In-service Inspection Workshop and NDT in Canada Conference*, Toronto (2012)

[2] M. S. Nixon and A.S. Aguado, *Feature Extraction and Image Processing,* 3rd ed. London, UK: Elsevier, ch. 4, pp. 140-173 (2012)

[3] *MathWorks – MATLAB and Simulink for Technical Computing.* Available: http://www.mathworks.com/

[4] G. Zack, W. Rogers, and S. Latt, "Automatic measurement of sister chromatid exchange frequency" , *Journal of Histochemistry & Cytochemistry,*Vol. 25, No. 7, pp. 741-753 (1977)

[5] F. N. Fritsch and R. E. Carlson, "Monotone Piecewise Cubic Interpolation", SIAM J. Numerical Analysis, Vol. 17, No. 2, pp. 238-246 (1980)

[6] E. W. Dijkstra, "A note on two problems in connexion with graphs", *Numerische mathematik,* Vol. 1, No. 1, pp. 269-271 (1959)

Evaluation of Interface Property for Thin Film by Laser Interferometer

Hae-Sung Park[1], Sanichiro Yoshida[2], David Didie[2] and Ik-Keun Park[1]

[1]Department of Mechanical & Automotive Engineering, Seoultech
232 Gongneung-ro, Nowon-gu, Seoul 139-743, Korea
[2]Department of Chemistry and Physics, Southeastern Louisiana University
SLU 10878, Hammond, LA 70402, USA

E-mail address(corresponding author) : ikpark@seoultech.ac.kr

Thin Film systems are used in a variety of area such as fuel cell, semi-conductor, prosthetic joints, LED display…etc. Since the thin film is composed of dissimilar materials, the residual stress can be induced at the interface and it can significantly affect the life of thin film. Therefore it is important to evaluate the interface property for the thin film.

In this paper, we proposed optical method using laser interferometer which combined with acoustic method. In order to form the interference by specimens, these are replaced with end-mirror in conventional Michelson interferometer and oscillated from acoustic transducer which attached on backside of substrate. The contrast of fringe pattern depends on oscillation amplitude at the interface of thin film. Thus we can evaluate the behavior of interface by Fourier spectrum analysis on the fringe pattern.

Two kinds of platinum specimens which fabricated from different method were tested. The one was treated by pre-surface O_2-plasma before the deposition (treated Pt) and the other one was deposited on the substrate without treatment (untreated Pt). It is generally known that treated case has better interface property. Interestingly, however, the spectrum peak by Fourier spectrum analysis for the treat Pt was lower than those of the untreated Pt at the certain frequency. The result shows that the pre-surface O_2-plasma treatment not always makes the better performance.

Keywords: Thin Film, Acousto-optic system, Michelson Interferometer, Nondestructive Evaluation, Adhesion strength

Development of ultrasonic inspection techniques using a matrix array transducer for acoustical anisotropic media

Naoyuki Kono and So Kitazawa
Hitachi Research Laboratory, Hitachi, Ltd.
7-2-1 Omika-cho, Hitachi-shi, Ibaraki, 319-1221, Japan

E-mail address : naoyuki.kono.jm@hitachi.com

Ultrasonic inspection techniques utilizing a matrix array transducer have been developed for non-destructive evaluation of anisotropic media. In the ultrasonic phased array techniques, point focusing beams are transmitted and received by appropriate setting of delay laws applied to each transducer element. The delay laws in anisotropic media are derived by propagation paths calculation based on ray tracing method. From the ray tracing calculation, efficient insonification angles are also evaluated by density of propagating rays in the media. Inspection results are represented as cross section images, and image distortion due to beam skewing in anisotropic media is compensated by ray tracing for each beam of sector scanning. In this study, capability of the ultrasonic inspection techniques assisted ray tracing in anisotropic media are evaluated by sizing of artificial notches prepared in test pieces with homogeneous anisotropy, as the first step of development for anisotropic media, e.g. a weld metal. The test pieces are made of built-up welded austenitic stainless steel. Sizing accuracy for anisotropic material is improved with a combination of selecting appropriate insonification angles and distortion compensation of cross section images, derived from ray tracing calculation.

Keywords: phased array, anisotropy, ray tracing, matrix array

A Study of Laser Generated Guided Ultrasonic Waves for Measuring Elastic Modulus of Metal Thin Film Layers on Silicon Substrate

Taehoon Heo[1,2], Bonggyu Ji[1,2], Bongyoung Ahn[1], Gang-Won Jang[3] and Seung Hyun Cho[1]
[1]Korea Research Institute of Standards and Science, Center for Safety Measurement, 267 Gajeong-ro, Yuseong-gu, Daejeon 305-340, Republic of Korea
[2]University of Science and Technology, 217 Gajeong-ro, Yuseong-gu, Daejeon 305-350, Republic of Korea
[3]Sejong University, 209, Neungdong-ro, Gwangjin-gu, Seoul 143-747, Republic of Korea

E-mail address(corresponding author) : seungcho@kriss.re.kr

The accurate measurement of mechanical properties of thin films in MEMS/NEMS structures is very necessary to improve the reliability of their design and manufacturing. However, existing methods to measure them, such as a tensile test or a resonance test, cannot be applied to thin films because of its quite small thickness. In this work, the method of elastic modulus measurement using laser generated guided ultrasonic waves, which propagating through constant geometric boundaries, is concerns for noncontact and nondestructive measurement so guided wave excitation and detection system using a pulsed laser and a laser interferometry has been established. Also an elastic modulus extraction algorithm from the measured guided wave signal was developed to build dispersion relations between wave speed and frequency. Finally, it was applied to actual metal thin film structures of Al-Si and Ni-Si multilayers. From experimental results, we confirm that the proposed method has considerable feasibility to assess elastic properties of metal thin films on silicon substrate.

Keywords: Laser based ultrasonic, Guided wave, Thin films, Elastic modulus

Real-time Adaptive Imaging for Ultrasonic Nondestructive Testing of Structures with Irregular Shapes

Sébastien Robert[1], Léonard Le Jeune[1], Vincent Saint-Martin[1] and Olivier Roy[2]
[1]CEA-LIST, Centre de Saclay, 91191, Gif-sur-Yvette Cedex, France
[2]M2M, 1 rue de Terre-Neuve, 91940, Les Ulis, France

E-mail address: sebastien.robert@cea.fr

Immersion ultrasonic testing of structures with irregular geometries may be significantly enhanced by using phased-arrays and specific adaptive algorithms that allow to image flaws under a complex and unknown interface. The common principle of all immersion methods adaptive can be summarized in two key-steps: first, the surface is determined by recording and processing the interface echoes; second, the ultrasonic ray paths through the measured surface are calculated to update the focusing laws and to preserve the image quality inside the structure.

In the first part of this communication, we present an adaptive imaging method based on the Synthetic Transmit Aperture (STA) technique, also called Total Focusing Method (TFM). The acquisition scheme consists in transmitting a large number of cylindrical waves by firing the array elements one by one. For each transmission, the backscattered waves are recorded with the whole array. In the proposed method, the recorded signals are processed a first time to image the surface of the test specimen and to extract its geometry. Once the surface geometry has been measured, a second TFM image can be displayed in the material by processing the same acquisition with focusing laws adapted to the surface. This processing is implemented in the portable M2M systems (developed in partnership with the CEA-LIST) to perform real-time adaptive imaging, and several results are presented and discussed in this paper.

In the second part, a new approach is proposed in order to accelerate imaging frame-rates and to reduce both the noise and the attenuation effects. In this approach, all the array elements are excited simultaneously to transmit planes waves in the specimen (instead of cylindrical waves characterized by lower amplitudes). Because the plane waves are less sensitive to noise and attenuation, we demonstrate that it is possible to obtain high quality images in complex specimens with a very small number of transmissions.

Improved Inspection Technique for Large Rotor Shafts, Using a Semi-Flexible Phased Array UT Probe

Guy Maes [1], Dany Devos [1], Patrick Tremblay [1]
Nobuyuki Hoshi [2], Hiroki Nimura [2], Hideaki Narigasawa [2]

[1] Zetec, zNDT Solutions, Québec, Canada
[2] The Japan Steel Works, Ltd., Hokkaido, Japan

Abstract

A new generation of nuclear power plants is being deployed worldwide. These new designs require large rotor shaft forgings with dimensions never seen before. Such heavy components present new challenges for non-destructive testing.

Due to the long sound path, conventional UT techniques cannot provide adequate detectability of the reference reflectors required by the existing codes. Also, some standards (e.g. VGB) require multiple angle beams to be applied in addition to the straight beam inspection, and this leads to long inspection times.

This paper will address the implementation and validation of phased array UT techniques, using a semi-flexible 2D array probe, for the inspection of large mono-block rotor shaft forgings. It will be shown how "Depth-Zone Focusing" and "Beam Steering" can be used to overcome the issues occurring with conventional UT probes.

Results of detectability measurements and data acquisitions on representative test specimens will be presented, and compared with conventional UT performance.

Various aspects of the hardware and software specification will be addressed, as well as the considerable reduction of the total inspection time.

Keywords: phased array probe, large forging inspection, rotor inspection

1. Introduction

Generation III+ nuclear power plants, especially those with more than 1100 MWe, require forged components which are a lot larger than those of previous plant designs. For instance, the size of mono-block rotor shaft forgings, as manufactured by The Japan Steel Works, Ltd. (JSW) is increasing: the maximum diameter of these forgings is reaching 3200 mm.

The acceptance criteria for rotor inspections during manufacturing are based upon the equivalent flat-bottom hole (FBH) size. Reflectors equivalent with a FBH of 0.9 mm diameter should be detected by ultrasonic testing in order to assure the quality of the component.

This is a very challenging requirement, and with increasing rotor shaft diameters, these small indications at the center of rotor shaft forgings could not be reliably detected with conventional UT probes. Due to the long sound path and the corresponding acoustic beam spread, the small indications cannot be discriminated from the grain noise.

In addition, the inspection of large mono-block forgings is very time-consuming. Some inspection specifications require the application of several angle beam techniques in addition to the straight beam technique. For example, the European VGB standard requires the use of angle beams at ±7°, ±14°, ±21° and ±28°. When using conventional UT (C-UT) on mono-block rotor shaft forgings with a diameter of 2800 mm, it would take approximately one month to complete scanning with all beam angles required by the European specification. Obviously, this has a big influence on the manufacturing process, and might decrease productivity.

This paper will show that phased array UT (PA-UT) technology can overcome the challenges related to the inspection of large mono-block rotor shaft forgings, due to the following characteristics:

- The active aperture of the UT probe should be increased, to yield more acoustic energy on the reflector by a smaller divergence of the UT beam; this could be done using a larger conventional UT probe, but it will be better addressed by the PA technology: the use of multiple pulse generators and multiple smaller elements leads to a better pulse energy transfer as compared to a single generator and a large active surface of a conventional probe
- The capability to focus acoustic energy at various depths is another advantage of PA-UT technology; a single PA-UT probe can be used for the whole rotor and the focal depth can be optimized for each section, thus improving the signal-to-noise ratio of the small reflectors compared to the grain noise (see Figure **1**: Depth focusing with PA-UT probe to improve SNR on small reflectorsFigure **1**); in addition, being able to change the focal depth gives more flexibility in terms of specimen dimensions on which the probe can be used
- PA-UT probes can be used to generate multiple acoustic beams within the same scanning sequence, and therefore the total scanning time is expected to be drastically decreased (see Figure 2)

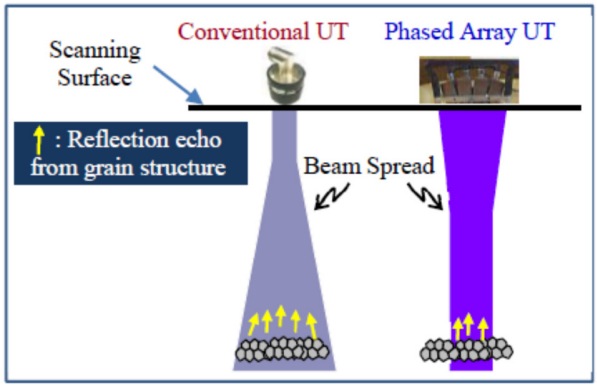

Figure 1: Depth focusing with PA-UT probe to improve SNR on small reflectors

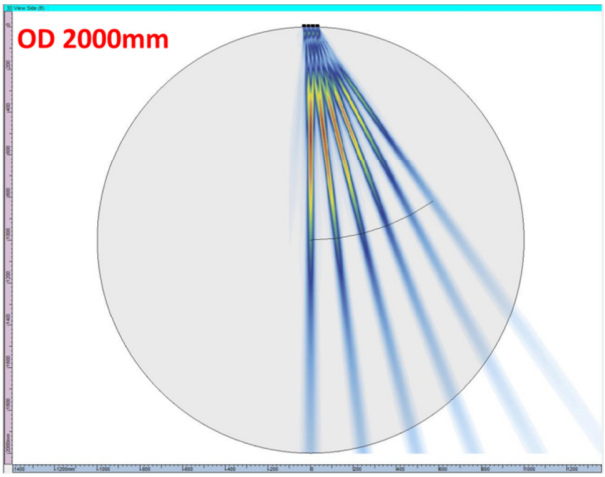

Figure 2: Example of beam steering with PA-UT probe on 2000 mm diameter rotor

2. Semi-Flexible Phased Array Probe Design

Zetec has designed an innovative new PA UT probe, which consists of 4 individual matrix arrays of 8 x 8 elements and aperture of 16 mm x 64 mm [1]. The 4 matrices are mechanically linked and are used as a single array (see Figure 3). Due to the mechanical linking, the 2M8x8E16-64-QUAD probe assembly allows an adequate direct coupling on diameters of 250 mm and up, thus allowing for conducting efficient inspection of a complete rotor with multiple stages. It also provides the benefit to mechanically focus the acoustic energy towards the center of curvature of the inspected specimens.

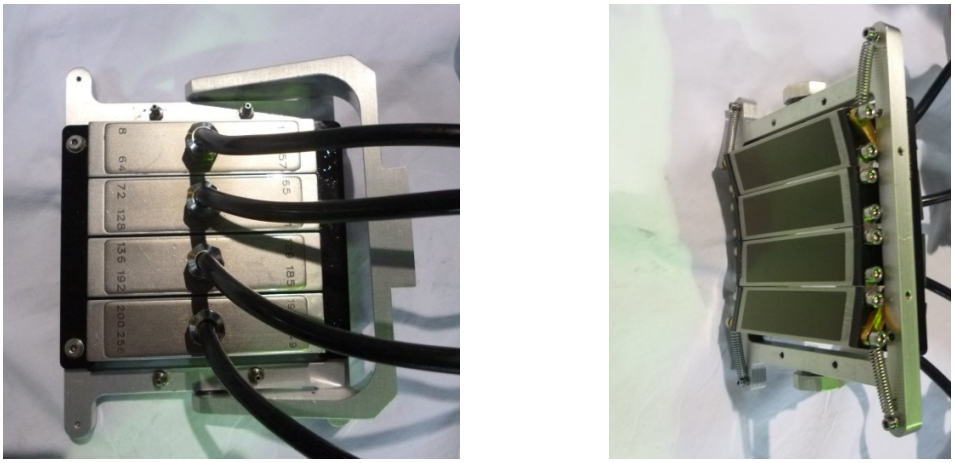

Figure 3: 2M8x8E16-64-QUAD Probe Assembly

The total active aperture of the PA-UT probe, 64 mm x 64 mm, has been determined by considering conflicting requirements: the long sound path required for rotor inspection requires high energy and thus large aperture, whereas the need for steering capabilities requires small individual elements. Another parameter that has been considered is the maximum number of elements that can be simultaneously managed by commercially available PA hardware and software (256).

The active surface of the QUAD probe is approximately 9 times larger than the typical C-UT probe used for this application. Figure 4 shows the effect on the beam diameter at 2000 mm sound path. The slightly elliptical cross section for the QUAD probe is due to the inter-array spacing.

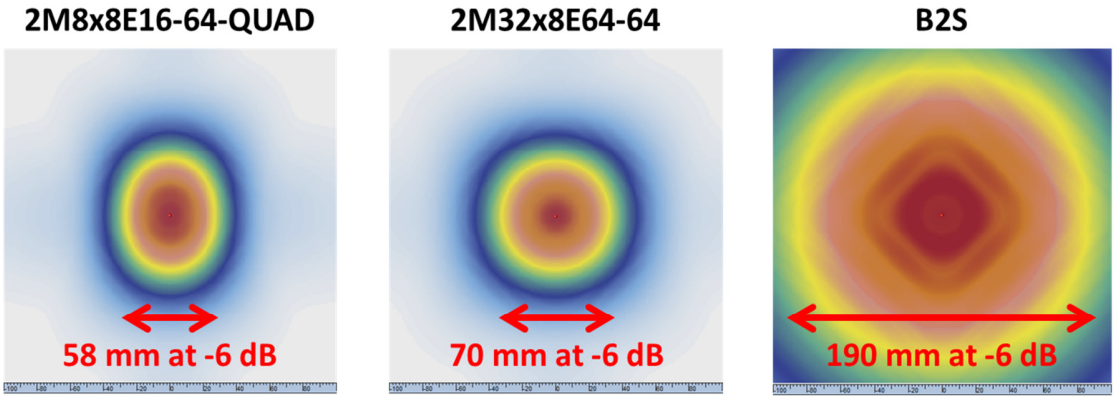

Figure 4 : Cross section of acoustic beam for QUAD probe (left), rigid PA-UT probe (middle) and typical C-UT probe (right)

Even with its large active aperture, the element size of the 2M8x8E16-64-QUAD still allows for steering the acoustic beam from 0°LW to ±35° on specimens from 250-mm OD up to flat, as can be seen on Figure 2 and Figure 5. For detection of indications at intermediate depths, a reduced aperture can be used. Finally, the design of the 2M8x8E16-64-QUAD probe assembly also provides the benefit of allowing the use of inter-array transmit-receive configurations for the detection of near surface indications.

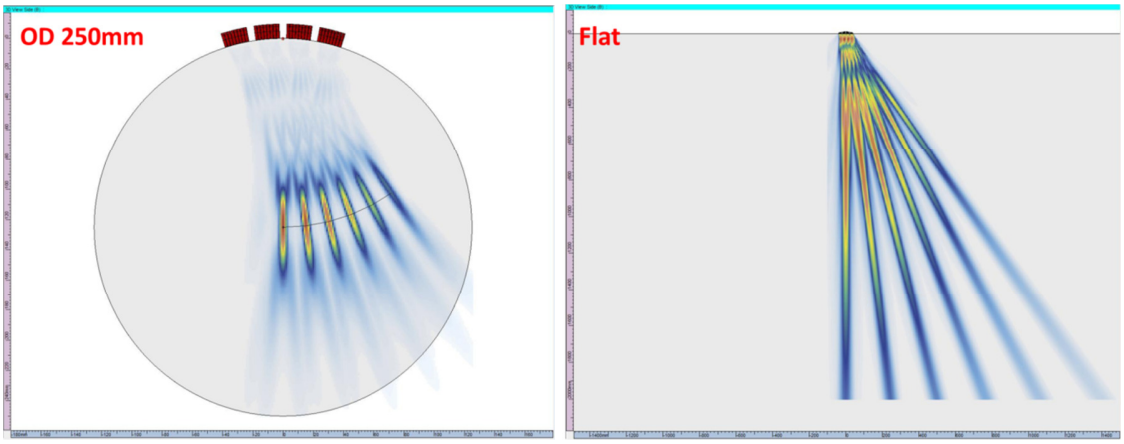

Figure 5 : QUAD probe steering capability from 0° to 35°LW for various diameters

3. Hardware and Software Innovations

To conduct the challenging inspections of large mono-block rotors efficiently, a high-performance UT PA system is required. The DYNARAY® system allows using up to 256 beam-forming channels simultaneously, and can efficiently drive large 2D matrix probes. This system can deliver an excitation pulse of up to 200V (loaded on 50 Ω) to every individual element of the probe in order to assure maximum energy transmission. The capability to record up to 256,000 points per A-Scan with an amplitude resolution of 16 bits at a rate of 30 MB/s really allows the DYNARAY to run efficient inspections through long sound paths.

The DYNARAY is controlled by UltraVision® 3. This software suite manages ultrasonic signal acquisition, displays real-time imaging of these signals, and provides online as well as offline data analysis and reporting. UltraVision 3 offers many advanced features and tools that improve the efficiency of UT inspections. In particular, it allows the control of custom arrays such as the 2M8x8E16-64-QUAD probe assembly which has multiple pitches [2].

Given the amount of data recorded when conducting inspections on large rotors and disks, the fact that UltraVision 3 can handle data files of more than 20 GB makes it a perfect fit for this type of work.

4. Development and Validation of Inspection Technique

4.1. Inspection Objectives

The objective was to develop an automated inspection methodology for large 2800 mm diameter mono-block rotors, satisfying the following requirements [3]:

- Indications with a size equivalent to a 0.9 mm diameter Flat Bottom Hole (FBH), and located between the near-surface and the center of the rotor shaft forging, can be reliably detected
- Indications with a size equivalent to a 1.6 mm diameter Flat Bottom Hole (FBH), and located between the center of the rotor shaft forging and the back-wall of the rotor, can be reliably detected
- Angle beam examination with refracted angles of 7°LW, 14°LW, 21°LW and 28°LW, in both CW and CCW orientations, can be performed using the same PA-UT probe, and simultaneously with the straight beam examination.

4.2. Straight Beam Inspection Technique

In order to achieve reliable detection of the target reflector over the complete sound path range, from the near surface to the back-wall, various straight beams (focal laws), focusing at different depths, have to be generated for the PA-UT probe. In order to allow the use of DAC curves for sizing of indications, the various beams (focal laws) should not be used in the near-field. Finally, 3 focal laws were selected to cover the complete depth range up 2800 mm.

A number of test blocks (see Figure 6), with 1.6 mm diameter FBH at depths from 5 mm to 2713 mm, were used to investigate the detection capability of the selected focal laws.

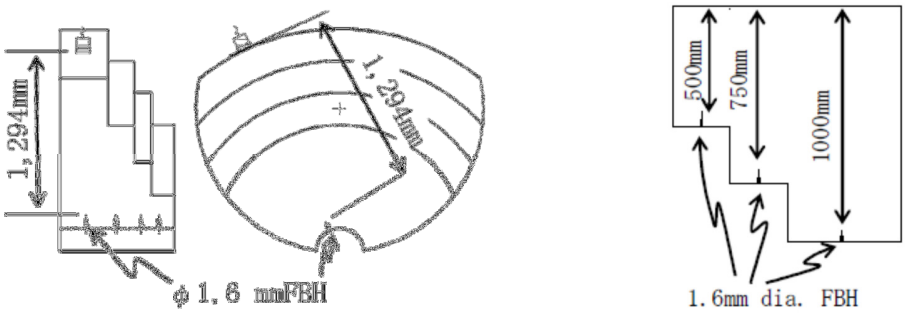

Figure 6 : Various curved and flat test specimens with 1.6 mm FBH

Typical UT responses obtained with the 3 focal laws at 0ºLW from the QUAD probe on FBH reflectors at various depths show excellent signal-to-noise ratio (SNR) (see Figure 7).

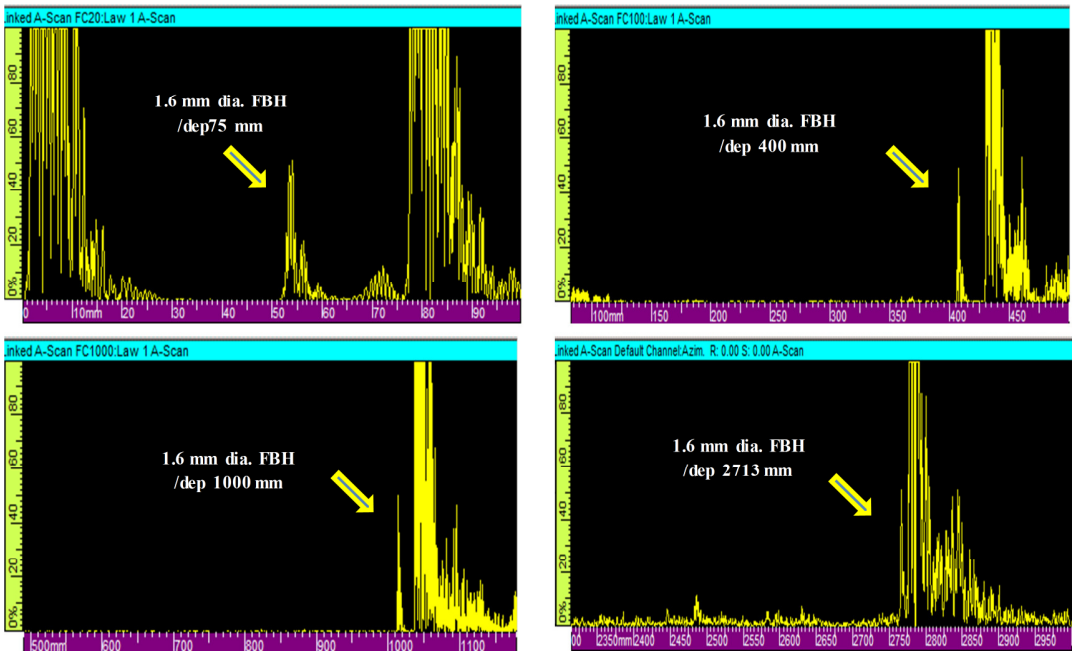

Figure 7 : A-Scan UT signals at 0°LW obtained from 1.6 mm diameter FBH at various depths

Based on the SNR obtained on the 1.6 mm diameter FBH reflectors, the minimum flaw size to generate a 6 dB SNR was calculated. Figure 8 shows a comparison of this minimum detectable flaw size for conventional UT and phased array UT at various depths. The conclusion is that a 0.9 mm diameter FBH located between the near surface (starting at 25 mm depth) and the center of rotor shaft forging (depth 1400 mm) can be clearly detected. In addition, it is obvious that a 1.6 mm diameter FBH located between the center of rotor shaft forging and back wall (depth 2800 mm) can be clearly detected.

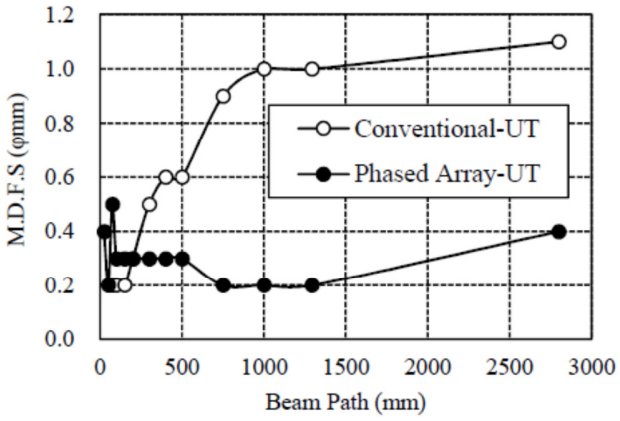

Figure 8 : Minimum detectable flaw size (SNR > 6 dB)

4.3. Angle Beam Inspection Techniques

Angle beams with refracted angles of 7°LW, 14°LW, 21°LW and 28°LW were generated using the QUAD probe, and were tested on 4.0 mm diameter SDH, at beam paths of 50 mm, 500 mm and 1000 mm, to compare the detection capability of angle beam examination with the straight beam examination. The UT responses in Figure 9 again show excellent SNR for all angles. The table in Figure 10 shows the complete results of the experimental comparison: the maximum decrease in sensitivity is 5 dB between the 0°LW and the 28°LW beams, generated with the QUAD probe.

In order to assess the detectability of the target reflector for angle beam examination, the SNR for the angle beams on a 1.6 mm diameter FBH was calculated. For this purpose, a correction factor was applied on the measured SNR on the 4.0 mm SDH, based on the theoretically calculated reflectivity difference between SDH 4.0 mm and FBH 1.6 mm (*), and the results of Figure 10 (**). From the results in the table of Figure 11, it can be observed that 1.6 mm diameter FBH at various depths between 50 mm and the back-wall of the rotor can be detected with a high SNR, using angle beam examinations up to 28°LW.

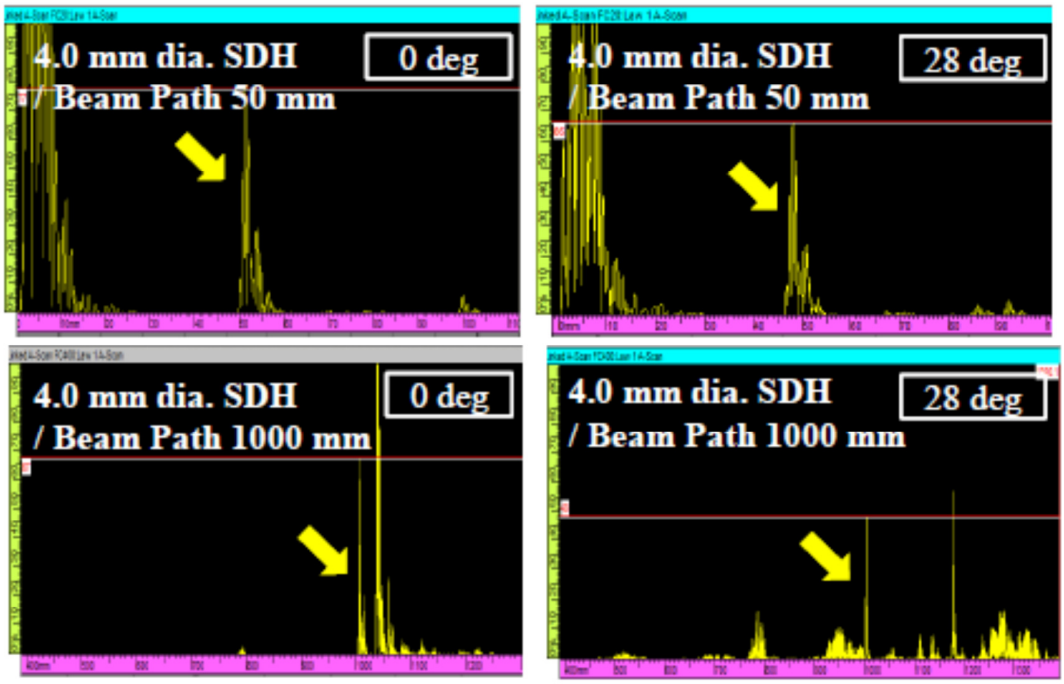

Figure 9 : A-Scan UT signals at 0°LW and 28°LW obtained from 4.0 mm diameter SDH at various depths

	Relative Sensitivity		
Refracted Angle	**Soundpath 50 mm**	**Soundpath 500 mm**	**Soundpath 1000 mm**
0 deg	0.0 dB	0.0 dB	0.0 dB
7 deg	-0.8 dB	-0.3 dB	-1.4 dB
14 deg	-1.9 dB	-1.8 dB	-0.9 dB
21 deg	-2.6 dB	-3.3 dB	-1.3 dB
28 deg	-5.0 dB	-3.0 dB	-3.0 dB

Figure 10 : Experimental comparison of sensitivity between straight beam and angle beams

	Soundpath 50 mm	**Soundpath 500 mm**	**Soundpath 1000 mm**
SNR for SDH 4.0 mm	48.0 dB	54.0 dB	54.0 dB
Correction Factor	17.1 dB (*) + 5.0 dB (**)	27.3 dB (*) + 3.3 dB (**)	30.3 dB (*) + 3.0 dB (**)
SNR for FBH 1.6 mm	25.9 dB	23.4 dB	20.7 dB

Figure 11: Detection capability of angle beam examination at various depths

4.4. Considerations for Automated Scanning

In order to perform automated UT scanning, the appropriate scanning resolution in axial and circumferential directions needed to be determined. Typically, the largest allowed scanning resolution is defined as 50% of the -6 dB beam spread of the narrowest acoustic beam in each direction, amongst the various applied focal laws. After experimental measurement of the beam spread of the applied beams using 1.6 mm FBH, the scanning resolution was set at 3.75 mm in the axial direction and 3.5 mm in the circumferential direction.

The automated UT scanning was set up as follows:

- Outer diameter of rotor shaft forging : 2811 mm diameter
- Number of PA-UT channels : a total of 11 channels, straight beam technique 3 channels, angle beam technique 8 channels (7°LW, 14°LW, 21°LW and 28°LW, CW and CCW)
- Scan Resolution : axial direction 3.5 mm; circumferential direction 0.12 deg
- Scanning speed : 50 mm/sec
- Mechanical scanning system : TUROMAN5, manufactured by Actemium Cegelec (see Figure 12)

It was confirmed that straight beam examinations and angle beam examination as mentioned above can be performed simultaneously using the DYNARAY phased array system, without loss of data. Although the scanning speed is only 50% of the speed of the typical conventional automated UT, the total scanning time can be reduced by 90%, because of the number of scanning sequences is drastically reduced.

Figure 12 : Mechanical scanning system (TUROMAN5)

5. Conclusions

From the work presented in this paper, the following conclusions can be drawn:

- The use of a large semi-flexible PA-UT probe for the inspection of large mono-block rotors provides improved detection performance compared to a standard conventional UT probe, due to the higher acoustic energy transmitted through the specimen and the smaller beam spread

- It was experimentally validated that a single PA-UT probe can be set up to meet the detectability requirements of the applicable codes, for both straight beam examination and angle beam examination

- Commercially available state-of-the-art phased array hardware and software allows for efficient application of this improved inspection technique in industrial conditions, resulting in a drastic reduction of the total inspection time

References

[1] P. Tremblay, D. Verspeelt, "Design and Validation of a Semi-Flexible Phased Array UT Probe for the Inspection of Large Forged Rotors", 9th Int. Conf. on NDE in Relation to Structural Integrity for Nuclear and Pressurized Components, Seattle, May 2012

[2] J. Berlanger, D. Reilly, D. Richard, G. Maes, "Advanced 3D Visualization and Analysis of Phased Array UT Inspection Data", 10th Int. Conf. on NDE in Relation to Structural Integrity for Nuclear and Pressurized Components, Cannes, September 2013

[3] N. Hoshi, H. Yoshida, H. Nimura, H. Narigasawa, R. Falsetti, F. Gatazka, "Establishment of Quality Evaluation Technique by PA UT for large Monoblock Rotor Shaft", 19th International Forgemasters Meeting, Tokyo, October 2014

Evaluation of dispersion characteristics for leaky surface acoustic wave on aluminum thin film with scanning acoustic microscopy

Byung-seok Jo[1], Tae-sung Park[1], Seung-bum Cho[1] and Ik-keun Park[1]

[1]Department of Automotive and Mechanical Engineering, Seoul National University of Science and Technology, 172, Gongreung-dong, Nowon-gu, Seoul, South Korea

E-mail address(corresponding author) : ikpark@seoultech.ac.kr

Leaky surface acoustic waves (LSAW) are generated in measurement process for V(z) curve technique of scanning acoustic microscopy (SAM) and have dispersion characteristics in multilayered thin film structure. The dispersion characteristics is used to evaluate the aluminum thin films which have a different thickness. To verify this relation, aluminum thin film with different thickness was deposited on the silicon (100) substrate by DC magnetron sputtering and scanning electron microscopy (SEM) is used to confirm the thickness of deposited thin film. Then the LSAW velocity of the thin films was measured using V(z) curve technique of scanning acoustic microscopy. The Rayleigh wave dispersion curves of multilayered structure (Al-Si) were also theoretically calculated to confirm the dispersion characteristics of measured LSAW velocities. As the thickness of aluminum thin film increased, the velocity of LSAW was decreased and this trend was similar to that of calculated dispersion curve. Consequently, we confirm the relation between the thickness of thin film and LSAW velocity and the similarity of dispersion characteristics between theoretical results and experimental results.

Keywords: Scanning Acoustic Microscopy, Leaky Surface Acoustic Wave, Dispersion Characteristics, Thin Film.

Study for Microcrack of steel wire rods using EMAR Method

Seung Wan Cho[1,2], Taehoon Heo[1,3] , Seung Hyun Cho[1]

and Zhong Soo Lim[4]

[1]Korea Research Institute of Standards and Science, Center for safety measurement, 267 Gajeong-ro, Yuseong-gu, Daejeon, Korea
[2]Sungkyunkwan Univ., 2066, Seobu-ro, Jangan-gu, Suwon-si, Gyeong gi-do, Korea
[3]University of Science and Technology, 217 Gajeong-ro, Yuseong-gu, Daejeon, Korea
[4]Research Institute of Industrial Science &Technology, 67, Cheongam-ro, Nam-gu, Pohang-si, Gyeongsangbuk-do, Korea

seungcho@kriss.re.kr

In a manufacturing process of a steel wire rod, lots of micro scale axial cracks usually occur on surface. Cracks over 30 micrometer of its depth may bring about severe problems, so it is very necessary to evaluate the depth of surface microcracks. Traditional UT Methods had a some difficulties to detect a micro crack because of its accuracy, this work concerns a nondestructive method to defect micro surface cracks in a steel wire rod using an electromagnetic acoustic resonance (EMAR) technique, which generates SH waves circumferentially in a cylinderical rod and measure the in-lane resonance of its cross section. The resonance frequency and attenuation coefficient were analyzed about healthy and damaged specimens. The results clearly showed the present method can detect surface cracks of a few tens of micrometers.

Keywords: EMAR, Resonance, Wire rod, micro crack.

Surface property measurement of the cylinder liner using the Honing polishing

Ho-Girl Lee[1], Taek-Gyu Lee[1], Hak-Joon Kim[1], Sung-Jin Song[1], Seung-Mok Kim[1], and Yeong-Jae Lee[1]

[1]Sungkyunkwan Univ. Natural Sciences Campus, Cheoncheon-dong, Jangan-gu, Suwon-si, Gyeonggi-do, Korea

E-mail address(corresponding author) : sjsong@skku.edu

Melting phenomenon of the inner wall of piston in or pump automatic engine has occur due to the friction and wear by high-speed reciprocating motion. As one of alternatives, the inner surface of a cylinder has been protected using cylinder liner. For the main material of the cylinder liner, casting and gray cast iron have been used as consideration of the economical efficiency and easy workability. And, honing polishing has been used to control the roughness of the cylinder liner. Honing polishing was observed to evaluate a difference in the surface with a change of roughness of the inner cylinder liners using a change in reciprocation. Thus, in this presentation, we will present measurement method and microstructure analysis results and relation between Rayleigh wave and surface properties. Using a Rayleigh wave, changes in physical properties of the specimen surface and the progress of the wear surface have been measured.

Keywords : ultrasound, Rayleigh wave, C-Scan

Study on ultrasonic method for detection of micro-defects in pipeline using the Rayleigh wave

Yun-Taek Yeom[1], Hak-Joon Kim[1*], Sung-Jin Song[1], Sung-Duk Kwon[2], Ki-Bok Kim[3]

[1]Dept. of Mechanical Engineering, Sungkyunkwan Univ., 2066, Seobu-ro, Jangan-gu, Suwon-si, Gyeonggi-do, Republic of Korea
[2]Department of Physics, Andong National Univ., Songcheon-dong, Andong-si, Gyeongsangbuk-do, Republic of Korea
[3]Center for Safety Measurement, Korea Research Institute of Science and Technology, 267, Gajeong-ro, Yuseong-gu, Daejeon, Republic of Korea

E-mail address(*corresponding author) : hjkim21c@skku.edu

Rayleigh surface waves is applied to detect defects on the surface area of the materials. Rayleigh wave propagate the surface of liquid-solid interface generating directional leaky wave. In the study, to measure the defects using the Rayleigh wave, we made SAW measurement system that generate and measure the leaky Rayleigh wave. SM45C specimens with artificial micro-surface defects were prepared. The incidence angle of the ultrasonic beam is fixed at Rayleigh angle. Signals reflected by surface defects were measured by pulse-echo technique and transmitted signals were measured by pitch-catch technique. We evaluate the size and depth of micro-surface defect (by reflection signals and transmission signal over defects of the surface wave.) The Correlation between surface defects and reflection and transmission signals showed the usefulness of leaky Rayleigh wave.

Key words : ultrasound, Rayleigh wave, surface defect, reflection, transmission

Accelerations of total focusing method for ultrasonic imaging

Ewen Carcreff[1] and Dominique Braconnier[1]
[1]The Phased Array Company, 9078 Union Center Blvd. #350 West Chester, Ohio, USA

E-mail address (corresponding author): ewen.carcreff@thephasedarraycompany.com

The total focusing method (TFM) has become a popular tool for the imaging of objects under ultrasonic testing. Compared to conventional imaging techniques, the benefits of TFM are optimal focusing and the possibility to reconstruct images of variable size with fine precision. Moreover, the process enables the use of arbitrary array geometries. The method requires the capture of time signals from every transmitter-receiver pair of an array transducer. The TFM algorithm is then applied to reconstruct an image by coherent summations over all elements. This procedure requires a large number of delay computations and summations according to the output image size. In a real-time imaging context, the computation of a single image needs to be as short as possible. For this purpose, implementations using multi-core and Graphics Processing Unit (GPU) have been developed. In this paper, we give an overview of such implementations and compare the computation times on real ultrasonic data. Reducing the number of operations can also shorten computation speed. This is achieved by using the array symmetry and by applying limited apertures. This paper also presents experimental results with those accelerations.

Keywords: Total focusing method, parallelization, multi-threading, graphics processing unit.

Experimental Visualization of Ultrasonic Pulse Waves Using Piezoelectric Films

Yoshinori Kamiyama[1] and Takashi Furukawa[1]

[1]Japan Power Engineering and Inspection Corporation, Japan

Abstract

The ability to predict the propagation path of ultrasonic waves is necessary for ultrasonic testing technicians who must be able to discriminate defect signals from noise. The visualization of ultrasonic propagation enhances understanding and prediction ability. Previously, we had developed a method to visualize ultrasonic propagation by mechanically scanning the surface of a test object with a piezoelectric ceramic transducer used as a receiver. This method did not lend itself to the measurement of transverse waves with isotropic sensitivity, and the spatial resolution of the method was limited. We have now developed a new visualization method that has uniform sensitivity to transverse waves and uses piezoelectric films in conjunction with a computer-controlled, mechanically scanned, miniature voltage probe to achieve high spatial resolution. In this paper, we explain the new method, compare our results with those obtained from photo-elastic measurements, and present the results of ultrasonic visualization in welded stainless steel.

Keywords : Piezoelectric film, Ultrasonic wave propagation, Visualization, PVDF, nondestructive testing

1. Introduction

In ultrasonic testing, it is important to track the propagation paths of ultrasonic waves emitted into a test object to perform an evaluation from the observed ultrasonic echoes. Thus, an improved understanding of ultrasonic propagation in actual test objects is important. The visualization of ultrasonic waves provides effective information for better understanding. In past studies, we developed a method to visualize ultrasonic propagation by scanning a two-dimensional area on the surface of a test object with a piezoelectric ceramic transducer used as a receiver [1]. A scanning mechanism holding the transducer was mounted on a surface parallel to the direction of travel of the ultrasonic waves propagating in the test object. Then, the ultrasonic propagation on this surface was visualized by means of the images created from the scanning results. However, this method had some inherent problems when detailed information about the ultrasonic propagation was required. Because the sensitivity of piezoelectric ceramics depends on the direction of shear strain in the transverse waves and the direction of shear strain varies according to the direction of wave propagation, this method could not observe transverse waves with uniform sensitivity. Furthermore, the spatial resolution of visualization images made by this method was limited because the resolution was restricted by the size of the piezoelectric ceramic element used as a receiver, and tiny piezoelectric ceramics are difficult to make. To solve these problems, we have developed a new visualization method using piezoelectric film that has uniform sensitivity to transverse waves and offers the possibility of higher spatial resolution. In this paper, we explain this new visualization method, compare its results to those of a photo-elastic measurement, and show a visualization of ultrasonic propagation in a welded stainless steel specimen.

2. The problems of the previous method and the solutions by the new method

Figure 1(a) shows the architecture of our previous visualization system. The strain is excited on the receiving surface of a test object by ultrasonic waves from a transmitter. In the previous method, the strain was received by a piezoelectric ceramic transducer, and visualized images of the propagating ultrasonic waves were obtained by scanning a two-dimensional area on the receiving surface with the transducer. Even though our method needs a surface that is orthogonal to the transmitting surface to serve as a receiving surface, it can visualize the ultrasonic propagation in actual metal materials. For example, an ultrasonic propagation path that curves because of anisotropic properties of materials and/or a scattering of ultrasonic waves caused by a discontinuity in the metal structure can be visualized by our previous method.

However, the previous method had some inherent problems. The first problem was anisotropic sensitivity. To visualize a

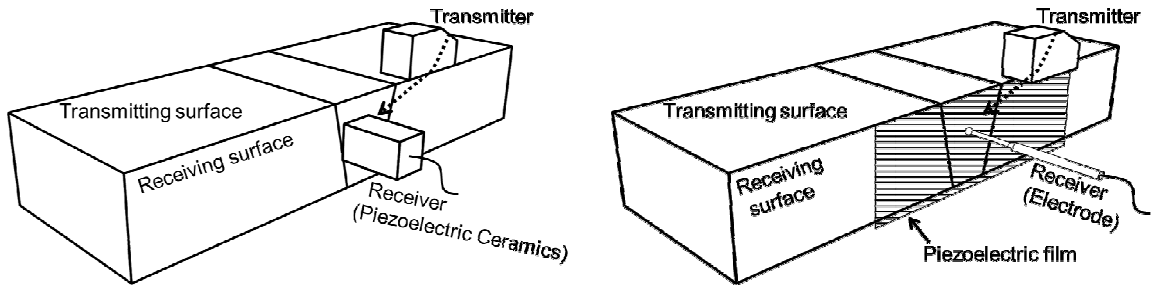

(a) Previous method using piezoelectric ceramics. (b) New method using piezoelectric films.

Figure 1. Previous and new methods of ultrasonic wave visualization.

transverse wave, we used a shear horizontal (SH) wave transducer as a receiver. The sensitivity of SH wave transducers depends on the direction of shear strain of the transverse waves and this direction will vary as a result of reflection or refraction. For example, when we evaluate the angled transverse ultrasonic wave before and after reflection from the bottom surface of a test object, we needed at least two separate measurement in order to evaluate each part of the wave with the same sensitivity. The second problem was limited spatial resolution. The resolution of the previous method was restricted by the size of the piezoelectric ceramic in the receiving transducer, and tiny piezoelectric ceramics are difficult to fabricate. The third problem was stability of transverse wave sensitivity. To visualize a transverse wave, we need an SH transducer as a receiver. The sensitivity of an SH transducer is a function of the contact conditions, which can easily become unstable unless slow mechanical scanning is employed.

Figure 1(b) shows the new visualization system. A piezoelectric film is mounted on the receiving surface of the test object with couplant or an adhesive. The ultrasonic wave is detected by an electrode scanning the surface of the piezoelectric film. In this study, we used PVDF (Polyvinylidene Difluoride) as the piezoelectric film. A PVDF film passed between rollers and polarized across the thickness direction has anisotropic sensitivity. However, a two-layer PVDF film, as shown in Figure 2, has uniform sensitivity [2]. To observe transverse waves, we laminated two films together with opposing directions of polarization and orthogonal anisotropic axes [2]. Such a two-layer PVDF structure solves the sensitivity problem of our previous method.

The spatial resolution of the new method depends on the nose shape of the electrode and the pitch of the mechanical scanning. Thus, the spatial resolution is improved by the new method from that of the previous method that was restricted by the size of the piezoelectric ceramic. Moreover, the stability and reproducibility of the measurement is improved for two reasons: (a) the electrode is now used as a receiver instead of the piezoelectric transducer whose sensitivity was strongly dependent on the contact conditions, and (b) couplant is not required between the PVDF and the electrode.

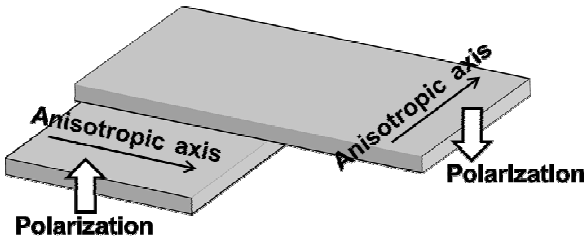

Figure 2. Laminated PVDF film for transverse wave measurement.

3. Equipment for the new visualization method using PVDF

Figure 3(a) shows the block diagram of the equipment for the new method and Figure 3(b) is an actual photograph. An electrode used as a receiver is connected to a pre-amplifier (fixed 20dB gain, LNA130WS, COSMOWAVE Co., Ltd.) that is grounded to an electrode layer on the laminated PVDF. An ultrasonic test instrument (USIP12, KRAUTKRAMER) is connected to an ultrasonic transmitter and the output of the pre-amplifier. The ultrasonic test instrument generates a single-pulse voltage waveform, and it excites an ultrasonic wave into the test object from the transmitter. After going through a bandpass filter and a variable amplifier in the ultrasonic test instrument, the received signal is sent to an A/D converter (16

bit, 25 MHz sampling, Turtle Industry Co., Ltd.). In the ultrasonic test instrument, a 2.25 MHz or 5 MHz narrow bandpass filter was employed in each experiment, and 80 dB gain was selected for the variable amplifier. A PC receives the outputs of the A/D converter and controls the drive motors of a two-dimensional mechanical scanner. The recorded data of positions and the A/D converted waves are reconstructed by software in the PC to form images of the ultrasonic wave patterns. The PVDF laminated film was attached to the receiving surface with soluble couplant (SHN-A5, TAIYO NIPPON SANSO CORPORATION). The laminated PVDF film consists of two PVDF films bonded with an epoxy adhesive, as shown in Figure 2; each layer is 110 μm thick, and there is also a thin Ag grounding electrode layer on the bottom side that is connected to the pre-amplifier and the test object. The strain caused by ultrasonic waves through the electrode layer excites electric signals in the PVDF layers. The receiving electrode that scans over the laminated PVDF film is 1 mm in diameter and has a hemispherical nose figure; it is internally spring-loaded to maintain constant contact pressure. In these experiments the ultrasonic wave was measured eight times at each point, the software recorded the averaged wave, and then the receiving electrode was moved to the next point. The interval between the recording points was 0.2 mm.

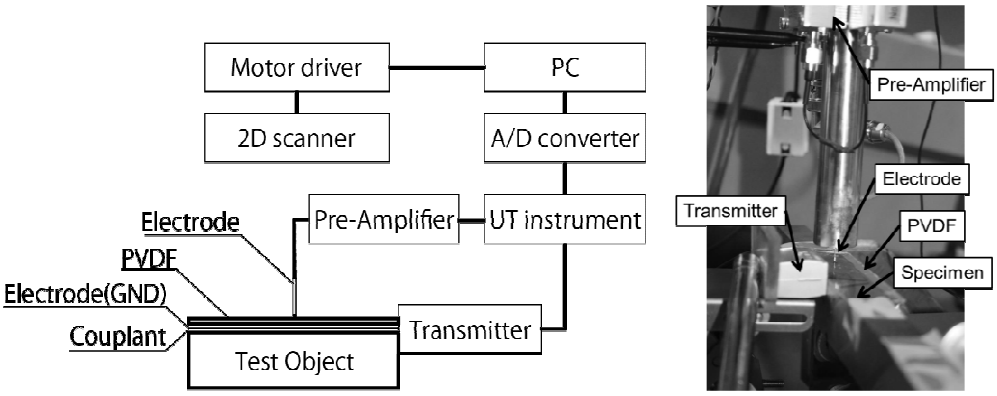

(a) Block Diagram (b) Equipment layout

Figure 3. Equipment configuration of the ultrasonic visualization system.

4. Comparing to photo-elastic visualization

We compared the result of the new method to that of a photo-elastic visualization method. Our method detects ultrasonic waves at the surface of a test object, whereas the photo-elastic visualization method observes inside of the test object.

In this experiment, we used a 2 MHz, 45 degree refracted transverse wave transducer (MWB45-2, KRAUTKRAMER). The photo-elastic method needs a transparent test object, therefore glass was used. The glass was 50 mm high, 15 mm thick and 300 mm long, and had a 3 mm diameter drilled hole placed about 15 mm from the top. In this experiment, the photo-elastic method used a pulsed strobe lamp (approximately 100 ns) and recorded the ultrasonic waveform at 40 ns intervals, using a CCD camera; this is nearly equivalent to sampling waves at each pixel at a 25 MHz rate.

Figure 4 shows the results of the two methods. Figure 4(a) is a result of the photo-elastic visualization. Figure 4(b) is a result of the new method using PVDF. Both results were obtained by a peak-hold procedure after an ultrasonic wave was reflected at the drilled hole. The peak-hold procedure involves searching for, and recording, the maximum value within a specified time period. Each of the visualization methods can be considered as an aggregate of time based waves in each pixel, thus we applied the same procedure to create the images in Figure 4.The photo-elastic visualization detects pressure as a brightness value proportional to the square of the pressure [3]. Thus, we show the square root of the obtained brightness value in Figure 4(a). Both results show reflected waves returning to a transmitter and fringe patterns caused by interference between the non-scattered portion of the incident waves around the drilled hole and the reflected waves. Comparing Figure 4(a) and Figure 4(b), confirms that the results of the new visualization method with PVDF correspond to the ultrasonic wave propagation inside the test object.

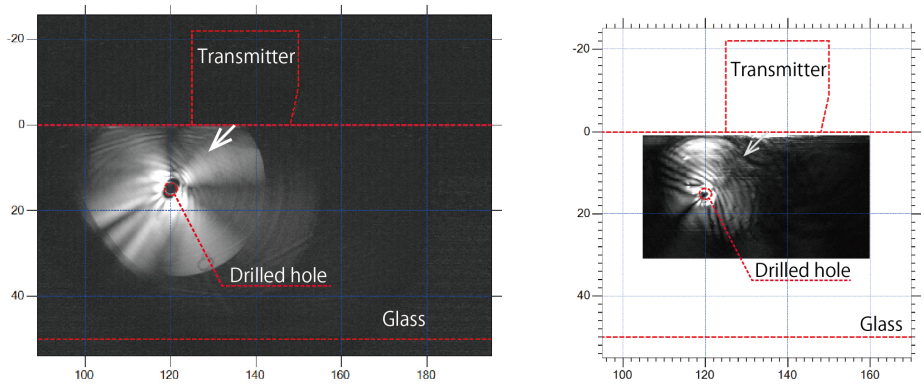

(a) Photo-elastic measurement (b) PVDF visualization system

Figure 4. The peak-hold results of the two methods after reflection by the drilled hole.

5. Visualization results of a welded stainless steel

Figure 5 is a visualization, by our new PVDF method, of ultrasonic wave propagation in a 16 mm thick stainless steel test object with a TIG weld. In Figure 5, the TIG welding area is indicated by a broken red line. A 5 MHz and 45 degree refracted transverse wave transducer (5C10x10A45, KGK) was used as the transmitter. Figure 5(a) shows the waveform shortly after the transmission into the base metal of the test object. Figure 5(b) shows the wave propagating in the welding metal. Compared with the waves in the base metal shown by Figure 5(a), the waves in the welding metal shown by Figure 5(b) denote relatively strong scattering caused by a metal structure. In Figure 5(c), an ultrasonic wave that passed through the welding metal and reflected at the bottom of the test object is observed. Because of attenuation in a metal structure, it is generally difficult to visualize waves that have passed a weld, but our new method has a high enough S/N ratio to observe the waves passing the weld. Figure 5(c) also shows an ultrasonic wave reflected at the bottom. When a vibration direction is varied as with Figure 5(b) to (c), the previous method required at least two separate measurements aiming to the each direction, but with the new method, the data can be obtained in a single measurement. Figure 5 confirms that the new visualization method using PVDF can be applied around a weld metal and offers the possibility of quantitative evaluation of ultrasonic wave propagation.

6. Conclusions

In previous studies, we developed an ultrasonic visualization method using piezoelectric ceramics. However, it had problems with anisotropic sensitivity, limited spatial resolution, and stability of transverse wave sensitivity. In this paper, we have presented a new visualization method using PVDF which offers the possibility of resolving those three problems, and we have shown the result of ultrasonic propagation in a stainless steel test object with a TIG weld. We intend to continue improvement of this visualization method to obtain quantitative evaluation of directional characteristics and attenuation, along with high spatial resolution.

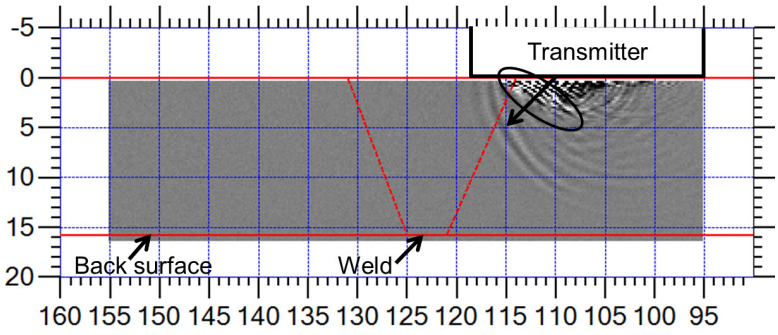

(a) About 5.8 μs after the triggering of the ultrasonic pulse.

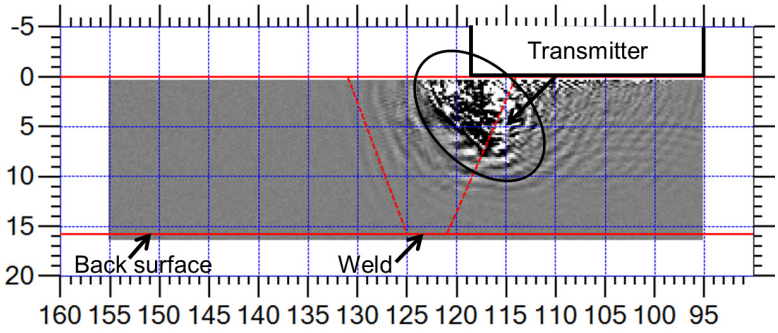

(b) About 8.2 μs after the triggering of the ultrasonic pulse.

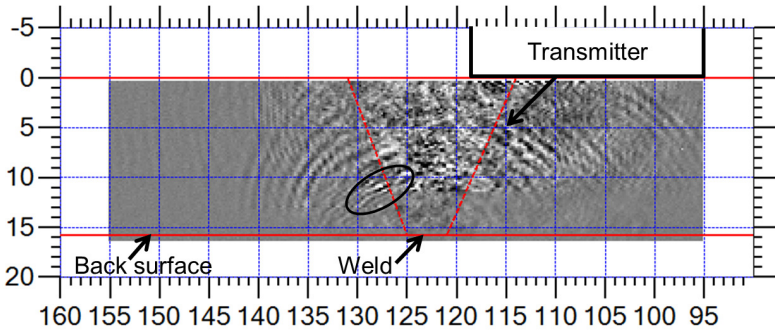

(c) About 14.1 μs after the triggering of the ultrasonic pulse.

Figure 5. Results of ultrasonic wave visualization using piezoelectric film. The dashed red lines denote the welded zone and the black ovals denote the transverse ultrasonic waveforms.

References

[1] K. Furukawa, H. Yoneyama, Y. Horii and N. Uesugi, "Measurement of ultrasonic wave propagation in austenitic stainless steel welds-(I)", Proceedings of the Second International Conference on NDE in Relation to Structural Integrity for Nuclear and Pressurized Components, pp. B195-201 (2000).

[2] Y. Tanaka, T. Ikeda, K. Toiyama, S. Kuwako, Y. Fujimoto, "Basic Study on Measurement of Guided Wave Using Piezoelectric Film", Transactions of the Japan Society of Mechanical Engineers. A, Vol.72, No.718, pp.951-956 (2006).

[3] H. Aizawa et al., "Shin Hihakaikensa Binran (New Handbook of Nondestructive Inspection)" (in Japanese), Nikkan Kogyo Shimbun Ltd., pp.732-736 (1992).

Monitoring of pipe wall thinning using high-temperature thin-film UT sensor

Takeshi KODAIRA , Isao SEKI, Naoto KAWASE, Takayuki MATSUURA,
Yuko YAMAMOTO and Seiichi KAWANAMI
Mitsubishi Heavy Industries, Ltd.

1. Abstract

Periodical measurement of pipe wall thinning for nuclear power plant is performed manually and it is performed based on JSME code which is Japanese rules on pipe wall thinning management. However, there are following concerns.

i. Measured values may vary depending on the stability of measurement position and condition of contact.
ii. The additional work for installation and removal of heat insulating material and a scaffold is required at every measurement.
iii. The stable measurement is difficult on complex geometry, such as T-jointing of small pipe, because of the curvature.
iv. The continuous wall thinning monitoring in plant operating is impossible because of high-temperature.

Therefore, we developed the thin-film UT sensor for high-temperature use. Since the thickness of the sensor is thin (less than 1.0mm), it can be installed under the heat insulator of pipe. And its flexibility enables to measure the thickness on complex shape, such as T-jointing of small pipe. Moreover, it has the high-temperature durability and it can be continuously attached during plant operation.

We performed verification tests of measurement accuracy and load test of heat and irradiation durability. Furthermore, field trial was performed at actual nuclear power plant.

In this paper, we introduce features of the thin-film UT sensor, results of the verification tests and field trial.

2. Summary of thin-film UT sensor and measurement system

The thin-film UT sensor is shown in Fig.1. The thin-film UT sensor consists of top electrode, piezoceramic film and bottom electrode. Since the thickness of the sensor is less than 1.0mm and it is flexible, it can be installed under the heat insulator of pipe. It is also possible to measure complex shape, such as T-jointing of small pipe. Moreover, it has the high-temperature durability and it is applicable to the location of the maximum temperature 200 degrees C or higher by selecting material of piezoceramic film.

The measurement configuration using the thin-film UT sensor is shown in Fig.2. The thin-film UT sensor is fixed using adhesive material under heat insulator. Each sensor is connected to the relay box placed outside of heat insulator in order to bundle signal wires. In case of periodical wall thinning measurement, portable measurement equipment is connected to the relay box. Therefore, it is possible to measure wall thickness without removing heat insulator. Moreover, in case of wall thinning monitoring, data acquisition station is connected to the relay box and collects the wall thickness data continuously with appropriate interval.

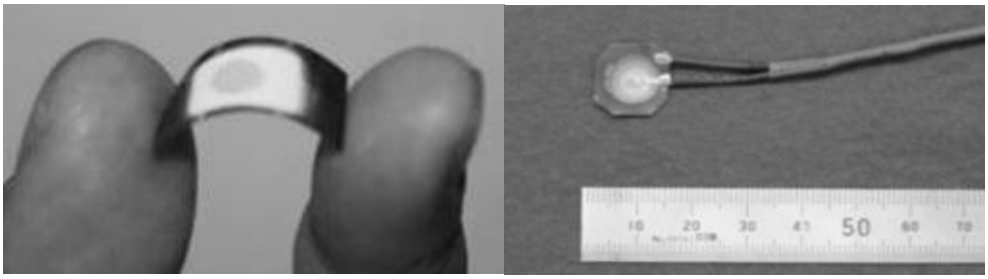

Fig.1 Thin-film UT sensor

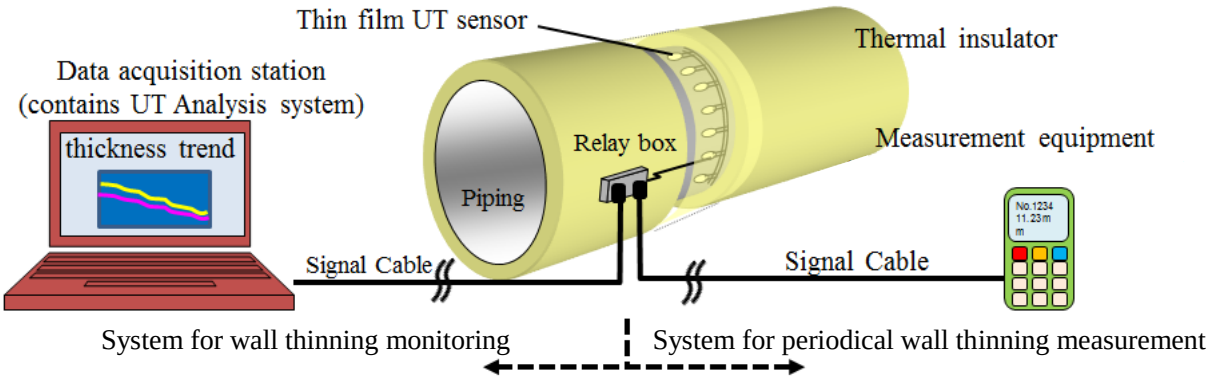

Fig.2 Measurement system

3. Verification test

3.1. Measurement accuracy of thickness

In order to confirm measurement accuracy of thin-film UT sensor, thickness is continuously measured on plate which is ground by 10μm unit using milling machine as shown in Fig.3. As shown in Fig.4, root mean square error between grinding value and measurement value was less than 2.3μm on the plate of approximately 10mm of thickness. Therefore, it is considered that thin-film UT sensor has enough accuracy to perform periodical measurement of pipe wall thinning.

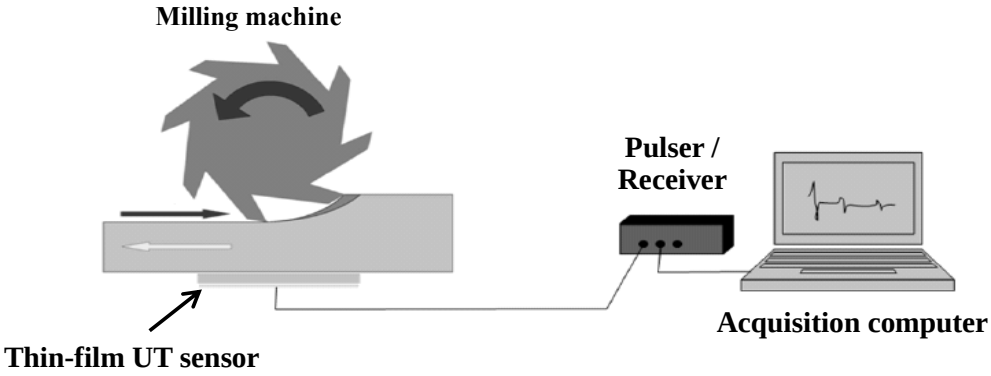

Fig.3 Measurement configuration on plate

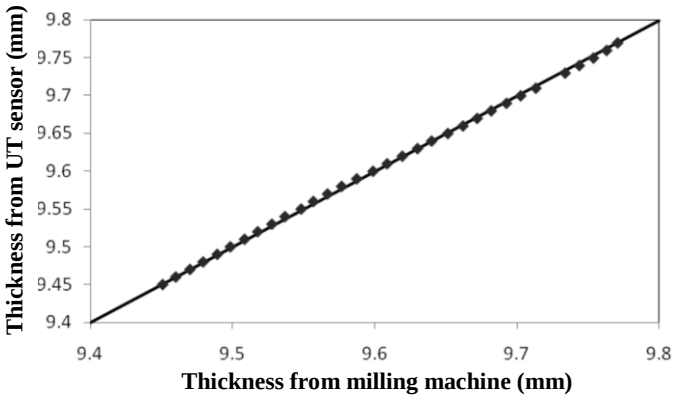

Fig.4 Measurement accuracy on plate

Moreover, in order to confirm measurement accuracy of thin-film UT sensor on complex shape, we measured wall thickness of T-joint piping and elbow piping by using both thin-film UT sensor and small size UT sensor as shown in Fig.5. The specification of mockup is shown in Table1.

As shown in Fig.7, maximum difference between both sensors was less than 0.1mm and it is considered that thin-film UT sensor has same measurement accuracy as small size UT sensor. On the other hand, although the stable measurement using small size UT sensor had a difficulty because of point contact. Thin-film UT sensor had an advantage of stable measurement because it could fit the surface of complex geometry because of its flexibility.

Fig.5 Measurement image of T-joint

Fig.6 Small size UT sensor

Table1 Specification of complex shape mockup

No.	Type	Nominal Diameter	Pipe Schedule
A	Elbow	3/4 inch	Sch80
B	T-joint	3/4 inch	Sch40
C	T-joint	1 inch	Sch40
D	T-joint	3/4 inch	Sch80
E	T-joint	1 inch	Sch80
F	T-joint	2 inch	Sch160

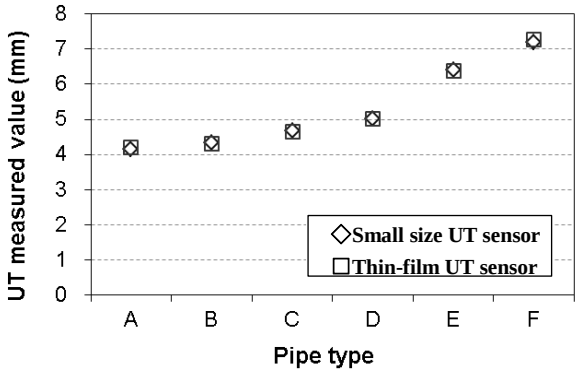

Fig.7 Measurement accuracy on complex shaped mockup

3.2. Verification of high-temperature durability

In order to confirm high-temperature durability of the thin-film UT sensor, the thermal cycle test and the continuous thermal test were carried out.

The thermal cycling test was carried out between room temperature and 200 degrees C by turns. The test condition of thermal cycle test is shown in Table2. As shown in Fig.8, the sensor could work after ten heat cycles without the indication of sensor flaking caused by heat expansion.

The continuous thermal test was carried out at 200 degrees C and the measurement is still ongoing. As shown in Fig.9, there were not remarkable signal distortion, noise and remarkable attenuation of signal amplitude after two years heating. Based on these results, it is considered that thin-film UT sensor has good high-temperature durability.

Table2 Test condition of thermal cycle test

Items	Condition
Number of thermal cycles	10 times
Heat temperature	approximately 200 degrees C

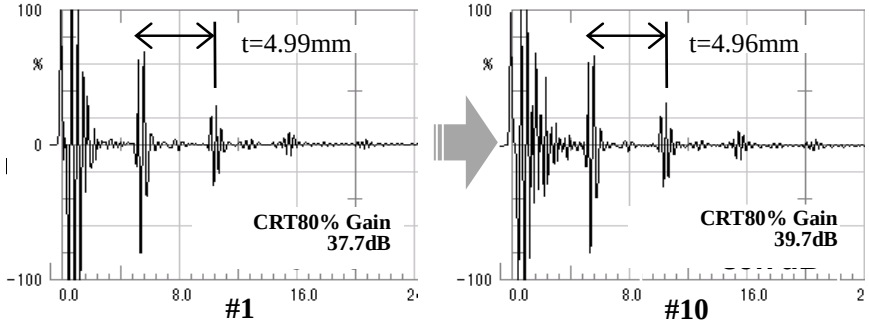

Fig.8 UT waveform of thermal cycle test

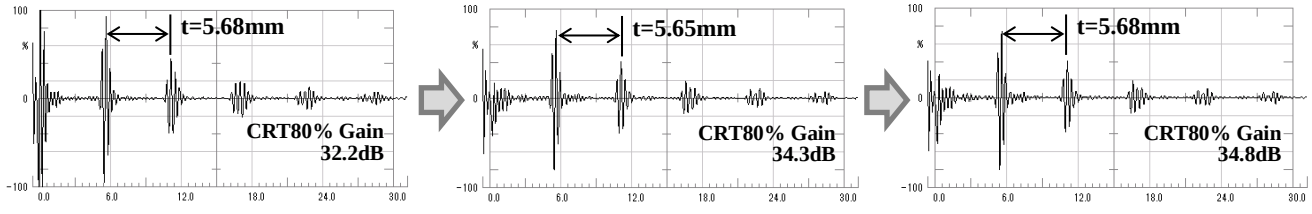

Fig.9 UT waveform of continuous thermal test

3.3. Verification of irradiation durability

In order to confirm irradiation durability of thin-film UT sensor, irradiation durability test was carried out. The test condition of irradiation is shown in Table3.

As shown in Fig.10, there were not remarkable signal distortion, noise and remarkable attenuation of signal amplitude after the irradiation test. 3300Gy is equivalent to the amount of irradiation for approximately 30 to 40 years on the surface of Main Coolant Pipes in nuclear power plant. Therefore, it is considered that thin-film UT sensor has long term applicability in nuclear power plant.

Table3 Test condition of irradiation

Irradiation source	cobalt 60
Irradiation time	11 hours
Dose rate	No.1 Location : 300Gy/H
	No.2 Location : 200Gy/H
Total irradiation	No.1 Location : 3300Gy
	No.2 Location : 2200Gy

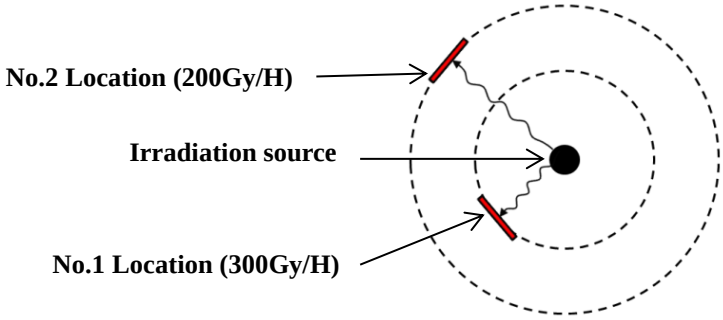

Fig.10 Irradiation layout

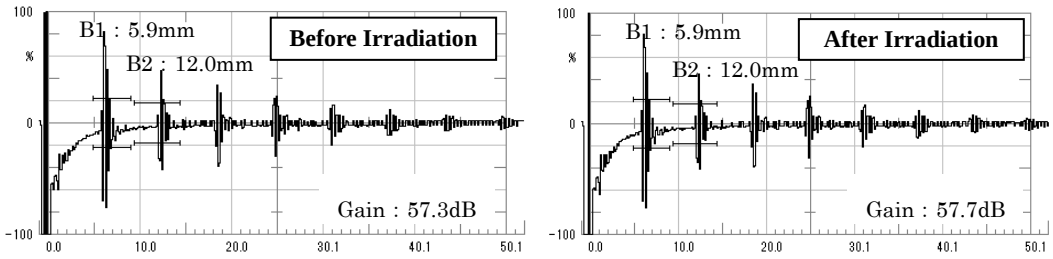

Sensor of No.1 Location

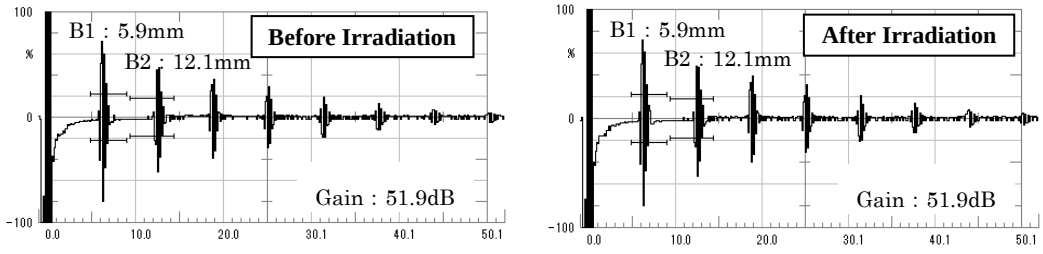

Sensor of No.2 Location

Fig.11 UT waveform of verification of irradiation durability

4. Field trial

In order to confirm applicability to actual plant of the thin-film UT sensor, we carried out the field trial at nuclear power plant as shown in Table 4. We installed thin-film UT sensors (Fig.12) to the pipe of actual nuclear power plant. It is planned that the measurement duration is 3 years and measurement frequency is shown in Table5.

An example of waveform is shown in Fig.13. There were not remarkable signal distortion and noise after test period of 4 months. As for two sensors, it is observed slightly attenuation. We consider that there is no issue in thin-film UT sensors and it was caused by changing of contact condition. There is an issue of install process and it needs to be modified for more stable measurement.

Table 4 Field trial condition

Items	Condition
Sensor numbers	4 sensors
Pipe wall thickness	approximately 6.0mm
Pipe temperature	Approximately 150 degrees C

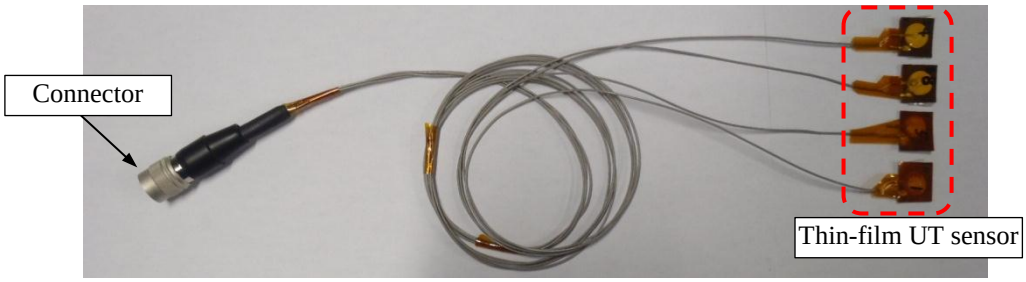

Fig.12 Thin-film UT sensor for field trial

Table 5 Measurement frequency of field trial

Period	Measurement frequency
from installation to 7 days	every day
from 8 days to 1 month	every two days
from 1 month to 1 year	every two weeks
after 1 year	every two months

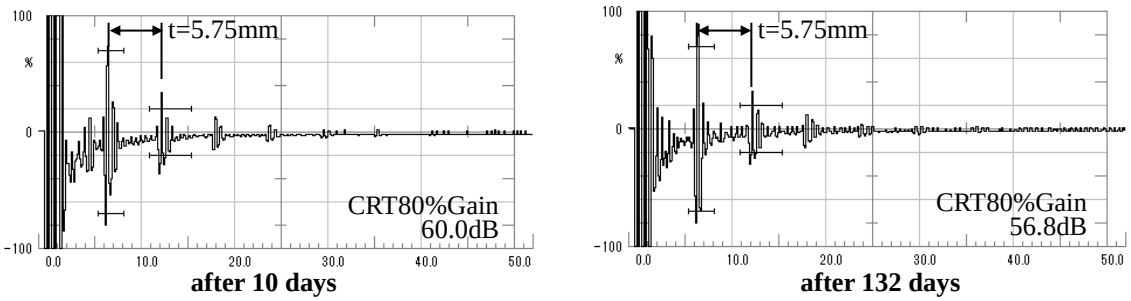

Fig.13 Waveform of field trial

5. Thin-film phased array UT sensor

In order to expand application of thin film UT technology, we developed a prototype of thin-film phased array UT sensor. Fig.14 shows the prototype. It is linear configuration phased array probe which has 8 elements. As it is known, this enables angle-beam examination by controlling oscillation timing as shown in Fig.15. Mockup test results are shown in Fig.16. This mockup is plate mockup of 22mm thickness and has several fatigue cracks. Tip echo of 3.7mm depth crack is clearly observed and the difference of crack depth is also clearly observed. These results suggest the possibility of continuous crack growth monitoring during plant operation.

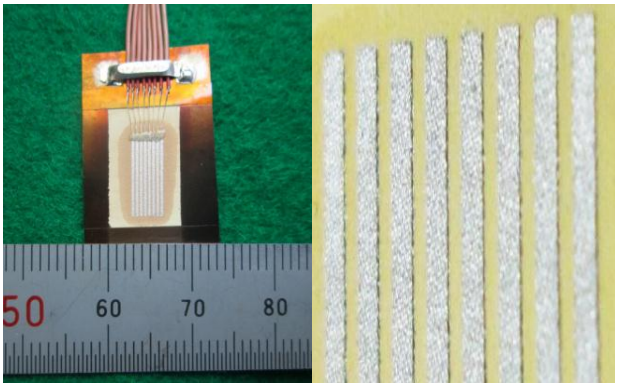

Fig.14 Thin-film phased array UT sensor

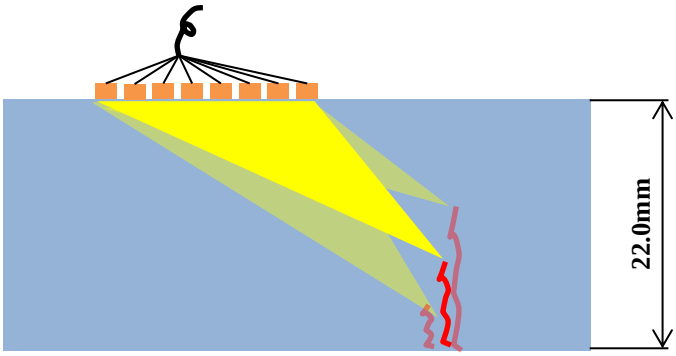

Fig.15 Concept of thin-film phased array UT sensor

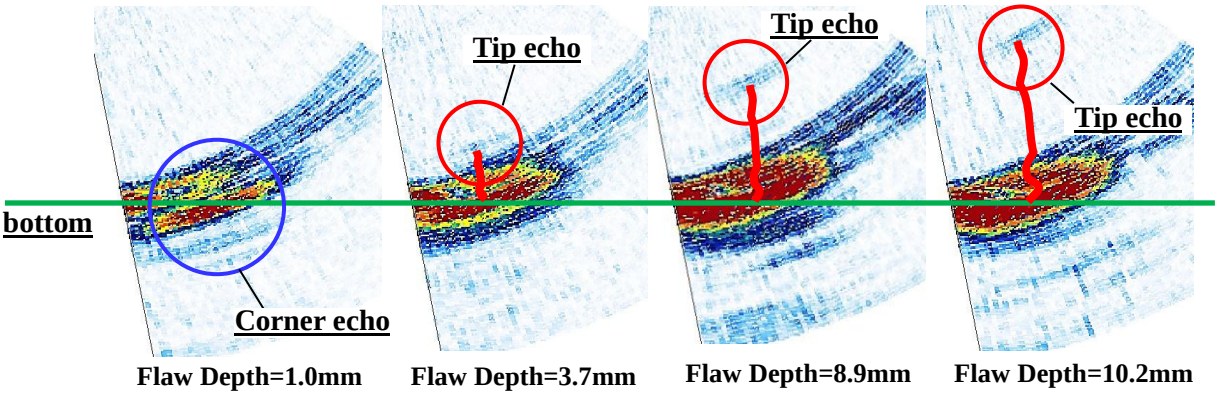

Fig.16 B-scope data of thin-film phased array UT sensor

6. Conclusion

We developed the thin-film UT sensor which is flexible and high temperature tolerant. We verified that thin-film UT sensor have high-measurement accuracy, high-temperature tolerant and irradiation durability. This thin-film UT sensor produces following advantage for pipe wall thinning management of nuclear power plant.

i. Measurement becomes stable because of continuous attachment.
ii. Additional work for installation and removal becomes unnecessary because of continuous attachment.
iii. Measurement on complex geometry becomes possible because of the flexibility.
iv. The continuous wall thinning monitoring during plant operating becomes possible.

Furthermore, we confirmed that thin-film UT sensor has possibility of continuous crack growth monitoring during plant operation.

We will investigate the suitability to Japanese standard and would like to replace all manual thickness measurement to continuous monitoring using thin-film UT sensor in the future.

References

[1] N. Fujita, I. Seki, T. Matsuura, Y. Yamamoto, M. Kurokawa, "Development of thickness measurement and thickness trend monitoring technology using high-temperature thin-film UT sensor", Japan Society of Maintenology, Vol.10, July 2013.

[2] M. Kobayashi, Cheng-Kuei Jen, Daniel Levesque, "Flexible Ultrasonic Transducers", IEEE Transactions on ultrasonics, and frequency control, Vol.52, No.8, August 2006.

[3] K. T. Wu, C. K. Jen, M. Kobayashi, A. Blouin, "Integrated Piezoelectric Ultrasonic Receivers for Laser Ultrasound in Non-destructive Testing of Metals", Journal of Nondestructive Evaluation (2011) 30:1-8

Residual stress evaluation of an IN 600 shot peening specimen by using the minimum reflection

Taek-Gyu Lee[1], Hak-Joon Kim[1], Sung-Jin Song[1], and Sung-Duk Kwon[2], Sung-Sik Kang[3],

[1]Sungkyunkwan Univ. Natural Sciences Campus, Cheoncheon-dong, Jangan-gu, Suwon-si, Gyeonggi-do, Korea
[2]Andong Univ., Songcheon-dong, Andong-si, Gyeongsangbuk-do, Korea
[3]Korea Institute of Nuclear Safety, 62 Gwahak-ro, Yuseong-gu, Daejeon 305-338, Korea

E-mail address(corresponding author) : sjsong@skku.edu

Inconel alloy is suitable for parts or system used in extreme environments like jet engine and nuclear reactor because it has high heat resistant and strong tensile strength. Especially, components made by IN 600, have applied ware shot peening process to produce residual stress. On the surface load in order to increase fatigue limit. So measurement of shot peening condition nondestructively is one of major issue in structure internally of the components. In this study, we applied minimum reflection method for measuring shot peening condition minimum reflected made based on reflection phenomena of generated Rayleigh waves. In this paper we will introduce minimum reflect method and measured results of shot peening at IN600 surface

Keywords: Inconel, shot peening, C-Scan, Rayleigh wave

Monitoring Microstructural Evolution in Steel Components with Nonlinear Ultrasound

James J. Wall[1,2,*], Kathryn Matlack[2,3], Jin-Yeon Kim[4], Jianmin Qu[5], Laurence J. Jacobs[2,4]

[1]Electric Power Research Institute, Charlotte, NC 28262
[2]G. W. Woodruff School of Mechanical Engineering, Georgia Institute of Technology, Atlanta, GA 30332
[3]Eidgenössische Technische Hochschule (ETH), Zurich, Switzerland
[4]School of Civil and Environmental Engineering, Georgia Institute of Technology, Atlanta, GA 30332
[5]Department of Civil and Environmental Engineering, Northwestern University, Evanston, IL 60208

[*]Corresponding Author (jwall@epri.com)

Material damage in structural components is driven by microstructural evolution that occurs at small length scales and begins early in component life. In metallic materials, these microstructural features associated with material damage are known to cause measurable changes in the acoustic nonlinearity parameter. Physically, the interaction of a monochromatic ultrasonic wave with microstructural features such as dislocations, precipitates, and vacancies generates a second harmonic wave with an amplitude that is proportional to the acoustic nonlinearity parameter. These nonlinear ultrasonic techniques thus have the capability to evaluate initial material damage, particularly before macroscale crack initiation and propagation occur. This talk will discuss how the nonlinear ultrasonic technique of second harmonic generation can be used as a nondestructive evaluation tool to monitor microstructural changes in steel, with a focus on characterizing neutron radiation- and thermally-induced embrittlement in nuclear reactor steels and model components. Experimental evidence in thermally and radiation damaged steels will be presented.

Corrosion Behavior of 304L stainless steel using confocal laser scanning microscopy (CLSM) and atomic force microscopy (AFM)

Joe-Ming Chang*, Tai-Cheng Chen, Hsiao-Ming Tung

Institute of Nuclear Energy Research Atomic Energy Council, No. 1000, Wenhua Rd., Jiaan Village, Longtan Dist, Taoyuan County 32546, Taiwan (R.O.C)

E-mail address(corresponding author) : joeming@iner.gov.tw

Dry Cask Storage System (DCSS) designs in Taiwan utilize a 304L stainless steel canister to confine spent nuclear fuel (SNF). These canisters were subjected to cold rolling and then welding during the fabrication process. Since these canisters are planned to be placed near the seacoast, chloride salts may deposit on the canister surface. The salts can deliquesce in specific environments, which may result in the aqueous solution necessary to initiate surface corrosion of the canister.

The purpose of this study was to investigate the effects of cold work on the corrosion behavior of 304L stainless steels. As-received and 20% cold-worked 304L stainless steels were used in the study. Corrosion tests were carried out in a salt spray system with a solution of 3.5% simulated seawater. The exposure time ranged from 0 to 12 h. Weight change and hardness were measured using a microbalance and a micro-hardness tester, respectively. Atomic Force Microscope (AFM) and Confocal Laser Scanning Microscope (CLSM) were employed to examine the surface morphology and surface roughness. In addition, the features of pitting corrosion, such as pitting area, width, length, depth and volume were characterized using OLS 4000 software.

The measurements of surface hardness exhibited no significant change before and after corrosion tests for both as-received and 20% cold-worked specimens. Surface morphology analyses revealed that corrosion products of the as-received specimen were observed after 2 h exposure. The degree of corrosion is more severe in the as-received specimen than that in the 20% cold-worked specimen.

Keywords: Corrosion, 304L stainless steel, Atomic Force Microscope, Confocal Laser Scanning Microscope

Water content distribution in concrete using the FDR method

Denis Vautrin[1], T. Clauzon[2], A. Courtois[2], F. Taillade[1]

[1]EDF R&D STEP, 6 quai Watier, BP 49, 78401 Chatou, France

[2] EDF DPIH DTG, Lyon, France

Abstract

This paper presents a diagnostic method for the estimation of the water content profile based on frequency domain reflectometry (FDR) measurements. The inversion algorithm allows estimating the inhomogeneous spatial profile of the water content into an electromagnetic dispersive material such as clay rock, concrete, etc. The principle of this method is validated on a synthetic data set corresponding to an inhomogeneous spatial water content profile and computed with a dispersive material model. Two experimental tests with sand have also been performed. The results show a good performance of the algorithm on the condition that different constraints are taken into account. The inversion algorithm requires a minimum of knowledge on the TDR sensor (no need for electromagnetic calibration of the TDR sensor head).

Keywords: water content, concrete, Frequency domain reflectometry, TDR sensors, inverse problem

1. Introduction

Electricité de France (EDF) operates 58 nuclear power plants in France, including a lot of concrete buildings, such as containment vessels and reinforced concrete natural draft cooling towers. These facilities have been in service for about 25 years and they are expected to provide electricity for the next 15 to 35 years. In order to support such long term operation project in high safety conditions, a specific Structural Health Monitoring (SHM) program has been established for each structure [1].

For nuclear structures, water content estimation is a major topic to understand and predict their behaviour at the end of the operating period. That is the reason why EDF is involved in research programs dedicated to concrete Thermo-Hydro-Mechanical (THM) modeling and to in-situ water content assessment technologies. It is well known that concrete delayed behaviour (shrinkage, creep…) is closely linked to the drying and moisture transfers within it. These phenomena are basically involved in the design of prestressed concrete civil structures, such as bridges, large LNG tanks, or nuclear power plant containments.

In order to get a better assessment of the delayed deformation for long term operation, EDF aims at enhancing the standard surveillance system provided for acceptance tests and in-service inspection (extensometer, displacement sensors, temperature probes, dynamometers). It turned out that the follow up of concrete water content over time could be a relevant method to reduce the uncertainties of the containment long term behaviour prediction. Among the sensing techniques able to measure water content in porous media, the Time Domain Reflectometry (TDR) probes appeared as a possible suitable monitoring tool for concrete moisture measurement. The TDR probes, interrogated by a method based on the Frequency Domain Reflectometry (FDR), enable to retrieve the water content distribution along the antennas (called also electrodes) of a TDR probe [2-4].

We present in this paper, a new formulation of the inverse problem taking the dispersive material (as concrete) and the water content distribution account in the telegrapher's equations. The new inversion algorithm is evaluated on numerical signals and tested on experimental measurements.

2. Theorical Background

2.1 Overview of some measurement technologies

Concrete is a porous material, made of cement, aggregates, sand, water, and sometimes other cement additive (Figure 1).

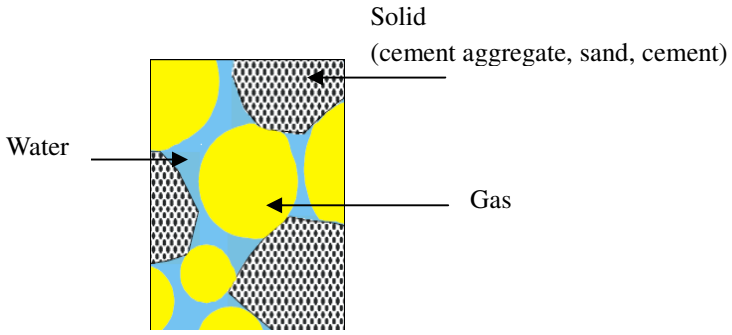

Figure 1. Porous network of concrete

The porous network resulting from the hydration of cement is characterized by its porosity Φ which corresponds to the fraction of void space in the material. Then we can define the saturation S_w (from 0 to 1) as the rate of full-water porosity volume versus the total porosity volume. At last, directly linked to the saturation, we can define the mass water content w:

$$w = \frac{S_w \cdot \rho_w \cdot \Phi}{\rho_c}$$

with ρ_w the water density (kg/m^3) and ρ_c (kg/m^3) the dry concrete density. In theory, saturation and concrete moisture are volumetric parameters, an average over an apparent and representative volume. The volumetric water content θ defined will be considered in the following:

$$\theta = \frac{\rho_c \cdot w}{\rho_w}$$

Capacitive sensors, Time Domain Reflectometry (TDR) sensors, tensiometric suction probes and neutron probes are sensors based on different physical phenomena able to provide a water content measurement. Ecole Centrale de Lille, ANDRA and EDF have launched a benchmark in order to compare the performance of these techniques and to collect data on the possible long term drifts. The tested technologies are presented in [5]. One of the outcomes of theses tests was the selection of two sensors suitable for structural monitoring: TDR and gas permeability "pulse" probes. Thanks to the high relative electric permittivity ε of the water (about 80) compared to the other concrete components (1 for air and about 5 for dry aggregates or cement paste), the electromagnetic methods are an attractive way to measure the water content. Moreover, the TDR sensors are especially robust for a use in industrial environment.

TDR is a well-known electromagnetic technique that has been used to determine the spatial location of cable faults. In the 1970's, the TDR technology has begun to be applied to geo-materials, in particular to evaluate soil water content [6-7]. The TDR sensors are constituted of two parallel rods placed into the probed material. The TDR method consists in recording the reflected voltage resulting from the emission and the propagation of a step pulse along the probe and in measuring the travel time and magnitude of all the echoes on the recorded signal (Figure 2). The relationship between the travel time τ and the material relative permittivity ε can be written as: $\varepsilon = c.\tau / (2.l)^2$ (where $c \approx 3 \times 10^8$ m/s is the velocity of light in vacuum and l is the electrode length).

Standard TDR devices (such as Campbell TDR100) make use of a broadband step voltage pulse, the frequency content of the measured TDR wave form extends from about *20 kHz* to roughly *1.5 GHz* [8]. However, this technique does not take into account the dispersive phenomenon: the relative permittivity of the concrete versus frequency is not a constant [9], called dispersive phenomenon. Moreover, it only provides a mean value of the water content and not an inhomogeneous distribution of the water content along the electrodes. For these reasons, we have preferred to use the FDR method.

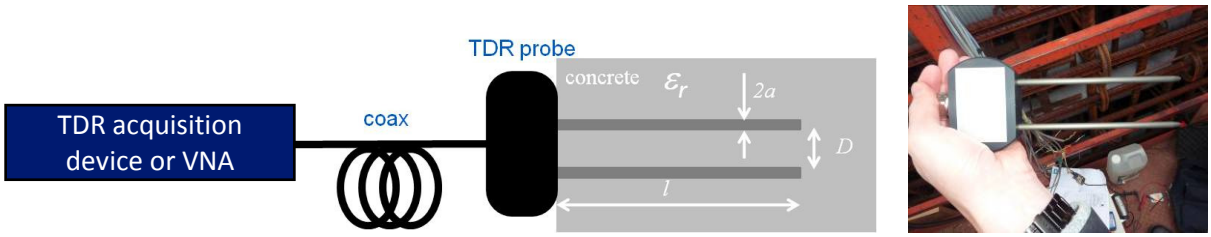

Figure 2. TDR device: measurement principle and picture of a TDR probe

2.2 FDR method & Electric model of the transmission line

The proposed technique is based on examining the concrete walls with the FDR method. The probe is connected to a calibrated vector network analyzer (VNA) using a coaxial cable (Figure 2). It measures the reflection coefficient $S_{11}(\omega)$ for different pulsations ω ($\omega=2\pi f$ where f is the frequency).

To model the propagation of an electric signal, the probe is considered as an electric line [10]. Generally, the electric signal transmission is modeled using the "telegrapher's equation" and characterized by the line parameters R, L, C and G, representing, respectively, the resistance, the inductance, the capacitance and the shunt conductance, per unit length (Figure 3). In the harmonic regime, telegrapher's equations are written as follow:

$$\begin{cases} \dfrac{\partial V(\omega,z)}{\partial z} + i\omega L(\omega,z)\, I(\omega,z) + R(\omega,z) I(\omega,z) = 0 \\ \dfrac{\partial I(\omega,z)}{\partial z} + i\omega C(\omega,z) V(\omega,z) + G(\omega,z) V(\omega,z) = 0 \end{cases}$$

with the intensity $I(\omega,z)$ and the voltage $V(\omega,z)$ depend on the space position z and the pulsation $\omega=2\pi f$ where f is the frequency. The following boundary conditions are verified at both ends at $z=0$ and $z=l$

$V(\omega,0) + Z_{srce}(\omega)\, I(\omega,0) = V_{srce}(\omega)$

$V(\omega,l) - Z_{extr}(\omega)\, I(\omega,l) = 0$

where $Z_{srce}(\omega)$ is the internal source impedance of the VNA connected at $z=0$ ($Z_{srce}(\omega)$=50Ω) and $Z_{extr}(\omega)$ is the terminal impedance connected at $z=l$ with $Z_{extr}(\omega) = 1 / (i\chi\omega\, \varepsilon'(\omega))$ where χ is determined by finite element simulation and it depends on geometries of the TDR sensors (for a typical TDR sensors: 2a = 6 mm and D = 40 mm, $\chi = 2.4 \times 10^{-3}$ m). $V_{srce}(\omega)$ represents the harmonic source generator

The transmission parameters along the line (as velocity and attenuation) depend on the complex permittivity of the material that is placed between the wires of the electric line (the TDR's electrodes). For two parallel rods, the electrical parameters depends on the permittivity as written below:

$L(z) = \mu_0\, \eta$ with $\eta = 1/\pi\ acos(D/2a)$

$C(\omega,z) = \varepsilon_0\, \varepsilon'(\omega)\, \eta$

$G(\omega,z) = \omega\, C(\omega,z)\, \varepsilon''(\omega, z) / \varepsilon'(\omega, z)$ where $\varepsilon(\omega, z) = \varepsilon'(\omega, z) - i\, \varepsilon''(\omega, z) = g(\omega, \theta(z))$ and $i=\sqrt{(-1)}$

$R(\omega,z) = 1 / (\sigma\, \pi\, a\, \delta_r)$ with $\delta_r = 1/\sqrt{\mu\sigma\pi f}$ and σ the electric conductivity of electrodes

The water content profile along the electrodes is introduced by a function $g(\omega, \theta(z))$ in the relative electric permittivity parameter ε which takes into account the dispersive phenomenon.

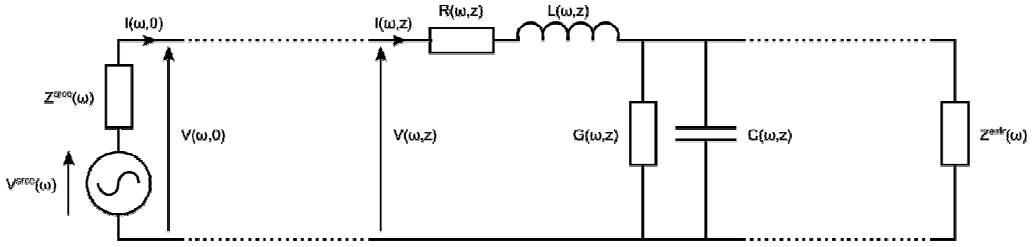

Figure 3. Transmission line model

For a given water content profile, the previous equations enable one to compute the voltage $V(\omega,x)$ and the electric current $I(\omega,x)$ for each spatial points of the electric line and each frequency. Taking the condition boundary at $z=0$ into account, the modeled reflection coefficient $S_{11}^{cal}(\omega, \theta)$ which depends on a water content profile θ as follows:

$$S_{11}^{cal}(\omega, \theta) = 2\, V(\omega,0) - 1$$

2.3 Inversion method

The inversion method is based on the minimization of a regularized least-squares criterion:

$$C(\theta) = \sum (S_{11}^{mes}(\omega) - S_{11}^{cal}(\omega, \theta))^2 + \phi(\theta)$$

where ϕ is a regularization term.

In order to speed up the inversion, the reflection coefficient are computed using a matrix formulation of the model based on sparse matrices. The criterion is minimized by means of the L-BFGS algorithm [11]. This quasi-Newton method only requires criterion and gradient computations. It is well suited to our problem since it enables to approximate the Hessian of the criterion with a small amount of storage. A similar approach was proposed in [12].

3. Simulations and validations

3.1 Result on synthetic data

In order to validate the proposed inversion method, results on a numerical simulation is presented in this section. Synthetic reflectometry measurements are computed by solving the forward problem presented in the previous section on a frequency range from *1 MHz* to *1 GHz* with a frequency sampling $\Delta f = 1$ *MHz*. To avoid the inverse crime problem, we add a white Gaussian noise sequence with a standard deviation such that the signal to noise ratio is *40 dB*. The following water content profile is used: $\theta(z)=8\%.(1-e^{10z}))+3\%$.

A model of the relative electric permittivity of the clay rock based on [13] is used so as to introduce a dispersive frequency dependence. In the first simulation, we have considered only the two parallel electrodes of the 600 mm of length as an electric line i.e. TDR sensors without head (junction between coaxial cable and two electrodes). A first-order Tikhonov regularization function is used to regularize the problem: ϕ corresponds to a quadratic penalty term applied to the differences in water content between all pairs of neighboring points. The first result is shown on the figure 4. The algorithm converges to a water content profile close to the exact solution. The solution found is relatively independent of the initialization of the inverse algorithm.

3.2 Results on experimental data

Experiments were carried out to check the validity of the numerical simulations. A TDR sensors with the electrodes of a 6 mm diameter, 40 mm inter-axis and 600 mm of length is used; the TDR is buried in a sand tank (Figure 5). The sand is a non-dispersive material but it allows us to test rapidly the inversion algorithm on experimental data. In a first test, the sand is considered as “dry” i. e. with the low relative humidity (HR). In the second test, a part of sand (between 240 and 600 mm) is moist and the HR is increased of few percent. The measurements $S_{11}^{mes}(\omega)$ are performed using a VNA of Anritsu MS2026 (Figure 6a). The TDR sensors is connected to the VNA through a coaxial cable of 2 m length. The measurements are performed on a frequency range of *1 MHz* to *1 GHz* with a frequency sampling of *1 MHz* (1000 points).

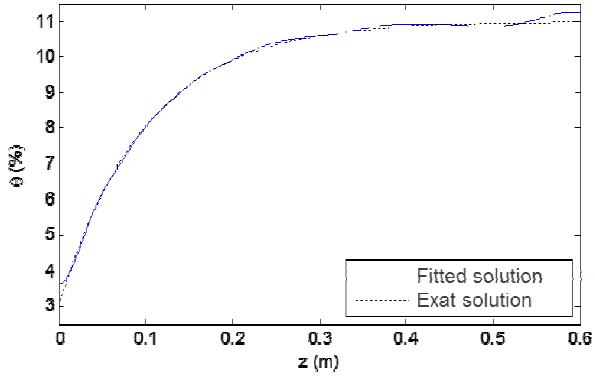

Figure 4. Water content profile: in dotted line the exact solution and in blue line the fitted solution

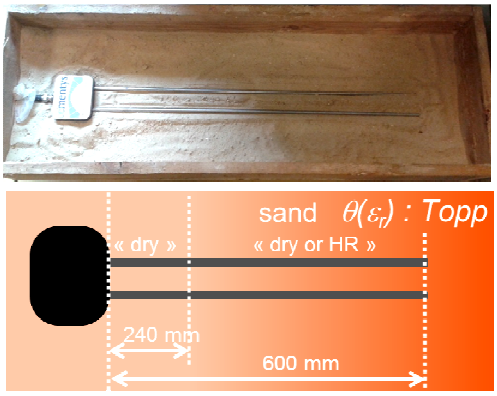

Figure 5. Mockup for a water content profile

We have considered a Topp [14] model to describe the relation between the relative electric permittivity and the volumetric water content of the sand. The inversion algorithm is performed on the experimental measurements. Unfortunately, the lack of knowledge of the TDR sensor head has introduced some perturbations in the inversion which does not allow to determine the water content profiles with a good accuracy. To compensate the lack of knowledge about the sensor head, additional prior information have been taken into account in the inversion algorithm. The results are presented in Figure 6b. In the first test (dry sand), the volumetric water content profile is relatively constant (of the order of 2%) along the electrodes. In the second test (dry + moist sand), the volumetric water content profile is close to the previous profile on the spatial range of 0 to 210 mm corresponding to a dry sand zone. On the spatial range of 210 mm to 600 mm, the volumetric water content profile is increased as expected qualitatively.

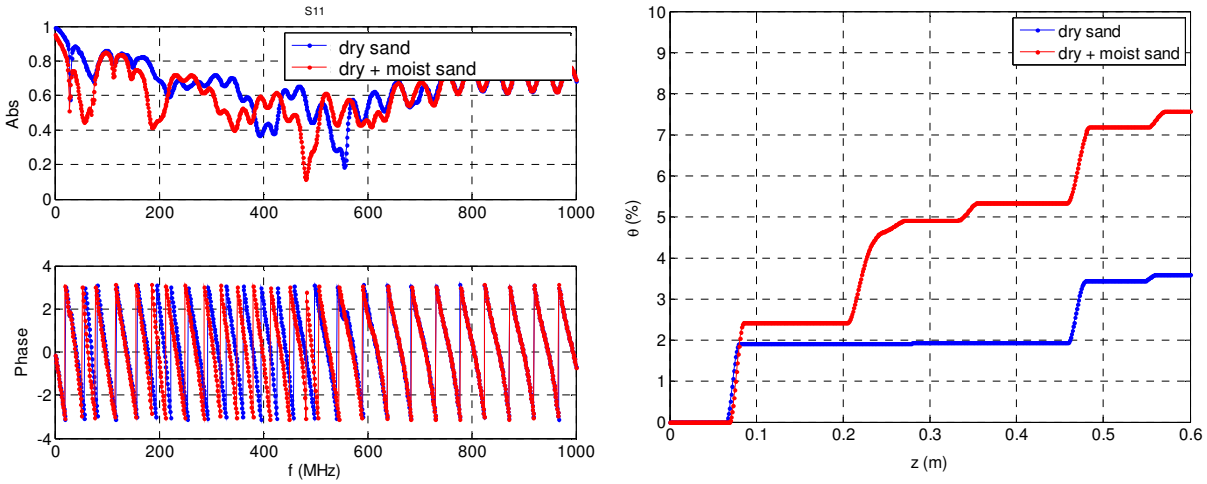

Figure 6. a) $S_{11}^{mes}(\omega)$ measurements, b) water content profile estimated

4. Conclusion

In this paper, we have presented an inversion algorithm for the water content estimation based on FDR measurements. The principle of this method is validated on a synthetic inhomogeneous spatial water content profile and using a dispersive material model. Two experimental tests where the probe is buried in a sand tank show that the proposed method is able to distinguish a homogeneous and inhomogeneous water content profile, on the condition that different constraints are taken into account. The inverse algorithm requires a minimum of knowledge on the TDR sensor (no need for electromagnetic calibration of the TDR sensor head).

Further research is needed to estimate the profile of the water content along the TDR sensor electrodes with a better accuracy. Another improvement relates to the design of the TDR probe itself and in particular the junction between the coaxial cable and two parallel electrodes, i.e. the TDR sensor head.

References

[1] P. Stephan, J. Salin, Ageing management of concrete structure: Assessment of EDF methodology in comparison with SHM and AIEA guides, Constr. And Build Mat., 37 924-933 (2012).

[2] H. Tang and Q. Zhang, Inverse scattering for lossy electric transmission line soft fault diagnosis, Antennas and Propagation Society International Symposium (APSURSI), (2010)

[3] Q. Zhang, M. Sorine, and M. Admane, Inverse Scattering for Soft Fault Diagnosis in Electric Transmission Lines, In 48th IEEE Conference on decision and Control, Shanghai, China, (2009).

[4] F. Visco-Comandini, T. Bore, G. Six, F. Sagnard, S. Delepine-Lesoille, G. Moreau, D. Placko and F. Taillade, FDR for non destructive evaluation: inspection of external post-tensioned ducts and measurement of water content in concrete, In 10th International Conference on Nondestructive Evaluation (NDE) in relation to Structure Safety for Nuclear and Pressurized Components, Cannes, France, (2009).

[5] Moreau G., Dubois J.-P., Agostini F., Salin J., Masson B., and Skoczylas F. (2010). "Survey of the future concrete structures lifetime measuring the water content: four types of embedded sensor under checking", International Symposium Fontevraud 7 - Contribution of materials investigations to improve the safety and performance of LWRs, Avignon, France, (2010)

[6] Davis J.L. and Chudobiak J.W. "In-situ Meter for Measuring Relative Permittivity of Soils", Geol. Surv. Can., Ottawa, Pap 75-1A, 75-79, (1975)

[7] Noborio K. "Measurement of soil water content and electrical conductivity by time domain reflectometry: a review", Comput. Electr. Agricult., 31, 213-237, (2001)

[8] Heimovaara, T., W. Bouten, and J. Verstraten (1994), "Frequency domain analysis of time domain reflectometry waveforms, A four-component complex dielectric mixing model for soils", Water Resour. Res., 30(2), 201-209.

[9] Al-Qadi I. L., Riad S. M., Mostaf R. and Su W. (1997). "Design and evaluation of a coaxial transmission line fixture to characterize Portland Cement Concrete", Constr. and Build. Mat. 11(3), 163-113

[10] D. M. Pozar, Microwave engineering, Wiley, New York, 3rd ed. edition, (2005)

[11] Hu, J.-L., Wu, Z., McCann, H., Davis, L., and Xie, C.-G., "BFGS quasi-Newton method for solving electro-magnetic inverse problems," IEE Proceedings Microwaves, Antennas and Propagation 153, 199–204 (2006).

[12] D. Vautrin, M. Voorons, J. Idier, Y. Goussard, S. Kerzal et N. Paul, Seismic imaging of transmission overhead line structure foundations, in Computational Imaging IX (IS&T/SPIE Symposium on Electronic Imaging), San Francisco Airport, CA, USA, jan. (2011).

[13] N. Wagner, T. Bore, J.-C. Robinet, D. Coelho, F. Taillade and S. Delepine-Lesoille, Dielectric relaxation behavior of Callovo-Oxfordian clay rock: A hydraulic-mechanical-electromagnetic coupling approach, Journal of Geophysical Research: Solid Earth 118 (9), 4729-4744, (2013)

[14] Topp G.C., Davis J.L., Annan P., Electromagnetic determination of soil water content: measurement in coaxial transmission lines. Water Resour. Res., 16(3), 574-582, (1980)

Two dimensional FEM simulation of ultrasonic guided wave propagation in multilayered pipe with delamination

Vu Anh Hoang[1], Hak-Joon Kim[1], Sung-Jin Song[1]
[1]Sungkyunkwan University, School of Mechanical Engineering, 300 Chunchun-dong, Jangan-gu, Suwon 440-746, South Korea

E-mail address : sjsong@skku.edu

Abtract:
Ultrasonic guided wave propagation in multilayered pipes can be modeled using Finite Element Method (FEM). The FEM uses various parameters which need to be optimized properly to obtain the solutions closer to the exact one. A two dimensional FEM model has been designed in COMSOL Multiphysics and has been simulated for having a better understanding of propagation and interference phenomena by creating a window of observation in the multi-layered pipe. A COMSOL simulation has been set up with the ultrasonic guided wave generated in the complete multilayered pipe without any defect. Then a delamination between two layers of the pipe has been created and again simulated for guided wave propagation with the presence of the delamination. The different modes of ultrasonic vibration were observed due to the presence of the delamination in the pipes.

Keywords: Ultrasonic, Guided wave propagation, FEM, Delamination, COMSOL

1. Introduction

The ultrasonic guided wave method has become successful in Non-Destructive Evaluation (NDE) because of its versatility and long-ranger inspection possibility in thin-wall structures. Understanding of ultrasonic guided wave propagation and its capability of flaw defection is an important aspect for proper evaluation of wave characteristics for nondestructive evaluation of material or defection of flaws [1]. Ultrasonic guided waves are suitable for long-range inspection and online monitoring of pipe [2-3]. Guided wave in piping are combination of various wave modes, each wave mode has a different sound velocity that depends on frequency. Therefore, guided wave inspection results are difficult to interpret so theoretical analyses tools, such as model analyses, mathematical calculation [4] and semi-analytic numerical calculation [5] help for optimization of the inspection setup as well as interpretation of the inspection results for simple situation. However, the ultrasonic guided wave propagation can be simulated using Finite Element Method (FEM) [6]. The simulation parameters used in FEM plays very important role for the usefulness of the obtained data. This paper presents Finite Element Method (FEM) simulation of ultrasonic guided wave propagation in delaminated multilayered pipes using COMSOL.

2. Two Dimensional FEM Model of ultrasonic guided wave propagation

A two-dimensional finite element method model for propagation of ultrasonic wave in the delaminated multilayered pipes has been studied with COMSOL.

2.1 Material and Ultrasonic guided wave properties

The materials chosen were Stainless steel, Teflon and Acrylic plastic with following properties as table 1.

Table 1. Materials and Ultrasonic guided wave properties

Material properties	unit	Stainless steel	Teflon	Acrylic plastic
Young's Modulus	Pa	2×10^{11}	7.5×10^{8}	3.2×10^{9}
Poisson's ratio		0.33	0.46	0.35
Density	Kg/m3	7850	2150	1190
Ultrasonic velocity	m/s	5950	1350	2730
Element size	mm	0.3	0.1	0.2

2.2 Incident ultrasonic guided wave

A 2 mHz frequency ultrasound has been transmitted to the pipes. The disturbance as the input signal is applied to a line of length 2.54cm which means the transducer has been modeled as the disturbances on a line. The initial disturbance is given as the displacements in perpendicular direction to the wedge surface only for modeling the normal incidence of ultrasonic wave. The input signal is provided from a date file and the linear interpolation is considered for the value of displacement at the undefined time in the data file.

The time domain representation of input displacement pulse used in the model is shown in the figure 1. The frequency content of the input signal was evaluated as the Fourier transform of the time domain signal and is as shown in figure 2.

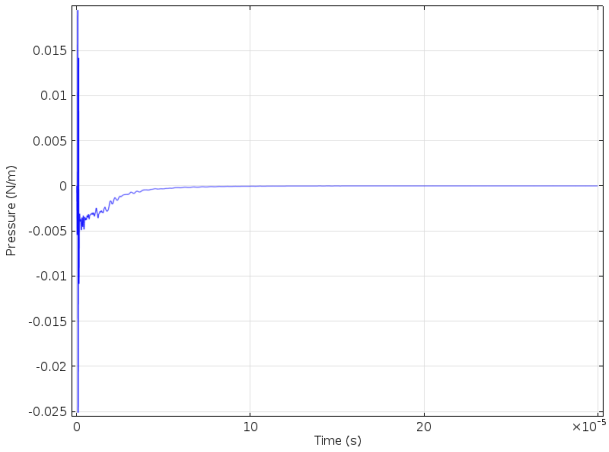

Figure 1. Input pulse as source excitation

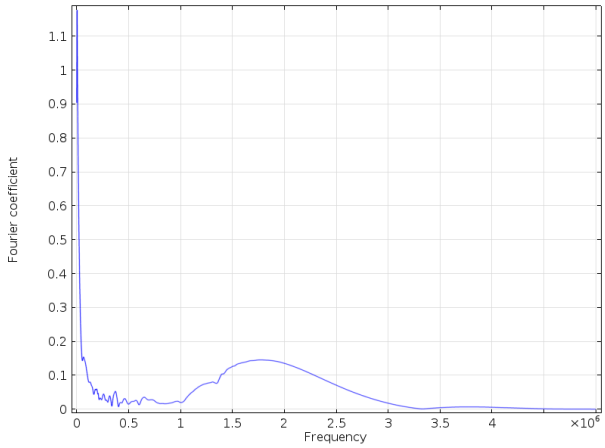

Figure 2. Input signal in frequency domain

2.3 Model Geometry

A circular geometry has been chosen as shown in figure 3 where the essential free boundary conditions were applied at the inner and outer diameters of the pipe wall. The initial disturbance was applied on a line of length 2.54 cm located at the top line of the designed wedge. As all the observation were made for the longitudinal wave only the signal was observed on the perpendicular line that passes through the middle of the source.

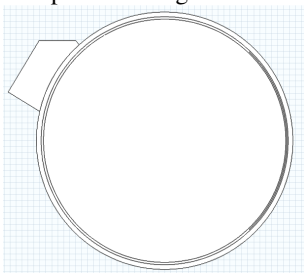

Figure 3. 2 dimensional multilayered sample pipe with delaminated area

2.4 Meshing

The mesh was generated automatically with the triangular elements. Free meshing provided in COMSOL was used for the generation of mesh. The elements were chosen as uniform throughout the domain. The mesh has been refined at the region below the excitation source. Minimum mesh quality that has been ensured for each of the model that has been solved is 0.1 with an element area ratio of about 0.03.

2.5 Application mode

For modeling of the two dimensional geometry, the plane wave radiation was applied. Time dependent analysis, free triangular type of element and time dependent solver was used for the solution. The duration of time span for the solution was chosen such that defect reflected signal appeared or from where excitation started.

3. Simulation result for ultrasonic guided wave propagation in Time domain

In this study, the maximum element size was chosen of $\lambda_L/12$ and the model was simulated for the ultrasonic guided wave propagation, λ_L is the wave length of longitudinal ultrasonic wave propagated in the direction of incidence. The time step chosen initially for simulation is $0.1 \times 10^{-6}\ s$. The calculation for the chosen time steps is as follows.

As per CFL criteria the time step should be less than $\Delta x/C_L$, in this case, for the maximum element length of $\lambda_L/12$ the time step should be $\leq \lambda_L/12 \times C_L$ that means if $\Delta x_{max} = \frac{\lambda_L}{12} \Rightarrow \Delta t \leq \frac{\Delta x_{max}}{C_L} = \frac{\lambda_L}{12 \times C_L}$. Corresponding the critical value of Δt was calculated to be

$$\Delta t = \frac{\Delta x_{max}}{C_L} = \frac{0.2m}{5850m/s} = 0.3 \times 10^{-6}\ s$$

The value of Δt used in the simulation was $0.1 \times 10^{-6}\ s$ which was less than the critical time step calculated above. The ultrasonic signals were plotted in time domain at different sizes of the delaminated area in different specimens for the same value of $\frac{\lambda_L}{\Delta x_{max}}$ at t = $3 \times 10^{-4}\ s$. A cross sectional plot (a cut line in the middle of the delaminated area) was also plotted at t = $3 \times 10^{-4}\ s$. The time t = $3 \times 10^{-4}\ s$ is chosen by the time the signal reaches to the defect. The above plots were used to evaluate the appearance of the delamination in pipes by comparing the arrival time and amplitude of the reflected and transmitted waves between different cases.

The signal at a various sizes of delaminated area in separated specimens was plotted for same size of element as shown below. The following plots (figure 4) show the onward propagating signal at a time of $3 \times 10^{-4}\ s$ plotted along the perpendicular line passing through the center of the line source.

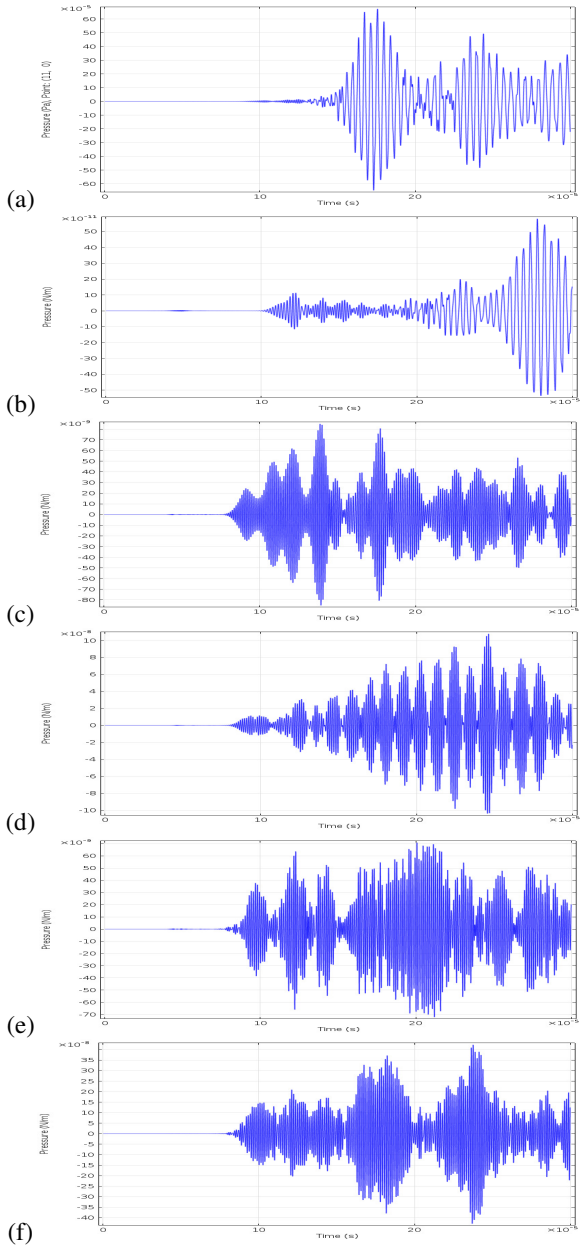

Figure 4. Onward propagating waves signal at various sizes of delaminated area in time domain corresponding to (a) D = 0, (b) D =3.75cm, (c) D = 5cm, (d) D = 7.5cm, (e) D = 12.5cm, (f) D = 15cm.

4. Frequency content of the forward propagated signal

The frequency content of the propagating wave has been evaluated by Fast Fourier transform of the onward propagating wave. The figure 5 shows the onward propagating waves in frequency domain for six cases of different sizes of delamination for $\Delta t = 0.1 \times 10^{-6}\ s$

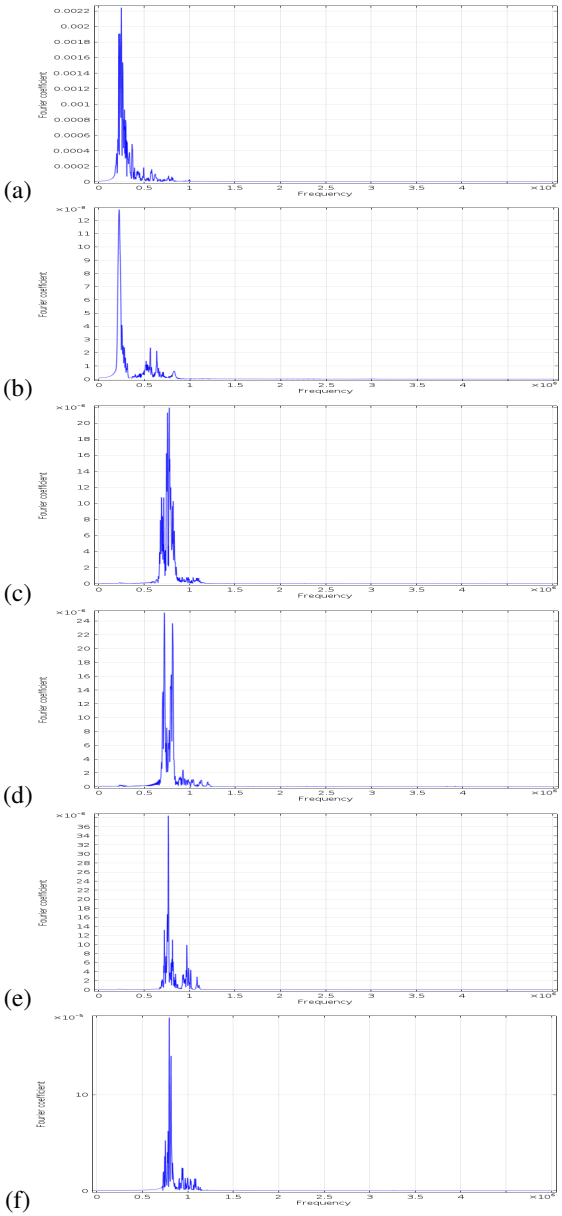

Figure 5. Frequency domain signal for on ward propagating wave corresponding to (a) D = 0, (b) D =3.75cm, (c) D = 5cm, (d) D = 7.5cm, (e) D = 12.5cm, (f) D = 15cm.

5. Discussion

All results shown in figure 4 were obtained for the time step of $0.1 \times 10^{-6}\ s$ which is well below the value calculated using CFL criteria. The time domain signal shown in figure 4 (a) that in the case that is no defect, signal acquired will show the high value of maximum amplitude, and the time arrival of reflected waves is around $15 \times 10^{-5}\ s$. For the following case in Figure 3 (b), (c), (d), (e), (f), when the wave encounters the delaminated area across it path, part of the wave gets reflected and travels in the opposite direction, and reflected wave reaches the transducer around the time of arrival of $10 \times 10^{-5}\ s$. Thus, the presence of the delaminated area will be indicated by a sudden decrease in the maximum amplitude of the signal between the initial and the delamination signal group that can be shown in figure 6.

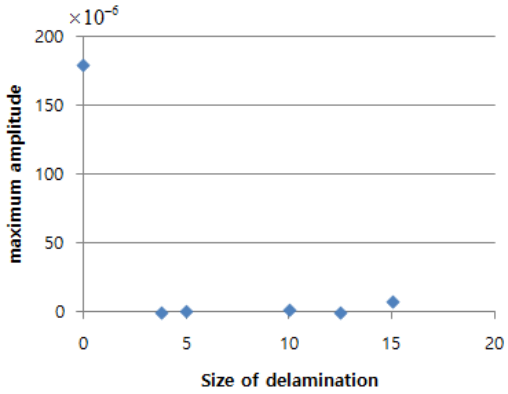

Figure 6. Maximum amplitude for different sized delamination in time domain

Figure 5 shows it is clear that the delaminated area can be determined by observing the change in the frequency domain signal for the onward propagating for various sizes of delaminated area in the final converged solution. Although there is no substantial change between the initial and the case with smallest sizes of delaminated area but when increasing the sizes of delaminated area difference can be observed as shown in Figure 7.

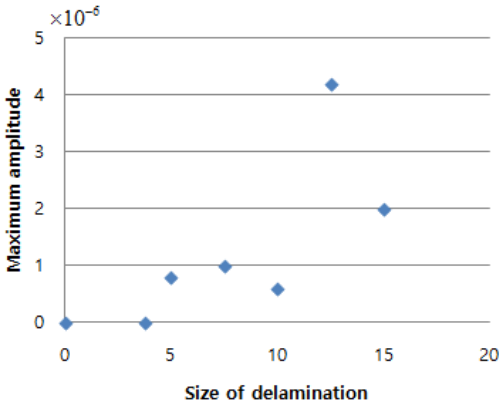

Figure 7. Maximum amplitude for different sized delamination at 1mHz

6. Conclusion

Ultrasonic Guided wave propagation can well be modeled using two dimensional Finite Element method with excitation on line segment as transducer. The free triangular element meshing can be used for the simulation of Ultrasonic Guided wave propagation for a value of $\frac{\lambda_L}{\Delta x_{max}} = 12$. Delaminated area can be determined by comparing the arrival time and amplitude of the reflected and transmitted waves between specimens with and without delamination in time domain also frequency domain. No substantial difference of the maximum amplitude in the frequency content of the onward solution between the initial and delaminated specimen with small size but if we keep increasing the size of delaminated area the difference becoming clearly.

References

[1] M.J.S Lowe, D.N. Alleyne , P. Cawley, “Defect Detection in Pipes using Guided Waves”, Ultrasonic, Vol. 36, pp.147-154 (1998)

[2] Joseph L. Rose, “Ultrasonic Guided Waves: An Introduction to the Technical Focus Issues”, Materials Evaluation, Vol. 61, pp.65(2003)

[3] P. Cawley, M.J.S. Lowe, P.N. Alleyne, B. Pavlakovic and P. Wilcox, “Practical Long Range Guided Wave Testing: Applications to Pipes and Rails”, Materials Evaluation, Vol.61a, pp.80-84(2003)

[4] Joseph L. Rose, Jing MU, Younho CHO, “Recent Advances on Guided Waves in Pipe Inspection”, 17th WCNDT, pp.25-28(2008)

[5] Takahiro, Hayashi and Joseph L. Rose, “Guided Wave simulation and visualization by a semi-analytical Finite Element Method”, Materials Evaluation, Vol.61, pp.75-79(2003)

[6] Friedrich Moser, Laurence J. Jacobs, Jianmin Qu, “Modeling Elastic Wave Propagation in Waveguideds with Finite Element Method”, NDT&E International, Vol.32, pp.225-234(1999)

Advanced Tools based on Simulation for Analysis of Ultrasonic Data

Souad BANNOUF[1], Sébastien LONNE[1], Florence GRASSIN[2], Stéphane LE BERRE[2] , David ROUE[2]

[1]EXTENDE, 15 Avenue Emile Baudot, 91300 MASSY, France

[2]CEA-LIST, Centre de Saclay, 91191, Gif-sur-Yvette Cedex, France

Abstract

The analysis of ultrasonic data occurs at the final step of nondestructive testing process, and is a critical element for its performance. Phased array technologies add an additional level of complexity, by their ability to combine several modes and several exploration areas. The use of simulation in order to facilitate the interpretation of data acquisition is a relatively untapped area, and opens the way for advanced characterization and automatic inversion.
The first part of this paper presents the module "CIVA Analysis" for ultrasonic NDT data. It includes imaging and reconstruction tools to identify the indications of an inspection. As an example, the segmentation will be described. This feature allows an automatic identification and characterization of indications in a large area of interest.
The second part of this communication will present the "Simulation on Acquisition" feature: from his first diagnosis, the analyst is able to quickly launch a simulation process to understand and interpret certain complex phenomena.

Keywords: CIVA, Analysis, Simulation, Acquisition, Characterization, Segmentation

1. Introduction: A software platform for UT data analysis and simulation

CIVA is a well-known versatile software for the modelling of NDT process that includes different simulation modules for various inspection methods: Ultrasound testing (UT), Guided-wave Testing (GWT), Eddy-Current Testing (ET), Radiographic Testing (RT) and Computed Tomography (CT). Along with its latest version CIVA 2015, this platform also includes now an analysis module for UT acquisition data. The main objectives of this analysis software are to display acquisition data in an easy and understandable way, to extract advanced information in an efficient manner, to put this data into a dynamic report and to avoid repeatable and time consuming operations. In addition to these essential tools for the analysis work, this module benefits from the long experience capitalized in CIVA in modelling innovative UT inspection methods in order to provide the users with advanced and easy to use tools. One example is the segmentation algorithm (now enhanced and automated) that has been used for years and has been qualified for the analysis of inspection data on French nuclear vessels. Innovative reconstruction methods associated to Phased-Array technologies such as the “Total focusing Method” is also available to process UT data, often acquired with the Full Matrix Capture mode. Signal processing tools are other features available to help for Signal to Noise ratio enhancement. Finally, the connection with the simulation part of CIVA provides to the user the possibility to compare easily real data and simulated trials. This helps to understand some phenomena or to highlight the need for an improvement in detection and characterization methods especially when the current results are ambiguous or lead to imprecise diagnosis. Some simplified simulation tools (“Simulation on Acquisition”) are even directly available in the CIVA Analysis module itself.

In this paper, after a description of the general process followed during a data analysis, some features of this new analysis software are described, such as the segmentation principle or the “Simulation on Acquisition” tool. Application examples are described to illustrate their use.

2. The process of UT data of analysis

The analysis of ultrasonic data obtained by automated or at least geo-localized acquisitions is usually performed according to one or several procedures and with the use of dedicated software. The analysis objective is to obtain an examination report that lists the operating conditions and the indications present in the inspected component.

The first step in the analysis process is to validate the acquisition, that is to say, to ensure that it is conform to the expected one. The acquisition parameters, its quality and the probes calibration are checked. Then, the analysis procedure may include some preliminary signal processing such as amplitude thresholding, application of Distance Amplitude Curve correction or reconstruction of the data in the accurate frame. For example, let's consider cracks analysis using angular scanning with a linear probe . The challenge is to optimize the visualization of the diffraction echo for an optimal characterization of the defect. In CIVA Analysis, the "limitation" tool allows to select data acquired at different angles. Figure 1 presents an analysis page where the top view (left) and section view (right) for each studied angle are displayed. This provides an overview of the acquired data.

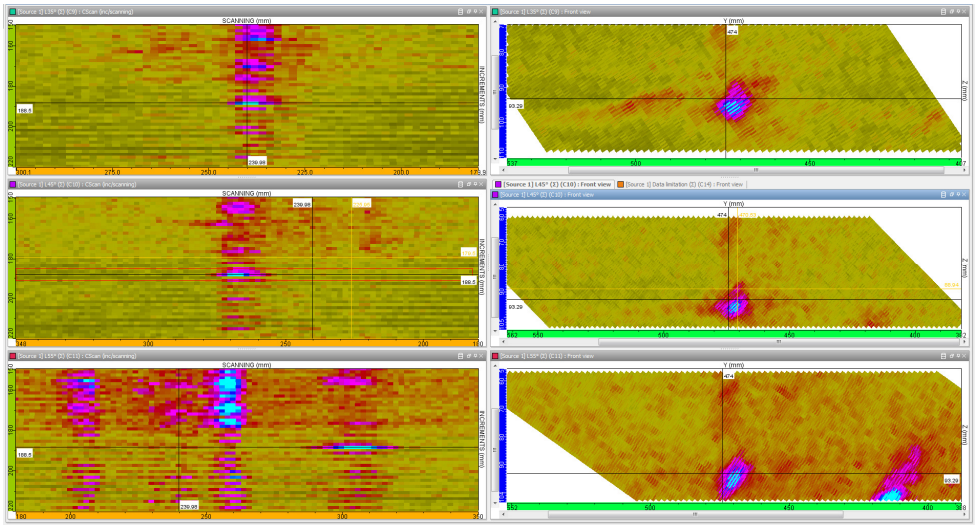

Figure 1: Overview of the data at different angles (35°, 45° and 55° from top to bottom). Images at left are top views and images at right are section views.

Synchronized cursors allow to optimize the limitation of the data (Figure 2) so the user may select the "best" angle to use for side view display. This allows to improve analysis.

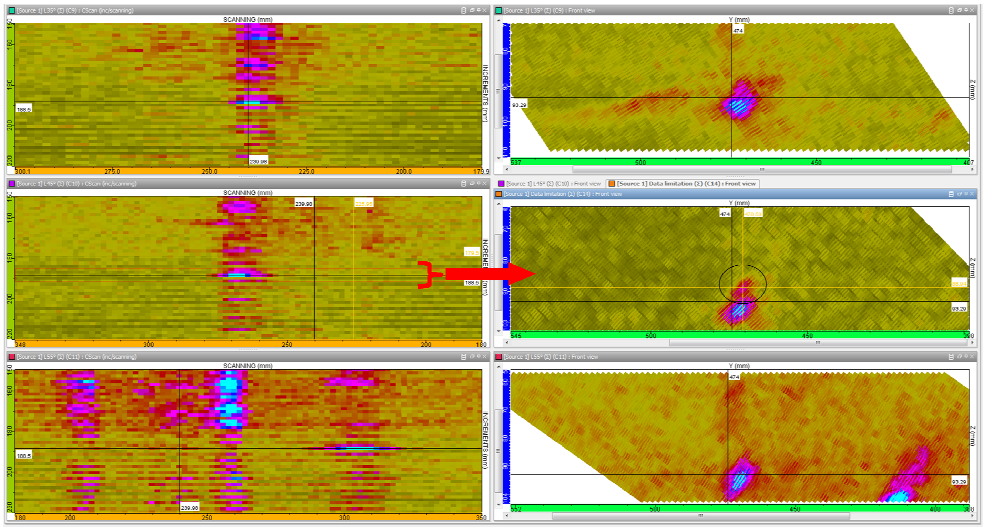

Figure 2: Optimization of the limitation to enhance the diffraction echo detection for the "best" inspection angle

This first step may take time but it needs to be realized only once. Indeed, all the actions described above (limitation, display of specific views,…) can be recorded thanks to the "template" tool and be reapplied to files corresponding to similar controls. Thus, the "template" automates this preliminary step, allowing the user to save time and to focus on the analysis itself.

Once it is done, the procedure imposes detection and characterization thresholds, most of the time defined by standards or codes. The goal is to eliminate false calls or small defects which do not fall within the search criteria. Clustering and segmentation algorithms help quickly determining the echoes of interest which are then studied more finely. The signals evolution according to the probe position, the shape and the position of the echoes, distance

measurement and so on are analyzed and noted in an indication table that is resumed in the final examination report. Figure 3 shows the results of application of the segementation tool to the previously studied angular scanning of a crack. The algorithm will be described more precisely in section 3.

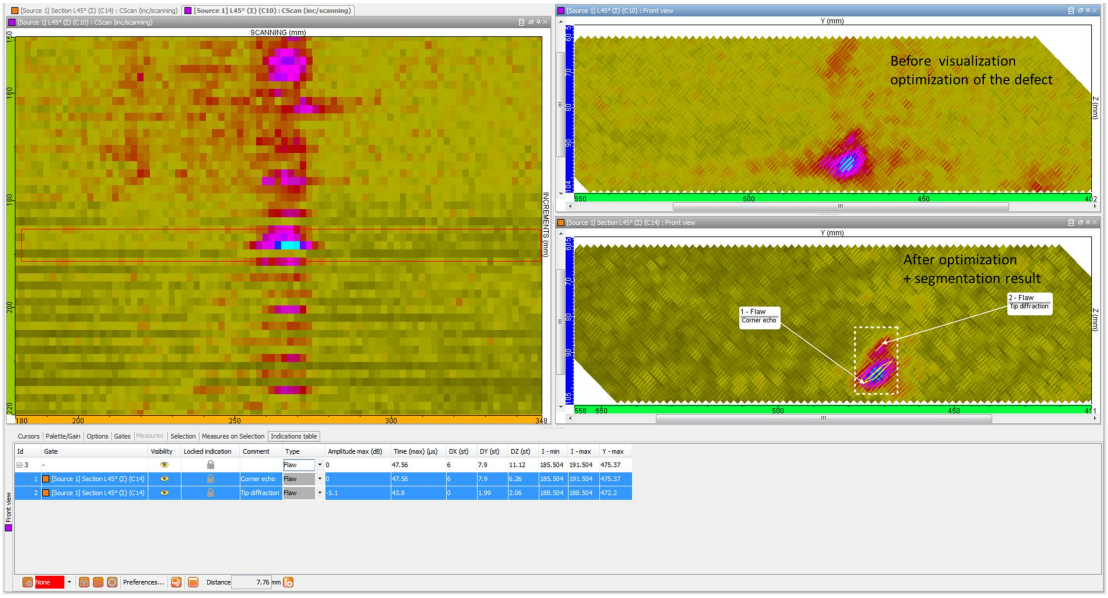

Figure 3**:** Segmentation result for the defect

Some inspection cases need particular process for both acquisition and analysis. Systems including analysis software were developed and dedicated to these particular cases such as pipe inspection with “zonal discrimination” method. Several suppliers propose solutions. However, these solutions have to be adapted to each case and vigilance is required in order to make sure that influent parameters are under control. In the French nuclear industry, qualification is based on the RSEM code. CIVA simulation software and its associated analysis tools are dedicated for the analysis of inspection data.

3. Segmentation: A powerful algorithm for indications grouping

The goal of the segmentation algorithm is to group signals that come from the same defect or part of a defect. This grouping is based on an algorithm that ensures a more efficient association than a geometrical one (only based on geometrical proximity). This algorithm assumes that locally, the wave front is planar. Thus, the grouping is based on a physical behavior of the ultrasound wave and reduces drastically grouping of false calls such as noise.

The parameters used to set segmentation can also be determined by a physical approach that increases the confidence level of grouping (based on the frequency, the bandwidth and other essential parameters of the transducer). Segmentation is a process that uses experimental or simulated data to compute segments that represent the various echoes. Segmentation can be 2D (applied to a single scan line) or 3D (applied to several consecutive scan lines).

Once the grouping is done, the groups and all relevant information (various possibilities depending on the procedure) can be managed to create the data for the examination report in the way they are required by most codes and norms. Multiple indications can also be grouped as one indication (tip diffraction echoes from a crack for example). One example of segmentation analysis performed in the CIVA UT analysis software is presented below.

5. Analysis of a UT acquisition on a given component

Hereafter, an acquisition performed with M2M systems will be used to illustrate the Smart Segmentation tool of CIVA Analysis and other functionalities. This acquisition corresponds to the inspection in immersion of a composite plate with a 5 MHz phased-array probe of 64 elements. An electronic scanning of 16 elements with null delay law and 1 element step is associated with a Cscan displacement of the probe.

The first thing to do before using the analysis tools of CIVA Analysis when dealing with such acquisition mixing electronic scanning and mechanical scanning is to concatenate the data. This allows to visualize the data coming from these two collinear axes of scanning (electronic and mechanical) on the same view. This also eases the reading and

understanding of the recorded signals. Figure 4 shows the differences in the Cscan view after application of the concatenation tool.

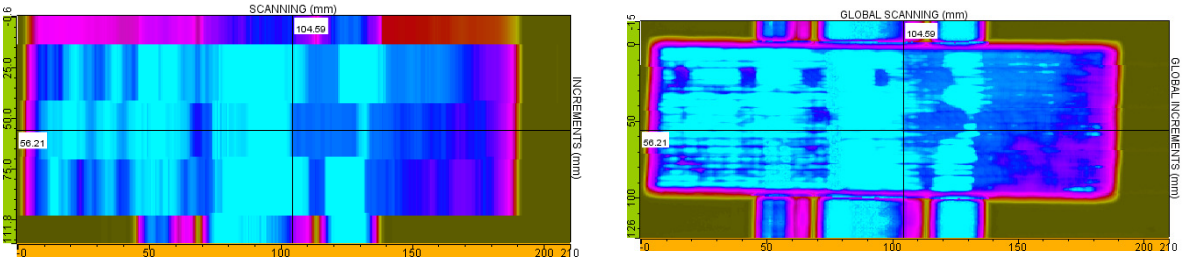

(a) (b)

Figure 4. Modification of the Cscan view after application of the concatenation tool – (a) before concatenation, (b) after concatenation.

Figure 5(a) shows the Bscan view for a specific increment index of the probe. The defects to be identified are located between the surface and backwall echo. The use of temporal gates will allow to isolate the flaw's responses in CIVA Analysis. As it can be seen, the surface echo is not perfectly horizontal. This is due to a slight mismatch in parallelism between the probe and the specimen. Therefore, a simple gate between the 2 geometry echoes is not sufficient since it will not be defined with the same time bounds for all probe positions. In CIVA Analysis, it is possible to define several gates and synchronize them in order to display only the different views in the desired temporal gate. For this particular case, two additional temporal windows will be used. The first one is associated with the entry echo (pink gate on Figure 5(b)) and the last one (blue gate) and includes the signals between the geometry echoes. This one is synchronized with the maximum echo of the entry echo in order to overcome with the change in time of flight of the entry echo.

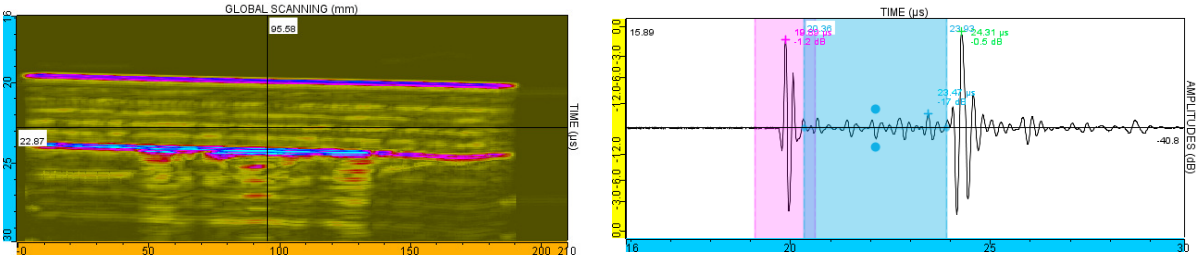

(a) (b)

Figure 5. Use of temporal gates in CIVA Analysis.

The result of the application of the temporal gates is presented on Figure 6 where several indications, certainly flaw echoes can be observed.

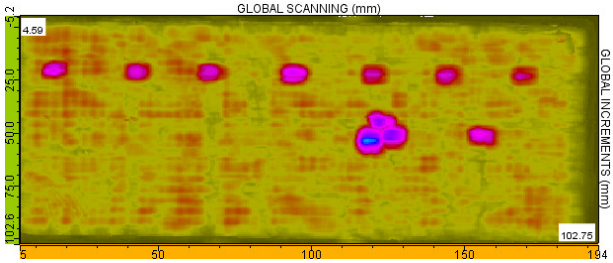

Figure 6. Cscan after application of temporal gates.

Then, the "Smart Segmentation" is a tool to assist in analysis. It allows the user to detect, in a Region Of Interest (ROI), indications that correspond to a predefined set of criteria.

First, the user defines a ROI containing the data to be segmented with the "selection" tool. Then, clicking on the segmentation button makes Segmentation (parameters) and Segmentation results toolboxes (Figure 7) appear. The user can adjust the "threshold" on the amplitude, the spatial and temporal resolution defining the grouping parameters, and the "tempo" parameter. The threshold corresponds to an amplitude level above which the signal will be taken into

account during the analysis. The spatial resolution is the number of successive shots considered to group information. The temporal resolution is the time window in which the processing will join two points of consecutive shots by a segment. Finally, the "tempo" parameter is the time window in each Ascan in which we keep only one echo. This must be in correspondence with the width of the signal (and the bandwidth). Note that all these parameters are set to pertinent values by default and should give an interesting result by a simple click with no adjustment except the threshold that has to be in accordance with the procedure and the noise level.

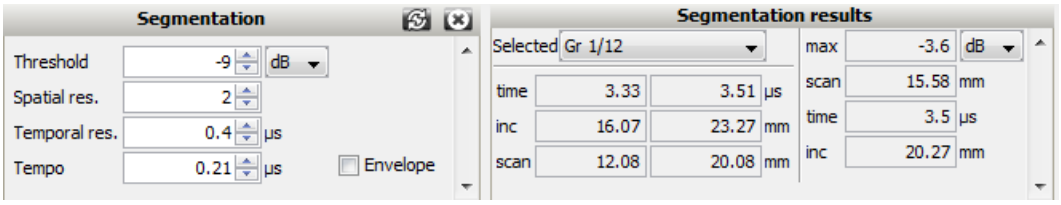

Figure 7. Segmentation toolboxes.

The results of the segmentation are displayed on the views in the layout (Figure 8). Twelve indications were found, corresponding to 12 possible defects.

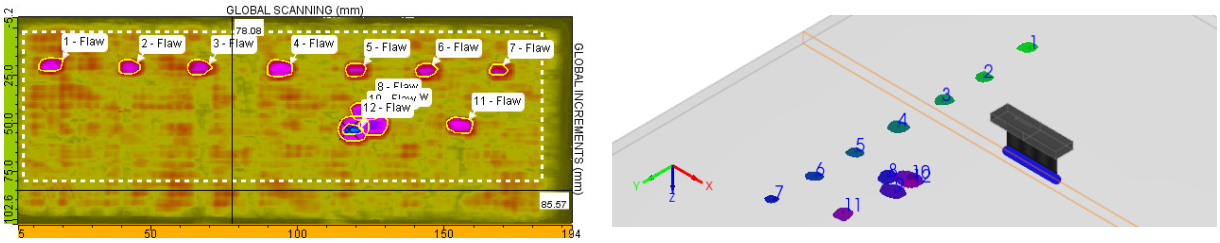

(a) (b)

Figure 8. Display of the groups after segmentation (a) on the Cscan, (b) on the 3D view.

Relevant information (amplitude, position, size…) is included in an indication table in one click: images, distances, type of indication or other comments can be added. Multiple indications can be grouped as one indication. Columns of this indication table can be selected, sorted among a long list of available data. This indication table can be exported in CSV format or an HTML report can be generated in one click.

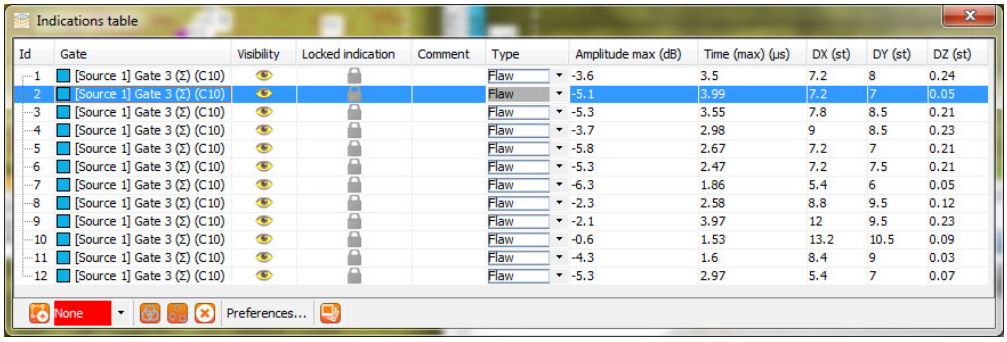

Figure 9. Indication table.

In parallel, to help with the diagnosis, multiple functionalities are available: a wide range of signal processing methods, some are classical (filters, etc.), others are more sophisticated (wavelet transforms, deconvolution methods, Split Spectrum).

5. Simulation on Acquisition: To help the diagnosis

The stand-alone version of CIVA UT Analysis module also proposes to perform a simulation in a ROI of the acquisition in order to enhance diagnosis.

To illustrate the usefulness of the "simulation-acquisition" tool, let's consider the following acquisition corresponding to the inspection of a mock-up representative of a NDT configuration. The component is made of homogeneous stainless steel; the surface is disturbed by a butt weld while the backwall is made up of two slopes of ±10° linked by a bead weld. The control is performed with a 2 MHz phased-array probe of 48 elements. A focused angular scanning is applied to cover the region of the welding (Figure 10).

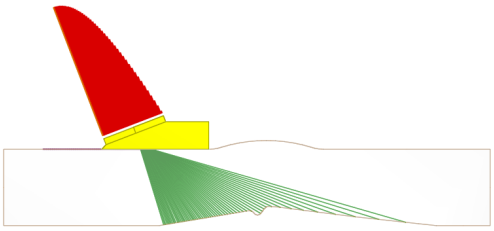

Figure 10. Configuration of the inspection.

Figure 11 shows the S-scan obtained after acquisition. Three echoes can be distinguished. There is no uncertainty on the origin of echoes n°1 and n°2 which correspond to geometry echoes from the backwall (respectively direct echo and conversion mode echo). On the other hand, the origin of echo n°3 is less clear. This echo may be a geometry echo from the bead weld or the echo from a flaw, probably from a tilted planar defect.

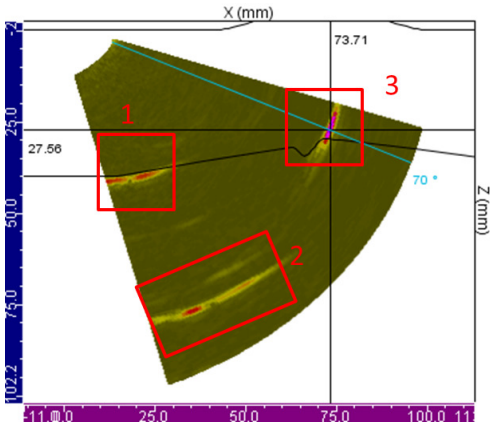

Figure 11. Result from the acquisition.

Because such uncertainty may not be acceptable for safety reason, CIVA Analysis users may remove doubt with the "simulation on acquisition" tool. To access this option, a ROI must be selected then the user activates the "Simulation on acquisition" tool.

A new page opens and offers to choose the options for simulation (Figure 12).

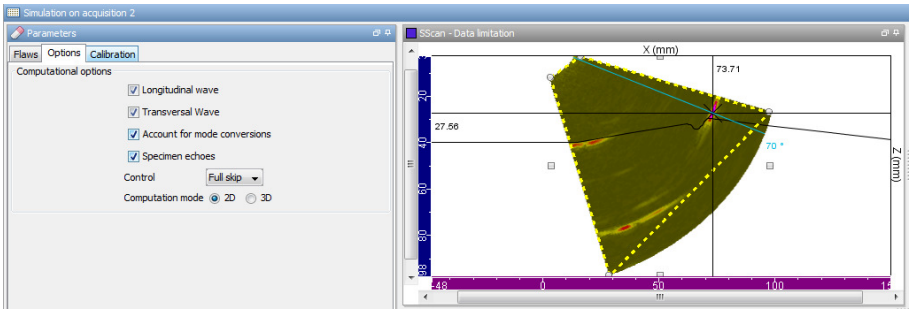

Figure 12. Simulation on acquisition panel.

The simulation is performed in the ROI where specimen echoes and flaws (planar defects and side drilled holes only) responses may be calculated. As a first step, let's consider that echo n°3 is a geometrical echo. Thus, no defects

will be simulated. The calculation result is shown on Figure 13 (image on the right) where it can be seen that the echoes n°1 and n°2 are well simulated whereas echo n°3 is absent.

Note that, the user has the choice between automatic and manual calibration of the amplitude of the simulated data. With automatic calibration, the maximum of amplitude in the simulated area is calibrated with the maximum one of the acquisition in the same zone. However, it is possible to adjust the dynamic afterwards.

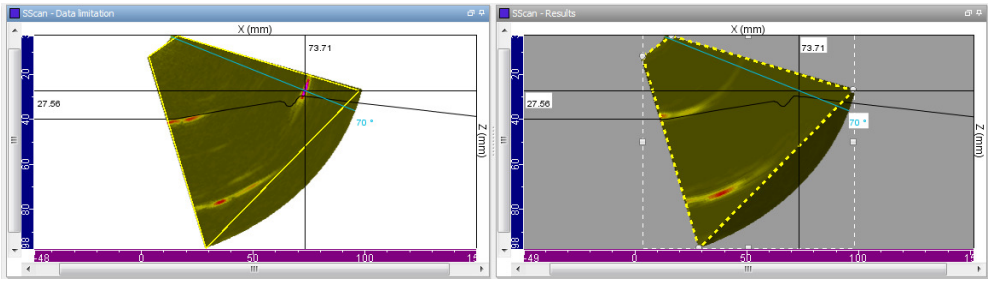

Figure 13. Comparison of the experimental S-scan (on the left) and the simulated one (on the right) without flaw.

The comparison of Figure 13 allows to confirm that echo n°3 is not a geometrical echo from the bead weld. The "simulation on acquisition" is then used with flaw response to check that the echo of interest comes from a planar flaw. This time, the ROI where will be applied the simulation is located around the zone of echo n°1 (Figure 14)

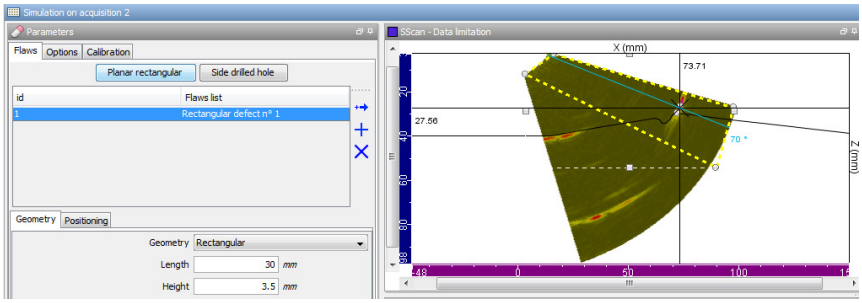

Figure 14. Flaw panel of the simulation on acquisition tool.

In the flaw tab of the simulation on acquisition panel, one rectangular defect is added which position and characteristics (height, tilt…) were based on the position of the echo (Figure 15). The defect location in the specimen can be adjusted with the mouse directly in the True image (e.g. True Bscan or True Sscan) where is shown the ROI. It is also possible in the 3D view where the S-scan can be dropped. This allows better fitting of the flaw position and orientation according to the one of the echo.

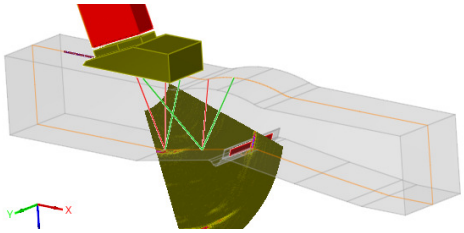

Figure 15. 3D view of the specimen and flaw with the S-scan.

Figure 16 show the result of the simulation in the ROI on the S-scan.

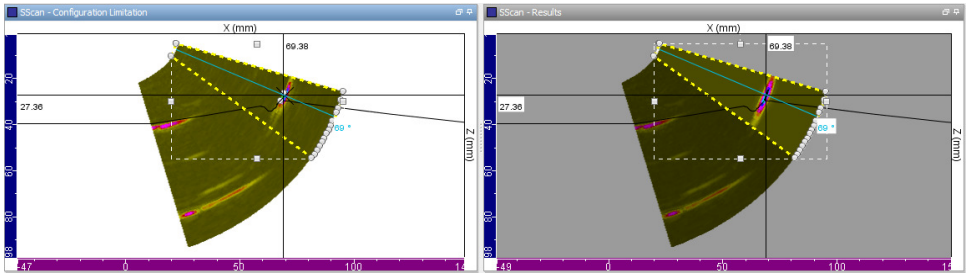

Figure 16. Comparison of the experimental S-scan (on the left) and the simulated one (on the right) with flaw.

An echo close to the experimental one has been obtained by simulation. This confirms that the echo n°3 belongs to a notch. The Ascans and echodynamic curves of the simulated data can be superimposed to experimental ones in order to compare the result (Figure 17). There is a good agreement between experiment and simulation. Simulations may be computed in 2D or 3D. In a first approach, 2D computation can be used. It presents the advantage of fast computation (in this example 2D simulation takes 3 seconds). Then, 3D computation which requires more computation time (1 minute 20s) may be considered especially when dealing with 3D cases and phenomena. The result will be thus more accurate for complex configurations.

Note that only planar defects and side drilled holes may be simulated in the CIVA Analysis module. Simulations with many more complex flaws may be performed in the full simulation software "CIVA 2015".

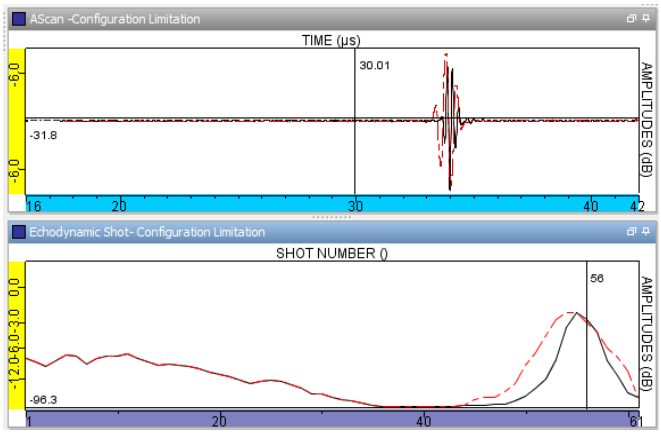

Figure 17. Comparison of experimental and simulated Ascans and echodynamic curves. In red, the result of simulation, in black the experimental data.

This example and the associated results show that the "simulation on acquisition" tool may help to better diagnosis of experimental acquisitions.

6. Conclusion

This article has introduced some of the tools available in the new UT analysis software, available with the CIVA platform. Among them, the principle and application of the segmentation algorithm have been detailed, this one being now available as an automatic tool. The interest of the "Simulation on Acquisition" feature has also been illustrated on an example where it can help to confirm or disprove a given diagnosis, especially when the acquisition data involves complex signals. Thus, CIVA Analysis module is a tool providing manual data inversion assisted by simulation. Ongoing developments at CEA aim to develop increasingly automated tools in order to improve and ease the detection and characterization of the flaws. Today, this software can be used to process acquisition data from various formats (M2M systems, Gekko, Olympus Data). As an option, full simulation modules can be used along with the analysis part to help in expertise or design works.

Model-aided Design of Purpose Built Ultrasonic Probes

Lars Skoglund,
WesDyne Sweden AB
Kemistvägen 5
18379 Täby
Sweden
E-mail address: skoglule@westinghouse.com

Abstract

For In-Service-Inspections (ISI) of components in a nuclear environment, limited access is often one of the challenges. The restrictions can be of several types, narrow gaps, varying geometries, obstacles etc. Aging of the nuclear fleet is causing an extended need for inspection, possibly at areas considered as non-inspectable before. To access these hard-to-reach areas, a purpose built ultrasonic probe is often the solution.

An unexpected inspection often requires a quick response which in turn means rapid development of a special purpose probe with no room for trial-and-error, the first design must deliver the quality required for the job.

Classical “standard” probe design is often a simplified model using ray-tracing, Snell’s law and assuming the sound beam to be a line or a cone. This gives acceptable results for plane geometries and crystal sizes relatively big, but when the probe size is restricted (and thus the crystal size), for curved geometries or higher refracted angles, this simplified design is often not sufficient. The focal depth can end up at an unexpected depth, the beam shape can be non-symmetric, surface waves can affect the sound pressure maxima etc.

As an aid for improved designing of ultrasonic probes, there are a number of modelling softwares available on the market. However, modelling softwares can have limitations that can cause unexpected results if not considered.

This paper will discuss some of the main benefits of simulated probe design including a few examples of modelling pitfalls. A reference case is the Heysham Boiler Spine inspections 2014 where the weld area was only accessible ca 1500mm down an 8mm gap.

Keywords: Ultrasonic, NDE Probes, Purpose built, Probe design, Modelling, Simulation,

Inspection of inaccessible areas

The Heysham Case

Martin Bolander

WesDyne International

Abstract

Most utility owner's fear to have a call from their Non-Destructive Examination (NDE) group stating that "we have an indication we can't explain". In the Heysham case this is what happened late 2013. During normal in-service inspection of the Heysham boiler spines one of the eight boilers indicated an anomaly placed in an inaccessible location.

During the first half of 2014 the EDF-Energy team and a number of Nuclear Service companies, Westinghouse and WesDyne included, developed procedures and methods to enable WesDyne to inspect the area in question using ultrasonic and eddy current techniques. In parallel a backup solution was developed by Phoenix Ltd and an X-ray approach using a second entry point was developed by AMEC.

The essence of the inspection challenge was to inspect a 360 degree weld. The weld area was only accessible via an 8 mm gap and located ~2000 mm down the said gap. The deployment was to be executed in a 60 C° environment of inside a gas cooled reactor. The inspection solution including factory acceptance tests needed to be developed and completed within six months.

This paper is primarily focused on presenting the rapid development process of the inspection solutions chosen and the associated lessons learned of this project.

Keywords : Boiler spine, Ultrasonic, Eddy Current, Unapproachable, Accessibility

Background

At the end of 2013 EDF Energy (EDF-E) identified an anomalous result during routine Teletesting using guided waves which was carried out at Heysham unit 1 power station at the routine maintenance shutdown. This result was found on the central support column (spine) of one of the eight boilers (1D1) attached to Reactor 1. Heysham needed to understand more about the nature of the anomalous results and its possible cause and initiated and investigation project.

This project soon became EDF Energy's number one risk and highest profile project during 2014. The two main reasons for the high focus were:

- The extended shut down created a significant loss of generation
- If the anomalous test results weren't properly understood and corrected lifetime production of 2.4 G Watt (until 2019) was at risk.

Customer Request

Westinghouse and WesDyne were approached by EDF-E in early 2014 and asked to develop bespoke inspection tooling and inspection technique to access the space where the anomalous reading was indicating.

More specifically the challenge given was to develop remotely operated tooling that would fit into a 20mm wide and 2m deep gap. This narrow slot formed an annular space between a thermal shroud and the boiler spine itself. To make the situation even more challenging the temperature of the boiler during the requested inspection was expected to be i n the excess of 50 degrees C and the radiation rates also expected to be high.

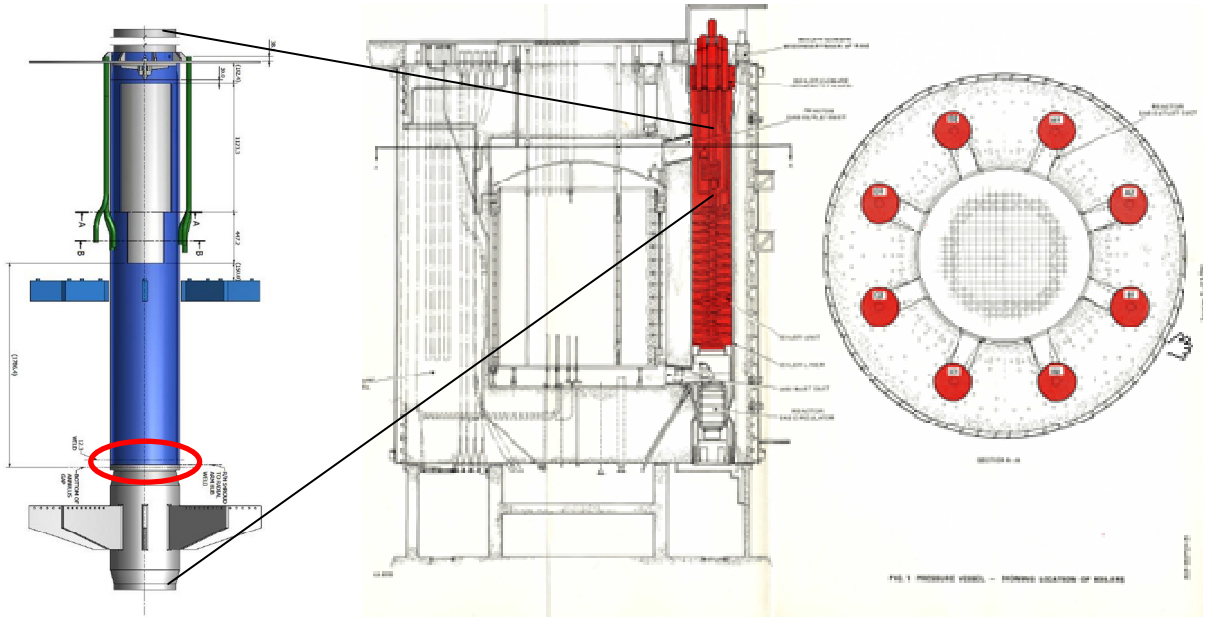

Figure 1 Inspection area (encircled)

The inspection task as initially described was to detect, characterize and size the anomaly. Actual inspection and acceptance criteria were to be developed during the course of the project but the true undertaking was to develop probes that would fit into the gap and survive the radiation and temperature levels.

Site execution was requested to mid-June. Hence we were given a six months window to develop tooling and technique, build test blocks, validate tooling and techniques, train personnel to install and service equipment in the full scale mock-up and execute on site.

Functional Requirements

Based on limited condition information WesDyne started to develop an inspection concept. The key initial specifications are presented below.

Component Access Specification

- V weld without cap
- Stainless steel parent material and weld material
- All couplant used to be retrieved
- Narrow gap
  (initially 20mm, in the end design criteria 8mm used)
- Component ~60°C
- Radiation level ~2mSv/h at 1m

Inspection Requirements

- Inspection area weld center line +/- 200mm
- Detection of surface breaking defects (ID and OD)
- Sizing of detected defects
- Positioning of detected defects

Equipment Requirements

- Able to be installed in reactor by trained “Divers”
- Robust to manage transport inside reactor
- Foreign Material protocol
- NDE instrumentation to be positioned in “cool” area

Personnel Requirements

- Project manager with high communication skills
- NDE UT & ET Level III to lead development
- Experienced in first of a kind project development
- Mechanical and Electrical designers experienced with remote NDE

Challenges

Besides the restricted time to develop an inspection solution there was three key challenges.

Unknown inspection targets

All data and in depth analysis on mock-ups indicated that the indication was circumferential and covering 360 degrees. If it was a real defect it had to be in-service induced and would consequently be initiated from either outer or inner surface.

Unknown defect location

As the guided waves was penetrating down the center column and the geometries keeps changing the accuracy of the location was initially given with +/- 200 mm from the theoretical weld center line of the 12.3 weld. This uncertainty in turn created some challenges for the detection technique.

Unknown object dimensions

As the object dimensions wasn't completely understood at the start of the project but the time pressure forced us to initiate development prior to have a complete picture. The major challenge was the continuously changing requirements related to the available gap. During our initial meeting in January 2014 the gap was presented as 20mm at the end of the development it had shrunk to "8 mm – can be less at some points".

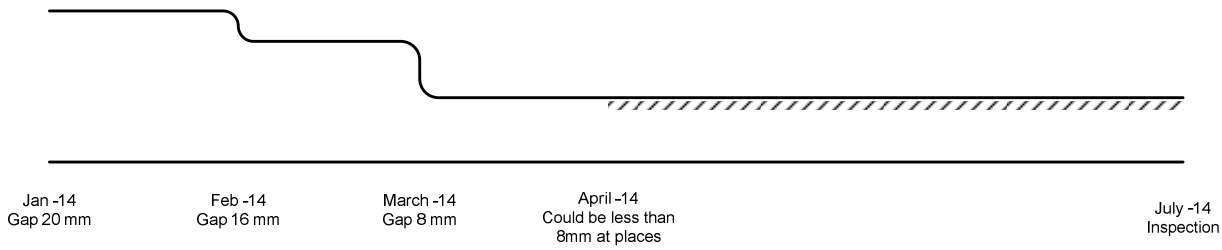

Figure 2: Reduction of estimated gap over time

Creating the solution or How to design a Swiss watch

Basically the development concept was divided into Inspection and Mechanical delivery. However, as the time constraints was quite aggressive all development was done in parallel communication and understanding of all work streams were essential.

For example, if the probe width needed to be adjusted the mechanical team was immediately notified in order to evaluate if this was acceptable or if a new inspection solution should be pursued as an alternative. This iterative process was continuously ongoing between the work streams and was enabled by in-house production of all of the essential parts.

Inspection concept

The team decided to focus on detection of inner (ID) and outer (OD) surface defects. As the extent was expected to be 360 degrees but not confirmed. The customer and the NDE companies decided that a detection target of 10mm*5mm surface breaking defect needed to be justified.

The as the initial inspection area was quite wide the selected solution needed to be very flexible. Inspection was to be performed from above the heat affected zone to below the thermal shield.

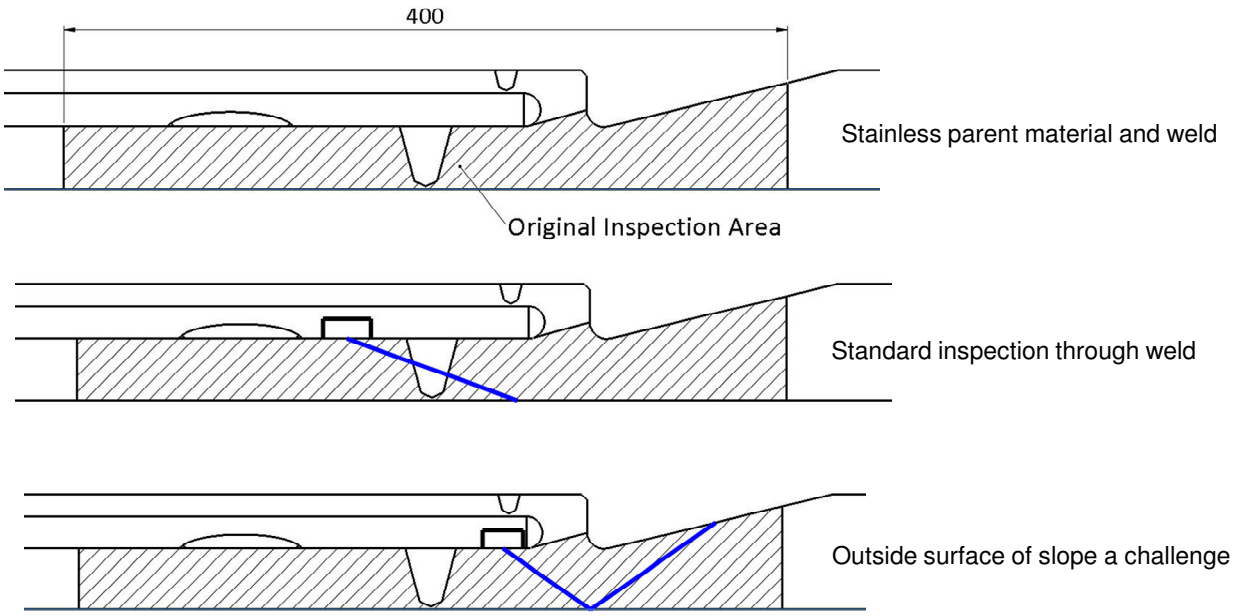

Figure 3: Inspection volume

The solution selected was to use Eddy Current for detection of OD surface breaking defects and for weld positioning along the spine axis. For defects originating from the ID and defects below the thermal shield various bespoke UT pulse echo probes was developed. The inspection area below the thermal shield areas however unlikely still needed to be covered as the inspection solution. The challenge given was to cover all areas.

On a high level the ultrasonic solution relied on low frequency 60°TRL, 70°TRL and 45°S with various focal depths. This is not an unconventional inspection solution but the height restriction of the probe posed the challenge to the probe design. The limitation in probe height, temperature and schedule drove the development team to abandon the phased array solution that from a pure NDE perspective was a most attractive route forward.

Mechanical Concept 360 Scanner

Access to the gap was given via a cut in the thermal shield ~2m above the area to be inspected. There is access to approximately 90 degrees of the spine circumference at this level and the opening is approximately 45 degrees. These restraints give the need to do a raster scan 2000 mm down an 8 mm gap 180 degrees from your access point!

Initially there were a number of design ideas but the selected one basically consists of three parts:

- Frame and motor drive.
  A frame is fitted in the opening of the thermal shield and this frame holds the vertical and rotational movements.

- Hinged ring
  A hinged ring is fitted into the gap and locked to create 360 degrees and then connected to the rotational motor. Three different rings was produced to compensate for the uncertainties related to the spine dimensions.

- Probe sword
  A curved 2 m long hinged sword is fitted down the gap and connected to the ring. In the end of the blade three probes, water spray, two cameras and lights are fitted. (refer figure 4)

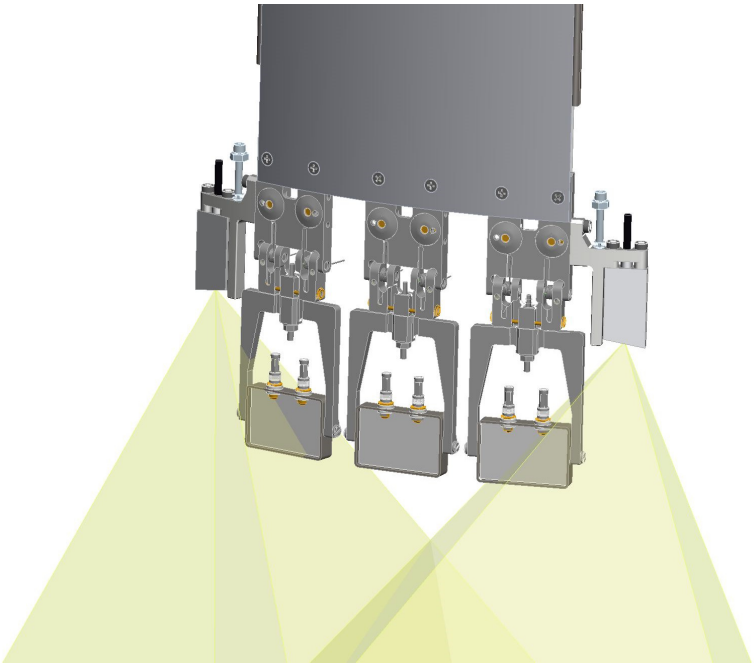

Figure 4 Probe head of 360 scanner

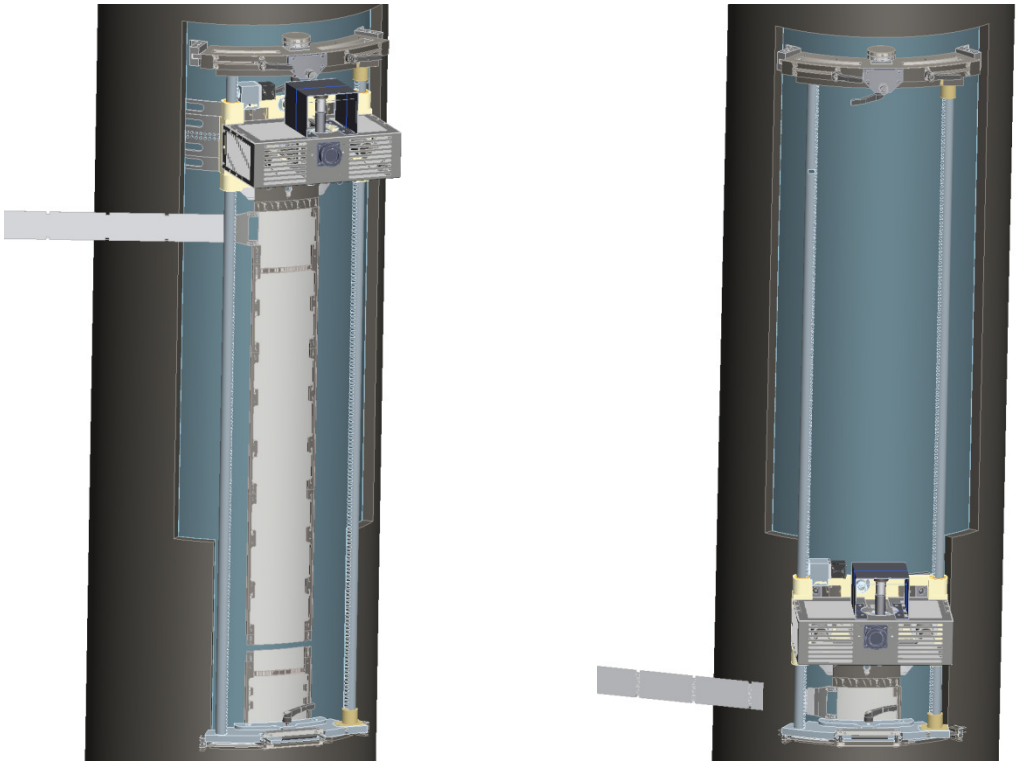

Figure 5: 360 scanner installed in thermal shield opening

Mechanical Concept Helical Scanner

In April 2014 the project was informed by the customer that they had indications that the gap could be less than 8mm at some areas. If this was the case the 360 scanner concept would not work as the ring and the blade both had their design criteria of 8mm and needed an 8mm gap 360 degrees the full length of the gap. Given this new challenge WesDyne presented a "best effort" concept to the customer named the Helical Scanner.

The basis of the concept was that "any inspection is better than none". If we could find areas with 8 mm gap we would be able to push the probes down to the inspection area and still validate the nature of the anomaly although we might not be able to cover the whole 360 degrees. The Helical scanner was created around three major parts

- Frame fixture
  A small frame is fitted in to the opening.

- Probe pusher and circumferential movement
  The vertical movement is performed by a probe pusher and the circumferential movement is done by moving the probe pusher outside the shroud. The circumferential movement is approximately 30 degrees and full circumferential coverage is achieved by entering the probe in 5 different angles.

- Flexible blade and turtle probe head
  A 2m and 1mm thick blade with a probe head holding one UT and ET probe under a "turtle back" to secure the probes from getting caught in obstacles.

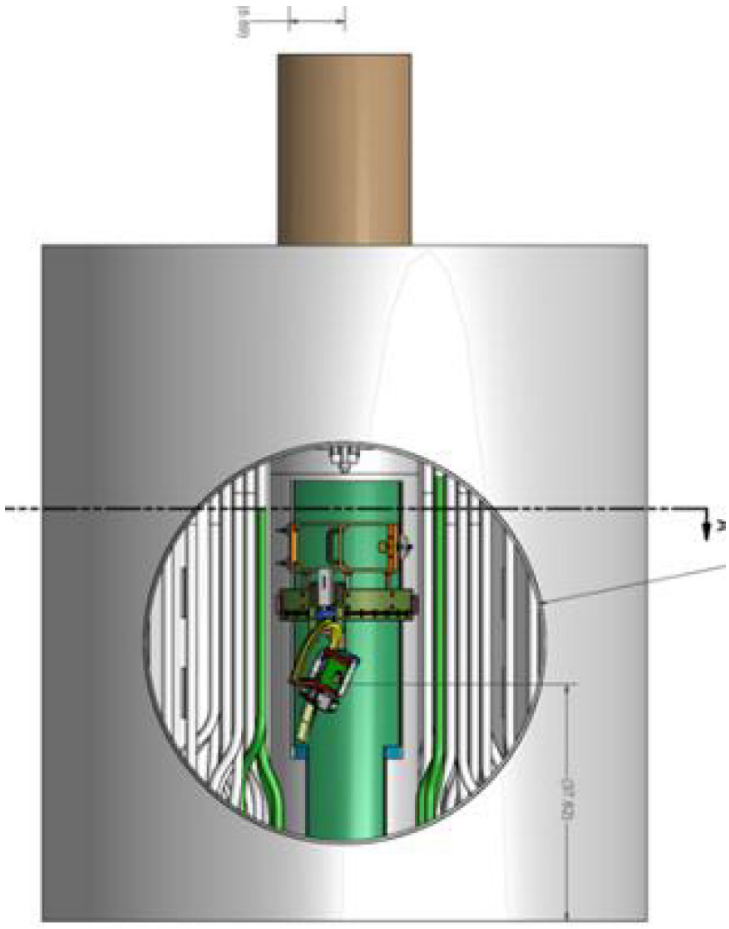

Figure 6: Helical scanner installed in the thermal shield opening

Helical scanner was developed and manufactured within three months during the final stages of the project and was the first ultrasonic tool to go into the gap!

Schedule

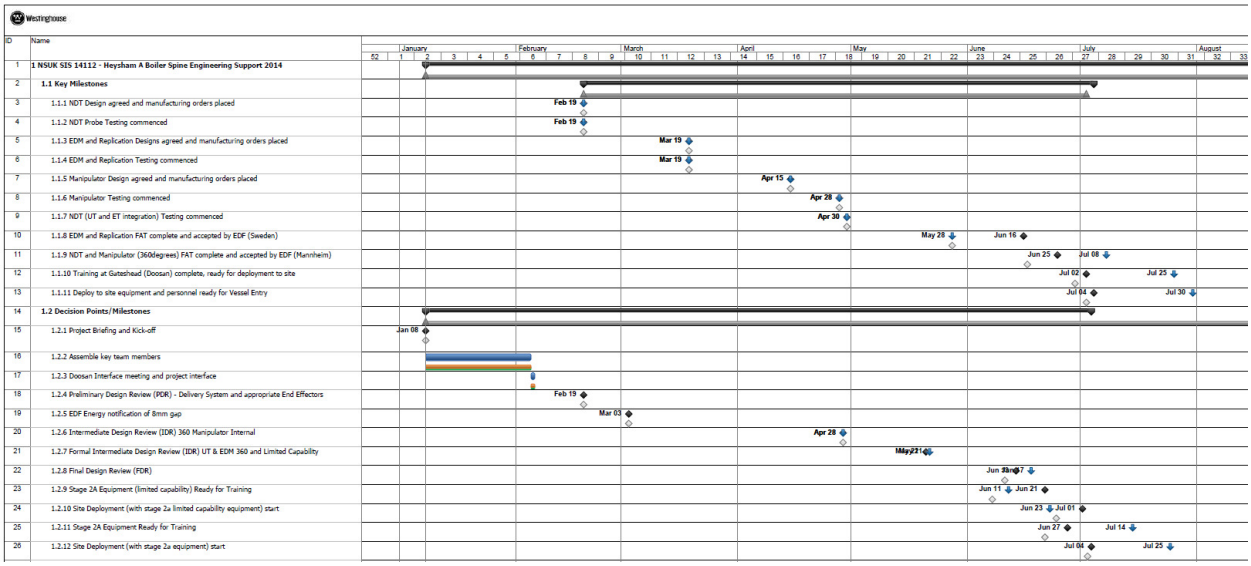

Figure 7: Milestones delivered during the 6 months

On-site execution

Due to Helical scanner quick installation and flexibility EDF-E choose to start with this as the defect was expected to be present 360°. The inspection went flawless in term of execution but there was no flaw detected in the space below the thermal shield opening.

The 360 scanner was deployed to scan the “dark side of the spine”. The scanner performed a 360° scan with a perfect result and the defects was found and sized. This too was a stellar performance and the customer applauded the crew and the tool as they executed with the “accuracy of a Swiss watch”.

Conclusions

The fact that WesDyne and Westinghouse were able to support EDF-E in this urgent predicament comes down to a number of key points.

- Our long history of bespoke mechanized remote NDE equipment for complex environments
- Our understanding of development and qualification processes in various countries
- Our ability to do probe development in parallel with conceptual design of inspection solutions
- Our capability to build everything from probe to manipulator in house in order to shorten lead times and re-work.
- Our ability to quickly mobilize resources globally with nuclear experience and understanding to support the challenge ahead.

However, the WesDyne and Westinghouse delivery had not been possible had EDF-E not taken the approach to the challenge they did. Without the following we would not have been able to be successful.

- EDF-E quickly built a team of key Nuclear Service providers and pursued parallel solutions for vital areas as redundancy (NDE being one of them)
- EDF-E also created a non-hostile environment where companies normally being competitors work together for the same goal and a feeling that we all succeed together.
- Although specifications were “floating” in the beginning of the project EDF-E made sure that the suppliers had access to the information as soon as EDF-E themselves had it.
- EDF-E’s ability to establish a creative and trusting environment.

As to further highlight the successful collaboration Westinghouse, Doosan AMEC and RR was given EDF-E collaboration award 2014.

Figure 8: Westinghouse, Doosan, AMEC, Atkins and RR receives the EDF-E collaboration award

Thanks

WesDyne and Westinghouse would never have been able to perform and support EDF-E had it not been for the support from:

- James Wenham, Project manager EDF-Energy
- Adrian Smith, Technical Lead – EDF-Energy
- Kim Sharp, NDE Level III – EDF-Energy

WesDyne

WesDyne Int.is the Non Destructive Inspection branch of Westinghouse Electric Company and is a leading supplier of mechanized Non-Destructive Examination products for all inspection needs worldwide. WesDyne provides turn-key and one-off type solutions with focus on the nuclear market. The expertise spans all aspects of remote and mechanized inspections, from problem analysis & solutions generation, development and manufacturing to field deployment of personnel & equipment. Inspection capabilities cover all key NDE areas such as Ultrasonic, Visual, Eddy Current, Magnetic Particle, Dye Penetrant and X-ray.

Short-Range Guided Wave Testing of Dry Cask Storage Systems Using EMATs

Matthew S. Lindsey[1], Jason K. Van Velsor[1] and Owen M. Malinowski[1]
Jeremy Renshaw[2] and Nathan Muthu[2]

[1]Structural Integrity Associates, Inc.
1951 Pine Hall Road, Suite 100
State College, Pennsylvania 16801
United States of America

[2]Electric Power Research Institute
1300 West W.T. Harris Boulevard
Charlotte, North Carolina 28262
United States of America

E-mail address (corresponding author): jvanvelsor@structint.com

With the defunding of the Yucca Mountain Nuclear Waste Repository, the U.S. nuclear power industry is without a remote long-term storage option for spent nuclear fuel. As a result, individual nuclear power generation facilities have turned to storing spent nuclear fuel on-site in Dry Cask Storage Systems (DCSSs). With many of these DCSSs having resided near saltwater for nearly 20 years now, the NRC has expressed concern over the potential of Chloride Induced Stress Corrosion Cracking (CISCC) damage occurring in the stainless steel storage canisters and has encouraged the industry to proactively address this issue. This paper will review the development of a volumetric inspection approach that utilizes high-frequency ultrasonic guided waves excited by low-profile Electromagnetic Acoustic Transducers (EMATs). This technique enables relatively significant portions of the canisters to be inspected for CISCC from the limited space available between the stainless steel canister and the concrete overpack. Furthermore, EMATs can operate without liquid couplant, at elevated temperatures, and within high radiation environments. Experimental results will be presented that demonstrate the ability of the short-range guided wave testing (SR-GWT) EMAT technique to detect the flaw geometries and sizes of interest for this application.

Keywords: EMAT, short-range guided wave testing, dry canister storage system, volumetric inspection, chloride induced stress corrosion cracking, spent fuel

Detection of corrosion on non-accessible areas using Rayleigh-like waves

Laura TAUPIN[1], Frederic JENSON[1], Sylvain MURGIER[2] and Pierre-Emile LHUILLIER[3]
[1]CEA, LIST, Digiteo Labs, Bât. 565, PC 120, F-91191 Gif-sur-Yvette, France
[2]EDF CEIDRE, 93206 Saint-Denis Cedex, France
[3]EDF R&D, EDF Lab Les Renardières, 77818 Moret sur Loing, France

E-mail address (corresponding author) : laura.taupin@cea.fr

Nuclear plants contain pipes which are maintained by supports or concrete walls. These components might experience corrosion which may induce loss of thickness. Due to the presence of metallic or concrete supports, some region of those pipes are non accessible. Bulk wave ultrasonic testing has a proven good sensitivity for the detection of corrosion defect. However this method requires to have a local access to the inspected part. Consequently no conventional non-destructive methods are available to inspect pipes under supports or concrete walls.
To control these non-accessible areas, EDF and CEA have started a collaborative work aiming at exploring the potentialities of an innovative inspection method based on the use of Rayleigh-like waves.
Rayleigh-like waves can be interpreted as the superposition of the first anti-symmetric and the first symmetric guided wave modes. Their propagation is characterized by beating phenomenon showing a periodic transfer of energy between both sides of the plate with a characteristic distance called the beatlenght. As a consequence, unwanted reflections and mode conversions at pipe supports can be avoided. It might also increase the detection performances of defects located under supports. To match the support dimension, the beatlenght can be adjusted by selecting the probe frequency.
As a first step, this method has been investigated on flat structures. Corrosion-induced losses of thickness have been modeled by rectangular notches. Simulations, using the NDT platform CIVA, and experimental works were compared. During the first experiments, it has been shown that an appropriate choice of the beatlenght and probe position allows to avoid support effect on the transmitted wave echoes.

Keywords: Rayleigh like waves, pipes support, corrosion defect.

Use of creeping wave/head wave ultrasonic method for inspection of a carbon steel pipe hidden areas under bedplate

S. MURGIER[1], C. HERAULT[1], P. BERGALONNE[2]
[1] EDF CEIDRE, 93206 Saint-Denis Cedex, France
[2] COMEX Nucléaire, 13276 Marseille, France

E-mail address(corresponding author) : sylvain.murgier@edf.fr

Non-destructive examinations are an important part of the preventive maintenance strategy of the EDF Group nuclear power plants. Some inaccessible components, such as buried pipes or covered areas under pipe bedplates for example, have not been designed to be serviced inspected. Despite the several examinations techniques used by EDF, there were no NDT methods available to inspect these areas.

Nevertheless, in the context of preventive maintenance and in order to extend the operating life of these power plants, EDF wished to have a detailed thickness mapping of these types of components, in order to support the establishment an industrial maintenance strategy.

In partnership with COMEX Nucléaire, a methodology for the inspection of unreachable areas in carbon steel pipes lines was developed by adapting an ultra-sonic transmission approach based on generated creeping wave/head wave type all-around the pipe diameter, using a robotic carrier to insure the coupling between the transmitter and receiver probe.

This new method has been successfully implemented on large diameter carbon steel pipes (24 inches) of the raw water system and allowed to carry out a detailed mapping of the remained steel thickness of the four areas under pipe bedplate for each section of the pipe.

This technique can be implemented outside of unit outages and thereby provide information for any necessary maintenance of the line. The results obtained in this examination campaign gave EDF the first elements to establish an industrially relevant maintenance strategy.

Keywords: corrosion mapping, pipes support, creeping wave, head wave.

A new State of the Art portable Phased Array equipment dedicated to defect characterization

Philippe Benoist (M2M), Olivier Roy (M2M), François Cartier (CEA)

Phased-Array Ultrasonic Testing brings efficiency and flexibility for testing of various components in the nuclear industry. Function of the applications, new ways to use Phased Arrays are developed: powerful systems for the manufacturing sectors as well as portable instrumentation during in service inspection. Now portable industrial equipment allows handling full parallel systems, matrix probes, 3D imaging and advanced techniques for optimal focusing. Associated to an intuitive user interface, the new system permits an optimal use of ultrasonic phased arrays in order to achieve rapid and reliable inspections. Among the new features, a new real-time inspection method is presented: Image reconstruction using Total Focusing Method permits a better characterization of the defects during inspections. Associated to Phased Array portable equipment and to matrix probes, this technique will be able to improve the results of an examination: this method includes different type of reconstruction (Direct, corner, mode converted). Moreover, it becomes possible to obtain, associated to Total Focusing Method, real time adaptive inspection taking into account of the variability of the examination surface. During the presentation, examples providing of different industrial sectors will be shown.

Detection and sizing of cracks in bolts based on ultrasonic phased array technology

Shan LIN[1]

[1]Cental Research Institute of Electric Power Industry, Japan

Abstract

It is necessary to check for any cracks that may be present in anchor bolts used in nuclear power plants after a massive earthquake. Moreover, there have also been reports of cracks in bolts in aging nuclear and thermal power plants. Phased array ultrasonic testing is an effective technology for detecting such cracks. In this study, linear-array probes with different frequencies are used to investigate the detectability of cracks, investigations show that 1-mm- deep crack can easily be detected using 10-MHz frequency, which is more appropriate than 2- and 5-MHz frequencies for detecting small cracks. Moreover, a new method for the depth sizing of cracks in bolts using ultrasonic phased array technology is addressed. More specifically, the finite element method (FEM) is used to predict sectorial views of various crack depths when a linear-array probe is used to inspect the bolts. Numerical results show that a peak associated with the vicinity of a crack's tip can be observed in the curve of echo intensity versus refraction angle for deep cracks. The refraction angle with respect to this peak decreases as crack depth increases. To verify the numerical results, experiments are performed on bolt specimens in which electrical discharge machining slits with different depths are introduced. The experimental and numerical results are in good agreement with each other. Therefore, based on the refraction angle associated with the peak, a new method for the depth sizing of cracks in bolts is proposed. Comparisons between determined and actual depths show that accurately determining a crack's depth from the inspection results by the proposed method is possible.
Keywords : Ultrasonic testing, Ultrasonic phased array technology, Bolts, Cracks, Detectability, Depth sizing

1. Introduction

Massive earthquakes may cause cracks in anchor bolts that are used to fix components to foundations in nuclear power plants. Moreover, numerous fatigue cracks have previously been found in aging nuclear and thermal power plants [1-2]. To assess the integrity of anchor bolts, cracks must be reliably detected and their respective depths must be determined. Currently, hammering and visual tests are used to detect cracks in bolts; however, detecting underground defects is impossible via a visual test. Further, results of a hammering test are strongly influenced by environmental and human factors; however, in contrast with hammering and visual tests, ultrasonic tests offer a more effective technique for detecting such cracks [3].

Because a crack tip echo is overwhelmed by a reflection echo, determining the crack depth via a conventional tip echo technique is difficult. In a previous study, we showed that (1) phased array ultrasonic testing (PAUT) is a promising candidate for detect such cracks and (2) the concrete surrounding anchor bolts and engraved number marks on bolt ends cause the intensity of crack echoes to decrease slightly, but they scarcely affect the detectability of cracks in anchor bolts [4]. Nonetheless, there remain two unsolved problems in the application of PAUT to bolts. First, how can small cracks be detected? Second, how can crack depths be determined from measured results?

In the present study, bolt specimens with different slits and fatigue cracks were prepared. These specimens were measured by three linear-array probes with respective frequency of 2, 5, and 10 MHz. To find a method for determining crack depth from measured results via PAUT, wave propagation in the specimens was performed. On the basis of this study's numerical results, a procedure to determine crack depth was proposed and applied to the specimens, and the determined crack depths were compared with actual values.

2. Detecting fatigue cracks in bolts via PAUT

2.1 Specimens

For convenience, the parameters related to the definition of a crack are shown in Figure 1. The geometry of the bolt specimens made of SS400 is shown in Figure 2. The length of the specimens was 300 mm for those in which a slit was introduced and 150 mm for those with a fatigue crack. The thread length is the same as the bolt length. Considering the

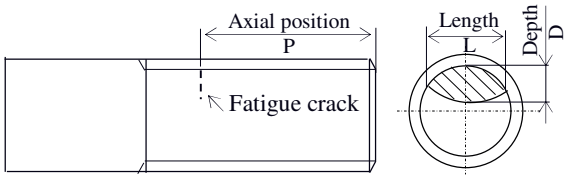

Figure 1 Definition of fatigue crack parameters

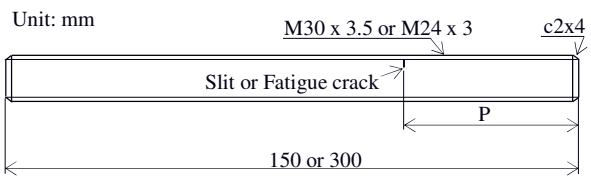

Figure 2 Geometry of bolt specimen

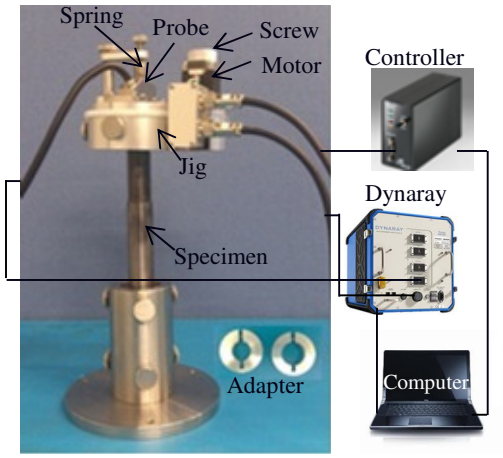

Figure 3 Measurement setup

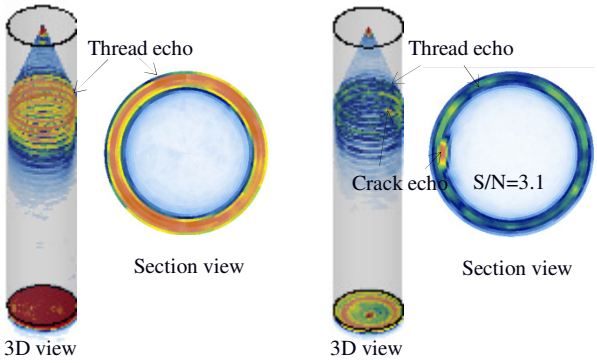

(a) P = 50 mm, D = 0.48 mm (b) P = 50 mm, D = 1.39 mm

Figure 4 Measurement results for different cracks

dimensions of a base plate and nut, the axial position of a slit or fatigue crack was determined to be 100 or 50 mm. Fatigue cracks were introduced to M30 and M24 bolts via the bending fatigue test. Slit depths ranged from 0.5 to 10 mm, whereas the targeted fatigue crack depths were 0.5, 1, 2, 4, 6, and 8 mm. After ultrasonic testing had been performed, fracture surface was observed and actual fatigue crack depths were measured. As such, depths corresponding to fatigue cracks are hereafter actual values.

2.2 Measurement setup

Figure 3 shows the system used to detect cracks in the specimens; the system comprised a jig, a probe, a controller, a phased array instrument, and a computer. Different adapters were used for bolts with different diameters. In this study, three 64-element probes with respective frequencies of 2, 5 and 10 MHz were used. The active aperture was set as 32 and the refraction angle ranged −20° to 20°. The focusing depth for transmission was 60 mm, but it ranged from 10 to 150 mm for reception in the dynamic depth focusing mode.

To determine an appropriate frequency, three linear-array probes are used to measure a bolt specimen in which a slit was introduced. The slit had a depth of 0.5 mm and an axial position of 100 mm. Measurement results showed that this slit could be easily detected via the 10-MHz probe and difficult to be detected via the 2-MHz probe. Therefore, 10-MHz frequency was considered to be suitable for the detection of cracks in bolts.

2.3 Detectability of fatigue cracks

Figure 4 shows measurement results for two M30 bolt specimens with cracks. The axial position of the cracks was 50 mm, and crack depths were 0.48 and 1.39 mm, respectively. As shown in the figure, there was no echo observed for the 0.48-mm-deep crack, but the crack echo from the 1.39-mm-deep crack was obvious; the signal-to-noise ratio of the crack echo was 3.1 dB. In another study, a 1.03-mm-deep crack in an M24 bolt specimen was easily detected [5]; the axial position of the crack was 90 mm. From these facts, it can be concluded that detecting 1-mm-deep cracks in bolts is possible.

3. Proposal for determining crack depth by FEM

3.1 Predicted measurement results with FEM

To develop a method for determining crack depth, wave propagation in bolts was performed via FEM. Figure 5 illustrates the numerical model used. In this model, a slit is introduced to a bolt whose diameter is 30 mm. The axial position of the slit is 50 or 100 mm, and slit depth varies from 0.5 to 10 mm. A 32-element linear-array probe was used to detect this slit. The pitch, width, and length of the element in the linear array are 0.6, 0.5, and 10 mm, respectively.

For this computation, wave mode was set to be longitudinal, and the central frequency of an incident wave was 5 MHz, which is different from the frequency used in experiment to reduce computation time. The refraction angle ranged from -5° to 20° with a step of 1°, and the focus depth was 60 mm.

Figure 6 shows the sectorial scan for a slit with a depth of 6 mm. As shown in the figure, thread echo (SE), slit echo (DE), echo that resulted from the second reflection at the slit (MDE), and back echo (BW) were all observed. The slit echo had two parts with a large intensity. Figure 7 depicts the dependence of echo intensity on reflection angle with a varying slit depth. As shown in the figure, when slit depth was a minimum of 2 mm, two separate peaks could be observed. The reflection angle corresponding to Peak 1 in the figure was constant, whereas that of Peak 2 decreased as slit depth increased. This indicates that the reflection angle of Peak 2 has a strong correlation with slit depth, i.e., determining slit depth based on Peak 2 it is possible.

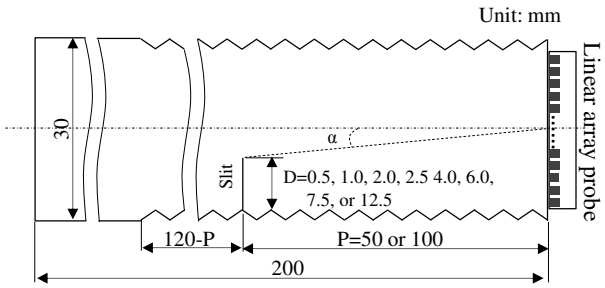

Figure 5 Simulation model for propagation of waves excited by linear array probe

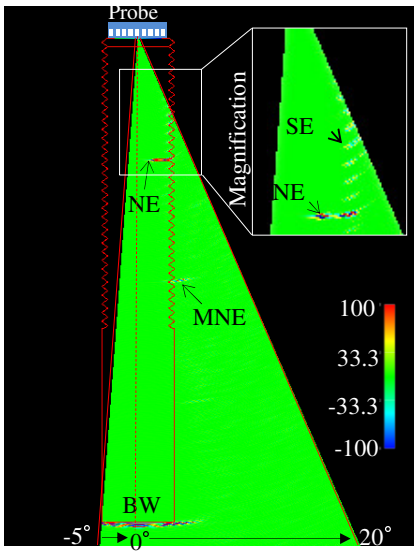

Figure 6 Predicted sectorial view by FEM

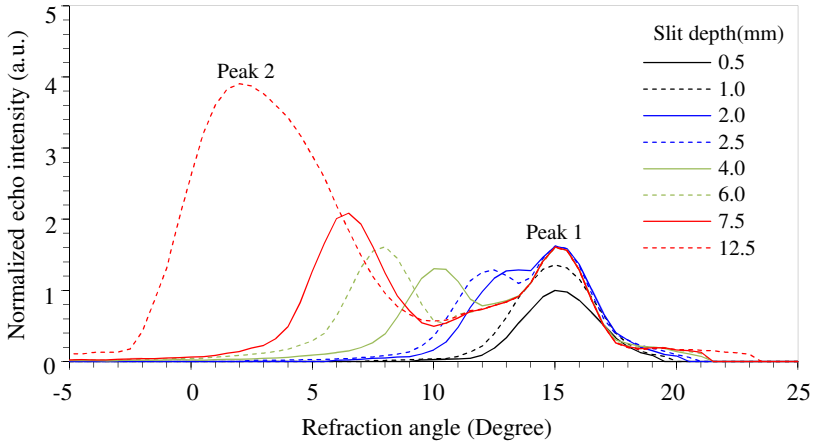

Figure 7 Dependence of echo intensity on refraction angle

3.2 Determination of crack depth

To determine slit depth based on Peak 2 from the previous subsection, making clear how Peak 2 occurs is necessary. Figure 8 illustrates how waves propagate in bolts when the central beam impinges the slit tip. In the figure, L, S, RL, DL, and DS indicate longitudinal, shear,
reflected longitudinal, diffracted longitudinal, and diffracted shear waves, respectively. As shown in the figure, longitudinal waves excited by the linear-array probe propagated toward the slit tip and reached the tip before 9.5 μs. Diffracted longitudinal and shear waves were generated while longitudinal waves impinged the tip. These diffracted waves propagated in all directions with circular wave fronts and were scattered by the thread, which resulted in the intensity of diffracted longitudinal waves becoming weaker with such propagation. In contrast, reflected longitudinal waves propagated toward the probe with a much larger intensity than that of diffracted longitudinal waves, which were received by the probe and therefore showed up as Peak 2.

As described in Section 3.1, determining crack depth using Peak 2 is possible. Figure 8 depicts the study's proposed procedure for determining crack depth from measurement results via ultrasonic phased array technology.

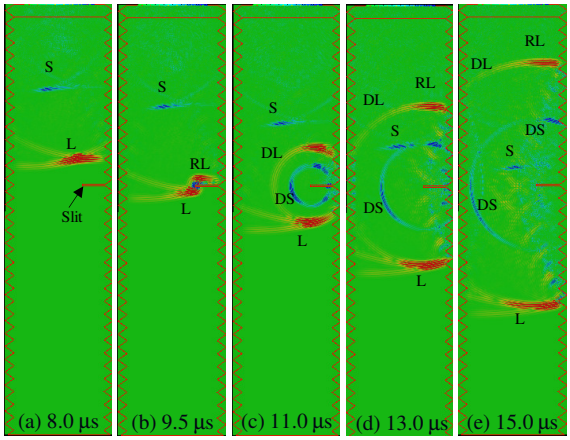

L: Longitudinal wave S: Shear wave
RL: Reflected longitudinal wave
DL: Diffracted longitudinal wave DS: Diffracted shear wave

Figure 8 Wave propagation in bolts

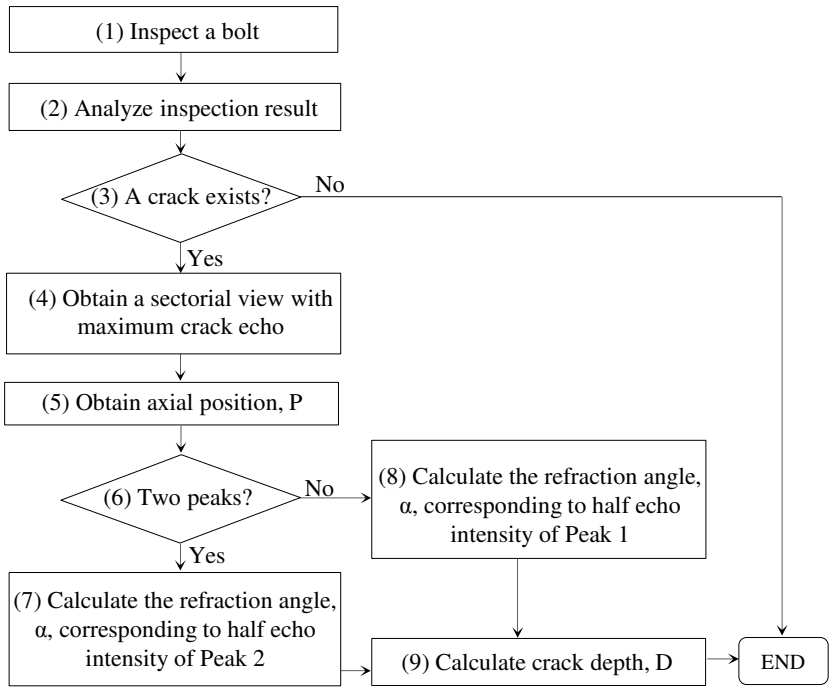

Figure 9 Procedure for determination of crack depth

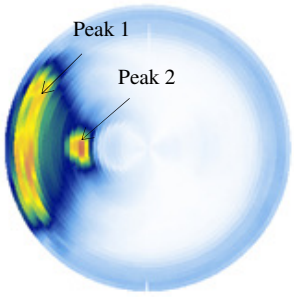

Figure 10 Section view of echo of 6-mm-deep slit at axial position of 50 mm in M30 bolt

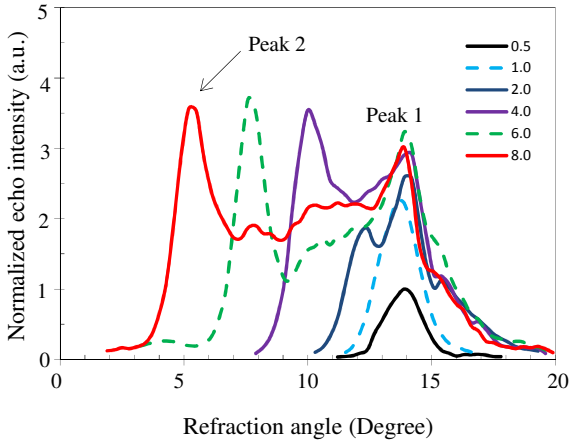

Figure 11 Dependence of echo intensity on refraction angle for slit at axial position of 50 mm.

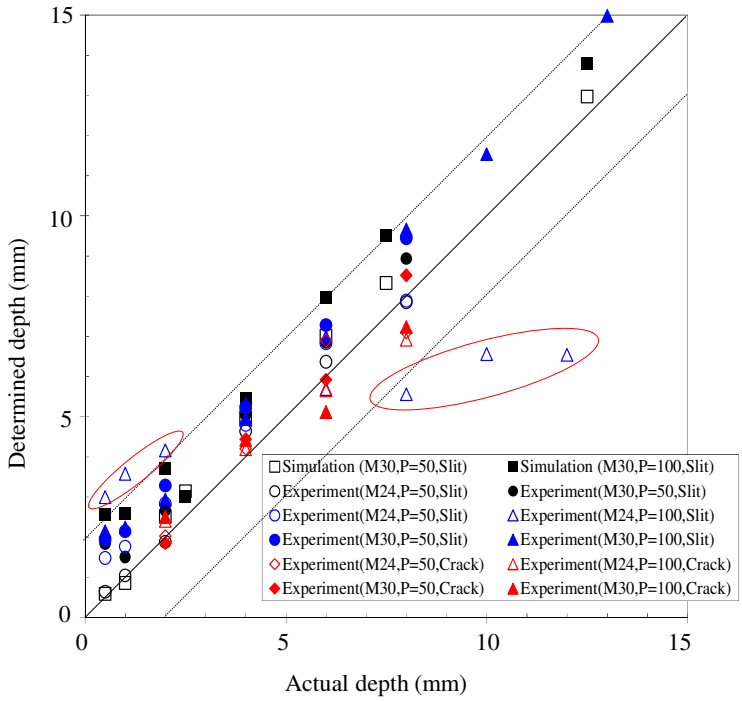

Figure 12 Comparison between actual depths and depths determined by experimental results.

Crack depth, D, can be obtained via $D = d - P * \tan(\alpha)$, where d, P, and α are the minor diameter, axial position, and refraction angle, respectively, obtained from the procedure. If Peak 2 exists, then α is the smaller one of two refraction angles corresponding to the half echo intensity of Peak 2. Otherwise, Peak 1 is used to calculate α instead of Peak 2.

4 Experimental verification

4.1 Experimental results

Figures 10 and 11 show this study's measurement results for the specimens with a slit at an axial position of 50 mm. Figure 10 shows section views, and Figure 11 shows curves of echo intensity versus refraction angle. These curves were normalized by the maximum echo intensity of a 0.5-mm-deep slit. As observed in these simulation results, the slit echo in the section view had two obvious parts with a large intensity, and two separate peaks appear in the curves of echo intensity when slit depth was minimum of 2 mm.

4.2 Crack depth

The procedure proposed in Section 3.1 was applied to the specimens to determine slit and fatigue crack depths. Figure 12 shows a comparison between actual depths and depths determined from measurement results via ultrasonic phased array technology. As shown in the figure, there is no problem in determining crack depth with a maximum error less than 2 mm for M30 bolts when P $\leqq$ 100 mm, and M24 bolts when P $\leqq$ 50 mm.

5. Conclusion

In this study, three linear-array probes with respective frequency of 2, 5 and 10 MHz were used to detect different fatigue cracks in bolt specimens. Measurement results showed that the 10-MHz probe was more appropriate for detecting cracks as compared to the 2-MHz and 5-MHz probes; further, the study showed that detecting 1-mm-deep cracks via this probe was possible.

Numerical computations were performed via FEM to discover a method for determining crack depth. The predicted intensity of crack echo showed that the reflection at the vicinity of the crack tip formed a peak in the curve of echo intensity versus refraction angle, and this phenomenon was verified via an experiment. On the basis of this phenomenon, a procedure to determine crack depths in bolts was proposed. For cracks at axial positions less than 100 mm in M30 bolts, determining crack depths via this procedure within an error of less than 2 mm is possible.

References

[1] Yi-Bin Chen, Shen-Yu Lai, Ta-Kang Hsiung and Ting Chow, "Degradation and Failure of RPV Support Skirt Anchor Bolts at Taipower's Kuosheng Nuclear Power Station," 1st ICMST Conference 2012, 2012, pp.63-64.

[2] Resolution of Generic Safety Issue: Issue 29: Bolting Degradation or Failure in Nuclear Power Plants (Rev.2) (NUREG-0933, Main Report with Supplements 1-34), http://www.nrc.gov/reading-rm/doc-collections/nuregs/staff/sr0933/sec3/029r2.html.

[3] Dong M. Suh and Whan W. Kim, Journal of Nondestructive Evaluation, Vol. 14, No. 4, 1995, pp. 201-206.

[4] Shan Lin and Hiroyuki Fukutomi, "Investigation of detectability of cracks in anchor bolts for application of phased array ultrasonic testing", Proceedings of the 10th International Conference on NDE in Relation to Structural Integrity for Nuclear and Pressurized Components, pp.1001-1007(2013)

[5]Shan Lin, Hiroyuki Fukutomi and Katsumi Shimomura, "Development of Ultrasonic Testing Technique for Anchor Bolt - Part 1: Basic Investigation of Evaluation of Fatigue Cracks by Phased Array Ultrasonics", CRIEPI Report, Q12009 (2013)

Ultrasonic Phased Array Inspection of Small Bore Tubing - a Replacement for Radiography

Toufik Cherraben[1] ; Francis Hancock[1], Jérôme Delemontez[2], Thierry Le Guevel[3], Philippe Cornaton[3]

[1]Doosan Babcock, NDT Department, Porterfield Road, Renfrew, PA4 8DJ, UK
[2]EDF, Division Technique Générale, Service Contrôle Matériaux Mécanisme, 21 Avenue de l'Europe, Grenoble, France
[3]EDF, Centre d'Ingénierie Thermique, 7 allée de l'Arche, Paris La Défense, France

E-mail address(corresponding author) : toufik.cherraben@doosan.com

As part of the follow-up monitoring of welds in heat exchangers, EDF wished to implement an alternative to radiographic examination (to eliminate the use of ionizing radiation). Any replacement system would have to undergo formal qualification.

To meet this requirement, Doosan Babcock has qualified an ultrasonic phased-array system for inspection of butt welds in small diameter (21mm to 80mm), thin-walled (2.8mm to 9mm) tubing.

The inspection system had to meet the requirements defined by the French decree AM1978. A qualification exercise, based on the european standard *FD CEN/TR 14748* methodology, was undertaken to demonstrate that the phased-array equipment and techniques applied meet those requirements (which were conceived for radiographic examination); indeed, regarding planar defects, the requirements are exceeded.

This qualification was based on a combination of open and blind trials on representative tests pieces with artificial and real defects supported by the *FD CEN/TR 14748* based technical justification.

This paper describes the process put in place to achieve this qualification and the results obtained in terms of performance in comparison with radiography.

Keywords: Qualification, Phased array, Small bore

Development of alternatives to radiographic testing at AREVA. Comparison and challenges

Frédéric LASSERRE[1], Sophie HEM[2], Bruno BADER[3] and Jean-Marc CRAULAND[4]
[1, 2]« Engineering & Project » department, AREVA Nuclear Power ; Paris, France
[3]«Reactors & Services» BG, installed base BU, AREVA Nuclear Power, Chalon France
[4]«Reactors & Services» BG, equipment BU, AREVA NP, Chalon / St Marcel France

E-mail address (corresponding author): frederic.lasserre@areva.com

For productivity reason and with a view of optimization of Non Destructive Testing (NDT) at the end of manufacturing or site installation, several departments of AREVA NP came within a common generic process for the development of alternatives to Radiography Testing (RT).

Some developments have thus been launched, for the examination of thick ferritic welds in heavy components (steam generator "SG", pressurizer "PZR" and reactor pressure vessel "RPV"), ferritic welds in piping (e. g. steam line) and thin ferritic welds in containment liner.

The implementation of alternatives to RT will at the end be acceptable provided that the quality guaranteed by the new techniques is demonstrated as at least as stringent as the quality insured (according to RCC-M) by the former NDT.

The NDT involved is RT, plus eventually Ultrasonic Testing (UT) as a complement (1 or 2 methods to replace). The replacing method is UT using different advanced techniques, mainly Pulse-Echo (PE) technique with Phased Array (PA) equipment and Time of Flight Diffraction (ToFD) technique with or without PA equipment. Alternatives are systematically proposed through automation of the NDT.

For replacement of conventional RT plus conventional manual UT required by RCC-M code for the examination at the end of manufacturing of the SG and PZR circumferential ferritic welds with large thickness, the foreseen techniques are automated UT/PE with PA and ToFD.

For replacement of RT in the examination of steam line ferritic piping welds (approximately 40 mm thick) as required by RCC-M code for level 2 welds, the foreseen technique is automated UT pulse-echo technique only, using phased array.

For replacement of RT in the examination of the containment liner welds (6 mm thick) as required by ETC-C (EPR™ Technical Code for Civil works) code, automated UT/PE with PA is foreseen.

For all these projects, the main issues are the shift between two methods (RT and UT) which deal with different physical principles and defect representations, and the necessary set up of new acceptance criteria (PA and ToFD not permitted so far in the applicable codes).

The present paper aims at presenting a step by step comparison of the replaced and replacing methods and techniques for each project of interest, also highlights how the emerging challenges are solved or overcame and shows how the improvements could finally be accepted through the same generic principles and process.

Keywords: ultrasonic testing, radiographic testing, alternatives, weld inspection.

6. List of participants and exhibitors

No.	Country	Participants & Exhibitors	E-mail	Affiliation
1	Austria	**Harri Varjonen**	h.varjonen@iaea.org	IAEA
2	Canada	**Evan Choi**	evan.choi@candu.org	CANDU Owners Group
3	Canada	**Guy Maes**	gmaes@zetec.com	Zetec, Inc.
4	Canada	**Ray ten Grotenhuis**	ray.tengrotenhuis@opg.com	Ontario Power Generation Inc.
5	Canada	**Colombe Dalpe**	sfranchi@eddyfi.com	EDDYFI
6	Canada	**Michael Sirois**	sfranchi@eddyfi.com	EDDYFI
7	China	**Jianhai Zhang**	jhzh1986@skku.edu	Sungkyunkwan Univ.
8	China	**Maodan Yuan**	yuanmaodan@skku.edu	Sungkyunkwan Univ.
9	China	**Ziqiao Tang**	tangziqiao@skku.edu	Sungkyunkwan Univ.
10	China	**Li Ying**	liying@granpect.com	Granpect Company Limited
11	China	**Tang Liang**	liying@granpect.com	Granpect Company Limited
12	China	**Bai Xiaobao**	baixiaobao@matrixndt.com	MATRIX U/E TECHNOLOGIES LIMITED
13	China	**Zhou Ping**	baixiaobao@matrixndt.com	MATRIX U/E TECHNOLOGIES LIMITED
14	Croatia	**Sergio Galosic**	zrinka.corak@inetec.hr	INETEC-INSTITUTE For Nuclear Technology
15	Croatia	**Zrinka Corak**	zrinka.corak@inetec.hr	INETEC-INSTITUTE For Nuclear Technology
16	Czech	**Pavel Kopcil**	miroslava.pribylova@cedok.cz	CEZ, a.s.

17	Denmark	**Anne Marie Thommesen**	amt@force.dk	NDT engineer
18	Finland	**Ari Koskinen**	ari.koskinen@vtt.fi	VTT Technical Research Centre of Finland Ltd
19	Finland	**Jorma Ahonen**	jorma.ahonen@fortum.com	Fortum
20	Finland	**Jukka Härkola**	jukka.harkola@stuk.fi	STUK
21	Finland	**Petri Luostarinen**	petri.luostarinen@fortum.com	Fortum
22	Finland	**Tapani Packalén**	tapani.packalen@inspecta.com	Inspecta Sertifiointi Oy
23	France	**Arnaud Vanhoye**	arnaud.vanhoye@cea.fr	CEA Saclay
24	France	**David Tisseur**	david.tisseur@cea.fr	CEA
25	France	**Duprat Joel**	joel.duprat@vallourec.com	Vallourec Heat Exchanger Tubes
26	France	**Frederic Jenson**	frederic.jenson@cea.fr	CEA LIST
27	France	**Frederic Taillade**	frederic.taillade@edf.fr	EDF R&D
28	France	**Hervé Gac**	hgac@sgndt.com	SGNDT
29	France	**Laura Taupin**	laura.taupin@cea.fr	CEA
30	France	**Patrice Jardet**	patrice.jardet@edf.fr	EDF
31	France	**Philippe Benoist**	p.benoist@m2m-ndt.com	M2M
32	France	**Pierre Thomas**	pierre.thomas@edf.fr	EDF
33	France	**Pierre-Emile Lhuillier**	pierre-emile.lhuillier@edf.fr	EDF
34	France	**Steve Mahaut**	steve.mahaut@cea.fr	CEA-LIST
35	France	**Sylvain Murgier**	smurgier@gmail.com	EDF
36	France	**Vincent Massol**	vincent.massol@snecma.fr	Safran - Snecma
37	France	**Yann Gelebart**	yann.gelebart@free.fr	EDF
38	France	**Audrey Gardahaut**	audrey.gardahaut@cea.fr	CEA

39	France	**Roman Fernandez**	caroline.quintanilha@extende.com	EXTENDE
40	France	**Sébastien Lonné**	caroline.quintanilha@extende.com	EXTENDE
41	France	**Jérôme Poguet**	no@imasonic.com	IMASONIC
42	France	**Stéphane Oster**	no@imasonic.com	IMASONIC
43	France	**Laurent Le Ber**	o.pichard@m2m-ndt.com	M2M
44	France	**Olivier Roy**	o.pichard@m2m-ndt.com	M2M
45	Germany	**Martin Bolander**	bolandms@westinghouse.com	Westinghouse
46	Germany	**Erhard Anton**	Anton.Erhard@bam.de	19th WCNDT 2016/German Society for NDT
47	Germany	**Purschke Matthias**	mz@dgzfp.de	19th WCNDT 2016/German Society for NDT
48	Hungary	**Peter Trampus**	trampusp@trampus.axelero.net	Trampus Consulting & Engineering
49	Japan	**Toshiyuki Takagi**	takagi@ifs.tohoku.ac.jp	Tohoku University
50	Japan	**Hajime Shohji**	shohji@criepi.denken.or.jp	Central Research Institute of Electric Power Industry(CRIEPI)
51	Japan	**Haruo Miyadera**	haruo.miyadera@toshiba.co.jp	Toshiba Corporation
52	Japan	**Hitoshi Ishida**	ishida@inss.co.jp	Institute of Nuclear Safety System, Incorporated
53	Japan	**Keiji Watanabe**	wkeiji@criepi.denken.or.jp	Central Research Institute of Electric Power Industry
54	Japan	**Ken Endoh**	endo@hihakaikensa.co.jp	Non-Destructive Inspection Co., Ltd
55	Japan	**Koichi Saruta**	saruta.koichi@jaea.go.jp	Japan Atomic Energy Agency

56	Japan	**Masaki Nagai**	nagai@criepi.denken.or.jp	Central Research Institute of Electric Power Industry
57	Japan	**Miho Morikawa**	miho_morikawa@mhi.co.jp	MITSUBISHI HEAVY INDUSTRIES, LTD.
58	Japan	**Naoyuki Kono**	naoyuki.kono.jm@hitachi.com	Hitachi, Ltd.
59	Japan	**Ovidiu Mihalache**	mihalache.ovidiu@jaea.go.jp	Japan Atomic Energy Agency
60	Japan	**Ryosuke Kobayashi**	ryosuke.kobayashi.xc@hitachi.com	Hitachi, Ltd.
61	Japan	**Shan Lin**	shanlin@criepi.denken.or.jp	Central Research Institute of Electric Power Industry
62	Japan	**Shuji Tanioka**	shuji_tanioka@mhi.co.jp	E-Techno Ltd.
63	Japan	**Takashi Yatoh**	tyatoh@neltd.co.jp	NUCLEAR ENGINEERING, Ltd.
64	Japan	**Takeshi Kodaira**	takeshi_kodaira@mhi.co.jp	Mitsubishi Heavy Industries, LTD.
65	Japan	**Tetsuya Uchimoto**	uchimoto@ifs.tohoku.ac.jp	Tohoku University
66	Japan	**Toshihiro Yamamoto**	yamamoto-toshihiro@japeic.or.jp	Japan Power Engineering and Inspection Corporation
67	Japan	**Yasushi Ikegami**	yasushi.ikegami@ctc-g.co.jp	ITOCHU Techno-Solutions Corporation
68	Japan	**Yoshinori Kamiyama**	kamiyama-yoshinori@japeic.or.jp	Japan Power Engineering and Inspection Corporation
69	Korea	**Byungsik Yoon**	bsyoon88@khnp.co.kr	KHNP-CRI
70	Korea	**Hakjoon Kim**	hjkim21c@skku.edu	Sungkynkwan University

71	Korea	**Hogirl Lee**	mckuza@skku.edu	Sungkyunkwan Univ.
72	Korea	**Jaeha Park**	jaehapark@skku.edu	Sungkyunkwan Univ.
73	Korea	**Jungwon Park**	park9037@skku.edu	Sungkyunkwan Univ.
74	Korea	**Seulgi Lee**	sglee1026@skku.edu	Sungkyunkwan Univ.
75	Korea	**Sungjin Song**	sjsong@skku.edu	Sungkynkwan University
76	Korea	**To Kang**	tkang@kaeri.re.kr	Korea Atomic Energy Research Institute
77	Korea	**Yong Seok Kang**	yskang94@khnp.co.kr	KHNP CRI
78	Korea	**Yongsik Kim**	yongskim21@gmail.com	Central Research Institute, KHNP
79	Korea	**Koo Kab Chung**	k211ckk@kins.re.kr	KINS
80	Korea	**Seung Seok Lee**	sslee@kriss.re.kr	KRISS
81	Korea	**Inchul Kim**	inchulkim@khnp.co.kr	KHNP(Korea Hydro & Nuclear Power Co. LTD)
82	Korea	**Bongjae Sheen**	bjsheen23@khnp.co.kr	KHNP(KOREA HYDRO $ NUCLEAR POWER CO.,LTD)
83	Korea	**Byeong-Hee Han**	bhhan@kriss.re.kr	Korea Research Institute of Standards and Science
84	Korea	**Byeongkwan Lee**	bklee0300448@khnp.co.kr	KHNP(Korea Hydro & Nuclear Power Co. LTD)
85	Korea	**Byung-Seok Jo**	jbee22e@gmail.com	Seoul National University of Science and Technology
86	Korea	**Changkuen Kim**	changkuen.kim@doosan.com	Doosan Heavy Industries & Construction
87	Korea	**Donghoon Kang**	dhkang@krri.re.kr	Korea Railroad Research Institute

88	Korea	**Dong-Jin Yoon**	djyoon@kriss.re.kr	Korea Research Institute of Standards and Science (KRISS)
89	Korea	**Dong-Yeol Kim**	east10kim@dsme.co.kr	DSME(Daewoo Shipbuilding&Marine Engineering)
90	Korea	**Duck-Gun Park**	dgpark@kaeri.re.kr	KAERI
91	Korea	**Euisoon Doh**	dohes@kps.co.kr	KEPCO KPS
92	Korea	**Geonwoo Kim**	gumppang01@kriss.re.kr	Korea Research Institute of Science and Standards
93	Korea	**Hae Sung Park**	acas_hs@naver.com	Seoultech
94	Korea	**Hunhee Kim**	hunhee1.kim@doosan.com	Doosan Heavy Industries
95	Korea	**Hwan-Sik Yoon**	aprobe50@khnp.co.kr	KHNP(KOREA HYDRO & NUCLEAR POWER CO.,LTD)
96	Korea	**Hyucksik Jang**	janghyucksik@khnp.co.kr	KHNP(Korea Hydro & Nuclear Power Co. LTD)
97	Korea	**Hyunjoon Cho**	impegasus@nate.com; impegasus@icloud.com	ISAQ
98	Korea	**Ik-Keun Park**	ikpark@seoultech.ac.kr	Seoul National University of Science and Technology
99	Korea	**Il-Sik Kim**	ilsik@kriss.re.kr	Korea Research Institute of Standards and Science (KRISS)
100	Korea	**Jaehyun Bae**	tmac1@skku.edu	Sungkyunkwan Univ.
101	Korea	**Jaeseok Park**	hunhee1.kim@doosan.com	Doosan Heavy Industries
102	Korea	**Jaesun Lee**	jaesun@pusan.ac.kr	Pusan National University

103	Korea	**Jin Ki Hong**	hongjk@kins.re.kr	Korea Institute of Nuclear Safety
104	Korea	**Jinyi Lee**	jinyilee@chosun.ac.kr	Chosun University
105	Korea	**Jonmin Park**	jmpark09@khnp.co.kr	KHNP(Korea Hydro & Nuclear Power Co. LTD)
106	Korea	**Jungil Song**	lovesong@khnp.co.kr	KHNP(Korea Hydro & Nuclear Power Co. LTD)
107	Korea	**Junsoo Park**	hunhee1.kim@doosan.com	Doosan Heavy Industries
108	Korea	**Junyoung Park**	890311pjy@khnp.co.kr	KHNP(KOREA HYDRO $ NUCLEAR POWER CO.,LTD)
109	Korea	**Kaige Wu**	kaigewu@kaeri.re.kr	Korea Atomic Energy Research Institute
110	Korea	**Ki Bok Kim**	kimkibok@kriss.re.kr	Korea Research Institute of Stndards and Science
111	Korea	**Ki-Hyoung Lee**	shirimp@kins.re.kr	KINS
112	Korea	**Kim Chi Yup**	kcy@kriss.re.kr	KRISS
113	Korea	**Koo Ahn Kwon**	912oppa@naver.com	KRISS
114	Korea	**Kyeongmin Lee**	ableman1@khnp.co.kr	KHNP(Korea Hydro & Nuclear Power Co. LTD)
115	Korea	**Kyungcho Kim**	kck@kins.re.kr	KINS
116	Korea	**Kyung-Young Jhang**	kyjhang@hanyang.ac.kr	Hanyang University
117	Korea	**Man Yong Choi**	mychoi@kriss.re.kr	KRISS
118	Korea	**Mingeun Song**	msong@epri.com	EPRI(Electric Power Research Institute)

119	Korea	**Moo-Song Shin**	moosong.shin@khnp.co.kr	KHNP(KOREA HYDRO $ NUCLEAR POWER CO.,LTD)
120	Korea	**Seungwan Cho**	csw790320@naver.com	Korea Research Institute of Standards and Science
121	Korea	**Sung-Sik Kang**	sskang@kins.re.kr	Korea Institute of Nuclear Safety
122	Korea	**Taehoon Heo**	heotaehoon@kriss.re.kr	Korea Research Institute of Standards and Science
123	Korea	**Taek-Gyu Lee**	ltk1214@skku.edu	Sungkynkwan University
124	Korea	**Wonjae Choi**	w.choi@kriss.re.kr	KRISS
125	Korea	**Yong Sang Cho**	yscho@kepco.co.kr	KEPCO KPS
126	Korea	**Yong-Moo Cheong**	ymcheong@kaeri.re.kr	Korea Atomic Energy Research Institute
127	Korea	**Yongtae Lee**	kidary97@nate.com	ISAQ
128	Korea	**Yoonsang Lee**	yslee@kps.co.kr	KEPCO KPS
129	Korea	**Young-Gil Kim**	kimyg@kriss.re.kr	Korea Research Institute of Standards and Science
130	Korea	**Youngin Hwang**	justgrace@skku.edu	Sungkyunkwan Univ.
131	Korea	**Young-Joo Kim**	yjkim@kriss.re.kr	Korea Research Institute of Standards and Science (KRISS)
132	Korea	**Youngwon Kim**	young9898@khnp.co.kr	KHNP
133	Korea	**Yuntaek Yeom**	yeomtaek7@skku.edu	Sungkyunkwan Univ.
134	Korea	**Young-Ho Son**	yhson@kims.re.kr	KIMS
135	Korea	**Sang-Hoon Lee**	sunghlee@kims.re.kr	KIMS
136	Korea	**Keun-Bong Yoo**	yookb@kepco.co.kr	KEPCO KPS

137	Korea	**Kwang-Hee Im**	khim@woosuk.ac.kr	Woosuk Univ.
138	Korea	**Byung Kook Lee**	ri0604@hanbiteds.co.kr	Hanbit EDS.CO.,Ltd
139	Korea	**Cha Sanggyeong**	chassgg1@naver.com	OMP CO., LTD
140	Korea	**Sung-Sik Lee**	chassgg1@naver.com	OMP CO., LTD
141	Korea	**Hong Joo Chung**	ksnt@ksnt.or.kr	The Korea Society for NDT
142	Korea	**Hyunmin Cho**	ksnt@ksnt.or.kr	The Korea Society for NDT
143	Korea	**Hyun Sun Jung**	sshin@zetec.com	Zetec, Inc
144	Korea	**Ki Hang Choi**	sshin@zetec.com	Zetec, Inc
145	Singapore	**Dennis Chai**	dennis.chai@olympus-ap.com	Olympus Singapore
146	Spain	**Rafael Martínez-Oña**	rmo@tecnatom.es	Tecnatom, S.A.
147	Sweden	**Erik Strindö**	erik.strindo@ssm.se	Swedish Radiation Safety Authority
148	Sweden	**Giselle García Roldán**	giselle.garciaroldan@ssm.se	Swedish Radiation Safety Authority
149	Sweden	**Jonas Jinnestrand**	jjinnestrand@tuv-nord.com	TÜV NORD
150	Sweden	**Lars Skoglund**	skoglule@westinghouse.com	Wesdyne Sweden
151	Sweden	**Peter Alzén**	peter.alzen@sqc.se	Swedish Qualification Centre
152	Sweden	**Tommy Zettervall**	tommy.zettervall@gmail.com; tommy.zetterwall@sqc.se	SQC Swedish Qualification Centre
153	Sweden	**Peter Merck**	torbjorn.sjo@dekra.com	DEKRA Industrial AB
154	Sweden	**Torbjorn Sjo**	torbjorn.sjo@dekra.com	DEKRA Industrial AB
155	Switzerland	**Patrick Graedel**	patrick.graedel@bkw.ch	BKW Energie AG
156	Switzerland	**Jens Beyer**	jens.beyer@ensi.ch	Switzerland Federal Nuclear Safety Inspectorate ENSI

157	Switzerland	**Klaus Germerdonk**	klaus.germerdonk@ensi.ch	ENSI
158	UK	**Andrew Brockett**	andrew.brockett@doosan.com	Doosan Babcock Ltd
159	UK	**Christopher Greener**	chris.greener@rolls-royce.com	Rolls-Royce
160	UK	**David Duxbury**	david.duxbury@rolls-royce.com	Rolls-Royce
161	UK	**Fraser Hardie**	fraser.hardie@doosan.com	Doosan Babcock
162	UK	**Oliver Nowers**	oliver.nowers@rolls-royce.com	Rolls-Royce plc / University of Bristol
163	UK	**Neil Hankinson**	nhankinson@phoenixisl.com	PHOENIX INSPECTION SYSTEMS LTD
164	USA	**Erica Schumacher**	erica.schumacher@extende.com	EXTENDE INC.
165	USA	**Benjamin Jackson**	ben.jackson@intertek.com	Intertek AIM
166	USA	**Greg Selby**	gselby@epri.com	EPRI
167	USA	**Myles Dunlap**	mdunlap@epri.com	EPRI
168	USA	**Nicholas Cardillo**	ncardillo@zetec.com	Zetec, Inc
169	USA	**Philip Ashwin**	pashwin@epri.com	EPRI
170	USA	**Ryan Meyer**	Ryan.Meyer@pnnl.gov	Pacific Northwest National Laboratory
171	USA	**Jason Van Velsor**	asnodgrass@Structint.com	Structural Integrity Associates
172	USA	**Joe Agnew**	asnodgrass@Structint.com	Structural Integrity Associates
173	USA	**Dominique Braconnier**	dominic@braconnier.com	The Phased Array Company
174	USA	**Gavin Dao**	contact@thephasedarraycompany.com	The Phased Array Company
175	Vietnam	**Anh Hoang Vu**	vuanhhoang89@gmail.com	Sungkyunkwan Univ.

Europe Direct is a service to help you find answers to your questions about the European Union
Free phone number (*): 00 800 6 7 8 9 10 11
(*) Certain mobile telephone operators do not allow access to 00 800 numbers or these calls may be billed.

A great deal of additional information on the European Union is available on the Internet.
It can be accessed through the Europa server http://europa.eu

How to obtain EU publications

Our publications are available from EU Bookshop (http://bookshop.europa.eu),
where you can place an order with the sales agent of your choice.

The Publications Office has a worldwide network of sales agents.
You can obtain their contact details by sending a fax to (352) 29 29-42758.

LD-NA-27790-EN-N

JRC Mission

As the Commission's in-house science service, the Joint Research Centre's mission is to provide EU policies with independent, evidence-based scientific and technical support throughout the whole policy cycle.

Working in close cooperation with policy Directorates-General, the JRC addresses key societal challenges while stimulating innovation through developing new methods, tools and standards, and sharing its know-how with the Member States, the scientific community and international partners.

Serving society
Stimulating innovation
Supporting legislation

doi:10.2790/13215

ISBN 978-92-79-57266-1